UNIVERSITY OF LILLE (FRANCE)

Doctoral School Material Science, Radiation and Environment (ED SMRE 104)

DOCTORAL THESIS

Presented by

Gaia Travan

Entitled

INTERACTIONS BETWEEN SALT TECTONICS AND CRUSTAL TECTONICS IN THE MEDITERRANEAN AND IN THE BARENTS SEA

To obtain a doctorate from the University of Lille

Speciality: Geosciences, Ecology, Paleontology, Oceanography

Earth and Universe Sciences

Defense date: 25 November 2022

In front of a jury consisting of:

Juan SOTO	Professor– Bureau of Economic Geology, The University of Texas, Austin (USA)	Rapporteur
Thierry NALPAS	Lecturer HDR - Univ. Rennes 1, CNRS, Géosciences Rennes, UMR 6118 (FR)	Rapporteur
Agnès MAILLARD	Lecturer HDR - GET, Observatoire Midi-Pyrénées, Univ. Toulouse, CNRS, IRD, UMR 5563 (FR)	Examinator
Jacques DÉVERCHÈRE	Professor – Univ. Brest, CNRS, Ifremer, GEO-OCEAN (FR)	Examinator, President of the Jury
Virginie GAULLIER	Professor – Univ. Lille, CNRS, Univ. Littoral Côte d'Opale, UMR 8187, LOG, Laboratoire d'Océanologie et de Géosciences (FR)	Thesis supervisor
Sverre PLANKE	Professor - Universitetet i Oslo (NO), Volcanic Basin Petroleum Research (VBPR)	Invited member

Funded by the European Union's Horizon 2020 research and innovation programme under the Marie Skłodowska-Curie grant agreement n° 765256.

Institute: Univ. Lille, CNRS, Univ. Littoral Côte d'Opale, UMR 8187, LOG, Laboratoire d'Océanologie et de Géosciences, F59000 Lille, France

Secondments: VBPR (Volcanic Basin Petroleum Research) (Oslo, Norway), University of Trieste - OGS (Oceanography and applied Geophysics) (Trieste, Italy)

UNIVERSITÉ DE LILLE (FRANCE)

Ecole Doctorale Sciences de la Matière, du Rayonnement et de l'Environnement (ED SMRE 104)

THÈSE DE DOCTORAT

Présentée par

Gaia Travan

Intitulée

INTERACTIONS ENTRE LA TECTONIQUE SALIFERE ET LA TECTONIQUE CRUSTALE EN MEDITERRANEE ET DANS LA MER DE BARENTS

En vue de l'obtention du grade de docteur de l'Université de Lille

Spécialité : Géosciences, Écologie, Paléontologie, Océanographie

Sciences de la Terre et de l'Univers

Date de soutenance : 25 Novembre 2022

Devant un jury composé de :

Juan SOTO	PR - Bureau of Economic Geology, The University of Texas, Austin (USA)	Rapporteur
Thierry NALPAS	MCF HDR - Univ. Rennes 1, CNRS, Géosciences Rennes, UMR 6118 (FR)	Rapporteur
Agnès MAILLARD	MCF HDR - GET, Observatoire Midi-Pyrénées, Univ. Toulouse, CNRS, IRD, UMR 5563 (FR)	Examinateur
Jacques DÉVERCHÈRE	PR - Univ. Brest, CNRS, Ifremer, GEO-OCEAN (FR)	Examinateur, Président du Jury
Virginie GAULLIER	PR - Univ. Lille, CNRS, Univ. Littoral Côte d'Opale, UMR 8187, LOG, Laboratoire d'Océanologie et de Géosciences (FR)	Directrice de thèse
Sverre PLANKE	PR - Universitetet i Oslo (NO), Volcanic Basin Petroleum Research (VBPR)	Invité

ACKNOWLEDGMENTS

First of all, thanks to the members of my thesis commission, Juan Soto, Thierry Nalpas, Agnès Maillard, Jacques Déverchère and the invited member Sverre Planke. I'm really grateful for the time you spent in the revision and evaluation of my work.

I want to thank my supervisor Virginie Gaullier, who decided to be part of the European project SaltGiant and chose me as her PhD student. Thanks for the knowledge you transmitted me during the scientific discussions, both in terms of seismic data interpretation, salt tectonics mechanisms and analogue modelling, and for having pushed me to do my best, not only in the 'purely scientific' work of my thesis and scientific dissemination but also involving me in the coordination of conferences sessions and proposal writing, and making me participate to the surveys GEOBAS 2018 and METYSS IV, therefore transforming these years of thesis in a moment of professional and personal growth. We shared quite a number of travels, and a beer in at least 6 different countries. Cheers to the next one!

I want to thank all the VBPR team for the secondment in Oslo (Norway). First of all, thanks to Sverre Planke and Ellen Eckhoff Planke for opening their door and allow me to collaborate with their team in the interpretation of the stunning TGS seismic data. Thanks to all of them for the shared moments and discussions. A particular thanks to Benjamin Bellwald, that daily supported me and answered to one thousand questions. Thanks to TGS ASA for the possibility to interpret the data and show them in this work, with a special mention to Reidun Myklebust for the useful comments on the figures and for approving all the last minute permission I asked.

Talking about secondments, thanks to OGS and the Department of Mathematics and Geoscience of the University of Trieste (Italy) for having welcomed me even during COVID times, when the bureaucracy made it almost impossible. In particular, I want to thank Anna Del Ben, that introduced me to salt interpretation during my master studies and supervised me during my master thesis and during the PhD secondment, marking the beginning of my love for seismic data interpretation and salt tectonics. After 7 years, is still huge the amount of knowledge you can transmit me during our scientific discussions, and the pleasure to share a coffee during the break. And thanks to Edy Forlin, that patiently introduced me to the magic world of seismic data processing. I'm sure one day we'll depth migrate a stunning diapir. Meanwhile, we can go on complaining about how much these salt structures messed up everything. Thanks to Angelo Camerlenghi, part of my master thesis jury in 2017, and key component of the SaltGiant PIs during my thesis. I'm grateful to OGS for sharing the data I worked on, well accessible in the Seismic data Network Access Point (SNAP), and a special thanks to Paolo Diviacco for his helpfulness. Talking about Trieste, thanks to Lorenzo Bonini that first introduced me to analogue modelling, I hope we'll be able to play with the silicone in your lab one day.

Thanks to Jacques Déverchère, that accepted to share with us the seismic reflection data on the Algerian margin, and thanks to Johanna Lofi and Jacques Déverchère (yes, again!) for the constructive inputs during my thesis monitoring committees (CST).

Thanks to the European Union that fully financed this project. This thesis is part of the European project SaltGiant, funded by the European Union's Horizon 2020 research and innovation program under the Marie Skłodowska-Curie grant agreement n° 765256. The SaltGiant project has been precious for the continuous interdisciplinary training and for the fundamental opportunity to exchange knowledge and experiences with other researchers from many European Universities but also from research centres and private companies. I want to thank the scientific coordinator Vanni Aloisi for having created the project, together with all the PIs, and to have kept his kindness and good mood even in the face of unforeseen events, it was a real pleasure to have you as the supreme SaltGiant boss. Thanks to the project manager Julia Champagnac and her efficiency, and thanks to all the ESRs, PI, PO and everybody that shared part of the SaltGiant journey, for the scientific discussions and for the late night deep conversations. Sharing joys and struggles with such a mixed group of people added so much to the thesis experience (company in distress makes trouble less!). You have been amazing, deep and lighthearted, reflective and ready to party, quiet and talkative, but always interesting, and I wish to all of the ESRs the best for their careers.

Thanks to the people that shared with me the time on the boat, the working part and the apéro one: researchers, technicians and the shipboard personnel, these last one communicating with me with an improvised sign language.

Thanks to Monique Gentric, who never stopped smiling even when I was bothering her with the mission orders, reimbursement requests and way more, in a French that was far from being understandable. Your efficiency is astonishing.
Thanks to the SMRE doctoral school, and to Nicolas Tribovillard for his helpfulness and kindness.
To all the team 6 of LOG, and to all the members of the lab, thanks for the daily support. And to all the colleagues, MCF, Professors, technicians of SN5, that made the lunch break a moment of interesting discussion about politics, science, food, cultures and languages, and enriched my diet with delicious buttery cakes!
A warm hug to the 'SN5 addicts' that entered in my life as colleagues and fastly became the best buddies for the Lillois days (and nights!). You have been invaluable, especially when COVID-19 froze our lives and the funny Lille became way less funny. I'll thank you in person, so don't look here for a proper acknowledgments of the time spent together. Thanks to my office mate Fabien, that shared with me the good and the bad days, and the good and bad dosettes. Thanks to Aurore, that is waiting for the end of my thesis to leave for Canada, that's very touching. Thanks to Maïwenn and Muriel for the best cakes in town and Little Leonie for all the smiles and all the ricotta (still convinced it will be your first word!), and to Marie for the best jokes. Thanks to Cesar, for having shown me the best of Wazemmes's nightlife, and to German and Brenda that always have the best music addresses, and the three of you for having helped my poor Spanish to improve. Louise and Matthias for the boardgame and beer afternoons, Romain for having done a huge effort to learn my language and eat my seeds. To Mathilde for having cut all our fruits, to Rachid for being the smiling glue of our group, to Roy –our dear Professor- for the best baklava I ever had, to Imene, Marina, Aboubacar, Zhenyu, Yi, I'm sad to leave before having had the time to know you better, but I'm happy for the moments we spent together.
A special mention to all the expats I met in Lille, that shared with me some of the feelings of being a foreign, both the good and the bad ones. You taught me that being lost is not a big deal.
And the warmest thank to my Italian support network. Grazie Giulia, per le note vocali infinite, il supporto e gli aneddoti sempre freschi. Sappi che sei la prima persona a cui penso quando mi macchio. Grazie a Ilaria e Gian, e a tutta la compagnia, per avermi chiesto una volta a settimana quando penso di ritornare, e per esserci stati tutte le volte che effettivamente riuscivo a farlo. A tutti gli ex compagni di geologia e agli ex colleghi, un po' sparsi per il mondo ma con i quali si tenta sempre di condividere una serata. A Veronica, che mi ha motivata quando non avevo voglia di partire. E a tutti gli amici che non nomino per paura di dimenticarne qualcuno.
Grazie alla mia famiglia, ai miei genitori per avermi sempre sostenuta, a Cate per le lunghe telefonate e a Massimo per aver camminato da solo durante le lunghe telefonate, e grazie ad Agnese per tutti i vestiti che mi cucirà nei prossimi 3 anni. Grazie per avermi riempito la valigia di cibo ad ogni partenza, è stato un miracolo riuscire a passare i controlli di sicurezza. E grazie a Coccadezia, che mi ha motivata negli step finali della stesura.

And thanks to who I forgot to thank, there's always someone. I'm sure I thought about you as soon as I printed this thesis.

To salt, the only tasty rock.

ABSTRACT

Salt tectonics is defined as a tectonic deformation that involves evaporites, as a substratum or as a source layer. Considering geological times, the behaviour of the salt can be approximated to a Newtonian fluid (i.e. viscous behaviour) compared to the brittle behaviour of the surrounding rocks, and their interaction can be modelled through scaled analogue models of a viscous material and a brittle one, e.g. silicone and sand. Crustal tectonics, both extensional and contractional, have often a fundamental role in the evolution of the salt structures, and becomes the main cause of salt deformation in many study areas.

The aim of this thesis is to analyze the timing and mechanisms of salt tectonics in three study areas characterized by different salt ages and increasing influence of crustal tectonics on the salt tectonics processes: the Western Sardinian margin and Northern Algerian margin in the Western Mediterranean, and the Sørvestsnaget Basin in the Southwestern Barents Sea. This has been done through the interpretation of 2D and 3D seismic reflection data from TGS (Norway), OGS (Italy) and UMR GEO-OCEAN (France), as well as through the integration with other geophysical data, wells data and the comparison with scaled analogue models we produced.

In the Western Mediterranean the salt layer deposited during the Messinian Salinity Crisis (5.6 Ma) so salt tectonics is relatively young, the overburden is limited to the Late Messinian and Plio-Quaternary sedimentation and the marks of the first stages of salt deformation are usually imaged. On the Western Sardinian margin, where the sedimentary load is limited, the salt structures are mainly the consequence of the basinward slope of the base of the salt, resulting from the differential subsidence particularly strong after the refilling of the Mediterranean at the end of the MSC. Moving towards the center of the Sardo-Provencal basin, where the sedimentary load of the Rhone Deep Sea Fan forms a thick salt overburden, gravity spreading dominates. While in this area there is no influence of crustal tectonics on salt deformation at a regional scale, we recognized on the Southwestern Sardinian margin the presence of a flower structure active during Pliocene, offsetting the Messinian sequence more than 0.5 s TWT. Considering the position of this crustal structure, we propose it to be part of the North Balearic Fracture Zone, i.e. the dextral strike-slip fault of the Sardo-Provencal basin opening. This structure has been interpreted in literature in the eastern Valencia Basin, but this would be the first time that the NBFZ is recognized in this area and with such a recent activity, opening a new chapter of discussion on the topic.

As recognized in literature, the southern sector of the Western Mediterranean is reactivated in compression since 8 Ma thanks to the Africa-Europe convergence, and this compression is expressed through thrusts on the Algerian margin. Here salt tectonics is mainly the consequence of crustal tectonics, and in particular of the increased potential energy consequence of the localized uplift (e.g. the uplifted plateau offshore Dellys, the Hannibal High uplift). The analogue models produced show that the uplift of the plateau is at the origin of the lateral thickness variations in the salt layer and of the polygonal minibasins formation in the area offshore Algiers. A component of gravity gliding related to the basin subsidence is present.

The third study area is the southern Sørvestsnaget Basin in the southwestern Barents Sea. Here the Late Carboniferous to Early Permian salt formed structures that are the result of hundreds of millions years of deformation, manly through reactive and active salt diapirism consequence of the Mesozoic extensional tectonics due to the Atlantic Ocean opening. This crustal extension enabled

the salt to migrate many kilometers through the stratigraphic sequence, leading to the formation of massive allochthonous salt structures and locally to their deflation. After the end of the crustal extension, the main influence on the salt deformation is attributable to the Quaternary glacial sedimentary wedge and the consequent glacio-isostatically controlled crustal movements, leading to internal redistribution of the salt in the allochthonous salt structures. Part of the hypothesis on the salt tectonics mechanisms in the Sørvestsnaget Basin were confirmed through analogue modelling.

Thanks to the diversity between the three study areas in terms of geological setting, we offer not only a broad picture of different levels of interaction between salt and crustal tectonics, but also of the effect of salt basal slope and differential sedimentary load on the salt structures evolution, as well as different levels of maturity of salt structures, from the younger ones (e.g. salt rollers) to the more mature ones (e.g. salt sheets).

RÉSUMÉ

À l'échelle des temps géologiques, le comportement du sel peut être approché d'un fluide newtonien (comportement visqueux) par rapport au comportement fragile des roches environnantes. La tectonique crustale, extensive et compressive, joue souvent un rôle fondamental dans l'évolution des structures salines et devient la principale cause de déformation dans de nombreuses zones d'étude. Le but de cette thèse est d'analyser le calendrier et les mécanismes de la tectonique salifère dans trois zones d'étude caractérisées par différents âges du sel et l'influence croissante de la tectonique crustale sur la tectonique salifère : la marge sarde occidentale et algérienne septentrionale (Méditerranée occidentale) et le bassin de Sørvestsnaget (mer de Barents sud-ouest). Cela a été fait par l'interprétation de données de réflexion sismique 2D et 3D de TGS (Norvège), OGS (Italie) et UMR GEO-OCEAN (France), ainsi que par l'intégration avec d'autres données géophysiques et la comparaison avec des modèles analogiques.

Dans la Méditerranée occidentale, le sel déposé pendant la crise de salinité (5,6 Ma) est relativement jeune, la couverture est mince et les marques des premiers stades de déformation sont visibles. Sur la marge sarde occidentale les structures salines sont principalement dues à la pente de la base du sel, résultant de la subsidence différentielle après le remplissage de la Méditerranée à la fin de la crise.

En se déplaçant vers le centre du bassin sardo-provençal, où la charge sédimentaire du Rhône Deep Sea Fan forme une lourde couverture au-dessus du sel, l'étalement par gravité domine. Bien que dans cette zone il n'y ait aucune influence de la tectonique crustale sur la déformation du sel à l'échelle régionale, nous avons reconnu sur la marge SW-sarde la présence d'une structure en fleur active pendant le Pliocène. Nous proposons qu'elle fasse partie de la North Balearic Fracture Zone, i.e. la faille de glissement dextre de l'ouverture du bassin sardo-provencal, jamais reconnue dans la région.

Le secteur sud de la Méditerranée occidentale est réactivé en compression depuis 8 Ma en raison de la convergence Afrique-Europe, et cette compression s'exprime par des chevauchements sur la marge algérienne. Ici, la tectonique salifère est principalement la conséquence de la tectonique crustale, et en particulier de l'augmentation de l'énergie potentielle résultant de l'élévation localisée. Les modèles analogiques produits montrent que le soulèvement du plateau est à l'origine des variations latérales d'épaisseur de la couche saline et de la formation des minibassins polygonaux dans la zone au large d'Alger. Une composante de glissement par gravité liée à l'affaissement du bassin est présente.

La troisième zone d'étude est le bassin de Sørvestsnaget dans la mer de Barents. Ici le sel permocarbonifère a formé des structures qui sont le résultat de centaines de millions d'années de déformation, principalement par le diapirisme de sel réactif et actif conséquence de la tectonique extensive mésozoïque due à l'ouverture de l'océan Atlantique. Ceci a conduit à la formation de structures de sel allochtones massives et localement à leur déflation. Après la fin de l'extension de la croûte, l'influence principale sur la déformation du sel est attribuable au prisme sédimentaire glaciaire quaternaire et aux mouvements de la croûte contrôlés par glacio-isostasie, ce qui entraîne une redistribution interne dans les structures de sel allochtones comme mis en évidence par la modélisation analogique.

Grâce à la diversité géologique entre les trois zones d'étude, nous offrons non seulement une vue d'ensemble des différents niveaux d'interaction entre le sel et la tectonique de la croûte, mais aussi de l'effet de la pente basale du sel et de la charge sédimentaire différentielle sur l'évolution des structures de sel, ainsi que des différents niveaux de maturité des structures, des plus jeunes (par ex. salt rollers) aux plus matures (par ex. salt sheets).

TABLE OF CONTENTS

INTRODUCTION

This PhD is part of the European project SaltGiant, funded by the European Union's Horizon 2020 research and innovation program under the **Marie Skłodowska-Curie grant agreement n° 765256**. The SaltGiant ETN is a four-year European cross-disciplinary network of natural and social scientists initiated in 2018 and dedicated to understand one of the largest salt deposits on Earth, the Messinian salt that characterizes the Mediterranean basins. One of the main objectives of the SaltGiant ETN is to train the PhD candidates to a multidisciplinary approach, both creating networks and collaborations between Universities, Research Institutes and industry, both broadening the personal knowledge of the single students with field courses, short courses and transferable skills trainings. This thesis is part of the Work Package 'Drilling Hazard' (coordinator: A. Camerlenghi, OGS), aimed at the understanding of early salt deformation and sub-salt overpressure development to mitigate the risks associated with drilling in salt-capped hydrocarbon provinces.

While the main part of the work has been carried out at the **University of Lille (LOG-CNRS)** under the supervision of V. Gaullier both in terms of bibliographic research, seismic data interpretation and analogue modelling production, this PhD included two secondments for a total of five months of work abroad. The first **secondment** took place at the **Volcanic Basin Petroleum Research (VBPR)** of S. Planke in Oslo (Norway) during September 2019, January-February 2020 and end September 2021. There we collaborated with the VBPR team, and in particular with S. Planke, B. Bellwald and D. Maharjan, at the interpretation of a 2D and 3D dataset (owned by **TGS ASA**, Norway) imaging the salt structures of the Sørvestsnagets Basin, Southwestern Barents Sea. The secondment at the **University of Trieste** and at the **Institute of Oceanography and Applied Geophysics (OGS)** in Trieste (Italy) during September 2020 and end July 2021 was focused on the processing and interpretation of seismic reflection data on the Western Sardinian margin and Sardo-Balearic basins, under the supervision of A. Del Ben, E. Forlin and A. Camerlenghi.

The **aim of this work** is to decipher the timing and mechanisms of salt tectonics and the **interactions between salt and crustal tectonics** in the **Western Mediterranean** and in the **Southwestern Barents Sea**, through the interpretation of **2D and 3D seismic reflection data** and the integration with data of gravity and magnetic anomalies. The hypothesis formulated resulting from the seismic data interpretation have been corrected and validated through the production of **analogue models** at the University of Lille.

The difficulties in studying salt tectonics and in particular its interactions with crustal tectonics are due to three main factors:

.A strong acoustic impedance contrast between salt and sediments prevents an accurate seismic imaging of the sub-salt deep structures. Moreover, the lack of internal reflection of the salt rock make it impossible the reconstruction of the internal deformation of this layer.

.The evaporites act as a decoupling layer (thin-skinned tectonics), preventing the propagation of the crustal structures towards the surface.

.The horizontal and vertical movements due to crustal tectonics can trigger a gravitational response both in the salt and in the overburden, blurring the deep tectonic signal.

As a result of the international collaboration and data sharing, this work is based on the interpretation of three datasets located in three different study areas, presented here in order of increasing influence of crustal tectonics on salt deformation: the Western Sardinian margin and the Algerian margin in the Western Mediterranean, and the Sørvestsnaget Basin in the Southwestern Barents Sea. The salt giants considered have respectively 5.6 Ma in the Mediterranean and around 300 Ma in the Barents Sea, with the consequence that the salt structures studied are not just the result of different geodynamical settings but are also at very different stages of maturity. For every area we analyzed salt tectonics both in terms of timing and mechanisms and in terms of influence of the crustal tectonics on the salt deformation. As already mentioned, the analysis of salt tectonics is based on the interpretation of geophysical data (mainly multichannel seismic reflection data, both 2D and 3D), and the comparison between the geometries interpreted in the natural example with the results of the analogue modelling of the formulated hypothesis.

In the **Western Mediterranean**, the deposition during the Messinian Salinity Crisis (MSC, 5.96 – 5.33 Ma) of a thick layer of evaporites and especially of a mobile halite unit has deeply influenced the architecture and evolution of the Mediterranean margins. The Mediterranean has characteristics that set it apart from most classic salt-bearing basins, where salt was deposited after (or right after) the rifting stage. We focused both on an area that did not underwent important crustal deformation after the deposition of the Messinian salt (the **Western Sardinian margin**) and an area in which the margin reactivated, influencing the deformation of the ductile salt layer (the **Northern Algerian margin**).

Very different is the situation in the **Southwestern Barents Sea**, where the salt imaged in the seismic reflection data was deposited during Permo-Carboniferous (~300 Ma), and due to the thick overburden the seismic imaging is limited to the allochthonous salt structures. This area underwent extensional crustal tectonics related to the Atlantic opening, and the reconstruction of the first phases of salt tectonics is result of the integration between the literature in terms of crustal tectonics in the area and the knowledge in terms of salt deformation. On the other hand, the most recent salt deformation has been analyzed through seismic data interpretation and its comparison with analogue models.

For what concerns the organization of the thesis, in **Chapter I** we will describe the main characteristic of the evaporites, the nomenclature of the salt structures and the mechanisms of ductile deformation, both related to gravity-driven failure and in response to crustal tectonics.

Chapter II will start with an introduction to the seismic reflection method, both in terms of acquisition, processing and characteristics of the signal, and an introduction to the swath bathymetry method and the gravity and magnetic potential methods. Will follow a description of the characteristics of the different datasets used in this study, and the data interpretation both in terms of theory (e.g. the principle of seismic stratigraphy) and the procedures used for the interpretation of the datasets in this work (e.g. attribute analysis). The end of the chapter is dedicated to analogue modelling, in particular its application for the study of salt tectonics.

Chapter III is dedicated to the Western Mediterranean. After the bibliographic synthesis of the geological setting of the area, particularly focused on the Messinian Salinity Crisis and its markers,

we present the results of the seismic data interpretation -with main focus on the salt tectonics structures- and analogue modelling of the Western Sardinian margin and Northern Algerian margin, and discuss the results in terms of timing and mechanisms of the salt deformation and influence of the crustal tectonics on the salt tectonics.

In **Chapter IV**, we start from the synthesis of the geological setting of the Barents Sea, with a focus on its Southwestern sector (Sørvestsnagets Basin ad Senja Ridge). We present the results of the 3D seismic data interpretation, here again focused mainly on the salt structures and the geometry of the salt overburden, and compare it with the results of the analogue models produced. We finish the chapter with the reconstruction of the long lived salt tectonics in the area and the influence of both salt tectonics and glacial phenomena on salt deformation.

Chapter V contains a general discussion of the outcomes of the work presented in the previous chapters, the differences and similarities between the Mediterranean and the Arctic salt, and the perspectives in terms of further studies and publications and data acquisition.

Two annexes conclude the thesis manuscript.

Chapter I: EVAPORITES DEPOSITION AND SALT TECTONICS

The evaporite is defined as a mineral sediment precipitated from a saturated brine by hydrologies driven by solar or non-solar evaporation, brine cooling etc. (Warren, 2006, 2021) resulting in a concentration of the solution exceeding the solubility value of a certain mineral. The evaporite minerals precipitation can be extremely fast compared to other rocks, with deposition rates up to more than 10 cm/yr compared to the few mm/kyr of other rocks.

Due to the topic of this thesis, we will focus more on the geological evolution of these minerals after their deposition, especially in terms of deformation of the so-called saltgiants **(Figure 1.1)**. Salt tectonics *sensu stricto* is defined as a tectonic deformation that involves evaporites -as a substratum or as a source layer- without the need to have significant tectonic forces (i.e., crustal tectonics), and the study of salt tectonics is therefore aimed at analyzing the deformation of salt rocks to reconstruct their geological history and potentially predict future scenarios. While other evaporites as gypsum can also deform, the lower viscosity values are characteristic of the halite rock (commonly referred to as salt or salt rock), that is therefore the main rock studied in terms of salt tectonics. The peculiarity of the salt tectonics is the **low temperature geological deformation** that consists in both lateral and vertical movement: considering geological times, the behaviour of the salt can be approximated to a Newtonian fluid **(viscous behaviour)**, i.e. the rate of shear stress is proportional to the rate of shear strain (Warren, 2006 and references therein).

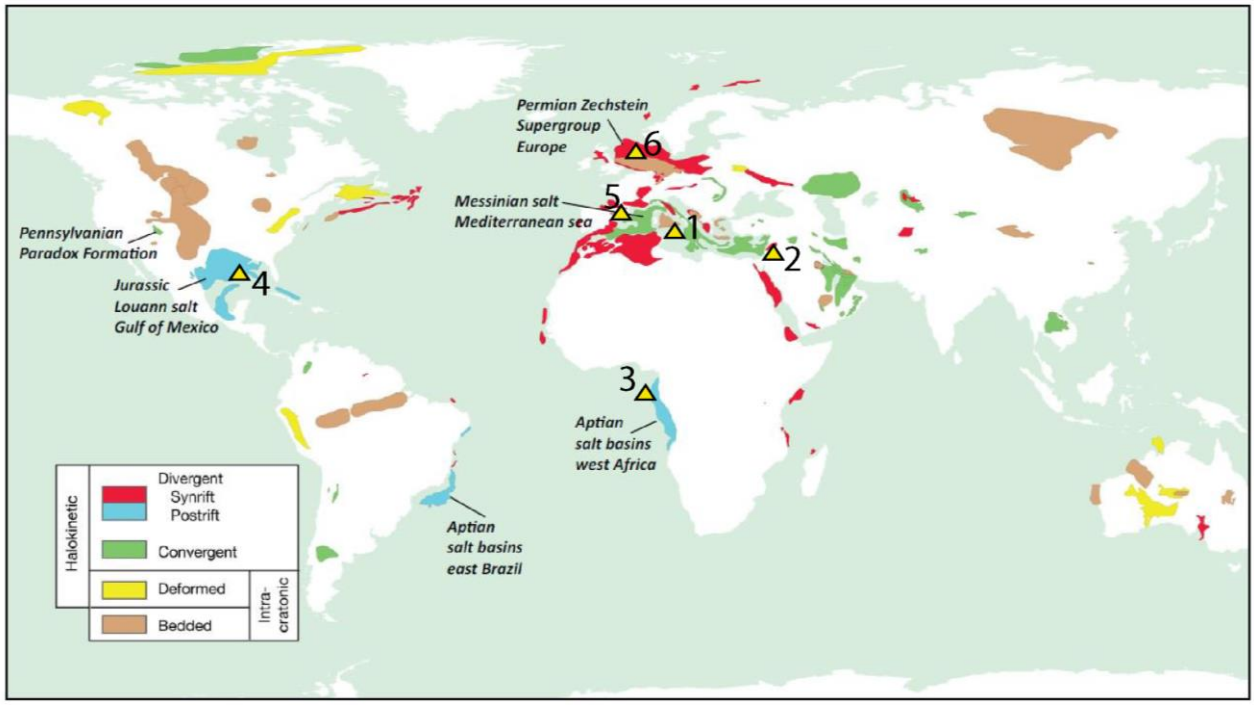

Figure 1.1: *Map of the world showing some of the ancient salt giants divided by tectonic setting, modified after Warren, 2010. Position of the examples shown in this chapter: 1- Realmonte saltmine (Figure 1.2) 2- Dead Sea (Figure 1.4) 3- Gabonese margin (Figure 1.19) 4- Gulf of Mexico (Figure 1.21) 5- SW Alpine belt (Figure 1.24) 6- Central North Sea (Figure 1.30).*

The study of salt tectonics and in general of the salt deposits (Figure 1.1) is often strongly connected to oil industry for the potentiality of salt structures to trap gas and oil. In fact, the presence of sealing

salt layers or salt-related anticlines led to the formation of some of the most important hydrocarbon provinces in the world, as the Gulf of Mexico, the North Sea and the Campos Basin ones (Figure 1.1) (Gearing et al., 1976; Warren, 2010). On land, evaporites deposits are exploited for both food and chemical industry (e.g. the salt mine in Realmonte, Sicily, **Figure 1.2**).

Nowadays, the study of salt tectonics is also linked to the research of sites for CO2 stocking in the -almost- global attempt to reduce the carbon dioxide emissions in the atmosphere. On the other hand, a side effect of the presence of these sealing layers is the potential development of **overpressures** below the salt, with consequent drilling hazard.

In this chapter we will describe the characteristics of the evaporites –with particular focus on the halite- and then describe the mechanisms of deformation of the salt rocks, giving some examples from different geological settings.

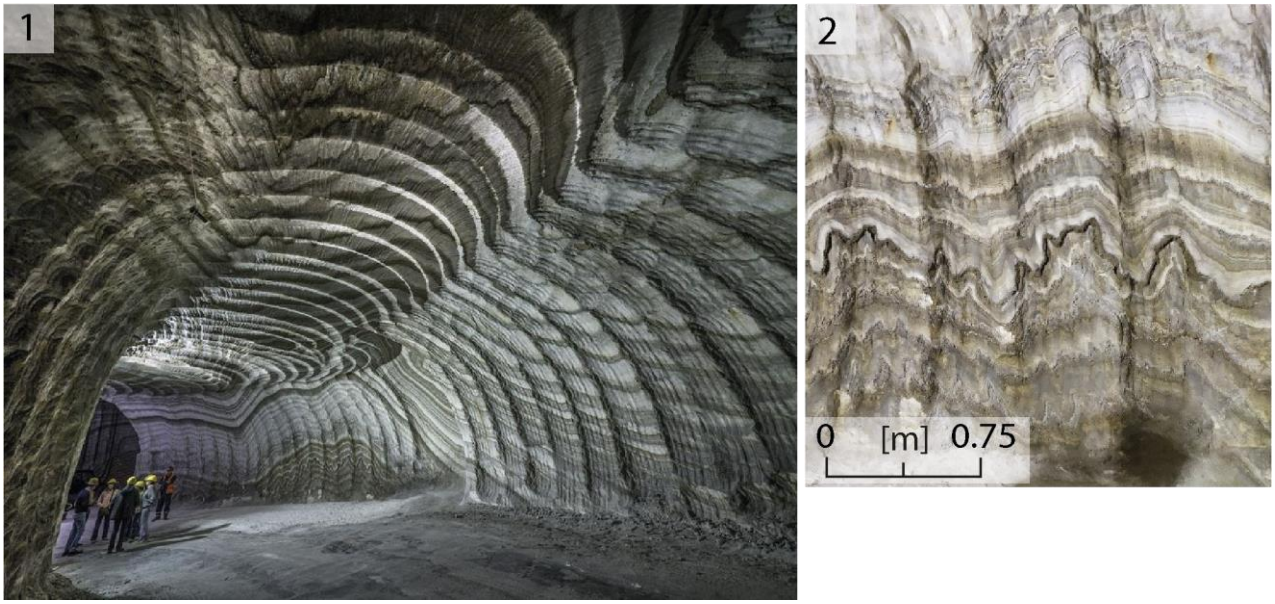

Figure 1.2: 1. *The Realmonte Saltmine (Sicily) dug in the Messinian Salinity Crisis deposits.* ***2.*** *Small scale folding.*

I.1. Deposition and main characteristics of evaporites

• Evaporites deposition

As already mentioned, the evaporite is a water-soluble mineral that result from the precipitation from a brine (saline solution), More than 80 evaporites minerals form in nature (Steward, 1963), but only 12 of them can form significant deposits and have therefore. Their classification in chlorides, sulfated and carbonates, together with their chemical composition, is presented in **Table 1.1**.

While both marine and non-marine environments can give origin to evaporite deposits, the marine ones are generally the most extended ones and consequently the most studied. The experiment of Usiglio (1849) shows the order of **precipitation** of different minerals resulting from the evaporation of a sea water column **(Figure 1.3)**, with a total of 17 meters of evaporites formed from the complete evaporation of a column of 1 km of seawater. The evaporation of 1 km of seawater with 38.45‰ of salinity (ρ=1.025 g/cm^3) leads to the precipitation of 0.1 m of carbonates ($CaCO_3$) when the salinity

Mineral class	Mineral name	Chemical Composition
Chlorides	Halite	$NaCl$
	Sylvite	KCl
	Carnallite	$KMgCl_3 \cdot 6H_2O$
	Kainite	$KMg(SO_4)Cl \cdot 3H_2O$
Sulfates	Anhydrite	$CaSO_4$
	Gypsum	$CaSO_4 \cdot 2H_2O$
	Kieserite	$MgSO_4 \cdot H_2O$
	Langbeinite	$K_2Mg_2(SO_4)_3$
	Polyhalite	$K_2Ca_2Mg(SO_4)_6 \cdot H_2O$
Carbonates	Dolomite	$CaMg(CO_3)_2$
	Calcite	$CaCO_3$
	Magnesite	$MgCO_3$

Table 1.1: *Common marine evaporite minerals and their composition (Stewart, 1963).*

is more than 53.3‰, followed by 0.6 m of gypsum ($CaSO_4x2H_2O$) when the salinity is 190‰, and anhydrite ($CaSO_4$) when the salinity is 310‰.

Halite (NaCl) starts to precipitate when the salinity reaches the 380‰, so ten times the initial conditions, producing 13.3 m of deposits. Only when a concentration of 3800‰ is reached, the first potash and magnesium salts start to precipitate, with deposition of ylvine, carnallite (potassium and magnesium chlorides), polyhalite, langbeinite and kieserite (potassium and magnesium sulphates) and kainite (a mixed mineral). As it can be noticed from the percentages of salinity necessary to precipitate them, the gypsum, anhydrite, halite and potash/magnesium salts all testify extreme conditions, and the abundance of these rocks in nature follow the same order of the precipitation one, i.e. the carbonate rocks are the most present one. Due to the continuous deposition of different salts depending on the concentration – often fluctuating in nature -, the evaporites deposits are commonly composed of mixed mineralogies. The precipitation conditions mentioned above are mainly the result of a basin isolation and climate aridity: the loss of water for evaporation is not balanced by oceanic and fluvial inflows, so the concentration increases allowing the precipitation of the evaporites.

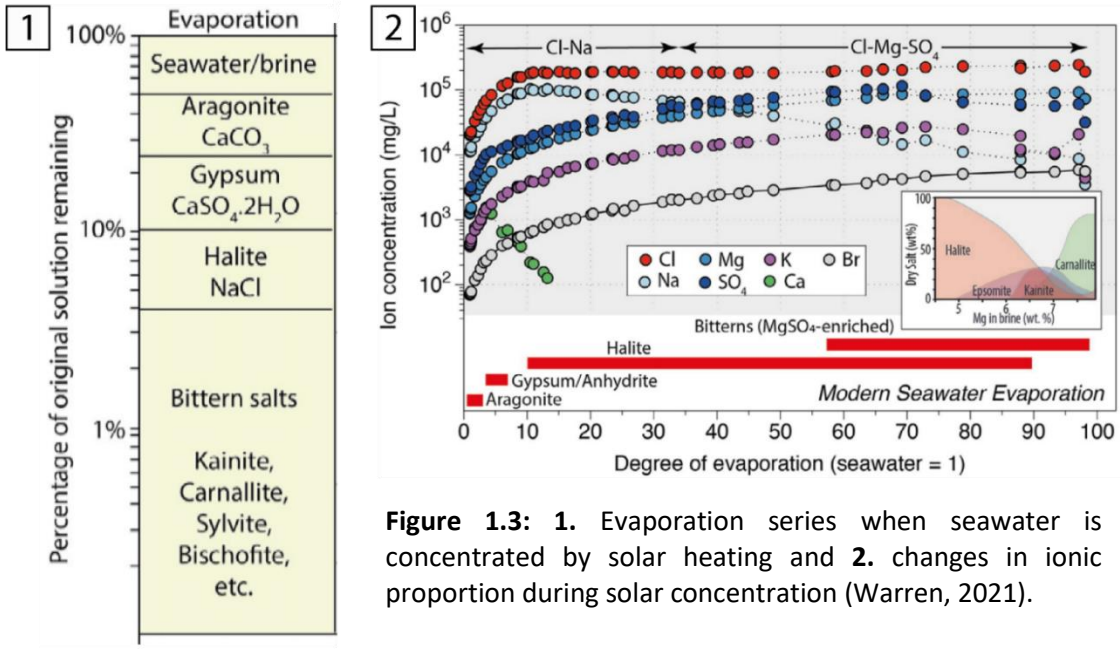

Figure 1.3: 1. Evaporation series when seawater is concentrated by solar heating and **2.** changes in ionic proportion during solar concentration (Warren, 2021).

While we will see in chapter III.A.4 (Messinian Salinity Crisis) the hypothesis about the formation of the Messinian salt giant, a nowadays analogue of this situation is the Dead Sea (**Figure 1.4**). The Arabian – African transform plate boundary led to the formation of a pull-apart trough, expressed as a 5 to 20 km wide valley (Girdler, 1990). The Dead Sea is located in the deeper part of this basin, and despite its name it is a terminal lake of 320 m depth with the shores at more than 420 m below sea level. During Pliocene, Mediterranean water flooded the depression, leading to the deposition

of the Sedom Formation evaporites, a layer of 2.3 km of halite with interbeds of anhydrite, dolomites etc. When the marine water supply stopped, the deposition became mostly siliciclastic, with chalk and thin evaporites layers (Zak, 1967).

The nowadays situation of the Dead Sea **(Figure 1.4.1)**, with a salinity of 192‰ at the surface and 266‰ at 300 m depth (Sirota *et al.*, 2018) is an interesting comparison to what happened in the Mediterranean Basin during the Messinian Salinity Crisis, and the data obtained from the measuring of different parameters of the Dead Sea waters are helpful to progress in the study of ancient salt giants (Sirota *et al.*, 2020).

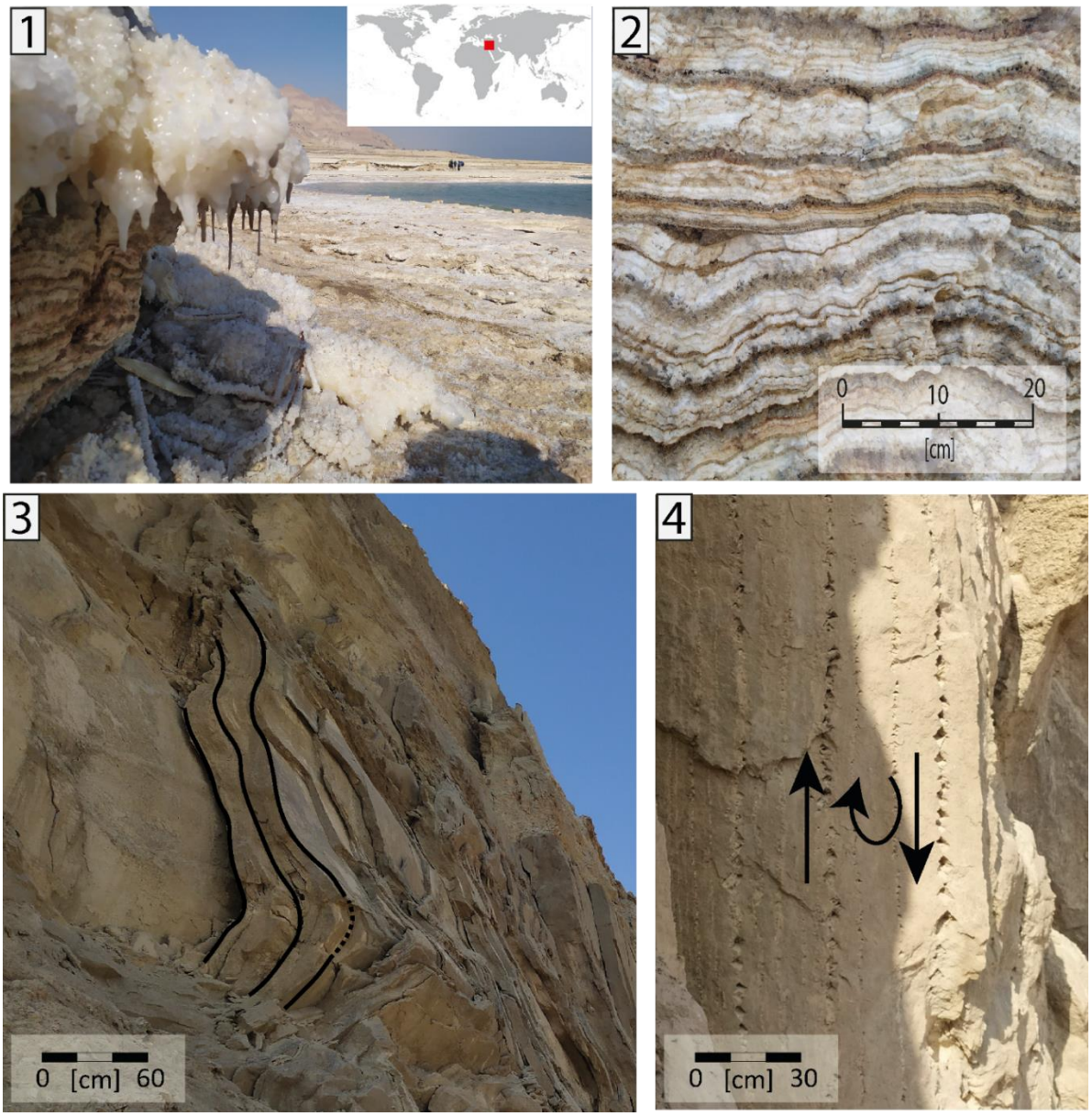

Figure 1.4: *The area of the Dead Sea shows both examples of modern salt deposition (1 and 2) and salt deformation (3 and 4).* ***1.*** *The Dead Sea shores are characterized by active deposition of salt.* ***2.*** *Outcrop of the halite deposits with terrigenous intercalations, testifying the thick salt deposition of the last years, around 10 cm/y.* ***3. and 4.*** *Detail of the outcrops of the Pliocene Mt Sedom diapir, southwestern Dead Sea Basin. The salt layers -horizontal at the moment of the deposition- are nowadays almost vertical, due to salt tectonics. The internal stratification (highlighted in black, in Figure 1.4.3), shows a deformation linked to the movement of the single layers of salt. The arrows in Figure 1.4.4 represent the relative direction of movement of the layers and the consequent internal deformation of the halite.*

In fact, this is the only modern example of salt layers accumulation on the floor of a brine lake of hundreds of meter of water depth. The brine volume is 147 km^3, and the drainage basin more than 40 000 km^2. With rainfalls of 45 to 90 mm and evaporation of 1500 mm, the water balance is negative, but in addition to the natural conditions the water level fall accelerated due to river diversion for irrigation and water pumping in the southern basin to maintain the water level in the saltworks, started in the '60s. The nowadays sea level fall is of around 1 meter per year, with around 10 cm of halite deposition per year (Figure 1.4.2) (Alsop *et al.*, 2015; Warren, 2006 and Weinberger, 2006). The seasonality of halite accumulation is due to the differences in temperature, that result in slight supersaturation during summer and high supersaturation during winter (Warren, 2021). Located at the western side of the Dead Sea Basin, the 4.5 km tall Sedom diapir (Figure 1.4.3 and 1.4.4) has a visible shape of 11 km long and 200 m above the lake level.

• Evaporites physical properties

This subchapter is not aiming to give a complete description of all the evaporite physical properties - (see e.g. Warren, 2006*)*- but to list some of the main physical properties of halite that can contribute to the comprehension of salt tectonics. As mentioned before, the salt deposits are generally composed of different evaporites, with anhydrite and gypsum commonly present. **Anhydrite** deforms more competently and has a higher viscosity compared to **halite**, but it is still weaker than most other rocks -especially at 200-300°C- and can act as a detachment layer. **Gypsum** is one of the most ductile and weakest rocks, so it is very efficient for what concerns detachment of fold and thrust belts. The average densities of anhydrite and gypsum rocks are respectively 2.90 and 2.31 g/cm^3 (Warren, 2006).

- **Viscosity and plasticity**: The most important characteristic of the salt rocks for the study of salt tectonics is the plasticity of this material. In fact, at low temperature and in geological times and scales, the salt moves as a fluid (solid state flux) due to the low viscosity values of 10^{10} to $10^{17\text{-}19}$ Pa.s., up to 10 orders of magnitude lower than the average values for rocks (Carter and Hansen, 1983; LeCompte, 1965; Warren, 2006) **(Figure 1.5)**.

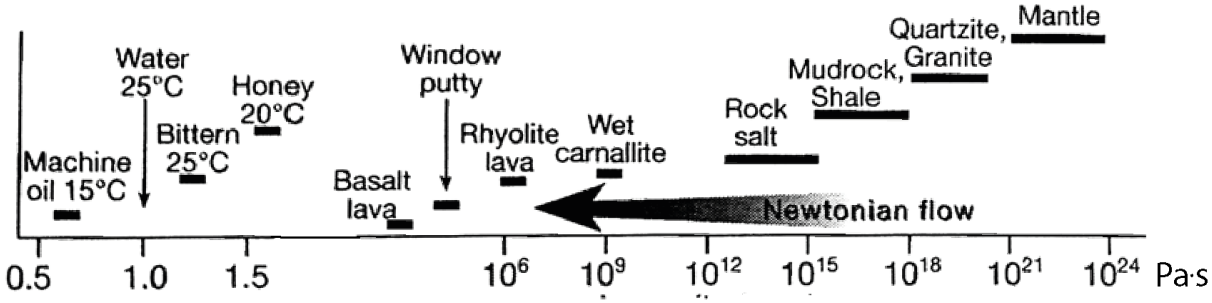

Figure 1.5: *Viscosity of different materials (non linear, logaritmic horizontal axis). We can notice that between the geological materials, rock salt has one of the lower viscosity values (*Warren, 2006*).*

The viscosity of the halite is strongly influenced by the following factors:

a. Mineralogy – Not only the chemical composition but also the dimension and geochemical organization of the grains have a fundamental influence on the plastic behaviour of the mobile salt (i.e. halite). Halite rocks have a mean grain size of 2 to 30 mm, coarser for the recrystallized salt. The smaller grains size constitutes a favorable condition for salt movement. From the grain

composition point of view, a higher amount of anhydrites and carbonates intercalation inside the halite results in a lower plasticity of the rock, and slows down the creep (Warren, 2006).

b. Content of water: the presence of water molecules in the salt lowers the viscosity of the rock, facilitating the movement.

c. Temperature: An increase of the temperature leads to enhanced cohesion and ductility, that results in an increase of the rupture strength (fracture point in **Figure 1.6**) in the stress-strain curve while decreasing the yield strength (or elastic limit), this last one being an indicator of the maximum stress that can be developed in a material without causing plastic deformation (Robertson *et al*., 1958): higher temperature reduces the viscosity and increases the plasticity of the evaporites, increasing therefore the strain resulting from a certain amount of stress but allowing the rock to resist to higher stress values without fractures.

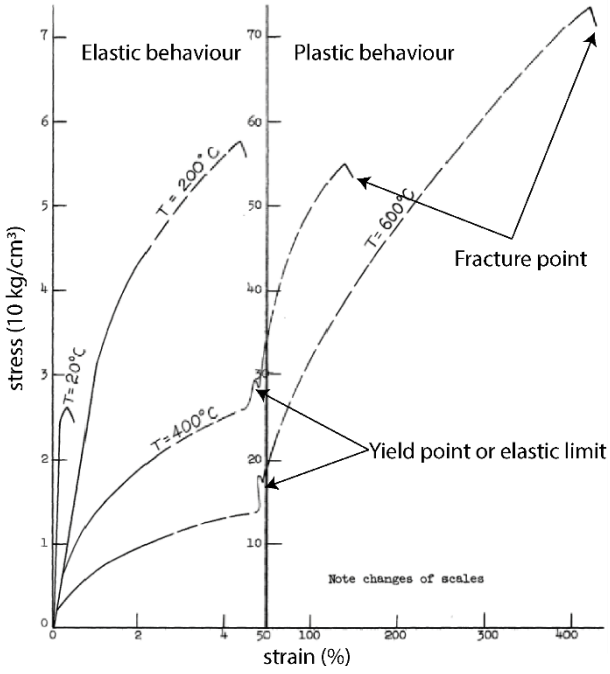

Figure 1.6: *Effect of the temperature on the deformation of salt: at higher temperatures, lower values of stress are necessary to produce a certain amount of strain, but higher stress values can be reached before the fracture point* (modified after Robertson *et al.*, 1958).

While in the past the temperature was considered fundamental for salt mobilization **(Figure 1.7)** (Gussow, 1968; Jackson and Talbot, 1986), more recent studies have scaled down its role: while its widely demonstrated that the viscosity of the salt is reduced by higher temperatures (Figure 1.6) and therefore the temperature effect of the viscosity could have a role in the study of the deep late mobilization of the salt, the studies on the real impact of temperature on the formation of salt structures around the world are not yet conclusive. While the presence of thermal

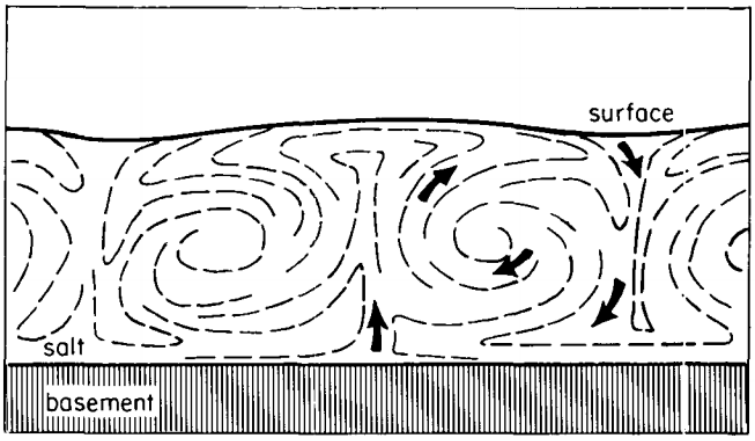

Figure 1.7: *Thermal convective halokinesis, with the dashed lines representing partly homogenized layering* (Jackson and Talbot, 1986).

anomalies related to basement transfer zone could possibly have a role in the salt deformation (Maillard *et al.*, 2003), the high heat flow up to 153 mW/m2 measured in the Gulf of Lions are conversely the result of the thermal refraction due to the diapirs presence (Poort *et al.*, 2020).

d. Pressure effect: the pressure lowers the viscosity of the halite, that reaches its plasticity threshold at 50-80 bars (around 300-meter depth), and becomes ductile under low strain rates (Jackson and Hudec, 2017). The viscous behaviour that we can observe at depth is lost under low confining pressure, meaning that at or near the surface salt loses its sealing characteristics and the rock salt is damaged by micro-fractures.

- **Strain value**: the strain value of Iran salt glacier has been measured to be 10^{-9} s^{-1}, while the medium value of the rocks is around $10^{-15}s^{-1}$, so the strain value of evaporites is approximately 1 Million times lower. These differences can also be seen in the tensional and compressional strength **(Figure 1.8).**

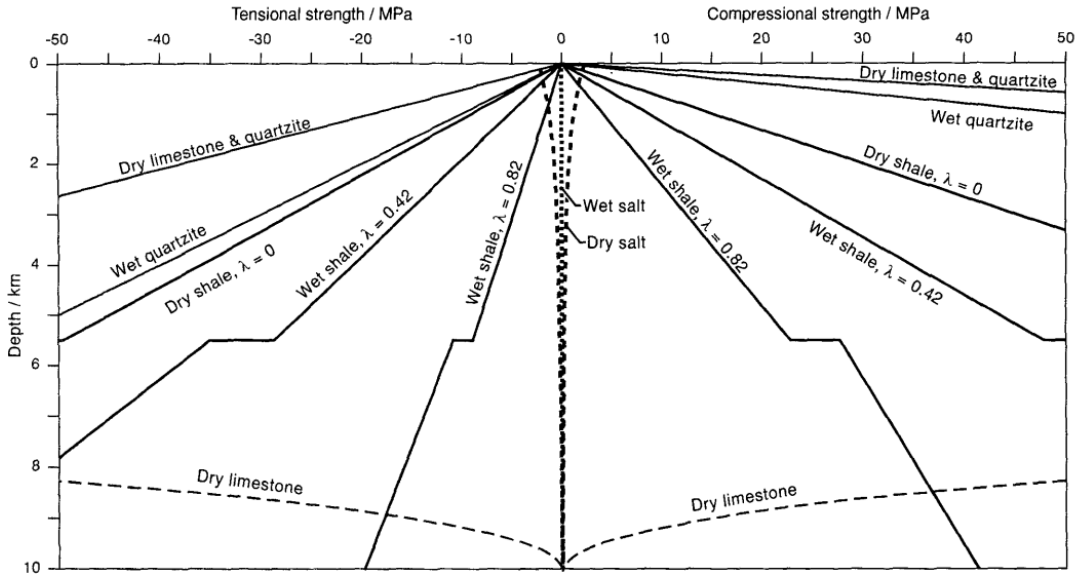

Figure 1.8: *Tensional and compressional strength of dry and wet salt (central part of the graph) compared to the one of other geological material (Jackson et al., 1994). The tensional strength is the maximum load that a material can support without fracture when being stretched divided by the original cross-sectional area of the material, while the compressional strength is the ability of a material to resist the direct pressure of applied compression force divided by the cross sectional area. In the graph, λ represents the pore pressure coefficient (ratio of pore pressure to lithostatic pressure).*

- **Relative incompressibility/constant density:** The halite rocks are characterized by a density of about **2040 kg/m^3**, reached very quickly in the first hundreds of meters of burial; this value can be approximated as constant until the evaporites reach a depth of 6-8 km, when the density changes for chemical and physical phenomena. In isothermal conditions, a pressure of 260 MPa (around 10 km depth) produces a density increase of the 0.7% (16 kg/m^3). Also the **temperature** influences the density of salt, with a decrease of 6% when the temperature changes from 0 to 800°C, and 18% above the 800°C (Gussow, 1968). But if we consider also the thermal expansion, the result is that the density of halite decreases with increasing depth (Jackson and Hudec, 2017; Odé, 1968; Warren, 2006). The density of the salt rocks is lower than the average density value of most carbonates and moderate-compacted siliciclastic rocks (Jackson and Talbot, 1986)

(Figure 1.9), so the **depth of density crossover** -or level of neutral buoyancy- is at about 1 km depth (Warren, 2006). So far we were referring to the measured density values for pure halite, but it worth mention that in most of the modelling or inversion studies a value of 2200 kg/m^3 is used, in order to include the presence of a low percentage of anhydrite (density of almost 3000 kg/m^3). As previously mentioned, the low and almost constant density of the salt makes this material 'unstable'. The density inversion has been long considered as the main mechanism of diapir formation at the beginning of the salt tectonic studies, while with the scientific progress it became clear that the density inversion not only is not a sufficient condition to deform salt, but it is not event a necessary one.

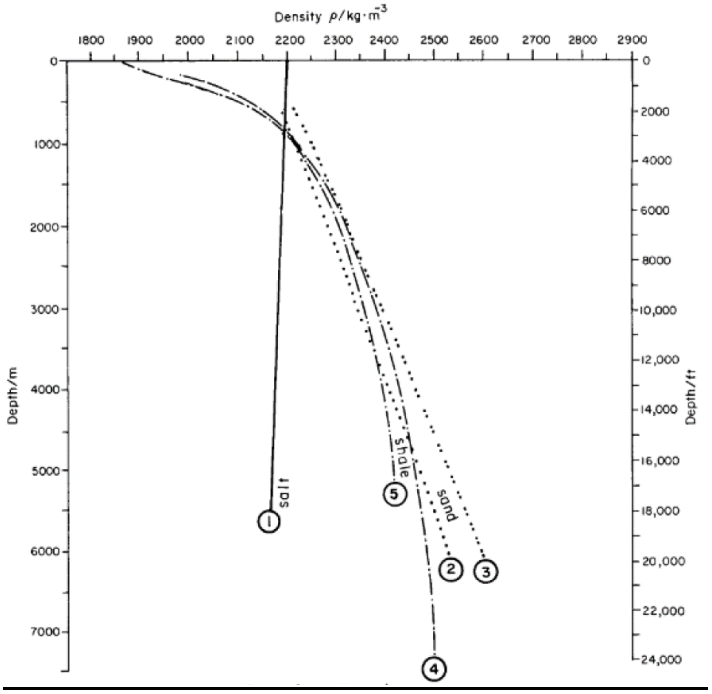

Figure 1.9: *Burial depth versus density for salt rock (1), shales (4 and 5), sandstone (2 and 3). In this graphic is considered not only the thickness of the overburden but also the geothermal gradient of 30°C/km, so the salt density slightly decreases with depth due to thermal expansion. The depth of density crossover between halite and the other geological materials is at around 1 km depth, depending on the density of the material (Jackson and Talbot, 1986).*

- **Sealing characteristics**: the main interest of the oil industry in the salt tectonics studies is due to the sealing characteristics of halite - and in general evaporitic rocks - when their shale content is limited. In fact, the permeability of halite is around one nanodarcy, being a permeability of 1 darcy the one permitting on an area of 1cm² the flow of 1cm/s of a fluid with 1mPa s under the pressure of 1 atm/cm. The same sealing characteristic that can be a benefit for the oil industry in terms of oil **traps** has to be carefully evaluated during drilling, because the presence of a salt layer can generate strong overpressure below the salt, exponentially increasing the drilling hazard. Moreover, the salt is considered safe -if it meets certain criteria- also from the point of view of the CO_2 trapping/storage, and many studies are nowadays going in that direction. The possibly permeable channels present in the salt rock can be scaled with a low pressured floating water solution, reducing more than 100 times the permeability (Robertson *et al.*, 1958).

- **Thermal conductivity**: The thermal conductivity of halite has values of about 5.15W/m-K at 43°C, significantly higher than other rocks **(Figure 1.10)**, with an influence on the temperature in the sedimentary basins: the presence of a layer of salt relatively increases the temperature above the salt and decreases the temperature below it (Nagihara *et al*., 1992). The presence of a layer of salt has therefore to be considered for its influence on rock maturity by the oil industry,

with the increased maximum depth of hydrocarbon burial before their deterioration (Warren, 2006). Moreover, the thermal expansion is high and could potentially trigger diapirism, especially if the **geothermal flux** is high (Warren, 2006), but the studies have not been conclusive due to the fact that the high thermal conductivity influences the measured values of geothermal flux, making the correlation between salt tectonics and thermal flux quite complex.

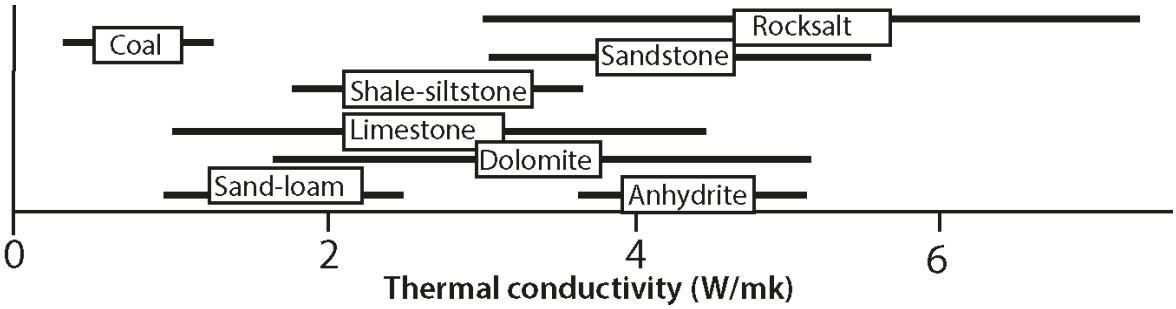

Figure 1.10: *Thermal conductivity of different geological materials (modified after Warren 2006).*

I.2. Salt tectonics

As mentioned in the previous part, the salt rocks have a viscous behavior in geological times. The deformation of the salt has been the subject of many studies –and contrasting theories- since the 19th century. We start by briefly retracing the history of salt tectonics studies and then talk about the nowadays state of art.

Introduction

The history of the study of salt tectonics has been divided by Jackson (1995) in three phases. Between the 1856 and the 1933, the ***"pioneering era"*** is characterized by a general lack of data that let the space for all sort of hypothesis (e.g. salt structures have been interpreted as residual islands). The studies start to take a common direction in 1933, with the beginning of the "***fluid era***": both salt and overburden were modeled as fluids with different viscosity, and the models followed the laws of Rayleigh-Taylor describing the instabilities at the interface between fluids with different densities (Nettleton, 1934). In this particular kind of models, small irregularities in the surface separating the two fluids are sufficient to give origin to diapirs, which grow thanks to the density contrast between the modelled fluids **(Figure 1.11)**. During this phase of the salt tectonics studies, the importance of external trigger mechanisms was highly underestimated (Warren, 2006).

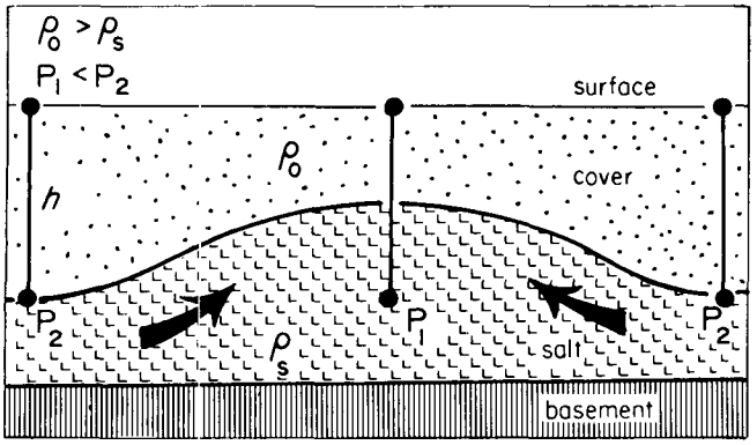

Figure 1.11: *Buoyancy halokinesis with density inversion, i.e. when the density of salt is lower than the density of the overburden (Jackson and Talbot, 1986).*

The modern salt tectonics studies start at the end of the '80s, with the beginning of the '***brittle era***': the '*fluid era*' concepts were too simplistic to properly model the relationship between salt and overburden, and were completely excluding the concept of the contrast between ductile and brittle behaviours. The most efficient way of modelling the salt has been reached considering the evaporitic layer as a pressurized fluid and the above sediments as a brittle cover, so the relative strength of the two layers acquired importance in the models. The new models were able to demonstrate the importance of the processes of gravity gliding and gravity spreading (Vendeville, 1987), and the external trigger mechanisms are analyzed (Jackson and Talbot 1986; Vendeville and Jackson, 1992a, 1992b). In the late '90s, **differential loading and extensional tectonics** started to be considered equally important for salt tectonics, and the relative importance of the buoyancy has been downsized (Gaullier and Vendeville, 2005; Vendeville, 2005).

I.2.1. Salt tectonics structures

Despite salt tectonics structures are described at any scale -from microscopic to basin one- we will introduce here the standard nomenclature used to describe the structure that we can resolve in the seismic reflection data, that is nowadays the primary mean to study the salt giants offshore. The final shape of the displaced salt depends not only on mechanism of formation of the salt structure, but also on the thickness of the salt and on the maturity of the salt structure (i.e. duration of salt tectonics). The classification of the different structures **(Figure 1.12)** is based both on the relationship between the salt and its overburden (i.e. the sedimentary sequence above the salt layer) and on the shape of the salt body:

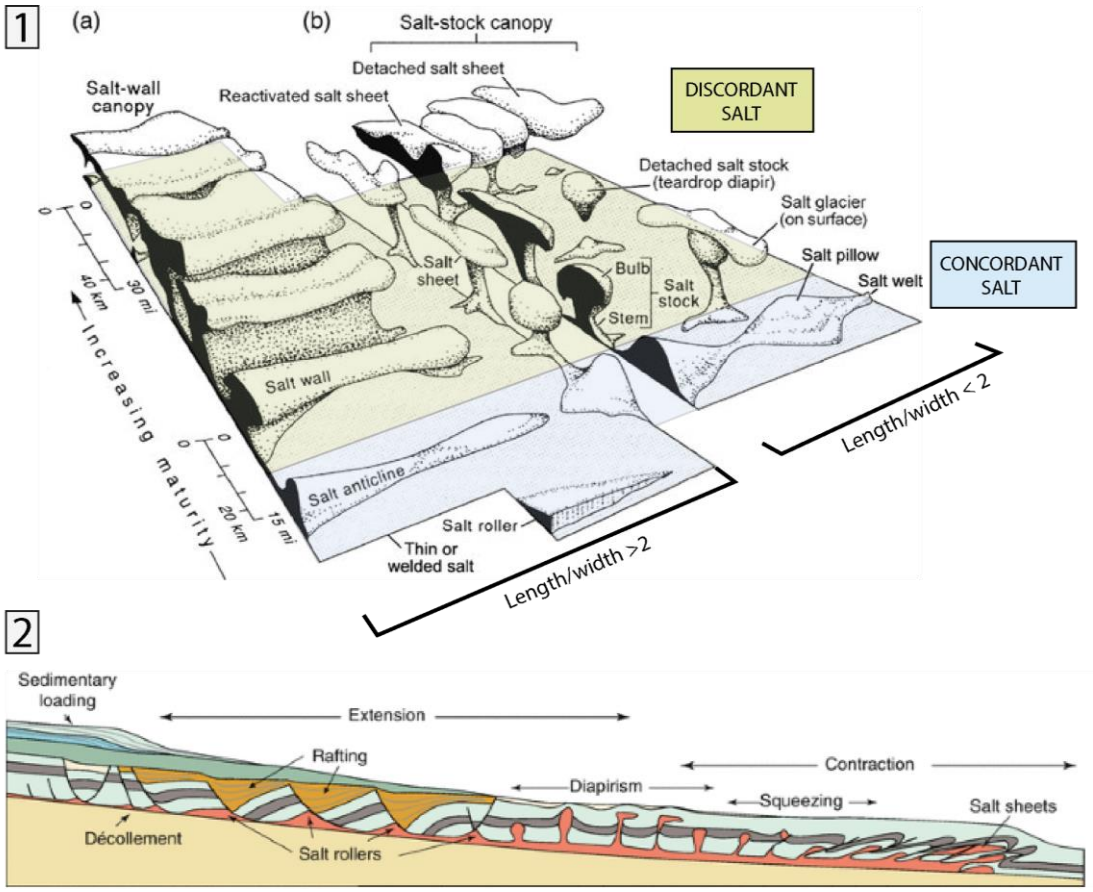

(caption on next page)

Figure 1.12: 1. *Schematic shape of the main salt structures in 3D, with increasing maturity and size (note the changing in the scale) towards the upper part of the image (modified after Hudec and Jackson, 2007). Part (a) has a linear source of salt, while (b) has a point source of salt.* ***2.*** *Schematic profile of the different salt tectonics domains and associated structures in the case of gravity gliding (Warren, 2016).*

- **Salt pillows and salt anticlines** are salt structures having **concordant overburden**; they are called salt pillows if in map view the length-to-width ratio is less than 2, or salt anticlines if this ratio is higher. They generally form as contractional folds or in the core of normal-faults rollovers. Contractional salt anticlines can be recognised from the generally long pre-kinematic phase and a short sin-kinematic one. Another salt structure with concordant overburden is the **salt roller**, that is a asymmetrical salt anticline located below normal –generally listric- faults of the overburden (Figure 1.12.2) (Vendeville and Cobbold, 1992; Brun and Mauduit, 2009).
- **Diapirs** are structures of salt having **discordant overburden** (i.e. cuts across the overburden beddings) (Jackson and Talbot, 1986), and are the most common structure especially in relatively young salt basins, as the Mediterranean one. A possible division in this broad cathegory of salt structures is the one between salt stocks and salt walls, respectively with axial ratio minor and major of 2 (Jackson and Hudec, 2017) but this division is not strictly applied in literature and other criteria of division have been proposed by other authors. Salt stocks and salt walls are the discordant equivalent of salt pillows and salt anticlines.
- **Allochthonous salt:** The allochtonous salt is emplaced at stratigraphic levels above the autochtonous salt layer and at the moment of its formation present an horizontal development, which can later be deformed for secondary salt tectonics. The allochthonous salt is generally characteristic of a mature phase of salt tectonics (i.e. Barents Sea salt structures, chapter IV.B), and take place when the salt supply exceeds the sediment accumulation. We can distinguish between **salt sheets**, when the source is a single feeder, and **salt canopies,** when 2 or more salt sheets compose a single structure. In the case of salt canopies, the boundary between the previously disconnected salt sheets is marked by sutures (allosutures), not always detectable in the seismic reflection data. The presence of allochthonous salt can have an important role in the gravity driven failure (Rowan, 2020). A particular kind of salt sheet is the **salt glacier**, that is a salt sheet moving beneath water of air, without significant overburden**.**

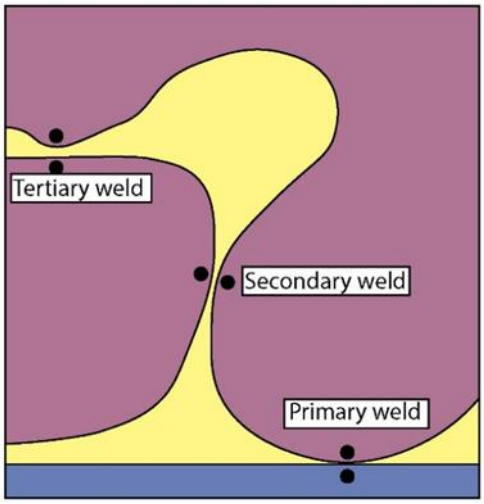

Figure 1.13: *Schematization of different salt welds (primary, secondary, tertiary).*

- **Salt welds:** The salt weld is defined as a layer of **50 meters or less** of remnant salt, testifying the previous presence of a thicker salt layer, moved or dissolved **(Figure 1.13)**. From the mechanical point of view it often acts as a surface, and limitates the salt tectonics due to the thinnes of the salt rock. In the seismic profiles, in which the thin salt layer cannot always be resolved, the salt welds can be recognised thanks to the common angular unconformity (e.g. apparent downlap), consequence of the fact that salt welds join pre- and post- salt strata, and these last ones are generally rather deformed (Warren, 2006). The salt welds are chategorized as **primary, secondary and tertiary** (Figure 1.13): the primary salt

weld concerns the allochthonous salt in place, while the secondary sald weld joins strata previously separated by a salt diapir. The welding of an allochthonous salt structure –of first or higher order- is called tertiary salt weld and can have a fundamental influence on the allochthonous salt structure evolution. Salt weld can be complete, incomplete (less than 50 meters of evaporites) or discontinuous.

- **Minibasin:** The minibasin is a small depression that subsides in a thick layer of salt, forming a synform of sediments **(Figure 1.14)**.

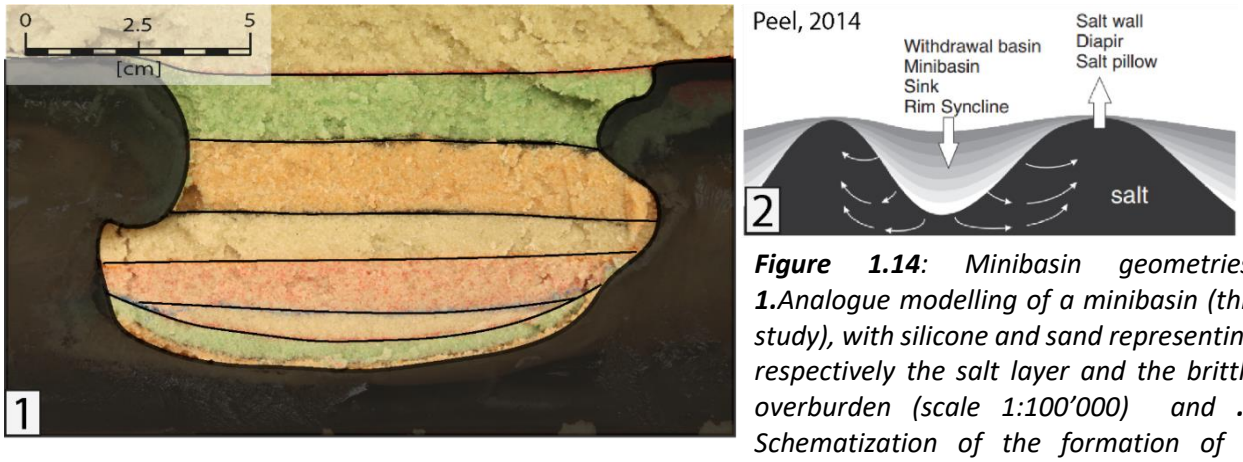

***Figure 1.14**: Minibasin geometries. **1.**Analogue modelling of a minibasin (this study), with silicone and sand representing respectively the salt layer and the brittle overburden (scale 1:100'000) and **.2** Schematization of the formation of a minibasin (Peel, 2014).*

At the initial stage, the minibasin is surrounded and floored by salt, that flows from beneath the minibasin towards its margin, creating new space for the vertical development of the minibasin and forming a network of salt structures surrounding the minibasins. The evolution of the structure stops when the salt layer at the base of the minibasin becomes a salt weld (Peel, 2014).

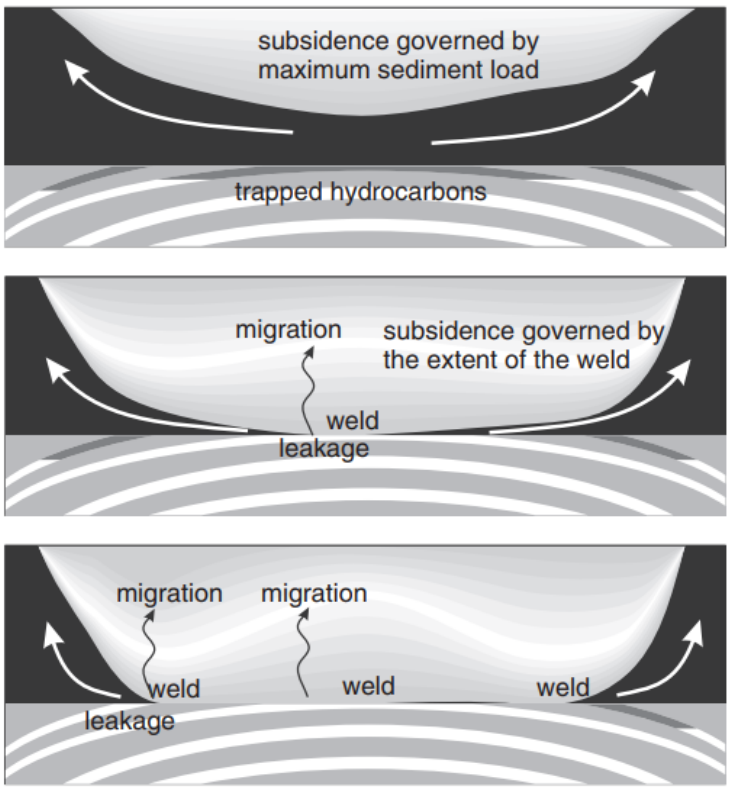

***Figure 1.15:** Evolution (from top to bottom) of a turtle structure, with the salt marked in black (Peel, 2014). When the structure forms above a subsiding diapir, it is called mock turtle anticline (Vendeville and Jackson, 1992b).*

- **Turtle back anticline**: The turtle back anticline **(Figure 1.15)** is the result of the inversion of a salt minibasin, and in most of the cases its formation dates the weld formation at the base of the minibasin. The turtle back anticline is recognisable by the flat base and the rounded crest, with a sedimentary sequence thick at the core and thinning laterally. The turtle back anticlines are particularly interesting in terms of hydrocarbon exploration, constituting potential traps (Peel, 2014).

- **Mock turtle anticline:** the origin of this anticline, which geometry is very similar to the turtle back anticline (Figure 1.15), is the formation of a depocenter on the crest of a subsiding diapir (Vendeville and Jackson, 1992b).

I.2.2. Salt tectonics mechanisms

Some of the characteristics of salt have been described in subchapter I.1., but it is worth mentioning that the salt layers object of our studies are most of the time constituted by different evaporites interbedded and variable amounts of non evaporitic materials. These stratifications lead, on a smaller scale, to surfaces of weakness along which the movement is concentrated. These surfaces and the effect of the movement is well visible in the outcrops (Figure 1.4.3 and Figure 1.4.4) but not detectable on the seismic reflection data, where the salt is imaged as a single transparent body without or with limited internal reflections. Considering that our study is based on the interpretation of seismic reflection data, in this thesis we will consider the salt layers as a single body, both from the point of view of the geometry and of the salt movement.
As seen in the introduction of this subchapter, the density inversion is no longer considered the driving mechanism of salt tectonics, that is actually mostly the result of pressure differences (Gaullier, 1993), as already discussed by Jackson and Talbot (1986). Different types of forces come into play for what concerns the basin-scale deformation processes. In particular, the external forces are the gravitational force -which depends on density, size and gravity acceleration- and the pressure constraint -which depends on the differential stress applied and the body dimension (i.e. crustal tectonics), while the internal forces are the viscous and frictional ones (Ramberg, 1981). The vector sum of these forces and constrains determines the movement of the salt in terms of magnitude and direction. Nowadays, the different mechanisms of salt tectonics –despite being often copresent in nature- can be divided in:

- Salt tectonics due to gravitational loading (subchapter I.2.2.a).
- Salt tectonics due to crustal tectonics (subchapter I.2.2.b).

I.2.2.a. Salt tectonics due to gravitational loading

The movement of salt can be treated as a fluid mechanics problem, and in terms of gravitational failure the main element to consider is the **hydraulic head**, that controls the magnitude and direction of salt flow (Meinhold, 1956). Mathematically, the hydraulic head (h) can be factored in elevation head and pressure head. The **elevation head (z)** is the height of the top of the salt layer above an arbitrary reference datum chosen for the system, while the **pressure head** $(\rho_0/\rho_s)*h_N$ is the overburden density ρ_0 divided for the salt density ρ_s, and multiplied for the thickness h_n of the overburden, giving information about the overburden in terms of pressure **(Figure 1.16)** (Jackson and Hudec, 2017 and references therein; Rowan, 2020 and references therein).
Elevation head and pressure head lateral variations are responsible respectively for the gravity gliding and the gravity spreading (Vendeville, 1987; Gaullier, 1993; Vendeville, 2005; Rowan *et al*., 2012, 2020) which however can initiate movement only if these forces exceed the strength of the

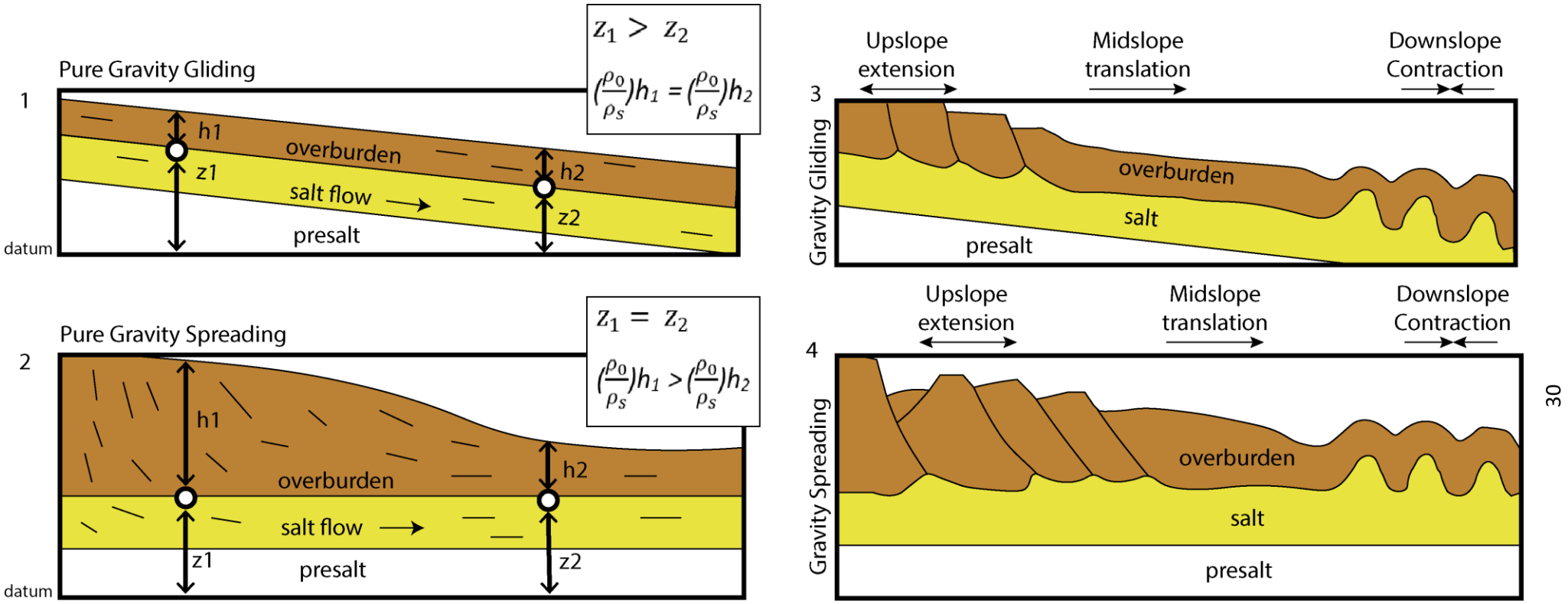

***Figure 1.16**: Theoretical model of gravity gliding and gravity spreading based on the hydraulic heads. **1.** Schematization of gravity gliding, where the driving mechanism is the elevation head (z). **2.** Schematization of gravity spreading, where the driving mechanism is the pressure head $(\rho_0/\rho_s)*h_N$. These mechanisms are independent by the density of the overburden if the density is constant. Both gravity gliding and gravity spreading mechanisms result in the formation of three domains: an upslope extension, a midslope translation, and a downslope contraction **(3. and 4.)**. Modified after Hudec and Jackson, 2007; Rowan, 2020; Vendeville, 2005.*

overburden, that resists deformation together with other forces as the viscous and frictional ones (Rowan, 2020 and references therein).
Gravity gliding and spreading, both consisting in a loss of energy potential of the system, are the end-members of a range of composite systems. Both phenomena tend to be reduced over time, due to the increase of the overburden thickness and the decrease of the salt flow with the thinning of the salt layer (Rowan, 2020).

- **Gravity Gliding**: a sedimentary body that presents at its base a layer characterized by low viscosity (i.e. a mobile layer), will slide on its basal dip under the effect of the downslope shear stress component of gravity (i.e. lateral variation of elevation head), without necessarily undergoing deformations and with a flow internal to the body in a direction **parallel to the basal slip surface** (Figure 1.16a) (Rowan *et al.,* 2012; Warren, 2006). A basal slope, that starts to be efficient for gravity gliding with a dip of less than 2°-3°, can form as a consequence of crustal tectonics and is also commonly present as the result of subsidence of the passive margins, that are consequently often characterized by this kind of deformation (Vendeville, 1987; Rowan *et al*., 2012). No bathymetric slope is required to trigger the gravity gliding process, that can in fact develop also when the bathymetric slope has a dip opposite to the direction of sediment movement (Vendeville, 1987; Rowan *et al*., 2012). Depending on the different schools of thought, gravity gliding is considered the dominant process of salt tectonics (Brun and Fort, 2011) or a process that strongly characterizes mainly the **first phase of margins evolution** because of the rifting –and consequent tilted blocks- and early thermal subsidence of oceanic crust (Rowan *et al*., 2012; Rowan, 2020). The possibility to have movement mainly depends on the dip of the top salt surface -with higher dips leading to higher probabilities of salt movement- but also on the thickness of the overburden, that decrease the probability to have movement (Rowan, 2020).

The three domains that result from the salt movement can generally be distinguished by changes in the salt structures formed and are the following (Figure 1.16.3):

- **Extensional province**: A proximal area of extensional stress field presents normal listric faults basinward dipping and resulting tilted blocks, sediment wedges, salt rollers at the foot of the listric faults and salt welds as a consequence of the movement of the salt towards the basin (Cobbold *et al*., 1989; Vendeville, 1987, 2005) (Figure 1.16.3).
- **Translational province**: The continental rise is generally characterized by midslope translation, with the salt moving towards the basin with absent or limited deformation and showing an almost tabular geometry (Vendeville, 1987) (Figure 1.16.3).
- **Downslope contractional province**: a distal region with a compressional stress field presents salt anticlines and diapirs. In this area it is often accumulated also part of the salt deposited in the upslope and midslope domains (Figure 1.16.3). The wavelength of the salt structures (e.g. salt diapirs and salt walls) depends on the thickness of the overburden, with small wavelength forming when the overburden is thin and longer wavelength resulting from thicker overburden (Rowan, 2020). This phenomenon can be seen at the scale of the seismic imaging but also in the salt outcrops (Figure 1.2). Salt minibasins are typically more developed in this province, because the flux of salt downslope inflates the diapirs separating the minibasins, creating more space for the minibasin sediments to deposit.

Due to sedimentary and tectonics factors, these domains are not always present or equally developed on the margins, especially when the margin is steep.

The influence of sedimentation on gravity gliding has been studied in detail by Vendeville (1987), that distinguished different styles of gravity gliding based on the uniformity and rate of the sedimentation **(Figure 1.17)**. An uniform sedimentation mainly results is the translation of the blocks, while a non-uniform one causes rotation of the block; slow sedimentation gives block translation if the sedimentation is uniform and rotation if it is not, while a high sedimentation rate leads to coexistence of deformation kinds.

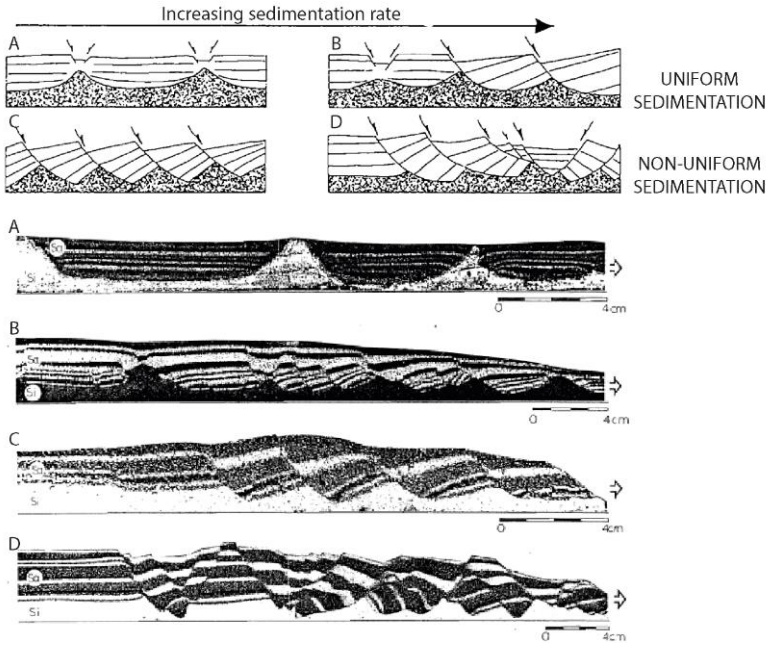

Figure 1.17. *Influence of rate and mode of sedimentation on the resulting geometries of gravity gliding (Vendeville, 1987), in a schematization (above) and in the analogue modelling (below).*
A: low sedimentation rate, uniform sedimentation.
B: high sedimentation rate, uniform sedimentation.
C: low sedimentation rate, non-uniform sedimentation.
D: high sedimentation rate, non-uniform sedimentation.

Moreover, the gravity gliding can be divided in ideal **parallel** gliding, where the particle paths are parallel straight lines, and ideal **radial** gliding -divergent (Vendeville and Cobbold, 1987) or convergent (Cobbold *et al.,* 1989)- where the margin is shaped as a circular cone and the particles paths are radii of a circle **(Figure 1.18).** The reality is actually composed of **mixed situations**, in which we find divergent gravity gliding off coastal salients and convergent gravity gliding off coastal re-entrants (Cobbold and Szatmari, 1991).

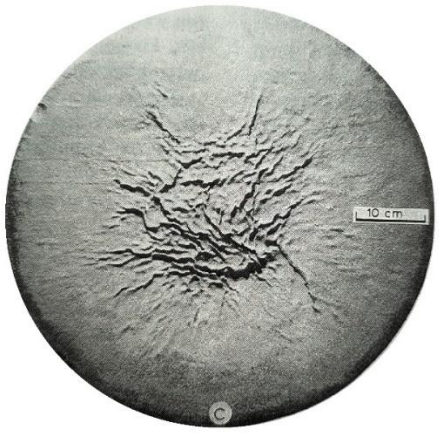

Figure 1.18: *Silicone putty of an analogue modelling, simulating the convergent gravity gliding as a result of a concentric 5° slope (Cobbold and Szatmari, 1991).*

One of the most important salt regions in terms of gravity gliding is the **West Africa** syn- to post- rift salt basin (Fgure 1.1). This basin extends from northern Namibia to southern Cameroon, and is characterised by a thick layer of salt deposited in the proto South-Atlantic during Aptian. The study of salt tectonics has been particularly detailed because of the interest for hydrocarbon exploration, considering the impact of salt movement on the shape and geographical distribution of the oil traps in the area (Duval *et al*., 1992; Spathopoulos, 1996). The analysis of salt tectonics is here facilitated by a relatively thin brittle overburden of 3 to 6 km.

After the salt deposition of the salt, the margin tilted towards the basin, resulting in a movement of gravity gliding of the salt, the overlying carbonate platform and Upper Cretaceous sedimentary sequence **(Figure 1.19)**. The brittle cover broke into blocks, and the salt deformed into salt rollers, salt diapirs etc.

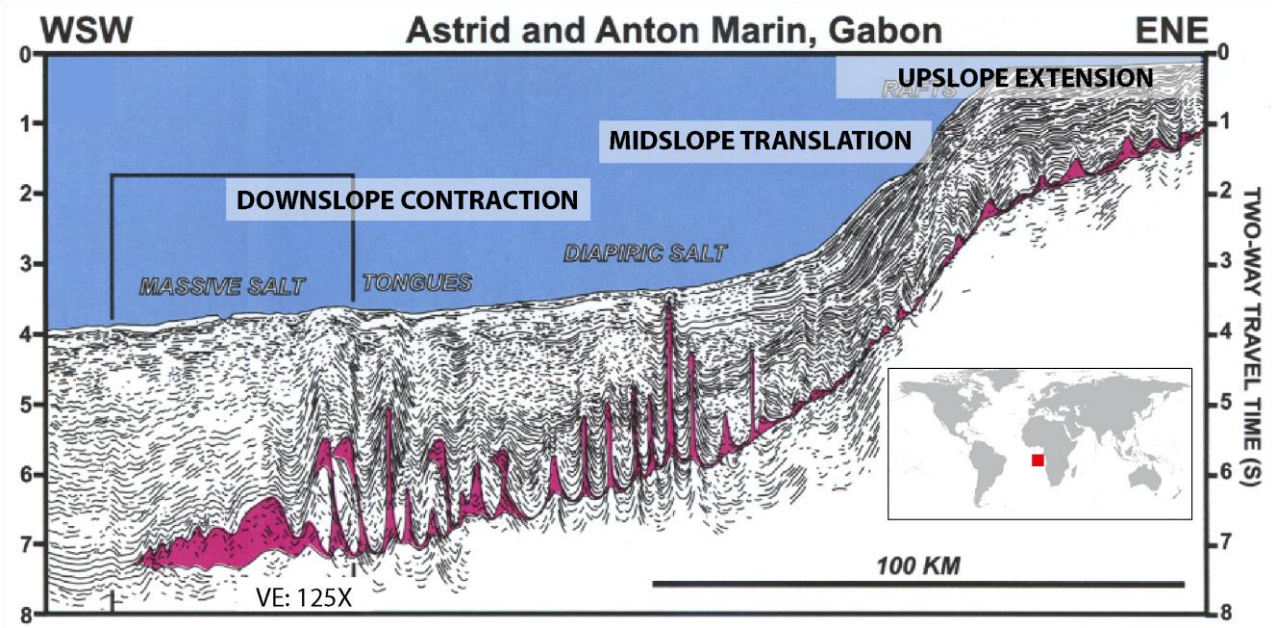

Figure 1.19: *Regional seismic profile from the Gabonese passive margin, with the post-rift salt layer interpreted in magenta and the division in extensional, translational and compressional domains (modified after Tari et al., 2003).*

- **Gravity spreading:** The differential loading (i.e. lateral variation of pressure head) on the salt is commonly the result of lateral **overburden thickness variations**, but can also result from density variations in the overburden. If we approximate to an overburden of laterally constant density, only few degrees of bathymetric slope - often present on the continental margins and favoured by high sedimentation rates - are necessary and sufficient to trigger the movement of a salt layer and the deformation of the sedimentary overburden, with a displacement direction parallel to the local slope (Figure 1.16.2). This condition is quite common when we have deep-sea fans with prograding sequences (e.g. Rhone deep-sea fan, Gaullier et al., 2008). This process thins the proximal part of the sedimentary wedge trough horizontal extension and thickens the distal part of the wedge trough horizontal shortening (Ge *et al*., 1997; Gaullier and Vendeville, 2005; Vendeville, 2005; Gaullier,2010; Rowan *et al*., 2012). As well as the direction, also the timing of spreading is controlled by regional depositional events, but in turn the bathymetric consequence of the spreading can locally influence the sediment depositional geometry (Gaullier and Vendeville, 2005). While the gravity spreading has been recently considered by some authors a process 'difficult to reconcile with geological evidence' (Brun and Fort, 2011), this has been disproved by various following publications: for Rowan *et al*. (2012) and Rowan *et al*. (2020), gravity spreading often becomes the main salt tectonics process on the margins after a first phase characterized by gravity gliding, and it generally affects the passive margins in presence of a high sedimentation rate as prograding sedimentary body in deltaic areas (e.g. Nile deep-sea fan, Ge *et al*., 1997; Vendeville, 2005; Gaullier, 2010; Loncke *et al*., 2010). In fact, the main mechanisms at the origin of the tilting

(tectonic subsidence during and after the rifting, thermal tilting) are time-limited and can not affect the older margins, so the long-lived salt tectonics is often linked to the sedimentary load (Rowan *et al*., 2012; Vendeville, 2005).

The gravity spreading mechanism is controlled by different factors, but while the shear strength of the salt is a secondary factor, the geometric and mechanical characteristics (i.e. compressional strength) of distal sediments have a relatively high influence. In fact, these sediments can act as a frontal buttress and prevent the spreading, so a thickness of the proximal overburden of 3 times the thickness of the distal one is necessary to have gravity spreading (Vendeville, 2005; Rowan *et al*., 2012;).

The same three salt-related structural domains described for gravity gliding (upslope extensional province, midslope translational province, downslope contractional province) are present also in the case of gravity spreading, and are therefore not diagnostic of the mechanism of formation (Rowan *et al*., 2012).

The gravity spreading has been studied both in 2D and in 3D **(Figure 1.20)** through analogue models of silicone and sands, respectively for the salt and the brittle overburden (Gaullier and Vendeville, 2005; Vendeville, 2005). The result of these model show that the presence of a brittle, semicircular lobe of sediments above a silicone layer leads to the formation of both radial and concentric normal faults and grabens in the brittle overburden, as well as the formation of concentric folds in front of the lobe (Gaullier and Vendeville, 2005). The thin-skinned grabens visible in the models open the space to the formation of salt ridges, and the brittle sedimentary sequence between the ridges subsides, marking the beginning of the minibasins formation. This subsidence causes the accumulation of more sediments in this bathymetric low, these last ones producing increased subsidence.

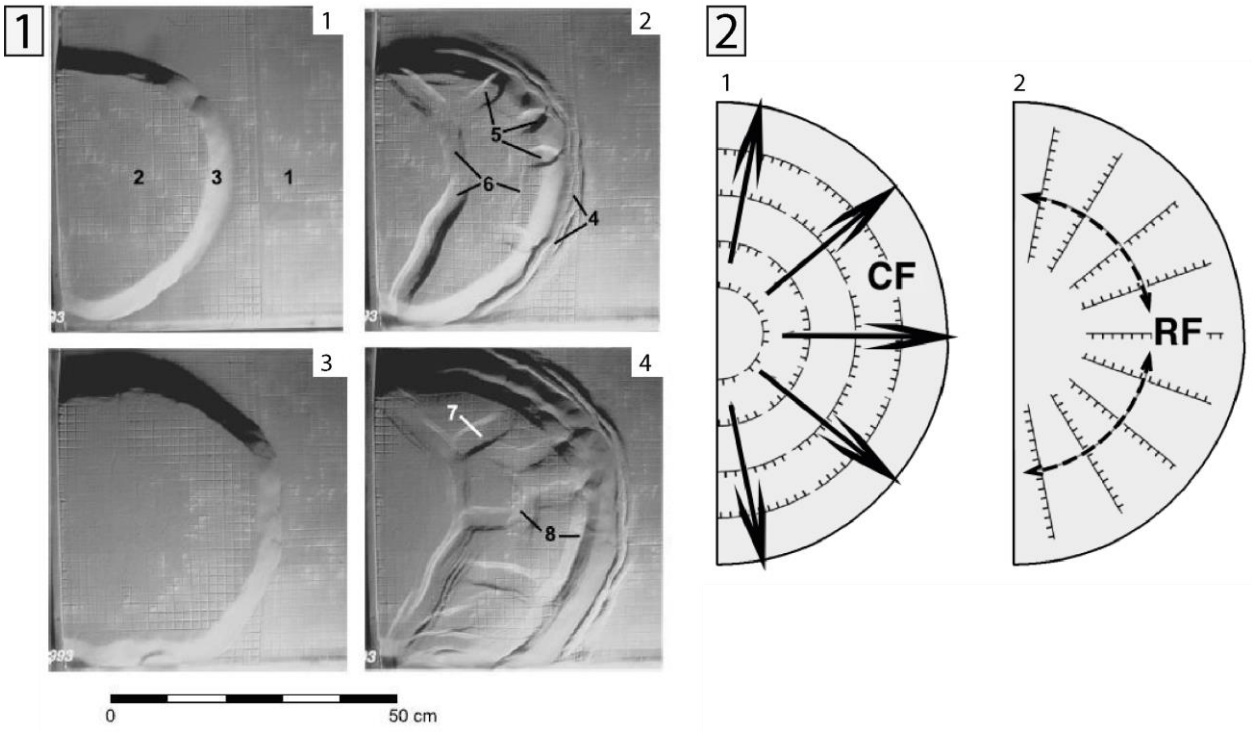

Figure 1.20: *(caption on next page)*

Figure 1.20: *Analogue modelling of gravity spreading in 3D (Gaullier and Vendeville, 2005).* ***1.*** *The presence of a brittle, semicircular lobe of sediments above a silicone layer lead to the evolution of the system thanks to the plastic behaviour of the silicone and the consequent gravity spreading. As a result of radial gravity spreading, both radial (5) and concentric (6) normal faults form in the brittle overburden, and concentric folds form in front of the lobe. Radial grabens (7) and concentric grabens (8) can be identified.* ***2.*** *The schematization in of the concentric (CF) and radial (RF) faults shows that the two tipologies of faults form due to the increase of both the radius and the perimeter.*

We described here the end members of gravity-driven failures, but in the natural examples all the intermediate cases are possible and the pure gravity gliding or spreading are rare, so it is more realistic to consider the influence and direction of both gravity gliding and spreading in a certain system, as in the case of the **Gulf of Mexico** (Figure 1.1 and **Figure 1.21**). Formed as a result of the Triassic-Early Cretaceous rifting, the Gulf of Mexico is one of the most spectacular example of gravity spreading dominated system (Rowan, 2012), thanks to the thick Jurassic salt and the many kilometers of brittle overburden. The important sedimentary input from the margin leads to the inversion of the margin tilting, with the salt base shallowing basinward (Figure 1.21.3). Despite this, salt tectonics continues vigorously thanks to the sedimentary load coming from the margin, and the main mechanism of salt tectonics is gravity spreading, with pulses of movement corresponding to the timing of depositional events (Wu, 1993; Rowan, 1999, Vendeville, 2005). The most evident of these correlations is the middle Pliocene rejuvenation of the salt bodies in the southeast Mississippi Canyon (deep-water Gulf of Mexico) (Vendeville *et al*., 2000; Rowan *et al*., 2004). A phase of gravity gliding is recognized in the earliest stages of evolution of the area, when the margin tilted basinward as a result of the differential thermal subsidence (Rowan, 1999). Nowadays in the area both authochthonous and allochthonous salt diapirs and sheets, canopies and welds are encountered (Figure 1.21.3), and very well developed minibasins can be visualized in the seafloor bathymetric data (Figure 1.21.1 and Figure 1.21.2) (Wu *et al*., 1990; Peel and Hossack, 1995).

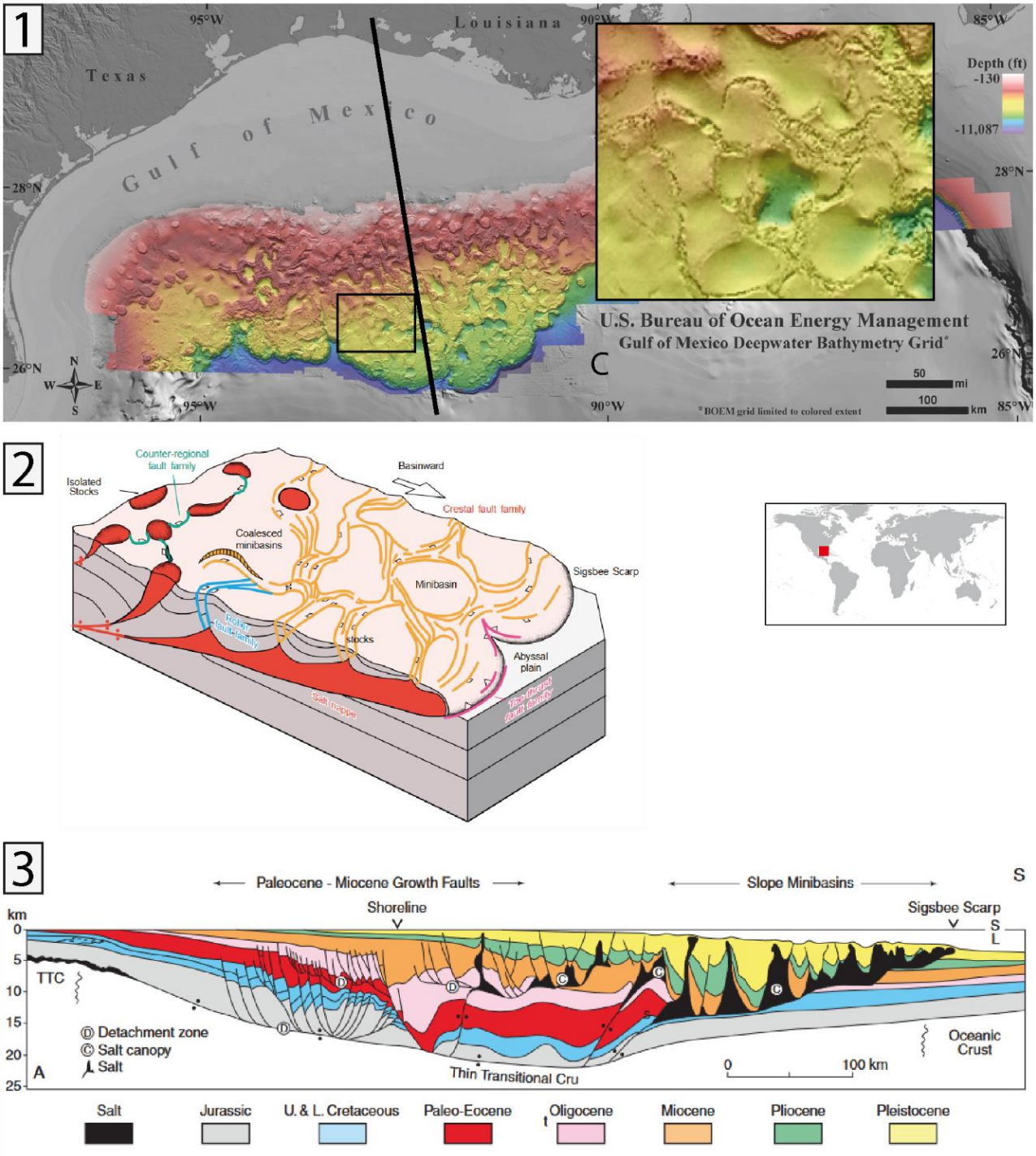

Figure 1.21: *The Gulf of Mexico.* ***1.*** *Detailed bathymetry of the Bureau of Ocean Energy Management with approximate position of Figure 1.21.3 and zoom of the minibasins geometry on the seafloor.* ***2.*** *Schematization of minibasins evolution above a salt nappe (Rowan et al., 1999).* ***3.*** *Cross-section of the northern Gulf of Mexico continental margin (Galloway, 2008).*

Salt deformation for downbuilding

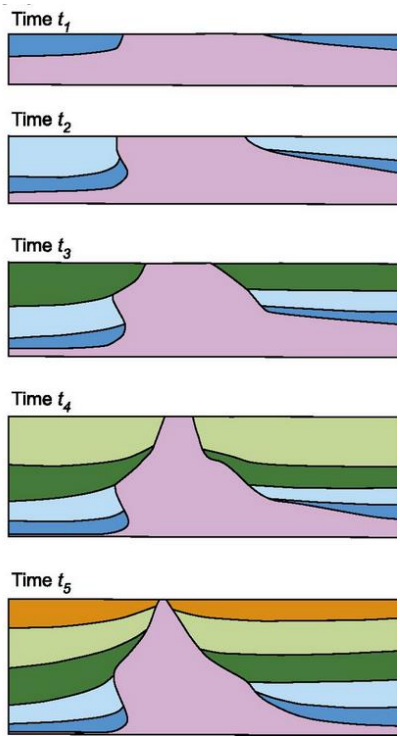

Despite the recent literature about downbuilding tends to consider it a synonym of passive diapirism (Hudec and Jackson, 2007), or even suggesting to abandon the use of this term (Rowan and Giles, 2021), we suggest that the term downbuilding should be kept to describe the early development of salt structures in areas in which there is no necessarily density inversion or crustal tectonics, and the growth of salt structures is purely the result of brittle sedimentation accumulating around a salt structure while the top of the salt structure keeps its positon at the surface **(Figure 1.22)** (Barton, 1933).

Figure 1.22: *Schematization of the evolution of a salt diapir for downbuilding (Nikolinakou et al., 2017, modified after Barton, 1933).*

I.2.2.b Salt tectonics due to crustal tectonics

Crustal tectonics is nowadays considered one of the principal causes of salt structures initiation, so the effect of contractional and extensional regimes in an area characterized by the presence of salt layers will be briefly described in this subchapter.

- **Salt tectonics in contractional settings**

The orogenic shortening of an area characterized by the presence of a salt layer form *chevauchement* structures in which salt acts as a *décollement* **(Figure 1.23)**, decoupling the stratigraphic succession involved in the compression from the underlying rock units (Davis and Engelder, 1985). The presence of a pre-kinematic salt rock during the formation of fold-and-thrusts belts results in larger and lower prims: the thicker the salt, the wider will be the orogeny, with resulting low mountain belts (Callot et al., 2022). The fold wavelength is also controlled by the thickness of the overburden, with thicker layers corresponding to longer fold wavelength (Jackson and Hudec, 2017). Moreover, early salt tectonics in the orogenic wedge becomes a structural inheritance, that influences the final shape of the orogenic wedge and becomes at a local scale the main source of heterogeneity in the deformation of the area *(Letouzey and Sherkati, 2004; Callot et al.*, 2012; Célini *et al.*, 2020). Another effect of the presence of the *décollement* is the faster propagation rate of the deformation. The contractional salt tectonics can be divided in thin-skinned (typical of the external fold belts of orogens) and thick-skinned one (typical of the internal zones of the orogens or inverted extensional basins) **(Figure 1.23.1 and 1.23.2).**

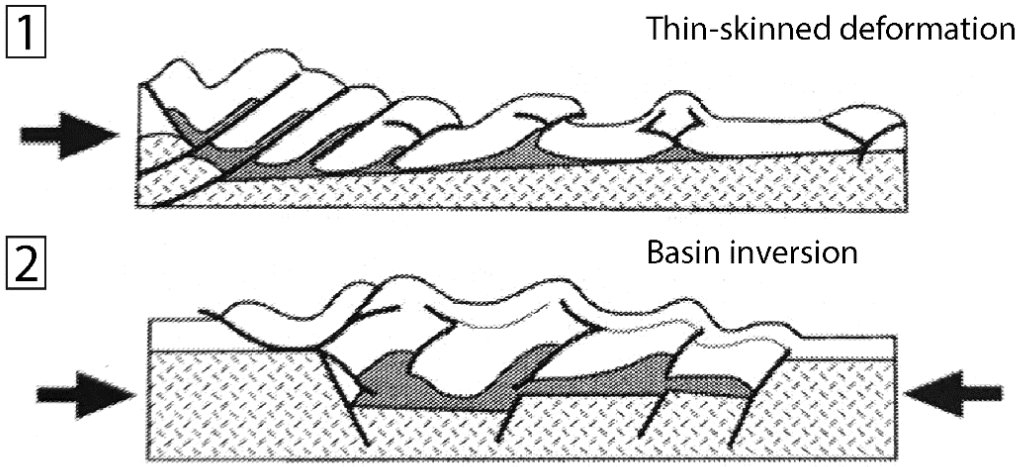

Figure 1.23: 1. *Contractional salt tectonics in the case of thin-skinned deformation and* ***.2*** *in the case of thick-skinned deformation due to basin inversion, after Letouzey et al. (1995).*

During compressional tectonics salt core anticlines can form, and if the pressure of the salt is enough and the roof of the anticline is thin enough (for early formation of the anticline or for erosion), the salt can break through the roof (Rowan, 2020). These structures are observed in mountain chains all around the world, as the Appalachian Plateau, the Franklin Mountains in northwestern Canada, the Jura of the western Alpine belt and the Pyrenees.

An example of fold-and-thrust belt affected by the presence of salt structures is in the Southwestern sub-alpine belt (position in Figure 1.1), where we can appreciate the effect of the pre-rift salt presence on the geometries of the inverted passive margin (Célini *et al*., 2020) **(Figure 1.24)**. The salt tectonics structures in the area mostly initiated during the rifting (Upper Triassic) and were active during mostly during early Jurassic, date of activity of salt walls as the La Bigue one (Figure 1.24) (Célini *et al*., 2020). The Liassic depocenters were later deformed by the Alpine orogenesis (Célini *et al*., 2020). The salt walls visible in the sections are affected by the regional compressional stress, while the effect of the compression is only slightly visible in the basins separating them (Célini *et al*., 2020).

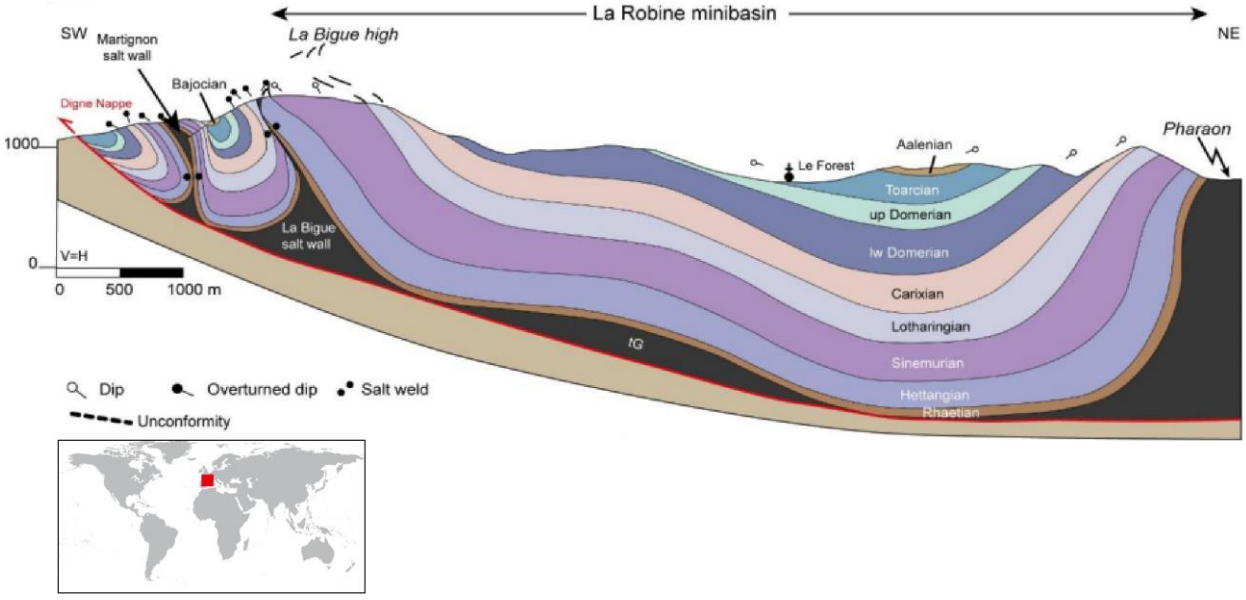

Figure 1.24: *SW-NE cross section of the Southwestern Alpine belt, showing La Robine minibasin and the compressed salt walls (Célini et al., 2020).*

Tectonic contraction is also an efficient mechanism for diapirs rejuvenation**,** because the compressional tectonics squeezes the already formed salt structures, often resulting in narrowed diapir stem eventually evolving in a vertical salt weld, as just seen in 'La Bigue salt wall' (Jackson and Hudec, 2017; Rowan, 2020) (Figure 1.24). In the case of minibasins fields, the salt absorbs the compressional stress and deforms, while the thick minibasin is stronger than the salt and maintains its general shape (Peel, 2014). The same geometries produced in the case of crustal compression are also produced in the compressional domain of salt tectonics as a result of gravity gliding or spreading (Figure 1.16).

- **Salt tectonics in extensional settings**

The presence of the *décollement* represented by the evaporitic rocks leads to different degrees of coupling between the basement, the salt and the overburden during extension. While complete coupling and complete decoupling are the extreme cases, a partial coupling is common. Regardless of the degree of connection with deep crustal structures, the extensional setting is particularly 'efficient' for the formation of salt structures, thanks to the thinning of the overburden through the formation of grabens and semi-grabens. This thinning results in a differential load on the salt, that can therefore move through three main mechanisms **(Figure 1.25)**:

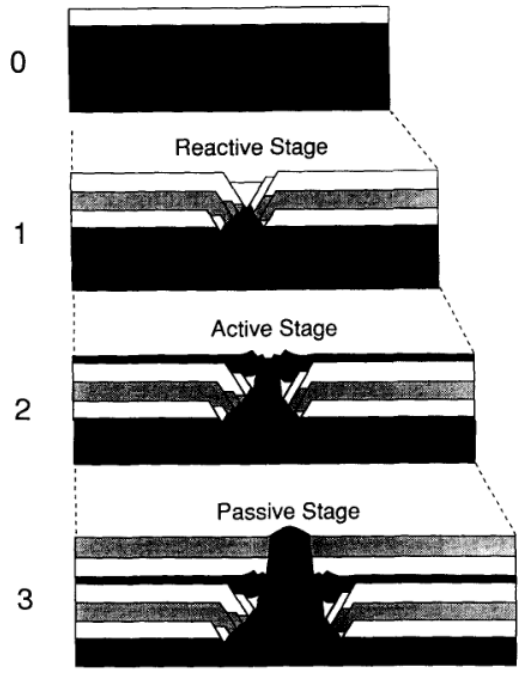

Figure 1.25: *Schematization of the phases of reactive, active and passive diapirism during thin-skinned extension (Vendeville and Jackson 1992a). From the calculation of Jackson et al. (1994), the thickness of the roof has to be <20% of the thickness of the nearby sediments flanking the diapir to initiate the salt movement.*

Reactive diapirism

In an extensional context, the formation of normal faults, grabens and half-grabens creates space in the overburden that is consequently filled by the salt (Figure 1.25 and **Figure 1.26**), regardless the presence or absence of a density inversion (Vendeville and Jackson, 1992a; Warren, 2006). When the extension stops, reactive growing of the diapirs stops (Vendeville and Jackson, 1992a).

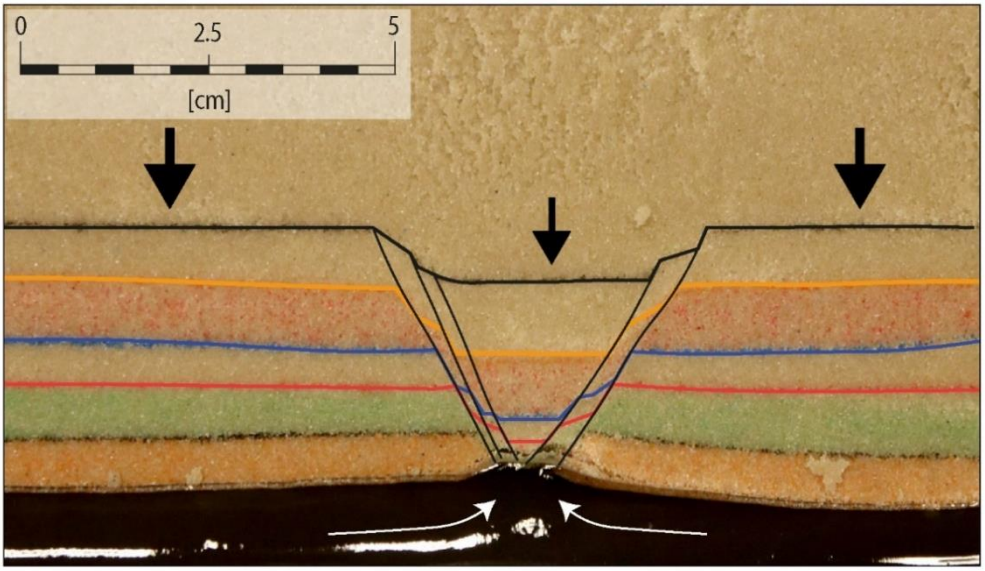

Figure 1.26: *Analogue modelling B03 (this study) with silicone and sand representing respectively the salt layer and the brittle overburden, scale 1:100'000. The dimension of the black arrows is a qualitative representation of the different pressure of the overburden on the silicone layer (black), which result in the initiation of reactive diapirism. The white arrows represent the movement of silicone in the model.*

Active diapirism

If the diapir is shallow enough (i.e. the brittle overburden is thinner than the threshold thickness), the diapir actively lifts and shove aside the overburden. This is generally the result of a **local thinning of the overburden**, due to erosion or to normal faulting (Figure 1.25 **and Figure 1.27**) or a result of the previous reactive diapirism. The density inversion can collaborate in the active growing of the salt structures but is not a key element for this mechanism, that is common also in areas where the density inversion is not present (e.g. Mediterranean Basin) (Gaullier and Vendeville, 2005; Vendeville, 2005; Warren, 2006; Jackson and Hudec, 2017). A particular kind of active diapirism is due to regional shortening.

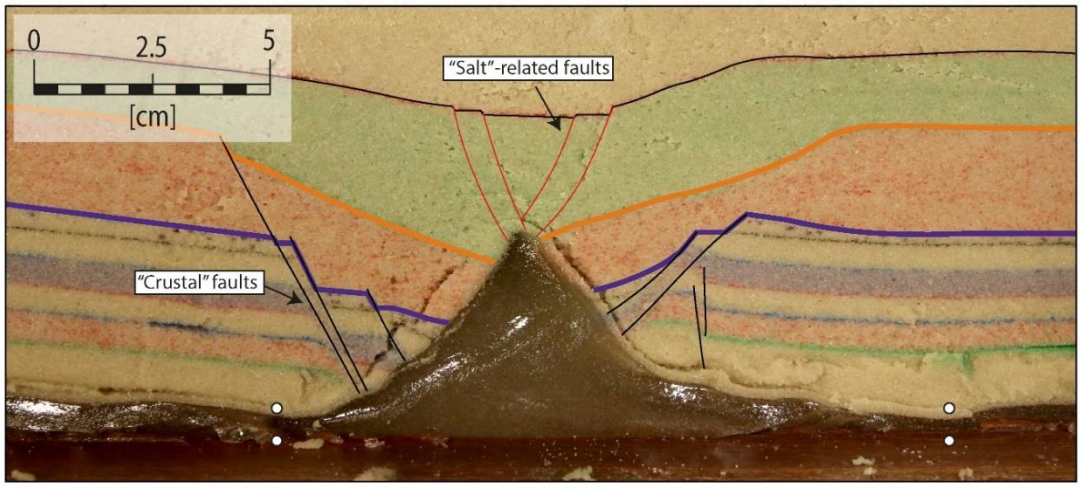

Figure 1.27: *Analogue modelling S01 (this study) with silicone and sand representing respectively the salt layer and the brittle overburden, scale 1 :100'000. The growth of the salt diapir for active diapirism leads to the formation of faults in the overburden above the diapir (i.e. keystone graben or crestal faults).*

An example of reactive and active diapirism is the Mt Sedom in the Dead Sea region (Figure 1.4). The mechanism of formation is suggested by its position inside a releasing band (i.e. extensional stress), and the reactive diairism is followed by a phase of growth for passive diapirism. The calculated Holocene rise of the diapir is 6-9 mm/y, and the same value is calculated through InSAR (Alsop *et al.*, 2015; Weinberger *et al*., 2006).

Passive diapirism

When salt reaches the surface, the surrounding sediments accumulate around it and the top of the diapir maintains its position near or at the surface, with a resulting growth defined as passive diapirism (Figure 1.25 **and 1.28**). The passive diapirism can be a phase that follows the active diapirism or the result of other phenomena as the erosion of an anticline crest (Jackson *et al*., 1994; Warren, 2006).

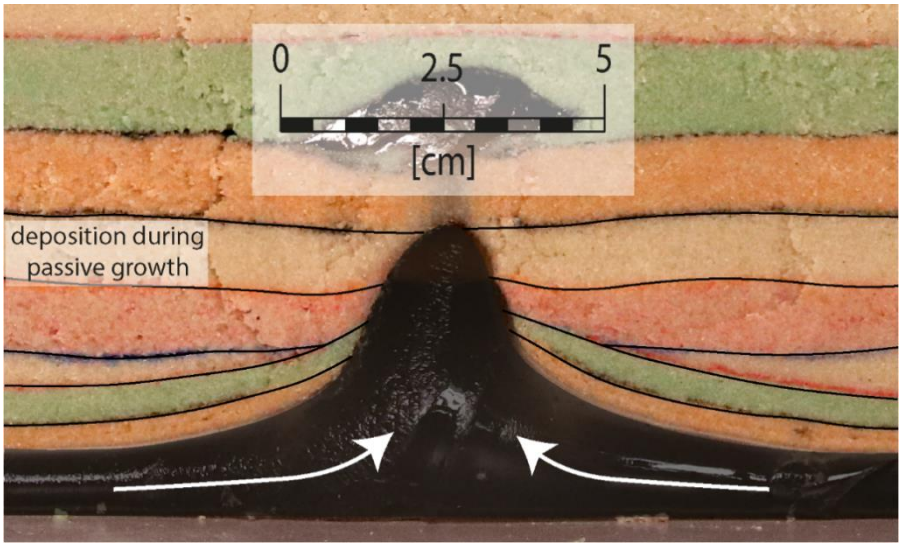

Figure 1.28: *Analogue modelling B01 (this study) with silicone and sand representing respectively the salt layer and the brittle overburden, scale 1:100'000. The white layer, crosscut by the silicone, testify the passive growth of the structure (passive diapirism).*

These three phases are not necessarely consequent, and depend by factors as extension, sedimentation rate and source layer depletion (Jackson *et al*., 1994).

Considering that the growth just described is the result of the extensional regime, the presence of salt can create the phenomenon of 'cryptic extension', in which the extensional tectonics of an area does not result in faulting because the extension is entirely absorbed by the growing salt structures (Vendeville and Jackson, 1992a; Rowan, 2020).

Fall of the salt structures: Extensional tectonics can produce the diapir rise, but it can also lead the diapir to fall if the salt supply is restricted **(Figure 1.29)** (Vendeville and Jackson, 1992b). In this situation, the top of the diapir becomes an area of subsidence and deposition through the formation of new depocentres (Figure 1.29) (Vendeville and Jackson, 1992b), and this can evolve in a mock-turtle anticline if the flanks of the depocentre roll over (Figure 1.29.E). A diapir that has undergone fall will show some particular geometries, notably the presence of salt horns (salt indentations) which represent a high-water mark of the original position of the salt.

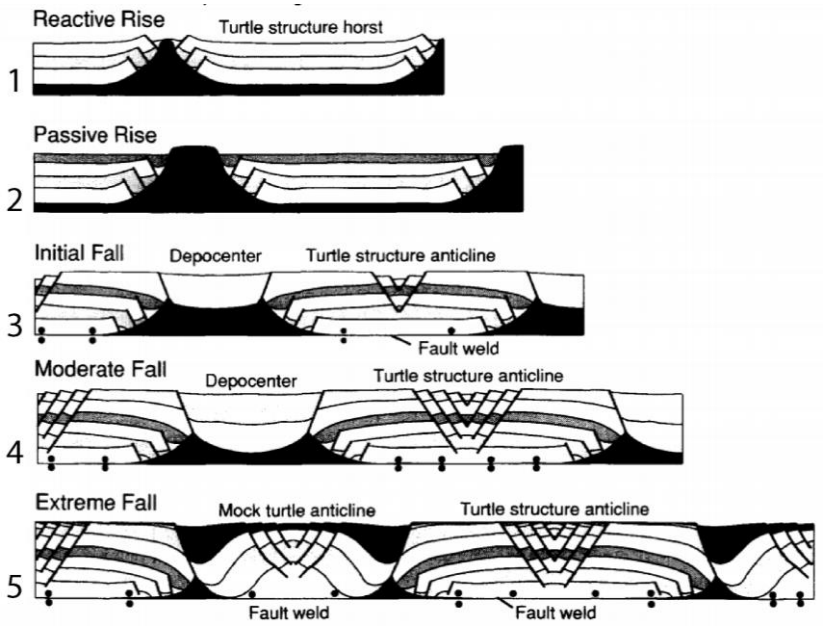

Figure 1.29: *Schematic rise and fall of diapirs during sedimentation (Vendeville and Jackson, 1992b).* ***1.*** *Regional extension during the reactive rise of diapirs.* ***2.*** *Passive rise of the salt structur.* ***3. to 5.*** *Initiation and progression of the salt structures fall, up to the formation of the mock-turtle anticline (5).*

The example of the **Central North Sea** (Figure 1.1 and **Figure 1.30**) is particular from the point of view of salt tectonics because here the phenomena of **extensional and compressional salt tectonics are co-present**.

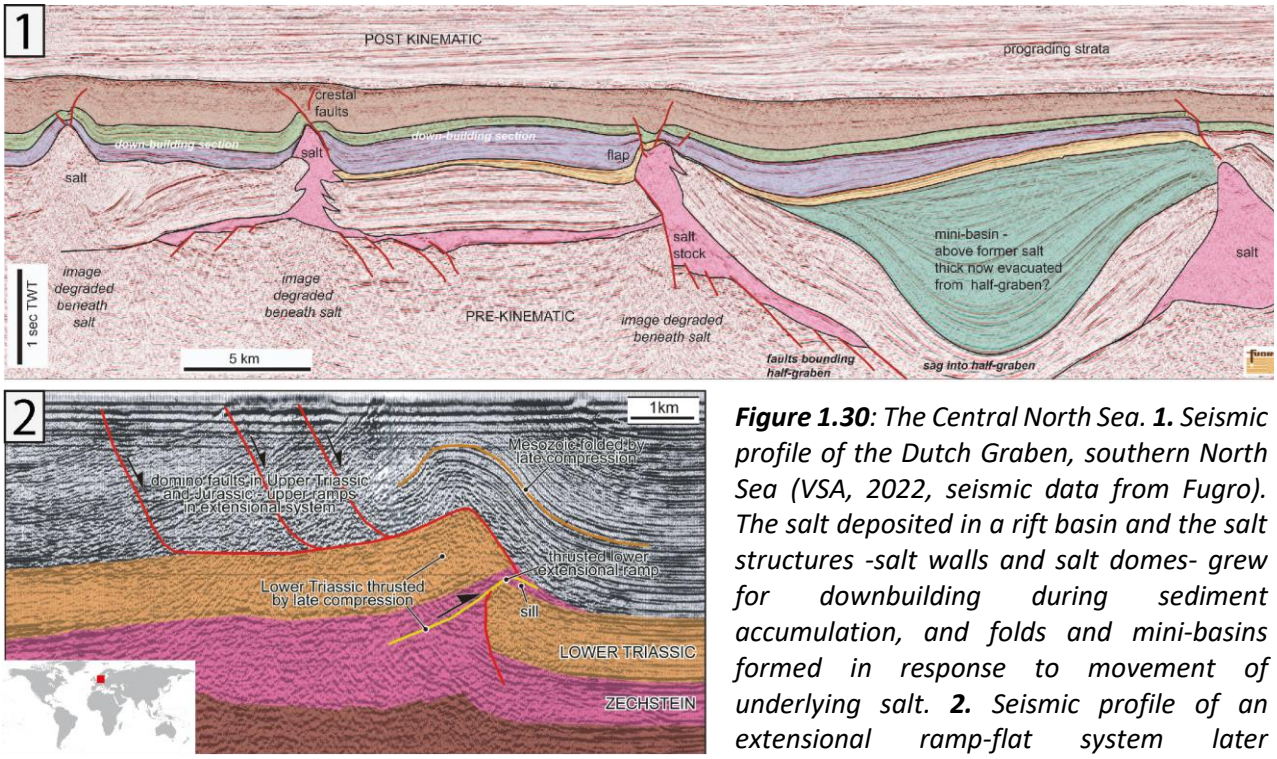

Figure 1.30*: The Central North Sea.* ***1.*** *Seismic profile of the Dutch Graben, southern North Sea (VSA, 2022, seismic data from Fugro). The salt deposited in a rift basin and the salt structures -salt walls and salt domes- grew for downbuilding during sediment accumulation, and folds and mini-basins formed in response to movement of underlying salt.* ***2.*** *Seismic profile of an extensional ramp-flat system later compressed (Stewart, 2007).*

During early Permian a sag basin -reaching a depth of 200-300 m below sea level- formed in this area, and during Late Permian the Arctic waters flooded the basin creating the Zechstein Sea. This sea covered vast areas in the northern and central Europe, and two salt giants deposited in two separate basins reaching around 1 km of salt thickness in the basin center. The salt deposition stopped as a consequence of a global low stand towards the end of the Permian, that stopped the water influx. The Permian Zechstein salt deformed mostly as a consequence of crustal tectonics: in

fact, with the beginning of the opening of the North Atlantic Ocean intense rifting interested the area during Triassic-mid Jurassic. The results are firstly thick-skinned reactive diapirism in the Central graben, and then, later in the Triassic, thick-skinned salt tectonics (Nalpas et al., 1995; Stewart, 2007). Despite the rifting ended in the mid-Cretaceous, the North Sea Zechstein salt has 2 different steps of deformation during Mesozoic to Tertiary, due to the Alpine Orogeny (i.e. the reactivation in compression) (Figure 1.30.2) (Ziegler et al., 1982). The thickness of salt in the area is not sufficient to form salt canopies, but the area presents massive diapirs and salt sills from the intrusion of the Permian salt along Triassic salt in the southern North Sea (Stewart, 2007) (Figure 1.30.1).

As well as for the compressional salt tectonics, the geometries formed for crustal extensional can be found in the extensional domain of salt tectonics due to gravity gliding or spreading.

Chapter II: DATA AND METHODS

In this chapter will be illustrated some key concepts about the geophysical data used in this work, with the principles of the seismic reflection and swath bathymetric methods and the potential fields method. Will then be listed the main characteristics of the dataset for each of the three study areas, followed by an explanation about the interpretation criteria and techniques, and the particularity of salt structures in terms of seismic data interpretation. An introduction on analogue modelling of salt tectonics will conclude the chapter.

II.1. Introduction on seismic reflection and swath bathymetry methods

Among the numerous geophysical methods available nowadays, the seismic reflection method is the most commonly used to image the subsurface due to its high resolution. This method uses reflected elastic waves, applying the principles of seismology but using an active source, to map the changes in acoustic impedance of the subsoil and consequently obtain information about the layers constituting it (Badley, 1987; Yilmaz, 2001; Dentith and Mudge, 2014). The importance of the seismic reflection method for the oil industry, especially offshore, has always been a great opportunity also for research, thanks to the significant amount of resources that oil companies have invested in this geophysical method and the consequent fast improvement of both acquisition and processing tools and interpretation software. The characteristics of the seismic reflection data we interpret are strictly dependent on acquisition methods and parameters (e.g. frequency of the source) and processing sequence, so the first part of this chapter will give an overview on these topics.

Another geophysical method which proved to be very important for this thesis is the multibeam (or swath) bathymetric data acquisition, providing a 3D image of the seabed thanks to high frequency acoustic waves, which do not penetrate the subsoil. This data becomes particularly interesting when studying recent geological events, that therefore deform the seafloor.

II.1.1. The seismic reflection method

The **seismic reflection method (Figure 2.1)** is a form of echo-sounding, in which an energy source generates a sound pulse (P-wave) that penetrates up to many tens of kilometers in the subsoil. As an effect of the discontinuity in the elastic properties of the material (densities and P-waves velocities), the wavelet created by the source changes its direction for diffraction, reflection or refraction, and a percentage of the energy reaches the detectors which register this echo with time and spatial information (Dentith and Mudge, 2014).
In the case of the offshore acquisition, the echoes are recorded by hydrophones located at regular intervals on the streamer, which is constituted by a flexible tube filled with oil in order to create neutral buoyancy (Dentith and Mudge, 2014; Yilmaz, 2001). Depending on the acquisition material, we obtain single-channel data (when we use a single detector for the reflected waves) or multichannel data (when multiple detectors register the reflected waves in different locations).

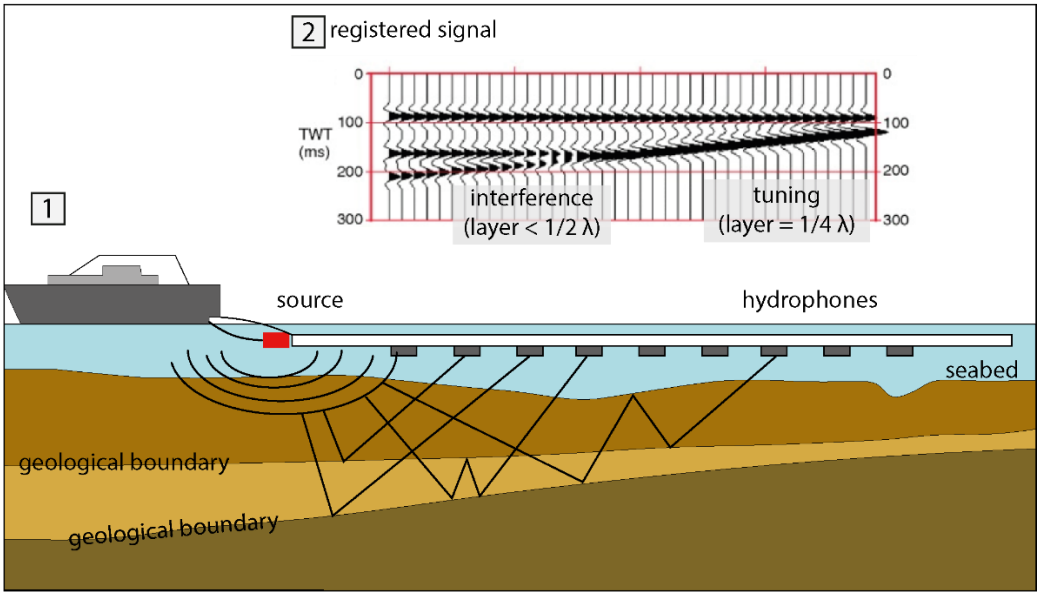

Figure 2.1: 1. *Schematized image of the seismic reflection acquisition offshore.* ***2.*** *Raypaths examples and resulting oscillographic trace showing the effects of interference and tuning* ***(.2)****. After Verma (1986) and Ashcroft (2011).*

The **two-way travel time,** the time necessary for the seismic wave to travel from the source to a reflector and back to a receiver, depends on the relative position of the objects and on the seismic velocity of the crossed layers. Therefore, from the processing of the seismic reflection data can be defined not only the geometry of the strata but also information concerning the velocities and consequently some petrophysical characteristics. The velocities obtained through seismic processing are not punctual absolute velocities, but depend on the layers on which is calculated (e.g. interval velocity) or the raypath through the different subsurface layers (e.g. Root Mean Square velocity).

II.1.2. The seismic wavelet characteristics

While the term seismic wave is commonly used, the seismic reflection method is actually based on wavelets, i.e. the result of the interference of waves of different amplitude, frequency and phase (Dentith and Mudge, 2014). As a result, the seismic signal will have a range of frequency (bandwidth), with a dominant frequency and wavelength.

The **amplitude** of the seismic wavelet depends on the source of the seismic wave, the impedance contrast of the reflectors and a series of factors attenuating the seismic wave during its propagation. The **amplitude** of the normal reflection (90°) of the seismic wave on a certain geological surface is determined by the contrast in acoustic impedance (ρ*v) across the surface. In fact, the reflection coefficient R at the interface between layer 1 and 2 is defined as

$$R = \frac{(\rho_2 V_2 - \rho_1 V_1)}{(\rho_2 V_2 + \rho_1 V_1)}$$

with ρ_1, ρ_2 being the density of medium 1 and 2 and V_1, V_2 being the velocity of the two media. The resulting reflection coefficient value ranges between -1 and +1, with negative values producing a reflection with negative polarity (e.g. the base of the halite layer in the Mediterranean Basin) (Ashcroft, 2011; Badley, 1987). Due to the wider range of variability of this parameter, we can simplify considering the reflection coefficient as mainly dependent on the velocity. As a general rule, acoustic impedance increases with the compaction of the rocks typical of increasing depth values, but at the same time the acoustic impedance contrast between rocks becomes smaller and smaller making the reflection weaker (Badley, 1987). A change in lithology that does not lead to a change in acoustic impedance will not produce a reflection and therefore will not be detectable with the seismic reflection method. The amplitude of the seismic wave is partly modified during seismic processing mostly by applying a gain filter.

The **velocity** of the wave propagation depends on the rock in which the wave is traveling, so it can be considered as a property of the medium. In a general case the medium is anisotropic and the velocity varies both vertically and laterally, but it tends to increase with depth because of the porosity reduction with compaction. The value of the velocity can be measured through acoustic logs, laboratory tests and vertical profiles or can be derived from velocity analysis during seismic processing. The formula for the velocity of the P waves is the following:

$$v_p = \sqrt{\frac{k + \frac{4\mu}{3}}{\rho}} = \sqrt{\frac{\lambda + 2\mu}{\rho}}$$

k = Bulk modulus
μ = Shear modulus
ρ = density
λ = Lame's lambda constant

$$\lambda = k - \frac{2}{3}\mu$$

As we can see, the value of v_p depends from different parameters. A larger value of the Bulk modulus (k) represents a material with low compressibility values, while the Shear modulus (μ) describes the resistance to shear, and the v_P is directly proportional to both these moduli. Conversely, in the formula there is an inverse proportionality between velocity and density, but when we consider a velocity-versus-density graphic **(Figure 2.2)** there is a clear direct proportionality; this is possible just because strength controls the velocity, and rocks with higher strength are generally the denser ones (Ashcroft, 2011). In the case of evaporites, a relatively low value of density of the rock correspond to high velocities.

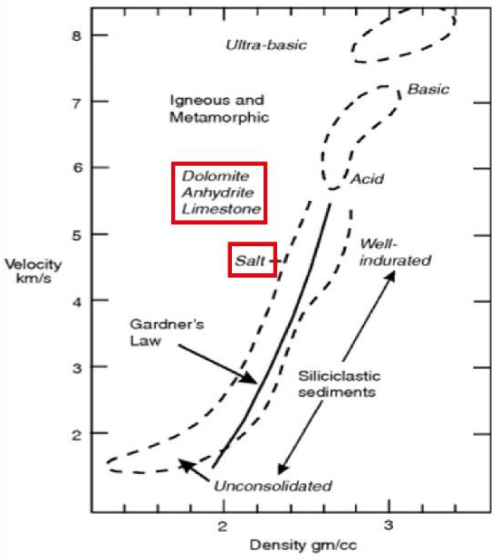

Figure 2.2: *Relationship between velocity of the seismic signal (km/s) and density of the geological material (g/cc). Evaporitic materials as salt, dolomites and anhydrites do not follow the main trend, and have high velocity compared to their relatively low density (Ashcroft, 2011).*

Higher temperatures, higher pressures and solid phases will produce a higher velocity, while the presence of pore fluid pressure causes a decreasing in the seismic velocity because of the decreasing of the inter-grain forces. Moreover,

many other parameters like grain bonding and composition have to be considered, so the evaporite minerals, having a generally low density, present high seismic velocities **(Table 2.1)**.

Mineral	Composition	Hardness	Density ($kg\,m^{-3}$)	Seismic velocity (ms^{-1})
Halite	$NaCl$	2.5	2200	4500
Gypsum	$CaSO_4 \cdot 2H_2O$	1.5–2	2300	5700
Anhydrite	$CaSO_4$	3.5	2900	6500
Tachydrite	$CaMg_2Cl_6 \cdot 12H_2O$	2	1660	3500
Sylvite	KCl	1.5–2	1990	4110
Carnallite	$KMgCl_3 \cdot 6(H_2O)$	2.5	1600	3900
Kieserite	$MgSO_4 \cdot H_2O$	3.5	2550	?
Langbeinite	$K_2SO_4 \cdot 2H_2O$	3.5–4	2820	5860
Polyhalite	$K_2SO_4 \cdot MgSO_4 \cdot 2CaSO_4 \cdot 2H_2O$	2.5–3.5	2790	5300
Dolomite	$CaCO_3 \cdot MgCO_3$	3.5–4	2870	6300

Table 2.1: *Physical properties of main evaporitic minerals (Jones and Davison, 2014).*

The **frequency of the seismic signal** is defined as the number of times a wavelet repeats per second, and it is measured in Hertz (Hz) or s/λ (ms) (Badley, 1987). The frequency has to be considered when we evaluate a seismic signal because it controls both the penetration capacity of the signal and the resolution of the data, fundamental in giving us an idea of how deep will be the subsoil imaged and what is the smaller structure that can be detected and/or resolved (Ashcroft, 2011).

The **vertical resolution** of seismic data determines how thick must be a unit to be resolved by the seismic signal (Badley, 1987). To be properly visualized in the data, a layer must be thicker than ½ wavelength, while smaller layers produce interference (Figure 2.1). The maximum interference is produced by a layer thickness of ¼ wavelength, which produce tuning (Figure 2.1) (Widess, 1973; Badley, 1987). Despite the fact that commonly used formulas to calculate the resolution are just based on the frequency content of the signal, wavelets with the same bandwidth but different shapes and consequent different side lobe energy resolve differently the same horizon (Koefoed, 1981; Simm and Bacon, 2014 and references therein).

The **horizontal resolution** is defined by the dimension of the Fresnel Zone **(Figure 2.3)**. Inside the Fresnel zone, arrival times differ by less than half a period from the first break, so most of the energy of a reflection is returned and the waves that interfere constructively will be detected as a single arrival. Subsurface features smaller than the Fresnel zone usually cannot be detected using seismic waves (Ashcroft, 2011; Badley, 1987).

As we can see from the following formula, the dimensions of the Inner Fresnel Zone (Df) are directly proportional to the wavelength (λ) and the average velocity (v), and inversely proportional to the frequency (f), meaning that geological material with higher seismic wave velocity will have lower horizontal resolution while a higher frequency of the seismic wavelet gives a higher horizontal resolution.

$$\boldsymbol{Df = \sqrt{d * \lambda}} = \sqrt{\frac{\boldsymbol{d * v}}{\boldsymbol{f}}}$$

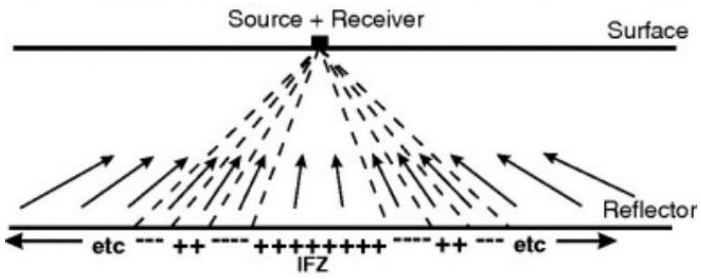

***Figure 2.3**: The IFZ (Inner Fresnel zone) here schematized represents the bigger zone of reinforcement (+) of the seismic signal. Zone marked by '-' are the areas of cancellation of the signal (Ashcroft, 2011).*

In order to have the higher vertical and lateral resolutions, the ideal seismic signal is a spike-like impulse with high energy and an infinitely extended frequency spectrum, called white spectrum for the analogy with the spectrum of the white light **(Figure 2.4)**. In fact, wider is the bandwidth in the frequency domain, sharper is the wavelet in the time domain, and consequently higher the resolution (Dentith and Mudge, 2014; Yilmaz, 2001).

Nowadays all the processing techniques use as an input a digitalized signal, so the old seismic sections have been digitalized. During the digitalization of old seismic lines, as well as during the recording of seismic signal in the acquisition process, it is necessary to consider the **Nyquist frequency** (f_N), the highest frequency that is correctly recorded with a certain frequency of sampling (f_s). The value of the frequency of sampling must be at least two times the Nyquist frequency.

Nyquist frequency $\boldsymbol{f_N = \frac{1}{2\Delta t}}$

For example, with a sampling period of 4 ms the sampling frequency is ¼, i.e. 250 Hz and the Nyquist frequency is consequently 125 Hz. If this simple rule is not respected the signal will contain alias signal so in order to avoid this problem the signal is generally cut by an 'anti-alias' filter.

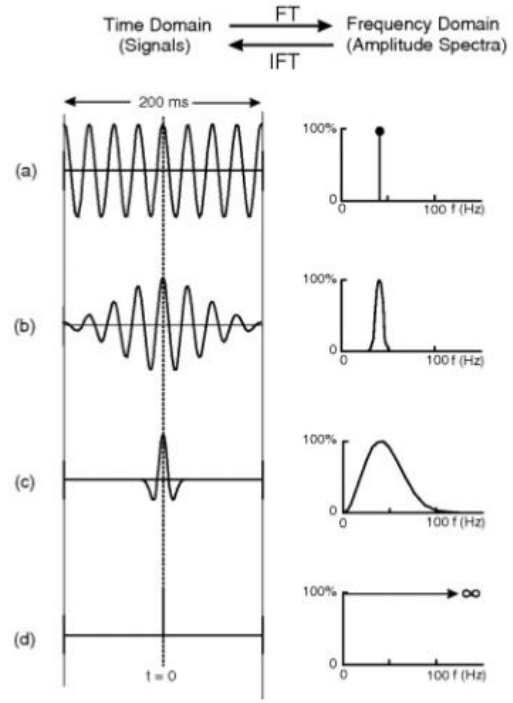

***Figure 2.4:** Time and frequency domains can be considered complementary, so if one domain is compressed, the other one is extended. The wavelet c) can be considered a standard one, while d) is the ideal spike with white frequency spectrum (from* Ashcroft, 2011).

Seismic signal attenuation

From the moment the seismic wave is produced by the source, the **attenuation** of the wave energy starts, with a decrease in the amplitude and frequency content and a change in the shape (Yilmaz, 2001; Dentith and Mudge, 2014). There are many factors that contribute to the attenuation of a P-wave, but the most important in terms of magnitude are:

1. Geometrical spreading/spherical spreading: the enlarging of the wavefront causes a fall off of the amplitude initially as the inverse of the square distance from the source and after as the

inverse of the distance from the source. This attenuation decreases the amplitude but has no effect on the shape of the wavelet (Yilmaz, 2001; Dentith and Mudge, 2014).

2. Being the behavior of the rocks not perfectly elastic, there is a dissipation of the seismic energy due to **inelastic deformation**, mostly friction and cracks. This process is called **absorption**, and is frequency depending as it attenuates with an exponential trend mainly high frequencies (loss of bandwidth) with production of heat (Yilmaz, 2001; Dentith and Mudge, 2014).
The fact that the higher frequency content of the waves is attenuated faster than the lower frequencies leads to a poorer resolution with depth (Badley, 1987).

Seismic signal disturbance

Every signal that is recorded but has not been originated by a geological object, and is therefore a disturbance or an unwanted information, is classified as **noise** (Dentith and Mudge, 2014; Mukherjee and Misra, 2017). The noise can be related to the seismic source (e.g. air wave, cable noise, 50-60 Hz power lines noise, multiples) or can be random (e.g. wind and wave motion, electrical noise of the recording instruments). Most of the random noise can be attenuated during the processing phase, applying some filters with the purpose to cut particular frequencies range related to a certain disturbance, e.g. a low-cut filter to remove the ~5-20 Hz wave noise (Yilmaz, 2001; Dentith and Mudge, 2014; Mukherjee and Misra, 2017).

One of the main disturbances of the seismic sections is the presence of **multiple** reflections, due to the repeated reflection of the seismic wave with a time delay equal to the time thickness in which the seismic wave 'bounces' (Badley, 1987; Ashcroft, 2011). As schematized in **Figure 2.5**, surface multiple, ghosting, water reverberation and the short-path peg-leg multiple are the main pathways that originate multiple reflections (Yilmaz, 2001). The surface multiple is the one with the highest reflection coefficients, but at the same time the easiest to recognize because of its characteristics. In fact, it has a reflection time and a dip of two times the one of the surface that generates it, and a reverse polarity. This kind of multiple reflection is a problem mainly in shallow water, where reverberation can partly or completely cover the main signal.

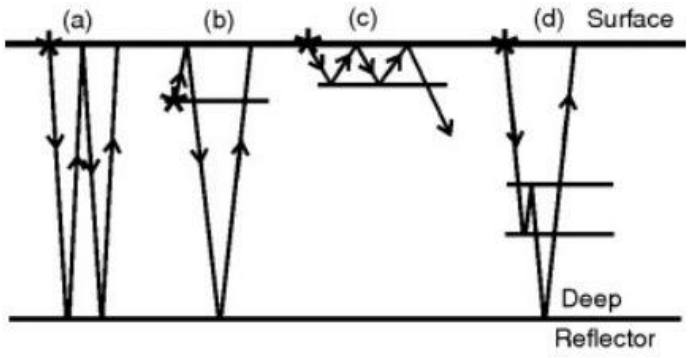

Figure 2.5: *Multiples are secondary reflections that can have interbed or intrabed raypath. a) surface multiple b) ghosting c) water reverberation d) peg-leg multiple (from Ashcroft, 2011).*

The diffraction is another main disturbance in the seismic signal and is due to the scattering of the seismic wave on a sharp interface. Its attenuation is carried out through seismic data processing (Badley, 1987), but the possibility to remove this disturbance is strongly related to the quality of the data.

II.1.3. Seismic data processing

A fundamental step between seismic data acquisition and its interpretation is the processing of the seismic data, aimed both at solving issues as the multiples and diffraction hyperboles ones and at enhancing the quality of the seismic signal. Despite the processing is a complex and time consuming technique, we can synthetize the principal operations as follows (Yilmaz, 2001; Ashcroft, 2011):

- **Pre-processing**: This phase, that prepares the raw data for the seismic processing, mainly consists of data format conversions and quality control.
- **Stacking**: The stacking of the seismic signal consists in summing the single traces, attenuating the random noise and therefore improving the signal-to-noise ratio. The evaluation of the best stacking results is one of the methods to obtain the velocity of the seismic waves (i.e. stacked velocities).
- **Deconvolution** or inverse filtering: this operation aims at removing the effect on the wave of its passage through the subsoil (the "Earth filter" effect), the multiple reflections or any disturbance related to the acquisition system. The common result is a compressed, zero-phase wavelet, therefore a higher temporal resolution of the seismic reflection data. It can be repeated at different steps during the processing (Dentith and Mudge, 2014; Yilmaz, 2001).
- **Migration**: the process of migration consists in moving (migrating) all the components of the traces to their 'real' position. This is particularly important for the inclined reflectors and for the folded one, for the effects of reflector's pull-up or pull-down, and for the diffractions **(Figure 2.6)**. The migration can be a time or a depth migration, this last one giving as a result the vertical axis in space instead of in time.

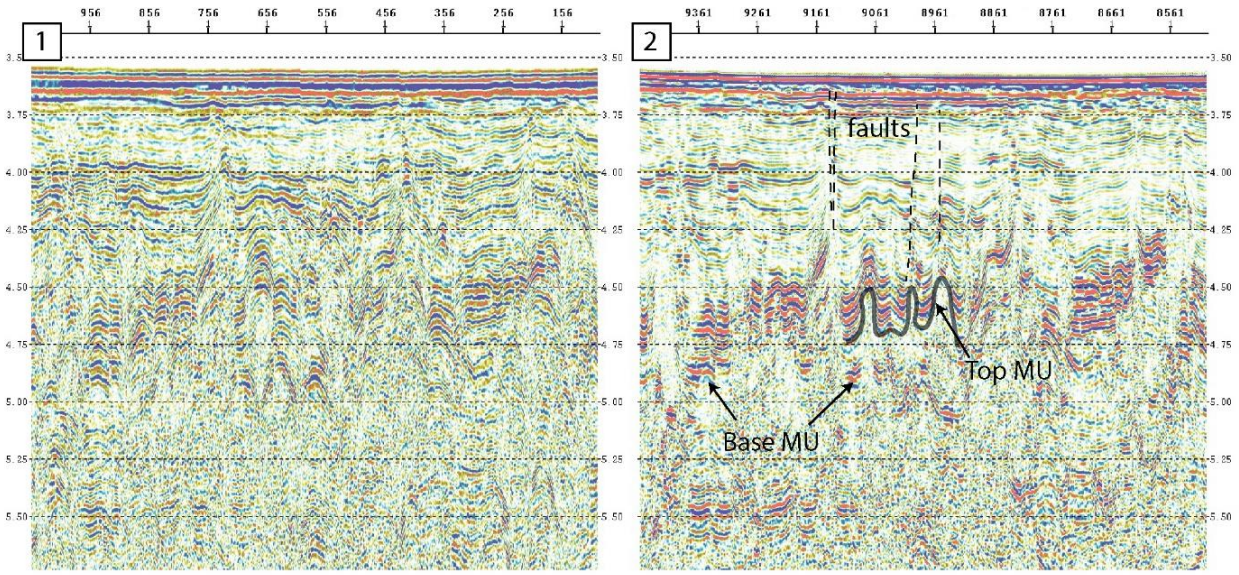

Figure 2.6: *Comparison between seismic data pre and post PSTM (Pre-Stack Time Migration).* ***1.*** *In the pre-processing the imaging of the salt is challenging.* ***2.*** *The migration removed the ringing and improved the imaging of the faults and the base salt, and the continuity of the deeper reflectors (5.5 s TWT).*

These different steps described do not necessarily follow the order of the above list, and depend on the data (2D, 3D, quality) and the characteristics of the area. For example, a pre-stack time migration is often applied in case of 2D seismic datasets in areas affected by salt tectonics **(Figure 2.6.2)**.

II.1.4. The multibeam bathymetry

While the seismic reflection method gives information about the subsoil, the multibeam bathymetry provides a detailed image of the seabed. Multibeam echosounders are composed of a transmitting antenna parallel to the vessel direction and a receiving antenna perpendicular to the vessel direction. The first one emits a **fan of narrow acoustic beams** with several tens to hundreds of kHz frequencies, while the second one receives the signal after its reflection on the seafloor **(Figure 2.7).** The interaction between the transmitted beams and the receiving antenna beam position allows to image a narrow section of the seafloor, obtaining the **time delay (depth) and intensity of the signal (back-scattering imagery),** i.e. both the depth and 3D geometries of the seafloor, and information about the nature of the sediments at the seafloor. The dimension of the area imaged by the instruments depends both on the instrument characteristics and on the distance between the instrument and the target, i.e. the water depth, and can reach tens of kilometers (Hughes Clarke, 2018). Considering that the resolution of the acquired data is inversely proportional to the distance between signal beams, the resolution will be higher when the seafloor is shallower and a smaller portion of the seafloor is imaged. The multibeam bathymetry method becomes really important in areas in which the tectonics –salt or crustal one- is still active and deforms the seafloor, allowing to extend in 3D the structures interpreted in the seismic reflection data.

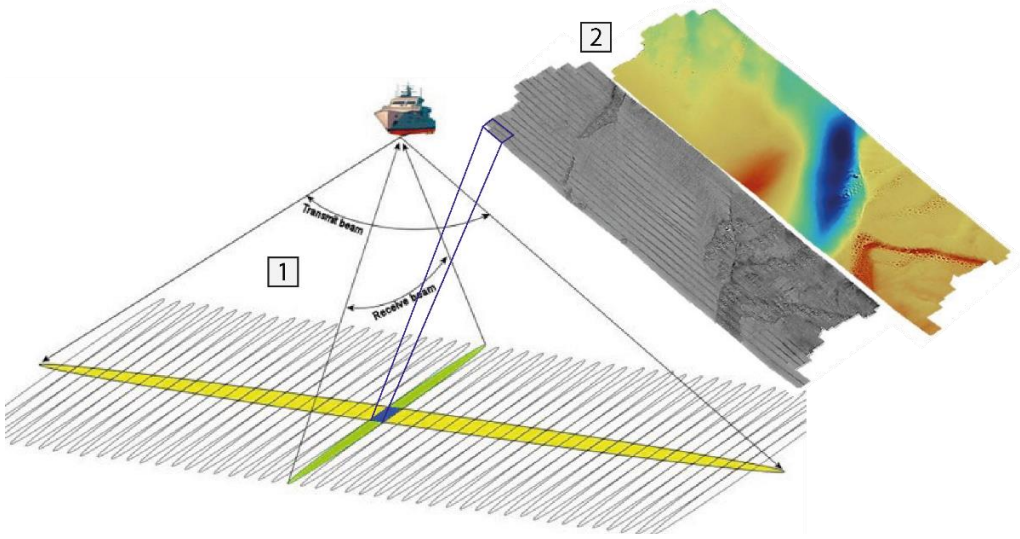

Figure 2.7*: Schematization of the multibeam echosounder acquisition.* ***1.*** *The intersection between the transmit and the receive beams represents the area imaged by the instrument (blue rectangle) (Zwolak, 2015).* ***2.*** *Both the intensity of the signal, i.e. backscatter imagery (on the left), and the time delay, i.e. the bathymetry (right) are registered (https://www.flotteoceanographique.fr).*

II.2. Introduction on gravity and magnetic potential methods

The variations of the gravimetric and magnetic potential fields are due respectively to variations in density and magnetism of the rocks, giving information about the geology of the subsurface (Dentith and Mudge, 2014). These two methods are relatively inexpensive compared to the seismic reflection data acquisition, and constitute an important source of constrains for the seismic interpretation.

II.2.1. Gravity method

A body presenting a positive **density contrast** compared to the surrounding material results in an excess of mass and a positive **gravity anomaly** in a sedimentary sequence (e.g. a basement high), while a lower density body produces a mass deficiency and consequent negative gravity anomaly (e.g. salt diapirs below the density cross-over depth) (Nettleton, 1971; Lines and Newrick, 2004; Dentith and Mudge, 2014). Considering the complexity of the subsoil and the co-presence of different bodies influencing the resulting potential field, this one will be the vector sum of the single fields (Nettleton, 1971). The base for the calculation of gravity anomalies on Earth is the **geoid**, which corresponds to the gravity equipotential surface of the Earth (Dentith and Mudge, 2014) **(Figure 2.8 and 2.9.3)**. The geological features and the correlated density changes produce changes in gravitational acceleration, which are extremely low compared to the total Earth field (Dentith and Mudge, 2014). Therefore, instead of using the acceleration unit [m/s^2] of the SI or the acceleration unit gal [cm/s^2] of the cgs system, the gravity acceleration is measured in mgal, with 1mgal = 10^{-5} m/s^2), or in gu (gravity unit ; 1mgal= 10 gu) (Dentith and Mudge, 2014). After the acquisition, the gravity data have to be corrected for the so-called topographic effect applying the **corrections of Free air, Bouguer and Terrain**, which correct the data respectively for the difference in height between the station of measurements and the datum level, the density of the material of which the height interval is constituted, and the shape of the geological material with that particular density (Nettleton, 1971; Dentith and Mudge, 2014).

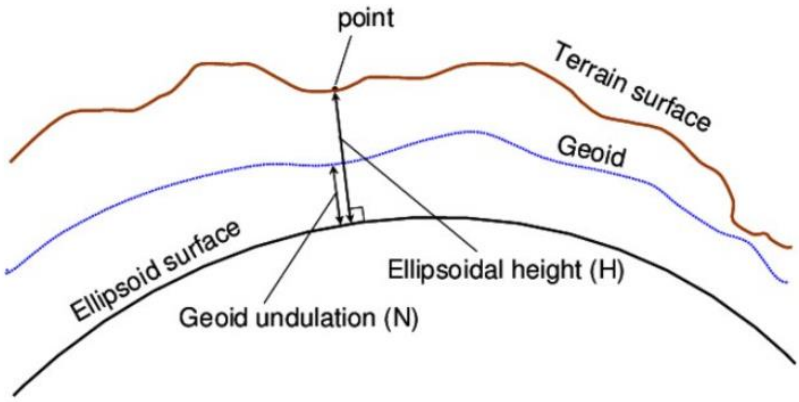

Figure 2.8: *Relationship between the geoid (blue line), the ellipsoid (black) and the terrain surface (brown line) (Forsberg et al., 2022).*

The magnitude of the corrected gravity anomaly is directly proportional to the density contrast and the volume of the body that produce the anomaly (Dentith and Mudge, 2014), but it also depends on the distance between the source of the anomaly and the measuring station. The measured amplitude will decrease with the distance with an **algorithm of decrease** strongly dependent on the shape of the source of the anomaly, with the maximum trend of decreasing -a square of the distance- occurring with a spherical body, while in case of more complex shapes the reduction of the amplitude is lower, and the body can be detected also at a relatively long distance (Dentith and Mudge, 2014).

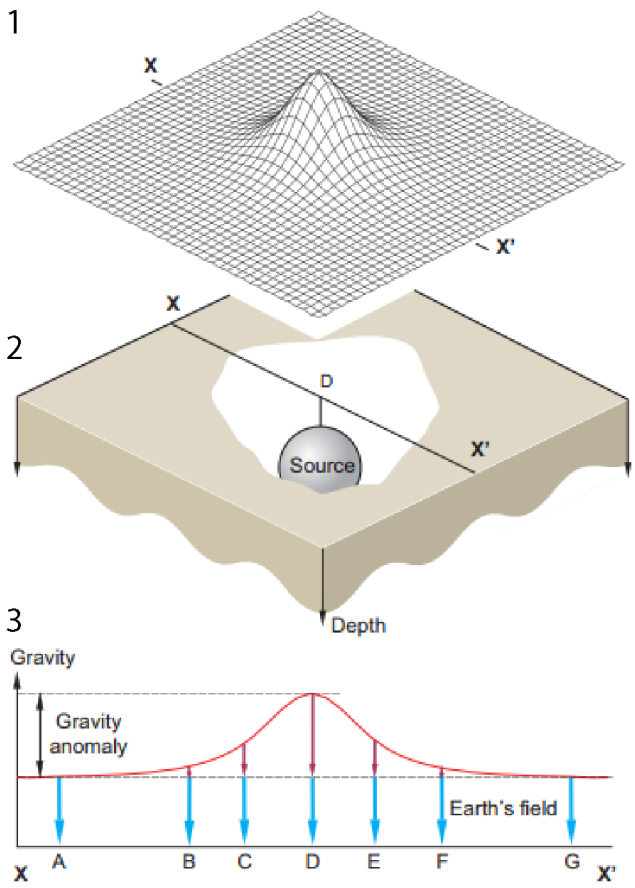

***Figure 2.9**: Gravity field of a sphere (Dentith and Mudge, 2014). The gravity measured values **(.1)** above the spherical source **(.2)** is the result of the two fields due to the Earth and the sphere, respectively blue and red in the representation **(.3)**.*

While the amplitude decreases with distance, the wavelength of the anomaly increases (Dentith and Mudge, 2014), making the application of filters fundamental to distinguish between various sources of anomalies. Different high-pass filters are applied to the data to obtain a higher resolution of the shorter wavelength: for example, the high-pass filtered data at 100 km and 30 km will respectively give information about the more regional and more local geological features (Dentith and Mudge, 2014).

As every method, also the interpretation of gravity data is susceptible to interpretation pitfalls linked to the acquisition and processing of the data or to the presence of anthropogenic or natural disturbances and topographic effects (Dentith and Mudge, 2014). Moreover, the same concept of non-uniqueness that characterizes the lithological interpretation of a seismic profile is valid also for gravity data, in which a certain value of gravity anomaly can correspond to a potentially infinite series of possible density value, shapes and depths of the anomaly source (Dentith and Mudge, 2014). Despite this, gravity anomalies interpretation has been used extensively for the mapping of offshore salt domes since the Gulf Coast exploration (Nettleton, 1971): with an almost constant density of 2.20 g/cm^3, the salt is denser than the surrounding sediments at shallow level and less dense at a depth major than the density cross-over one (Figure 1.8) (Nettleton, 1971). The interpretation of gravity anomalies is therefore a first, preliminary but efficient way to map the salt structures at a large scale.

II.2.2. Magnetic potential method

While the gravity field affects all the objects, the magnetic field affects exclusively the objects that are magnetic (Dentith and Mudge, 2014). Changes in the magnetic field are due to variations in rock magnetism, mostly controlled by **magnetic susceptibility**. The unit of the SI to measure the intensity of the magnetic field is the Tesla (T), but due to the weakness of the variations in the magnetic field the used unit is the nanotesla (nT), or the gamma (γ, with 1γ= 1nT) in the cgs system (Nettleton, 1971; Dentith and Mudge, 2014).

Unlike the gravity data, the magnetic anomaly depends on the position of the magnetic body in relation to the **Earth's magnetic field**, the latter consequence of the Earth's core. The magnetic field

measured by the instruments is the vector addition of the two **(Figure 2.10)**, and the earth magnetic field in a certain position can have an opposite direction to the one produced by the object of the study. The maximum positive anomaly effect of the sum of the earth and body's magnetism are when both are verticals (Figure 2.10.1), while the induced magnetism can be lower than the regional one above a body at the magnetic equator (Figure 2.10.3).

After the acquisition of geomagnetic data, a reduction has to be applied to remove the effect of the back-ground value of the magnetic field, the Earth's field variations (planetary-scale variations and elevation related ones), as well as the effect of the acquisition platform (Dentith and Mudge, 2014).

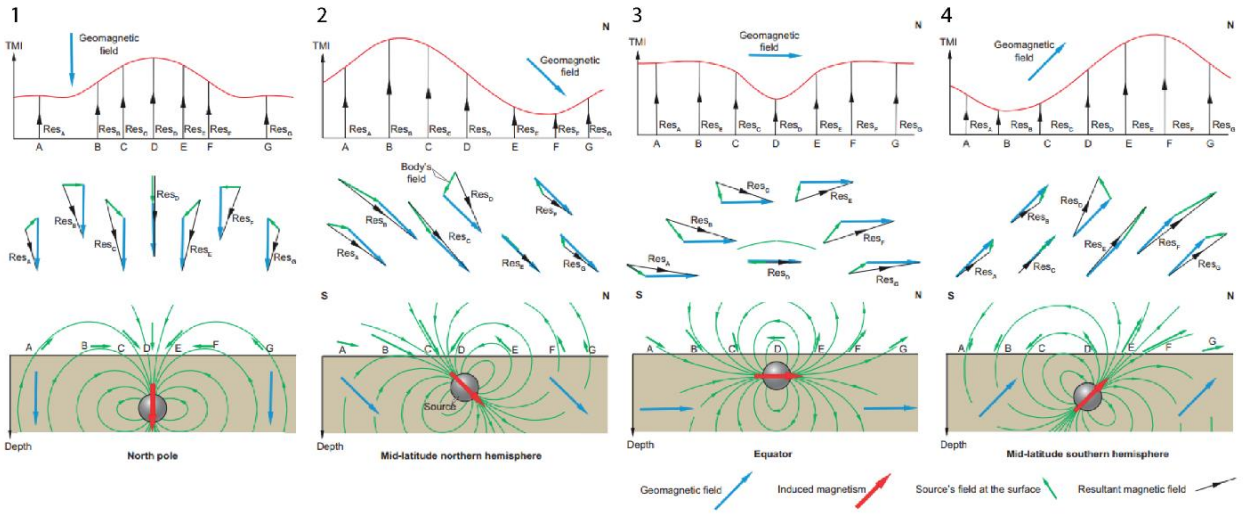

Figure 2.10: *Induced magnetic field of a spherical source:* ***1.*** *at the magnetic north pole* ***2.*** *at mid latitude northern hemisphere* ***3.*** *at the magnetic equator and* ***4.*** *at mid latitude southern hemisphere. The TMI is the scalar strength of the field (Dentith and Mudge, 2014).*

As in the case of the gravimetric data, the algorithm of the magnetic field decrease depends on the **shape of the source** of the anomaly: for a sphere the value is 1/distance^3, while in the extreme case of a semi-infinite horizon -which models a very largely extended body- it is possible to consider the amplitude of the magnetic field as independent from the height of the measuring station (Dentith and Mudge, 2014). The non-uniqueness already mentioned for the gravity anomalies interpretation is even more complex in the case of magnetic modelling, where also the direction of the magnetism act as a variable (Dentith and Mudge, 2014). As explained for the gravity field, also the magnetic data are **high-pass filtered** to obtain information about different ranges of wavelength of the anomaly.

The gravimetric and magnetic potential fields are often interpreted together to give complementary information on the geology of an area. Gravity data can generally detect anomalies deeper than magnetic data, but at the same time the resulting value of anomaly will be more strongly influenced by the deeper gravity anomalies (Dentith and Mudge, 2014). The union of potential field data and seismic reflection data, together with wells data and the knowledge of the local geology, provides constrains to limit as much as possible pitfalls and uncertainties in the interpretation. For example, a salt body is characterized as a general rule by a transparent seismic facies, a negative gravity anomaly and a negative magnetic anomaly, and the gravity and magnetic field can be used to map the possible presence of salt in case of absence or scarcity of seismic data coverage (Cunneen *et al.*, 2015). Seismic and magnetic data are therefore a very useful complementary to the seismic data interpretation and especially useful for large scale studies, but

they cannot reach the precision of the seismic data in terms of geometrical description of the structures.

II.3. Data

For the studies presented in this thesis we used various datasets **(Figure 2.11)**, belonging to both public institutes -as GEO-OCEAN (previously UMR Domaines Océaniques) (France) and OGS (Italy)- and oil and gas companies -as the TGS ASA (Norway)-, which authorized the data visualization and interpretation for scientific purposes. Due to the technical and geographic differences between them, we will here describe the datasets of this thesis dividing it in study areas, first the Western Mediterranean (Western Sardinian margin and Northern Algerian margin) and then the Southwestern Barents Sea (Sørvestsnaget Basin).

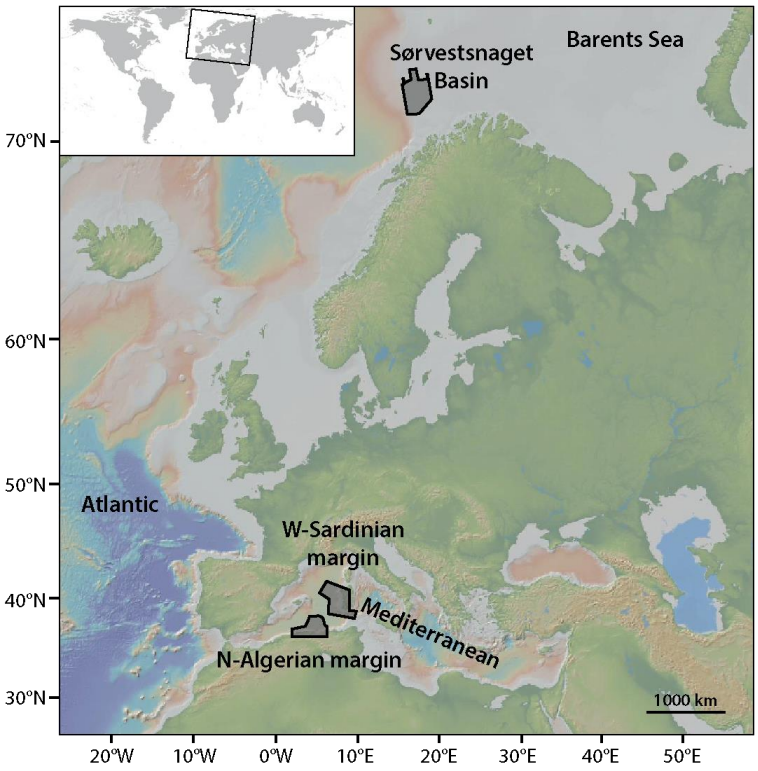

***Figure 2.11**: Position of the 3 datasets used for this study: the Northern Algerian margin and the Western Sardinian margin in the Western Mediterranean, and the Sørvestsnaget Basin in the Southwestern Barents Sea.*

II.3.1. Western Mediterranean

II.3.1.1. Western Sardinian margin

During the thesis secondment at the University of Trieste and OGS and in continuation of a collaboration already consolidated with these institutions, different datasets were made available for the analysis of salt tectonics in the Western Sardinian margin and Central Sardo-Provençal basin **(Table 2.2 and Figure 2.12)**.

Survey	Year	Zone	Data acquired	Number of profiles/km available	Acquired by
MS	1972	Mediterranean Sea	Flexotir seismic profiles 24 channels	5 profiles	OGS (Italy)
CROP	1991	Mediterranean Sea	Airgun seismic profiles 30 channels	2 profiles	CNR-OGS (Italy)
WS10	2010	W-Sardinian margin	Gi-gun seismic profiles 30 channels	7 profiles	OGS (Italy)

***Table 2.2**: Characteristics of the dataset used on the Western Sardinian margin.*

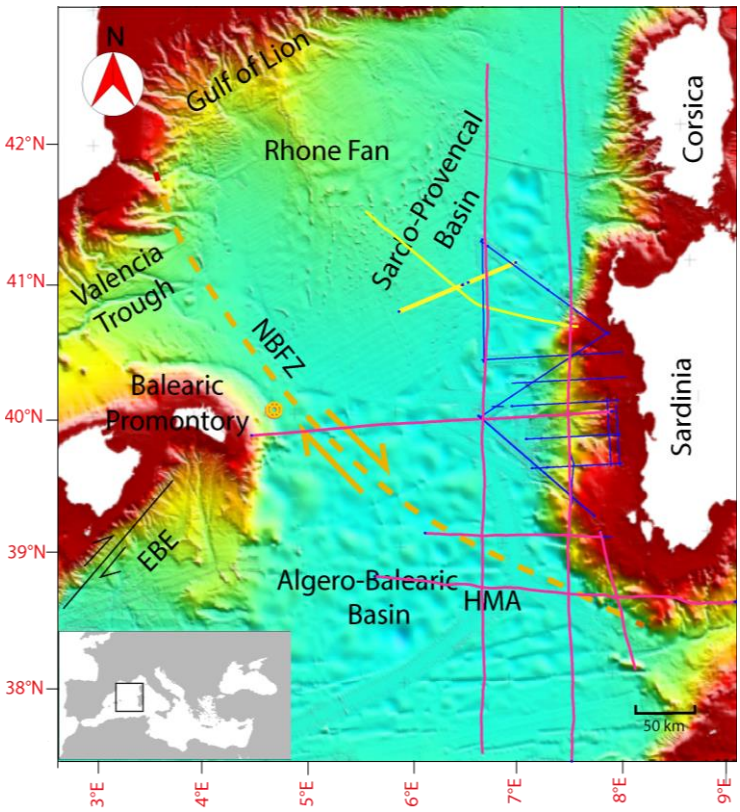

Figure 2.12: *Position of the datasets used for this study on the Western Sardinian margin: MS (pink lines), CROP (yellow lines) and WS (blue lines). The position of the area is marked in Figure 2.10. NBFZ: North Balearic Fracture Zone. HMA: Hamilcar Magnetic Anomaly. EBE: Emile Baudot Escarpment.*

MS (Mediterranean Sea) Survey: the MS dataset has been acquired between 1969 and 1980 by the National Institute of Oceanography and Applied Geophysics (**OGS**) of Trieste (Italy) onboard the Italian R/V "Marsili". The project was aimed at investigating the deep structures of a large area of the Mediterranean Sea, and was locally able to image the Moho. The instrumentation consisted in a Flexotir source and a 24-channel streamer of 2400 m, and the 28000 km of seismic profiles have been acquired with a mean registration length of 6-10 seconds with 4 ms sample rate. Dal Cin *et al.* (2016) calculated that the vertical resolution of the MS profiles is around 6-7 m if we apply the Rayleigh criterion and consider the maximum source frequency and a velocity of 2000 m/s. The MS seismic lines used in this thesis are located in the Eastern Sardo-Provençal and Algero Balearic basins, and were partly reprocessed during my Master degree and during the secondment at OGS (Italy), in order to obtain a clearer image of the Messinian salt structures (Figure 2.6).

CROP (CROsta Profonda) Project: The CROP Project results from the union of scientific and industrial interests, and was led by CNR (Italy) in collaboration with industrial partners as AGIP and ENEL (Italy), and a major part of the data acquisition and elaboration offshore was made by OGS (Italy). The profiles of the CROP Mare survey were acquired onboard the Italian R/V OGS Explora, with a 80 litres airgun and a 30 channel streamer of 4.5 km (Finetti, 2005). The registration length was the double than the MS survey, with records of up to 20 seconds, locally penetrating below the Moho. Seismic profiles CROP M1 and M2A1 (from literature) were particularly useful for this work, because they give information on the central Sardo Provençal Basin not imaged by the other dataset.

Project WS10: The seismic reflection profiles of the WS10 project have been acquired in 2010 onboard the research vessel "OGS Explora" of **OGS** (Italy) and had the target of the eastern sector of the Sardo-Provençal basin and the Sardinian passive margin. The acquisition project was based on the knowledge obtained thanks to the MS and CROP seismic reflection profiles, and aimed

at integrating these data with higher resolution ones about the Messinian and post-Messinian sequences, with a good compromise between resolution and penetration. The energy source were 2 GI-guns -for a total of 710 cubic inches- and the seismic signal had a registration length of 8s, with 1 ms sample rate. The length of the digital 120 channels streamer was of 1500 m with 12.5 m group interval, a 25 m near offset and 1512.5 far offset and a shot interval of 25 m. The calculated vertical resolution obtained with this dataset is of about 3-4 m (Geletti *et al.*, 2014; Dal Cin *et al.*, 2016). Seven WS10 seismic reflection profiles have been used for this thesis.

II.3.1.2. Algerian Margin

In the framework of the Western Mediterranean geodynamics, the Algerian margin plays a particular role due to its active tectonics and the consequent risk in terms of destructive earthquakes. After the earthquake of Boumerdès of 2003, two oceanographic surveys **(Table 2.3 and Figure 2.13)** have been acquired by UMR Domaines océaniques (Brest, France), giving new inputs to the scientific research in the area and integrating the data acquired by previous oceanographic surveys. The data were made available for this study thanks to the collaboration with Professor J. Déverchère.

Survey	Year	Zone	Data acquired	Number of profiles/km	Acquired by
MARADJA I	2003	NW Algerian margin Oran to Dellys	Multibeam bathymetry: Kongsberg EM300 and EM1000	6500 km	J. Déverchère for UMR Domaines océaniques onboard R/V "Le Suroît"
			Air-gun mini-GI SODERA high resolution seismic data	6-channels: 4169 km 24-channels: 802 km	
MARADJA II	2005	NE Algerian margin Dellys to Béjaïa	Multibeam bathymetry: Kongsberg EM300	4200 km	
			Air-gun mini-GI SODERA high resolution seismic data	24 traces: ~4000 km	

***Table 2.3**: Characteristics of the main dataset used on the Northern Algerian margin.*

MARADJA I: The "MARge Active el DJAzaïr" oceanographic survey has been acquired by J. Déverchère in **2003** onboard the French R/V "Suroît" (IFREMER, France). This survey images the north-west Algerian margin, from Habibas Island-Oran to Dellys, and interests the area from the limit of the continental platform up to the deep basin 40-50 km from the coastline. Main objective of the survey was the characterization of the margin in terms of deformation, structure and risk evaluation, because of the high seismic risk in the area (Déverchère et al., 2005b). For this reason, the density of the seismic lines in the area of Boumerdès is higher.

Using as an energy source 2 air GI-guns SODERA, **6 and 24 channel profiles** were registered, leading to the acquisition of 4169 km of 6-channel profiles -for a total of 93000 shots with 12 seconds interval- and 802 km of 24 channel profiles -with total 62000 shots and 5 seconds interval-. The seismic profiles registered with 24 channel have very high resolution in the Plio-Quaternary sequence but cannot image properly the evaporitic sequences because of the low penetration. On

the other side, the 6 channels give a lower resolution image of the Plio-quaternary data but a deeper penetration, resulting more useful for the aim of this thesis.

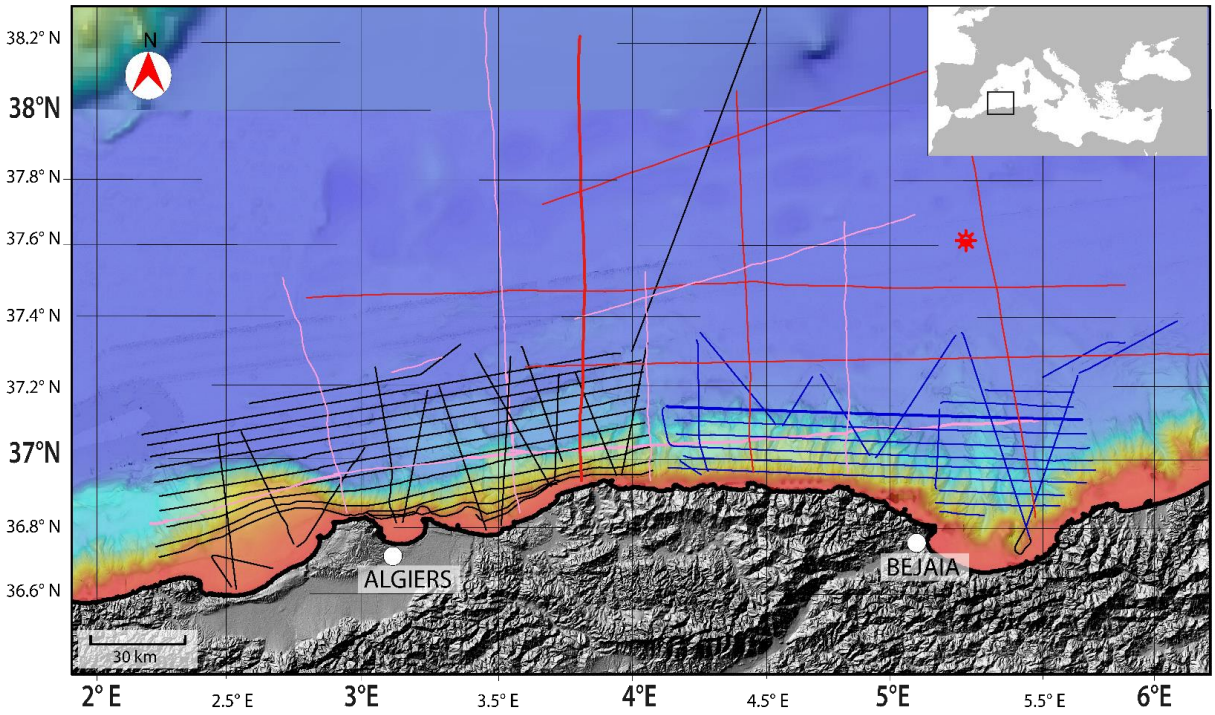

***Figure 2.13**: Position of the datasets used for the study on the Algerian margin: MARADJA I (black lines), MARADJA II (blue lines), SH73 (pink lines) and ALE77 (red lines). The red star shows the location of well 371. The position of the area is marked in Figure 2.11.*

Moreover, 6500 km of continuous multibeam bathymetry were acquired through the Simrad Kongsberg EM300 multibeam, a 32-kHz multibeam system composed of 135 beams for a total aperture of 140° and horizontal planes antennas. This multibeam echo-sounder has a swath coverage of 5 times the water depth, a lateral resolution of 25-35 m at 1000 m depth and a vertical accuracy of 2-10 m, and it is efficient up to a water depth of 4000 m (Domzig *et al.*, 2006). The EM1000, with a higher frequency of 95 kHz, 60 beams and a total aperture of 150° with circular antennas, is designed for shallower waters (0-1500 m) and has been used to image the sea bottom of ten profiles on the continental platform. The DEM constructed after the processing with CARAIBES Software and used for this thesis has a maximum grid of 50 m. The bathymetric data in the Algerian margin are particularly interesting as a complement to the seismic reflection data because both salt tectonics and crustal tectonics are still active in the area, and therefore visible on the bathymetry.

MARADJA II/SAMRA: aimed at completing the data acquired during MARADJA I, this seismic survey onboard the French R/V "Suroît" led to the acquisition in **2005** of around 4000 km of **24 and 72 channels seismic profiles**, with respectively 2 and 5 airguns of energy source and 50-55 Hz and 50-250 Hz of frequency. These characteristics of the seismic source have produced a seismic signal with a vertical and lateral resolution of respectively 5 and 25 m for the 24 channel profiles and up to 2 and 10 m for the 72-channel profiles. The seismic source, improved in terms of penetration from the first MARADJA survey, led to the imaging of up to the base of the salt layer in the 24 traces profiles. Around 4200 km of bathymetric data have been acquired through the EM300 bathymetric system.

Six profiles from the **ALE survey** (**Total**, **1974**) and eight profiles of the **SH survey** (**Sonartrach**, **1977**) integrate the seismic data coverage in our study area, imaging the central parts of the basins up to more than 38°N. These **industrial seismic data** differ by the Maradja I and II in terms of amplitude spectra **(Figure 2.14)** and consequently in terms of resolution and penetration.

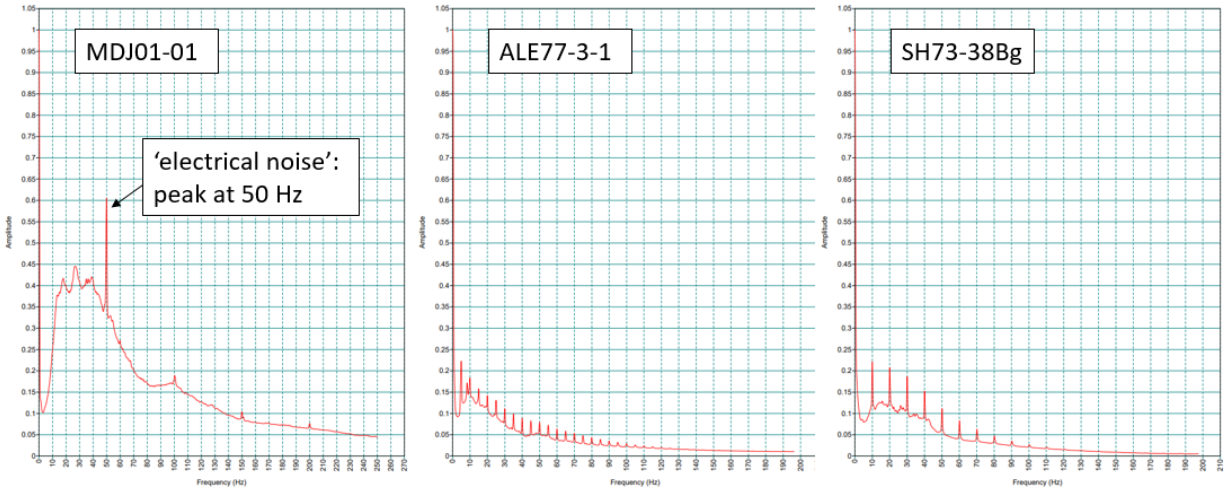

***Figure 2.14**: Variations in amplitude as a function of the frequency (amplitude spectra) of the 3 seismic reflection datasets on the Algerian margin.*

II.3.2. Southwestern Barents Sea

The Barents Sea region has been object of many seismic acquisition surveys related to the oil and gas exploration. The seismic data used for this study **(Figure 2.15 and Table 2.4)** have been provided by TGS (Norway) and interpreted during my secondment at the VBPR under the supervision of Sverre Planke (Oslo, Norway).

Survey	Year	Data	Area
Carlsen 3D	2017	3D seismic	5 500 km²
CFI_NBR	2009-2012	2D seismic	200 000 km²
Merged gravity data	2010-2018	Bouguer gravity anomalies	200 000 km²
Merged magnetic data	2010-2018	Magnetic anomalies	200 000 km²
7117/9-1, 9-2, 7216/11-1S, 7218/11-1	1982, 1983, 2000, 2013	Wells data	2400 km²

***Table 2.4**: Characteristics of the different dataset used for the study of the salt tectonics in the SW Barents Sea. All the data are property of TGS.*

We mainly focused on the interpretation of the 5500 km² of very high quality time migrated **3D seismic reflection data**, acquired by TGS in 2017 in the southern part of the Sørvestsnaget Basin, between the Senja Ridge and the Senja Fracture Zone. The 3D dataset was integrated by 2D regional seismic profiles acquired by TGS between 2009 and 2017 and imaging the southern Sørvestnaget Basin up to the Marginal High, the Senja Ridge and the western Tromsø Basin. Moreover, the seismic interpretation was constrained by potential field data -gravity and magnetic anomalies highpass filtered at 30 and 50 km wavelength-. In particular, the Bouguer gravity anomaly has been useful for the identification of the salt and the crustal structures, that present respectively a negative and a positive density anomaly compared to well compacted sedimentary sequences. The potential field

data have been used in a qualitative way, but they could be useful in the future to produce an inversion model, in order to constrain the deep development of the salt structures. The seismostratigraphic interpretation was constrained by the wells 7117/9-1, 7117/9-2, 7216/11-1S and 7218/11-1 contained in the perimeter of the 3D cube (position in Figure 2.15), partly penetrating up the Early Cretaceous (well 7117/9-2 and 7218/11-1) but none of them reaching the evaporitic bodies. All these wells, drilled for hydrocarbon exploration purposes, were declared dry.

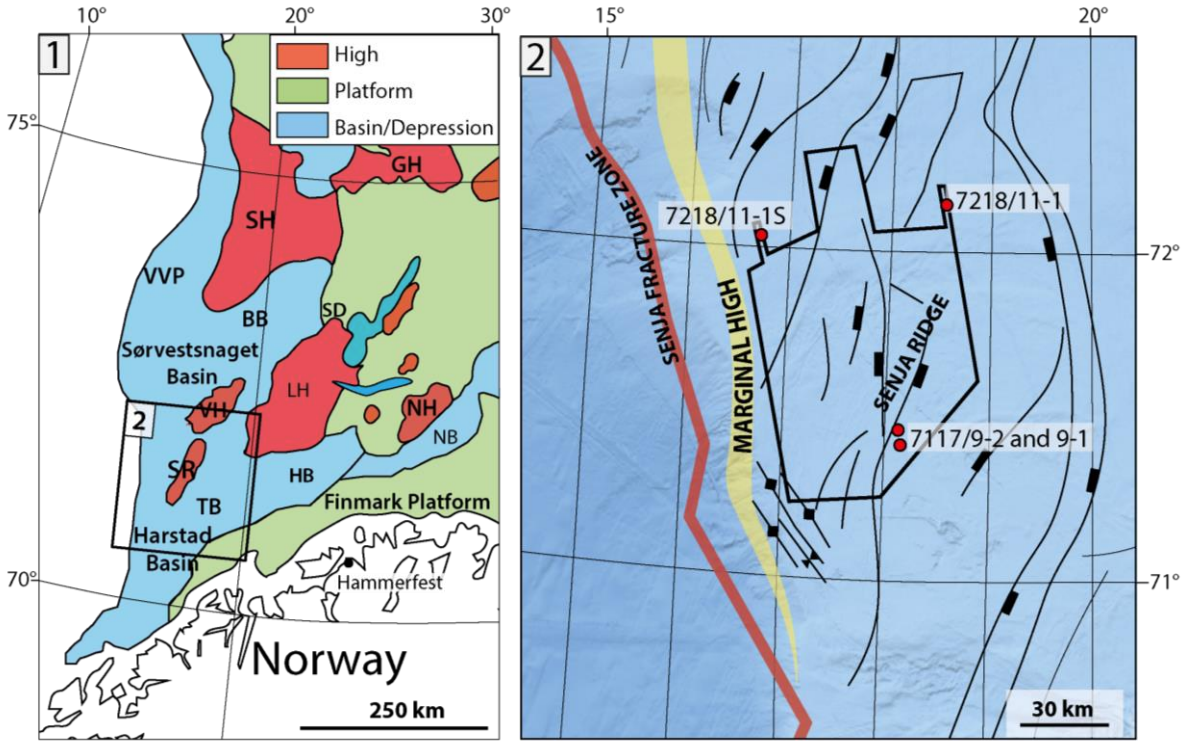

***Figure 2.15**: **1.** Location of the study area in the Southwestern Barents Sea with position of the main highs, platforms and basins. **2.** Detail of the 3D dataset and wells position in the Southern Sørvestsnaget Basin with position of the main structural elements.*

II.4. Data interpretation

II.4.1. Seismic stratigraphy

The first step in the interpretation of a seismic dataset is the identification of the truncations (i.e. horizons terminations) and of the different **seismic units** present in the data, based on the principles of sequence stratigraphy (Mitchum *et al.*, 1977; Vail *et al.*, 1977) **(Figure 2.16)**. The seismic unit is defined as a group of reflectors which characteristics differ from the adjacent ones, and are therefore recognizable, interpretable and mappable (Mitchum *et al.*, 1977). After the identification of the seismic units present in the data, the interpretation of their geometries is extended to the whole dataset. The number of seismic units identified in a certain dataset depends on the characteristics of the area but also on the characteristics of resolution and penetration of the seismic data, as well as on the topic of the study and the consequent level of detail requested by the interpretation. The division in sequences leads to the production of **isobaths and isopach maps**, which give information on the geometries of the units' boundaries and regional and local variations of the units' thickness.

The second step of seismic interpretation consists in the analysis of the reflectors inside the sequences, when present (Figure 2.16) (Badley, 1987). The relationship between reflections can be used to understand the **chronology**, while the geometry and attributes of the reflection give information about the **depositional setting** and the physical characteristics (Badley, 1987).

All these definitions are referred to the initial geometry of the reflectors, because following tectonics, compaction etc. strongly modify the inclination and in general the geometry of the horizons, and it is the role of the interpreter to distinguish between deposition geometries and the result of post depositional deformation. These concepts about the geometries of the internal reflections are not applicable for salt deposits, which generally present a transparent seismic facies. In the study of salt tectonics, we therefore focus on the depositional geometries of its brittle overburden, which register the phases of movement of the salt.

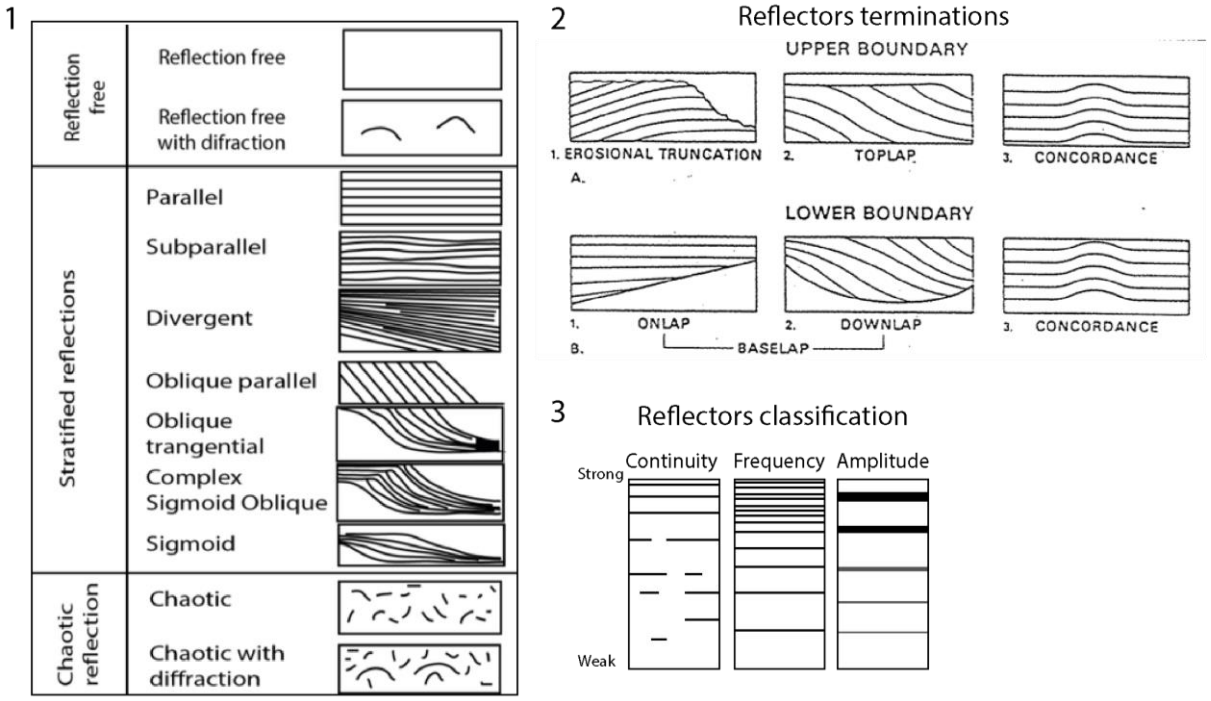

***Figure 2.16**: Seismic stratigraphy classifications. **1.** Schematization of the main seismic units' characteristics **2.** Schematized geometry of the reflectors terminations. **3.** Reflector classification based on the continuity, frequency and amplitude of the reflection. After Catuneanu et al., (2011); Mitchum et al., (1977) and Vail et al., (1977).*

For what concerns the identification of the **lithologies** imaged in the seismic data, the uncertainty is often quite strong if there are no wells in the area. Clays and silts are generally thin bedded with moderate to low amplitude reflections and moderate to good continuity, but can be imaged as reflection-free due to destructive interference or very low amplitude reflections (Badley, 1987). Coarse grained sediments have a higher accumulation rate compared to clay and silts, and most of the time they present mounded configurations or sheet-like forms (Badley, 1987). The top of the carbonate platforms is mostly marked by a strong positive reflection due to high velocity, but this is not valid in case of porous or fractured platforms (Badley, 1987). Salt deposits are generally easy to recognize because of the high amplitude at the top and the often inversed polarity seismic reflection

at the base, together with the particular geometry of the deformed sediments (salt diapirs, pillows etc.) and the high seismic velocities (around 4 km/s for the p-waves).
Seismic facies and relative lithologies will be described separately for each study area.

II.4.2. Seismic structural analysis

The seismic structural analysis is based on the interpretation of the seismic data, and therefore limited to the resolution of the latter. The visible structures are analyzed in 3D, in order to understand the geographical and temporal relationship between faults, folds, salt structures etc. Higher the quality of the seismic data, more precise will be the seismic structural analysis also in complex settings characterized by different tectonic phases.

In this thesis we will do a descriptive structural analysis of horizons, faults and folds, and the analysis of the temporal relationship between sediments deposition and faults movement, folds forming, salt tectonics and in general all the episodes of movement. It will follow a kinematic analysis, with the study of the movement, and a dynamic analysis, in which we will consider the stress that gave origin to the movement identified (Mukherjee and Misra, 2017). Considering the topic of this thesis, particular attention will be given to the kinematic and dynamic analysis of the salt bodies, which however cannot be isolated from the regional tectonics.

Faults and folds interpretation

The presence of **faults** offshore – regardless of whether they are normal, reverse strike-slip- can be interpreted in the seismic profiles, in the horizon maps and in the time slices of 3D dataset, as well as in the bathymetry for recently active structures (Mukherjee and Misra, 2017).
For what concerns the interpretation of the faults in the seismic profiles, this is performed mainly through the identification of offsets in the stratigraphic markers. The identification of the fault-plane reflection is less common, and is linked to the accumulation of fluids, to mineralization on the fault plane or to a difference in the pore fluid pressure along the plane (Mukherjee and Misra, 2017).
Three families of faults will be considered in this thesis:

- **Regional faults**: The regional faults often present the larger throws, and affect both the basement and the sedimentary sequence; through the large scale deformation these faults control the basin architecture (Mukherjee and Misra, 2017). The identification and analysis of these faults give us information about the regional stress and strain history.
- **Salt-related faults**: This family of faults is a consequence of the presence of a salt layer, which deforms viscously causing brittle deformation (i.e. faults) in the overburden. The faults do not propagate in the salt but create complex patterns above the salt structures.
- **Polygonal faults**: The polygonal faults are closely spaced and multidirectional small-scale normal faults with modest throws values of typically 10-100 meters (Mukherjee and Misra, 2017 and references therein). They are mainly found in fine grained sediments and they originate through dewatering contraction, dissolution-induced shear failure, density inversion, gravitational loading etc.

While the basin architecture is due to the regional faults, smaller scale faults as the salt-related ones and the polygonal ones play a major role in the control of fluid flow (Mukherjee and Misra, 2017).

The **folds**, divided in anticlines and synclines, can be the result of compressional and transpressional strain, salt or clay tectonics or related to fault propagation (Mukherjee and Misra, 2017).

II.4.3. Wells to seismic ties

Wells data present good vertical resolution but they lack lateral extent, and are therefore complementary to seismic reflection data. The well to seismic tie allows to relate the data obtained from the well to the seismic reflectors picked in the dataset. This procedure generally comprehends the computing of the acoustic impedance and the creation of a synthetic seismogram from the calibrated well logs, followed by the correlation between the seismic data at the well location and the synthetic seismogram (White and Simm, 2003).
Depending on the kind of well and on the analysis performed during the drilling and on the cores, it is possible to have a datation of certain horizons –based on paleontological studies, isotopes analysis etc.- and/or the lithological composition.

II.4.4. Salt imaging and interpretation

Despite the salt is one of the easiest lithologies to detect in the seismic reflection data, the detailed interpretation of the salt structures presents some issues. Being aware of the possible **pitfalls** becomes therefore essential to being able to distinguish between seismic artifacts and real geological objects, and to know the **level of confidence** of each interpretation. The main problem is related to the salt structures geometry, often complex especially in the case of long-lived salt movement, and offering endless possibilities in terms of travel path options and out of plane reflectors, particularly disturbing in the 2D seismic data (Jones and Davison, 2014). Moreover, the movement of the salt tilts the surrounding horizons, and the imaging of the interface between salt and sediments becomes challenging when this interface is steep. In this case, it is the role of the interpreter to use all the available data to reconstruct a **geologically reasonable** salt tectonics structure, considering the age of the salt and the geological history of the area when known (Jones and Davison, 2014).

Another issue is the velocity of the P-wave in the salt. The value for pure halite is 4500 m/s, but for seismic processing and conversion the value used is the average velocity resulting from the different evaporites and co-present inclusions (Jackson and Hudec, 2017). In particular, gypsum and anhydrite (respective Vp of 5700 m/s and 6500 m/s) are commonly found, increasing the average seismic velocity and the common anisotropy, but all the non-evaporitic inclusions decrease this value, ending up with common **velocities of around 4 km/s** for the salt bodies. The high velocity of the seismic wave in the salt layer results in the pull-up velocity effect, which deforms the horizons below the salt structures and has to be corrected through migration. Another effect of the seismic velocity, and specifically of the passage between materials with strongly different seismic velocities, is the seismic wave diffraction, that produces a disturbance in the seismic signal (Jackson and Hudec, 2017).
Due to the absence of identifiable internal reflectors in the salt bodies we analyze in this work, the salt interpretation will be limited to the geometrical definition of the top and base salt horizons.

Top salt interpretation: The top of the salt structures can be identified by a strong positive reflection when the overburden is composed of slightly compacted siliciclastic sediments, while the amplitude can be low or negative when the surrounding rocks are well compacted. In this case, the top of the salt is identified as the top of the seismically transparent zone. Once again, also this method presents some exceptions, due to the fact that the salt is not always seismically transparent, because of the presence of coherent and incoherent noise and non-halitic inclusions. Another exception is the fact that the overburden can be seismically transparent as well, as in the case of some shales or mass transport deposits (Jackson and Hudec, 2017).

Base salt interpretation: as well as the top of the salt, the base salt can be a negative reflection (e.g. in the Western Mediterranean) or a positive one (e.g. if the subsalt is a crystalline basement), but it can also vary laterally due to different subsalt lithologies or compaction. While it should constitute the base of the transparent lithology, its interpretation is quite challenging due to the seismic signal attenuation when crossing the salt. In this case, the interpretation of the base salt is mainly based on the salt weld, which generally allows a better imaging of this horizon (Jackson and Hudec, 2017). While in terms of seismic interpretation we can only use all the possible constrains and keep in mind all these rules, this issues can be partly prevented during seismic data acquisition, thanks to longer offsets that both allows a better subsalt illumination and a better velocity resolution and consequent seismic processing (Jones and Davison, 2014).

Other biases in salt seismic interpretation

Seismic coverage: This issue is more evident in terms of interpretation of the salt structures due to their fast lateral variations: as we will see in the grids of the salt in the Mediterranean, the grid of the salt top and the thickness map of the salt are not representative of the 3D development of the salt structures but give punctual information and a long wavelength trend if present. When the bathymetry is influenced by the salt structures, it is possible to suggest corrections in the grid of the top salt based on the geometries visible on the bathymetric data **(Figure 2.17).**

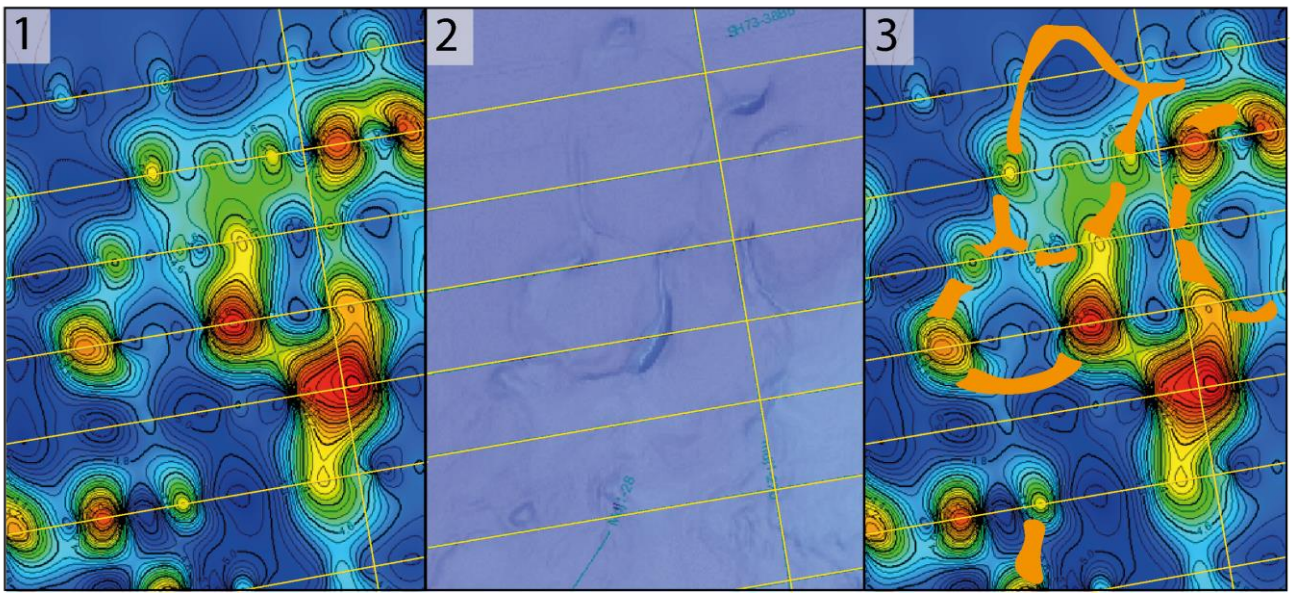

Figure 2.17: *(caption on next page)*

***Figure 2.17**: Data integration in the Algerian margin. **1.** Grid of the top salt. **2.** Bathymetric data. **3.** Possible correction of the grid. The grid of the salt top strongly depends on the position of the seismic profiles (yellow thin lines), but it can partly be corrected with the bathymetric data if the salt structures deform the seafloor. We can therefore track the 3D geometry of the salt structures in the area (.3). While the illustrated corrections have not been applied to the maps presented here, they have been considered during the analysis of the salt tectonics in the area.*

Seismic data penetration: Seismic data penetration depends both on the seismic source and on the subsoil characteristics, and is therefore different in the three study areas. In the Western Mediterranean the salt layer covers the whole deep basin and is post-rift, so the absence of a clear imaging of the subsalt structures makes the analysis of the influence of crustal tectonics on salt movement more complex. In the case of the Southwestern Barents Sea, the seismic data penetration mostly depends on the position of the allochthonous salt structures: below the allochthonous salt the penetration is very limited, while the seismic data reach up to 6 s TWT between the salt structures.

II.4.5. Procedure for seismic imaging and interpretation

The procedure of interpretation and analysis of the seismic data is composed of a series of steps - during which we use different softwares- that partly differ between the study areas. We describe here the standard procedures and the peculiarities of the 3D seismic data interpretation **(Figure 2.18)**.

After a first visualization of the 2D seismic reflection data in **SeiSee software**, the georeferenced data are loaded in the seismic interpretation **IHS Kingdom software** (Figures 2.18.1 and 2.18.2). Following the definition of the seismic units and consequent horizons dividing them, the horizons and the faults have been picked, and the picking of the horizons has been gridded to create time structures maps, showing the 3D morphology of the stratigraphic surfaces. Moreover, the calculation of the time thickness between definite horizons and the consequent gridding has produced the isochron maps, which illustrate the vertical thickness of the seismic units (Figures 2.18.3 and 2.18.4). This vertical thickness is higher than the real thickness when the layer is deformed, but gives a good approximation of the layers' thickness variations. Seismic attribute analysis has been calculated on some of the layers interpreted in the 3D dataset (Figure 2.18.5).

The produced grids have been exported and loaded, visualized and implemented through the softwares **Surfer** and **Eiva Navimodel Viewer** (Figures 2.18.6 and 7).

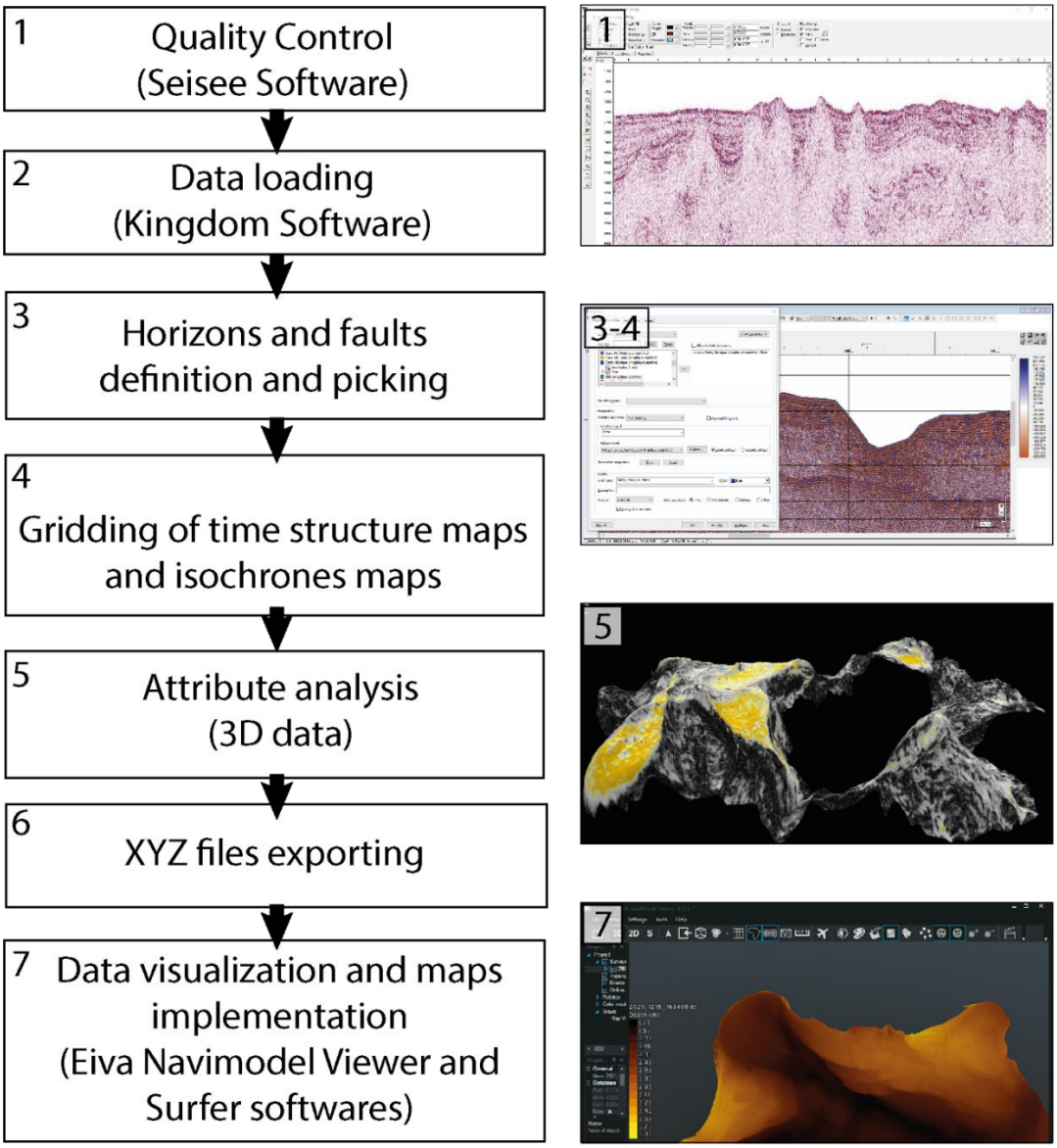

***Figure 2.18**: Flowchart of the seismic data interpretation. For details, see text.*

Interpretation of the 3D dataset

The interpretation of the 3D dataset in the Southwestern Barents Sea consists in some more steps integrating steps 3 and 4 of figure 2.18, aimed at improving the quality of the resulting grids. The 3D dataset is interpreted iteratively with increasingly shorter distance between the interpreted seismic profiles, both parallels and perpendiculars to the data acquisition direction (i.e. inline and crossline profiles). After the whole dataset has been interpreted every 8th inlines and crosslines, the interpretation has been gridded, and the grid has been snapped to an horizon, extending the interpretation to the 7 inlines and crosslines located between the real interpretation. To improve the quality of this extrapolation, we applied the **Vatmax volume attribute (Figure 2.19)**, which is able to detect the maximum value of amplitude in a certain **vertical window** above and below the horizon, e.g. 50 ms above and 50 ms below in the case of the top of the allochthonous salt structures in the Barents Sea.

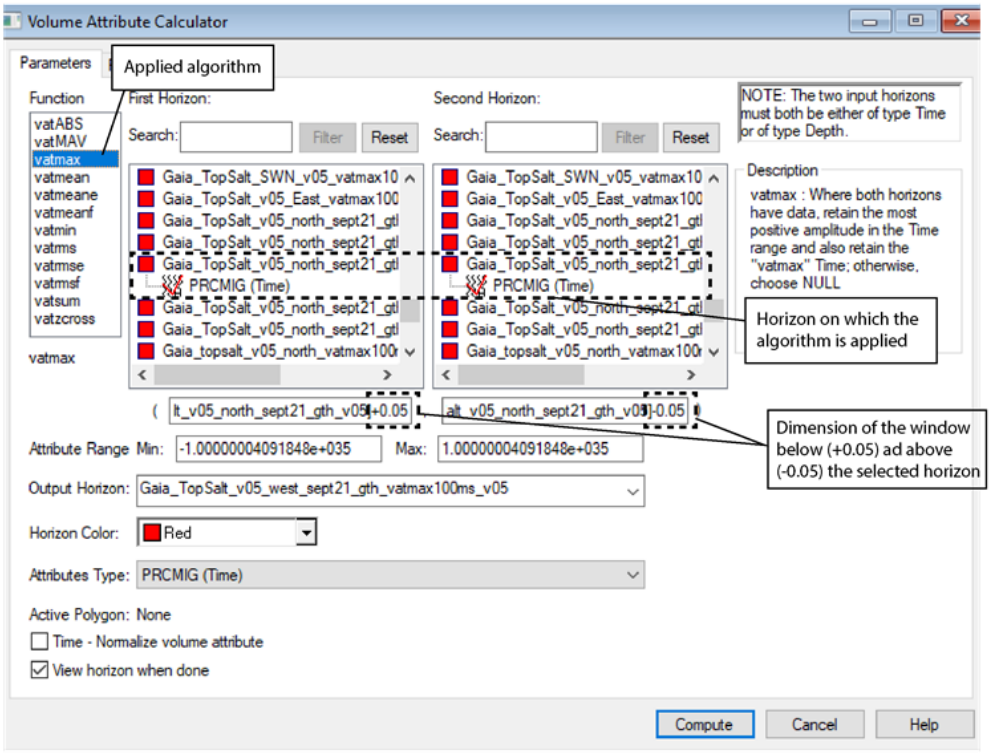

***Figure 2.19**: Volume attribute calculator in HIS Kingdom software.*

The dimension of this window is decided by the interpreter, which has to find the best compromise between a window large enough to contain the target horizon, but small enough to avoid to contain other horizons of equal or higher amplitude and same polarity. If the horizon is a negative reflection (e.g. base of salt in certain conditions) the Vatmax volume attribute is substituted by the **Vatmin volume attribute,** that detects the maximum amplitude of negative polarity.

This flowchart works very well when the horizon we are working on has a high amplitude, as in the case of the top of the allochthonous salt in the Sørvestsnaget Basin. Some errors are present on the steep flanks of the salt, due to both the lower amplitude of the reflection –therefore more difficult to detect- and the limits related to the vertical window. After the calculation of the Vatmax or Vatmin volume attribute, the horizon is gridded again. This procedure produces a **considerable detail improvement** of the final grid (bin size of 12.5 m), and the error introduced by such extrapolation is negligible.

- ## Gridding algorithms

2D seismic reflection profiles are not always regularly distributed in a certain study area, so the data are gridded –i.e. interpolated on a regular network based on the data present near to the node (Dentith and Mudge, 2014)- based on the general assumption that the spatial variation of the parameters is continuous. The step of gridding of the interpreted horizon follows a first step of picking of the main reflectors and can be applied iteratively with the refinement of the interpretation. In fact, a good grid of the horizons is at the same time an efficient tool to illustrate the results and a fundamental step to understand the geology and the problematic of the area.

The gridding algorithms are divided in **mathematical and data adaptive (Figure 2.20).** The mathematical modeling algorithms (Cubic Spline Algorithm, Flex Gridding Algorithm, Minimum Curvature Algorithm) do not use data sample values directly, but first fit some form of mathematical

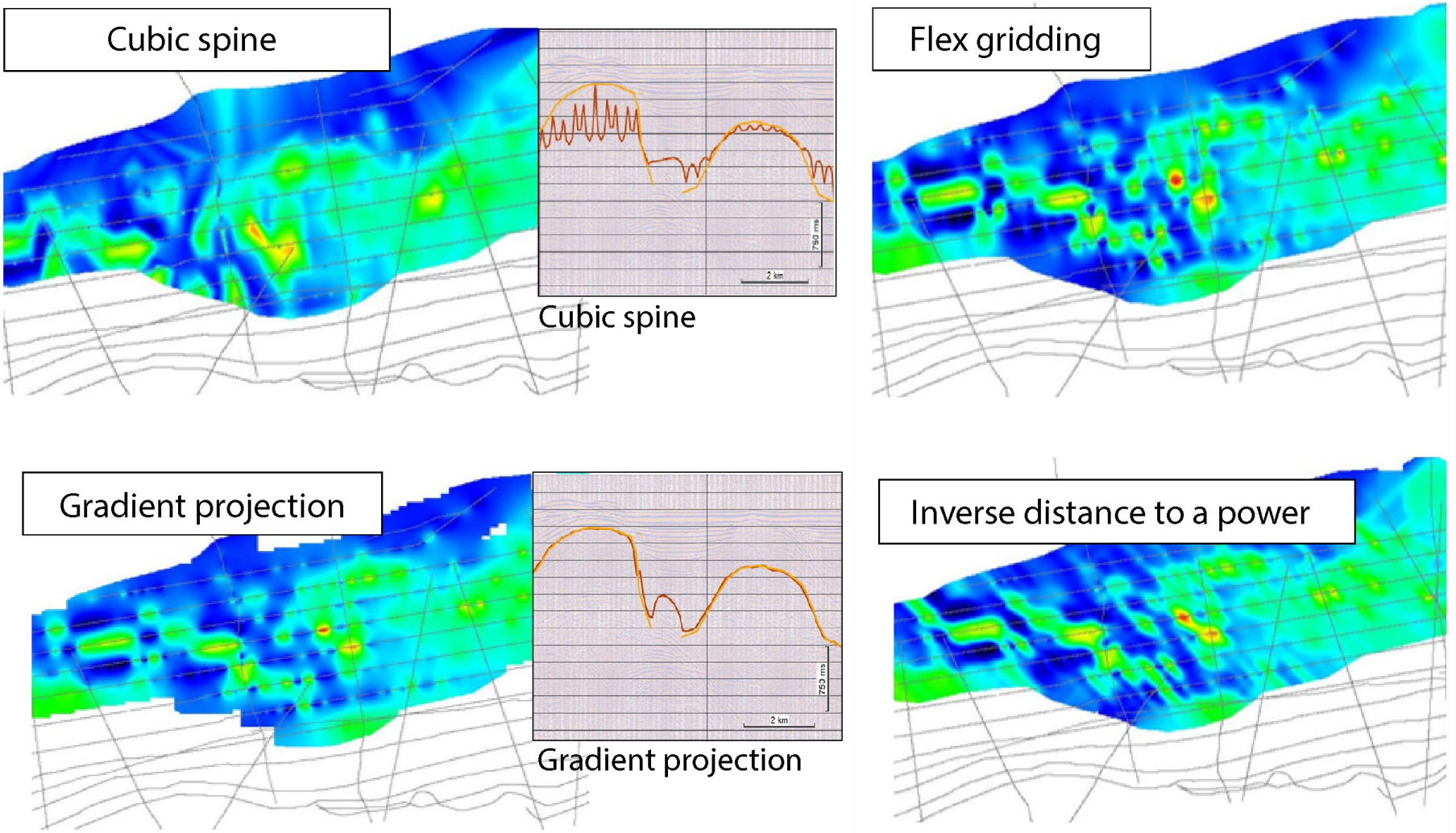

***Figure 2.20**: Comparison between the different gridding algorithms available in Kingdom Software and applied on the salt top horizon, divided in mathematical modelling algorithms (upper line) and data adaptive algorithms (bottom line). All the calculated grids presented in this work have been constrained by a polygon, delimitating the area in which a seismic facies is present. The segment of seismic reflection profiles shows the cubic spine and gradient projection algorithms results (dark red line), applied on the data (yellow line).*

surface to the data values and then interpolate by finding the value of the surface passing through the desired location. For example, the minimum curvature algorithm is the second derivative of the values of the grid nodes, so this kind of interpolation is a valid one just for the data that vary smoothly, as the gravity and magnetic fields (Dentith and Mudge, 2014), but it is not compatible with the fast lateral changes characterizing the salt structures.
On the other side, the data adaptive algorithms (Gradient Projection Algorithm, Inverse Distance to a Power Algorithm, Natural Neighbor Algorithm) are more faithful to variations in the sampled data but not always compatible with a less dense dataset.
Due to the particular geometry of the salt structures, we tried different algorithms in order to choose the one able to introduce the minimum level of errors while maintaining the interpreted geometries. Flex gridding, gradient projection and minimum curvature algorithms give the better results, but considering the characteristics of the salt structures on the Algerian and Western Sardinia margins (high spatial variability, also at very short scale), the gradient projection algorithm has been used for most of the maps.

• Seismic attributes analysis and their applicability

Seismic attributes are defined as *measured, computed or implied derivatives from seismic data* (Mukherjee and Misra, 2017) and can give to the interpreter information not visualized in the seismic sections or enhance the present ones, consequently helping in the correct interpretation of the data. The second, important aim of seismic attributes is to partly automatize the time consuming interpretation process. Only the amplitude attributes have been applied during our work, but it worth mentioning other methods that could be useful in a future continuation of the work presented here.

- The **amplitude attributes** are quantitative attributes that use the amplitude of the seismic signal as a base of the computation. Between them, the **Root Mean Square Amplitude** consists in the square root of the sum of squared amplitudes divided for the number of samples in the calculation window, and give therefore a scaled estimate of the trace envelope, highlighting in this way the presence of bright spots and anomalies in the seismic reflection amplitude. Compared to the reflection strength attribute, the RMS amplitude gives smoother results depending on the window dimension. A negative point of this attribute compared to other amplitude seismic attributes is the sensitivity to noise (Koson *et al.*, 2014). An example of the application of this seismic attribute is in chapter IV.B.1.

- The **coherence attributes** measure the continuity between neighbouring seismic traces along an interpreted horizon in a calculation window, considering the waveform and not the amplitude. This is particularly helpful in the identification of spatial patterns like faults, fractures, channels and in general any discontinuity. It can also be applied to a time slice to enhance the discontinuities (Cooke *et al.*, 1999; Mukherjee and Misra, 2017).

- The **instantaneous frequency** -the most used of the frequency content attributes- is the first derivate of the instantaneous phase and analyzes the rapid changes which could indicate the passage between salt and sediments. For a better use of this seismic attributes it is recommended

to use a Continuous Wavelength Transform filter, that 'cleans' the salt from random high frequency noise. This leads to a better visualization of the salt boundary highlighted by the frequency attribute (Halpert and Clapp, 2016).

- **Dip and azimuth attributes** are calculated on an interpreted horizon and are respectively the dip in degree and the direction of maximum deep in degree clockwise from the north of that horizon (Halpert and Clapp, 2016; Mukherjee and Misra, 2017).

- The **curvature attribute** measures the tightness of a curve at a particular point. The maximum and minimum curvature are combined to obtain secondary parameters that describe the characteristics of the curvature of a surface in terms of magnitude and direction (Mukherjee and Misra, 2017).

Different sequences of algorithms have been created to try to detect specific geological targets because a single attribute can fail or give false positives (Berthelot *et al.*, 2013 and references therein). Between the different methods linked to salt, we will briefly describe a texture-based method that includes 3 different texture attributes valid both for 2D and 3D data (Hegazy and AlRegib, 2014). This method consists in the application of the 3 following attributes:

a. Directionality: it is based on the eccentricity of the scattered plot of the gradient components. The salt seismic imaging lacks of directionality, therefore it is easily detected by the attribute. On the other hand, this seismic attribute gives some false positive results, so it has to be integrated by the next two seismic attributes that filters the false positives.

b. Smoothness of texture: this algorithm makes a sum of the magnitudes of the gradient over a neighborhood window. In the salt areas, this gradient is significant.

c. Edge content. This algorithm eliminates rough regions that actually belong to edges and not to a salt body region

For all these seismic attributes a value of threshold is chosen, and a nonlinear transformation is applied. In this way, the higher values are emphasized and the lower values are de-emphasized, improving the visualization of the anomaly.

II.5. Analogue modelling of salt tectonics

The analogue modelling is intended to represent in a simplified way and at a **smaller space-time scale** a natural phenomenon, complying with the similitude rule: relationships of time, space, forces and deformation (geometric, dynamic and kinematic scaling) have to be maintained, ideally during all the duration of the experiment (Hubbert, 1937). This method allows not only to reproduce the natural example at a smaller time-space scale, but also to test the different parameters (e.g. sedimentary thickness, timing of the deformation etc.) and analyze the influence of each of these parameters on the final geometries of the model. Since the beginning of analogue modelling in the geological field (Hall, 1815) **(Figure 2.21)**, analogue modelling has been used to study geological phenomena at every scale, and at any depth from the earth surface (e.g. erosion models) to the deep mantle convection models.

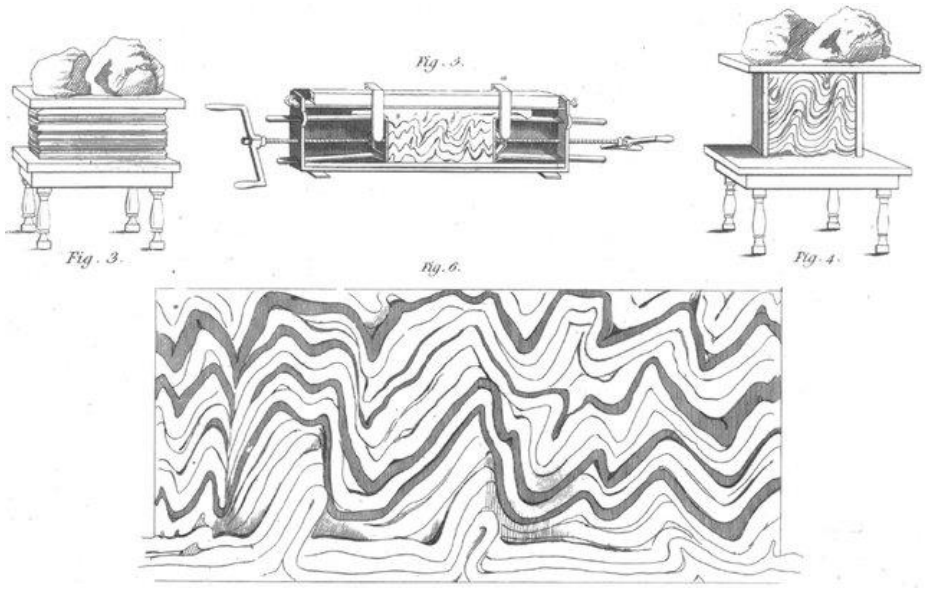

***Figure 2.21**: Original sketch of the first analogue models applied to geology, from Sir James Hall (1815).*

The models commonly consist in a space limited by vertical walls (generally wooden or glass ones) containing a sequence of layers. One or more of the lateral walls can be connected to a motor, that applies a compressional or extensional stress to the box model. Different geometries of the box, especially in terms of base of the sedimentary sequence, simulate different structural elements.

The laboratory experiments can be classified based on the experimental approach in three macro categories: the external approach, the combined approach and the internal approach (Schellart and Strak, 2016). The first two are open systems, and energy is added to the model in the form of materials, stress etc. In the external experiment all the deformation is consequence of this energy, while in the combined one part of the deformation is due to the internal forces (Schellart and Strak, 2016, and references therein). All the models performed in this work are based on the combined approach, with layers of materials added or partially removed during the experiment and in some cases compression of the box model.

While for more than 100 years the models where just a qualitative representation of the natural prototype, Hubbert (1937) introduced the concept of scaling. Based on his theory, an analogue model and a natural prototype are geometrically similar if all the relationships between the lengths (l) in the model and the length in the prototype are equivalent (l_n^m/l_n^p = constant, with superscripts m and p being respectively the model and the natural prototype) and all the corresponding angles are equal (Hubbert, 1937; Schellart and Strak, 2016). Moreover, to respect the kinematic similarity the model and the natural example need to undergo similar deformations and in a proportional amount of time (t_n^m/t_n^p = constant). If this scaling is respected, the velocity of eventual crustal deformation can be easily obtained through the following formula: $v^p = v^m (l^p t^m/l^m t^p)$ (Hubbert, 1937; Ramberg, 1967; Schellart and Strak, 2016).

The similitude rule also means that for every geological material modelled we need to find a valid substitute in terms of similar properties of deformation, and during the history of analogue modelling different materials have been used: syrups, honey and silicone for the viscous materials, microspheres, sugar and sand for the brittle ones (Schellart and Strak, 2016). Nowadays, the viscous behavior of the salt is commonly simulated through a polymer of silicon while quartz sand simulates the brittle behavior of the sand. In particular, we used a silicone polymer (Xiameter, produced by Dow Corning, U.K.) with a density of around 1 g/cm^3, while the sand we used has a grain size

between 125 et 315 μm and a density of 1.5 g/cm^3, an angle of internal friction around 30°, and negligible cohesion.

The halite has a density of around 2.2 g/cm^3, while the silicone used has a density of around 1 g/cm^3, giving a $\rho^* = \rho^m / \rho^p \sim 0.5$. In terms of viscosity (μ), the viscosity of the silicone at room temperature is around $\mu=10^5$ Pa.s, while the viscosity of halite is around $\mu=10^{19}$Pa.s. Consequently, $\mu^* = 10^{-14}$.

For the geometrical scaling, we considered that 1 km in the natural example corresponds to 1 cm in the model, obtaining a value of $l^*=l^m/l^p=10^{-5}$.

No gravity acceleration is applied on our models, so g* is 1 (Hubbert, 1937)

Recording pictures of the models at constant time intervals allows qualitative and quantitative analysis of the experiment. In particular, the surface view is useful to compare the model surface to bathymetric data and to have a partial 3D image of the evolution of the model. Side view are often registered when the box is composed of transparent lateral walls, but due to the lateral effect (i.e. friction above the box walls etc) these data are not always representative of the situation in the model. Large laboratories are recently using non-intrusive techniques as the X-Ray Computed Tomography, which can give a 4D image of the model, i.e. the evolution in time of the internal structures of the model. The info obtained by cameras or X-Ray tomography can be used in post-processing to obtain kinematic measurements, e.g. the velocity field of the model (Schellart and Strak, 2016).

Despite being an efficient tool to improve the understanding of the geology of an area, the analogue modelling presents some limitations, namely the limited choice of the materials compared to the variability of the natural one, and the general isotropic behavior of the models layer, in contrast with the mostly anisotropic geological layers. This problem is particularly evident in salt tectonics, where the mobile evaporitic layers are often composed of several sublayers of evaporites with different viscosity values. Considering that we do not have any information about the anisotropy in our study areas, neither in the brittle nor in the ductile layers, and that the coefficient of internal friction of the sand are well compatible with the one of the brittle overburden, the limitations do not affect the applicability of the method to this study.

Analogue modelling has been in this study a very efficient tool to analyze the geometries of the different study areas: following the seismic data interpretation phase, a comparison was made with scaled analogue models, in order to better understand the mechanisms at the origin of the interpreted salt structures. The analogue models, produced in the Analogue Modelling Laboratory of the LOG, University of Lille (France) will be discussed in detail in chapters III.C.2 and IV.B.2.

In our model the scaling is partial, because we are not modelling the temperature, the difference of rheological characteristics with depth etc. Some approximations are the result of technical constrains -as the limit in the box models dimensions- and human ones, as the impossibility to access the analogue modelling laboratory during the night.

Chapter III: THE WESTERN SARDINIAN MARGIN AND THE ALGERIAN MARGIN (WESTERN MEDITERRANEAN)

III.A. Geological setting of the Western Mediterranean

Located between a latitude of 30° and 46° N and a longitude of 6°W and 36° E, the Mediterranean Basin is almost completely enclosed by land, with the exception of the 14 km wide Gibraltar Strait that connects it with the Atlantic Ocean. Despite the relatively limited extension of this basin, strong differences are present at a local scale, both from the geodynamic and the sedimentary point of view. The Mediterranean can be divided in Eastern, Central and Western Mediterranean, this last one characterized by younger crust while the Central and Eastern basins are relics of Mesozoic to Cenozoic Tethys Ocean (Rehault *et al.*, 1984).

We will here mostly focus on the formation and nowadays characteristics of the Western Sardinian and Northern Algerian margins in the Western Mediterranean **(Figure 3.1).** These two study areas are quite close geographically but different from the point of view of formation and current tectonic activity, which is absent on the Western Sardinian margin and active and strong on the Algerian one, that reactivated in compression since 8 Ma (Mauffret *et al.*, 1992). These differences strongly affect the salt tectonics that we will analyze in the following chapters.

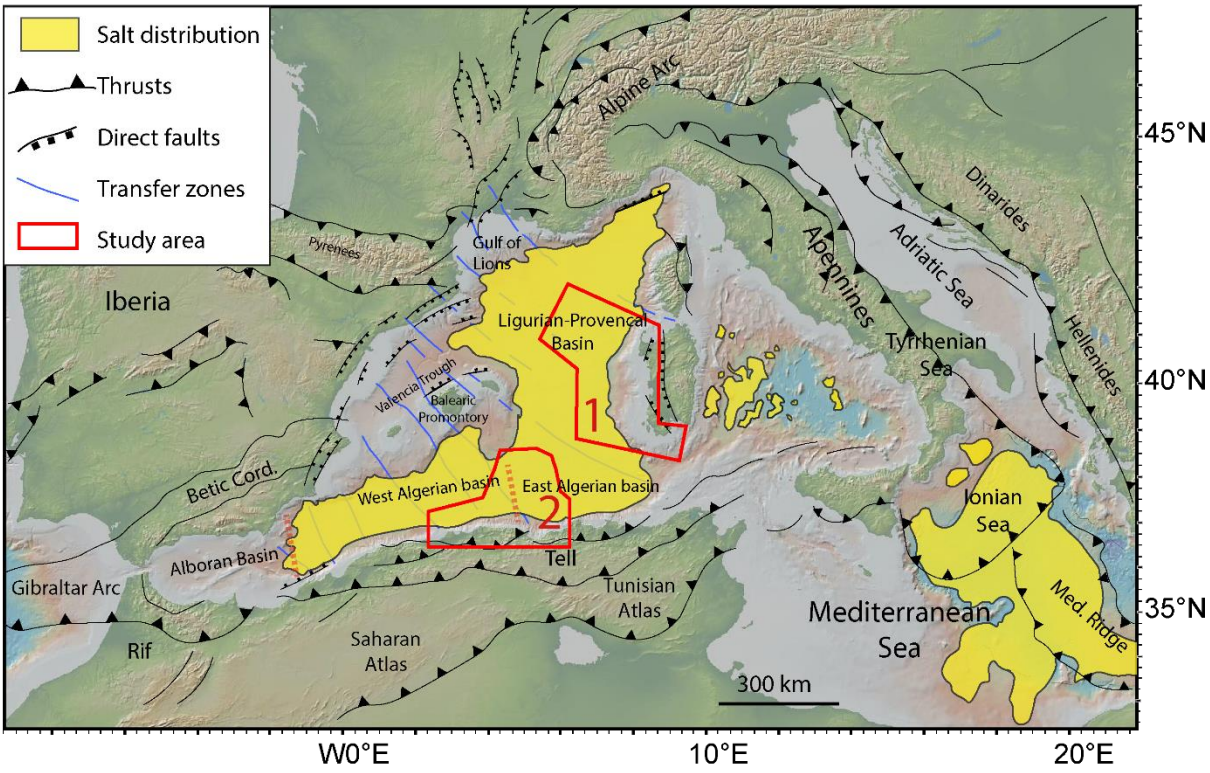

Figure 3.1: *Bathymetric map of the Mediterranean (from GeoMapApp) with the location of the study areas in relationship with the Messinian salt deposits (MU) and the main structural lineaments (Domzig et al., 2006; Jolivet et al., 2006; Lofi et al., 2011a; Lymer et al., 2018). In red are marked the two study areas in the Western Mediterranean: 1 – the Western Sardinian passive margin and 2 – the recently reactivated in compression Northern Algerian margin.*

III.A.1. Physiographic setting

The present day physiography of the Mediterranean is the consequence of the geodynamical evolution and of the vertical movement that affected the margins mainly after the Messinian Salinity Crisis (Nesteroff, 1973). The main geomorphological units in the western Mediterranean **(Figure 3.2)** (Gennesseaux and Vanney, 1979; Rehault *et al.*, 1984) are:

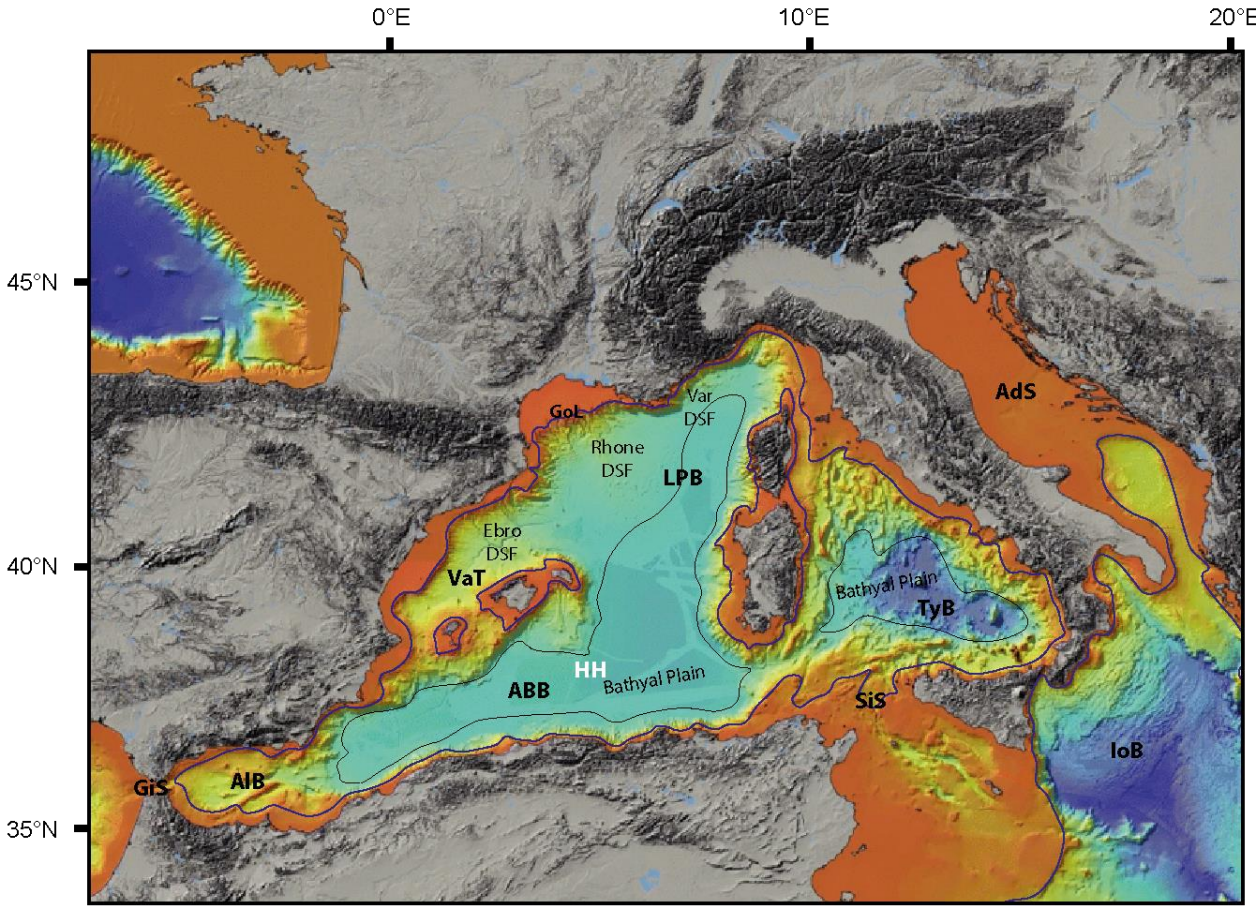

Figure 3.2: *Morpho-bathymetry of the Mediterranean Sea (Brosolo et al., 2012), with the shelf break (blue line) and the limit of the abyssal plain (black line). ABB: Algero-Balearic Basin; AdS: Adriatic Sea; AlB: Alboran Basin; DSF: deep-sea fan; GiS: Gibraltar Strait; GoL: Gulf of Lions; HH: Hannibal High; IoB: Ionian Basin; LPB: Liguro-Provencal Basin; SiS: Sicily Strait; TyB: Tyrrhenian Basin; VaT: Valencia Trough.*

. Continental shelf and slope: The continental shelf in the Western Mediterranean has a depth of 100-200 m, and is generally narrow with the exception of the northwestern margins, especially the Gulf of Lions. While the Western Sardinian margin has an average 25-km-wide continental shelf –narrower in the northern part and wider in the southern one-, the Northern Algerian continental shelf has a way more limited width of average 5 to 10 km, reaching the minimum of less than 2 km where the mountains are closer to the coastline, and the maximum of 40 km in the embayments (Cattaneo *et al.*, 2010; Sage *et al.*, 2011).

The continental shelf break is at a water depth of 100 to 200 m (Cattaneo *et al.*, 2010), and the Western Mediterranean slope is average 6-10° steep, reaching a depth of more than 2000 m (Rehault *et al.*, 1984). The slope is steep in the northern and southern sectors of the Western Sardinian margin and moderate in the central sector, in correspondence with the Oristano Amphitheatre (Sage *et al.*, 2011; Del Ben *et al.*, 2018). The variably narrow and steep continental

slope of the Algerian margin (average 5-20 km wide ad c. 10°, up to 20° steep) is characterized by the presence of deep canyons and gullies that transport the sediments towards the basin (Capron *et al.*, 2011; Cattaneo *et al.*, 2010). Active tectonics structures influence the geomorphology of the area through the formation of abrupt escarpments, common on the central Algeria slope (Déverchère *et al.*, 2005b; Cattaneo *et al.*, 2010).

. **Deep-sea fans and continental rises**: The major deep-sea fans of the Western Mediterranean are, in order of extension, the Rhone deep-sea fan, the deep-sea fan of the rivers Var and Roya, and the composed fan of Ebro canyon and other smaller contributions (Rehault *et al.*, 1984). As a consequence of the different sedimentary inputs, the continental rises of Corsica-Sardinia, Liguria and Algeria are narrow, while on the Provençal margin the continental rise is wide and well developed thanks to the presence of the above mentioned deep-sea fans. The continental rise on the Western Sardinian margin is mainly developed in the area of the Gulf of Oristano, while on the Northern Algerian margin the continental rise -when present- is at 2000 to 2700 m, with 2-3° of slope and the presence of deep-sea fans as the Algiers one (Cattaneo *et al.*, 2010, Babonneau et al., 2017).

. **Bathyal plain**: Marked by the isobath of 2700 m, the bathyal plain has a depth of up to around 2850 m in the Sardo-Balearic and Algerian plains (Rehault *et al.*, 1984). The abyssal plain geomorphology is characterised in the Western Mediterranean by the presence of numerous salt diapirs resulting from the Messinian Mobile Unit deformation, so a high resolution bathymetric data acquisition becomes here a fundamental input for the study of salt tectonics at a regional scale.

This division is particularly important in terms of salt tectonics, because as we saw in Chapter I there is a strong influence of the margins geometry on salt movement. The different development of the physiographic units is the first element to consider when we study the salt tectonics in a certain sector of the Mediterranean margins.

III.A.2. Geodynamic and tectonic setting

III.A.2.1 Basins formation

The Western Mediterranean counts several sub-basins, namely the Alboran, Valencia, Provençal, Algerian and Tyrrhenian Basins, developed during the last 40-30 Ma (Figure 3.2 and **Figure 3.3**) (Carminati *et al.*, 2012). The phases of development of the Western Mediterranean and the events that led to its actual structure have been studied through paleomagnetic, geophysical and heat flow data, as well as subsidence values in the basin. The details of the Mediterranean evolution of the last 50 Ma have been largely debated, and we will here consider the schematization of Carminati *et al.* (2012) integrated with the studies of Rehault *et al.* (1984), Carminati and Doglioni (2005) and Jolivet *et al.* (2021a, 2006).

The geodynamical evolution of the Mediterranean can be divided in a phase in which the deformation was mostly controlled by large scale movements of the large plates (150-35 Ma), a phase in which the slab retreat mechanisms controlled the deformation (35/32-8 Ma), and a still ongoing phase in which the slab retreat stopped and the main mechanism of deformation is again the large scale plates interaction (Rehault *et al.*, 1984; Jolivet *et al.*, 2021a).

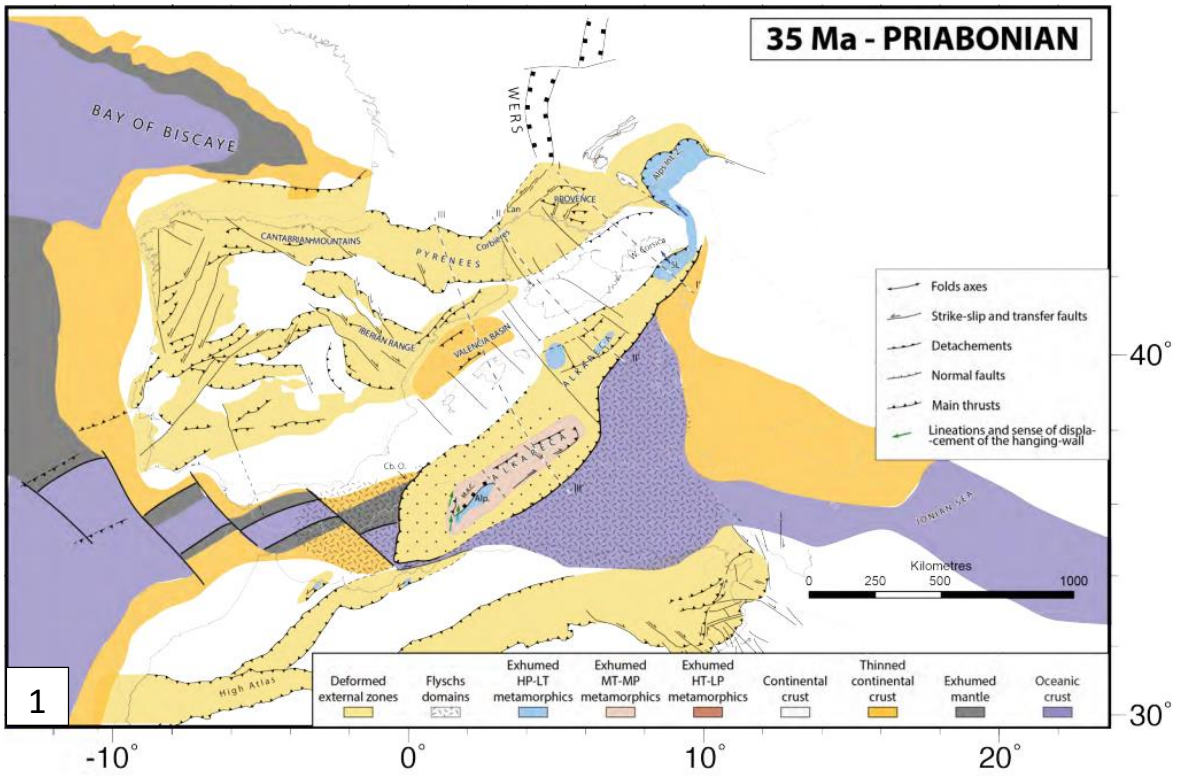
35 Ma - PRIABONIAN
BAY OF BISCAYE
CANTABRIAN MOUNTAINS
PYRENEES
IBERIAN RANGE
VALENCIA BASIN
PROVENCE
ALPINE CHAIN
ALKAPECA
JONIAN SEA
High Atlas
Folds axes
Strike-slip and transfer faults
Detachements
Normal faults
Main thrusts
Lineations and sense of displa-cement of the hanging-wall
Kilometres
0 250 500 1000
Deformed external zones
Flyschs domains
Exhumed HP-LT metamorphics
Exhumed MT-MP metamorphics
Exhumed HT-LP metamorphics
Continental crust
Thinned continental crust
Exhumed mantle
Oceanic crust
1
40°
30°
-10°
0°
10°
20°

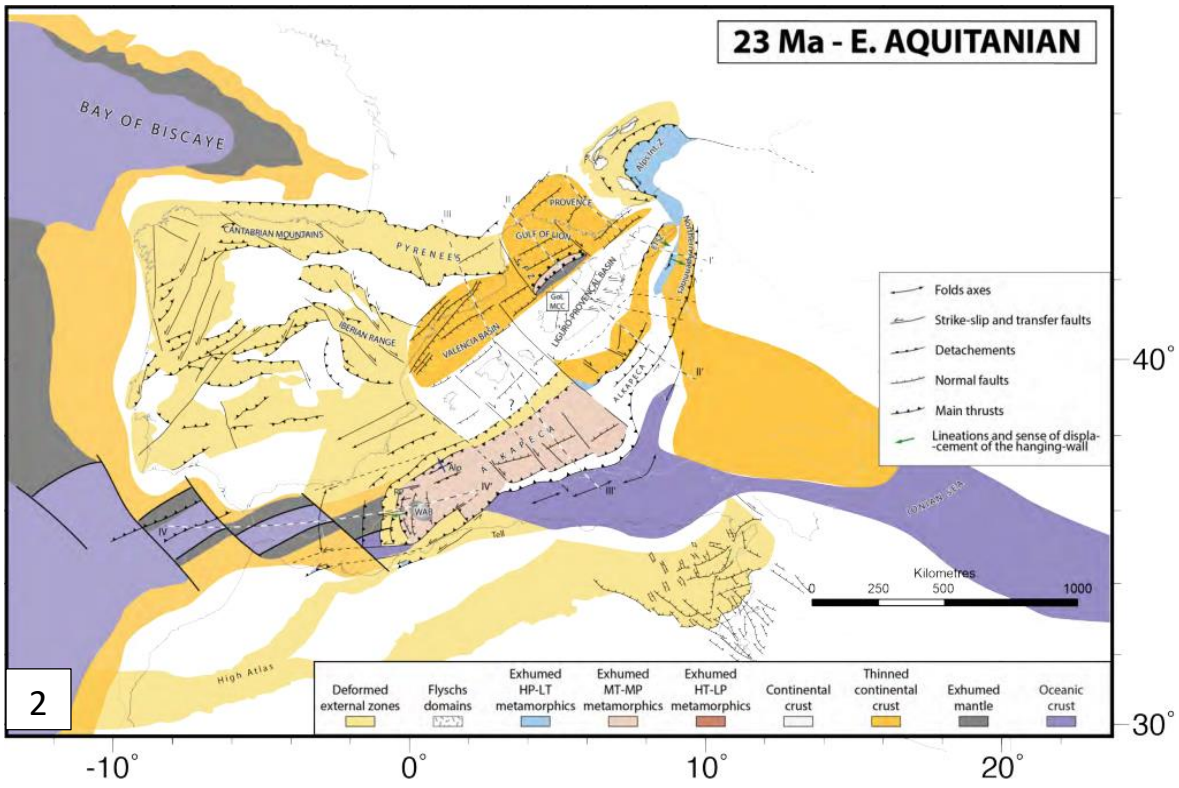
23 Ma - E. AQUITANIAN
BAY OF BISCAYE
CANTABRIAN MOUNTAINS
PYRENEES
PROVENCE
GULF OF LION
IBERIAN RANGE
VALENCIA BASIN
ALKAPECA
JONIAN SEA
High Atlas
Folds axes
Strike-slip and transfer faults
Detachements
Normal faults
Main thrusts
Lineations and sense of displa-cement of the hanging-wall
Kilometres
0 250 500 1000
Deformed external zones
Flyschs domains
Exhumed HP-LT metamorphics
Exhumed MT-MP metamorphics
Exhumed HT-LP metamorphics
Continental crust
Thinned continental crust
Exhumed mantle
Oceanic crust
2
40°
30°
-10°
0°
10°
20°

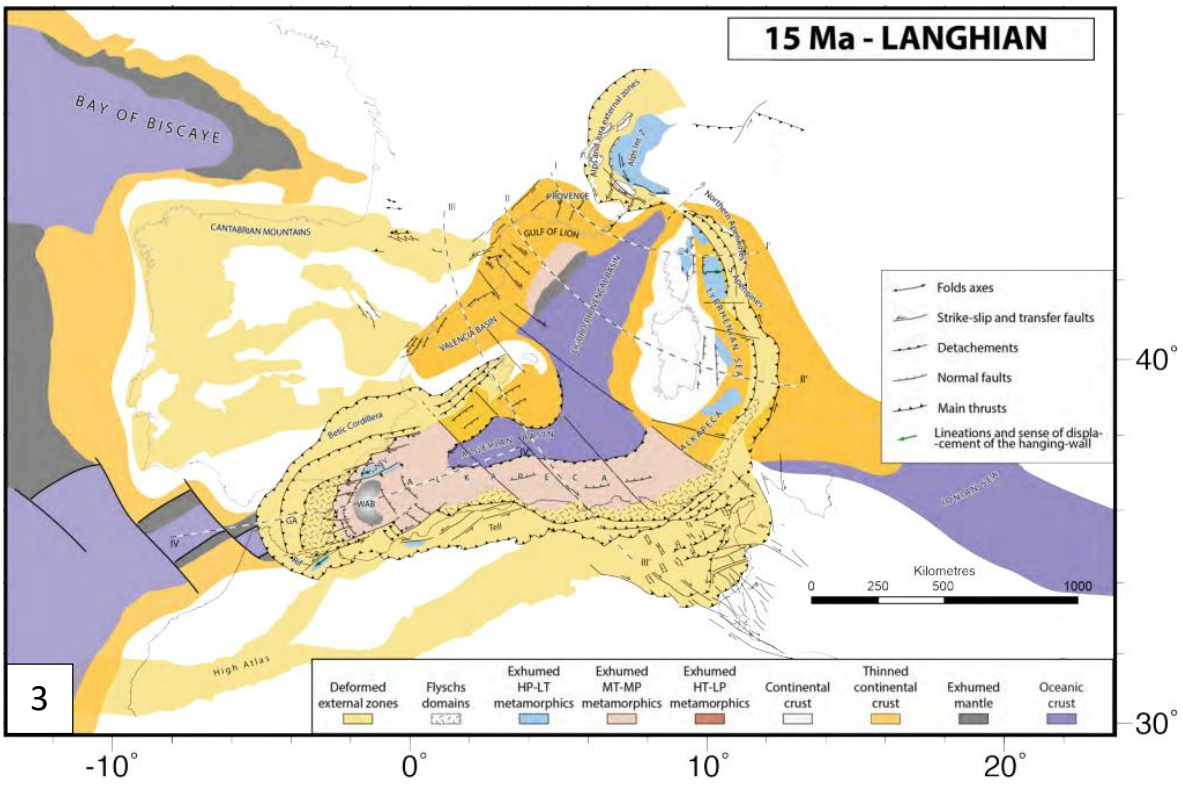
15 Ma - LANGHIAN
BAY OF BISCAYE
CANTABRIAN MOUNTAINS
PROVENCE
GULF OF LION
VALENCIA BASIN
Betic Cordillera
ALGERIAN BASIN
TYRRHENIAN SEA
IONIAN SEA
Tell
High Atlas
Folds axes
Strike-slip and transfer faults
Detachements
Normal faults
Main thrusts
Lineations and sense of displa-cement of the hanging-wall
Kilometres
0 250 500 1000
Deformed external zones
Flyschs domains
Exhumed HP-LT metamorphics
Exhumed MT-MP metamorphics
Exhumed HT-LP metamorphics
Continental crust
Thinned continental crust
Exhumed mantle
Oceanic crust
3
40°
30°
-10°
0°
10°
20°

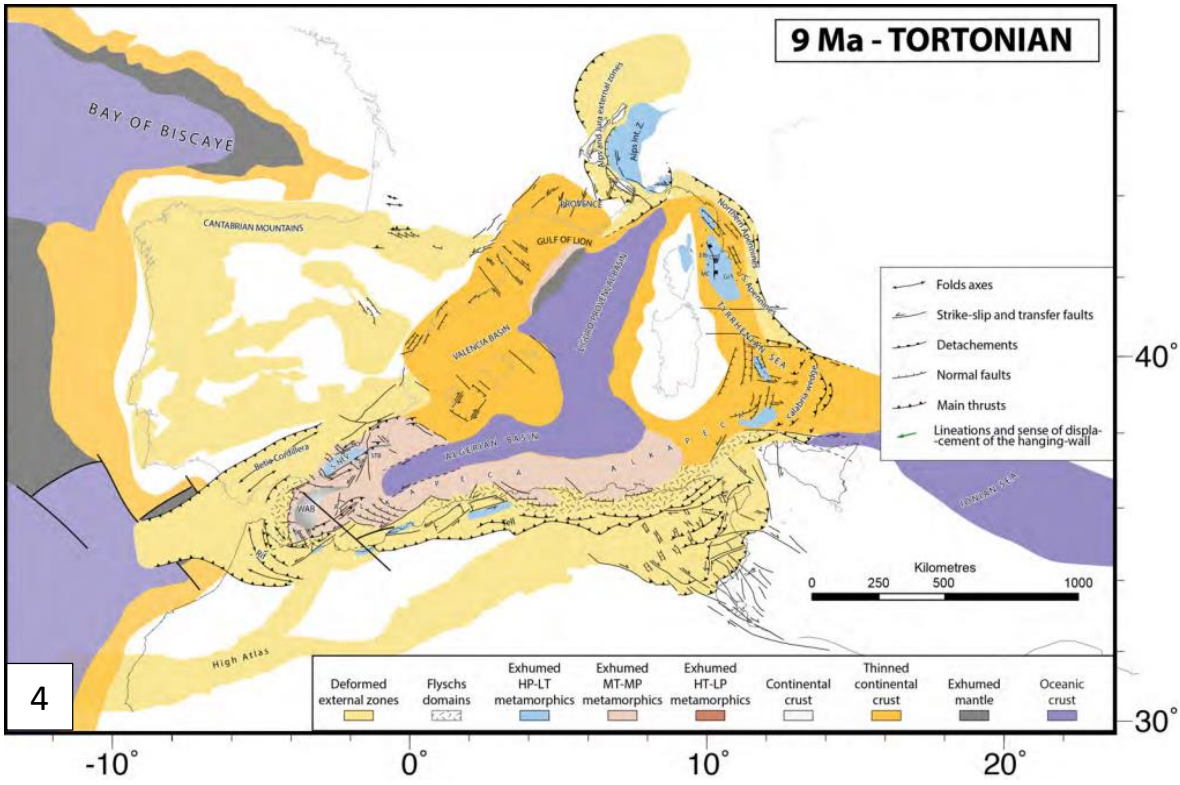
9 Ma - TORTONIAN
BAY OF BISCAYE
CANTABRIAN MOUNTAINS
PROVENCE
GULF OF LION
VALENCIA BASIN
Betic Cordillera
ALGERIAN BASIN
TYRRHENIAN SEA
IONIAN SEA
Tell
High Atlas
Folds axes
Strike-slip and transfer faults
Detachements
Normal faults
Main thrusts
Lineations and sense of displa-cement of the hanging-wall
Kilometres
0 250 500 1000
Deformed external zones
Flyschs domains
Exhumed HP-LT metamorphics
Exhumed MT-MP metamorphics
Exhumed HT-LP metamorphics
Continental crust
Thinned continental crust
Exhumed mantle
Oceanic crust
4
40°
30°
-10°
0°
10°
20°

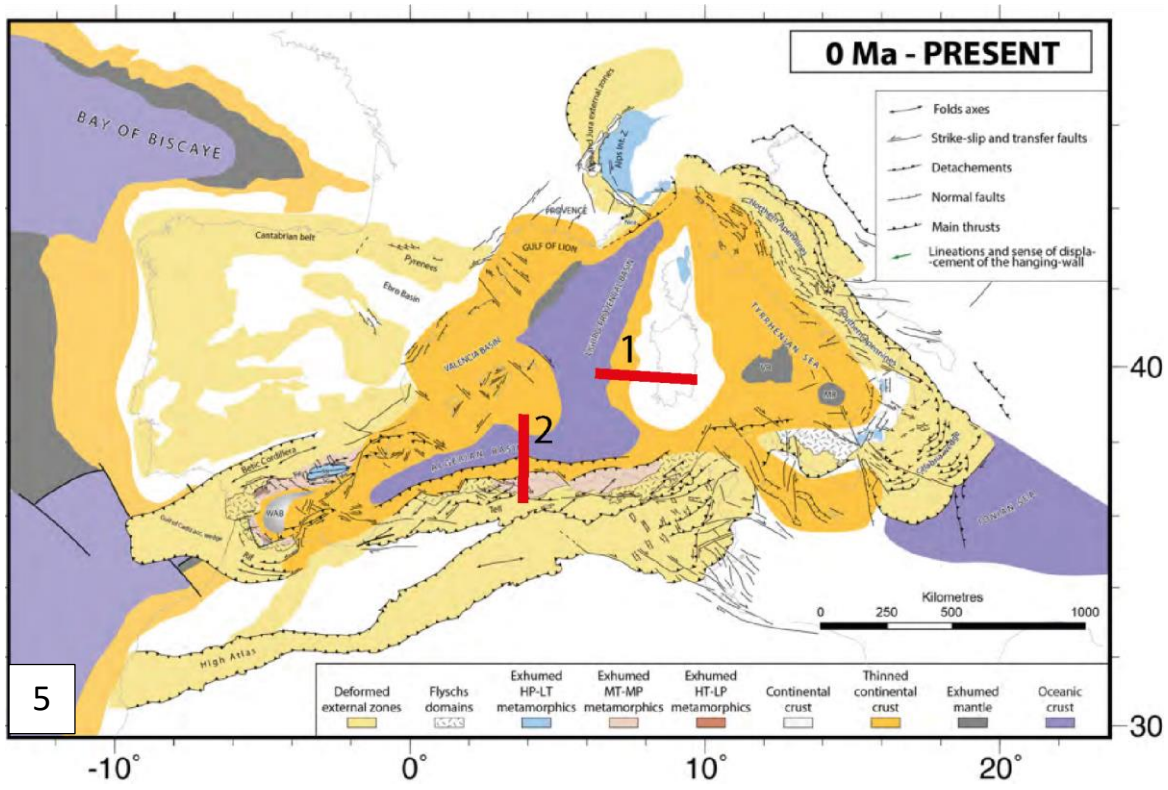

***Figure 3.3**: Reconstruction of the Western Mediterranean geological evolution: **1.** Priabonian **2.** Early Aquitanian **3.** Langhian **4.** Tortonian and **5.** present day situation with position of the schematized margins architectures of figure 3.4. (Romagny et al., 2020).*

Up to 35/32 Ma - Phase of plates scale interactions

Since 74 Ma the Mediterranean is in a plate convergence context, in which the interactions between Africa, Adria, Europe and subplates shaped the area through a complex system of belts and subduction zones (**Figure 3.3.1)**, with the not negligible influence of inherited structures like the lithosphere thickness and the lithosphere heterogeneous composition consequence of the Mesozoic rifting (Carminati and Doglioni, 2005).

32 to 20-15 Ma – Phase of opening of the Liguro-Provençal basin and Corso-Sardinian block rotation, and beginning of the Alboran Sea formation (Jolivet *et al.*, 2021a)

The relative convergence between Europe and Africa (or Africa and Adria depending on the model) was in the past considered the cause of the opening of the Western Mediterranean basins. The data about convergence (135 km of in the last 23 Ma between Africa and Europe) and the ones about the migration of the Appennine arc (more than 700 km eastward in the last 23 Ma), conversely suggest that the migration of the Appennines-Maghrebides arc is the result of the Appennine-Maghrebides subduction roll-back, due to slab pull or mantle flow (Carminati and Doglioni, 2005).

Around 30 Ma the Apennines developed along the Alps–Betics retrobelt to the east, in which oceanic or thinned pre-existing continental lithosphere was present (Carminati and Doglioni, 2005). The subduction rate of the Apennines subduction trench was slowed down in the NE and SW portions, because of the friction with the continental lithosphere of the Adria and Africa margins. This led, together with an 'easily subdactable' oceanic lithosphere in the central part of the system, to an increase of the curvature of the trench (convex shape in Early Oligocene time) (Carminati and

Doglioni, 2005). Relatively coevally (30-35 Ma) the absolute velocity of Africa decreased, and the convergence velocity between Africa and Eurasia increased: the slowing down of Africa may be imputed to the **collision between the two plates** (Jolivet and Faccenna, 2000 and references therein) and can be the cause of the extensional processes in the Mediterranean region because it increased the retreat velocity -and consequently the extensional stress- of the African plate in the locked oceanic subduction zone (Jolivet and Faccenna, 2000): as a result, the extensional basins of the Aegean Sea, the Liguro-Provençal Basin and Alboran Sea formed in the overriding plate (Jolivet *et al.*, 2021a). Within these dynamics, the opening of the Sardo-Provencal Basin is the result of the 30° counter-clockwise rotation of the **Corsica-Sardinia block** (Rehault *et al.*, 1984) **(Figure 3.3.2 and 3.3.3)**. The relative movement between Sardinia and Balearics was possible during the spreading phase through the dextral strike-slip motion along the **North Balearic Fracture Zone**, an approximately NW-SE fault system (Rehault *et al.*, 1984; Granado *et al.*, 2016, Jolivet *et al.*, 2021b; Maillard *et al.*, 2020b). The evolution of the rifting led to spreading of oceanic crust due to the extreme stretching of the continental crust, during a timeframe of some millions years: 23-19 Ma (Cherchi and Montadert, 1982) or 21-18 Ma (Rehault *et al.*, 1984). Calc-alkaline magmatism of 33-13 Ma and related to the subduction characterizes the western Sardinian margin (Rehault *et al.*, 1984).

At 20-15 Ma the **AlKaPeCa** (Alboran, Kabilia, Peloritani, Calabria) block collided with the African margin (Figure 3.3.3), marking the end of this phase of basins opening (Leprêtre *et al.*, 2018; Romagny *et al.*, 2020; Jolivet *et al.*, 2021a) and starting the phase in which the retreating slab was divided in two. The slab retreating towards east led to the opening of the Tyrrhenian Sea, while the part of the slab retreating westward led to the opening of the Algerian Basin and the Alboran Sea (Jolivet *et al.*, 2021 and references therein).

In the last decades, different authors tried to shed some light on the geological history of the **Algerian Basin**, still the most controversial in the Western Mediterranean in terms of both rifting processes and direction of opening. The classical model of opening considers that the Liguro-Provençal Basin, the Valencia Thrust and the Algerian Basin opened in an approximately NW-SE direction, respectively during Late Oligocene-Early Miocene the first two, and during Middle Miocene the Algerian Basin (Rehault *et al.*, 1984; Schettino and Turco, 2006; Carminati *et al.*, 2012). More recently, Mauffret *et al.* (2004) and Medaouri *et al.* (2014) proposed that the NW-SE direction of opening is valid just for the Valencia Trough and the Liguro-Provencal Basin, while in the case of the Algerian Basin a NE-SW or E-W opening direction would better explain the observed geometries. An hybrid model has been proposed by Driussi *et al.* (2015), who suggests a first NW-SE opening phase followed by a longer phase in a NE-SW direction, partly confirmed by Aïdi *et al.* (2018) that proposed a two-step model formation for the Western Algerian margin: a south to south-eastward drift of the AlKaPeCa domain, with consequent collision with the African plate and detachment of the slab (17 Ma), followed by oceanic crust formation as a consequence of the east-west opening (16-8 Ma) (Aïdi *et al.*, 2018 and references therein). More recent hypothesis suggest a fan-shaped opening of the Eastern Algero-Balearic Basin between 15.2 and 12.7 Ma (Haidar *et al.*, 2022).

Around 15 Ma **(Figure 3.3.4)**, the double-vergent Apennines–Maghrebides trench and the back-arc extensional wave moved eastward. At 10 Ma the formation of the Liguro-Provencal Basin, the Valencia Trough, and the North Algerian Basin was almost completed, and the extension migrated east of Corsica and Sardinia (Jolivet *et al.*, 2006 and references therein).

8 Ma to nowadays: The phase of Late Mediterranean tectonics

At about 8 Ma, extension stopped in most of the Western Mediterranean and a **tectonic inversion** propagated eastward from the Alboran and Southern Algerian Basin (c. 8 Ma) to the southern Tyrrhenian (<2 Ma) in a 'scissor-like' manner, following the same direction of the subduction cessation (Jolivet *et al.*, 2006, 2021a; Billi *et al.*, 2011; Carminati *et al.*, 2012). This phase of compression is considered partly responsible for the Messinian Salinity Crisis, through the reduction of the connection between the Atlantic Ocean and the Mediterranean (Jolivet *et al.*, 2006, 2021a) **(Figure 3.3.4 and 3.3.5).** Around 6 Ma, the Messinian Salinity Crisis (Chapter III.A.4) represents a geological event of vast impact for the following development of the Mediterranean Basin, especially in terms of sedimentary sequence and subsidence rates (Ryan *et al.*, 1973; Rehault *et al.*, 1984).

In the Western Sardinian margin, no mayor tectonics event happened after salt deposition (Ryan *et al.*, 1978) but the post-rift differential subsidence - particularly intense after salt deposition - increased the deepening of the Sardinian slope (Montadert *et al.*, 1978; Rehault *et al.*, 1984; Geletti *et al.*, 2014) as well as most of the Mediterranean Sea margins. Moreover, the sea-level drawdown probably induced a large isostatic rebound, and the Zanclean reflooding induced tilting and subsidence (Rabineau *et al.*, 2014; Heida *et al*., 2021).

III.A.2.2. Geological structures and present-day kinematics

- ### Margins architecture

The lithosphere of the Western Mediterranean is thinner than 60 km in the basins, with a range of values that varies between the 60 km in the Valencia Trough and the only 20-25 km in the Tyrrhenian Sea, and the same trend is followed by the crust (Carminati and Doglioni, 2005). In the Western Sardinian margin **(Figure 3.4.1)**, the continental crust thins from the 27 km thickness onshore to the 12 km along 70 km distance (Afilhado *et al.*, 2015), while in the Algerian margin **(Figure 3.4.2)** the crust thins from 15 km in the upper margin to around 6 km at the margin foot, along 50 km (Leprêtre *et al.*, 2013).

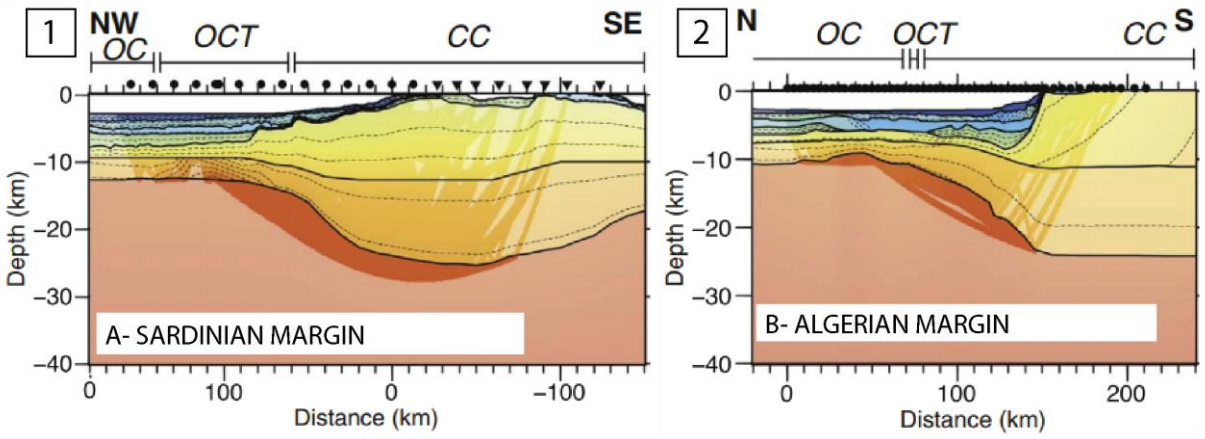

***Figure 3.4**: Comparison between the nowadays continental and oceanic crust thickness in different margins: **1.** The Western Sardinia margin **2.** The Algerian margin, position in figure 3.3.5. OC: Oceanic Crust; CC: Continental Crust; OCT: Ocean-Continent Transition (Aïdi et al., 2018, after Afilhado et al., 2015, Moulin et al., 2015).*

The OCT (Ocean-Continent Transition) on the Algerian margin is extremely narrow with a width of less than 10 km, distinguishing this margin from other Western Mediterranean margins formed in a similar contest and leading to the hypothesis of a multiphase formation of the margin west of Alger: a rollback of the Tethyan subduction zone, a transcurrent episode and a compressional reactivation (Leprêtre *et al.*, 2013). The nature of the crust, supposed to be a thin oceanic one because of the geophysical data, is debated due to the lack of samplings; in the area off Greater Kabylia it has a thickness range between 3 and 5.5 km (so thinner than the average 7 km) and is characterized by thickness changes, typical of basins of back-arc settings. In almost all the basin, the Moho is at a depth of maximum 14 km (Aïdi *et al.*, 2018). Different fault geometries reflect the complex geological evolution of the Algerian margin, and the recent change from extensional to compressional tectonics.

- ## Transfer zones

As already described in the previous subchapters, the geological history of the Western Mediterranean is characterized by different phases of back-arc opening of the basins and rigid blocks rotations. The crustal or lithospheric expression of the faulting in the slab accommodating the tearing are the transform zones **(Figure 3.5)**, areas of deformation several tens to hundreds of km wide (Jolivet *et al.*, 2021b and references therein). These have been largely hypothesized in the Mediterranean back arc regions, but often their position has been drawn based on kinematic considerations rather than magnetic or seismic data observations. We will focus here mainly on the **Catalan-Baleares Sicily Transfer Zone** (Jolivet *et al.*, 2021b).

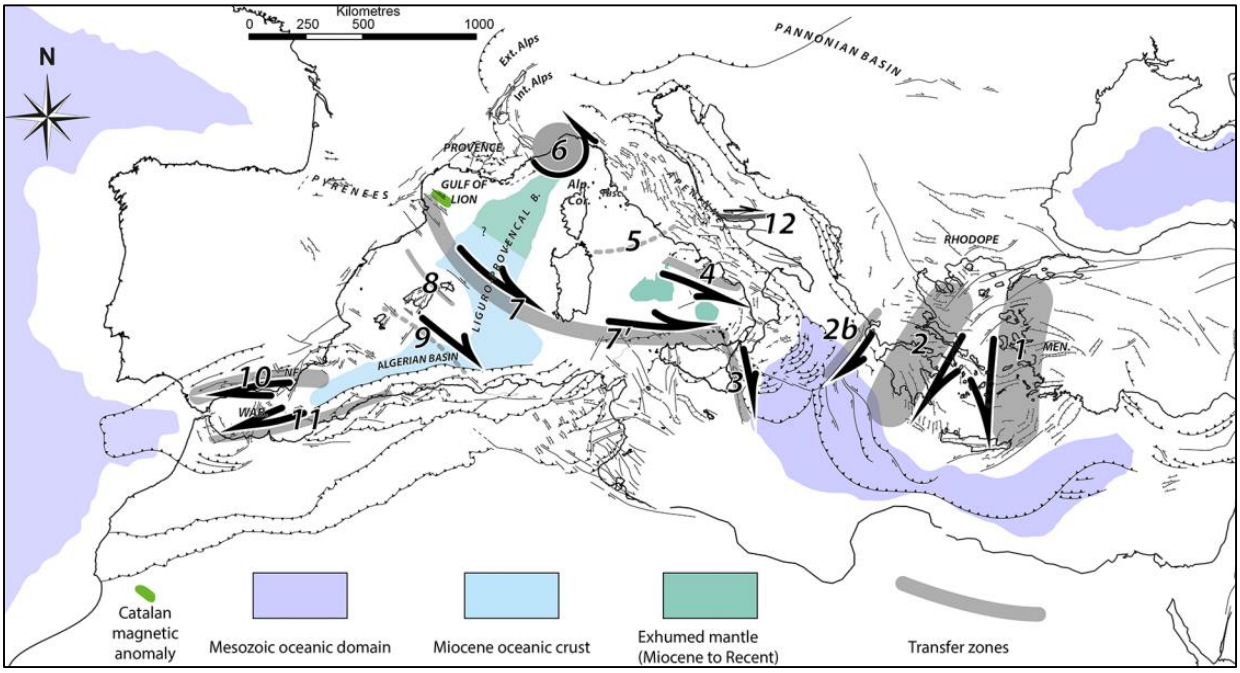

Figure 3.5*: Location of the transfer zones and nature of the crust in the Mediterranean region (*Jolivet *et al.*, 2021b*). 1: West Anatolia Transfer Zone, 2: Central Aegean Shear Zone, 2b: Kephalonia transfer fault; 3: western limit of the Calabria accretionary wedge, 4: transfer zone along the northern limit of the Southern Tyrrhenian oceanic/exhumed mantle domain, 5: 41st parallel fault, 6: Alps/Apennines transition, 7: Catalan-Baleares Sicily Transfer Zone (CBSTZ), 8: Central transfer zone (Valencia basin), 9: Transition between the Liguro-Provençal and Algerian basins, 10: Betic Cordillera, northern limit of the Alboran Sea, 11: Rif, southern limit of the Alboran Sea, 12: Trimiti transfer zone.*

The Catalan-Baleares-Sicily Transfer Zone (CBSTZ) (Figure 3.5) starts in the southern Gulf of Lions (eastern limit of the Pyrenees) and crosses the Sardo-Provençal basin reaching northern Sicily. This is the longer fracture zone of the Mediterranean, result of the rigid block rotation that led to the formation of the Sardo-Provençal Basin and the opening of the southern Tyrrhenian with the rotation of the Italian peninsula (Jolivet *et al.*, 2021b). This fracture zone groups previously described fracture zones as the Catalan Fracture Zone (Mauffret *et al.*, 2001, 1995) and the North Balearic Fracture Zone (NBFZ) (Maillard and Mauffret, 1999), recently described in more detail by Maillard *et al.* (2020b) based on seismic data interpretation of transtension structures and on the Catalan magnetic anomaly magnetic anomalies (Canva *et al.*, 2020). In the seismic profiles, grabens and half grabens filled with syn-rift volcanic rocks and sediments have been interpreted as part of this fracture zone (Maillard *et al.*, 2020b). The total displacement along this fracture zone increases towards southeast, going from zero to 800 km calculated (Jolivet *et al.*, 2021b; Romagny *et al.*, 2020). The faults were active first in the NW part and then in the SE one, due to the deformation migration (Jolivet *et al.*, 2021b); in the northern Sicily sector, this transfer zone is nowadays reactivated in compression (Sulli, 2000).

- ## Strain and seismicity

The relative motion between Africa and Europe (e.g. **NW-SE oblique convergence**) has nowadays a rate that varies between 3-7 mm/yr (N45W+-20 convergence direction) in the Central Mediterranean to 2-5 mm/yr (EW convergence direction) in the western limit of the Mediterranean (Gibraltar Strait) (Nocquet and Calais, 2004; Capron *et al.*, 2011) **(Figure 3.6).**

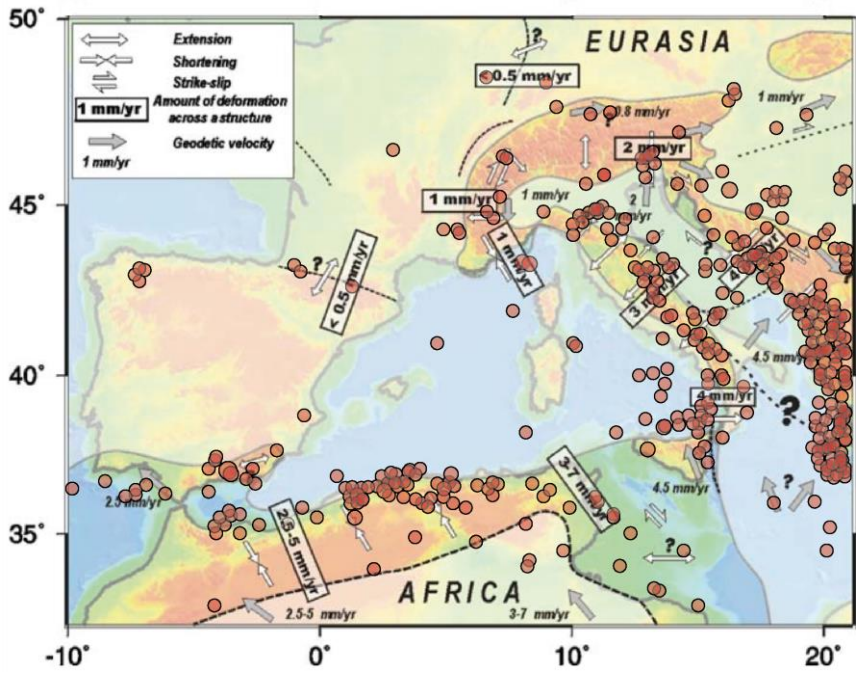

***Figure 3.6**: Map of the Western Mediterranean with the amount of deformation and strain regime (white arrows) of the highlighted active areas, while the grey arrows indicate the direction of the African plate with respect to the Eurasian plate (Nocquet and Calais, 2004). Juxtaposed is the map of the distribution of the earthquake with a magnitude of 5 or more in the Western Mediterranean between 1922 and 2022 (USGS catalogue 2022), which position corresponds to the area of maximum strain.*

This deformation is concentrated at the boundary between Nubia and Eurasia plates, and most of the earthquakes interest a narrow area of the coastal Africa (Figure 3.6, Nocquet and Calais, 2004). The **concentration of the stress and strain**, and consequently of the mostly reverse fault-type earthquakes, is probably due to the sharp transition between oceanic crust in the north and continental crust in the south (Nocquet and Calais, 2004).

In the **Algerian margin** up to 50% of this deformation is supposed to be concentrated in the offshore domain, where Déverchère *et al.* (2005) and Domzig *et al.* (2006) identified a serie of fault-propagation folds, 20-35 km long **(Figure 3.7)**. These are **south dipping north-verging structures** that are partly accommodating the Africa-Europe convergence, and that begin at about 1° of longitude and continue towards east (Déverchère *et al.*, 2005b; Domzig *et al.*, 2006). Westward, this structure of faults mapped after the MARADJA I cruise seems to be connected with the Yusuf fault (active transpressional fault), while eastward seems to be connected with the reverse faults of the Sardinia Channel (Bougrine *et al.*, 2019 and references therein). The integration between the study of seismic data and GPS velocity confirms the strain accumulation on an onshore reverse fault system (Bougrine *et al.*, 2019).

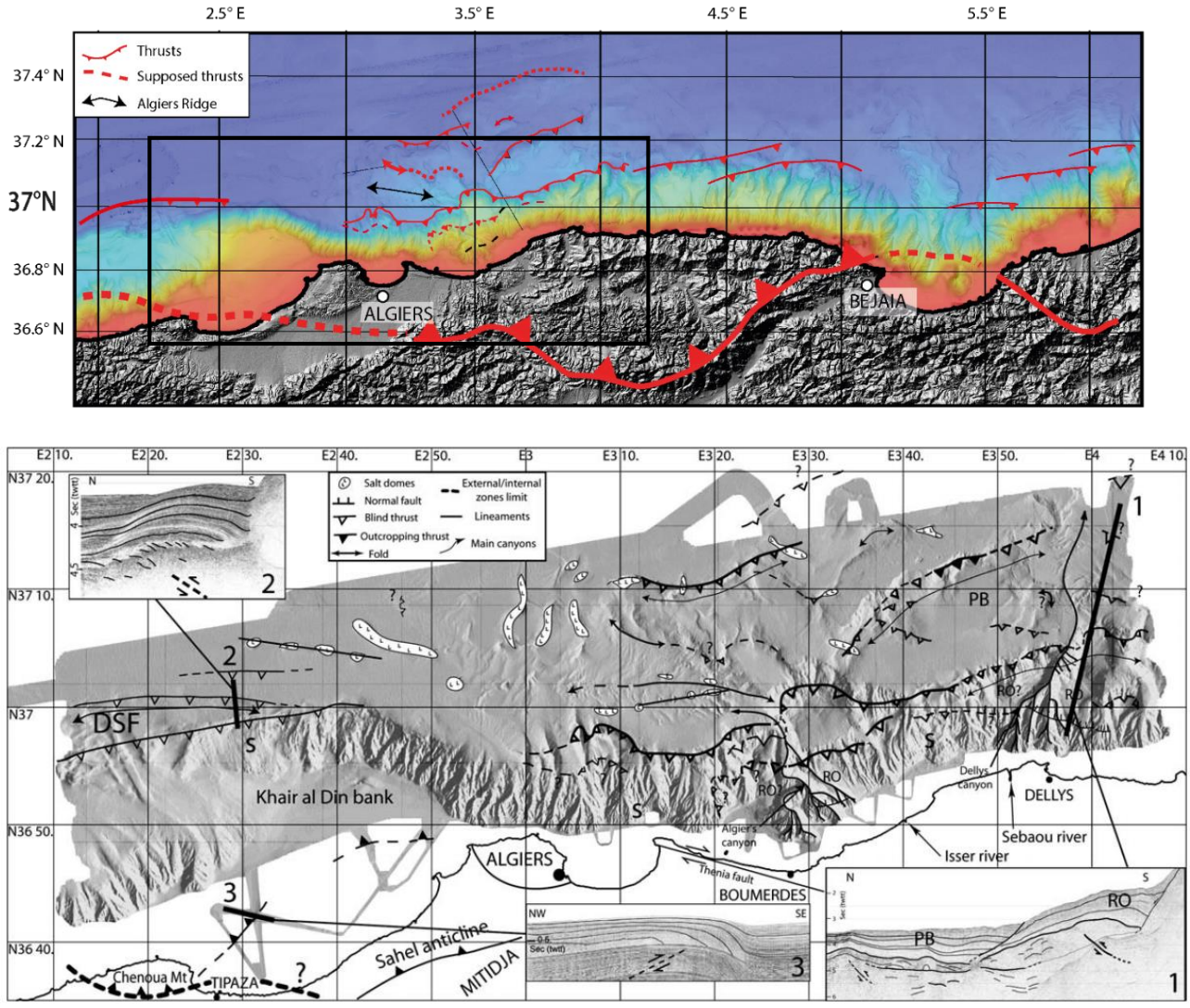

Figure 3.7: 1. *Bathymetric and topographic map of the study area, with the pattern of thrusts on the Algerian margin. After Babonneau et al. (2017), Bougrine et al. (2019), Déverchère et al. (2005), Domzig et al. (2006).* ***2.*** *Detail of the Tenes region with the main geological features identified (Domzig et al., 2006).*

The importance -not just scientific but also civil- of the studies in the area is due to the nowadays destructive seismicity, with catastrophic events as the Mw 6.8 earthquake of Boumerdes (Algeria) in 2003 on a ENE-striking, S-dipping reverse fault and a maximum potential magnitude of c. 7.3 (Yelles *et al.*, 2004; Ayadi *et al.*, 2008; Déverchère *et al.*, 2010; Billi *et al.*, 2011; Bougrine *et al.*, 2019).

The focal mechanisms of the recent earthquakes in the area describe mostly pure reverse faulting (Déverchère *et al.*, 2005). Despite the uncertainties are still high, this margin could be at an early stage of subduction (Auzende *et al.*, 1972).

Towards the center of the basin, the structure of the **Hannibal High** (position in Figure 3.2) is a "complex stacking of volcanoclastic formation over a thin crust" (Leprêtre *et al.*, 2013), but its origin is still discussed. The area corresponds to an important magnetic anomaly, leading Mauffret *et al.* (2004) to interpret the Hannibal High as a N-S trending accretion center, while more recent interpretations describe it as the offshore expression of the post-collisional magmatism already recognized in Greater Kabylia (Aïdi *et al.*, 2018). The Miocene to recent uplift is considered the result of important thermal uplift (Aïdi *et al.*, 2018).

III.A.3. The sedimentary sequence in the Western Mediterranean

The Paleozoic-Mesozoic basement in the Western Mediterranean has a depth of around 6 s TWT and is structured in horst and grabens due to the rifting. The shape of the basement and the sedimentary sequence above has been studied mainly trough seismic reflection profiles, partly calibrated thanks to DSDP and IODP wells and industrial drillings.

The sedimentary sequence in the Western Mediterranean has been divided in **(Figure 3.38)**:

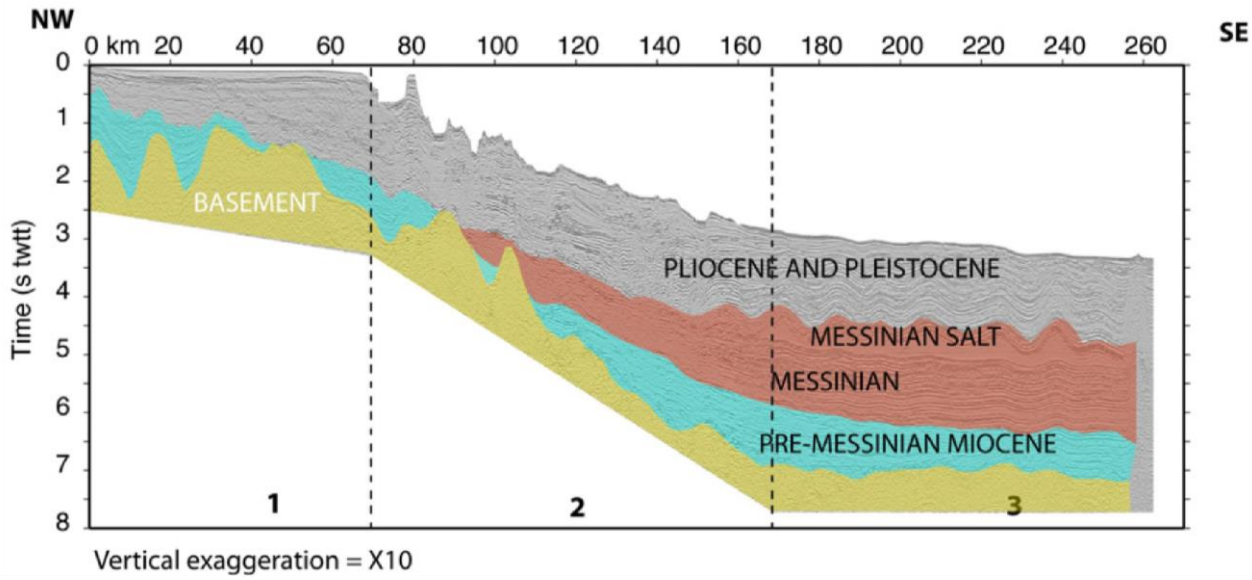

Figure 3.8: *NS-SE seismic profile ECORS 1, Gulf of Lions, showing the deepening of the Miocene depositional environment, the Messinian Trilogy and the Plio-Quaternary sedimentary sequence (Leroux et al., 2015).*

A **Lower and Middle Miocene** marly and probably detrital sequence, with an open sea depositional environment in the upper part (Rehault *et al.*, 1984). This sedimentary sequence has a seismic velocity of up to 5 km/s and a calculated thickness of 3-5 km (Hsü *et al.*, 1978; Leprêtre *et al.*, 2013). On the Sardinian margin, the pre-Messinian strata deposited in a basin with a different conformation; after the deposition, a strong and still active subsidence towards the centre of the basin tilted the strata. On the other hand, the pre-Messinian sediments on the Algerian margin have been mostly deformed by crustal tectonics.

A **Messinian** sequence of evaporitic and terrigenous sediments (Messinian trilogy) that deepens towards the margin toe (Aïdi *et al.*, 2018), landward substituted by a sedimentary gap

called MES – Messinian Erosion Surface (Lofi *et al.*, 2011a). This sedimentary sequence is particularly important for this work, and will be described in detail in subchapter III.A.4.2 (Markers of the Messinian Salinity Crisis in the Western Mediterranean).

The **Pliocene and Quaternary** sequence is composed of mainly marly sediments, as a consequence of the re-established marine conditions at the end of the crisis. The average calculated thickness varies between 400 m (foot of Sardinian Slope) and 1.6 km (Northwestern Mediterranean), with the strong local variabilities mostly due to the different sedimentary inputs. This post-Messinian sedimentary sequence has its maximum thickness in correspondence with the Rhone Deep Sea Fan, a turbiditic and mass transport deposits up to 3.6 km thick (Rehault *et al.*, 1984).

During Lower Pliocene, the deposition consisted in pelagic and hemipelagic clay, and became turbiditic during Upper Pliocene with the deposition of sand and clay, leading to a change in seismic facies between a **semi-trasparent Lower Pliocene** to a more **reflective Upper-Pliocene/Quaternary** (Rehault *et al.*, 1984). Climatic changes and consequent sea level fluctuations had a strong influence on the sedimentation of the upper Pliocene and Quaternary (Obone-Zue-Obame *et al.*, 2011 and references therein). The seismic velocity of this sequence strongly depends on the depth, because of the direct proportionality between compaction and seismic velocity. The Vp velocities calculated by Leprêtre *et al.* (2013) on the Algerian margin is in the range of 1.9 to 2.7 km/s.

The Plio-Quaternary sedimentary cover on the Western Sardinian margin is very limited, with a thickness of less than 0.3 s TWT (Sage *et al.*, 2011) that increases up to 2.5 s TWT going towards the center of the basin. On the Algerian margin, The Plio-Quaternary sediments have low amplitude and high frequency reflections, and present a maximum thickness of about 1.2 s TWT in the central Algerian margin. The main rivers of this area have high availability of clastic sediments due to the mountain reliefs, and their seasonal regime gives a seasonality to the sediment supply (Dan *et al.*, 2010; Capron *et al.*, 2011). The presence of canyons and the instability of the margins led to the deposition of numerous sedimentary bodies at the foot of the slope and in the basin; their generally limited dimension is supposed to be due to the high frequency of the earthquakes in the area (Domzig *et al.*, 2006), so they can be important to study the historical seismicity (Dan *et al.*, 2010).

III.A.4. The Messinian Salinity Crisis

The catastrophic event of the Messinian Salinity Crisis at the end of the Miocene is a central topic in the Mediterranean subsoil exploration since the middle 20th century. The presence of a layer of salt in the Mediterranean has been initially noticed thanks to the bathymetric data, that registered the presence of particular structures on the sea floor (Boucart, 1958).

Later, the acquisition of *flexotir* profiles **(Figure 3.9)** highlighted the presence of domes (Auzende *et al.*, 1971), that has been confirmed to be evaporitic thanks to the Deep Sea Drilling Project drillings in the site 124 and 134 (Ryan *et al.*, 1973) opening a new, still unsolved chapter in the history of the Mediterranean geology. It was clear since the very beginning that the deposition had to be the consequence of an extraordinary geological event, probably an **alternance of marine and shallower water conditions** (Nesteroff *et al.*, 1973), but different hypothesis originated due to the lack of data.

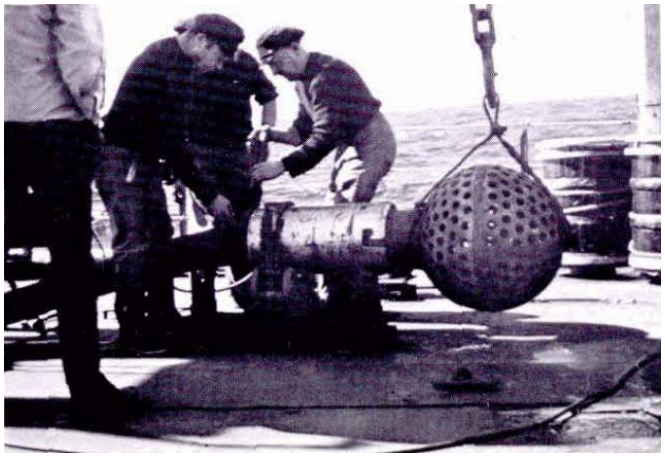

***Figure 3.9**: Preparation of the Flexotir sphere (photo CNEXO-Laubier), seismic reflection method used to image the subsoil during the 70's.*

Nowadays the most accepted hypothesis is a **1500 m sea level water drop** due to the **closure of the Gibraltar Strait** and the consequent evaporation of seawater (Hsü and Cita, 1973; Ryan and Cita, 1978; CIESM, 2008), but an alternative option proposed a shallow water desiccated basin, that would therefore consist in a less catastrophic event for what concerns the volumes of water involved (Nesteroff *et al.*, 1973). A third -less widely accepted- hypothesis considers the scenario of a deep not desiccated basin, with a relatively deep depositional setting of the Messinian Salinity Crisis sequence (Selli, 1973; Manzi *et al.*, 2005).

The still open questions on the MSC are mainly due to the fact that 80% of the MSC deposits are offshore and can be studied exclusively through indirect geophysical data (seismic data, gravimetric data, magnetic data etc.) without the constrain of direct data. In fact, just a few percent of the MSC sequence has been drilled for scientific purpose, and the industrial boreholes result in cuttings instead of complete cores of the sedimentary sequence (Kastens *et al.*, 1987; Hübscher *et al.*, 2008; Ottes *et al.*, 2008). The scientific community is now trying to overcome the boundary between onshore and offshore studies and to create a stronger interdisciplinary and international collaboration (i.e. MedSalt and SaltGiant projects).

III.A.4.1. Chronostratigraphy of the MSC

Based on the study of different paleontological and sedimentological records or study areas, the chronostratigraphy of the MSC present significant differences between authors. The possible chronology proposed in CIESM (2008), result of a critical analysis of the studies of the previous 30 years and accepted by a consistent part of the community working on this topic, divides the MSC in the following phases **(Figure 3.10)**:

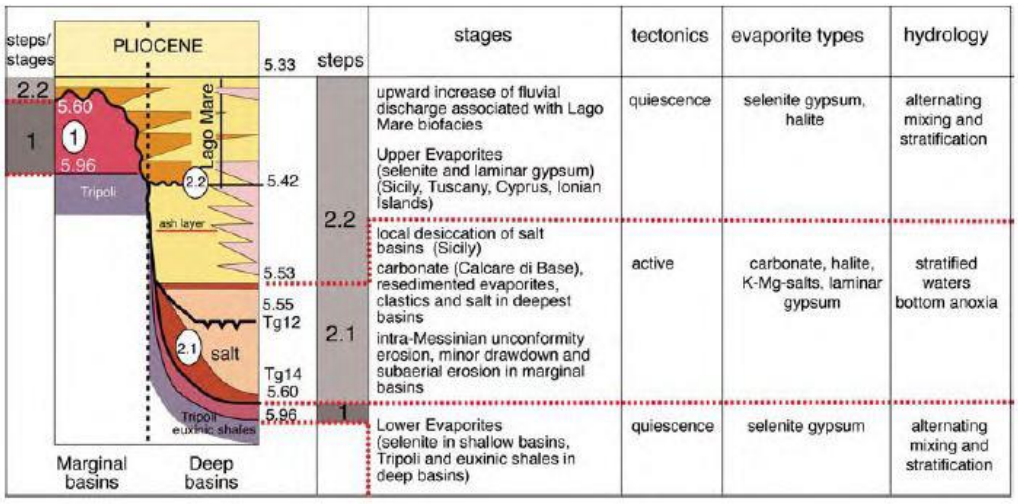

***Figure 3.10:** The MSC scenario proposed during CIESM (2008), explanations in the text.*

***Figure 3.11**: Gypsum crystals from the Sicilian outcrops of the Messinian Salinity Crisis deposits (Gessi di Cattolica).*

-7.251-5.97 Ma: Before the Crisis. A phase of pre-conditioning has been defined and dated from micropaleontological studies. The first occurrence of Globorotalia Miotumida (7.25 Ma) marks the beginning of the tectonic restriction of the Mediterranean-Atlantic connection, supposed to be related to the Africa-Eurasia convergence and the tectonic uplift in the Gibraltar Strait area. A drop in the diversity of calcareous plankton has been dated 6.7 Ma, and between 6.3 Ma and the beginning of the MSC the sedimentary sequence registered a peak of precipitation of authigenic calcite, dolomite and aragonite (Roveri *et al.*, 2014 and references therein).

-5.96-5.6 Ma, Stage 1: MSC onset and first evaporitic stage. At 5.96 (+- 0.2) Ma there has been the first important change in the salinity level, with deposition of evaporites (as Primary Lower Gypsum) in the so-called marginal basins. The deposition started in Sicily **(Figure 3.11)**, and was soon followed by evaporites deposition in Greece, Spain and Cyprus (Krijgsman *et al.*, 1999, 2002). During this stage, the deposition in the Eastern and Western Mediterranean was diachronous.

-5.6-5.55 Ma, Stage 2: MSC acme and halite deposition. A successive major sea-level fall -not accepted by all the scientific community- resulted in the erosion of the exposed margins, development of subaerial canyons and the consequent formation of the **Messinian Erosion Surface (MES)**, and deposition of the products of the erosion downslope (CIESM 2008; Lofi *et al.*, 2005; 2011a, 2011b). The products of the erosion have been largely studied (Maillard *et al.*, 2003, 2006, 2020a; Lofi *et al.*, 2005), being the only preserved evidence of the deposition that preceded the Messinian Salinity Crisis.

At the same time, in the deep basins the high salinity of the water resulted in the deposition of a 1500-3000 m thick layer of **evaporitic sediments**, during an estimated period of about 600k years (CIESM, 2008 and references therein) and with an areal extension illustrated in **Figure 3.12.1**. Thanks to the peculiar physical characteristics of the evaporites, the deposition of this layer created in the Mediterranean the conditions for the development of a thin-skinned tectonics that still affects the sediments of the last ≈6 Ma.

-5.55-5.33 Ma, Stage 3: water dilution. During the last phase of the MSC, as a consequence of the general shallow water dilution and the cyclic salinity fluctuations, **Upper Evaporites** and Lago Mare deposited (Orszag-Sperber, 2006; Andreetto *et al.*, 2021). The Upper Gypsum deposited between 5.55 and 5.42 Ma (Stage 3.1), while the beginning of the deposition of the Lago Mare has been dated 5.42 Ma (CIESM 2008).

-5.33 Ma: The end of the MSC is marked by the **Zanclean flooding**, which follows the initial collapse of the Gibraltar Strait (5.48 Ma) (Clauzon *et al.*, 2008). The wide catastrophic reflooding has been confirmed by the sharp paleontological and sedimentological contact between MSC and Pliocene

sediments and by a sedimentary body at the Sicily gateways, supposed to be the biggest megaflood deposit on Earth (Couvering *et al.*, 2000; Micallef *et al.*, 2018). The datation of the end of the MSC (5.33 Ma) has been defined with the base of the Trubi marls in Sicily, representing the sedimentary record of the Zanclean reflooding (GSSP at Eraclea Minoa, Sicily) (Couvering *et al.*, 2000).

III.A.4.2. Markers of the Messinian Salinity Crisis in the Western Mediterranean

The Eastern and Western Mediterranean basins present important differences for what concerns the MSC markers, possibly explained by the presence of the Sicily Strait that acted as a gateway during the Crisis (Micallef *et al.*, 2018). While the Western Mediterranean is characterised by the presence of the Messinian trilogy (Figure 3.12), the Eastern Mediterranean sedimentary record is limited to up to 2000 m thick Mobile Unit with 6-7 strong reflectors and an erosional surface at the top, in contrast with the mainly transparent MU of the Western Mediterranean (Lofi *et al.*, 2011a). Also for what concerns the nomenclature, there has been some confusion mainly due to the different deposits in the onshore domain and for the lack of data in the offshore domain. Just recently most of the scientific community started to use a common nomenclature for the Messinian Trilogy in the deep deposits of the Western Mediterranean (Figure 3.12.3 and 3.12.4) (Lofi *et al.*, 2011a), facilitating the comparison between studies in the different basins. We will now describe the main characteristics of the MSC markers in the Western Mediterranean, with some more details about the Western Sardinian and Algerian margins.

- ### Messinian surfaces in the Western Mediterranean

Several surfaces have been identified within, above and below the Messinian sequence (Figure 3.12.3-4 and **Figure 3.13**), marking the beginning and the end of the Messinian Crisis and subdividing the sedimentary sequence. Offshore and in shallower areas, these surfaces testify the erosional events consequence of the sea level drop.

Messinian Erosion Surface (MES): this surface is an angular unconformity between the pre-MSC and the Plio-Quaternary sediments, and it is the most largely extended of the Messinian surfaces (Ryan, 1976). Visualized as a strong erosional reflector in 2D seismic imaging (Figure 3.13), it often forms complex drainage networks in the 3D imaging, where can be appreciated the Messinian system of valley and incisions (Cameselle and Urgeles, 2016). Despite the doubts about the phases of formation of the MES, it is widely accepted that it is diachronous and polygenetic, a result of both the subaerial erosion due to the seawater drawdown –proved by direct observations on the slopes (Savoye and Piper, 1991; Cornée *et al.*, 2008)-, subaqueous erosion and carbonates dissolution (Lofi *et al.*, 2005, 2011b), and the erosional effect of the reflooding event at the end of the MSC (Roveri *et al.*, 2014 and references therein). Observed only at the upper slope of the Western Sardinian margin (Sage *et al.*, 2011), it is relatively continuous on the Algerian margin (Obone-Zue-Obame *et al.*, 2011).

Bottom Surfaces (BS, BES): The prolongation of the MES basinward is represented by the Bottom and Bottom Erosional Surfaces (BS and BES), a surface predating the evaporitic units (Ryan and Cita, 1978) and often not well imaged because of the seismic imaging disturbance linked to the salt layer. Its interpretation is discontinuous in the Western Mediterranean (Lofi *et al.*, 2011a).

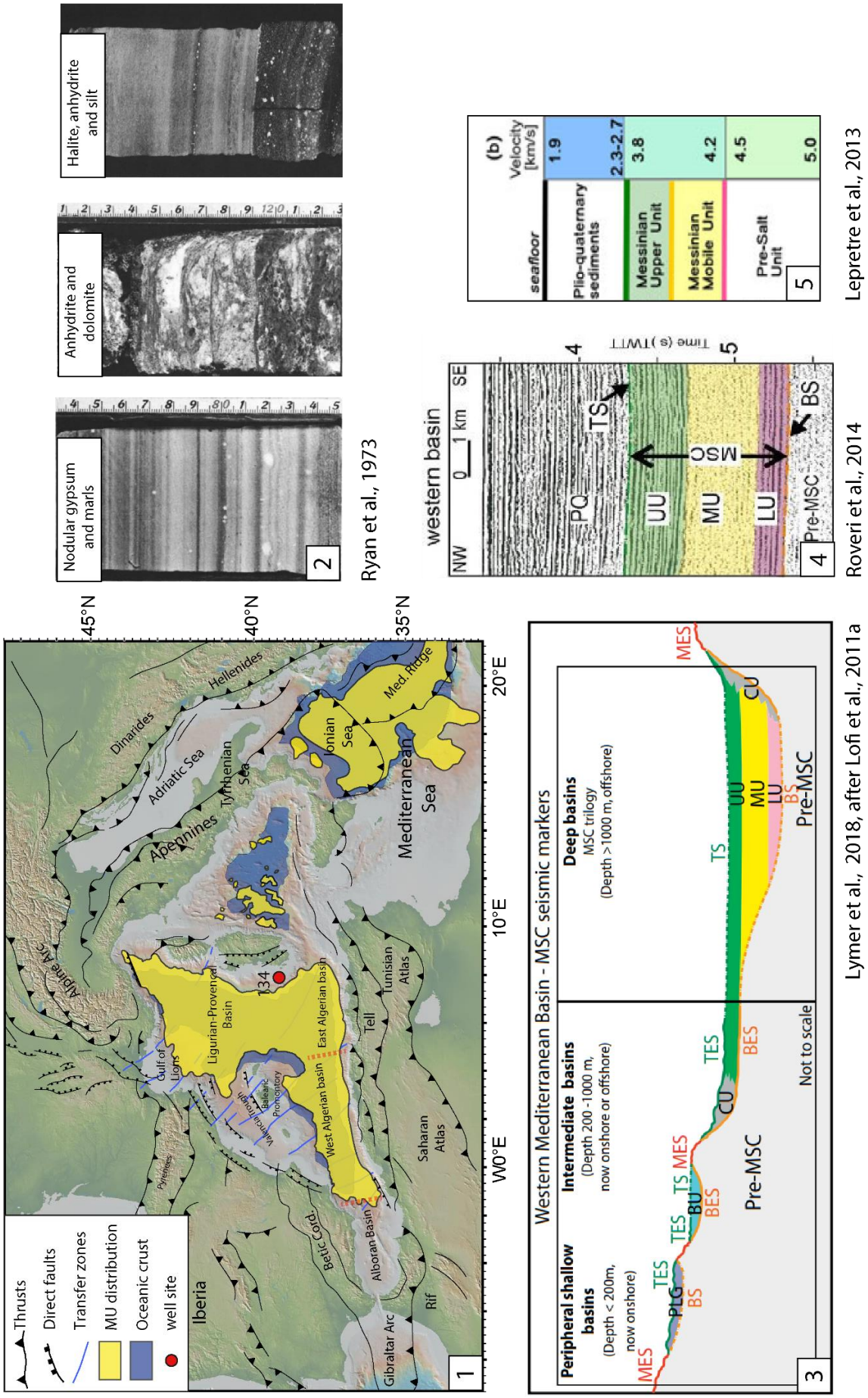

Figure 3.12: *(caption next page)*

Figure 3.12: *Schematic distribution and characteristics of the Messinian deposits in the Western Mediterranean.* ***1.*** *Map of the present-day extent of the oceanic crust and MU deposits, together with the main structural lineaments (after Domzig et al., 2006; Jolivet et al., 2006; Lofi et al., 2011a; Lymer et al., 2018) and position of the DSDP drilling site 134 (leg XIII) (Ryan et al., 1973).* ***2.*** *Details of the drilling site 134 recoveries: nodular gypsum in a matrix of dolomitic marl and silt -similar to the nowadays Sabkhas environment-, spherules of anhydrite in a dolomitic matrix and an interbedding of halite, silt and anhydrite (modified after Ryan et al., 1973).* ***3.*** *Schematization of the MSC surfaces and units in the Western Mediterranean (Lymer et al., 2018 after Lofi et al., 2011a).* ***4.*** *The Messinian Salinity Crisis deposits of the Western Mediterranean as imaged in the seismic reflection profiles.* ***5.*** *Velocities of the seismic waves in the Plio-Quaternary and Messinian sediments from velocity forward modelling (Leprêtre et al., 2013). The velocity of the p-waves in the Messinian sequence has values between 3.9 km/s and 4.2 km/s, higher for the MU and lower for LU and UU.*

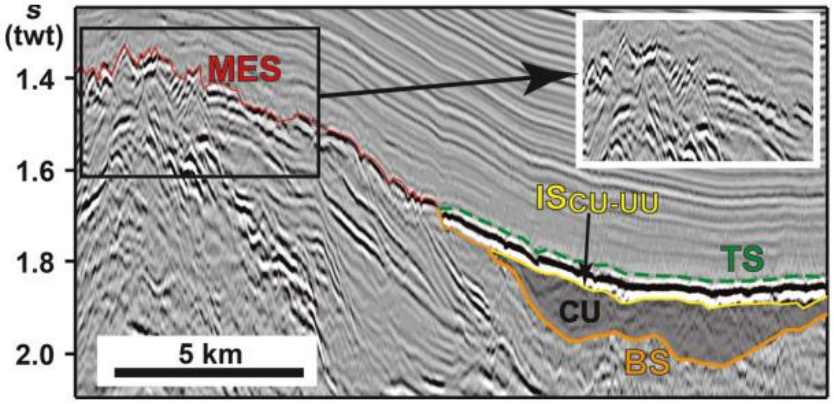

Figure 3.13: *The Messinian Erosion Surface (MES), the Top Surface (TS) and the Bottom Surface (BS) in the Western Mediterranean (Cameselle and Urgeles, 2017).*

Internal Erosion Surface (IES): The internal unconformities inside the UU or CU, locally displaying gullies morphologies, are labelled as IES (Maillard *et al.*, 2006). These internal surfaces are more common in the intermediate-depth basins while they have not been interpreted in the deep Western Mediterranean basins (Lofi *et al.*, 2011a)

Top Surfaces (TS, TES): As well as the Bottom Surfaces, the Top and Top Erosional Surfaces represent the prosecution basinward of the MES, and divides between Messinian and Plio-Quaternary sediments (Figure 3.12.3-4). The marks of erosion have been identified just in the shallower areas (Maillard *et al.*, 2006; Lofi *et al.*, 2011b).

- ## Messinian depositional units in the Western Mediterranean

The three main subunits of the MSC deposits (LU, MU, UU) form an aggrading sequence that fills the deep basins and onlaps the margins, while two secondary units (CU and BU) are locally identified (Figure 3.12.2-3-4).

Lower Unit (LU): The older of the Messinian trilogy units has been observed for the first time in the Gulf of Lions as a group of continuous low frequency and low to high amplitude reflectors for a total thickness of 450-600 m (Montadert *et al.*, 1970; Lofi *et al.*, 2005). The geometrical disconnection between onshore and offshore, together with the lack of direct sampling of the whole Messinian Salinity Crisis sequence, results in uncertainties about its rheology: if this unit has been deposited at the beginning of the drawdown, it is most likely composed of clastic sediments (Lofi *et al.*, 2005),

while if it postdates this event it is probably evaporitic (Krijgsman *et al.*, 1999). On the Western Sardinian margin, the Lower Unit is a package of parallel reflectors mostly recognisable where the MU is undeformed (Del Ben *et al.*, 2018). In the Algerian margin the LU presents low amplitude, low frequency and generally continuous reflectors, with an interpreted thickness comparable to the one of the UU (Capron *et al.*, 2011). Being just locally imaged in the seismic profile and never drilled, we don't have a datation of these layers, so we will refer to it as 'pre-salt' in our seismic interpretation.

Mobile Unit (MU): Deposited during the acme of the Messinian Salinity Crisis, this unit is constituted by halite, and results therefore seismically transparent **(Figure 3.14)** or very slightly stratified due to deposition of chemically and physically different evaporites and incorporation of clastic layers during salt tectonics (Lofi *et al.*, 2011a; Dal Cin *et al.*, 2016; Granado *et al.*, 2016). As a consequence of the high velocity of the seismic waves in this layer (Figure 3.12.5), the top is generally imaged in the seismic data as a high amplitude positive reflection, while the base is a negative high to medium amplitude one. The ductile deformation that characterize this layer made it the first unit of the Messinian Salinity Crisis to be recognized in the Mediterranean seismic sequence (Auzende *et al.*, 1971), but after more than 40 years the whole sequence has still never been completely cored, so as well as for the LU some uncertainties persist. Its areal distribution (Figure 3.12.1) has been mapped through seismic reflection data interpretation, with increasing detail in the last years. The retrodeformation of the salt layer gives as a result an average thickness of 1100 meters with the pinch out at around 3.5 s TWT, with maximum depth values of 4.0 s TWT on the western Sardinian margin (Sage *et al.*, 2011). In the Algerian Basin, the presence of larger salt structures near the margin and gentle salt-cored folds in the deeper basin suggest that the Mobile Unit was thicker near the margin and thinner in the basin (Soto et al., 2022).

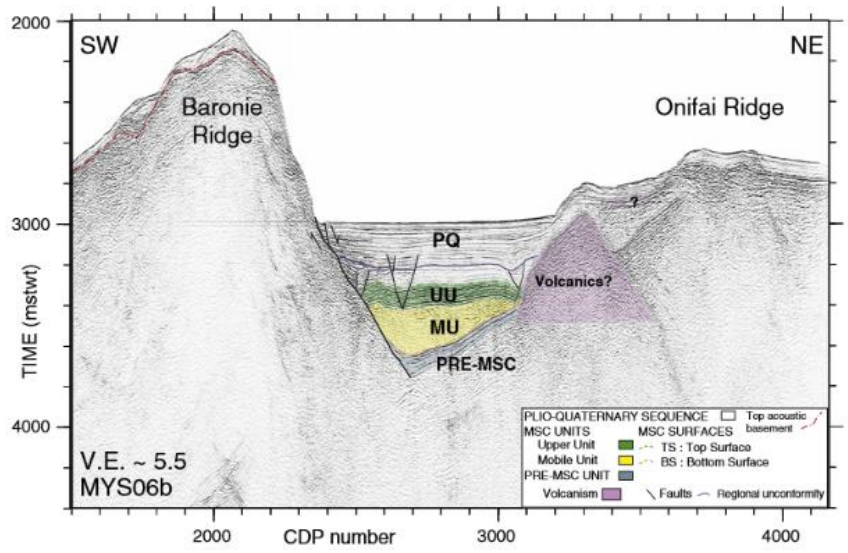

Figure 3.14: *Seismic reflection profile showing the MU and UU in the western Tyrrhenian basin (Gaullier et al., 2014).*

The salt tectonics which characterizes the MU has been active, depending on the area, since Late Messinian or Early Pliocene, locally until present (Gaullier and Bellaiche, 1996; Maillard *et al.*, 2003; Dal Cin *et al.*, 2016; Lymer *et al.*, 2018).

Upper Unit (UU): Deposited under oscillating sea-level conditions during the last phase of the Messinian Salinity Crisis, the nature of this unit is still partly uncertain. In fact, despite its upper part has been drilled during the DSDP Leg XIII expeditions -recovering dolomitic marls, anhydrite stromatolites and Sabkha deposits interbedded with marly levels (Figure 3.12.2)- the lithological information cannot be extended to the whole UU sequence in the Western Mediterranean because it is suggested to present strong lateral variations. The thickness is 250 to 500 ms TWT (calculated 440-880 m)

(Rehault *et al.*, 1984; CIESM 2008), and it presents parallel continuous reflectors (Figure 3.14) onlapping on the margins (Sage *et al.*, 2005; Maillard *et al.*, 2006; Lofi *et al.*, 2011a). The controversies on the environmental conditions towards the end of the Messinian Salinity Crisis are still strong, due to the presence of apparently discordant multidisciplinary evidences (for more details, see Annex B) (Krijgsman *et al.*, 1999; Roveri *et al.*, 2001; Andreetto *et al.*, 2021). The presence of a 70 ms TWT (about 160 m) autochthonous salt layer 's' in the Eastern Sardo-Provençal Basin (Geletti *et al.*, 2014) suggests a temporal low stand during the late MSC; this salt layer, as the MU, locally produces anticlines (Geletti *et al.*, 2014). The same 's' layer was identified by Dal Cin *et al.* (2016) also in the deepest part of the Algero-Balearic Basin.

Together with the Messinian Trilogy, two other units have been interpreted in the Western Mediterranean:

Complex Unit (CU): Present from the upper-middle slope to intermediate depth basins, this unit seems to be closely related to sedimentary supply sources, as it probably deposited during the first phases of the sea level fall and its consequent clastic input derives from both fluvial drainage and/or slope instability (Maillard *et al.*, 2006; Lofi *et al.*, 2011a; Obone-Zue-Obame *et al.*, 2011; Granado *et al.*, 2016). The Complex Unit has been sampled on the French continental slopes, where it contains sands, conglomerates and marly levels interpreted as Messinian fluviodeltaic deposits eroded during the drawdown phase. This poorly imaged fan shaped accumulations at the foot of the margin are generally chaotic, but present many internal configurations, with a seismic facies that varies from reflection free to chaotic to high amplitude semicontinuous reflectors.
The CU in the seismic profiles has been identified beneath or above the MU, and in some areas seems to laterally become MU/UU. The thickness -up to 1 s TWT- and lateral extent are irregular and influenced by the Messinian thalwegs (Lofi *et al.*, 2011a).
On the Algerian margin the **Complex Unit** is located at the foot of the margin, and because of its seismic facies and stratigraphic position it is supposed to be the prosecution offshore of flysch units onshore central Algeria (Aïdi *et al.*, 2018).

Bedded Unit (BU): As well as the CU, also this sedimentary sequence is often deposited at the river mouth. The seismic facies is constituted by relatively continuous parallel reflectors somewhere chaotic, for a total thickness of up to 0.2 s TWT (about 350 m). The chronostratigraphic relation between the CU and the BU is not defined, so depending on the areas and on the margin morphology the CU predates or postdates the deposition of BU.

III.B. The Western Sardinian Margin (Study Case 1)

The first of our case studies, mostly analyzed during the secondment at the University of Trieste and OGS (Italy), is the Western Sardinian passive margin. At the beginning of the Messinian Salinity Crisis, the opening of the Sardo-Provencal back-arc basin was already complete, making this area a suitable place for the study of the well preserved Messinian sedimentary sequence (Rehault *et al.*, 1984; Jolivet *et al.*, 2006).

This part of the study is mainly based on the interpretation of multichannel seismic reflection data acquired between 1972 and 2010 **(Figure 3.15 and Table 2.2).** A detailed seismic reprocessing has been performed on seismic reflection profiles WS10-02 and MS095, respectively located at the Western and Southwestern Sardinian margin, improving the imaging of the deeper reflectors. While most of the profiles image the Western Sardinian margin, some profiles of lower seismic resolution image the center of the basin, partly reaching the Rhone Deep Sea Fan and the North-Eastern Balearic margin. The southwestern and southern Sardinian margin has been studied during the last part of the secondment, and the data revealed here unexpected crustal geometries.

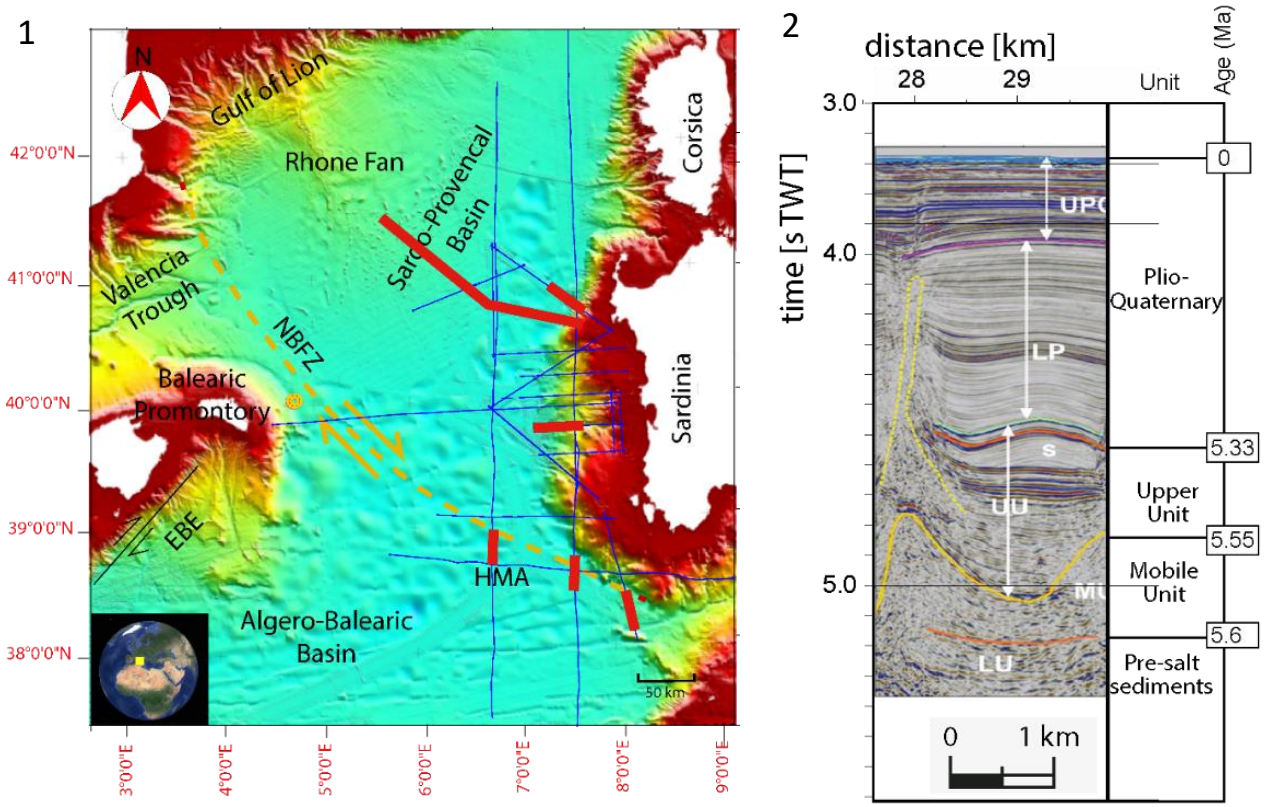

Figure 3.15: 1. *Bathymetric map of the Sardo-Provencal and Eastern Algero-Balearic basins and position of the multichannel seismic reflection dataset (blue lines). Marked in red is the position of the seismic profiles that follow. NBFZ: North Balearic Fracture Zone. HMA: Hamilcar Magnetic Anomaly. EBE: Emile Baudot Escarpment.* ***2.*** *Seismostratigraphic units interpreted in the dataset, based on the nomenclature of Lofi et al. (2011) and datation of CIESM (2008), modified after Geletti et al. (2014). The absence of drilling of the pre-salt sediments makes it impossible to place temporally these horizons, which could be Messinian (i.e. Lower Unit) or pre-Messinian.*

III.B.1. Results of the seismic data interpretation

We based our seismic data interpretation on the description of the Messinian Salinity Crisis deposits available in literature, and the nomenclature of CIESM (2008) and Lofi *et al.* (2011a) (Figure 3.15.2). Despite the dataset does not have a high data density, it allowed us to analyze the general trend of the main seismic reflectors **(Figure 3.16)** and units thicknesses. While the UU and the Plio-Quaternary sequences are well visible, in this study area is particularly difficult the interpretation of the MU geometries, especially for what concerns the base of the salt in the lower part of the slope and in the abyssal plain.

III.B.1.1. Seismic stratigraphy

Acoustic basement: Very few informations are available in the seismic data about the acoustic basement in the area. A deep reflector highlighted by the seismic reprocessing (pre-stack time migration) has been interpreted at 6-7 s TWT, but its nature is still under analysis.
Some seismically transparent bodies **(Figure 3.17)** -corresponding to positive anomalies in the magnetic data- act as local discontinuity of the MSC and Plio-Quaternary deposits. These structures have been interpreted in literature as volcanic bodies (Geletti *et al.,* 2014) and could be the result of the calc-alkaline magmatism of 33-13 Ma, related to the subduction (Rehault *et al.,* 1984, 2012; Franciosi *et al.,* 2003).

Pre-salt sedimentation (older than 5.6 Ma): While the imaging of the pre-salt sedimentary sequence is partly prevented by the screening effect of the salt layer, we interpreted the pre-salt geometries in most of the seismic reflection profile imaging the lower slope. When visible, the pre-salt seismic facies consists in medium amplitude continuous reflectors. On the slope, they are tilted with a calculated angle of 2.3 to 4° (Figure 3.16), so a slightly higher angle than the seafloor slope. In fact, as known in literature, the pre-Messinian strata deposited in a basin with a different conformation; after the deposition, a strong and still active subsidence towards the center of the basin tilted the strata. The Sardo-Provencal basin is one of the Mediterranean basins more strongly interested by subsidence phenomena, because of its depth (Carminati and Doglioni, 2004). The most recent of these deposits are supposed to be the Lower Unit, composed by clastic sediments (Lofi *et al.,* 2005) or evaporitic ones (Krijgsman *et al.*, 1999).

Mobile Unit (5.6-5.55 Ma): This layer of halite was deposited during the peak of the Messinian Salinity Crisis. It presents a reflection-free seismic facies, and forms salt tectonics structures varying from salt rollers and anticlines on the slope to up to 4 km thick diapirs downslope. Due to its ductile nature, this layer constitutes the main cause of recent deformation of the passive margin sedimentary sequence, acting as a *décollement*. Despite the seismic velocities values for the MU are different in different studies, we use a velocity of 4.2 km/s (Camerlenghi *et al.,* 2020), compatible with its composition. We describe here the geometry of the base and top of this layer.

Base of the MU (5.6 Ma) (Figure 3.18): The base of the MU is characterized by a reflector with high to very low amplitude and negative polarity, this last one due to the generally higher velocity of the seismic wave in halite compared to the one in relatively young brittle sediments. The locally very low amplitude is mainly due to the screening effect of the salt layer, so the precise interpretation of

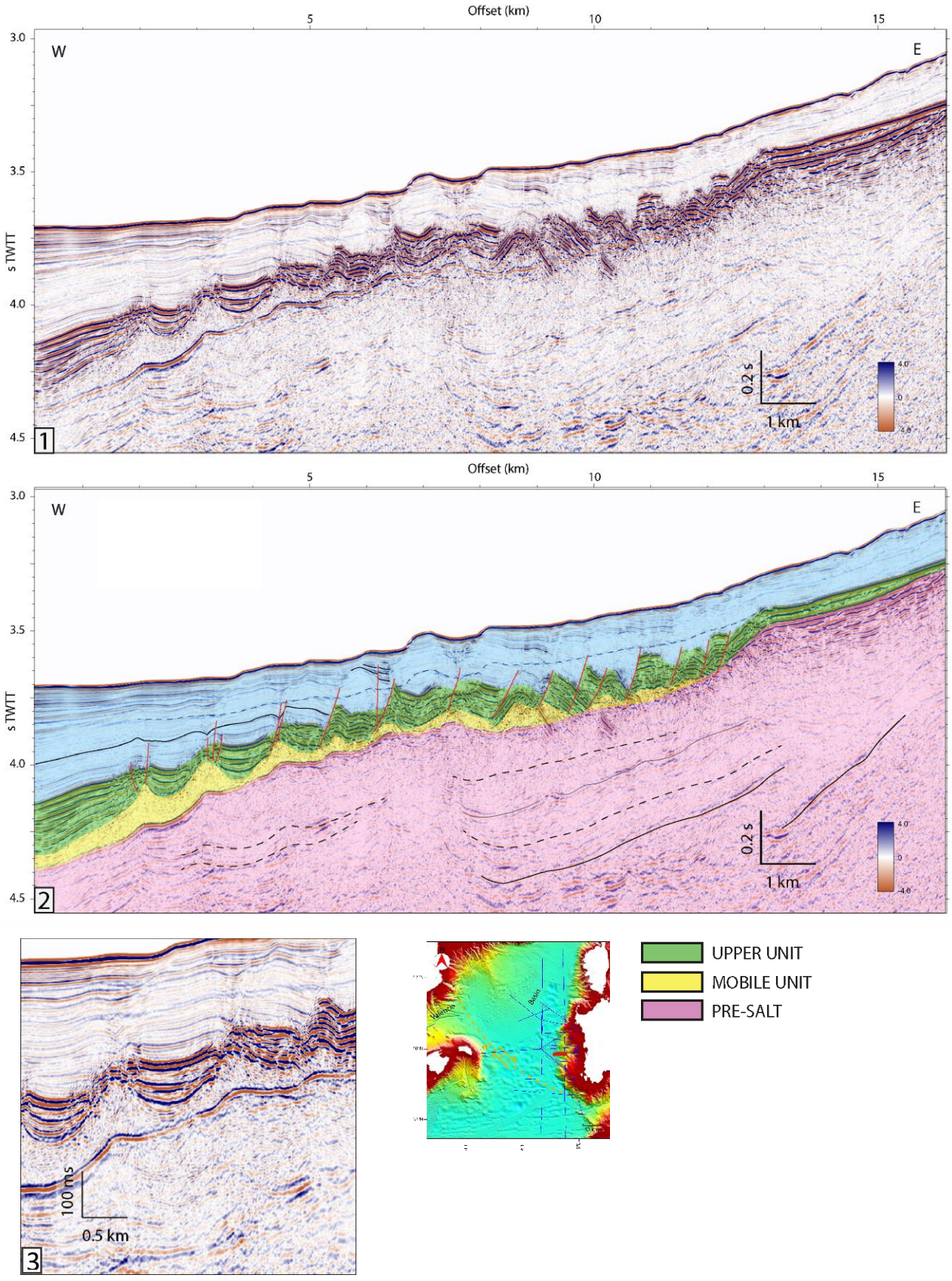

Figure 3.16: *Detail of seismic profile WS10_13.* ***1.*** *Uninterpreted* ***2.*** *Interpreted.* ***3.*** *Zoom of the pull-up effect on the base salt horizon. VE at the seafloor: 5.8X. The maximum calculated angle of the base salt is 4°.*

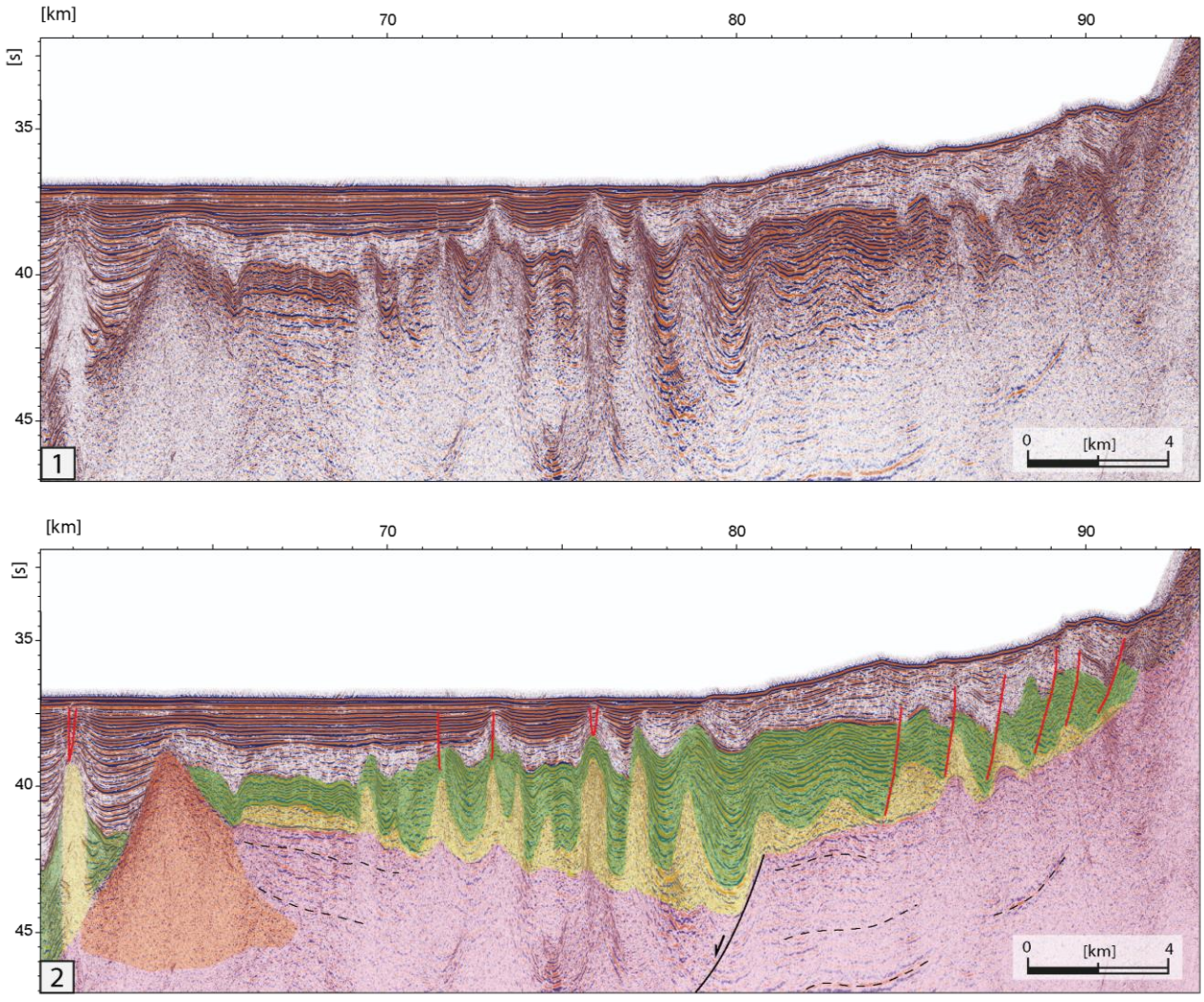

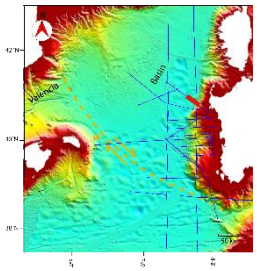

UPPER UNIT
MOBILE UNIT
PRE-SALT
VOLCANIC

Figure 3.17: *Seismic profile WS10-03 on the northeastern Sardinian margin.* ***1.*** *Uninterpreted* ***2.*** *Interpreted. V.E:~ 8X.*

this horizon is possible just when the thickness of the salt is limited, mainly on the slope (Figure 3.16) while in the deeper area the isobaths map of the MU base is based on the punctual interpretation of this horizon where visible (i.e. below the thinner salt). The high velocity of the salt is also at the origin of the pull-up effect on this horizon below the salt structures, well visible in the apparent undulation of this horizon below the salt anticlines of Figure 3.16.3. The base of MU horizon in the study area is located at a depth between 3.1 and 5.6 s TWT (Figure 3.18), with shallower values on the Sardinian and Balearic slopes and maximum depth values at the northwestern limit of the dataset (i.e. below the Rhone Deep Sea Fan) and in general towards the center of the basin with local exceptions.

As visible in Figure 3.17, together with the base MU slope towards the basin and the tilted blocks geometry we locally interpreted a component of dip landward of 1.5°. This slope is associated to

the volcanic structure already mentioned, and has the effect of locally block the downward mobilization of the salt layer.

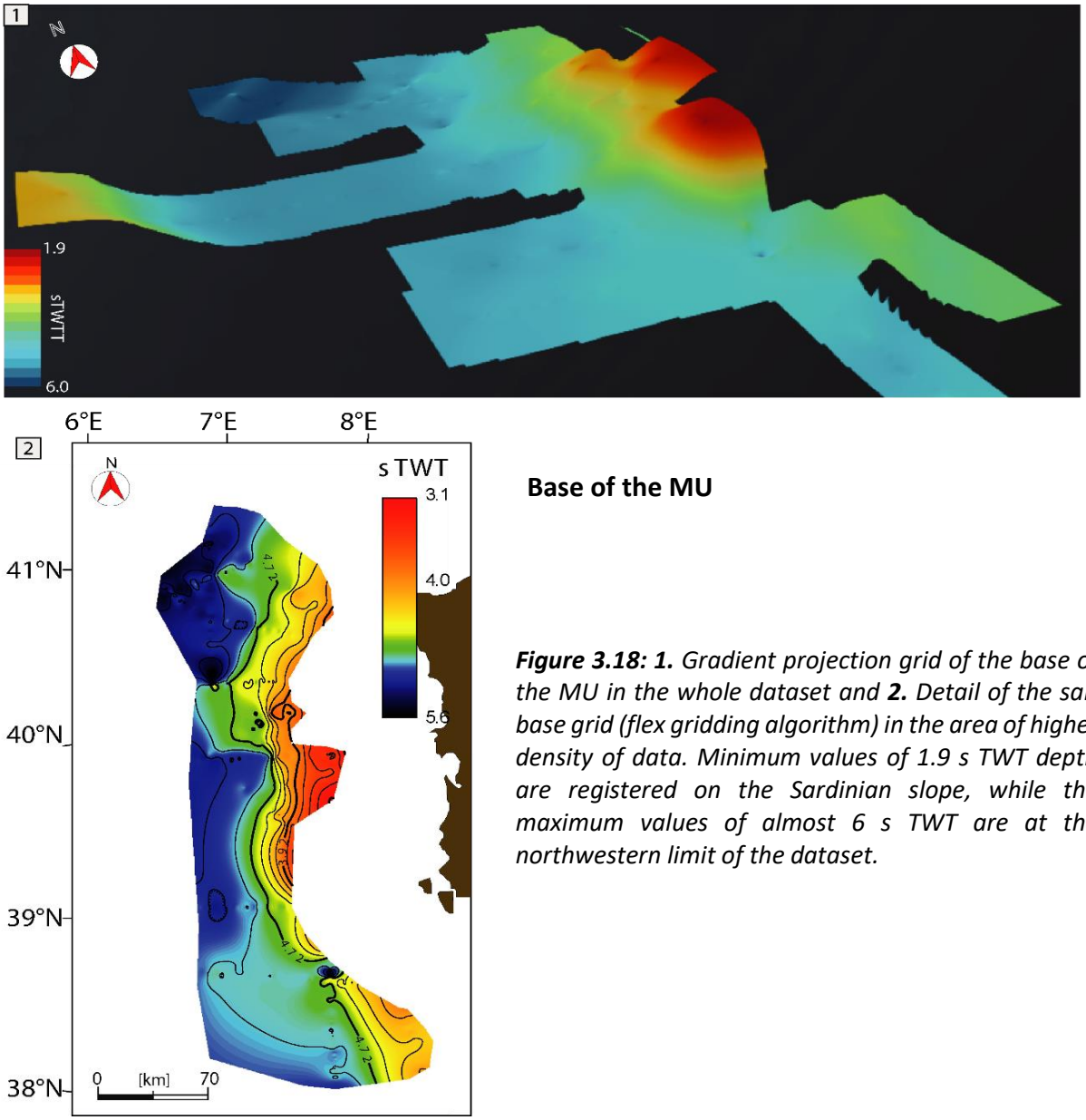

Base of the MU

Figure 3.18: 1. *Gradient projection grid of the base of the MU in the whole dataset and* ***2.*** *Detail of the salt base grid (flex gridding algorithm) in the area of higher density of data. Minimum values of 1.9 s TWT depth are registered on the Sardinian slope, while the maximum values of almost 6 s TWT are at the northwestern limit of the dataset.*

Top of the Mobile Unit (5.55 Ma) (Figure 3.19): The top of the halite layer is a high amplitude positive reflection horizon, thanks to the high velocity of the seismic wave in the halite (4.2 km/s). This horizon is strongly deformed by salt tectonics, that sometimes makes the interpretation tricky when the structures are complex, e.g. the verticalization of this horizon make it seismically transparent (Figure 3.17). When the top of the salt is not imaged, the position of the horizon is interpreted indirectly, i.e. as the top of the transparent seismic facies. When the salt structure is more complex and lateral reflections disturb the imaging, a useful hint is provided by the geometry of the deeper layers, i.e. the intensity of the pull-up deformation in the pre-salt horizons. The regional trend of the top of the MU is -as well as the one of the MU base- a deepening of this horizon towards the deep basin, passing from 3 to almost 6 s TWT (Figure 3.19). On this, overlaps another trend with considerably shorter wavelength of variation, better visualized on the seismic profiles: the top of the MU horizon varies significantly in a short distance because of salt tectonics.

Thickness of the MU: The thickness of the MU varies between 0 (pinch out on the margin, Figures 3.16 and 3.17) to almost 2 s TWT (4.2 km, major salt diapirs), with a general trend of thickening towards the center of the basin and towards NW. The small scale variation is due to the presence of salt structures, with salt welds both on the margin between salt rollers and in the basin between the major salt structures. Important variations are present where the salt layer is thicker.

Upper Unit (5.55-5.33 Ma): Sign of the water dilution at the end of the Messinian Salinity Crisis, the UU has been sampled in DSDP well leg 13 and is composed in the Western Mediterranean by marls and evaporites (Hsü *et al.*, 1973), resulting in a calculated interval velocity of 3.5 km/s (Camerlenghi *et al.*, 2020). The seismic facies shows high amplitude continuous reflections, often disrupted by the salt related structures. On the slope we can observe that the parallel horizons are tilted basinwards, as already discussed for the pre-salt horizons. Moreover, syn-kinematic geometries are present both on the slope (Figure 3.16) and in the abyssal plain, testifying an early salt deformation. The thickness of this unit is around 0.3-0.45 s TWT (500-800 m). On the Sardinian margin, a transparent layer characterized by ductile deformation has been previously interpreted in the UU sequence, suggesting the deposition of salt during this late phase of the Crisis ("s" salt layer, Geletti *et al.*, 2014).

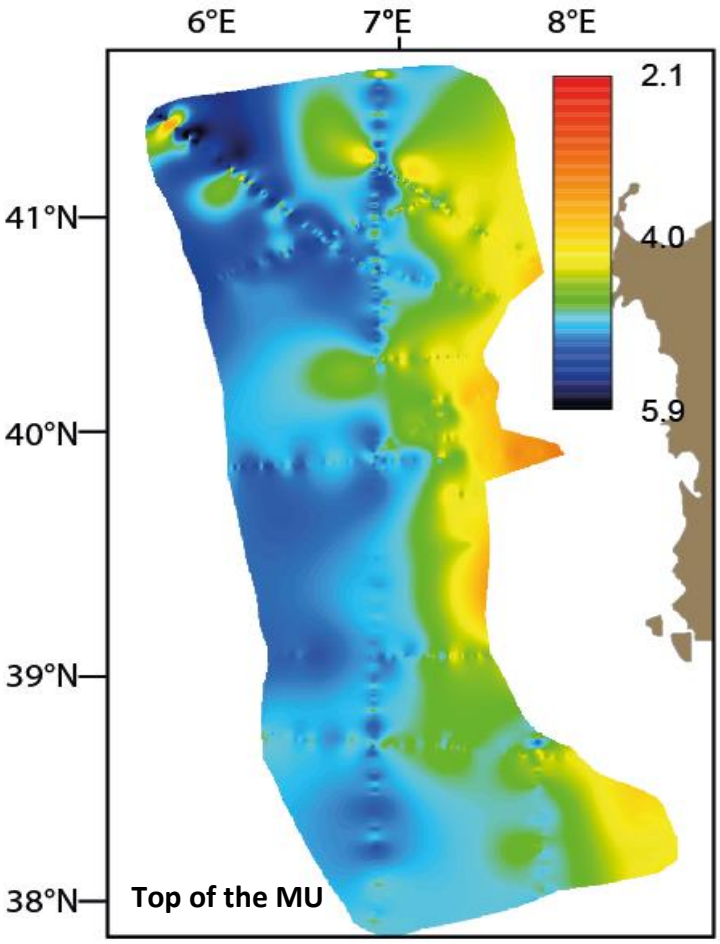

Figure 3.19: *Isobaths map of the top of the Mobile Unit in the area. Values range is between 3 and 5.9 s TWT, with increasing values towards the center of the basin and maximum depth values towards north.*

Plio-Quaternary (5.33-0 Ma): The Lower Pliocene is mostly pelagic and muddy (Trubi marls), resulting in a semi-transparent seismic facies with low amplitude continuous reflectors, while the Upper Pliocene and Quaternary are detritical and coarser and the seismic reflectors result therefore higher amplitude while maintaining their lateral continuity. Syn-kinematic geometries strongly characterize the sequence, mainly for what concerns the lower Pliocene. In the study area the thickness of the Plio-Quaternary sequence presents a general trend of thickening from the Sardinian slope towards the center of the basin, with maximum values towards the Rhone Deep Sea Fan where it reaches a thickness of more than 1.5 s TWT between the salt structures. This trend of thickening is partly visible in the bathymetric data, which show a gradual lifting of the water bottom towards the Gulf of Lions (Figure 3.15). Some localized deposits have been interpreted at the foot of the slope (Figure 3.17). The thickness of the Plio-

Quaternary sediments strongly depends also on the position of the salt structures, with local minimum thickness values of the PQ in the basin corresponding to the bigger salt diapirs.

Brittle cover (Figure 3.20): From the rheological point of view, the Upper Unit and the Plio-Quaternary can be considered as a single unit (the 'brittle cover'), characterized by brittle deformation in contrast with the MU ductile one. The brittle cover thickness varies between 0 and 2.5 s TWT (around 0 to 3 km), with a limited sedimentary sequence on the Western Sardinia starved margin and a general trend of thickening towards the center of the basin already described for the Plio-Quaternary. Maximum values are registered at NW in correspondence of the Rhone Deep Sea Fan, as visible in Figure 3.20: the limit of the Rhone DSF is marked in red, while the red arrows indicate the direction of sediments supply.

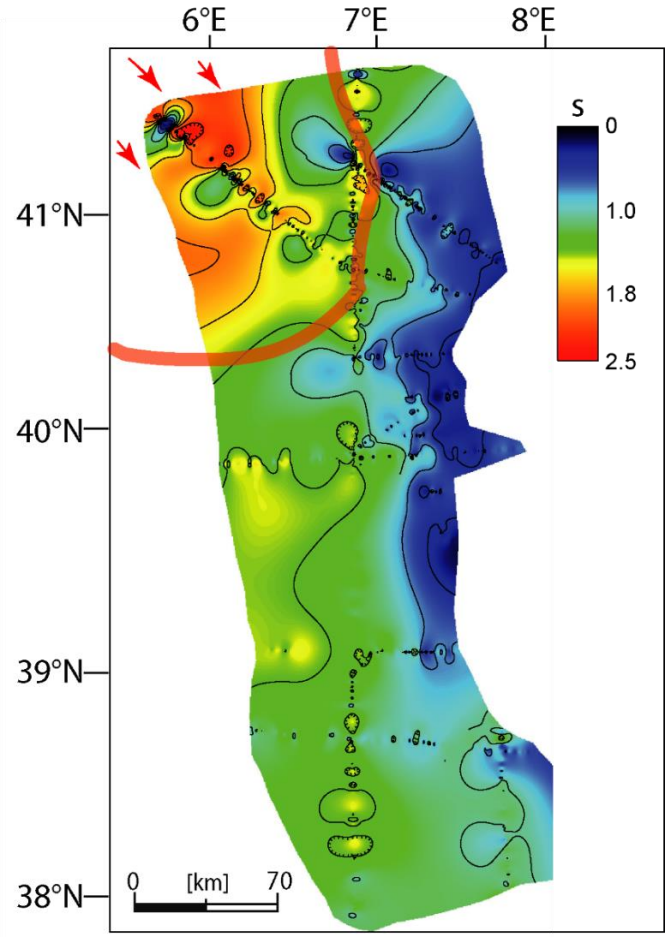

Brittle cover thickness

Figure 3.20: *Thickness map of the brittle cover, i.e. the PQ and UU deposits, on the Western Sardinian margin, with contour interval 0.3 s TWT. In red is marked the limit of the Rhone Deep Sea Fan influence, and the red arrows show the direction of the sedimentary influx.*

III.B.1.2. Salt tectonics structures

After having described the 3D grids of the Messinian and Plio-Quaternary layers, we analyze here the salt tectonics structures and relative domains. The analysis of the salt tectonics geometries on the Western Sardinian margin shows a division in domains, well visible in **Figure 3.21** (CROP profile) that give a regional image of what we already partly saw in the seismic reflection profiles of Figures 3.16 and 3.17.

- **On the slope** a first area of smaller salt structures, salt rollers, salt anticlines and minor diapirs is identified, and the base of the salt dips towards the basin with an angle of 2.3 to 4° (Figure 3.16). Locally we interpreted a slope towards the margin (Figure 3.17), that leads to a double direction of salt tectonics. The deformation of the brittle cover is mostly limited to normal faults and some early growth strata in the UU (Figures 3.16, 3.17, 3.21), these last ones being mainly a thickening of the sedimentary sequence between the salt structures and a thinning of the sequence towards the salt, with some onlaps geometries. As previously mentioned, the brittle cover is quite limited towards the margin, with the exception of local accumulation of sediments (Figure 3.17).
- **Basinward,** the slope of the base of the salt becomes weaker (few tens of degrees) while the salt structures become slightly thicker and more complex, with common diapirs (Figure 3.21.3). The UU is deformed by the salt structures, but for what concerns the Plio-Quaternary sequence the deformation is mostly limited to the lower Plio-Quaternary and to salt related normal faults. Some internal geometries of the UU are interpreted as fan shaped, but the quality of the data does not allow a conclusive datation of the beginning of the deformation, while we can confirm that most of salt tectonics ends before the Pleistocene.
- Reaching the area in which the base of the salt is deeper (km 0 to 80 of seismic profile CROP, Figure 3.21) the salt structures become bigger with around 3 km thickness of salt, up to reaching the maximum thickness of 4 km in the structure of Figure 3.21.2, actively deforming the seafloor. Here, the UU and PQ sedimentary sequence between the salt structures shows uptilted seismic horizons towards the salt diapirs, together with slight turtleback geometries in the Plio-Quaternary, making difficult the reconstruction of the internal geometries of this unit and to distinguish between syn-tectonics growth and post-depositional deformation. The Plio-Quaternary thickness is quite important with a thickness of up 1.5 s TWT and salt related faults cutting up to the most recent horizon, proving a still active salt tectonics deformation.

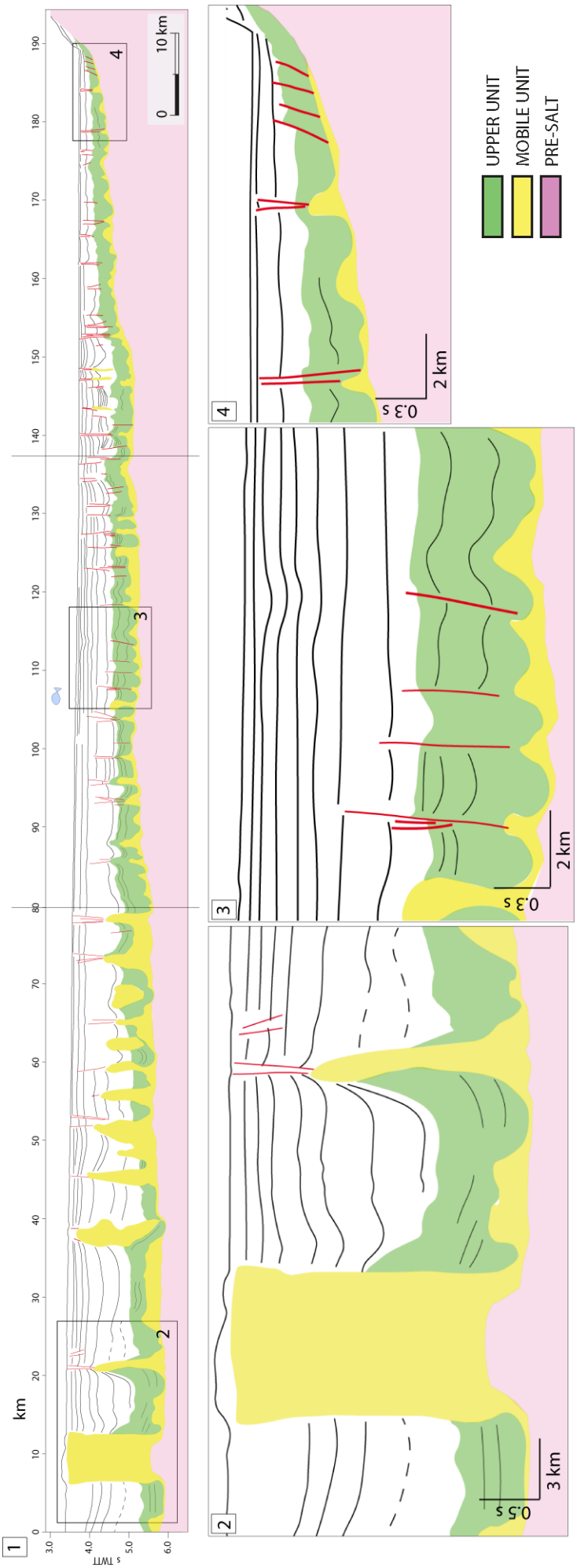

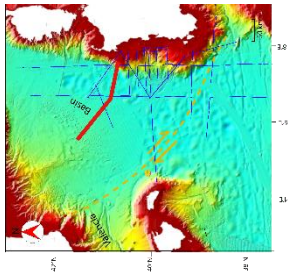

Figure 3.21: *Line drawing of CROP seismic reflection profile imaging between the Sardinian slope to the center of the basin, and zooms. Modified after Finetti (2005). VE: 6.7 X.*

III.B.1.3. Crustal structures

On the Southwestern Sardinian margin, we interpreted some crustal normal faults offsetting recent horizons. The imaging of the salt is here particularly challenging due to the characteristics of the seismic data and the complexity of the faulting.
The detail of sesmic reflection profile **MS044 (Figure 3.22)**, located on the Southwestern Sardinian margin, shows a fault structure affecting at least the Messinian and Pliocene sediments. We identified two main normal faults and at least three additional normal faults between the main ones, forming a negative flower structure, i.e. a structure of transtension generally widening upward where it splits in numerous faults. As visible in Figure 3.22, there are two factors that reduce the accuracy of this interpretation: first of all, the seismic facies of the pre-salt sediments and that of the UU does not differ significantly, with medium to high amplitude continuous reflectors. Therefore, in the absence of a salt layer separating the two units, it becomes challenging to mark the limit between them. Moreover, considering the complexity of the faults system, the interpretation of the salt is particularly tricky, and no salt has been interpreted in the flower structure. The layer interpreted as UU has parallel horizons with a total thickness of around 0.5 s TWT and without evident signs of syn-crustal tectonics growth, and the top of this unit is offset by the crustal faults of up to 0.5 s TWT. The Pliocene above the flower structure is up to 0.5 s TWT thicker than the average value in this seismic profile and form a symmetric anticline above the flower structure, while the Pleistocene sequence seismic horizons are mostly parallel to the seafloor and undeformed.
The most recent faults, that could potentially look as a continuation of the major normal faults, are interpreted here as a result of salt tectonics, and are present along all the seismic profile, where they constitute the most recent deformation up to the Quaternary.

Southeastwards, crustal faults geometries are interpreted in seismic reflection profile MS043 on the Southeastern Sardinian margin **(Figure 3.23)**. We interpreted a major normal fault and numerous other normal faults slightly southern, forming a flower structure. The major fault offsets both the top of the UU and the base of the salt, respectively of 0.2 and 0.35 s TWT. Due to the ductile nature of the salt, this difference in the offset cannot be considered as a proof of syn-tectonic sedimentation of the Messinian sequence. The imaging here is not as good as in profile MS044 due to the thickness of the salt layer, and in particular due to the fact that salt structures are particularly complex above the crustal structure, with part of the MU forming an allochthonous salt sheet at km 145.

The third profile imaging these crustal structures on the Southern Sardinian margin is the seismic reflection profile MS099 **(Figure 3.24)**. Here we interpreted a normal fault dislocating up to the early Plio-Quaternary sequence, while slightly southern an anticline deforming both the pre-salt layers and the UU is interpreted as a blind reverse fault. The salt has a limited thickness of a few tenths of a second, and the UU has isopach and tilted parallel horizons in most of the seismic reflection profile, with exception of the area of early salt deformation. The Plio-Quaternary sequence is deformed both by the crustal faults and by salt tectonics. In particular, above the crustal structure the Early Pliocene show fan shaped geometries thicker towards the north, suggesting a syn-crustal tectonics sedimentation. The normal faults that cut the UU and Lower Plio-Quaternary forming small scale steps on the seafloor are consequence of salt tectonics.

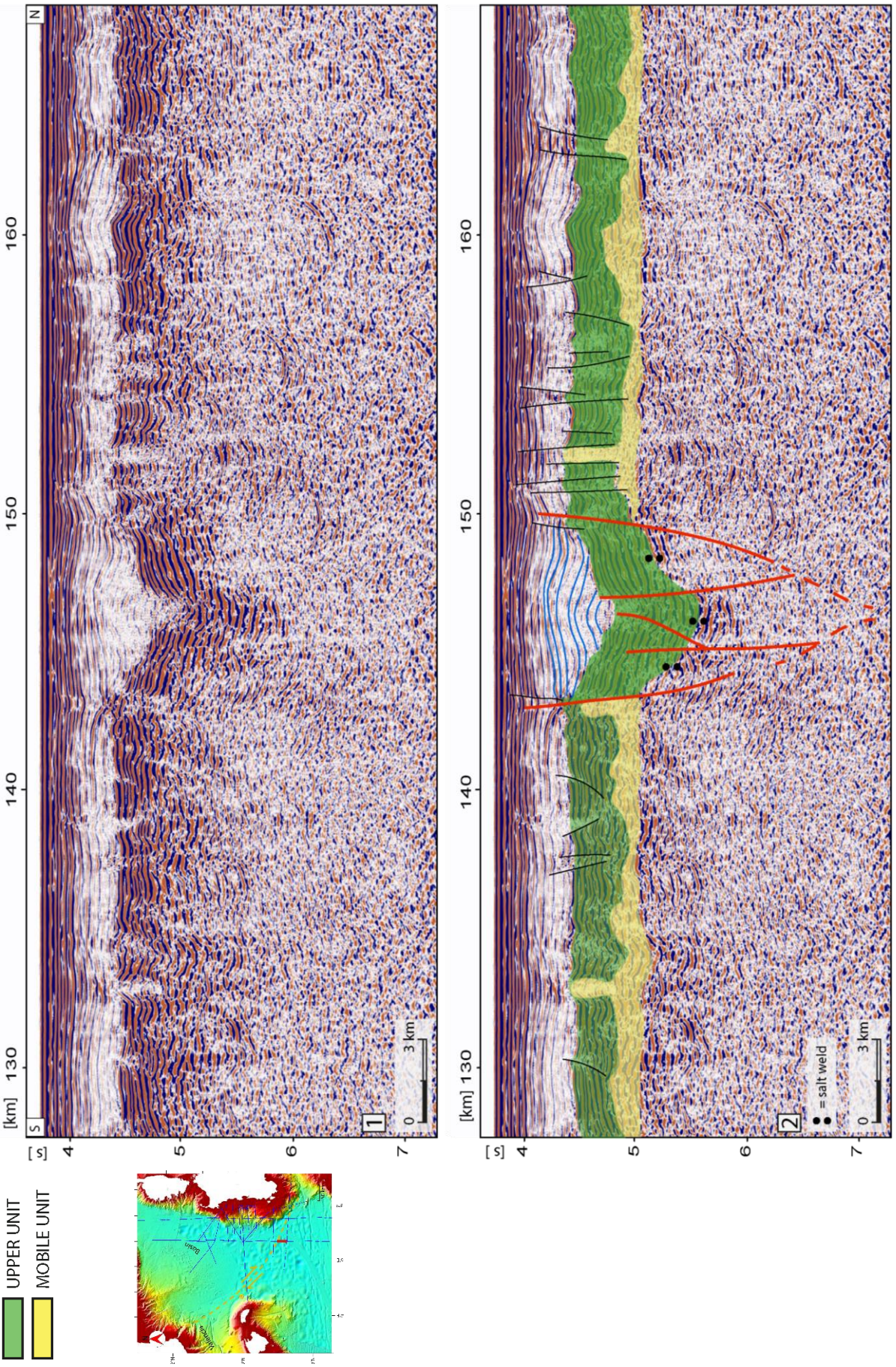

Figure 3.22: *Seismic profile MS044, southwestern Sardinian margin.* ***1.*** *Uninterpreted* ***2.*** *Interpreted. VE: 4X.*

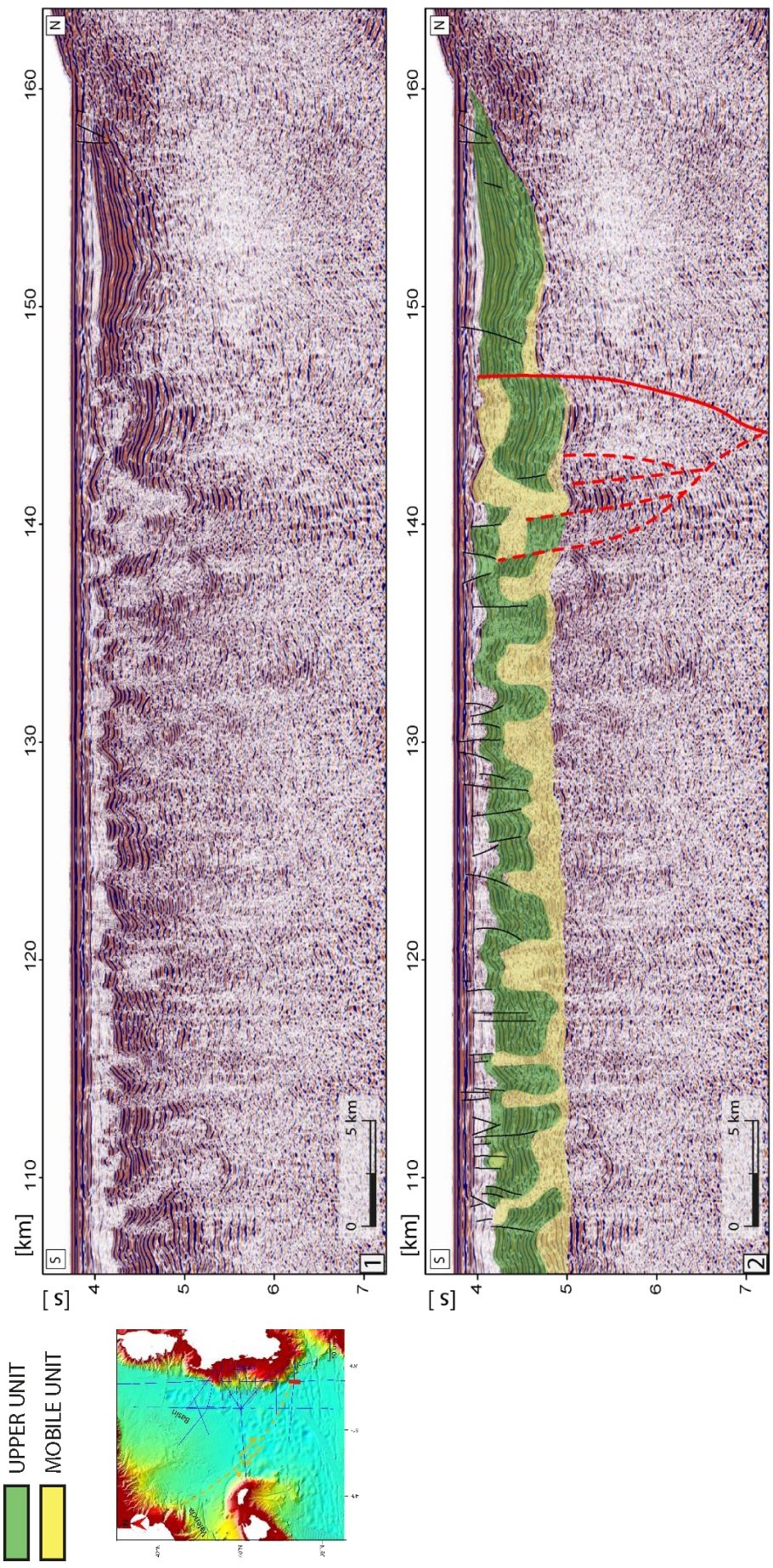

Figure 3.23: *Seismic profile MS043, southwestern Sardinian margin.* ***1.*** *Uninterpreted* ***2.*** *Interpreted. VE: 4X.*

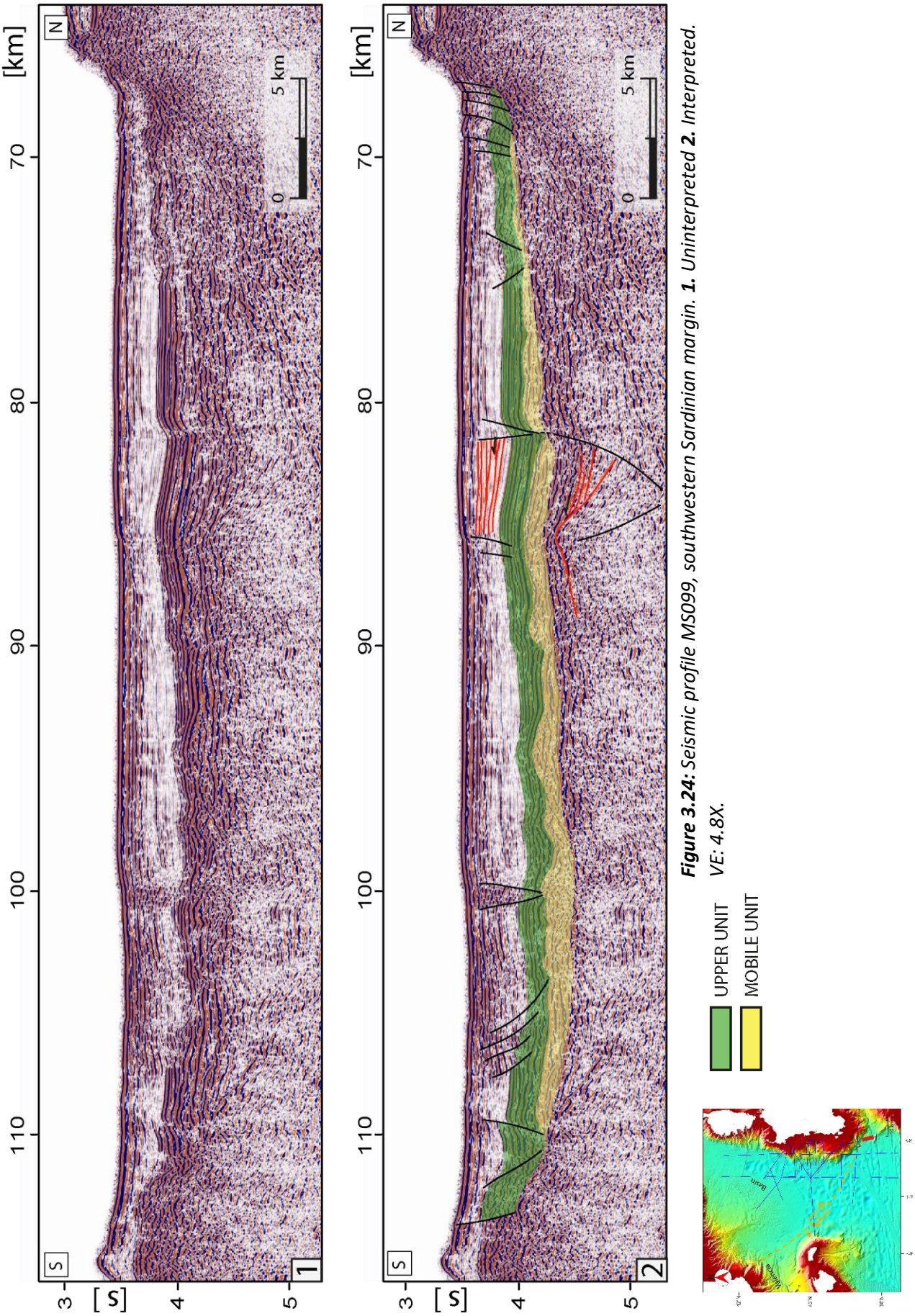

Figure 3.24: *Seismic profile MS099, southwestern Sardinian margin.* ***1.*** *Uninterpreted* ***2.*** *Interpreted. VE: 4.8X.*

III.B.2. Discussion and intermediate conclusions

- **Salt tectonics**

The salt deposited in an already open basin, that did not register major tectonics events after the MSC (Ryan et al., 1978) but encountered a post-rift differential subsidence, particularly intense after salt deposition and basin refilling. An important consequence is the tilting of the MU base, which presents a component of dip towards the basin. The Western Sardinian is a starved margin due to the scarce Sardinian rivers sedimentary input, therefore the influence of sedimentary load on salt tectonics can be considered neglectable; only locally we identified some sedimentary bodies present at the foot of the Sardinian slope (Figure 3.17). On the other hand, towards the center of the basin the presence of Rhone deposits at the northwestern limit of the area is noteworthy.
Therefore, considering the very limited sedimentary load from the Sardinian river and the slope accentuation after the end of the MSC, the main mechanism of salt tectonics recognized in the area is basinward gravity gliding **(Figure 3.25)**.

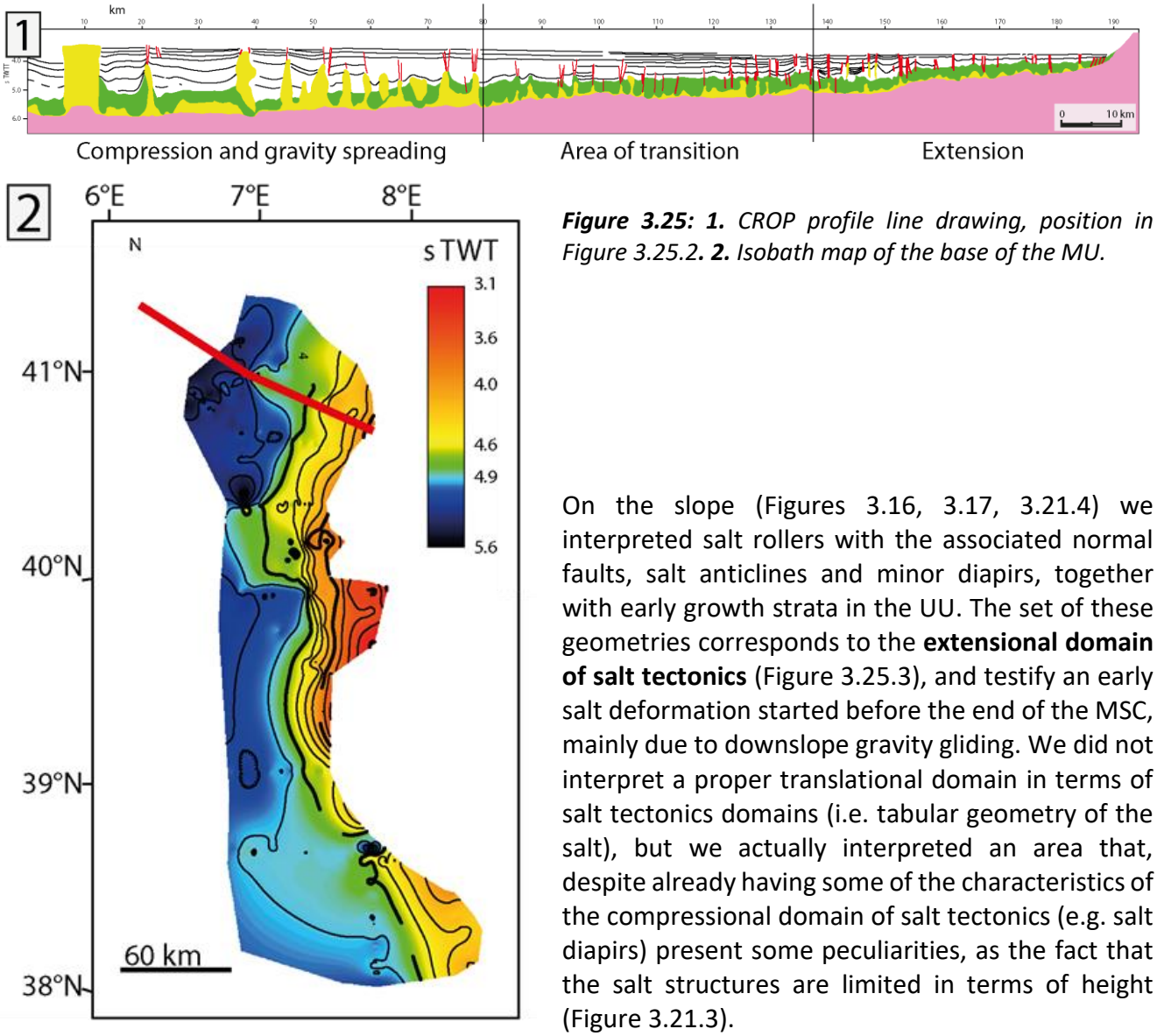

Figure 3.25: 1. *CROP profile line drawing, position in Figure 3.25.2.* ***2.*** *Isobath map of the base of the MU.*

On the slope (Figures 3.16, 3.17, 3.21.4) we interpreted salt rollers with the associated normal faults, salt anticlines and minor diapirs, together with early growth strata in the UU. The set of these geometries corresponds to the **extensional domain of salt tectonics** (Figure 3.25.3), and testify an early salt deformation started before the end of the MSC, mainly due to downslope gravity gliding. We did not interpret a proper translational domain in terms of salt tectonics domains (i.e. tabular geometry of the salt), but we actually interpreted an area that, despite already having some of the characteristics of the compressional domain of salt tectonics (e.g. salt diapirs) present some peculiarities, as the fact that the salt structures are limited in terms of height (Figure 3.21.3).

The deformation is mostly dated early Pliocene, testifying that salt tectonics stopped very early in this sector. This area is considered as an **area of transition** between the area of extensional tectonics on the slope and the downslope domain. The northwestern limit of this area is at kilometer 80 of

Figure 3.21, where there is an abrupt passage between the small salt structures with a wavelength of less than 2 km to a downslope area of km-height salt diapirs with a wavelength of around 6 km and a thicker brittle cover of around 1.5 s TWT, and strongly deformed lower Plio-Quaternary (Figure 3.21.2). This passage between different salt tectonics styles correspond to the external limit of the Rhone Deep Sea Fan, suggesting a strong influence of the Rhone sediments weight on the salt structures geometries of this third sector, in which the main mechanism of salt tectonics is **gravity spreading**. Moreover, the deep-sea fan deposits seem to have a buttress effect on the salt layer downslope movement from the margin.

Even if we did not produce specific analogue models for this study area, we compared the interpreted geometries with the results of new analogue models produced during this work, mainly focused on early salt deformation and gravity gliding. The model of **Figure 3.26** represents the situation that has been interpreted in the Gulf of Lions, with early downslope deformation and minibasins formation for downbuilding before the tilting of the model (Figure 3.26.1), followed by normal faults formation upslope and diapir growth downslope as a consequence of the tilting of the model (Figure 3.26.2 and .3). In Figure 3.26.4 we can appreciate the geometries of extensional salt tectonics (A) and compressional domain with early diapirs formation (B).

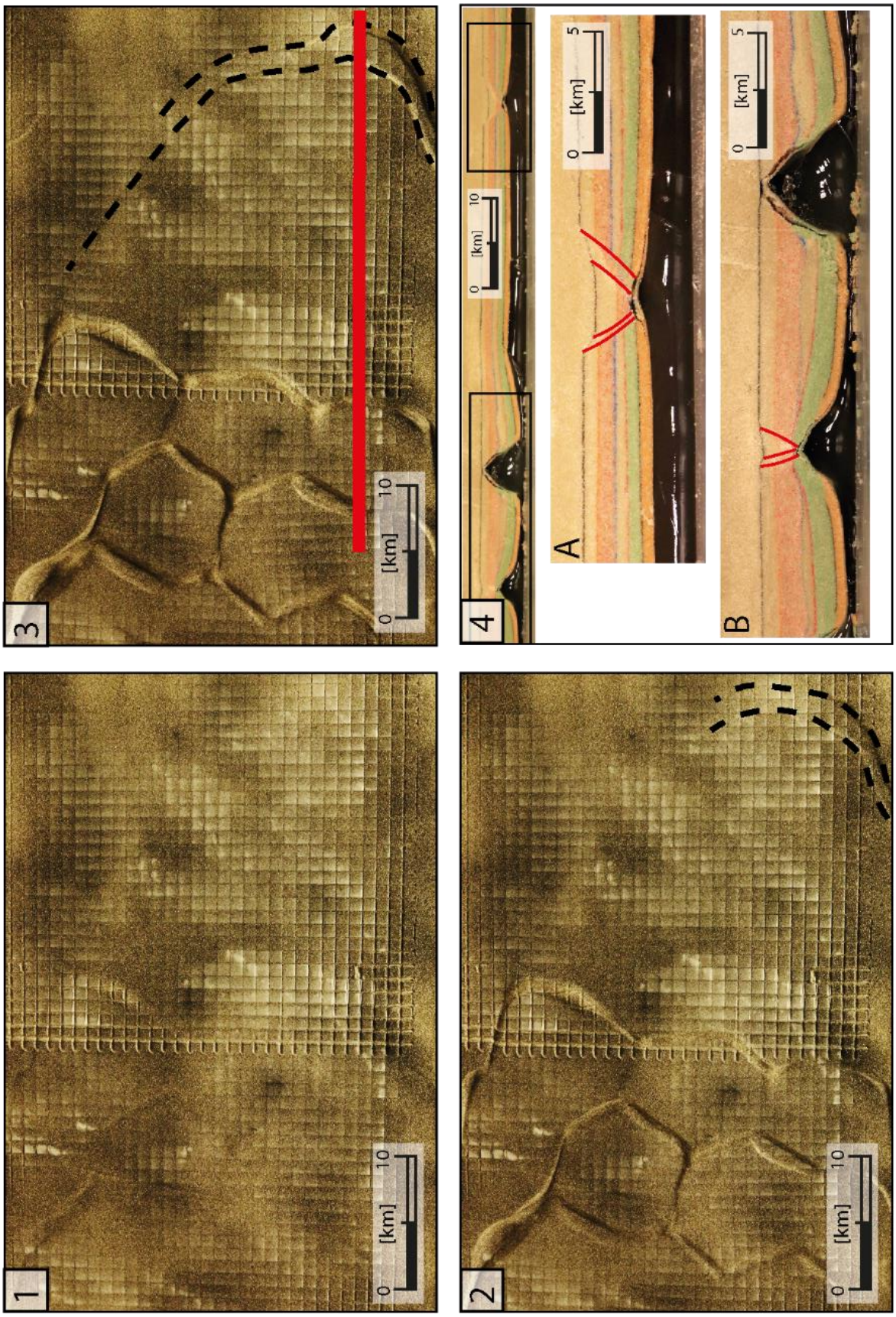

Figure 3.26: *Top View of model BO3, modelling the early salt tectonics* ***(1.)*** *and the gravity gliding consequence of the tilting of the box model* ***(2. and 3.)****, and section of the model at the end of the experiment* ***(.4)****. Gaullier et al., in prep.*

- **NBFZ reactivation**

The movement between the Sardinian and the Balearic blocks was possible during the spreading phase through the dextral strike-slip motion along the North Balearic Fracture Zone, an approximate NW-SE fault system (Figure 3.15.1) (Rehault *et al.*, 1984; Granado *et al.*, 2016; Maillard *et al.*, 2020b; Jolivet *et al.*, 2021b). The crustal structures that we analyzed in the seismic reflection profiles MS044, MS043 and MS099 (Figures 3.22, 3.23, 3.24) revealed the presence of a flower structure of direction NW-SE. Despite the precise geometries of the faults were not always interpretable with certainty and the study would benefit from a higher density of data, we propose the following retrodeformation of the analyzed geometries of seismic profile MS044 **(Figure 3.27)**:

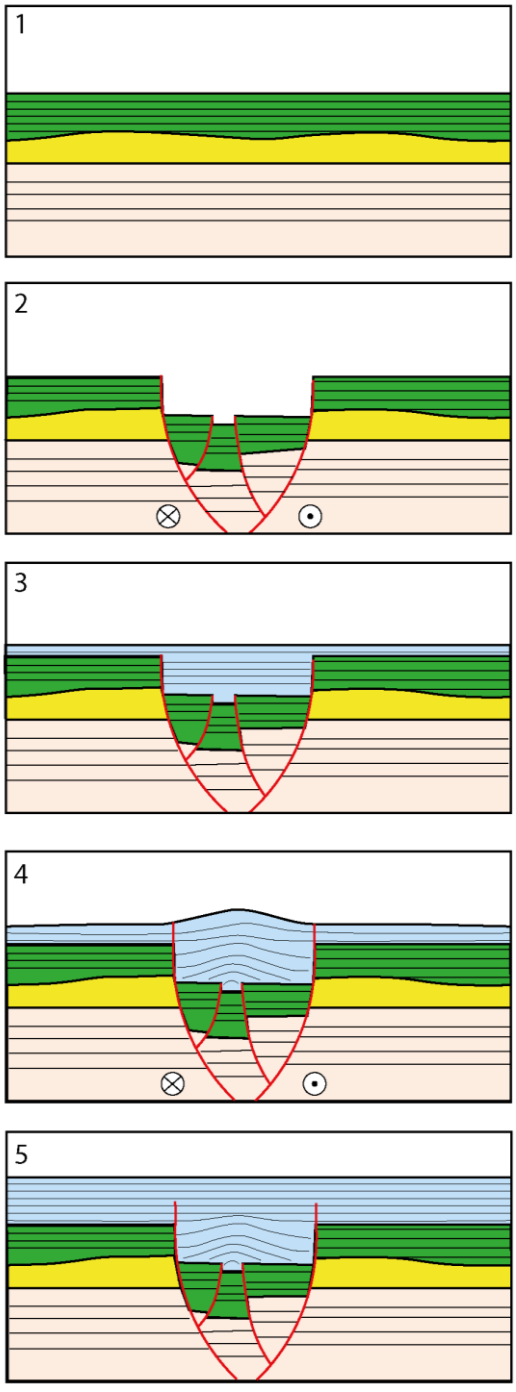

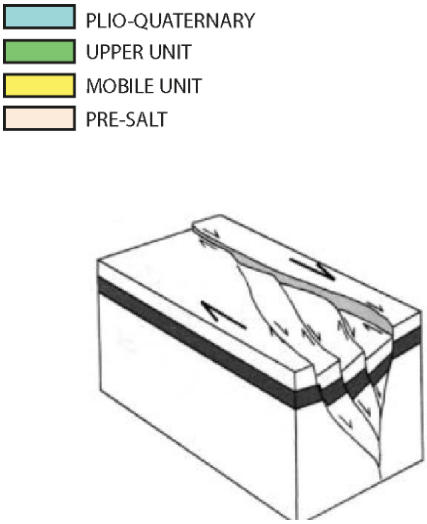

Figure 3.27: *Retrodeformation of the crustal structure interpreted in seismic reflection profile MS044.* ***1.*** *The sedimentary sequence of the MSC is deposited.* ***2.*** *The sequence is offset by transtension, leading to the formation of a negative flower structure (http://earthquake.usgs.gov).* ***3.*** *The early Pliocene sedimentary sequence fills the bathymetric low.* ***4.****The sequence is deformed by the transpressional stress* ***5.*** *The deposition of the Pleistocene sequence postdates the crustal activity.*

At the end of the MSC (Figure 3.27.1) we have limited lateral thickness variations in the UU, due to the formation of the first salt anticlines already during the deposition of the UU. Immediately after the end of the MSC, the area is deformed due to crustal tectonics, with an extensional strike slip mechanism that results in the formation of a negative flower structure or tulip structure (Figure 3.27.2), well visible in Figure 3.22 and partly visible also in Figure 3.23. Considering that we did not interpret salt in the flower structure of seismic profile MS044, we suggest that the Mobile Unit moved laterally during the crustal deformation, but uncertainties are present and the study would benefit from additional data. The crustal structure is already formed at the moment of the early Pliocene deposition (Figure 3.27.3), as testyfied by the onlap geometries of the Pliocene horizons and by the fact that the sedimentary sequence is thicker above the flower structure. The early Pliocene deposition is followed by a phase of compression, expressed in the formation of a simmetric anticline (Figure 3.27.4) above the flower structure. A phase of compressional tectonics has been interpreted as well is seismic profle MS099, where it is expressed in the fan shaped geometry in the Pliocene sequence. The Pleistocene sequence is deposited after the end of the reactivation of this fault system, and is therefore defomed only by salt tectonics.

Considering the nature of this fault (strike-slip) and its position, we consider it to be part of the North Balearic Fracture Zone. This crustal structure presents in our study area a double recent activity, postdating not only the opening of the basin but even the Messinian Salinity Crisis. A first extensional phase corresponds to the end of the MSC, while a second phase dated middle Plio-Quaternary is compressive.

• Intermediate conclusions

The interpretation of geophysical data, together with the reprocessing of seismic reflection profiles and the comparison with new analogue models, allowed us to decipher the mechanisms of salt tectonics on the Sardinian margin, that resulted to be mostly the consequence of gravity gliding due to the slope at the base of the MU, result of the margin tilting. Minor influence can be attributed to the scarce sedimentary input from the Sardinian rivers, while locally the Rhone Deep Sea Fan thick layer of sediments leads to a buttress effect on the salt gravity gliding from the margin and to gravity spreading below the salt. The presence of volcanic bodies locally inverts the slope of the salt base, blocking the basinward movement of the salt.

On the Southwestern Sardinian margin salt deformation is very locally influenced by the presence of a crustal strike slip fault, active in two phases (respectively extensional and compressional) after the end of the Messinian Salinity Crisis and recognized in this study as part of the North Balearic Fracture Zone.

III.C. The Algerian Margin (Study Case 2)

This part of the thesis aims at deciphering the different mechanisms of salt tectonics that interfere in the central Algerian margin offshore Algiers and Béjaïa, and in particular the influence of crustal tectonics on salt movement, thanks to the MARADJA I and II seismic reflection dataset integrated with some previously acquired deep penetrating seismic profiles (**Figure 3.28,** Figure 2.14, Table 2.3). As described in chapter III.A (Geological setting of the Western Mediterranean), the Algerian margin is reactivated in compression, but the presence of the halite layer (Messinian Mobile Unit) often prevents the correct imaging of pre-evaporitic sediments, limiting therefore the possibility to properly image the crustal structures that characterize the margin in our seismic dataset. This makes the role of salt tectonic analysis particularly important to reconstruct the crustal tectonics evolution of the study area, so we focused our attention on the sediments of the last 5.6 Ma, i.e. the Messinian Mobile Unit, the Upper Unit and the Plio-Quaternary sediments, both in terms of geometries of the base and top of the units, layers thicknesses and internal reflectors geometries.

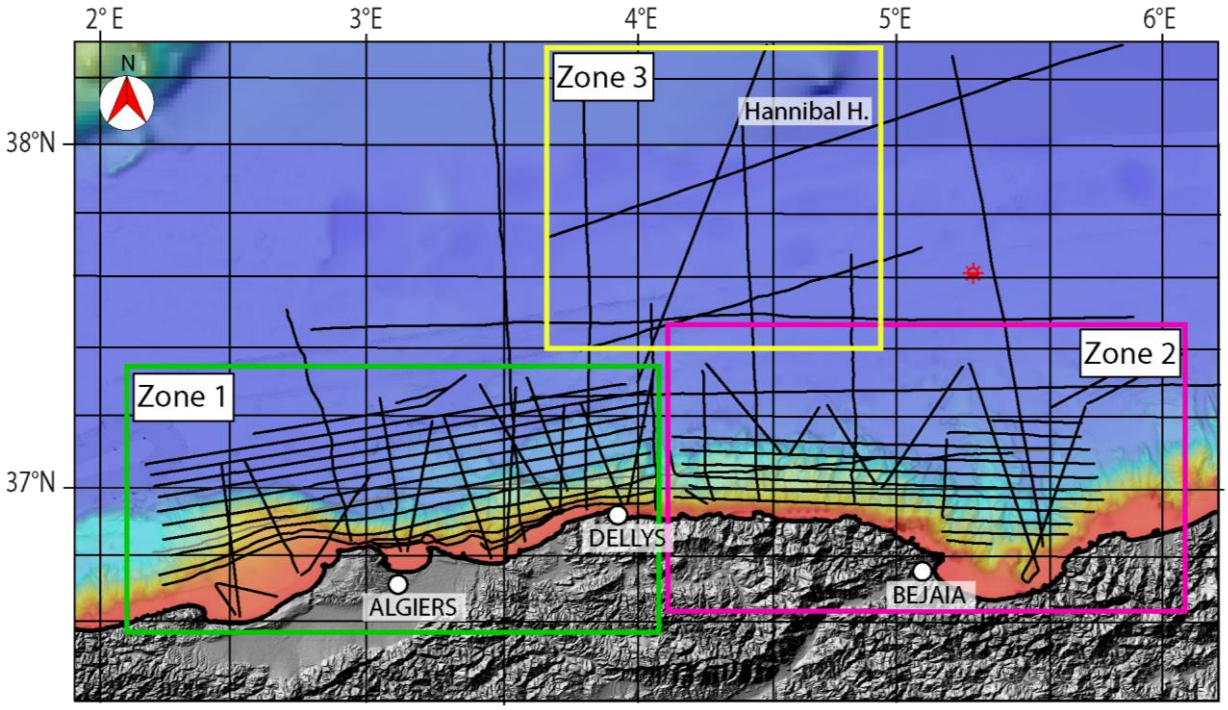

Figure 3.28: *Bathymetric and topographic map of the Algerian margin, with marked the position of the seismic reflection dataset and the division in western (zone 1: 2°20' to 4°E, 36°40' to 37°20'N), eastern (zone 2: 4 to 6° E, 36° 35' to 37°30' N) and northern (zone 3: 3°40' E to 5°E, 37°25' to 38°20'N) sectors.*

III.C.1. Results of the seismic data interpretation

As well as for the Sardinian margin study area, we based our seismic data interpretation on the characteristics of the Messinian deposits described in literature (CIESM, 2008) and the nomenclature of Lofi *et al.* (2011a) **(Figure 3.29 and 3.11)**. Due to the topic of this work and the limited data penetration, the interpretation is mainly focused on the Messinian Mobile Unit and Upper Unit and the Plio-Quaternary sediments. Locally, mainly in correspondence with salt welds, we were able to image pre-salt sedimentary geometries and locally the basement, obtaining punctual but essential information for the reconstruction of the margin's development. While most

of the interpretation is based on the academic seismic surveys MARADJA I and II, the integration with older seismic profiles acquired by the oil industries TOTAL and Sonartrach in the 70's has been particularly useful to extend the interpretation towards the center of the Algero-Balearic Basin, e.g. in the area of the Hannibal High.

In order to discuss separately areas that strongly differ in term of Messinian deposits and crustal tectonics –and consequently also in terms of salt tectonics-, we divided the study area in area 1 (western sector, 2°20' to 4°E, 36°40' to 37°20'N), area 2 (eastern sector, 4 to 6° E, 36° 35' to 37°30' N) and area 3 (northern sector, 3°40' E to 5°E, 37°25' to 38°20'N) (Figure 3.28), and this division will be maintained both for the results and for the discussion chapter. Due to the higher density of seismic profiles imaging the salt and the peculiar interpreted geometries, sector 1 will be described in more detail and in this chapter, and is object of a scientific publication that will be submitted in the near future.

III.C.1.1. Seismic stratigraphy

Acoustic basement: the acoustic basement is only locally imaged in our data, and limited to the oil industry seismic profiles. In zone 2 the top of the acoustic basement is interpreted only in one seismic profile parallel to the coast at a depth variable between 5.7 and 4.7 s TWT, and this reflector becomes shallower in area 3 towards the Hannibal High, with values of up to 3.9 s TWT.

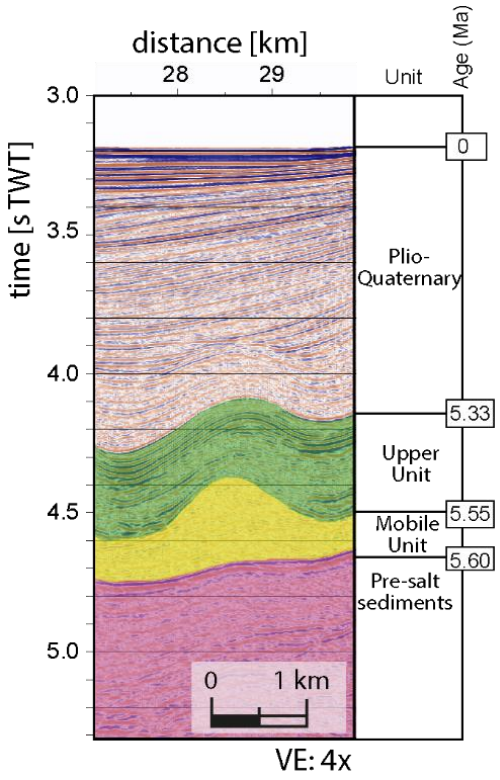

Figure 3.29: *Detail of seismic profile MARADJA 01-97, with the seismostratigraphic units interpreted in the dataset, based on the nomenclature of Lofi et al. (2011) and datation of CIESM (2008). VE: 4X.*

Pre-salt sediments (older than 5.6 Ma): The imaging of pre-evaporitic sediments is made difficult by the presence of the evaporitic layer, that has a shielding effect on the seismic signal. When they are imaged, usually below the salt welds or in correspondence with the thinner salt layer, the pre-salt sediments present **medium amplitude continuous reflections**, often deformed by the pull-up effect due to the salt high seismic velocity **(Figure 3.29)**. In the Algerian basin, the pre-salt sequence of pelagic marls thickens towards the base of the Algerian continental slope (Haidar et al., 2022; Soto et al., 2022). As already mentioned for the Western Sardinian margin, at least the shallower part of this sedimentary sequence is supposed to be the Lower Unit, deposited during Messinian and composed of clastics sediments (Lofi *et al.*, 2005) or evaporites (Krijgsman *et al.*, 1999).

The Mobile Unit (5.6-5.55 Ma): this reflection-free seismic facies, deposited at the peak of the Messinian Salinity Crisis and mainly composed by halite (Hsü *et al*., 1973), constitutes –together with the crustal tectonics- the main reason of recent deformation in the area. Being the Messinian

salt giant a central topic in this study, the Mobile Unit will be described with more detail, starting with the regional geometry of its base and top and the regional thickness of the unit to give an idea of the regional and local trends, to proceed then with the analysis of the geometries in the seismic profiles. Being mainly composed of halite, this unit has a calculated interval velocity of 4.2 km/s (Camerlenghi *et al.*, 2020), slightly lower than the 4.5 km/s of the pure halite.

Base of the MU (5.6 Ma) (Figure 3.30): The base of the MU is imaged in the seismic reflection data in the area as a **negative polarity horizon**, due to the generally lower acoustic impedance of the pre-salt sediments. The **reflection amplitude** is **medium to very low**, because of the effect of the salt layer on the seismic signal, but this also depends on the processing applied on the data and therefore changes in different datasets.

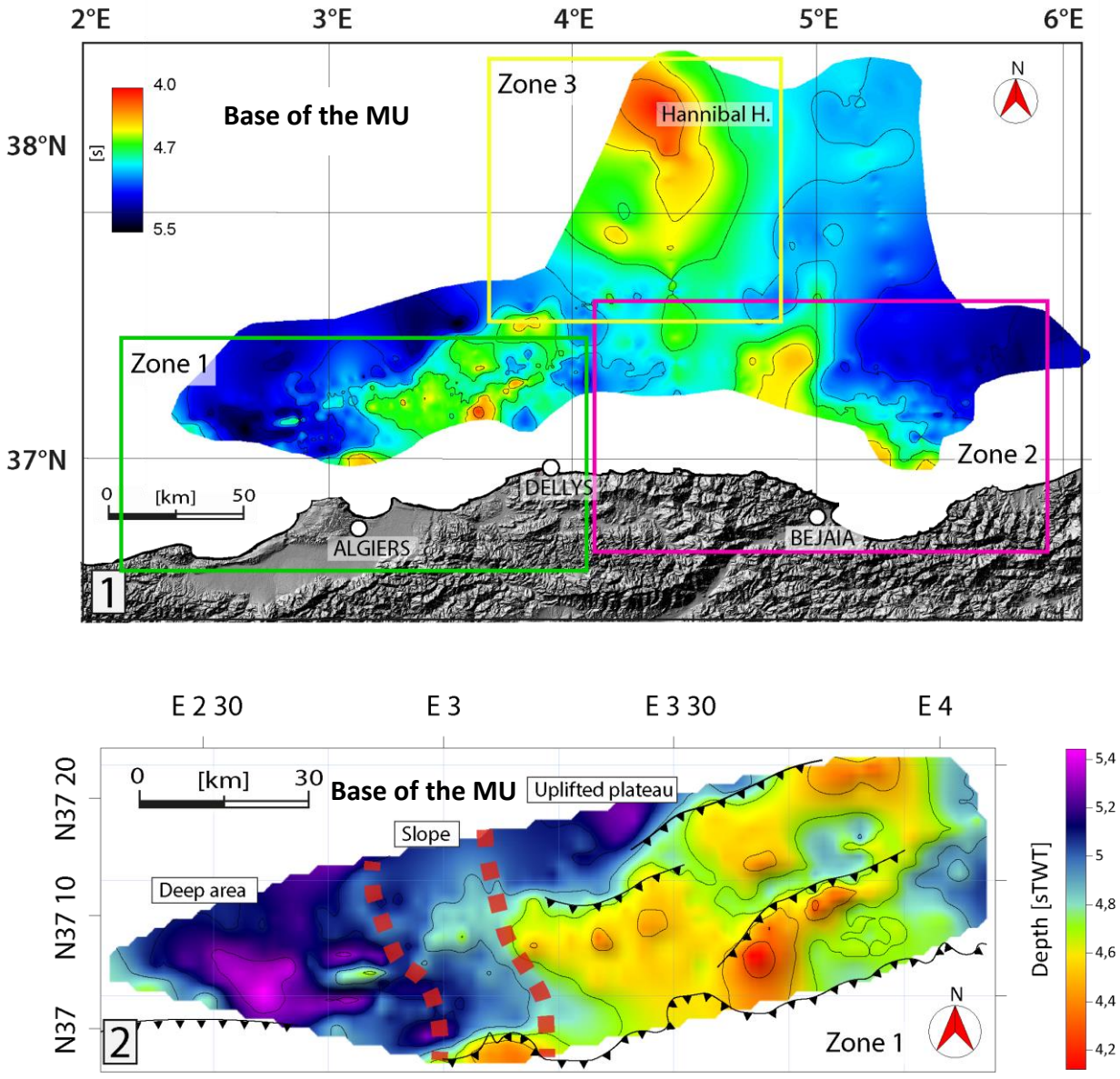

Figure 3.30: .1: *Isobath map of the base of the Mobile Unit on the Algerian margin, with contour lines every 0.2 s TWT and values between 4.0 and 5.5 s TWT. The geometry of this grid is partly deformed by the presence of pull-ups (see text for details).* ***2.*** *Detail of the base of the Mobile Unit in Zone 1, with contour lines every 0.2 s TWT. The position of the thrusts is from Déverchère et al. (2005) and Domzig et al. (2006), while the dashed red line shows the division between the uplifted plateau, the slope and the deep area.*

In correspondence with the major salt structures, the base of the salt results deformed due to the **pull-up effect** of the high seismic velocity in halite, and the seismic signal is often cancelled or very disturbed. Despite these difficulties, the base of the salt has been interpreted in the whole dataset with variable level of confidence, inversely proportional to the thickness of the salt. With a **depth between 4.0 and 5.5 s TWT**, the base of the MU presents different dipping directions: towards north, northwest and west for the western area, towards east and northeast for the eastern one and towards south -but with a very limited data coverage- for the northern one.

Area 1 (W): As we can see in Figure 3.30.2, the base of salt located between 2°20' and 4° East presents a strong discrepancy in its depth values between the eastern and western sectors, connected by a central slope dipping towards west: between 3°10' and 4°E, an uplifted plateau is characterized by values of base salt depth between 4.1 and 4.7 s TWT, with the trend of the shallower values presenting a good matching with the thrusts offshore Dellys and Boumerdes result of a fault propagation fold system below the salt layer (Déverchère *et al.*, 2005, Domzig *et al.*, 2006) as we will see in the seismic profiles that follows. The calculated uplift rate of these crustal structures is around 0.2 mm/yr, with a consequent northern bathymetric scarp of around 400 m (Déverchère *et al.*, 2005).

Moving towards west and towards north, these values present an abrupt change, rapidly reaching more than 5 s TWT (convertible in around 4.5 km depth) and then becoming shallow again with values of 4.7 s TWT. Another slope, less visible in the data due to the limited data coverage, is the continental slope. Some of the small scale variations of the base of the salt visible in figure 3.30.2 are the result of the pull-up effect, due to the high velocity of the seismic waves in halite (around 4.2 km/s).

Area 2 (E): Shallower values of 4.3-4.7 s TWT are present between 4 and 5° E, and the base of the salt deepens at around 5 to 6° E, reaching a depth of up to 5.5 s TWT (Figure 3.30.1), where again we can also notice a deepening of the base of the MU due to the continental slope.

Area 3 (N): Moving towards north, the base of the MU becomes more and more shallow, with minimum values of 4 s TWT corresponding to the positive magnetic anomaly of the Hannibal High.

Top of the Mobile Unit (5.55 Ma) (Figure 3.31): The top of the MU is in the seismic profiles a continuous high positive reflector, result of the very high velocity of the seismic waves in the halite and the consequent strong difference of acoustic impedance between the MU and the UU.

Local difficulties in the interpretation are due to salt tectonics and the consequent local verticalization of this horizon, therefore hardly imaged in the data. The top MU horizon on the Algerian margin is located **between 3.6 and 5.4 s TWT** (Figure 3.31), and as a consequence of the ductile behavior of the salt and the consequently formed salt structures, the geometry of the top of the MU is often characterized by small wavelength vertical changes of many hundreds of meters in its position. The wavelength of these variations in the map strongly **depends from the data distribution**, with shorter wavelength variations where we have a good data coverage and longer wavelength variations where there is no salt deformation or where the data coverage is lower.

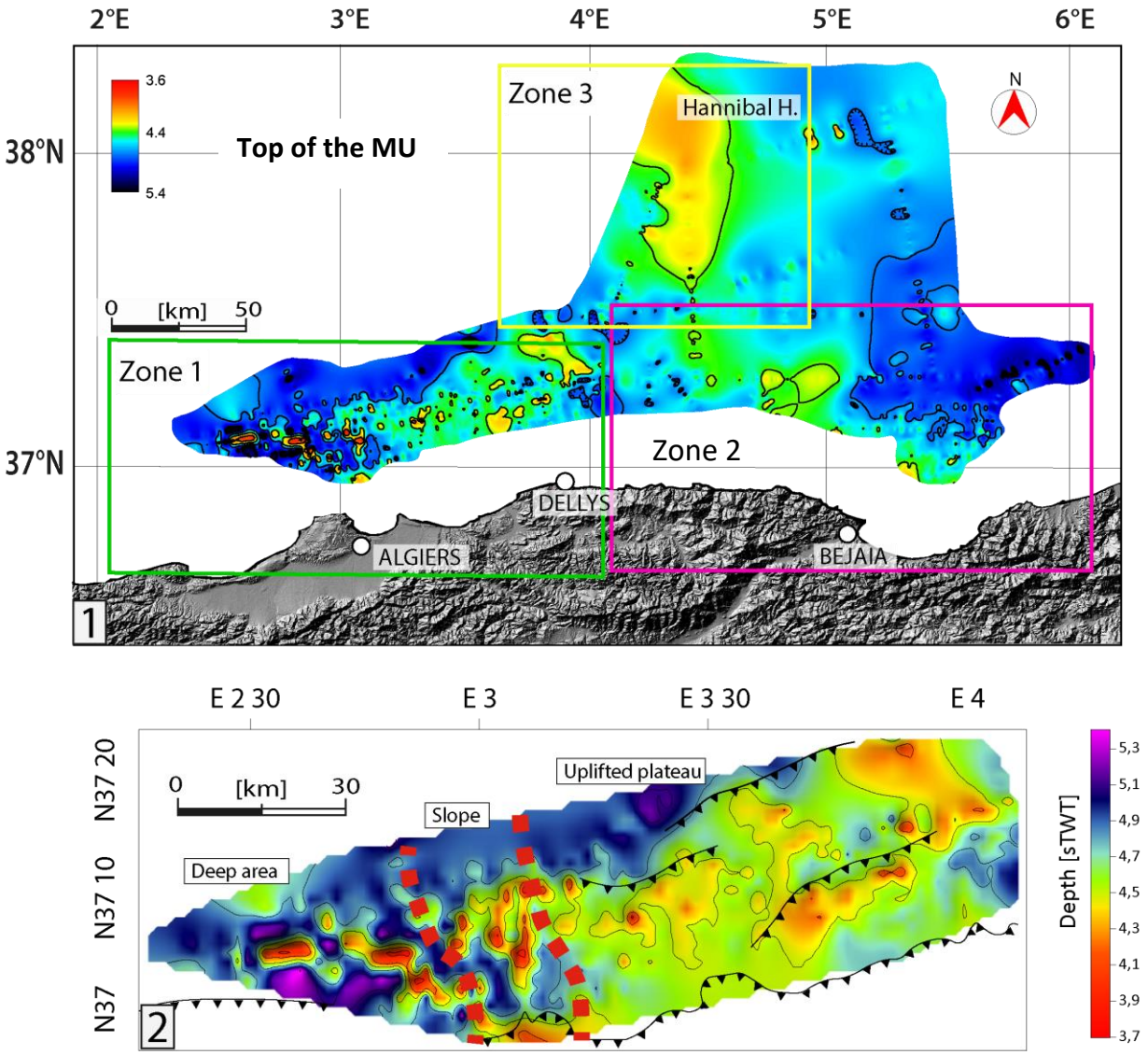

***Figure 3.31**: **1.** Isobath map of the top of the Mobile Unit on the Algerian margin, with contour lines every 0.5 and values between 3.6 and 5.4 s TWT. The apparent distribution of the salt structures is strongly dependent from the position of the seismic lines, particularly in areas of well-developed salt tectonics, in which the apparent distribution of the salt structures in the map is limited by the position of the seismic profiles. **2.** Detail of the base of the MU in Zone 1, with contour lines every 0.4 s TWT and values between 3.7 and 5.4 s TWT. As in Figure 3.30, the dashed red line shows the division between the uplifted plateau, the slope and the deep area.*

Area 1 (W): The grid of the MU top in area 1 (Figure 3.31.2) differs between the eastern and the western part with the same division seen in the base salt horizon: between 3°10’ and 4°E the top of the MU is shallow and quite regular, with average 4.5 s TWT depth. In fact, already from this map we can see that no major salt structures are located in this area. On the other hand, between 2°20’ and 4° E the MU top has an average depth of 5 s TWT and fast lateral changes, due to the presence of major salt structures.

Area 2 (E): In the eastern sector we can see that again there is a shallower area between 4 and 5 degrees where the base of the salt is between 4.7 and 4.4 s TWT and a deeper one eastward where the top of the MU is at a depth of more than 5 s TWT. In the deeper area, small wavelength variations are due to the salt structures, that results to be way smaller than in sector west and do not affect the seafloor morphology. Moreover, in the eastern area there seem to be fewer salt

structures, but this is mainly related to the fact that the MARADJA II profiles parallel to the margin are located further south, and consequently in an area of thinner salt layer. This result in a quite poor data coverage of the area of maximum development of the salt structures.

Area 3 (N): Less precise is the geometry of the MU top around 38°N, where the apparent scarcity of small scale deformation in Figure 3.31 does not have to be taken into account due to the low density of seismic data coverage. Few major structures can be visualized around 5°E in Figure 3.31, and are most likely present in the nearness not imaged by seismic data.

Thickness of the Mobile Unit (Figure 3.32): The thickness of the MU presents values between **0 and 1.6 s TWT**, so between 0 and 3-3.4 km if we consider that the average velocity of the seismic wave is 4.2 km/s (Camerlenghi *et al.*, 2020). The minimum thickness of salt is registered in correspondence with the structural highs (e.g. Hannibal High) and the salt welds, while maximum thicknesses are the salt walls and diapirs in area 1 (W). This unit, as well as the Upper Unit, pinches out towards the south.

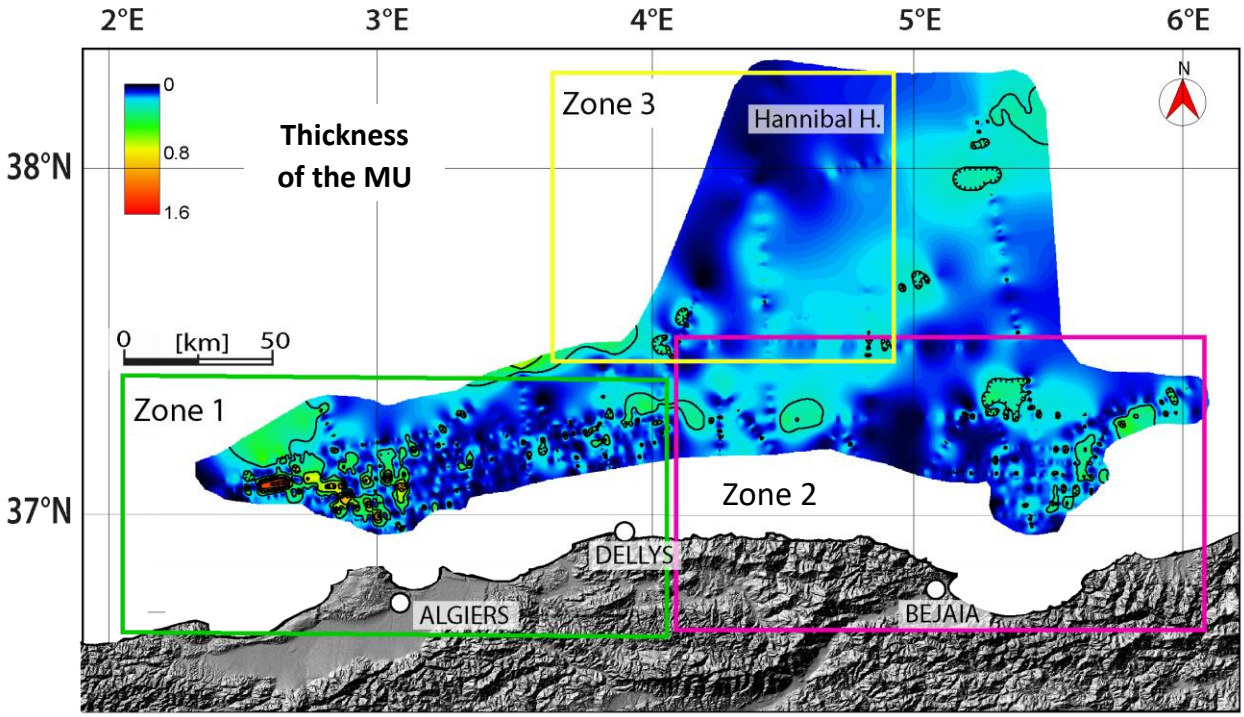

Figure 3.32: *Thickness map of Mobile Unit on the Algerian margin, with contour lines every 0.5 s TWT and values between 0 and 1.6 s TWT, corresponding respectively to the structural highs and to the bigger salt diapirs of Zone 1.*

Area 1 (W): Following the same internal division of Area 1 previously described for the base and top of the MU, the thickness of the MU can be divided here in an eastern part characterized by a thin salt layer above the uplifted plateau identified in the base salt grid, and a western area of a thick salt layer with well-developed salt structures (Figures 3.31.2 and 3.32). The bigger diapir have a thickness of 1.5 s TWT, that can be converted in more than 3 km height.

Area 2 (E): with a sort of specular symmetry with area 1 (W), we can divide between a sector of thinner salt on the west and one of thicker salt and salt tectonics structures towards east. But as

we already saw in the top salt map, the structures are not as developed as in area 1 (W), and the bigger structures identified here have around 500 ms TWT height, so slightly more than 1 km height.

Area 3 (N): Here again we have very few information, but the salt layer is rather thin with pinch outs towards the Hannibal Ridge and thicker salt towards south-east. The area will be better understood through the analysis of the few seismic reflection profiles.

Upper Unit (5.55-5.33 Ma) (Figure 3.33):

As already seen in the Western Sardinian margin, the UU is composed by marls and evaporites (Hsü *et al.*, 1973), and have a calculated interval velocity of 3.5 km/s (Camerlenghi *et al.*, 2020). In our data it presents a seismic facies of continuous, high amplitude reflectors, creating a strong contrast with the underlying MU ad with the lower amplitude continuous reflections of the lower Pliocene (Figure 3.29). The UU often shows syn-kinematic geometries (e.g. fan strata geometries) and frequent onlaps on diapirs and structural highs, that we will analyze in more details in the seismic reflection profiles. With a thickness between 0 and 0.7 s TWT, it has lower thickness values above the structural highs, while the salt diapirs correspond to absence of UU deposition**.** Maximum values are around 0.7 s TWT, i.e. 1.2 km.

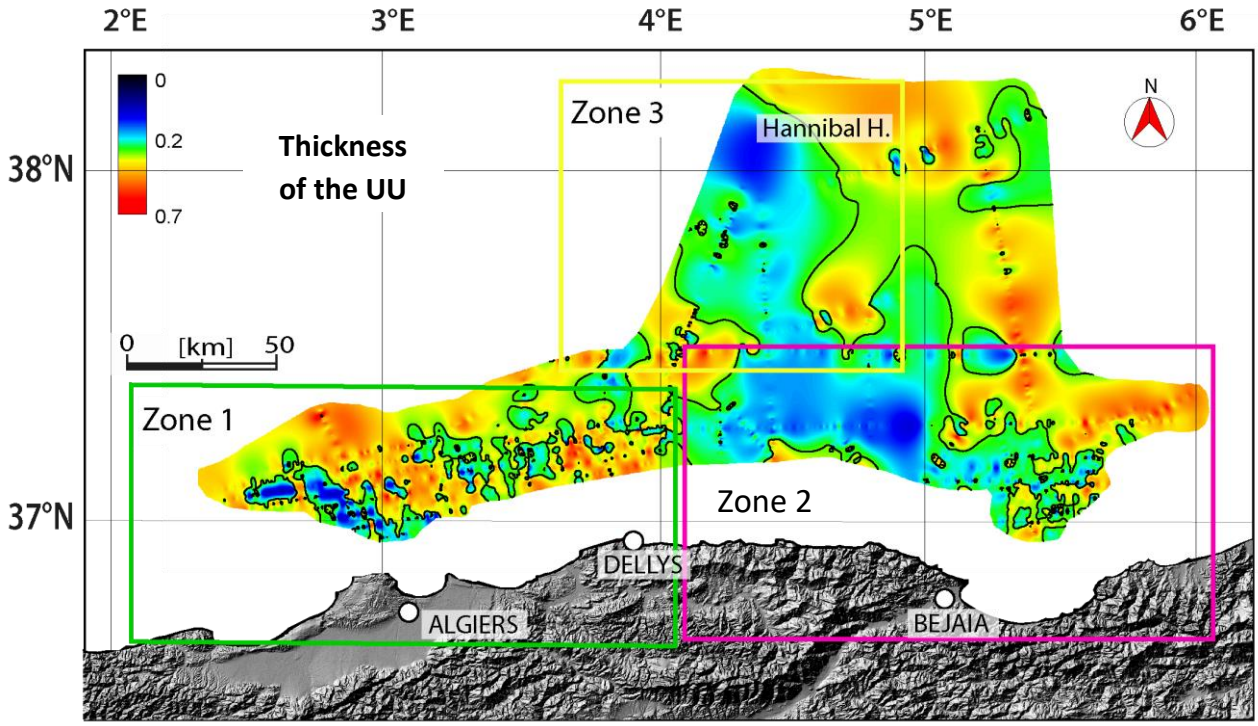

***Figure 3.33**: Thickness map of the Upper Unit on the Algerian margin, with contour lines every 0.4 s TWT and values between 0 and 0.7 s TWT, with the lower ones corresponding to the structural highs and to the major salt diapirs.*

Zone 1 (W): Considering the small wavelength variations in the UU thickness, it is problematic to evaluate the thickness of the UU at a regional scale, but its value does not present a clear thickening trend in Zone 1, except for slightly thinner values that correspond to the thrusts positions.

Zone 2 (E): In contrast with what we observed in zone 1, in zone 2 we can identify a regional trend (Figure 3.33). In fact, between 4.6° e 5° the UU thickness is limited to 0.1-0.2 s TWT (180 m to 350 m), while it reaches a thickness of 0.3-0.5 s TWT (0.5 to 0.8 km) towards east. At the eastern

limit, probably also thanks to the higher density of seismic reflection profiles, the thickness variations of the UU have a shorter wavelength in the grid, similar to the ones of Zone 1. The same area in which the base of the MU is uplifted (3°10' to 4°E) correspond to a thinner UU, suggesting the presence of a structural high predating the end of the Messinian Salinity Crisis.

Zona 3 (N): Values of UU thickness around zero correspond to the area of limited salt thickness and to the Hannibal High. Outside the area of influence of the Hannibal High, the maximum values of UU thickness are around 0.5 s TWT (i.e. 0.8 km), compatible with the regional values.

Plio-Quaternary (5.33 - 0 Ma) (Figure 3.34): After the end of the Messinian Salinity Crisis, the Mediterranean Sea went back to deep water conditions, and the sedimentary sequence recovered in the DSDP well 371 is composed of calcareous mud and mudstones. As a consequence of the pelagic and muddy nature of this sequence in the Western Mediterranean, the lower Plio-Quaternary has a generally low amplitude, high-frequency continuous reflectors seismic facies. This makes it locally difficult to visualize these horizons and consequently the geometries necessary to date the salt movement during the early Plio-Quaternary, as we will see in the salt tectonics subchapter. The seismic horizon reflection strength increases towards the Upper Plio-Quaternary, showing the detritical and coarser nature of this recent sequence.

The trend of Plio-Quaternary sedimentary thickness (Figure 3.34) shows thicker deposits near to the coast line, with maximum values of around 1.7 s TWT (2.1 km), and more reduced values going towards the center of the basin, far from the influence of the river sedimentary inputs. Fan shaped strata characterize most of the Plio-Quaternary, while infilling geometries are more common in the most recent sediments. We can observe, both in the seismic profiles, in the map of the brittle cover thickness and in the bathymetry, the formation of sedimentary minibasins around 10 km wide surrounded by salt structures.

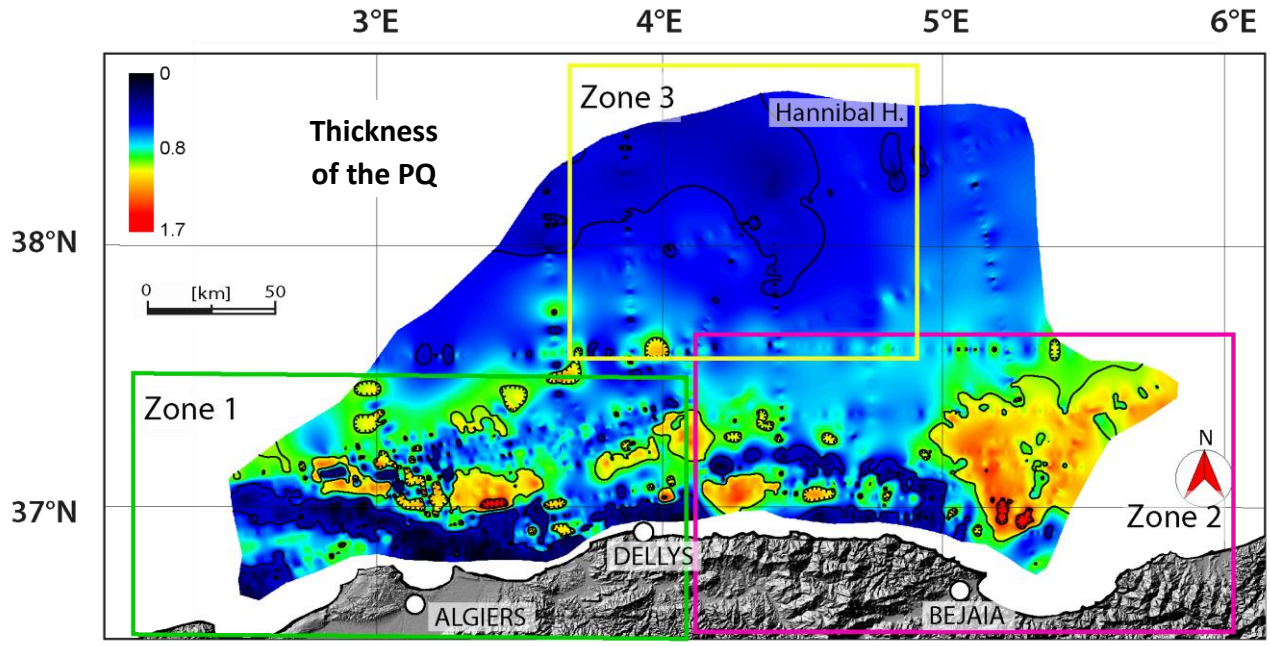

Figure 3.34: *Thickness map of the Plio-Quaternary deposits on the Algerian margin with contour lines every 0.5 s TWT. This map presents the higher areal extension, due to the greater ease in interpreting these shallower deposits and to the fact that they are present ubiquitously in all the seismic profiles.*

Brittle cover (Figure 3.35): As already discussed for the Western Sardinian case study, from the point of view of salt tectonics the Upper Unit and the Plio-Quaternary sediments can be considered as a single sedimentary body, defined as brittle cover as it is characterized by the brittle deformation in contrast with the ductile one of the MU.

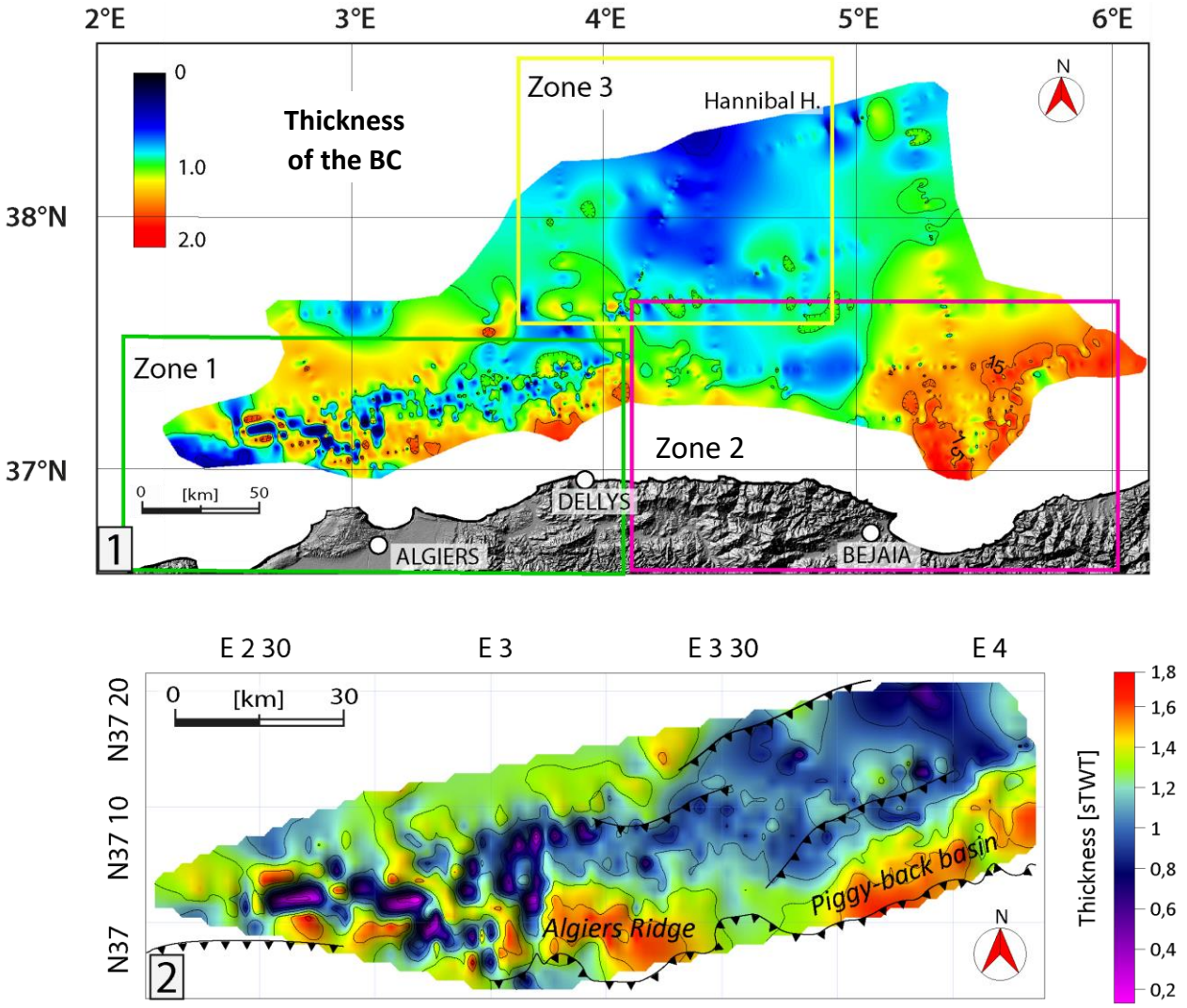

Figure 3.35: 1. *Thickness map of the brittle cover, i.e. Upper Unit and Plio-Quaternary deposits, on the Algerian margin with contour line every 0.5 s TWT and values between 0 and 2 s TWT. A major depocenter is present around 5°20' E, while minimum values are northward (i.e. Hannibal High).* ***2.*** *Zoom of the brittle cover thickness on area 1, with contour lines every 0.3 s TWT and values between 0 and 1.8. The two depocenters are here related to the sediments of the Algiers Ridge and to the piggy-back basin above the uplifted plateau.*

The sedimentary load constituted by the brittle cover has an influence on the geometries and distribution of the salt related structures, that tends to form where the sedimentary load is lower (e.g. external limit of a deep sea fan). The thickness range of the brittle cover is between **0 and 2 s TWT**, that -calculated with an average velocity of the seismic wave in the layer of 2500 m/s- correspond to values between 0 and 2500 meters of sediments. Some areas of major sediment thickness are proximal to the coastline, mainly in correspondence with the deep-sea fan offshore Béjaïa (5-5°30' E) that constitute the main depocenter of the area. This trend is superimposed on another one, that shows a lower thickness of sediments on the uplifted area of the three zones. Also

the MU has a strong influence on the thickness of these deposits; in fact, the lower values of thickness are registered above the main salt structures, and the small wavelength variations in sediment thickness are mostly attributable to the presence of salt diapirs, with absence of UU and very limited Plio-Quaternary in correspondence with the bigger diapirs. For what concerns **Zone 1**, the spatial variation in the brittle cover thickness map (Figure 3.35.1) shows a trend of major thickness of the brittle sedimentary cover near the coastline, with 2 main depocenters of different origins: the eastern one (3°40' to 4° E) is the result of the syn-tectonic sedimentation during the thrusts activity (piggy-back basins) and correspond to a local low of the bathymetry, while the one at 3°30'-4° E corresponds to the Algiers Ridge, and is a local high on the bathymetry. In Zone 2 the lower values correspond to the shallower area and the major ones to the deeper base salt, and to a river sedimentary input offshore Béjaïa. In zone 3, the thickness of the brittle cover follows the same trend as the MU, UU and Plio-Quaternary maps, with a marked thinning corresponding to the Hannibal High.

III.C.1.2. Salt tectonics and salt-related structures

After the description of the 3D grids of the Messinian and Plio-Quaternary units of the previous subchapter, the salt and overburden geometries in the seismic reflection profiles will now be described in detail. The seismic profiles more characteristics of the three areas (1- west, 2 - east, 3 - north) were selected, both parallel and perpendicular to the margin to better understand the tridimensional development of the area already seen in the grids. We will describe here the geometries of the basement and of the pre-salt sedimentation -when visible-, the Messinian Mobile Unit with focus on the salt structures formed, and the geometries of the brittle cover containing information on the timing of crustal and salt deformation.

Zone 1 (W): Starting from the analysis of the seismic profiles in zone 1 (western area), seismic profile MDJ01-03 parallel to the margin **(Figure 3.36)** clearly illustrates the different salt structures that characterize the uplifted plateau (E3°10 eastward), the westward slope, and the abyssal plain (3°10' to 4° E) (division in Figure 3.31.2). While very limited imaging of the pre-salt horizons is obtained here, the geometry of the salt structures and the brittle overburden is particularly significant to understand the relationship between salt and crustal tectonics on the Algerian margin.

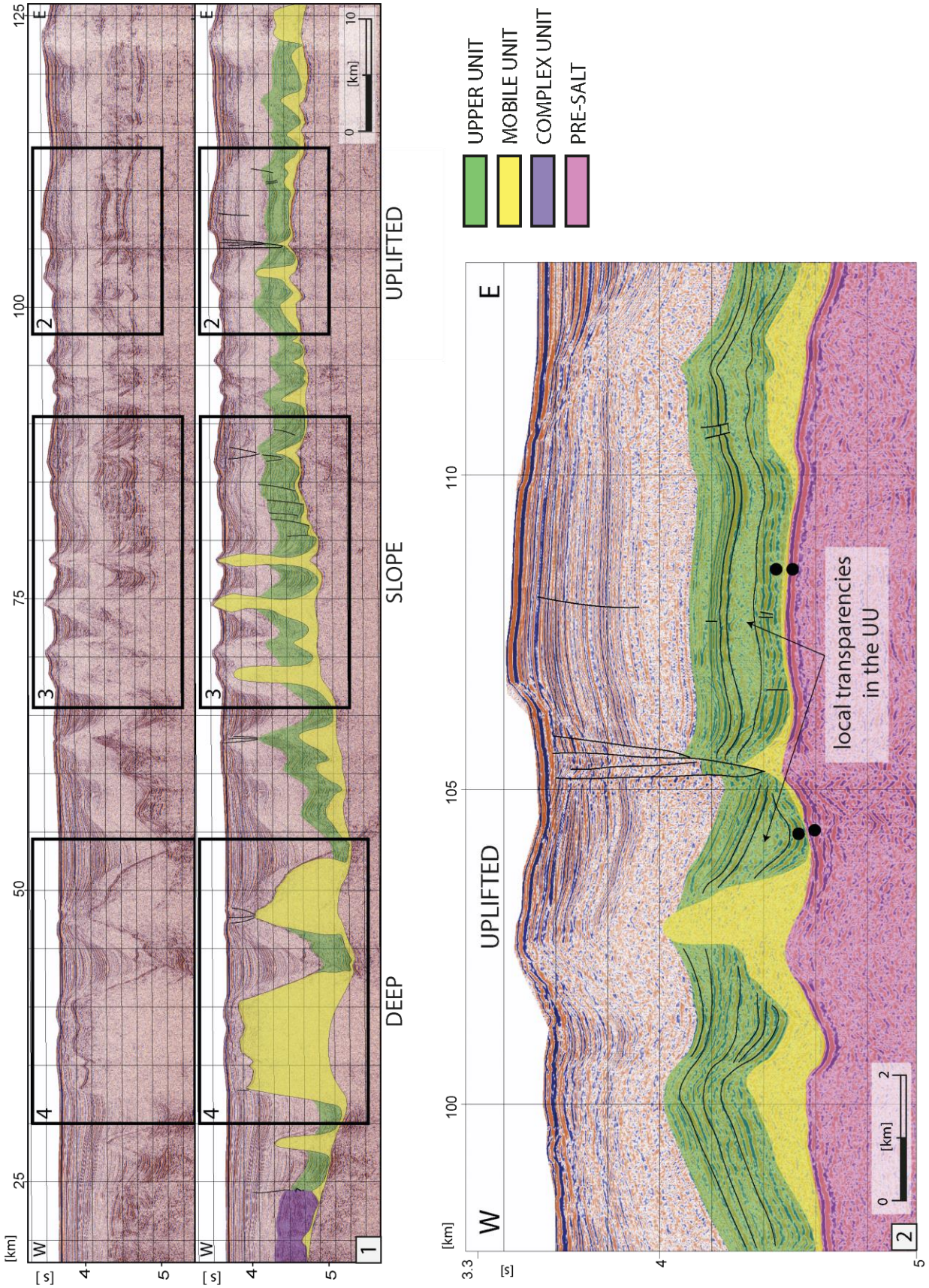
UPPER UNIT
MOBILE UNIT
COMPLEX UNIT
PRE-SALT
DEEP
SLOPE
UPLIFTED
UPLIFTED
local transparencies in the UU
W
E
[km]
[s]
0
10
2

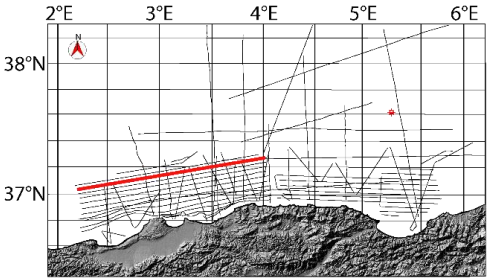

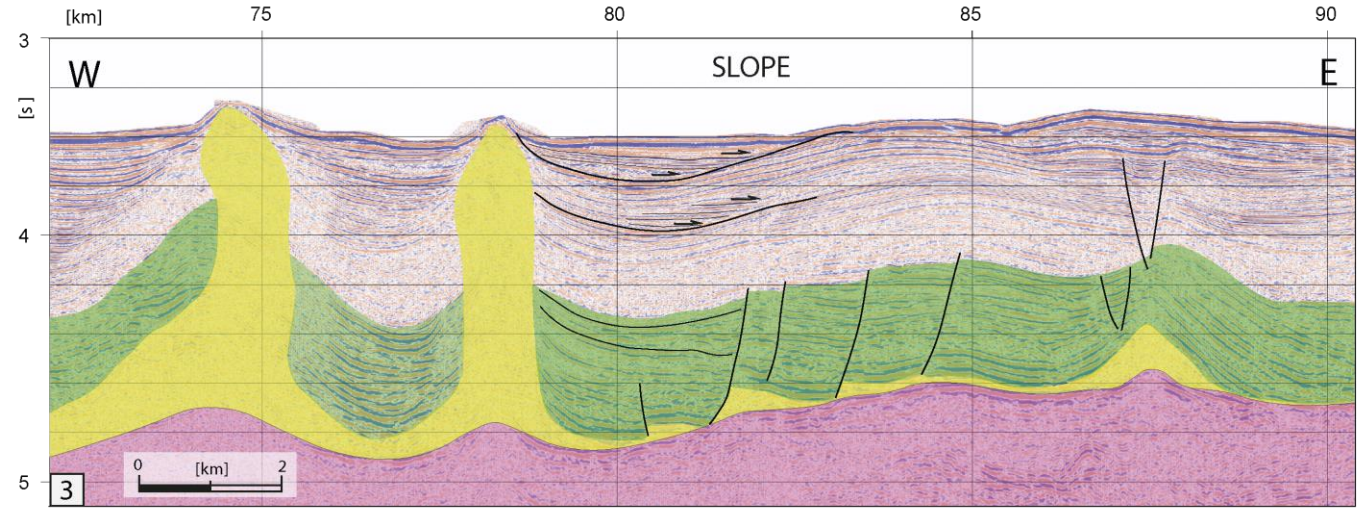

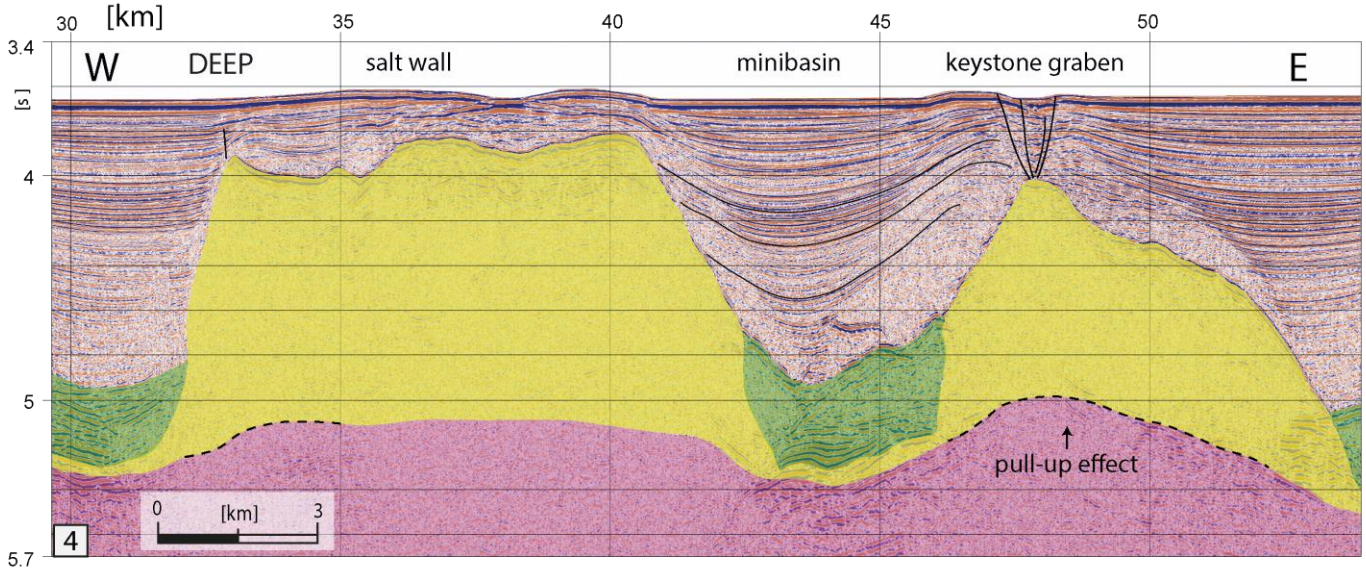

***Figure 3.36**: **1.** Seismic profile MDJ01-03, parallel to the margin offshore Algiers and Boumerdes, highlighting the presence of an uplifted area and a deeper one, connected by a slope. The black rectangle marks the position of figures 3.36.2, 3.36.3 and 3.36.4. VE: 8.8X. **2.** Detail of seismic profile MDJ01-03 located on the uplifted plateau. VE: 5.6 X **.3:** Detail of seismic profile MDJ01-03 located on the slope, at the transition between the uplifted plateau and the slope. The presence of extensional faults in the UU marks the extensional salt tectonics domain. VE: 5.6 X **4.** Detail of seismic profile MDJ01-03 in the deep basin, imaging the major salt structure of this study area. VE: 5.6 X.*

To have a clearer image of the differences, we will describe the uplifted plateau, the slope and the deeper area separately:

- **The uplifted plateau** is characterized by **reduced salt thickness** and by salt diapirs, salt anticlines and salt rollers mostly limited to 200-300 ms height (few hundreds of meters thickness) and spaced by 2-3 km of thin salt or salt welds (Figure 3.36.2). The internal reflectors in the UU show slightly fan shaped strata while they are truncated and uptilted in correspondence with the salt diapirs and deformed above the anticlines. Moreover, a seismic transparent layer of 120 ms thickness has been observed in the UU in this area, suggesting the presence of a salt layer that could be either salt migrated from the MU beneath or autochthonous salt resulting from a locally shallower environment (Figure 3.36.2). The Plio-Quaternary geometries of deposition imaged in the seismic profiles parallel to the margin are mostly the result of the geometries of deposition and erosion of the brittle sedimentary supply from the margin rather than linked to salt tectonics; during Plio-Quaternary the synkinematic depositional geometries that could be reconducted to salt tectonics activity are minimal and mostly restricted to the scarce salt diapirs above the uplifted plateau. Because of the strong influence of crustal tectonics on the development of the area, it is particularly interesting to analyze the profiles perpendicular to the margin and roughly-perpendicular to the thrusts **(Figures 3.37 and 3.38)**. As previously mentioned, the uplifted domain in which the base of the MU is deformed and lifted has been described in Déverchère *et al.* (2005) and Domzig *et al.* (2006) as the result of the thrusts activity, and is characterized by wedged, piggy-back basins. The internal reflectors in the UU show slightly fan shaped strata while they are truncated and uptilted in correspondence with the salt diapirs and deformed above the anticlines. In seismic profile MDJ01-95 **(Figure 3.37)** we can see the effect of the **blind thrust** at km 22 on the geometries of late Miocene to Plio-Quaternary sediments, deformed by a thrust anticline. Another possible blind thrust is present at km 40, but the presence of a salt diapir and the consequent seismic pull-up hides the hypothetical pre-salt sediments deformation. Together with the deformation due to the thrusts presence, the UU and PQ also present shorter wavelength anticlines attributable to salt tectonics. In this profile the CU deposition appears mostly coeval to the UU one, while for the datation of the deposition begin the uncertainties are higher because the base of the CU is not clearly imaged. The UU shows infilling geometries with onlapping horizons at km 35, testifying early salt deformation. The lower Plio-Quaternary presents an almost constant thickness along the profile and is strongly deformed by the salt related anticlines, while the upper Plio-Quaternary varies laterally and the sequence shows infilling geometries and flat horizons, with very localized salt related deformations. The integration of seismic reflection data with bathymetric data **(Figure 3.39)** allows us to follow the 3D development of these salt structures, that result to be salt ridges surrounding depocenters.

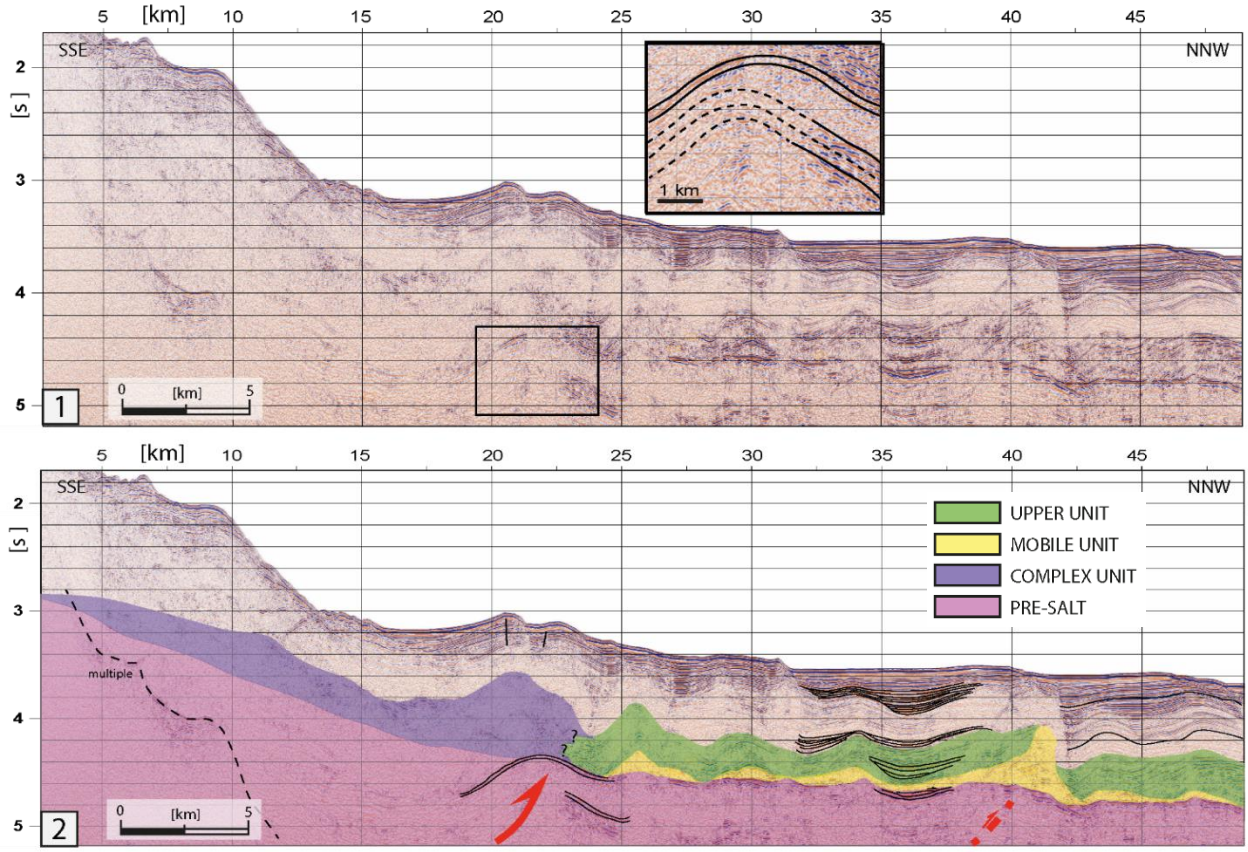

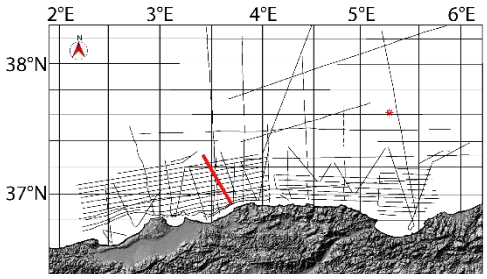

***Figure 3.37**: Seismic profile MDJ01-95, perpendicular to the margin in the area of the uplifted plateau. **1.** Uninterpreted **2.** Interpreted. The red arrows represent the supposed position of the thrust that leads to the formation of the anticlines, with major uncertainties concerning the one at km 40, where the visualization of the pre-salt geometries is disturbed by the presence of a salt diapir. VE: 5.6 X.*

The effect of the thrusts activity on the sediments geometry is particularly evident in seismic profile MDJ01-96 **(Figure 3.38)**, in which the uplift of the base salt in correspondence with the thrust anticline results in the formation of a **southward slope of 4°**, in contrast with seismic profile mdj01-95 (Figure 3.37), located only 2.5 to 22 km far, slightly sloping northward. While the UU has a rather constant thickness up to km 25, the presence of a blind thrust at km 27 and the consequent anticline formed has an effect already on the geometries of deposition of the UU, that result fan shaped. The earlier growth strata typical of the **piggy-back basins** are dated Lower Pliocene, while the evidences of salt movement seem to be mostly concentrated during early Pliocene and stopped quite early, despite the formation of the slope in the base salt continued, as testified by the piggyback geometries of the PQ and by the step in the bathymetry.

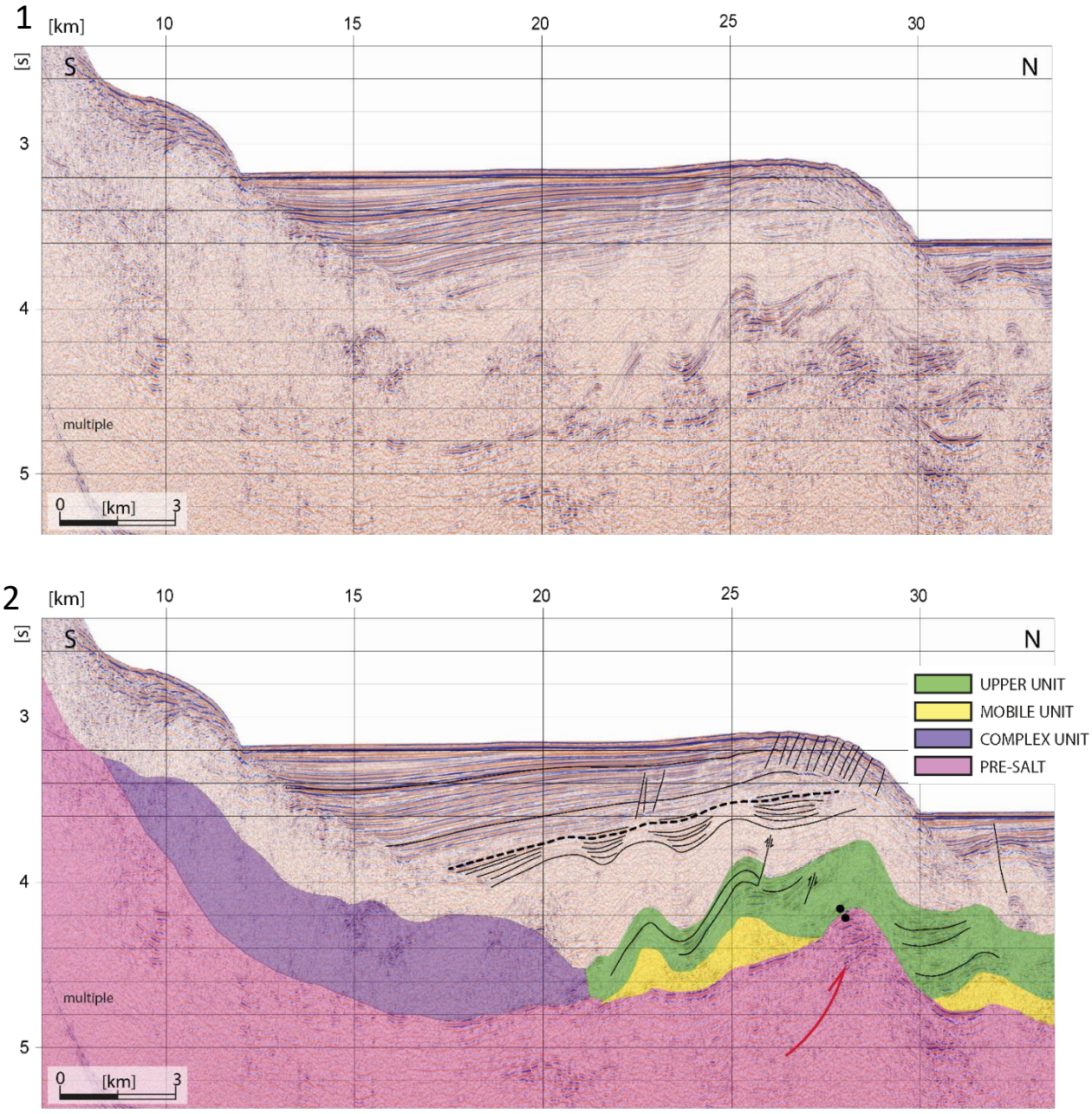

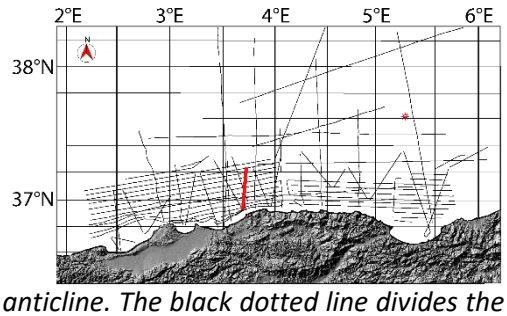

***Figure 3.38**: Seismic profile MDJ01-96, perpendicular to the margin in the area of the uplifted plateau. **1.** Uninterpreted **2.** Interpreted. The profiles perpendicular to the margin show some piggy back geometries (Déverchère et al., 2005a) due to the thrusts rooted below the Messinian sediments, that is also responsible for the southward slope of the base of the salt in this seismic profile. The red arrow represents the supposed position of the thrust that leads to the formation of the anticline. The black dotted line divides the Plio-Quaternary sediments in two subsets: a lower sequence in which are co-present the effects of the salt and crustal tectonics (i.e. anticlines and thickening of the sequence towards south) and an upper one in which the horizons geometries are exclusively the result of the thrust activity. VE: 5.6 X.*

- If we analyze the situation **on the slope** at the western limit of the uplifted plateau (Figure 3.36.2) we notice a sudden change in the geometries. The base of the salt deepens westward switching between a depth of 4.6 s TWT to 5.4 s TWT in 45 km, forming a calculated average gradient of 2.6° (Figure 3.36.3). The passage between the uplifted plateau and the slope produces an area of extensional salt tectonics, with extremely reduced salt thickness and direct faults rooted in the MU and dislocating the whole UU, followed westward by an area of well-developed salt structures on the slope, presenting the characteristics of the classical polygonal minibasins, i.e. a dish-shaped syncline of few km of diameters, subsiding into a salt layer.

The structures strongly affecting the seafloor morphology at km 77 of seismic profile MDJ 01-03, can be better analyzed with the help of high resolution bathymetric data, on which we can appreciate the 3D extension of these structures **(Figure 3.39)**. The salt diapir up to few km thick imaged in the profile corresponds on the seafloor to an annular salt ridge, while the smaller salt structure produces a crestal graben well visible on the seafloor. The UU internal layering shows lateral thickness variations and onlap geometries (Figure 3.39.2), while this unit is absent in correspondence with the salt diapirs, and the onlapping horizons are uptilted around the salt diapirs. The PQ horizons are deformed up to the seafloor, and onlapping geometries are present (Figure 3.39.2), while the PQ deposits are almost absent above the two salt diapirs. The seismic signal is chaotic not only inside the salt structure but also partly around it, so the shape of the interpreted structure is based on the seismic data but also on our knowledge of salt tectonics and wave propagation. The localized high amplitude seismic reflections inside the salt body are most likely a lateral reflection of the top of the MU, but could possibly be a layer of brittle sediments incorporated into the salt during the ductile deformation.

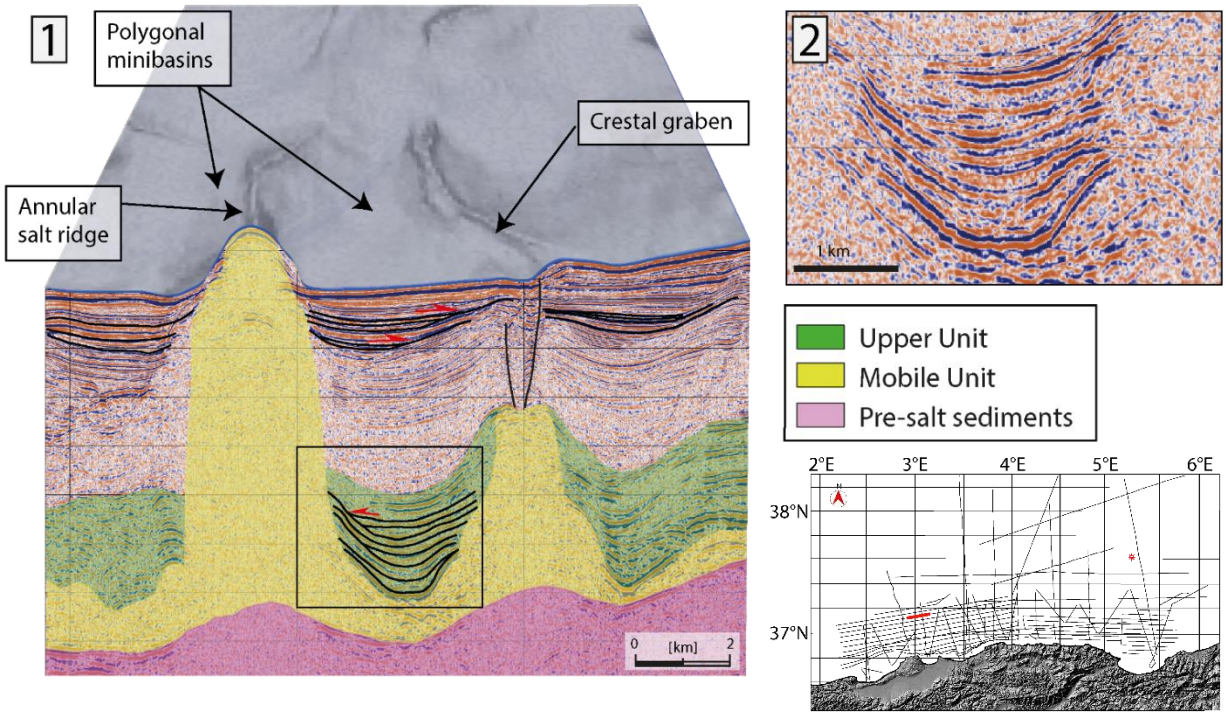

Figure 3.39: 1. *Detail of seismic profile MDJ 01-04, parallel to the margin and imaging the structures related to the minibasins, and* ***2.*** *The multibeam bathymetry data acquired during the MARADJA survey, allowing to interpret in 3D the salt structures which results to be annular salt ridges surrounding polygonal minibasins. Onlapping horizons and fan-shaped strata geometries are already present in the sediments that pre-date the end of the MSC. VE: ~6.7X.*

- The average value of the salt base depth reaches moving from east to west quite high depths, with values of 5-5.45 s TWT at 37°E (Figure 3.36.3) **(abyssal plain)** where we also find the major salt structures of the area. The maximum depth of the base salt is reached at 2°37'N 37°E, where the 5.4 s TWT depth corresponds to one of the shallower values of the top of the MU, therefore forming the massive salt structures imaged in Figure 3.36.3 and affecting the bathymetry. The difference in width between the two salt walls of figure 3.36.3 is the result of the way in which this seismic profile cuts the elongated salt structure, with the western, larger diapir being the consequence of an oblique section imaging. The UU seems to have an average constant value where the salt structures did not develop, while it is absent in correspondence with the massive salt diapirs. Due to the thick brittle cover -that reaches here its maximum values of area 1-, and to the presence of numerous lateral reflections, the eventual presence of growth strata in the UU is not imaged. Between the salt walls, the Plio-Quaternary thins towards the salt structures and forms the typical geometries of the salt minibasins already described on the slope.

Zone 2: As mentioned in the previous subchapter, in terms of MU the situation in Zone 2 was somewhat similar to that of the western one, with an area of thinner salt where the base and the top of the MU are shallower, and a part of thicker salt where the base and the top of the MU are deeper. This can be better appreciated in seismic profile ALE 77-33-1 **(Figure 3.40)** parallel to the coastline, that despite being part of an older dataset better represents the geometries in the area. These data have lower frequency of the signal, therefore lower resolution and higher penetration, allowing us to have information about the pre-salt geometries. The top of the acoustic basement is the top of a chaotic or transparent seismic facies and has a depth variable between 4.4 and more than 6 s TWT. Above this, a seismic unit of continuous medium amplitude and almost undeformed seismic reflectors has a thickness of up to 0.8 s TWT. While the upper part of this pre-salt sequence could be interpreted as Lower Unit, we do not have the elements to mark the beginning of the Messinian Crisis sedimentary sequence in the area.

Both the MU and the UU pinch out in the central part of this seismic profile. The salt thickens towards east and towards west forming numerous salt anticlines and diapirs, that deform not only the UU but at least the lower Plio-Quaternary, with some deformation reaching the seafloor. Normal faults cut the UU and PQ sequences with minimum offsets, confirming the presence of a very thin layer of MU that cannot be imaged in the seismic reflection data. The UU presents lateral thickness variation along the seismic profile, with lower values in the uplifted area (around 0.05 s TWT), while eastward it reaches values of 0.4 s TWT (700 m).

In the profile perpendicular to the coast MDJ02-70 **(Figure 3.41)** the presalt sediments are clearly imaged as parallel continuous horizons partially tilted towards north, and in contrast with Zone 1 no blind thrusts geometries have been interpreted. The MU has a thickness variable between few ms (salt welds) and 0.4 s TWT (800 m), with thicker salt anticlines towards NNW (i.e. downslope). Particularly interesting is the geometry of the UU, that shows thickness differences along the seismic profile and in particular fan shaped strata above salt anticlines of few hundred meters' height. Moreover, downlap geometries have been interpreted in the lower Pliocene sediments at km 55 to 60 (Figure 3.41.3). As we will see in the discussion chapter, these geometries are particularly important to reconstruct the movement of the Mobile Unit.

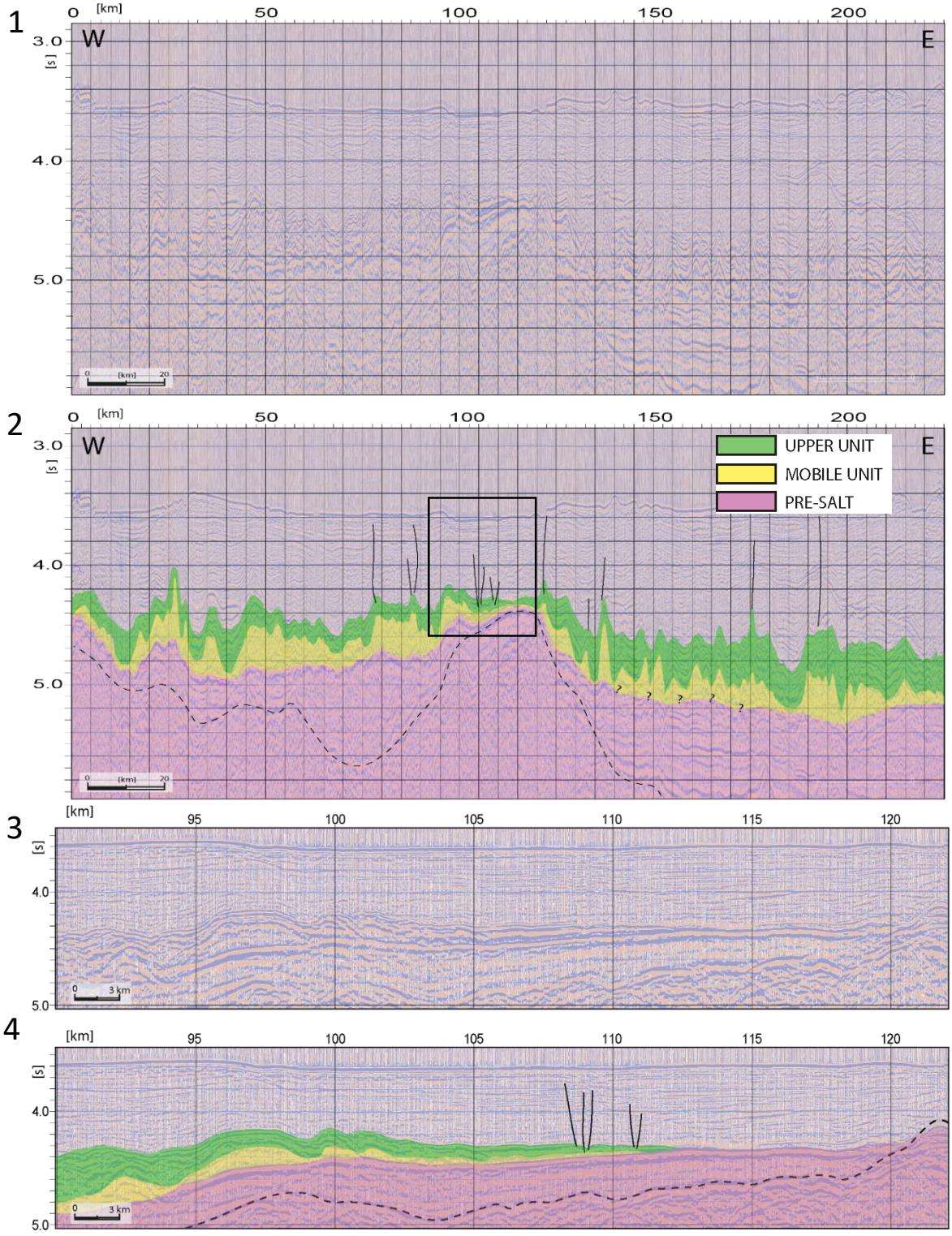

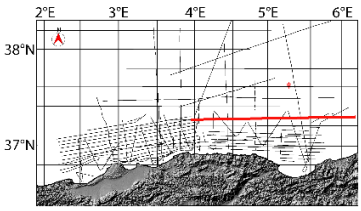

***Figure 3.40**: Seismic profile ALE 77-33-1 parallel to the coast line, in zone 2.* **1.** Uninterpreted **2.** Interpreted, *with position of the zoom of figures **.3** ad **.4** (uninterpreted and interpreted) (VE: 4.5 X). VE:~22.5 X The dotted lines represent the acoustic basement.*

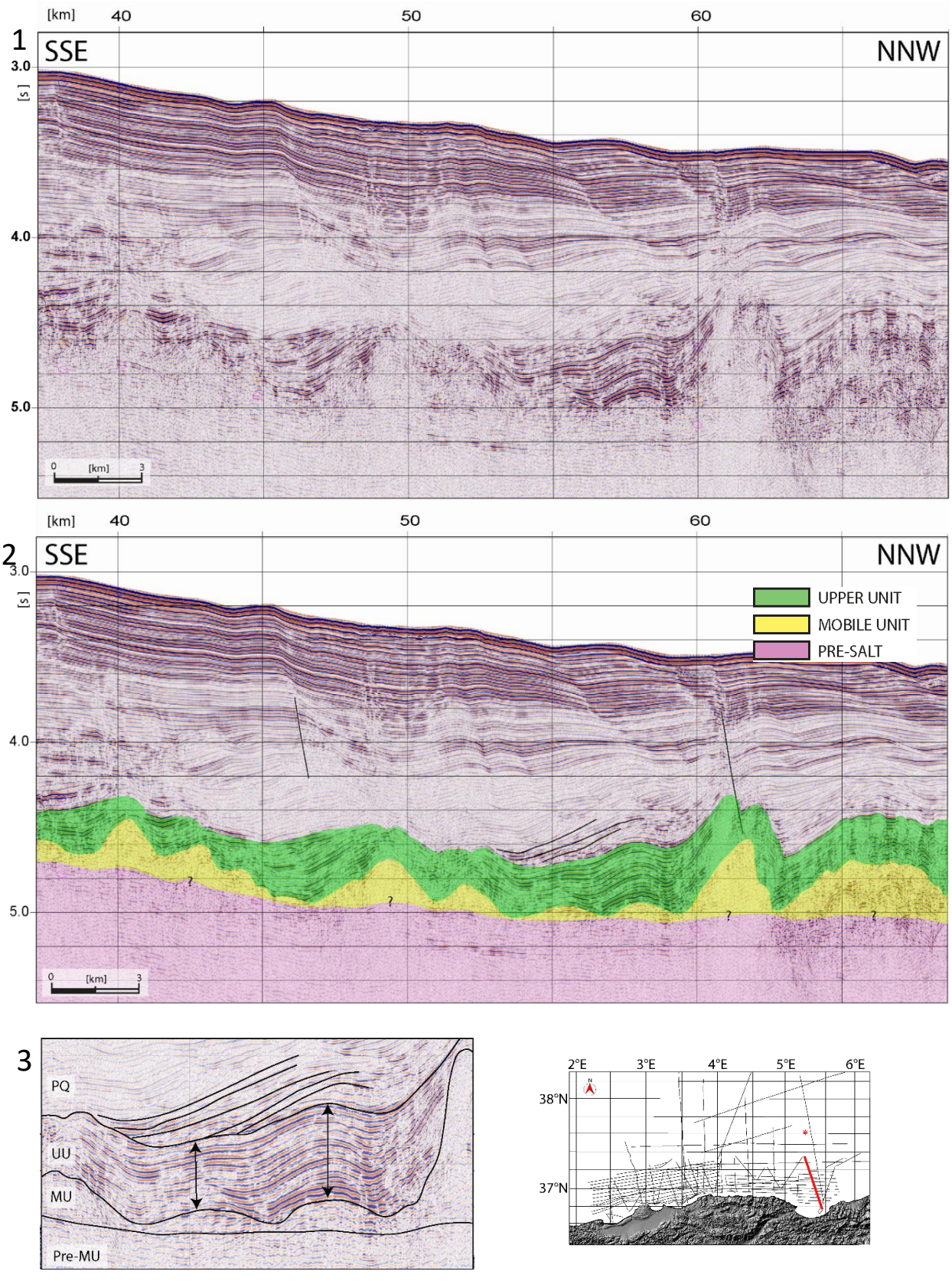

Figure 3.41: *Seismic profile MDJ 02 -70, perpendicular to the coastline in zone 2.* ***1.*** *Uninterpreted* ***2.*** *Interpreted. V.E.:~ 5X. As visible in the zoom* ***(3.)****, the UU has different thickness along the seismic profile, and apparent downlap geometries are interpreted in the lower Plio-Quaternary.*

Zone 3 (N): While the higher density of the dataset is mostly southern 37°25' N, some of the seismic profile image the area of the Hannibal High, up to 38°20' N **(Figure 3.42)**. Previously interpreted as a N-S trending accretion center (Mauffret *et al.*, 2004), the Hannibal High crustal structure (position in Figure 3.30.1) has been recently explained as the offshore expression of the post-collisional magmatism already recognized in Greater Kabylia (Aïdi *et al.,* 2018), and is constituted by a "complex stacking of volcanoclastic formation over a thin crust" (Leprêtre *et al.*, 2013).

The pre-salt horizons, continuous and parallel when visible, are strongly affected by the crustal deformation (Figure 3.42). The base of the MU have different directions of slopes, and the thickness of the MU varies between 0 –where it pinches out above the two highs- and 0.4 s TWT (800 m) where the base of the salt is deeper and the salt forms diapirs. Also the UU has strong lateral thickness variability, from the few meters thin UU above the major high at km 95 to the more than

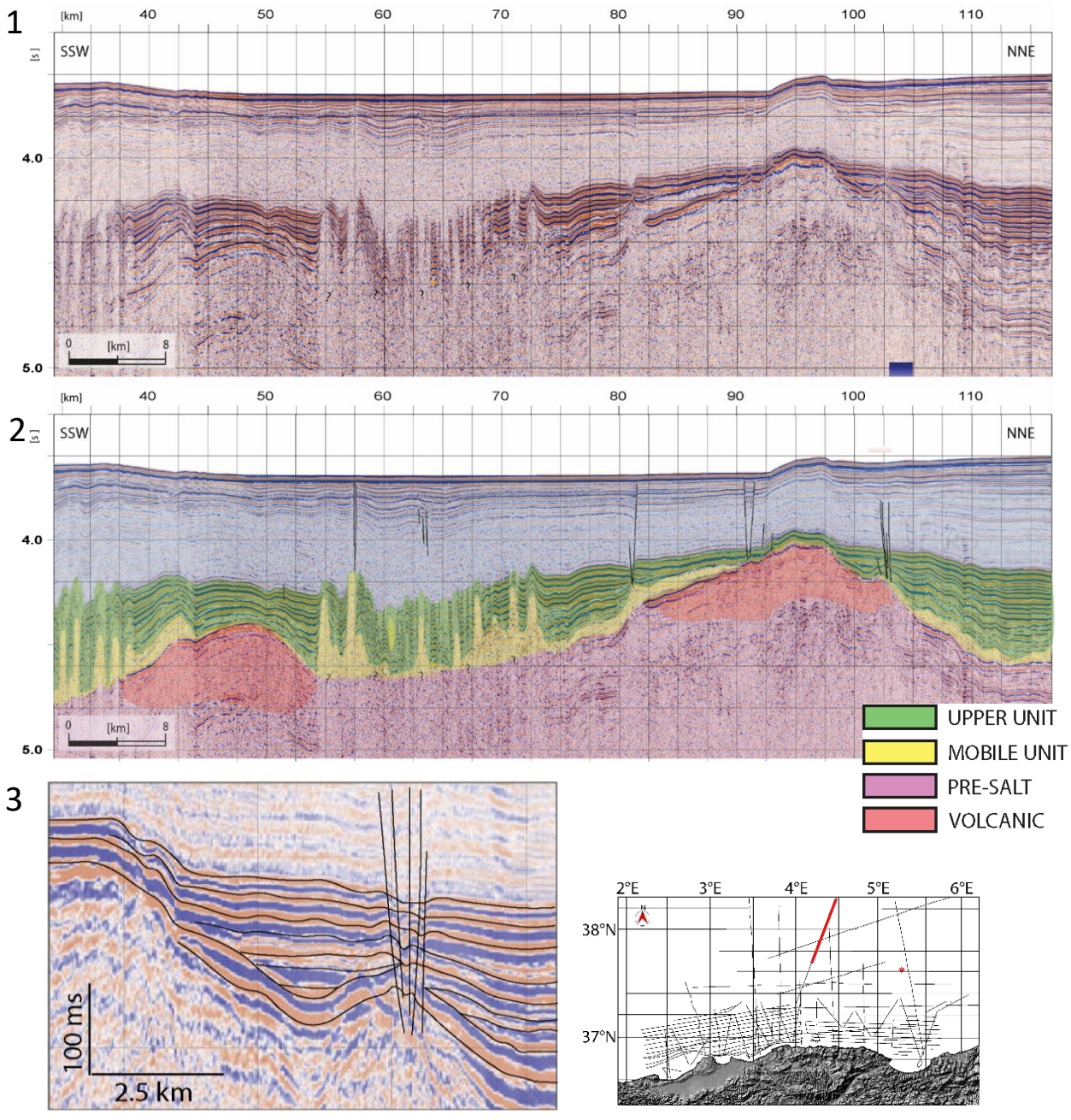

Figure 3.42**: Seismic profile MDJ01-01 (V.E.~ 22 X), imaging the area of the Hannibal High, **1.** Uninterpreted **2.** Interpreted, with marked the position of the zoom of figure **3.

0.4 s TWT (700 m) downslope. Onlap geometries in the UU are present above the Hannibal High, and are particularly well visibles above the major high. While the UU is strongly deformed both by the extensional faults related to salt tectonics -mostly above the major high- and to the formation of salt structures downslope, the deformation related to salt structures becomes less evident in the Upper Plio-Quaternary sequence, and the seafloor is only affected by the late and more localized step of movement of the Hannibal High, which led to a seafloor deformation of 6 km along this profile.

III.C.2. Analogue modelling of the salt tectonics on the Algerian margin

After the interpretation of the geophysical data, some doubts persisted concerning the observed geometries of salt deformation on the Algerian margin. In particular, given the heterogeneity of the salt and crustal tectonics in the study area, we decided to focus on **Zone 1** (i.e. the western one), located between 2°20' to 4°E and 36°40' to 37°20'N (Figure 3.28).

This area is characterized by certain elements that are schematized in **Figure 3.43** and will be considered in the model:

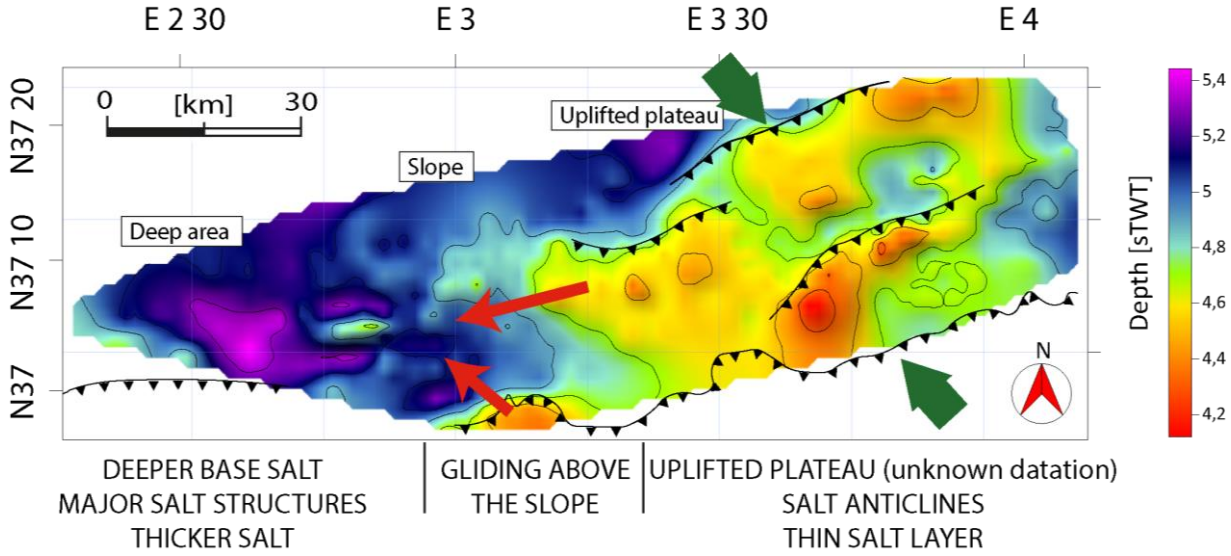

Figure 3.43: *Isobath map of the base of the Mobile Unit in zone 1 and schematization of the elements of the model representing the uplift of a plateau in an area characterized by the presence of a salt layer. The red arrows represent the slopes direction in the base salt, while the green ones represent the tectonic stress in the area.*

- A lack of detailed information about the pre-Messinian **crustal movements**, hidden by the ductile nature of the salt. As testified by the geometries interpreted in the seismic reflection profiles perpendicular to the margin, the beginning of the crustal activity predates the end of the MSC. Moreover, the MARADJA profiles does not present a deep penetration, therefore most of the thrusts interpretation is based on the seafloor deformation, piggy-back geometries and uplift of the Messinian deposits. Considering that we lack information about the pre-salt sediments thickness, we use in this model a thickness of sediments based on technical reasons.
- The presence in the eastern part of an **uplifted plateau** of crustal nature, above which the salt layer is thin and the base and top of the salt are uplifted. Associated to this, there is a **westward slope** of 2.6°.

- The presence in the western part of an area of deeper base of the salt, without signs of crustal activity and with major salt walls.
- A layer of salt that, as already mentioned, has different thicknesses. The viscous nature of the salt prevents us from having information about the initial thickness of the MU in a certain area.
- The UU does not present a difference in thickness at a large wavelength between the eastern and western sector (uplift plateau VS deeper area), suggesting that the uplift of the plateau began (or re-activated) after the end of the MSC. We know that the reactivation in compression is dated around 8 Ma in the area and therefore pre-dates the Messinian Salinity Crisis, but due to the evaporitic nature of the MU the Crisis cancelled any pre-Messinian bathymetric difference.

Based on these elements, we formulated the hypothesis that the direction of the salt movement is influenced by the reactivation in compression of the margin both in terms of timing and geometries, with the uncertainty regarding the initial distribution of the salt layer in the area.

To confirm this hypothesis, different analogue models have been produced in the analogue modelling laboratory of the University of Lille, aimed at better understanding the origin of the salt structures interpreted in the area offshore Algiers, and especially the relation with the uplifted plateau. The salt layer has been modelled through a layer of silicone, while the brittle behavior of the rocks has been modelled through layers of sand (granulometry 125-315 µm). We will describe here two of the analogue models produced, both modelling the hypothesis of a constant salt layer at the beginning of the plateau uplift. In fact, the production of an analogue model with inhomogeneous thickness of salt at time T=0 is technically complicated by the viscous nature of this material.

III.C.2.1. Experimental protocol

Scaling: We used a 1:10 000 geometrical scaling in our model, so 1 cm of material corresponds to 1 km in the natural example.

The **pre-salt layers** are not properly imaged in the seismic data, so the thickness of pre-silicone layers has been decided based on the amount of sand layers necessary to model the plateau uplift.

Salt thickness scaling: considering the ductile nature of the Mobile Unit -and the consequent high variability of its thickness in the area- there is an uncertainty about the thickness of this layer, for which we consider an average value of 1 km of salt, i.e. 1 cm of silicone in our models. A proper volumetric reconstruction could be possible only through basin scale 3D data coverage and corrections for dissolution and erosion.

Overburden thickness scaling: The brittle overburden is well visible in the seismic data, so the scaling was based on an average value of the interpreted layers thickness. The simplification applied is compatible with the nature of these layers and the lever of approximation that characterize the analogue models.

In terms of **temporal scale**, the duration of the different phases of the model is quite well constrained by the seismic data, but it is also dependent by few more factors related to modelling:

- The uplift of the plateau is produced by the compressional movement of the box model. The speed of the compression has to be slow enough to give time to the silicone to deform.
- Constrains related to the laboratory accessibility during the night **(human constrains)**: we have to pause the sedimentation during the night due to the impossibility to spend the night in the laboratory, but due to the viscous rheology of the silicone the model does not stop moving.
- The **silicon mobility**, which in turn depends on other factors such as temperature, sand content in the recycled silicone etc.

Experimental box

For this model we built a box **(Figure 3.44)** constituted by three fixed glass panels and a movable wooden one to which is connected a motor, in order to move the wall and compress the model in a S-N direction. The two glass panels of 1 meter each are positioned in a N-S direction, while the E-W walls are 60 cm long. The result is a delimited rectangle of 90 x 60 cm, and the maximum possible height of the model is constrained by the glass panels (20 cm height). A plate of 30 x 55 cm in model A01 and 25 x 45 cm in model A02 is present on the SE part of the box bottom, in order to create a preferential area for the modelled crustal deformation.

The model can be schematically divided in different areas (Figure 3.44), based on the layers of material (sand vs sand and silicone) and the actions that will be carried out during the experimental procedure:

Zone A: At the southern limit of the box model, this area of 20 x 60 (model A01) or 15 x 60 (model A02) respectively represent the area in which the sedimentary sequence is exclusively brittle, i.e. the Mobile Unit deposition is absent.

Zones B: The northern part of the box represents the area in which the Mobile Unit deposited, so the sedimentary sequence contains 1 cm thick silicone layer to model the presence of the salt.

Zone C: At the western and northern limit of the box model and only in zone B, this part of the model is strongly affected by edge effects, and silicone and sand will be regularly removed during the experiments to create a free edge and leave space to the model to develop. The width of this area is around 2.5 cm.

Plateau: As previously mentioned, a plate of 30 x 55 cm in model A01 and 25 x 45 cm in model A02 is placed at the SE boundary of the box model, constituting the base of part of zone A and B. In this way we are able to move towards north the effect of the box model compression, and to model the formation of the uplifted plateau offshore Algiers and Dellys.

The experimental protocol for this model consists in an active compression of the box model in order to simulate the reactivation in compression of the Algerian margin. To simulate the situation in Zone 1, we recreated both the area of the plateau uplift and the area where there is no effect of the compression on the salt layer. During the continuous deformation of the model we proceeded with the deposition of several sedimentary layers, that are not isopach but are regionally scaled to

the interpreted layers. Due to the presence of a silicone layer, the deformation has to be slow to give time to the silicone to deform in a ductile way.

We produced several analogue models, differing mostly in terms of dimensions of the box models and the plates, and we will describe here the last two models produced. The experimental design for every model is summarized in **Tables 3.1 and 3.2**, where all the actions carried out during the experiment (e.g. chronology, layers material and thickness, etc.) are recorded to allow the reproducibility of the model. This is followed by a general comment on the various stages, and a discussion on the models results. The differences between the two models procedures and results will be briefly described, while the comparison between the result of analogue modelling and seismic data interpretation will be discussed in chapter III.C.3.

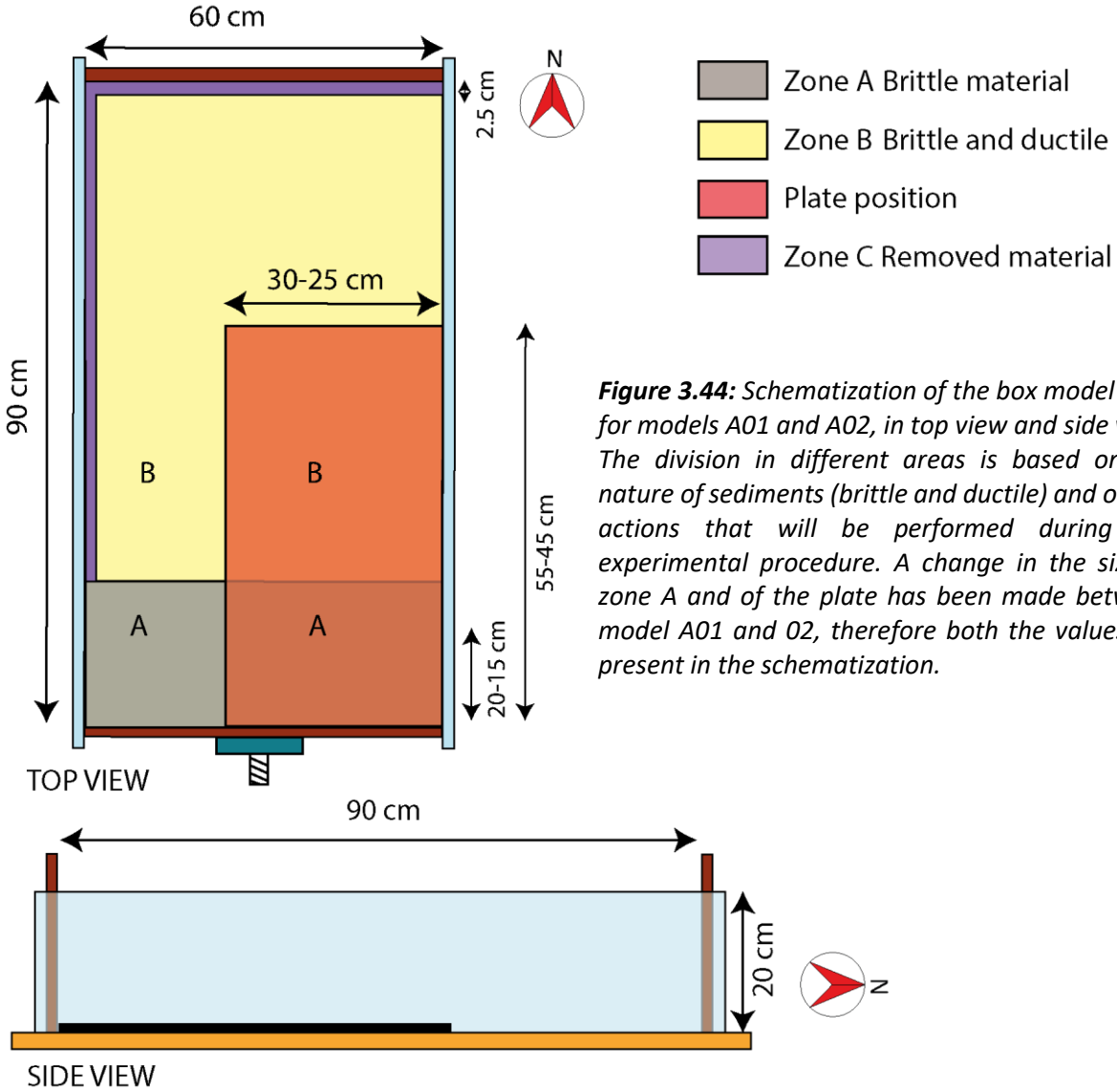

Figure 3.44: *Schematization of the box model used for models A01 and A02, in top view and side view. The division in different areas is based on the nature of sediments (brittle and ductile) and on the actions that will be performed during the experimental procedure. A change in the size of zone A and of the plate has been made between model A01 and 02, therefore both the values are present in the schematization.*

III.C.2.2. Model A01

• Experimental procedure

The first of the two models described here was mainly aimed at calibrating the ratio between the dimension of the plate -that will control the dimensions of the uplifted plateau- and the dimensions of the box model. Moreover, this model was also necessary to evaluate the speed of the engine during the plateau uplift and to understand the number of hours necessary to run the whole model. The first 6 layers of sand -for a total of 8 cm- are added to the whole box (Table 3.1).

Time	Layer	Material/activity	Thickness [cm]	Sand color	Top color	Location
-24h00'	1	Medium sand	2 cm	White	Blue	Whole box
	2	Medium sand	0.5 cm	Red	Brown	Whole box
	3	Medium sand	2 cm	White	Black	Whole box
	4	Medium sand	0.5 cm	Blue	Red	Whole box
	5	Medium sand	2 cm	White	Green	Whole box
	6	Medium sand	1 cm	Lavender	Blue	Whole box
	7	Medium sand	1 cm	White	Brown	Zone A
	8	Medium sand	0.5 cm	Red	Green	Zone A
	9	Silicone	1 cm	/	/	Zone B
0	10	Medium sand	1 cm	White	Red	Zone A
	11	Medium sand	0.5	White	Blue	Zone B
	/	Engine 0.59 cm/h	/	/	/	/
45'	/	Engine 4.92 cm/h	/	/	/	/
1h25'	/	Engine 1.05 cm/h	/	/	/	/
4h52'	/	Material removed	5	/	/	Zone C
5h35'	/	Material removed	5	/	/	Zone C
22h30'	12	Medium sand	0.3 – 0.5	Orange	Green	Zone B
22h50'	/	Engine 0.49 cm/h	/	/	/	/
27h45'	13	Medium sand	0.3 – 0.5	Blue	Blue	Zone B
29h45'	Final layer	Medium sand	>2	White	/	Whole box

Table 3.1: *Experimental procedure of model A01.*

The first 20 cm of the southern part (zone A) are covered with 2 more strata of 1 cm and 0.5 cm of sand. After the brittle sedimentation, 1 cm of silicone is added to zone B. In this model the silicone does not constitute the base of the model, so the silicone layer has to be prepared on a separate table and cut into sections to move it to the model. After this, the silicone needs around 24 hours to become flat. When the silicone is flat, 1 cm of sand is added on zone A and 0.5 cm of sand is added on zone B. At this point, the sedimentary sequence pre-dating the interpreted crustal movement is complete, and we turn on the engine to have 0.59 cm/h of model compression, marking the beginning of the experiment. At T=45', we increase the speed of the engine to 4.92 cm/h, because the initial low speed was leading to an unequal distribution of the strain in the model. At T=1h25', the plateau is partly formed, so we switch back to a velocity of 1.05 cm/h, that has a better proportion with the natural example. At T=4h50', silicone is removed from zone C. This operation has been necessary to de-block the system, and is repeated at T= 5h35'. At T=6h40', we significantly reduce the speed of the compression to 0.2 cm/h, in order to slow down the model during the night. After the night break, at T=21h45' the area above the plateau presents exposed

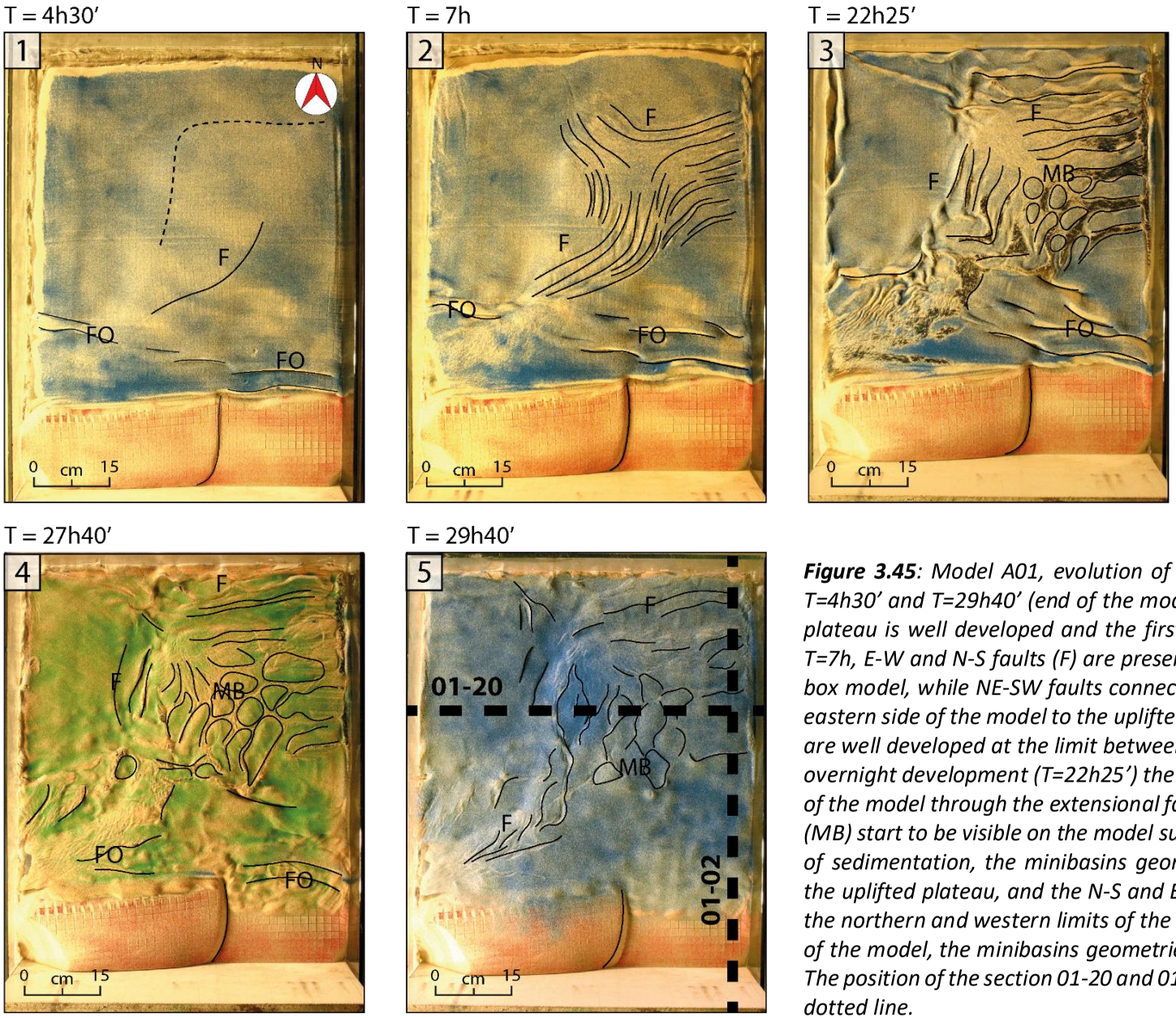

***Figure 3.45**: Model A01, evolution of the top view between time T=4h30' and T=29h40' (end of the model). **1.** T=4h30', the uplifted plateau is well developed and the first faults form above it. **2.** At T=7h, E-W and N-S faults (F) are present on the eastern side of the box model, while NE-SW faults connect the uplifted plateau of the eastern side of the model to the uplifted area on the SW. Folds (FO) are well developed at the limit between areas A and B. **3.** After the overnight development (T=22h25') the silicone reached the surface of the model through the extensional faults. Minibasins geometries (MB) start to be visible on the model surface. **4.** After another layer of sedimentation, the minibasins geometries (MB) are clearer on the uplifted plateau, and the N-S and E-W faults are visible only at the northern and western limits of the plateau. **5.** Towards the end of the model, the minibasins geometries are more and more clear. The position of the section 01-20 and 01-02 is marked with the black dotted line.*

silicone **(Figure 3.45.3)**. The compression is temporarily stopped at T=22h30', and sand is added to the model (layer 12, Table 3.1) to fill the lows formed by the deformation of the silicone. Immediately after, 5 cm of material are removed by zone C. At T=22h50', we turn on the engine at 0.49 cm/h and let the structures develop up to time T=27h45' (Figure 3.45.4), when 0.3 to 0.5 cm of sand are added to zone B. Sand and silicone are newly removed from zone C.
At time T=29h45' (Figure 3.45.5), we block the model adding a layer of sand of more than 2 cm. This last, thick layer of sand has to be thick enough to stop the deformation of the model and to allow us to wet the model without ruining the geometries of the sand layers. Due to the succession of layers with high and very low permeability, the model has to be wet slowly, in order to prevent the formation of bubbles of air below the sealing silicone layer. This problem locally affects the model above the plateau, but the damage to the geometries is minimal.

Considering the tridimensional nature of this model, we are interested in the observation of both the N-S and E-W sections, so a compromise has to be done. We start cutting N-S sections on the eastern side of the dataset to visualize the area of the uplifted plateau, cutting the sections 1 to 7 at 1.3, 3, 5, 7.3, 10 and 12.2 cm from the eastern wall of the box. After this, we cut E-W sections (numbers 8 to 14) located at a distance from the northern wall of 1, 3, 5.2, 9, 12, 15.1 and 17.9 cm. One more section is cut at this point in a N-S direction at 16.1 cm from the eastern side of the box, in order to visualize the salt geometries perpendicularly to the margin direction towards the western limit of the uplifted plateau. Then, 13 more sections are cut in a E-W direction, with sections 16 to 28 at a distance from the north of 21, 24.9, 27, 28.1, 31, 34.2, 35, 36.8, 38.7, 41, 43.5, 46.7 and 48.6 cm.

- ## Results and discussion

During this first experiment we observed the formation of the uplifted plateau in response to the compressional stress and the deformation of the salt layer as a consequence of this uplift.
Between time T=0 and time T=4h30', the major deformation visible on the model is the deformation related to the **uplift of the plateau** in the eastern part of the model and in a deformation of the southwestern part of the model due to the absence of the plate in this area (Figure 3.45.1). Moreover, folds are present in the southern part of the box model. The pattern of faults in the model starts from the NE-SW normal fault (F) that starts to be visible in Figure 3.45.1. After few more hours (T=7h, Figure 3.45.2) the pattern of faults above the plateau is well defined, with copresence of **E-W and N-S normal faults** locally forming grabens geometries. Few faults at the N-W limit of the box model are due to the edge effect and will not be considered. After several hours without sedimentation due to the night break, the silicone is exposed on the model surface, reached through the space opened in the overburden by the numerous faults (Figure 3.45.3). The first **minibasins geometries (MB)** are visible at this phase, but will be clearer after more sedimentation at time T=27h40' (Figure 3.45.4). At this point, the geometries of the fault pattern are less and less clear, and numerous fractures are present above all the plateau. At the end of the experiment (Figure 3.45.5), the deformation related to the plateau uplift reaches almost the northern wall, and we can clearly distinguish between an **eastern area of uplifted plateau with well-developed minibasins geometries** and a western area with minimal deformation at the model surface.

In this model it is also particularly interesting to evaluate the geometries visible in the sections, that strongly differ between the N-S and E-W sections.

- **N-S sections:**

In the N-S sections we can observe in detail the pop-up geometries result of the box model compression, and the resulting gravity gliding towards south due to the slope formed by the plateau uplift. The gravity gliding resulted in a thinner silicone layer above the plateau where few silicone anticlines formed and accumulation of silicone towards south, that is in proportion thicker than in the natural example. This leads to more complex salt structures, as visible in Figure 3.46. The northern limit of the model is not taken into consideration here, because the deformation related to the plateau reached the northern glass panel so the edge effects in the area are very strong. In model A02 the dimensions of the plateau will be reduced in order to obtain some information also about the area located northern the uplifted plateau.

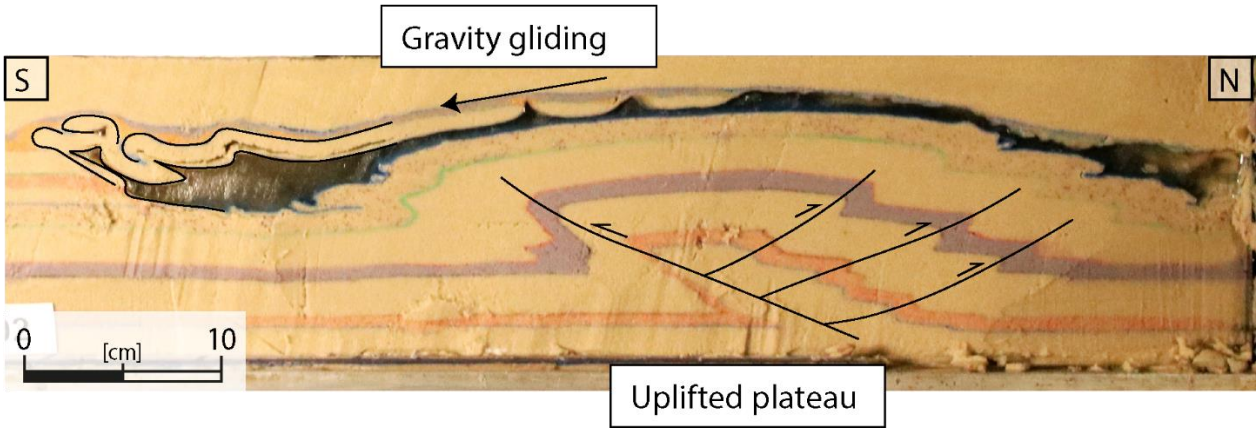

***Figure 3.46**: Section A01-02, cut in a N-S direction and located at 3 cm from the western limit of the box model (position in Figure 3.44). In black are interpreted the reverse faults of the pop-up, result of the compressional stress applied to the model. The silicone layer is thinned above the uplifted plateau, and forms thick structures towards the southern part of the model.*

- **E-W sections:**

In the E-W sections **(Figure 3.47)** it is possible to visualize the effect of gravity gliding due to the plateau uplift when the silicone has more space to move.

We can see above the uplifted plateau the presence of a thinned silicone layer of around 0.1-0.5 cm forming silicone anticlines and silicone rollers, as well as normal faults in the overburden. As visible in Figure 3.47.2, the geometries in the sedimentary sequence of the minibasins present between the silicone diapirs show slight anticlines geometries, with the orange and violet layers thickening towards the silicone structures and forming slight anticlines geometries, typical of the turtleback structures. Towards west the downslope area shows an accumulation of silicone reaching more than 2 cm thickness and formation of salt walls and marked anticlines in the brittle overburden.

Both the N-S and E-W sections clearly show the gravity gliding of the silicone layer and its overburden in response to the plateau uplift, as well as early silicone deformation for downbuilding.

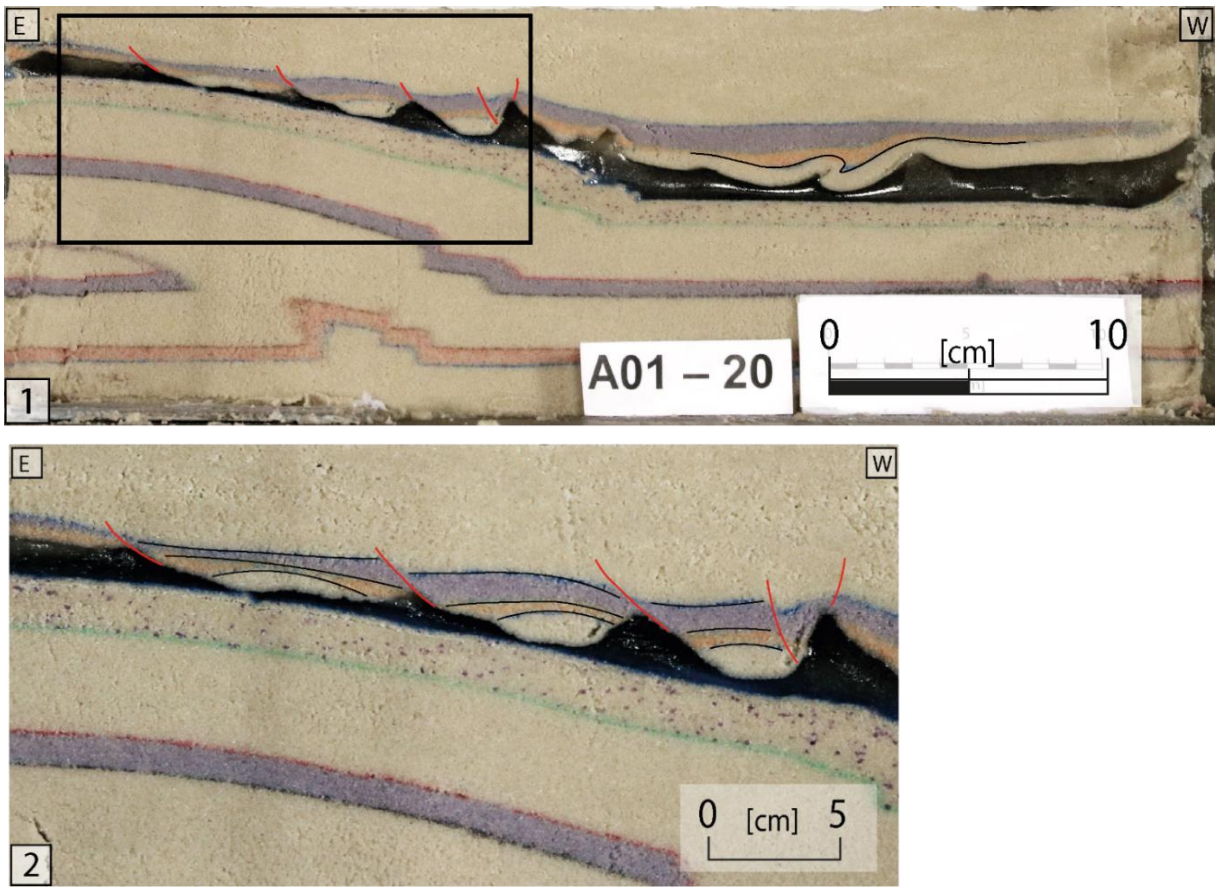

***Figure 3.47**: **1.** Section A01-20 (E-W direction) located at 31 cm from the northern limit of the box model. In red are interpreted the normal faults above the silicone layer, result of the downslope movement of the silicone due to the plateau uplift. Silicone anticlines formed downslope. **2.** The minibasins interpreted in top view (Figure 3.45) are particularly well visible in the zoom on the slope, where the sediments form turtle-back geometries.*

Aspects to be improved in the following models:

Considering the very good results of this first model, there are very few aspects to be considered for a better result in the next model.

- The dimension of the uplifted plateau is slightly too big, so we decide to use a smaller plate for the next model in order to have more space in which the effect of the compression does not have a direct consequence on the silicone deformation.
- Moreover, we saw in this first experiment that it is necessary to start the experiment with a higher speed of the engine in order to de able to start the faults that form the plateau. In the next model, we suggest to start with a speed of around 5 cm/h.

III.C.2.3. Model A02

- **Experimental procedure**

Due to the observation on the previous model, where the uplifted plateau occupied a big percentage of the box model, we decided to change the box configuration and reduce the dimensions of the uplifted plateau. The dimensions of the plate that we use to simulate the plateau are therefore reduced from 55x30 cm to 45x25 cm, and the N-S width of zone A is reduced from 20 to 15 cm, in

order to let more space to the development of the salt structures. Moreover, we realized that the model can be done continuously in a single day if the plateau uplift is started with a higher velocity; in this way we can avoid the lack of sedimentation during the night break. Considering that some explanations of the actions carried out have already been provided during the description of model A01, here we will mostly emphasize the differences between the two models.

As well as in model A01, the first phase consists in the sedimentation of 6 sand layers on the whole model, for a total of 8 cm **(Table 3.2)**. The last 2 layers, for a total of 1.5 cm, are limited to zone A. After this first brittle sedimentation phase we move the silicone patches –already prepared on a separate table- to the model, and let it flatten. The silicone needs around 24 hours to become completely flat and to lose the air inclusions. One cm of sand is then added on zone A, and 0.5 cm of sand (top marked with blue) are added on zone B (i.e. above the silicone). At T=0, we turn on the motor with a speed of 4.2 cm/h, and the experiment begins. This high velocity has been chosen based on the results of the first experiment, in which the low velocity at the beginning of the model resulted in a blocked system. Considering that the pop up geometry consequence of the compression of the box is already well developed and that the plateau is partly formed at time T=30', we decide to slow down the speed of the motor at 1.02 cm/h to use a velocity that has a better proportion with the natural example. To be sure that the system has the space to develop, we remove 2.5 cm of sand and silicone from the northern part of area C.

Time	Layer	Material/activity	Thickness [cm]	Sand color	Top color	Location
-24h00'	1	Medium sand	2 cm	White	Blue	Whole box
	2	Medium sand	0.5 cm	Red	Brown	Whole box
	3	Medium sand	2 cm	White	Black	Whole box
	4	Medium sand	0.5 cm	Blue	Red	Whole box
	5	Medium sand	2 cm	White	Green	Whole box
	6	Medium sand	1 cm	Orange	Blue	Whole box
	7	Medium sand	1 cm	White	Brown	Zone A
	8	Medium sand	0.5 cm	Red	Green	Zone A
	9	Silicone	1 cm	/	/	Zone B
0	10	Medium sand	1 cm	White	Red	Zone A
	11	Medium sand	0.5	White	Blue	Zone B
	/	Engine 4.92 cm/h	/	/	/	/
30'	/	Engine 1.02 cm/h	/	/	/	/
	/	Material removed	5	/	/	Zone C north
5h10'	/	Material removed	5	/	/	Zone C west
6h28'	12	Medium sand	1	White	Green	Zone A
6h45'	/	Material removed	5	/	/	Zone C
7h	13	Medium sand	0.3 – 0.5	Orange	/	Zone B - depoc
8h40'	/	Material removed	5	/	/	Zone C
8h45'	14	Medium sand	0.3 – 0.5	Blue	/	Zone B - depoc
10h15'	15	Medium sand	0.5	White	Red	Zone B
12h25'	Final layer	Medium sand	>2	White	/	Whole box

Table 3.2: *Experimental procedure of model A02.*

After around 5 hours of development of the model, we remove some silicone also from the western side of zone C. At T=6h28', we add 1 cm of sand on zone A, and after 20' around 2.5 cm of sand and

silicone are removed from zone C. At T=7h, the faults formed on the surface of the model **(Figure 3.48.2)** are filled with few mm of orange sand. Moreover, some depocenters of sand of 4 to 6 cm of diameter are added to the model, keeping few cm of distance between each of them (Figure 3.48.3). This procedure simulates the irregular deposition that happens in nature, especially at the deep-sea fans. At T=8h40', 2.5 cm of silicone and sand are removed from zone C. Immediately after, we add around 0.5 cm of sand on the previously formed depocenters, so strictly above layer 13. At T=10h15', we add a layer of around 0.5 cm of white sand an all zone B (Figure 3.48.4). Extensional faults go on forming both in E-W and in N-S direction, and minibasin geometries are visible on the surface of the model (Figure 3.48.5). The model is stopped at T=12h20' with a thick layer of sand. To be able to properly wet the model despite the layer of silicone, we have to remove around 2 to 3 cm of silicone along all the sides of the model, in order to avoid the problem of sub silicone bubble formation of model A01.

As well as for model A01, we try to obtain the maximum amount of information from both the N-S and E-W sections, so we start cutting N-S sections on the eastern side of the dataset to visualize the area of the uplifted plateau, cutting the sections 1 to 4 at a distance from the eastern wall of 5, 5.7, 7.6, 8.4 cm. After this, we cut E-W sections (5 to 22) located at a distance from the northern wall of 6.5, 9, 13, 17.2, 20.3, 21.8, 23, 24.6, 25.5, 26.8, 29, 30.6, 32.7, 33.6, 35.1, 37, 39 and 41.2 cm.

- ## Results and Discussion

Considering the similarities with model A01, the geometries we noticed in model A02 are comparable, with a difference related to the localized depocenters and the different dimensions of the uplifted plateau, as well as the absence of the overnight break in the sedimentation.

Between time T=0 and time T=5h35', the major deformation visible on the model is the deformation related to the uplift of the plateau in the eastern part of the model (Figure 3.48.1), as well as the formation of folds result of the compressional deformation (FO). As in model A01, the pattern of faults starts with the formation of a NE-SW normal fault (F) that starts to be visible in Figure 3.48.2, simultaneously with the development of the plateau. At time T=7h15', localized sedimentation is added to fill the synclines and to form depocenters on all the model (Figure 3.48.3). During the last 5 hours of deformation, the minibasins geometries are more and more clear on the model surface, and the N-S and E-W are clearly defined above the uplifted plateau (Figures 3.48.4 and 5).

- **N-S sections:**

Differently from the previous model, in model A02 both the slopes towards north and towards south are well visible in the sections **(Figure 3.49)**, and we can notice the gravity gliding towards north and towards south consequence of the plateau uplift. Above the uplifted area the silicone is thinned (0.1 to 0.7 cm) and forms silicone anticlines and small diapirs. Normal faults cut the sand overburden, testifying the movement of the silicone up to the end of the model. Thicker silicone is located both northward and southward. The main difference between the two downslope areas is the fact that southward the silicone is stopped by the brittle sedimentary layer of zone A and forms therefore several cm thick silicone structures, while northward it has more space to move and form salt anticlines.

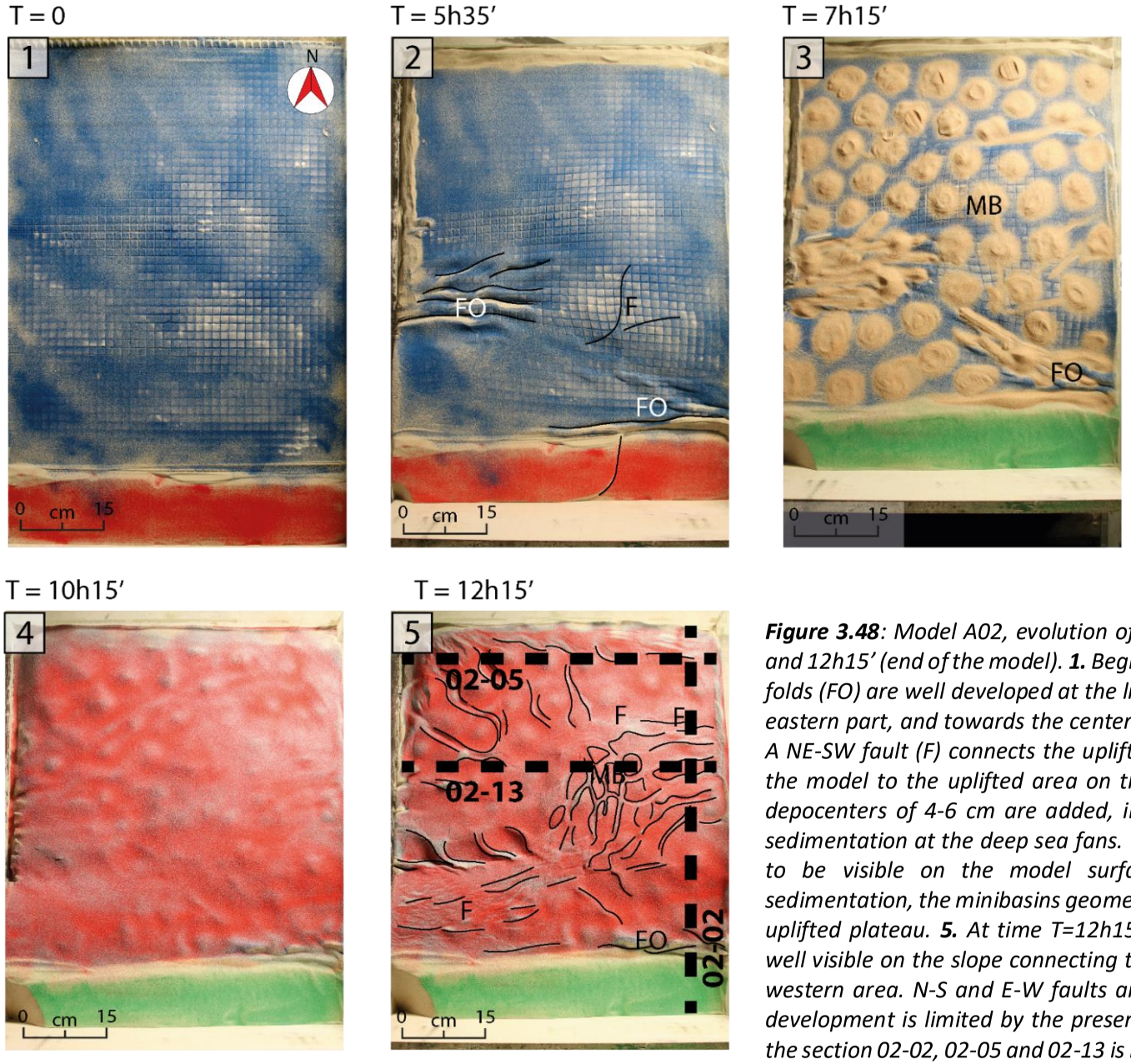

***Figure 3.48**: Model A02, evolution of the Top View between time T=0 and 12h15' (end of the model). **1.** Beginning of the model. **2.** At T=5h35', folds (FO) are well developed at the limit between areas A and B in the eastern part, and towards the center of the model in the western one. A NE-SW fault (F) connects the uplifted plateau of the eastern side of the model to the uplifted area on the SW. **3.** At time T=7h15', sand depocenters of 4-6 cm are added, in order to simulate the irregular sedimentation at the deep sea fans. Minibasins geometries (MB) start to be visible on the model surface. **4.** After another layer of sedimentation, the minibasins geometries (MB) are partly visible on the uplifted plateau. **5.** At time T=12h15', the minibasins geometries are well visible on the slope connecting the uplifted plateau to the deeper western area. N-S and E-W faults are partly visible, but their special development is limited by the presence of minibasins. The position of the section 02-02, 02-05 and 02-13 is marked with the black dotted line.*

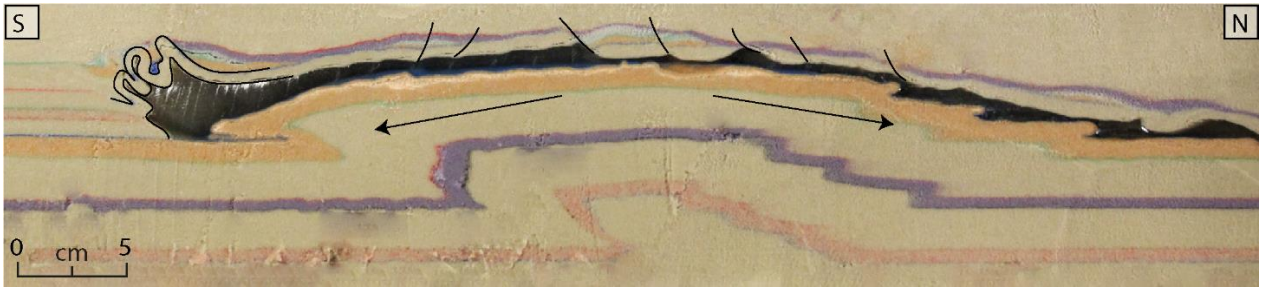

Figure 3.49: *Section A02-02, in a N-S direction and located 5.7 cm from the eastern glass wall. The double slope direction, both southward and northward, leads to gravity gliding in the two directions.*

- **E-W sections:**

Differently from model A01 and thanks to the more reduced dimensions of the uplifted plateau, we have here the possibility to distinguish in the E-W sections between the situation northward the effect of the uplifted plateau **(Figure 3.50.1)** and across the uplifted plateau (Figure 3.50.2). In section A02-05 (Figure 3.50.1) there is no sign of the plateau uplift, and salt diapirs formed ubiquitously with small minibasins dividing the few cm thick salt diapirs. In the sections A02-13 cutting the uplifted plateau (Figure 3.50.2) we can see that above the plateau we have the geometries of extensional tectonics and reactive diapirism already noticed in the N-S sections, i.e. reduced silicone thickness, normal faults and silicone anticlines. The silicone layer, homogeneous at the beginning of the experiment, is thinner above the uplifted plateau and thicker towards west, where it forms diapirs and salt walls up to several cm thick.

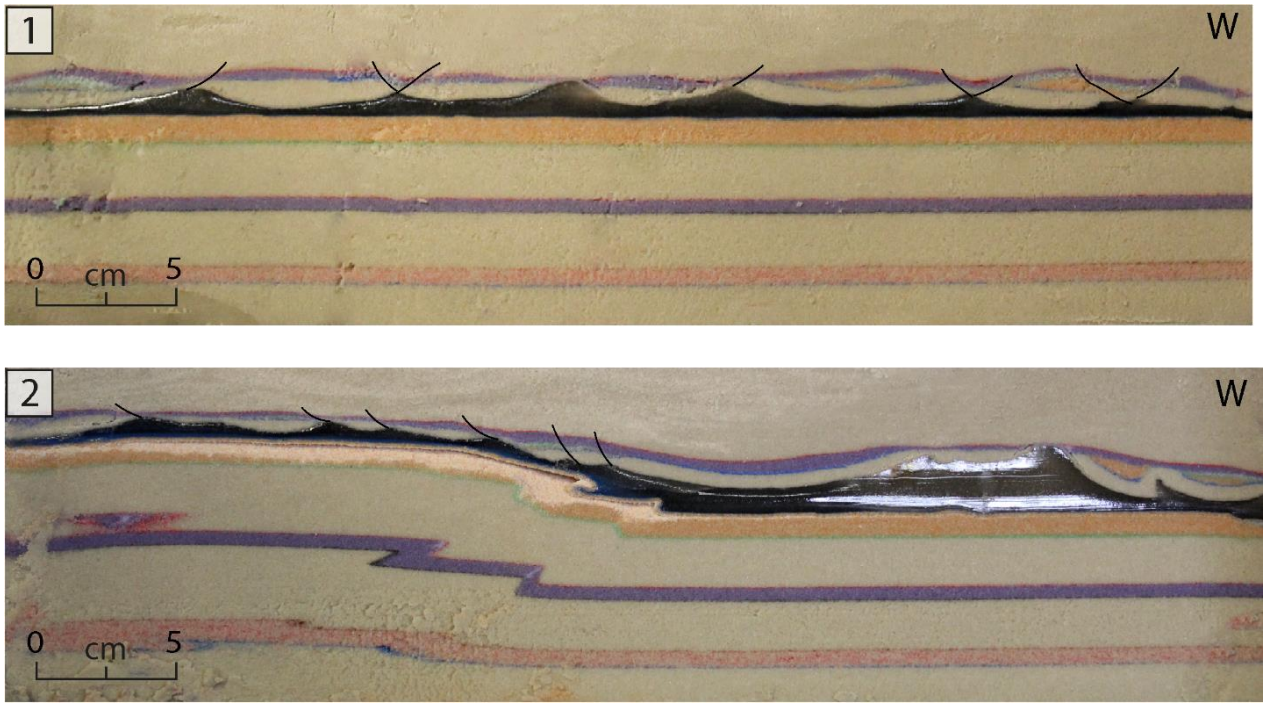

Figure 3.50: *E-W sections A02-05* ***(1.)*** *and A02-13* ***(2.)****, located respectively at 6.5 and 25.5 cm from the northern limit of the box model. In .1 the salt structures develop without the influence from the compressional stress, while in .2 the plateau uplift affects the silicone layer producing gravity gliding towards west.*

III.C.2.4. Outcomes of the study

In order to simulate the effect of compressional tectonics on salt tectonics offshore Algiers and Dellys, we produced some analogue models of the plateau uplift and analyzed the geometries formed by the silicone layer and its overburden. Despite the silicone layer at the beginning of the box modelling is isopach, the uplift of the plateau consequence of the compressional stress after the peak of the Crisis leads to the formation of an area of uplifted base and top of the silicone, thin silicone layer and limited silicone structures of early formation. On the northern and eastern side instead, the silicone is thicker and forms salt diapirs of several cm. The geometries observed in the analogue models A01 and A02 are compatible with the ones interpreted in the seismic reflection and bathymetric data, suggesting that the salt thickness differences observed can be exclusively consequence of the plateau uplift, that started towards the end of the MSC as suggested by the UU geometries in the seismic profiles.

Moreover, we proved that the minibasins structures form as a result of the uplift of the plateau also without inhomogeneous sedimentation.

III.C.3. Discussion and intermediate conclusions

• Discussion

In the Algerian Basin, salt is mostly present in the deep domain, limiting the basin-scale gravity gliding. Salt and crustal tectonics are co-present on the margin, resulting in a quite challenging reconstruction of the different deformations interpreted in the area. This is due to the fact that the crustal deformation can be partly accommodated by the salt movement and consequently the timing of the crustal tectonics is 'hidden'. Thanks to the interpretation of the seismic profiles of MARADJA I, MARADJA II and older seismic data, as well as the results of new analogue models produced, we analyze here the mechanisms of salt tectonics and its interaction with crustal tectonics in an area of more than 30k km². Where possible, we reconstruct the temporal evolution of the salt and its overburden deformation. This will be done separately for the western, eastern and northern sectors (areas 1, 2 and 3), due to the differences between the three areas and the different amount of data available that leads to different levels of detail in the reconstructions.

Zone 1 (W): 2°20' to 4°E, 36°40' to 37°20'N

The area offshore Algiers and Dellys has the higher data density on the MARADJA dataset, with numerous seismic profiles -parallel and perpendicular to the margin- imaging the salt structures and the thrusts. This data density allowed us to make detailed grids of the different Messinan surfaces, and in particular of the base and top of the MU. In these grids we observed that Area 1 presents a marked division between its eastern and western parts. Above the eastern uplifted plateau, where the base and the top of the MU are deformed and uplifted -with a strong correspondence with the anticlines identified by Déverchère *et al.* (2005) and Domzig *et al.* (2006)- the thickness of the salt is limited and the salt structures have a vertical development mostly limited to few hundreds of meters. The Plio-Quaternary deposits are around 700 meters thick and present growth strata related to the piggy-back basins. On the other hand, the western sector is not affected by crustal tectonics, and the base of the salt is deeper. The thick salt layer forms there major salt structures of 1.5 to 2 km height, and well developed salt walls are still deforming the seafloor as visible in the bathymetry. The PQ deposits have a thickness of up to 1.5 km, and in correspondence with the salt structures they are often deformed up to the most recent horizons. The two areas are connected by a slope, with intermediate characteristics in terms of salt and overburden thickness and still active salt deformation. The complexity of the area analyzed has given rise to several questions, mainly concerning the timing of the plateau uplift and the role of the crustal tectonics on the movement of salt. A pre-MSC uplift of the plateau could not be excluded a priori, because due to the limits in the imaging of the pre-salt sedimentary sequence the eventually present syn-kinematic geometries could have been missed. The normal faults prove that part of the salt previously located above the plateau moved westward, partially explaining the differences in the MU thickness between the uplifted plateau and the deeper area, but due to the ductile nature of this layer it is not possible to estimate the initial amount of salt initially deposited in the two sectors. Therefore, the difference in salt thickness between western and eastern sectors can be whether the consequence of a differential deposited thickness or a post-plateau uplift salt migration, or both.
This salt thickness difference, together with the interpreted geometries of the salt and overburden, gave rise to the hypothesis of early salt deformation by E-W thin-skinned gravity gliding above the

Messinian salt layer, consequence of the plateau uplift. This hypothesis has been analyzed also through the analogue models, in which it has been possible to recreate the uplift of the plateau and the response of the silicone layer to the uplift. As a result of the integration between geophysical data observations and new analogue models, we reconstructed the evolution in the area following the deposition of the Messinian Mobile Unit, i.e. since 5.6 Ma **(Figure 3.51)**.

Chronology of development of the area

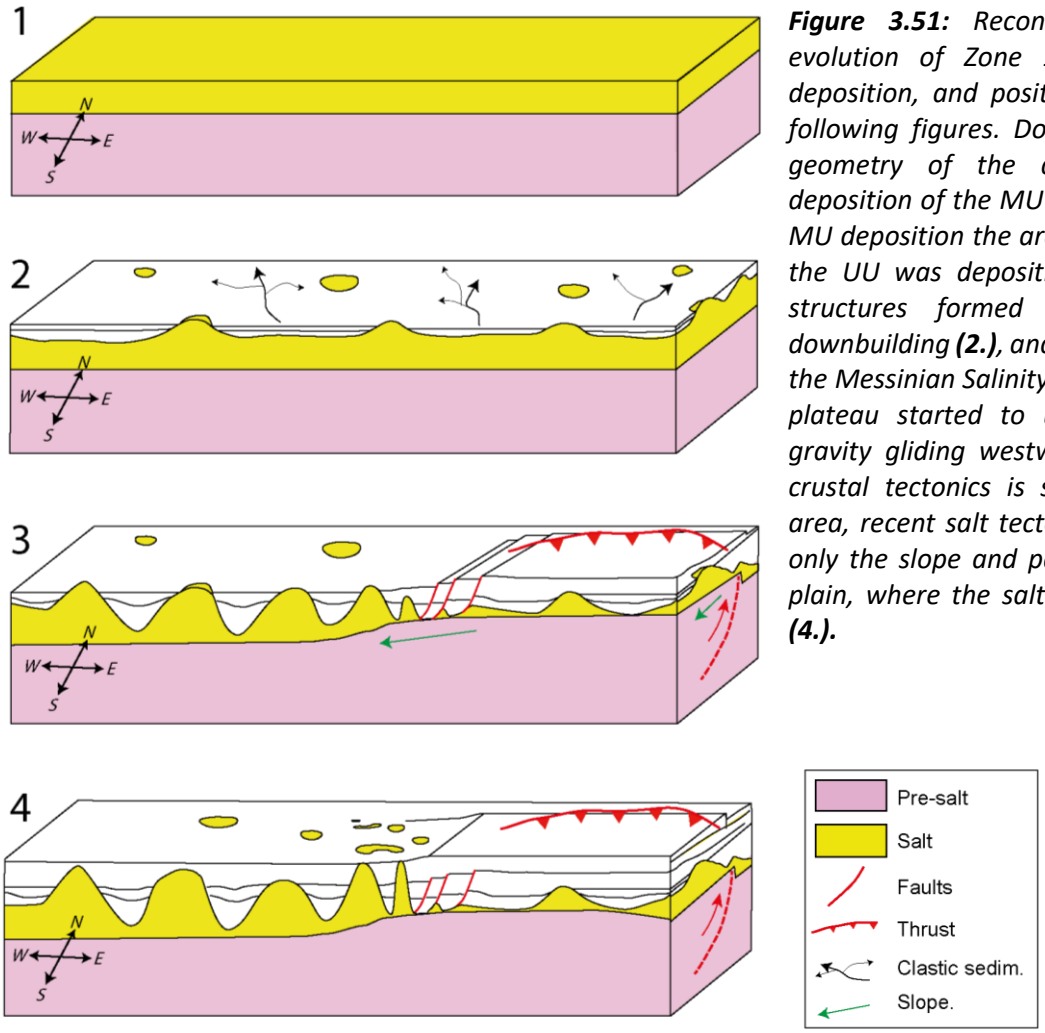

Figure 3.51: *Reconstruction of the evolution of Zone 1 since the MU deposition, and position (in .4) of the following figures. Doubts exist on the geometry of the area during the deposition of the MU **(1.)**, but after the MU deposition the area was flat. While the UU was depositing, the first salt structures formed ubiquitously for downbuilding **(2.)**, and before the end of the Messinian Salinity Crisis the eastern plateau started to uplift, leading to gravity gliding westward **(3.)**. Despite crustal tectonics is still active in the area, recent salt tectonics characterize only the slope and part of the abyssal plain, where the salt walls are thicker **(4.)**.*

Phase 1 - Deposition of the MU (Figure 3.51.1): Due to its evaporitic nature, the deposition of the salt cancelled the pre-existing bathymetric differences in the basin; at the end of the MU deposition, the area is flat. If bathymetric differences where present before the salt deposition, these differences in elevation were inferior to the MU thickness, or onlapping geometries of the UU would have been identified in the area.

Phase 2 - Downbuilding during the deposition of the lower UU (Figure 3.51.2): From the analysis of the depositional geometries, and in particular from the **growth geometries** in the UU **(Figure 3.52)**, we can affirm that the beginning of the salt movement predates the end of the MSC. The differential pressure due to the irregular clastic sedimentation leads to the ubiquitous formation of the first salt anticlines and diapirs, that growth for downbuilding in all the area. Aside from these

small scale variations, the lower UU does not present important regional thickness changes in Zone 1 except for the thinning and onlap on the margin, suggesting absence of tectonic activity during most of the UU deposition.

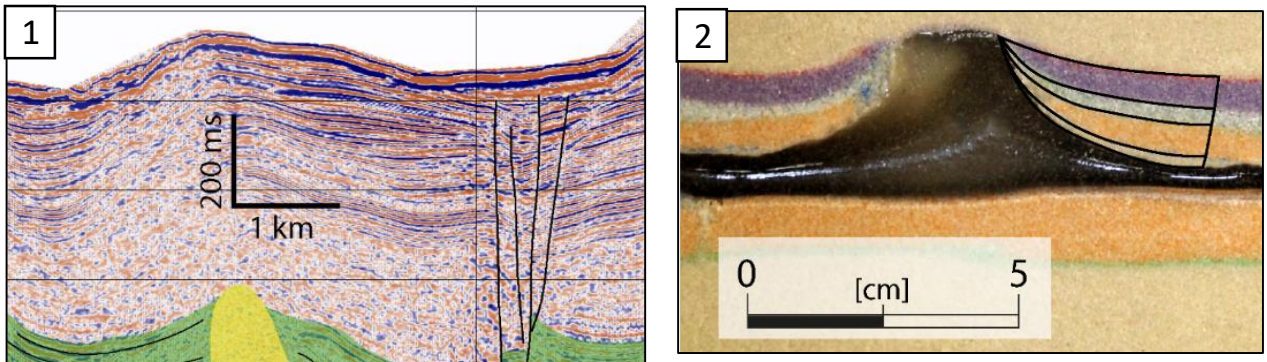

***Figure 3.52**: Growth geometries in the UU in seismic profile MDJ01-03 **(1.)**, parallel to the margin. The beginning of the salt movement predates the end of the MSC, while no activity is present during the late Plio-Quaternary. Similar geometries have been identified in the analogue models **(2.)**, where the silicone structures started to form very early during the UU deposition.*

Phase 3 - Uplift of the plateau (Figure 3.51.3): The compressional crustal tectonics led to the beginning of the plateau uplift before the end of the MSC, as testified by the fan shaped geometries of the UU at km 30 of seismic profile MDJ01-96 (Figure 3.38). The uplift of the plateau created two directions of local slopes, respectively landward above the plateau (Figure 3.38) and westward at the western limit of the plateau (Figure 3.36), this last one resulting in early Plio-Quaternary salt gravity gliding along an area of around 6 km **(Figure 3.53)**. The normal faults and associated salt rollers are comparable to the geometries observed in model A02, in which the uplift of the plateau led to a redistribution of the silicone, that flow westward towards the deeper area (Figure 3.53).

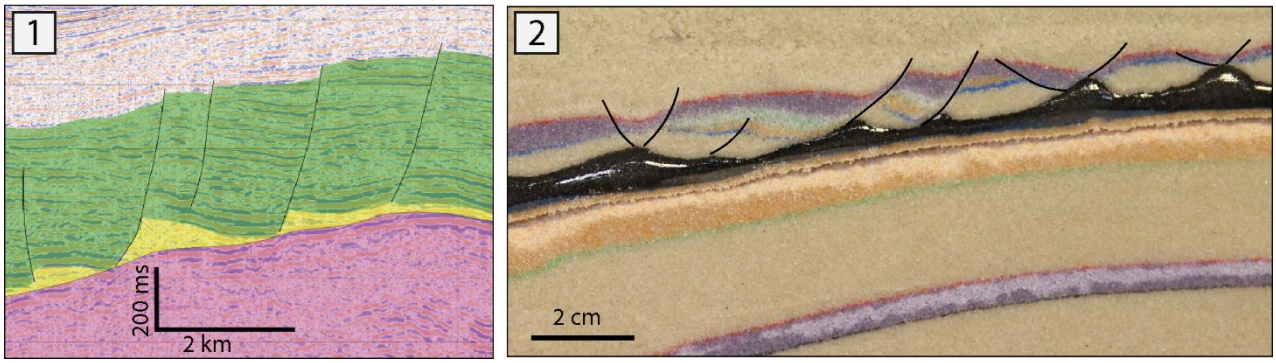

***Figure 3.53:** Comparison between the geometries interpreted in the seismic reflection profile parallel to the margin MDJ01-03 **(1.)** and the interpretation of the geometries in analogue model A02 **(2.)**.*

The major phase of crustal activity is concentrated during the Plio-Quaternary, as evidenced by the thickening typical of the piggy-back basins well visible in the Plio-Quaternary sedimentary sequence **(Figure 3.54, seismic profile MDJ01-96)**: in the sequence highlighted in pink we have at the same time a thickening of the sedimentary sequence towards the south and the formation of salt related

anticlines, highlighting the copresence of crustal and salt tectonics. In violet is highlighted a sequence that shows infilling geometries (onlapping horizons), while the blue layer shows no deformation related to salt tectonics but exclusively the southward thickening (piggy back geometries) due to thrusts activity.

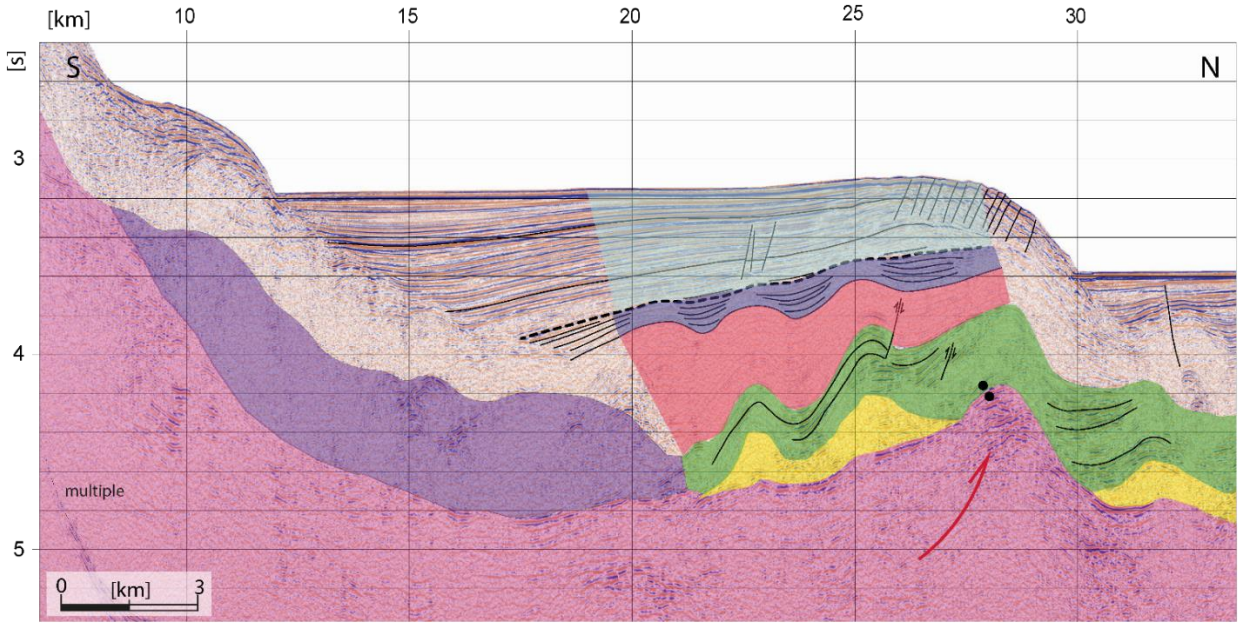

Figure 3.54: *Seismic profile MDJ01-96. VE: 5.6 X. The brittle overburden is here divided in a pink sequence of crustal and salt tectonics co-presence, an onlapping violet sequence towards the end on the salt related deformation, and a light blue sequence of crustal deformation (piggy-back geometries).*

Phase 4 - Recent development (Figure 3.51.4): As the plateau is going on uplifting, a net division between the eastern and western sectors is established, and the two areas evolve differently. The growth of salt structures for downbuilding persists in the western sector, while above the plateau the movement stops due to different factors. First of all, the salt thickness is limited and the salt welds are common, preventing the development of salt structures. Moreover, the presence of piggy-back sedimentation has a buttress effect on the salt (Figure 3.54), in contrast with the increased slope due to crustal tectonics that could have led to gravity gliding southward.

Nowadays, the salt activity is mostly active on the slope at the western limit of the plateau, in correspondence with the polygonal minibasins which form on the seafloor geometries matching with the ones visible on the analogue models **(Figure 3.55)**.

Salt tectonics is also active in part of the western sector (around 2°50') where the presence of a higher volume of salt could be related to a thicker deposition (i.e. the base of the salt was already deeper at the moment of the deposition) or to a localized salt supply consequence of gravity gliding from the surrounding areas.

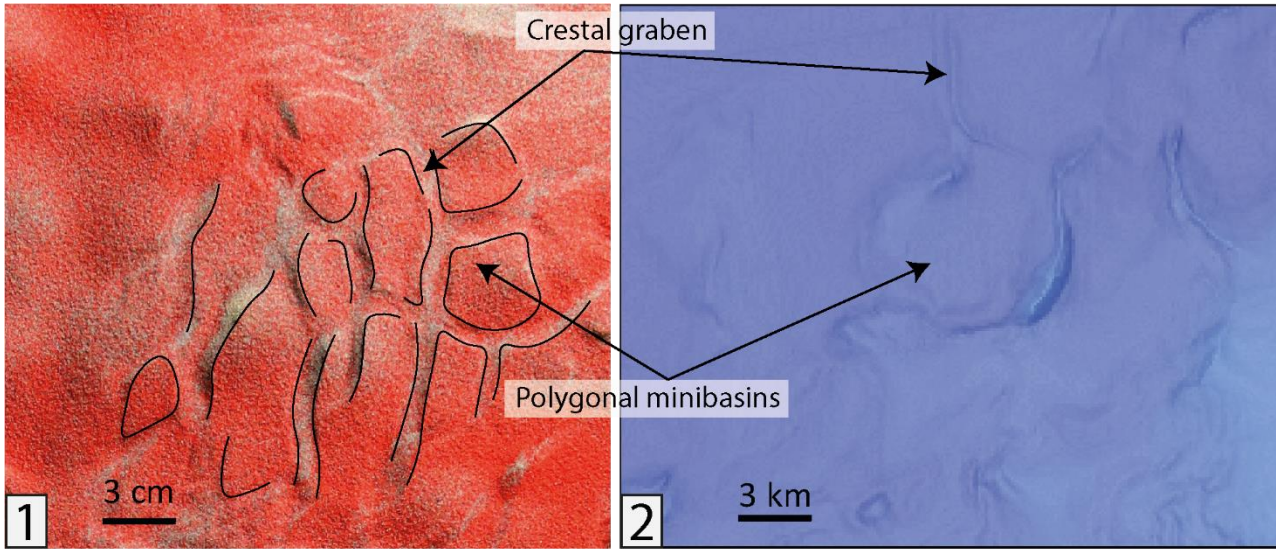

Figure 3.55: *Comparison between the geometries of the model surface* ***(1.)*** *and the bathymetric data* ***(2.)****.*

Minibasins position

As seen in the results chapter, the minibasins in Zone 1 are particularly well developed on the slope, where part of them are still active **(Figure 3.56)**. Considering that there is not always density inversion between the MU and its overburden in the Western Mediterranean, these minibasins are not the consequence of negative buoyancy, as visible also from their shape (e.g. absence of rims).

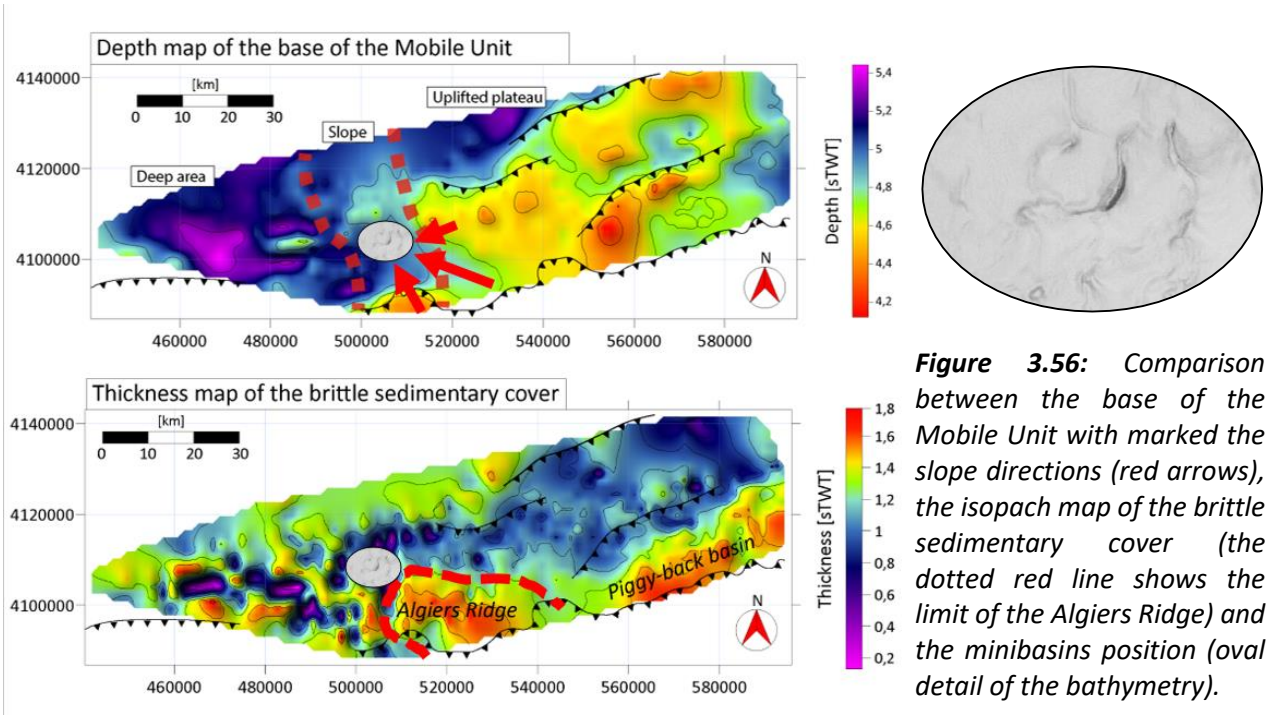

Figure 3.56: *Comparison between the base of the Mobile Unit with marked the slope directions (red arrows), the isopach map of the brittle sedimentary cover (the dotted red line shows the limit of the Algiers Ridge) and the minibasins position (oval detail of the bathymetry).*

Multiple factors alternative to the density inversion are considered to be at the origin of minibasins formation, as the presence of a slope, the compressional stress and the sedimentary load (Peel, 2014). The base of the MU in Zone 1 has multiple slope directions (Figure 3.30), both from the margin and from the uplifted plateau to the deeper basin, and the polygonal minibasins position corresponds to the compressional domain of salt tectonics as visible in Figure 3.36. We suggest that

the greater development of minibasins in the western sector of our study area is in the first place the result of this multiple slope directions, and consequent intersection between different zones of shortening: the downslope flow of salt inflates the diapirs separating the minibasins **supplying them with viscous evaporites**, so the growth of the minibasins is mostly the result of the surrounding diapirs uplift rather than the subsidence of the minibasins. The sedimentary load is another potential element for the minibasins formation (Peel, 2014). As visible in Figure 3.56, the salt diapirs are more developed at the external limit of the sedimentary load of the **Algiers Deep Sea Fan**, where the pressure is lower. A partial contribution of the deep-sea fan in the determination of the position of salt diapirs development cannot be excluded, but also thanks to the analogue modelling it is clear that the potential partial contribution of gravity spreading is not fundamental for the minibasins formation. In fact, as we saw in the analogue models just presented, the minibasins form both on the slope and on the uplifted plateau, but their development is probably stopped on the plateau due to the more limited salt availability.

Zone 2 (E): 4 to 6° E, 36° 35’ to 37°30’ N

Despite the more limited number of seismic profiles in area 2, we were able to analyze the trend of thinning and thickening of the Messinian units and the internal reflectors geometries in some seismic reflection profiles. In particular, along seismic reflection profile ALE-77-33-1 we observed a marked difference in the Upper Unit thickness (Figure 3.33) and onlapping geometries of the internal UU reflectors towards an uplifted region, testifying that the uplift of that area predated the end of the MSC. The movement of the crustal structure continued up to nowadays, resulting in gravity gliding towards W and towards E. The relative uplift of part of zone 2 after the end of the MSC is testified by the fact that the top of the UU is shallower where the acoustic basement is shallower. Due to the geometry of the salt and the overburden, as well as the presence of normal faults cutting the UU and Plio-Quaternary towards the uplifted structure, we can affirm that also in zone 2 the main mechanism of salt tectonics is gravity gliding. Thanks to higher resolution seismic reflection profiles perpendicular to the margin, we were able to analyze the timing of salt deformation in an approximate N-S direction (Figure 3.41). Considering the interpreted geometries (i.e. differences in the UU thickness with fan shaped depositional geometries and apparent downdip del lower Plio-Quaternary), we can affirm that the movement in that direction started very early, before the end of the Messinian Salinity Crisis. From the geometries of seismic profile MDJ02-70, we reconstructed the following temporal evolution of the gravity gliding perpendicular to the margin **(Figure 3.57)**:

Phase I (Figure 3.57.1): After the deposition of the halite (MU), the lower UU is deposited on a flat surface. The question marks represent the uncertainties concerning the geometries of the salt base at the moment of the salt deposition.

Phase II (Figure 3.57.2): As a result of the movement of diapir A, some onlapping geometries are registered in the late UU sedimentation.

Phase III (Figure 3.57.3): The lower Plio-Quaternary onlaps on diapir A, while the formation of diapir B still did not begin, as testified by the absence of lateral thickness changes in correspondence with the nowadays position of diapir B.

Phase IV (Figure 3.57.4): The salt continues moving towards the centre of the basin, forming salt diapir B. As a result, the Lower PQ onlapping horizons are tilted, creating a geometry of apparent

downlapping. Moreover, the sedimentary sequence in correspondence with diapir B are cut by a salt related direct fault. Some synkinematic geometries are now produced at NNW, due to the growing of a structure not represented in the reconstruction.
So, tu sum up, diapir A grow early, and then the salt moved basinward, ''deflating'' the first structures formed while new diapirs (B) are formed basinwards.

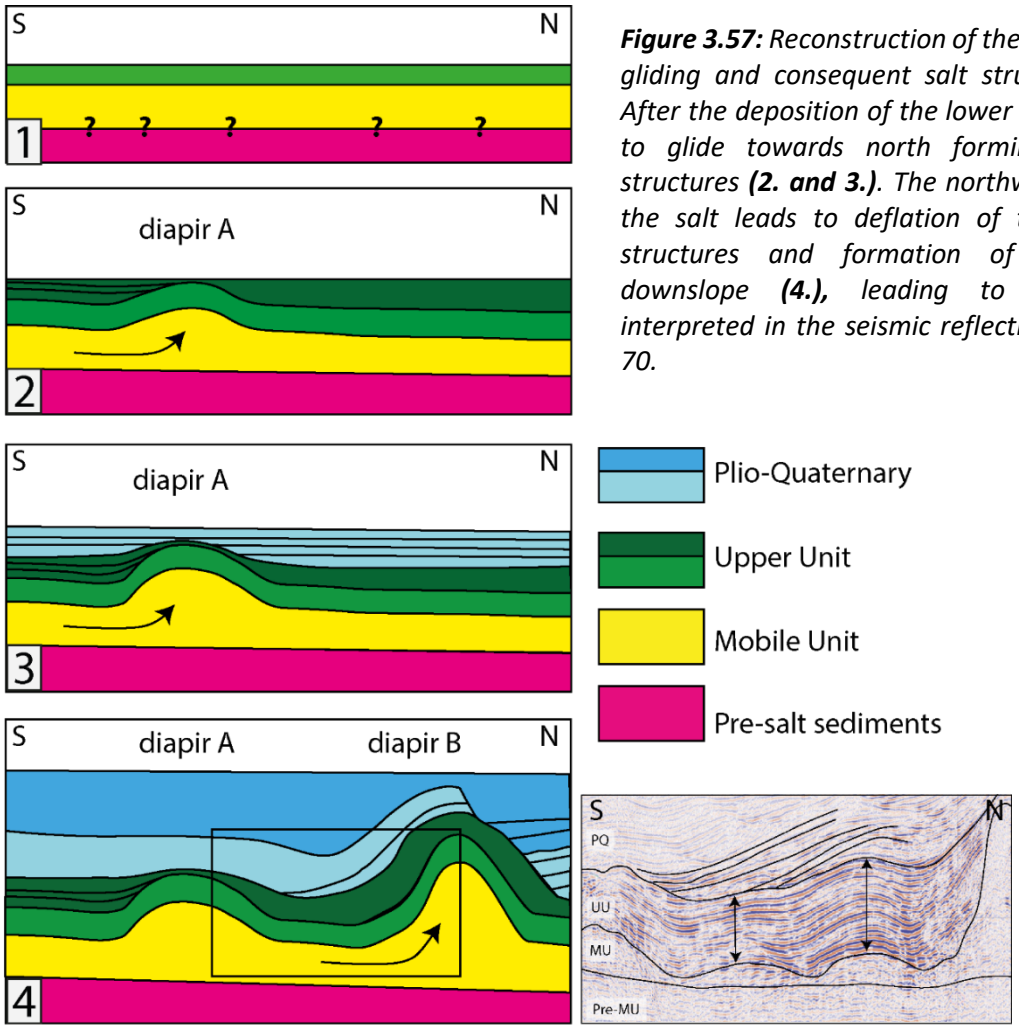

Figure 3.57: *Reconstruction of the northward gravity gliding and consequent salt structures formation. After the deposition of the lower UU* ***(1.)****, salt starts to glide towards north forming the first salt structures* ***(2. and 3.)****. The northward movement of the salt leads to deflation of the firstly formed structures and formation of new structures downslope* ***(4.),*** *leading to the geometries interpreted in the seismic reflection profile MDJ02-70.*

Zone 3 (N): 3: 3°40' E to 5°E, 37°25' to 38°20'N

This area is strongly characterized by the presence of the still active Hannibal High, which influences the geometries and thickness of the MSC sediments and the following movement of the salt. Despite the data coverage is quite limited, the main elements interpreted allowed us to reconstruct the timing of the crustal and salt deformation. Above the Hannibal High the salt layer is particularly thin and it pinches out, and the thin Upper Unit sediments show clear onlap geometries **(Figure 3.58)**.

Moreover, the deformation of the seafloor leaves no doubt about the still active crustal tectonics, with the Hannibal High uplift that continued during the deposition of the Messinian and post-Messinian sediments up to recent times. Based on the geometries of the seismic horizons and the knowledge in terms of salt tectonics, we propose the following reconstruction of the salt movement in the area **(Figure 3.59)**. In contrast with Zone 1, where the density of seismic reflection profiles allowed to reconstruct the 3D development of the area, here the 2D reconstruction is focused on

the very local effect of the Hannibal High on the recent salt tectonics, i.e. an increasing of potential energy of the system.

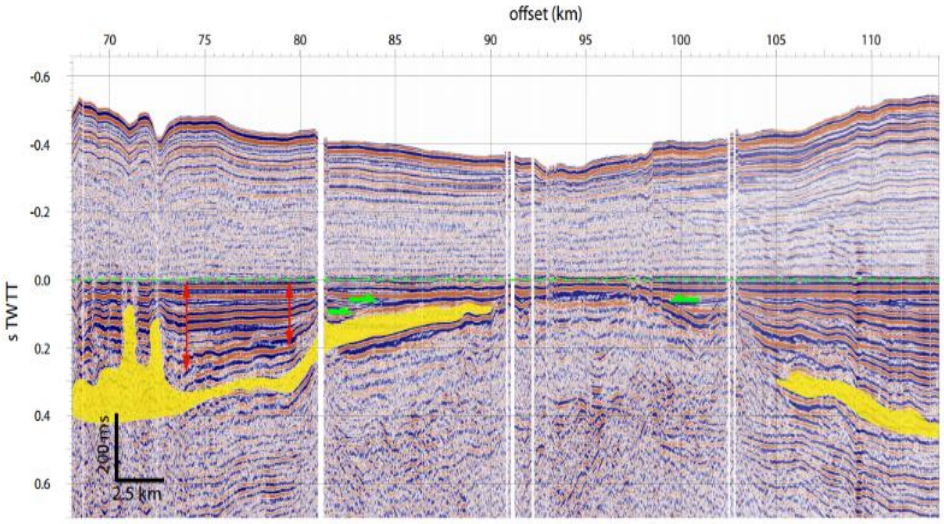

Figure 3.58: *Flattening of the top of the UU, showing the onlapping geometries and the lateral thickness changes of this unit.*

Phase I (Figure 3.59.1): At **5.6 Ma**, during the deposition of the MU, the positive topography of the Hannibal High is most likely already partly formed. Due to the fact that the MU seismic facies lacks internal reflectors and has a ductile behaviour, we cannot confirm if the Hannibal High uplift predates the deposition of the salt.

Phase II (Figure 3.59.2): At **5.3 Ma,** at the moment of the deposition of the UU, the Hannibal High was already a bathymetric high as testified by the onlap geometries and the important lateral thickness changes. During the deposition of the UU the growth of the Hannibal High led to the formation of a slope and to consequent salt gravity gliding, with extension upslope (normal faults that cut UU and PQ) and formation of salt diapirs downslope.

Phase III (Figure 3.59.3): During **Lower to Middle Plio-Quaternary** the movement of the Hannibal High is probably reduced, but uncertainties are high due to the low amplitude of the Lower Plio-Quaternary horizons and the consequent difficulties in recognizing the marks of the deformation.

Phase IV (Figure 3.59.4): Some of the salt structures continued to move up to the **late Plio-Quaternary**, forming anticlines with different kilometers of wavelength in the Plio-Quaternary sediments. The most recent movement of the Hannibal High, affecting the bathymetry, is limited to an area of 6 km along the seismic profile (Figure 3.42). Despite the presence of a slope at the base of the salt, the system reached the hydraulic equilibrium and the movement stopped during Upper Pleistocene.

To conclude, the factor of control of salt tectonics is the area is the crustal tectonics (i.e. uplift of the Hannibal High), but despite the crustal structure goes on moving there are no traces of recent salt deformation in our seismic reflection data.

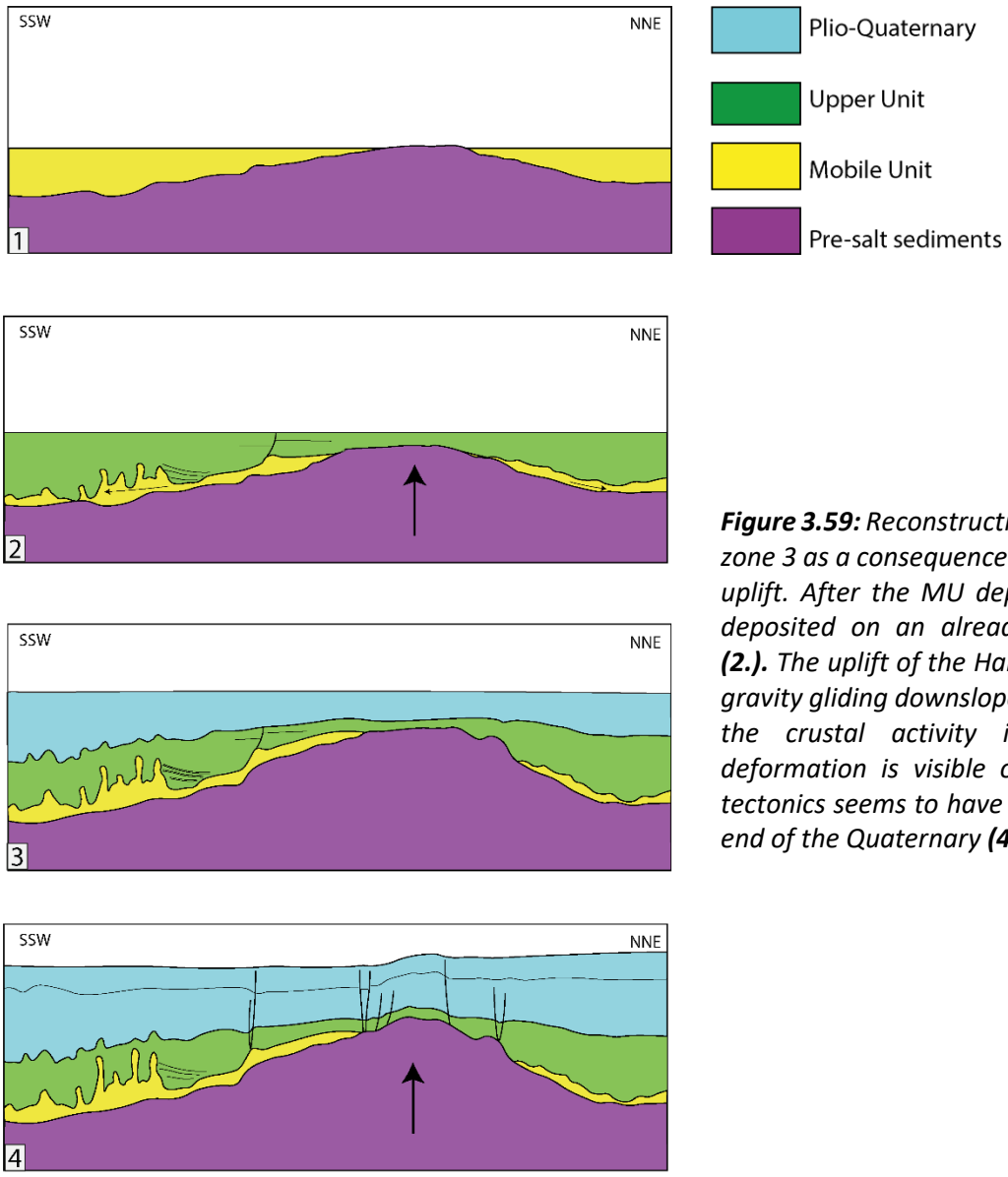

Figure 3.59: *Reconstruction of the evolution of zone 3 as a consequence of the Hannibal High uplift. After the MU deposition* ***(1.)****, the UU deposited on an already uplifted structure* ***(2.).*** *The uplift of the Hannibal High results in gravity gliding downslope* ***(2. and 3.)****. Despite the crustal activity is still active and deformation is visible on the seafloor, salt tectonics seems to have stopped towards the end of the Quaternary* ***(4.).***

- ## Intermediate conclusions

The seismic reflection data interpretation, and in particular the analysis of the geometry of the salt structures and the distribution and internal reflectors geometries of the brittle cover, together with its comparison with the produced analogue models used to corroborate the hypothesis formulated, led to the reconstruction of the timing and mechanisms of salt tectonics and the effect of the reactivation in compression of the Algerian margin on the salt deformation. Salt tectonics started early in all the area, possibly before the end of the Messinian Salinity Crisis, both for **downbuilding** and for **gravity gliding** consequence of crustal tectonics and differential subsidence. Due to the heterogeneity of the area, local differences are present:

In Zone 1 (2°20’ to 4°E, 36°40’ to 37°20’N), a first phase of early and ubiquitous development of salt structures for downbuilding was followed by the uplift of the plateau, which led to the movement of part of the salt towards the deeper western sector for gravity gliding and to a slowdown of the salt movement above the plateau. Salt walls of many km thickness developed, and thick **minibasins** deposited. Nowadays, the salt structures are active only where the relationship

between salt and overburden thickness is favorable, and classical polygonal minibasins geometries are visible on the seafloor.

In Zone 2 (4 to 6° E, 36°35’ to 37°30’ N), the early salt deformation for downbuilding is followed by northward **gravity gliding**, as a result of the basin subsidence following the refilling of the Mediterranean at the end of the Crisis and local gravity gliding due to crustal uplift. A higher data coverage of the areas of maximum development of salt tectonics structures, and in particular the external limit of the deep-sea fan, could bring new light on the possible influence of sedimentary load on the salt tectonics in the area.

In Zone 3 (3°40’E to 5°E, 37°25’ to 38°20’N), the deformation of the salt is again consequence of the **crustal tectonics**, and in particular the long lived uplift of the Hannibal High that led to gravity gliding. Despite the crustal structure is still active nowadays, there are no proofs of salt deformation in the area, probably due to the thickness of the overburden.

Chapter IV: THE SØRVESTSNAGET BASIN (SW BARENTS SEA)

The Sørvestsnaget Basin is particularly interesting for the study of salt tectonics because of the presence of a layer of salt deposited during the Carboniferous-Early Permian (Gipsdalen Group) and a long lasting extensional crustal tectonics. The interaction between salt and crustal tectonics in the area has lasted hundreds of millions years, producing mature and differing salt structures visible both in the seismic reflection data and in the Bouguer gravity anomalies. This third study area becomes therefore fundamental to analyze the behavior of salt layers in geological settings where the interaction between salt and crustal tectonics is particularly intense and long lasting.

IV.A. GEOLOGICAL SETTING OF THE SW BARENTS SEA

With an average water depth of 400 m, the Barents Sea covers around **1.2 million km^2** in the northwestern part of the Eurasian plate, it is limited to the north by the Arctic Ocean (Svalbard and Franz Josef Land), to the west by the continental slope of the Norwegian-Greenland Sea (Cenozoic passive margin), to the east by the Novaya Zemlya and to the south by the coasts of Norway and Russia **(Figure 4.1)** (Barrère *et al.*, 2009; Gabrielsen *et al.*, 1990). In the **Eastern Barents** the basins are **broad and N-trending** with a limited number of structural highs, while in the **Western Barents** the **narrow highs and basins** are mainly ENE-trending, with N or NNW trends in the Trømso Basin area (Gabrielsen *et al.*, 1990; Gac *et al.*, 2018). The complexity of the Barents Sea, formed by stretched continental crust, is due to the interaction between episodes of orogenic compression and crustal rifting, the effects of Carboniferous-Permian salt deposition both for what concerns the subsidence of basins and for salt tectonics, and the climatic influence of the Northern Hemisphere glaciations during Pleistocene (Faleide et al., 1984, 1996, 2008; Gabrielsen et al., 1990; Smelror et al., 2009; Gernigon et al., 2014; Omosanya et al., 2017).

The main structural elements of the Barents Sea have been set very early, possibly before the Carboniferous, and have been reactivated several times during the tectonic evolution of the Barents Sea (Gabrielsen *et al.*, 1990). In particular, the Southwestern Barents Sea highs and basins were formed by **four phases of extension**, namely during Carboniferous, Late Permian-Triassic, Late Jurassic-Early Cretaceous and Paleocene-Eocene (Clark *et al.*, 2014; Gac *et al.*, 2018).

IV.A.1. Geological evolution of the Barents Sea

The reconstructed geological history of the Barents Sea starts with the **NeoProterozoic-Cambrian Timanide Orogeny,** result of the collision between Arctica and Ferroscandia, that left in the southern Barents Sea a WNW-ESE structural trend. After this, the **Ordovician to Early Devonian Caledonian Orogenesis -**culminated around 400 Ma- was the consequence of the oceanic subduction and oblique continental collision between Laurentia and Precambrian Baltic Shield, with the consequent **closure of the Iapetus Ocean (Figure 4.2)**. This orogenesis resulted in a general NE-SW trend of the structures, with regional exceptions in the Southern Norwegian Barents Sea (NW-SE trend) and in the Western Barents margin (N-S trend) (Gabrielsen *et al.*, 1990; Smelror *et al.*, 2009 and references therein; Clark *et al.*, 2014 and references therein; Gac *et al.*, 2018 and references therein; Rowan and Lindsø, 2017 and references therein).

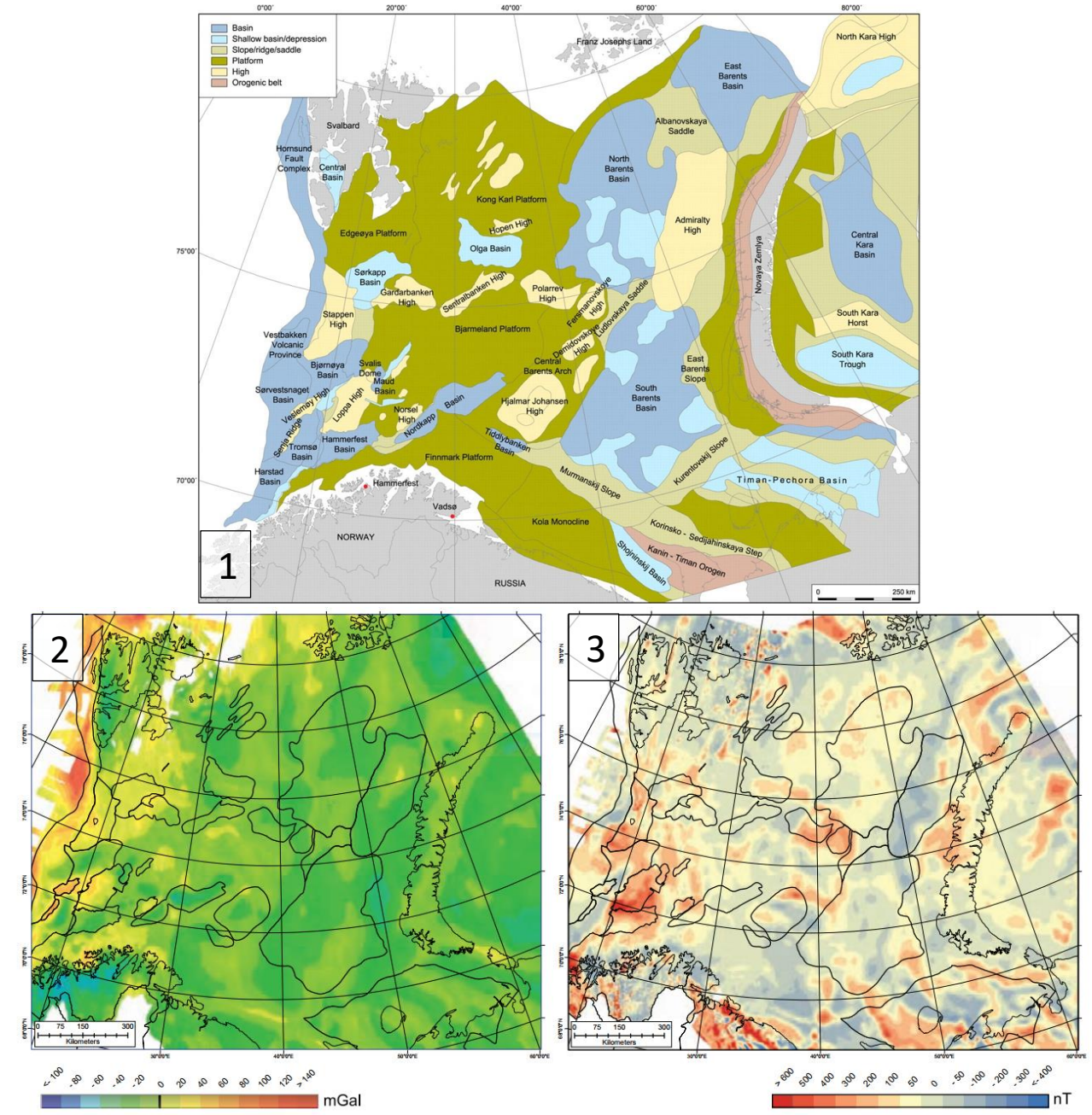

***Figure 4.1**: **1.** Structural map of the Sørvestsnaget Basin (Henriksen et al. 2011). **2.** Gravity anomalies map with the main features of the Barents Sea (Smelror et al. 2009). **3.** Magnetic anomalies map with the main features of the Barents Sea (Smelror et al. 2009). **4.** Depth to basement in the Barents Sea (Smelror et al. 2009).*

During **Devonian to Lower Carboniferous** the **collapse of the Caledonian orogeny** marks the beginning of the rift in the area (Figure 4.2), with formation of basins that mainly developed along the structural features of the Caledonian Orogeny (Smelror *et al.*, 2009). Crustal extension affected most of the Barents Sea, and the western Barents acted as a transfer area in this phase (Clark *et al.*, 2014 and references therein; Faleide *et al.*, 2008; Gac *et al.*, 2018 and references therein). The rift was followed by a post-rift thermal subsidence and formation of a broad sag basin (Gabrielsen *et al.*, 1990; Clark *et al.*, 2014).

The **rifting in late Permian-Triassic** is inferred, and would have contribute to the Triassic subsidence of the Southwestern Barents Sea, amplifying the relief of the Selis Ridge (Clark *et al.*, 2014 and references therein). The northward drift of the shelf and the consequent **climate shift**, together with the progressive drowning of the basin, led to the development of a **carbonate platform** between Sverdrup to Pechora Basin in **Late Carboniferous-Early Permian**, and the deposition of the Gipsdalen group, composed of evaporites, carbonates and siliciclastics (Faleide *et al.*, 1984; Smelror *et al.*, 2009). The presence of salt also in the SW Barents Sea basins, e.g. in the Tromsø and the Sørvestsnaget ones, means that an early phase of basin formation occurred here 320-300 Ma, hundreds of million years before the final shaping of these deep basins (Clark *et al.*, 2014 and references therein). The north-eastern and eastern Barents Sea have been relatively stable with reduced tectonic activity since Late Carboniferous, while the western part was strongly involved in the episodes of **opening of the North Atlantic**. In the **Late Jurassic to Early Cretaceous** the propagation of the North Atlantic led to regional extensional tectonics in the Southwestern Barents Sea (Figure 4.2), with rifting and strike-slip adjustments along old structures lineaments. The crustal extension resulted in the formation of the major highs and the narrow and deep basins of the Southwestern Barents (Gabrielsen *et al.*, 1990; Faleide *et al.*, 1993; Clark *et al.*, 2014; Omosanya *et al.*, 2017; Gac *et al.*, 2018) (Figure 4.1). A post-rift differential subsidence characterised the Cretaceous in these basins and in general in the Barents Sea (Faleide *et al.*, 2008). The extensional regime of the North Atlantic system and the rifting in the Western Barents Sea continued during **Late Cretaceous to Paleocene**, and the presence of younger, narrower and deeper basins going towards west suggests a focusing of the rift before the final breakup (Gabrielsen *et al.*, 1990; Clark *et al.*, 2014 and references therein). The extension culminated, at the beginning of Eocene, in seafloor spreading and the formation of the Norwegian-Greenland Sea (Faleide *et al.*, 2008).

During Middle Eocene the Sørvestsnaget Basin subsided, leading to deep marine bathyal conditions (Knutsen *et al.*, 1992; Ryseth *et al.*, 2003) followed by shallowing at the Eocene-Oligocene boundary (Ryseth *et al.*, 2003). The Sørvestsnaget Basin experienced during Cenozoic a strain partitioning with coeval development of fold and thrusts and normal faults, orthogonal to sub-orthogonal to each other (Kristensen *et al.*, 2018). The presence of compressional structures in the Sørvestsnaget Basin had been previously associated to a compressional phase during Oligocene to Miocene times, and possibly continuing through Plio-Pleistocene (Knutsen and Larsen, 1997), but more recently explained as the result of right-lateral oblique plate motions along the margin, with a climax of transtention during Upper Paleocene to Middle Eocene in the Southwestern Barents Sea (Kristensen *et al.*, 2018).

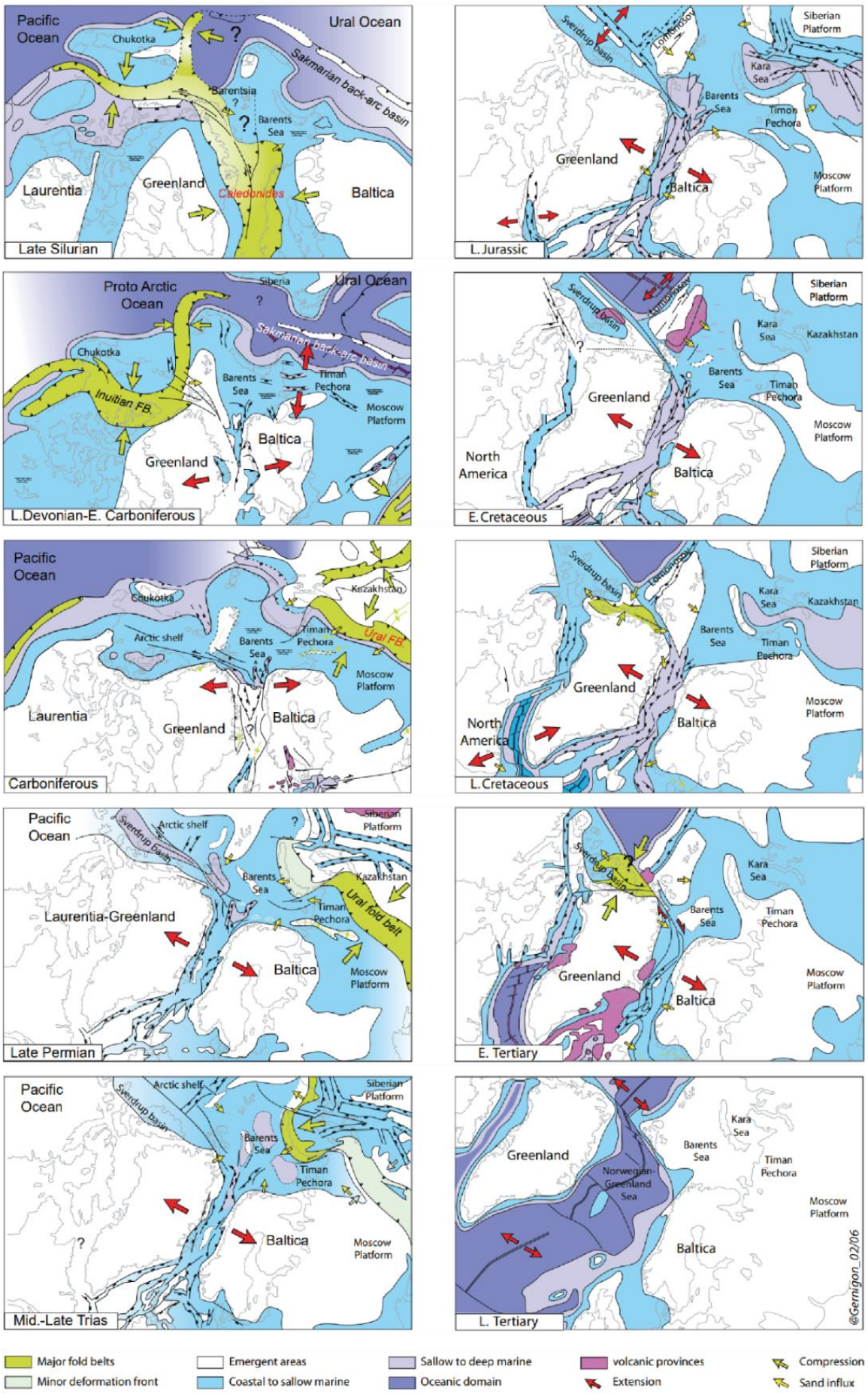

***Figure 4.2**: Geodynamic evolution of the North Atlantic and Arctic regions (Smelror et al., 2009).*

During Plio-Pleistocene the geological development of the Barents Sea region has been largely controlled by the glacial phenomena with sediment erosion and deposition, and glacio-isostatically controlled crustal movements **(Figure 4.3)** (Gabrielsen *et al.*, 1990; Faleide *et al.,* 2008; Knies *et al.,* 2009; Gac et al., 2018 ; Bellwald *et al.,* 2019).

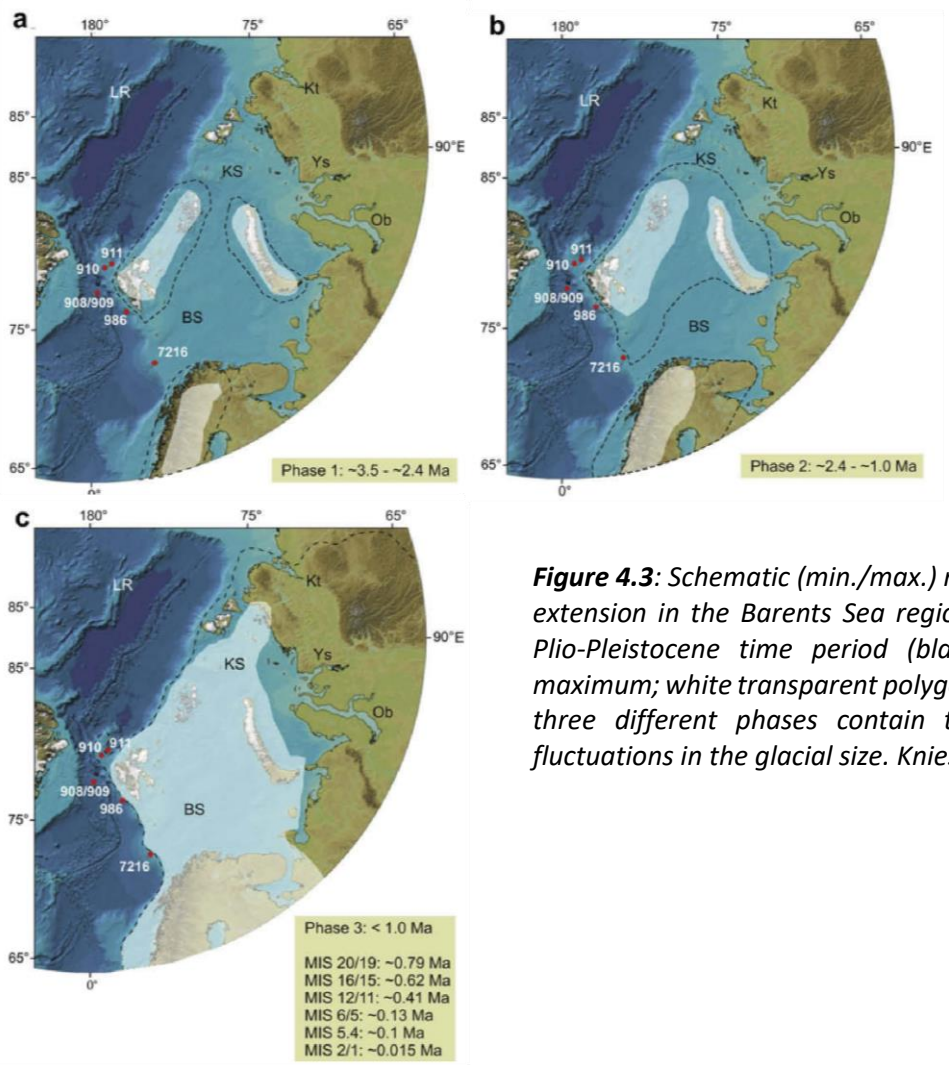

***Figure 4.3**: Schematic (min./max.) model of lateral ice extension in the Barents Sea region during the Late Plio-Pleistocene time period (black stippled lines: maximum; white transparent polygons: minimum. The three different phases contain themselves strong fluctuations in the glacial size. Knies et al. (2009).*

A sequence of different **glacial-interglacial cycles** characterized the last 4 Ma, with a variability of solar heating mainly controlled by Earth's orbit precession (19-23 ky cycles) and obliquity (41 ky cycles) (Ravelo *et al.*, 2004). The Nordic Hemisphere Glaciation (NHG) has been a gradual climate cooling ('initial growth phase' of Knies *et al.,* 2009) between 3.6 and 2.4 Ma that caused a growing of the ice volume with values of 0.4‰ (Knies *et al.*, 2009 and references therein). Shorter term glacial episodes have been dated 3.34, 3.295, 2.7 and 2.523-2.433 Ma, while a warmer period (middle Pliocene climate optimum) has been dated 3.25 to 3.05 Ma (Knies *et al.*, 2009 and references therein; Ravelo *et al.*, 2004). Particularly strong has been the glacial episode at the beginning of the Pleistocene (2.75 Ma, Ravelo *et al.*, 2004) with intensification of the glaciation in the circum-Atlantic and ice growing in Greenland, Scandinavia and North America. This global climate change resulted in the erosion of the shelf –also due to its tectonic uplift- and the formation of an unconformity that interested all the sedimentary basins (Mangerud *et al.*, 1996; Gabrielsen *et al.*, 1990; Knies *et al.*, 2002, 2009). In the study area the most important unconformity is the URU (Upper Regional Unconformity) surface (Sættem *et al.*, 1992; Bellwald *et al.*, 2019).

IV.A.2. Structural framework of the SW Barents Sea

As previously mentioned, the Basins in the SW Barents are generally narrow and ENE trending, and become narrower, deeper and younger moving towards west (Figure 4.1). Particularly deep is the **Sørvestsnaget Basin** (Ronnevik *et al.*, 1982), a sedimentary basin located at the southwestern limit of the Barents Sea between 71° and 73°N -widening in the northern part and and narrowing to the south- and between 15°E (oceanic crust) and 18°E **(Figure 4.1 and 4.4)** (Gabrielsen *et al.*, 1990; Faleide *et al.*, 2008).

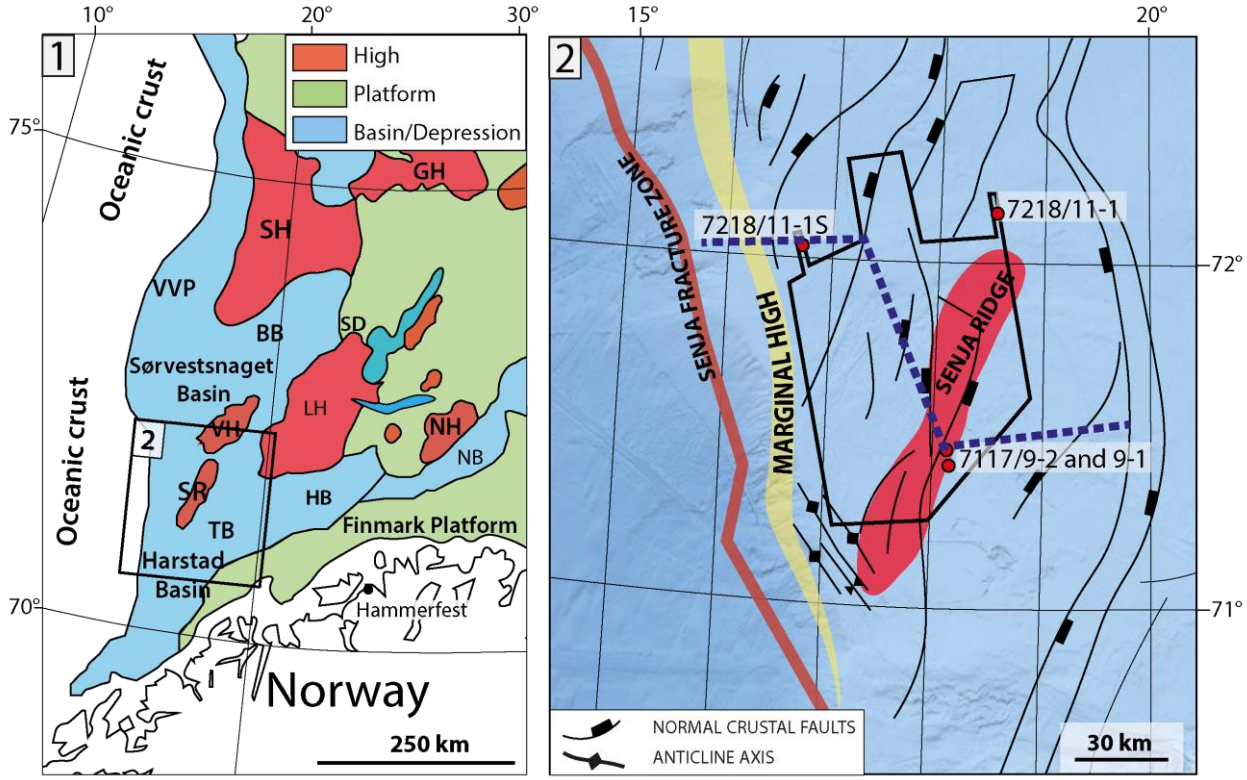

***Figure 4.4**: Main highs and basins of the SW Barents Sea and position of the study area. **1.** The black rectangle marks the position of figure 4.4.2. GH: Gardarbanken High; LH: Loppa High; BB: Bjornaya Basin; HB: Hammerfest Basin; NB: Nordkapp Basin; NH: Norsen High; SD: Svalis Dome; SH: Stappen High; SR: Senja Ridge; VH: Veslemoy High; VVP: Vestbakken Volcanic Province. Compiled after Henriksen et al. (2011). **2.** Position of the TGS 3D dataset and wells in the southern Sørvestsnaget Basin structural map, and position of the seismic profile of Figure 4.6. Compiled after Lasabuda et al. (2018), bathymetry from Emodnet bathymetry.*

Consequence of the particular location at the western limit of the Barents Sea, the development of this basin has been strongly controlled by the large scale tectonics movements (Faleide *et al.*, 2008): the evolution of the Sørvestsnaget Basin can be reconducted to the releasing bend along the Senja Fracture Zone during Latest Paleocene-Eocene (Planke *et al.*, 2012). Excluding some exceptions, the majority of the faults of the basin are north-northeast south-southwest trending normal faults and the southern Sørvestsnaget Basin is characterised by the co-presence of extensional and contractional structures, mainly oriented repectively NE-SW and NW-SE (Figure 4.4.2) (Kristensen *et al.*, 2018).

The **Stappen High** and the northeast-southwest trending **Knolegga Fault Zone** constitute the north and northwest limits of the basin. At the northeast, the limit of the basin is marked by a south-southwest north-northeast fault zone, which separates the Sørvestsnaget from the Bjmnoya Basin

(Figure 4.1). The southeastern limit of the Sørvestsnaget Basin is constituted by the Senja Ridge crustal high (NNE-SSW trend) and the Veslemoy High (NE-SW), separated from the basin by a fault zone **(Figure 4.1 and 4.4)** (Gabrielsen *et al.*, 1990). The formation of the **Senja Ridge** has been dated mid-Cretaceous to Late Pliocene, and has been active during several tectonic phases but positive since Late Cretaceous-Early Cenozoic (Faleide *et al.*, 1993). Despite some compressional tectonics cannot be excluded from the mechanisms of formation of this basement high, the faults dividing it from the surrounding basins are extensional **(Figure 4.4.2 and 4.6)** (Mjelde *et al.*, 2002). The result of the drilling on the Senja Ridge suggests that during Early Cretaceous the Senja Ridge was part of the subsiding basin, and during Upper Cretaceous was a positive structure as testified by the thinning, erosion and non-deposition of the Upper Cretaceous interval, more carbonate rich compared to the sediments in the Trømso Basin (Knutsen and Larsen, 1997).

The southwestern limit of the southern Sørvestsnaget basin is marked by the **Senja Fracture Zone** (SFZ, Figure 4.4.2) which is the southern sector of the western Barents Sea-Svalbard margin, composed of two shear segments and a central rifted segment (Faleide *et al.*, 2008; Kristensen *et al.*, 2018 and references therein). Its Cenozoic evolution is linked to the opening of Norwegian-Greenland Sea (Figure 4.2), with the continent-continent transform area of Early Eocene that becomes during Eocene-early Oligocene an ocean-continent margin. Later on, the spreading ridge shifted north and nowadays the area is a passive continental margin with no shear movement (Figure 4.4.2) (Vågnes *et al.*, 1998).

Another basin partially imaged by our dataset is the **Tromsø Basin** (Rønnevik *et al.*, 1975), separated from the southern Sørvestsnaget basin by the Senja Ridge. This basin is located between 71° to 72°15'N and 17°30' to 19°50' E, with a NNE-SSW axis and a south-central system of detached faults (Gabrielsen *et al.*, 1984).

IV.A.3. The sedimentary sequence in the SW Barents Sea

We describe here briefly the sedimentary sequence of the Barents Sea, with a focus on the reconstructed sedimentation of the Southwestern Barents Sea **(Figure 4.5)**.

'Presalt' sediments

The oldest sediments identified in the Barents Sea are the sediments of the Caledonian orogeny (500 Ma) in the eastern Barents, while in the western Barents they are significantly younger (e.g. Devonian in the Nordkapp Basin) (Smelror *et al.*, 2009). During Upper Devonian-Mississipian the deposition in the grabens consisted of mostly non-marine alluvional, fluvial, lacustrine sediments of humid and warm climates, followed by more arid conditions and sea-level rise that led to the deposition of deltaic and marine deposits and evaporites (Ronnevik *et al.*, 1982; Larssen, 2002).

Gipsdalen Group evaporites

The Gypsidalen Group (Cutbill and Challinor, 1965) covers 250 000 km^2 and presents a lithology composed of **evaporites** -halite and anhydrite-, **warm-water carbonates** often dolomitized and **red-coloured siliciclastics** (Figure 4.5) (Larssen, 2002; Rowan, 2017). Evaporitic sediments dominate in the basins, with mostly halite in the distal areas and anhydrite and carbonates near the margin of the platform and on the basement highs (Larssen, 2002; Rowan, 2017 and references therein). Slightly different periods and multiple phases of deposition of the Gipsdalen Group evaporites have been proposed but is nowadays accepted the Upper Cretaceous to Lower Permian age as the most

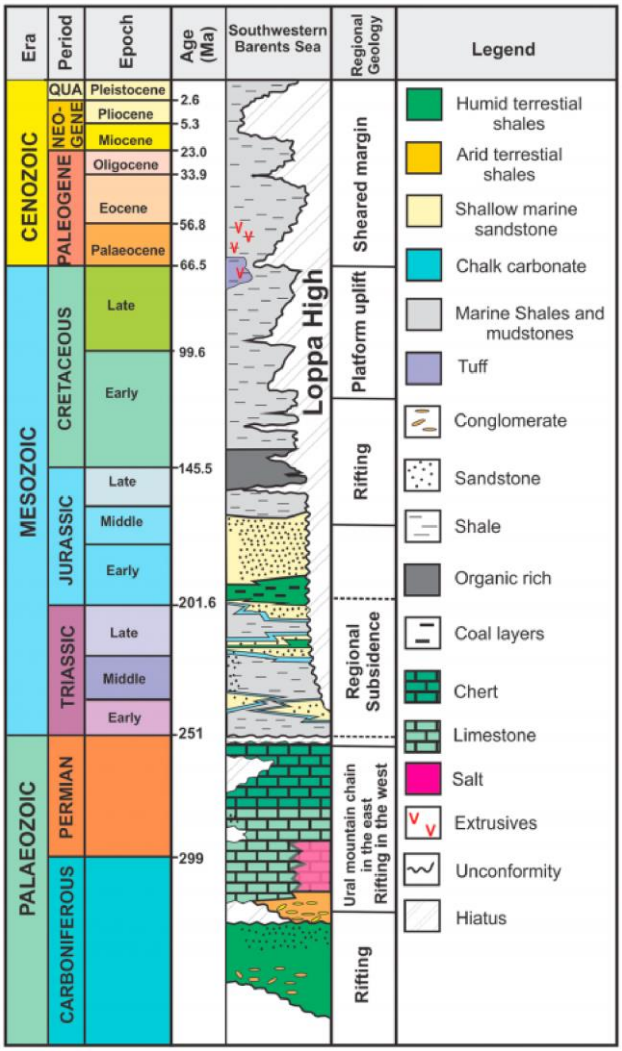

***Figure 4.5**: Lithostratigraphic column of the Southwestern Barents Sea, which the main regional tectonic events from the Paleozoic to the present* (Omosanya *et al.*, 2017).

probable (Faleide *et al.*, 1984; Ronnevik *et al.*, 1982). As well as the lithology, also the thickness of this formation highly depends on the depositional area, with thicker deposits in the rift structures and in the areas of subsidence. For what concerns the Sørvestsnaget Basin, strong uncertainties about the depositional thickness are due to the depth of this basin and to the consequent impossibility to image the Permo-Carboniferous layer with seismic reflection data. The salt in the Sørvestsnaget Basin is supposed to be mostly mobilized, but cannot be excluded the presence of a clastic fraction still in place (Mjelde *et al.*, 2008).

Permian-Cretaceous sedimentation

After the deposition of the Lower Permian evaporites, in the Middle to Late Permian the sedimentation shifted to **fine grained siliciclastic**, because of the Uralian Orogeny that changed the water circulation and consequently lowered the sea water temperature (Rønnevik *et al.*, 1982; Larssen, 2002). The Triassic is marked by the presence of a NNW trending **prograding delta** (Planke *et al.*, 2012), with cycles of transgression and regression dated Lower to Middle Triassic in the Western Barents Sea (Smelror *et al.*, 2009). In the Early Cretaceous an important uplift and subsidence mainly concentrated in the northern and eastern Barents led to the formation of the Base Cretaceous unconformity (Planke *et al.*, 2012). Simultaneously, the **Barents Sea Large Igneous Province** (BLIP) formed during Early Cretaceous, with episodes of intrusive and extrusive volcanism (Planke *et al.*, 2012). For what concerns the Sørvestsnaget Basin, the depth of the mid Jurassic horizon has been estimated from Ocean Bottom Seismographs (OBS) studies to be around 10-12 km, with maximum depth values of around 14-17 km in the depocenters (Mjelde *et al.*, 2002). The post-rift differential subsidence that characterize the area during Cretaceous created the depositional space for up to 9 km of Late Jurassic-Early Cretaceous and up to 6 km of Late Cretaceous sediments in the northern depocenter of the Sørvestsnaget Basin, confirmed by gravity models and 2D data interpretation (Mjelde *et al.*, 2002). The Cretaceous sediments drilled in the Sørvestsnaget Basin are mainly claystone with thin beds of limestone, dolomite, and siltstone, with an Upper Cretaceous interval rich in carbonate in the drilling near the Senja Ridge top (well 7117/9-2) (Knutsen and Larsen, 1997).

Cenozoic Sediments

Cenozoic strata are widely missing in the Norwegian Barents Sea because of Cenozoic uplift and consequent erosion (Rowan, 2017 and references therein), but the succession is quite complete in the Western Barents and in particular from early Paleocene (Danian) to middle Eocene in the Sørvestsnaget Basin **(Figure 4.6)** (Ryseth *et al.*, 2003).

In the post-opening scenario of the Middle Eocene, the Sørvestsnaget Basin subsided and significant **sandy submarine fans** were deposited in deep marine bathyal conditions (Knutsen *et al.*, 1992; Ryseth *et al.*, 2003). The sediments register a marine shallowing at the Eocene-Oligocene boundary, and the shallow conditions continue throughout Oligocene-Miocene with deposition of shallow marine, fine grained sediments (mud rocks) plus local Lower Oligocene sandstones (Ryseth *et al.*, 2003). The shallow marine Oligocene-Miocene package has minor deposition (Knutsen Larsen, 1997) and presents unconformities, probably due to phases of compression and inversion of the highs (Ryseth *et al.*, 2003) and local uplift in the Southern Sørvestsnaget that led to erosion (Knutsen *et al.*, 1992).

During Late Cenozoic the sedimentation was largely controlled by **Northern Hemisphere Glaciations,** and the consequent erosion of the continental shelves and deposition or large volumes of sediments on the continental slopes. Since the beginning of the glaciation, ice-rafted debris started to be deposited, forming prograding sedimentary bodies of sandy/silty muds that constitute in the Western Barents Sea more than half of the volume of post-opening sedimentary sequence (Faleide *et al.*, 1996, 2008). The ice-sheet had an important role in the compaction of the sediments (Bellwald *et al.*, 2019).

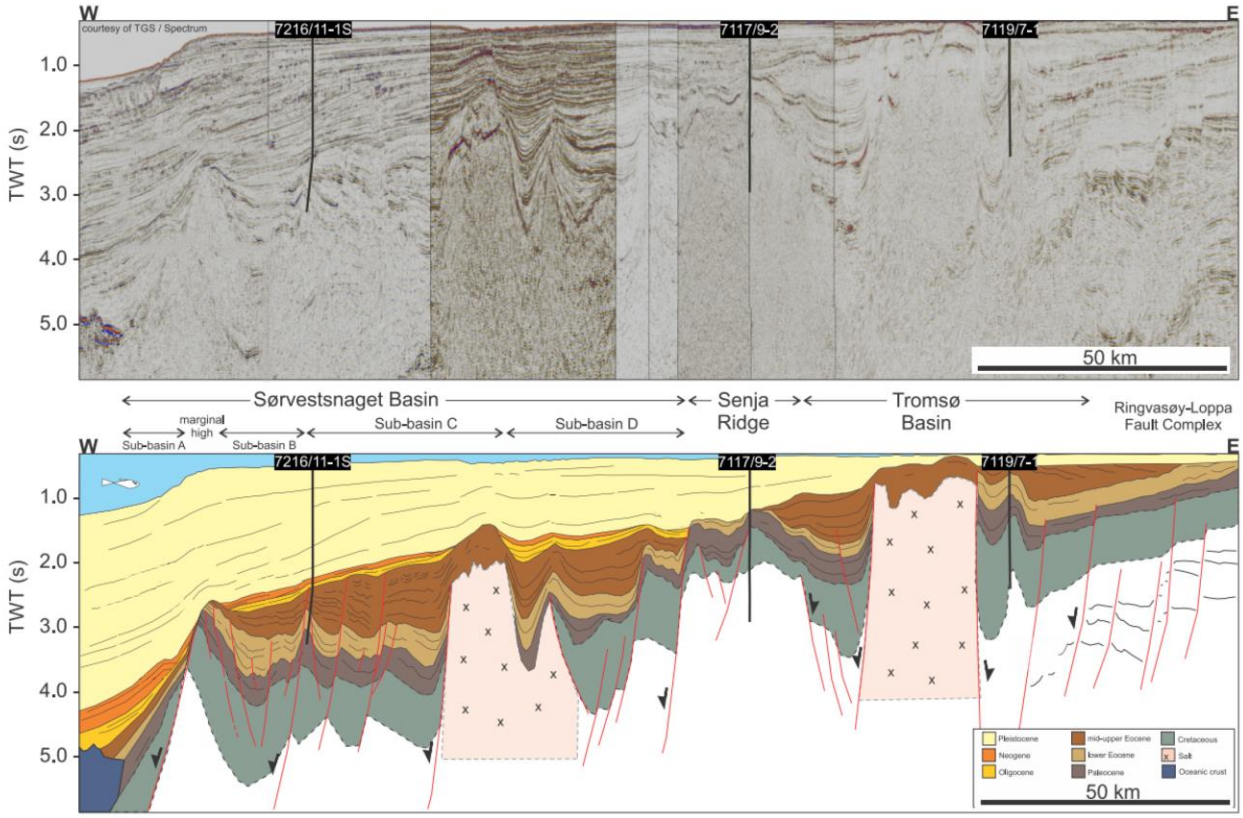

***Figure 4.6**: General section showing the stratigraphy of the Tromso and Sørvestsnaget basins, divided by the Senja Ridge (modified after Lasabuda et al., 2018). Location in Figure 4.4.2.*

The major unconformity in the area is the **URU** (Upper Regional Unconformity) surface, which divides the sedimentary rocks of the Lower Cretaceous/Jurassic from the thick wedge of mostly subparallel glacial sediments (Bellwald *et al.*, 2019; Sættem *et al.*, 1992).

IV.A.4. Previous salt tectonics studies in the Barents Sea

Due to the diachronous development of the basins in the Barents Sea, the relationship between crustal rifting and the Permo-Carboniferous evaporite deposition is highly variable: the salt of the Gipsdalen Group results **synrift** in the Tromsø Basin, **postrift** in the Tiddlybanken Basin, **syn to early post-rift** in the Nordkapp Basin (Rowan and Lindsø, 2017; Hassaan *et al.*, 2021a, 2021b). This aspect, together with the differences in terms of tectonics history and sedimentary thickness, led to a wide variety of salt tectonics mechanisms and structures in the Barents Sea, so the study of salt tectonics in one of the basins cannot be considered representative of the other areas.

One of the Barents most studied basins from the salt tectonics point of view is the **Nordkapp Basin** (position in Figure 4.1), where the studies are mainly based on seismic interpretation (Nilsen *et al.*, 1995; Rowan and Lindsø, 2017; Hassaan *et al.*, 2021b, 2021a) with an important integration of gravity and magnetic data (Fichler *et al.*, 2007; Gernigon *et al.*, 2018) and analogue modelling (Koyi *et al.*, 1995 a and b). In the Nordkapp Basin the salt movement seems to be strictly linked to the **regional tectonics** which controlled the initiation, growth and reactivation of the salt structures, formed through short periods of growth and long stops (Nilsen *et al.*, 1995; Rowan and Lindsø, 2017). The mid-late Permian **crustal extension** triggered the beginning of salt tectonics (Hassaan *et al.*, 2021a), while the main phase of salt movement is dated upper Lower to Middle Triassic (Nilsen *et al.*, 1995) with a **rejuvenation** of the salt structures during Triassic-Jurassic. The Mesozoic regional extension resulted in gravity gliding, which forced the vertical development of pre-existing diapirs, and a latest phase of rejuvenation has been dated early-mid Eocene. Despite the salt growth is mostly consequence of the crustal tectonics, the **sediments progradation** geometries is particularly important in terms of influence on the morphology of the resulting salt tectonics (Hassaan *et al.*, 2021a). The quality of the seismic imaging in the area allowed also the identification of different facies – and different reological characteristics- of the **Layered Evaporite Sequence (LES)**, caused by the basin architecture at the time of the Gipsdalen Group deposition (Hassaan *et al.*, 2021b). The studies in the area comprehend also the influence of salt bodies on the thermal evolution of the petroleum systems, and in particular the expansion of the hydrocarbon generation window in presence of salt structures (Cedeño *et al.*, 2019).

In the Tiddlybanken Basin (position in Figure 4.1) the rifting predates the deposition of the evaporites, and the salt deposited in a post-rift sag basin. Characteristic of this basin is the Tiddlybanken Diapir, an isolated structure that developed in different steps since early to middle Triassic (Rowan and Lindsø, 2017). Both in the Nordkapp and Tiddlybanken basins some large diapirs developed up to the shallower strata, influencing the bathymetry and locally reaching the seafloor (Gernigon *et al.*, 2018). For what concerns the Southwestern Barents, the sedimentary sequence of these basins is too thick to image the deep Permocarboniferous salt through seismic reflection data, and the studies are therefore concentrated on the shallower parts of the salt structures (Knutsen and Larsen, 1997; Perez-Garcia *et al.*, 2013; George *et al.*, 2017; Rowan and Lindsø, 2017). Despite the limitation in terms of imaging, the analysis of a salt diapir in the Tromsø Basin **(Figure 4.7)**

suggests that the salt tectonics is here consequence of the extensional crustal tectonics (i.e. reactive diapirism), while the successive growth is due to passive diapirism (Rowan and Lindsø, 2017). The rejuvenation of the salt diapir during Paleogene is attributed to crustal shortening (Rowan and Lindsø, 2017).

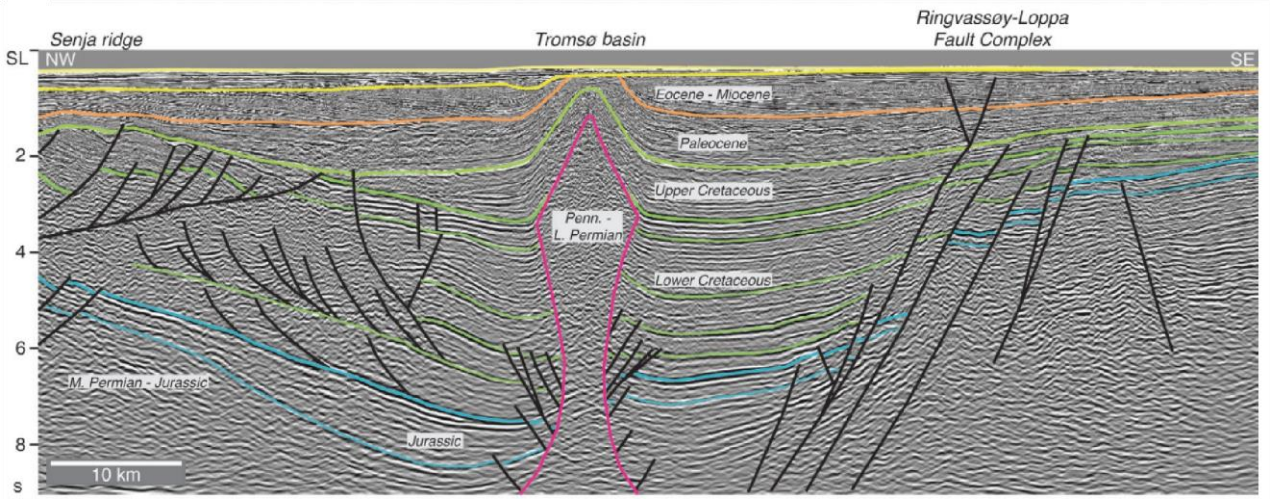

***Figure 4.7**: 2D Seismic reflection profile of a Salt Diapir in the northern Tromsø Basin (Rowan and Lindsø, 2017).*

Salt tectonics analysis in the Sørvestsnaget Basin is made more complex by the thickness of the sedimentary sequence and by the intense and various tectonic movements of this basin, located at the limit of the Barents Sea continental shelf. Previous studies on salt tectonics in the Sørvestsnaget Basin (Knutsen and Larsen, 1997; Perez-Garcia *et al.*, 2013) partly mapped some of the salt structures that we will describe in the results chapter and linked the major salt movement in the area with the opening of the Norwegian-Greenland Sea. As we can see in **Figure 4.8**, the study from Knutsen and Larsen (1997) first mapped four structures, and interpreted them as possible salt.
After fourteen years, 3D seismic reflection data allowed a more detailed mapping of the western side of one of the salt bodies (Figure 4.8.2) (Perez-Garcia *et al.*, 2013), while lot of uncertainties are still present in terms of deep and shallow salt geometries, and on the hundreds of millions years of salt tectonics in the Sørvestsnaget Basin.

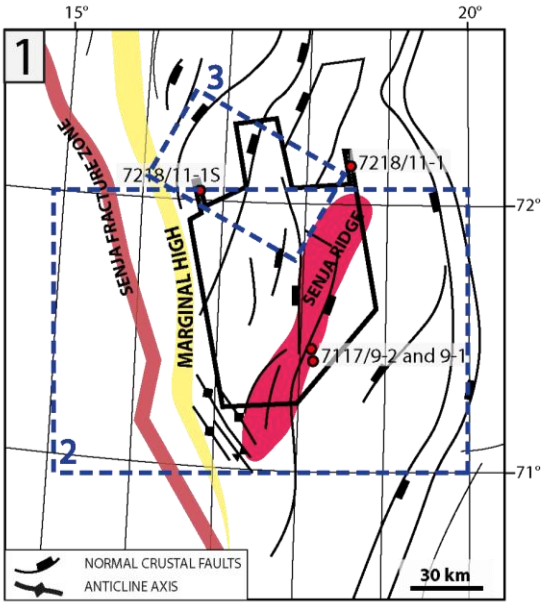

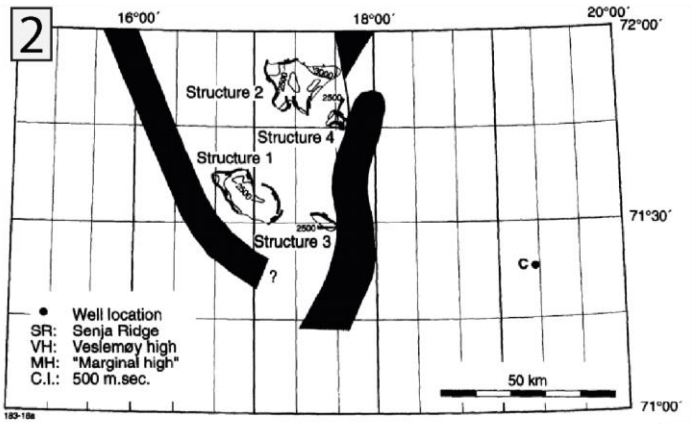

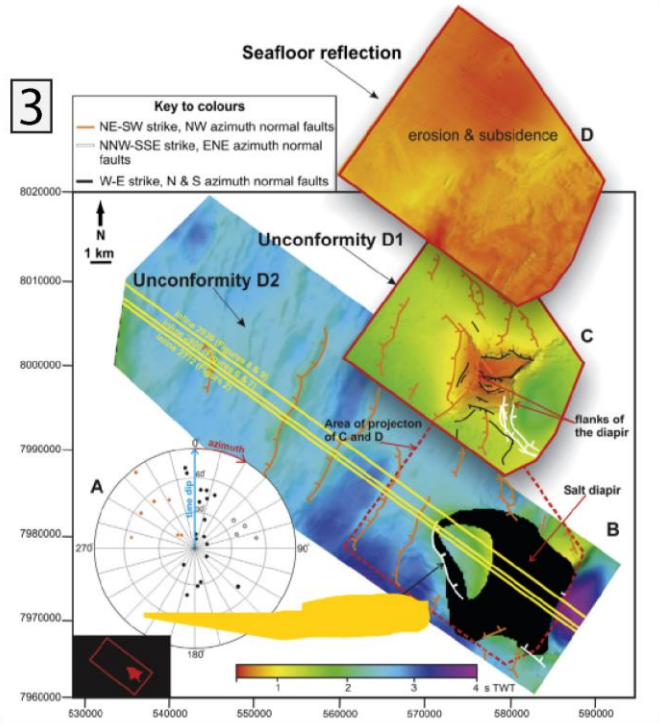

***Figure 4.8**: **1.** Position in map of the previous studies in the area. **2.** First map of the salt structures in the southern Sørvestsnaget Basin by Knutsen and Larsen (1997) and **3.** Mapping of the main horizons above a salt structure in the Southern Sørvestsnaget Basin (Perez-Garcia et al., 2013).*

IV.B. The Sørvestsnaget Basin (Study Case 3)

We present here the results of the collaboration with the Volcanic Basin Petroleum Research (Oslo, Norway), that led to the understanding of the interaction between salt and crustal tectonics in the Southern Sørvestsnaget Basin. The interpretation of the geophysical data was followed by the production of analogue models, and from the comparison between the results we reconstructed 300 Ma of salt deformation.

IV.B.1. Results

In this chapter we will focus on the seismic stratigraphy, on the structural analysis and on the salt structures shape and evolution in the Sørvestsnaget Basin, in order to reconstruct the salt tectonics in the area. The results are mostly based on the interpretation of a high resolution 3D seismic reflection dataset integrated by additional geophysical data **(Figure 4.9)**, ownership of TGS (Norway).

IV.B.1.1. Integration of geophysical data to optimize the accuracy of results

As already mentioned in chapter II (Data and methods), the study of the area is based on the interpretation of 3D seismic reflection data, regional 2D seismic data, Bouguer gravity anomalies, magnetic anomalies and wells data. The copresence of different geophysical data (Figure 4.9) constitute a valid aid in the correct interpretation of the dataset and a mean to avoid some of the major seismic interpretation pitfalls. In fact, every data is essential for a certain aspect of the interpretation, but it is from their integration that we can obtain the most accurate output.

- **Seismic data**: the quality of the **3D dataset** used for this study is very high, with detailed information of the subsoil geometries up to a depth of more than 4 s TWT (Figure 4.9.1). Despite the very good quality of the 2D reflection profiles, all the images presented in this chapter belong to the 3D seismic dataset, being it more useful for detailed salt structures interpretation. A particular way of visualizing seismic data are the **time slices (Figure 4.10)**, a horizontal display or map view of 3D seismic data having a certain arrival time, allowing us to visualize the different horizons present at the same time depth. A spatially high-frequency event on a time slice is either a steeply dipping event (as a consequence of the horizons deformation for salt tectonics, tilting of the margin, depocenter, differential compaction of the sediments etc.) or a high-frequency event in time (e.g. the thin sedimentary layers of the Upper Eocene to Pliocene sequence). The time slices in our dataset (Figure 4.10) allow to visualize very well the overburden deformation above the interpreted salt structures (time slices at 1300 and 2000 ms) and the transparent seismic facies of the salt resulting in a grey homogeneous area in the time slices (time slices at 2500 and 3000 ms), as well as the high frequency of the horizons around the salt structures, faults geometries, depocenters etc. When considering this, we have to keep in mind that the seismic facies is mostly transparent also below the salt due to the shielding of the seismic signal, so a time slice cut at a major depth would not give us more information about the salt geometries. We can also notice here the similarity between the seismic facies of the salt structures and the Senja Ridge.

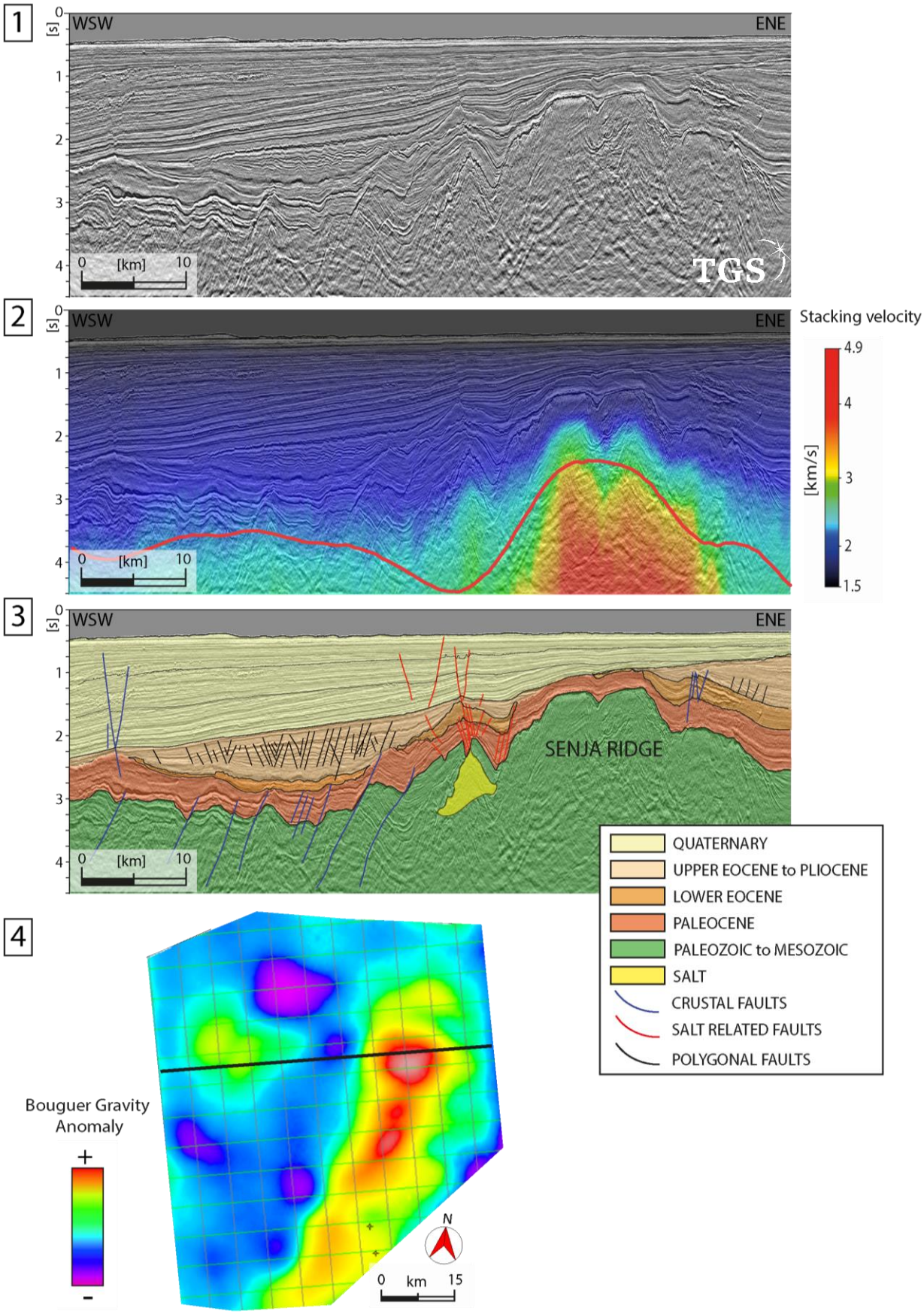

Figure 4.9: *Integrated use of the available data.* ***1.*** *Seismic reflection profile (position in figure 4.9.4) of the 3D Carlsen dataset. The positive and negative amplitudes reflections are respectively black and white. VE at the seafloor: 7.7 X.* ***2.*** *Seismic reflection profile with superimposed the stack velocity values and the relative value of the 30 km high-pass filtered Bouguer gravity anomaly (red line), this last highlighting a*

difference in density of the subsoil. ***3.*** *Interpreted seismic profile, result of the integration between seismic reflection data and the velocity data derived from it, Bouguer gravity anomaly and wells data. The division in faults families is based on their genesis: crustal faults (blue), salt related faults (red) and polygonal faults (black).* ***4.*** *Relative values of Bouguer gravity anomaly, 30 km high-pass filtered. The black line shows the position of the seismic profile in 4.9.1, .2, .3. Seismic data courtesy of TGS.*

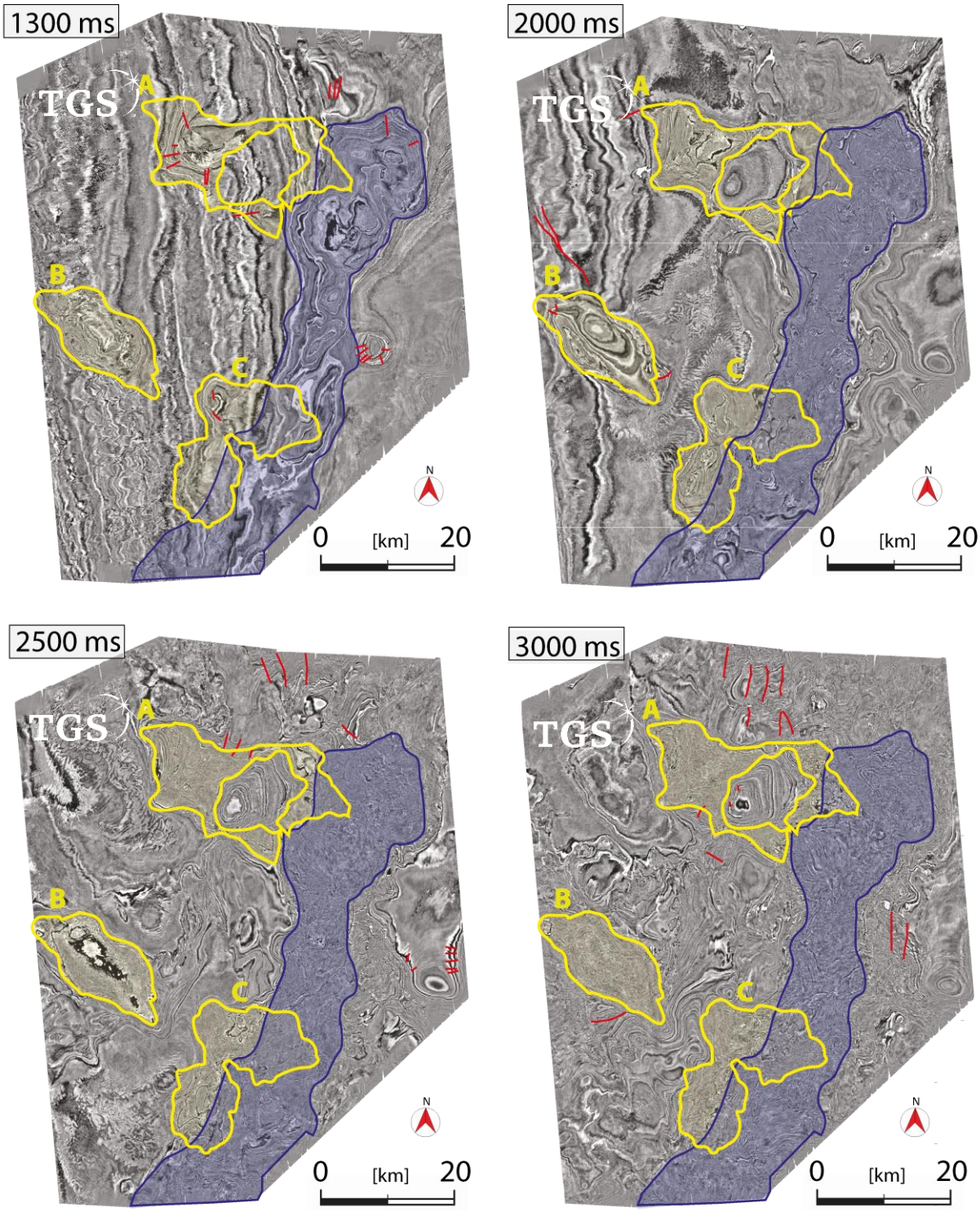

Figure 4.10*: Time slices of the 3D dataset at 1300, 2000, 2500 and 3000 ms TWT. In violet is marked the position of the Senja Ridge and in yellow the position of the interpreted allochthonous salt structures (respectively A, B and C from north to south). Seismic data courtesy of TGS.*

From the seismic data processing were derived by TGS the **stacking velocities** (Figure 4.9.2), defined as the value of the seismic velocity obtained from the best fit of the travel time curve by a hyperbola (Yilmaz, 2001). The range of values of the stack velocities in the 3D dataset is between 1.5 km/s for the water column to 4.9 km/s for the Senja Ridge crustal high, and the velocity data are particularly useful when interpreting salt structures surrounded by clastic sediments, due to the high velocity of seismic waves when crossing the halite as visible in Figure 4.9.2. More challenging is the distinction between the Senja Ridge and the salt, distinction for which it becomes essential the use of Bouguer gravity data discussed later. At a smaller scale, the velocity data can help in tracing the vertical limit between two geological bodies presenting comparable seismic facies and in which the horizon dividing the two bodies is not imaged, as in the very common case of vertical boundaries **(Figure 4.11)**. In this case, the salt body -partly detected thanks to the fault pattern above it- presents a slightly higher stacking velocity than the Cretaceous sediments.

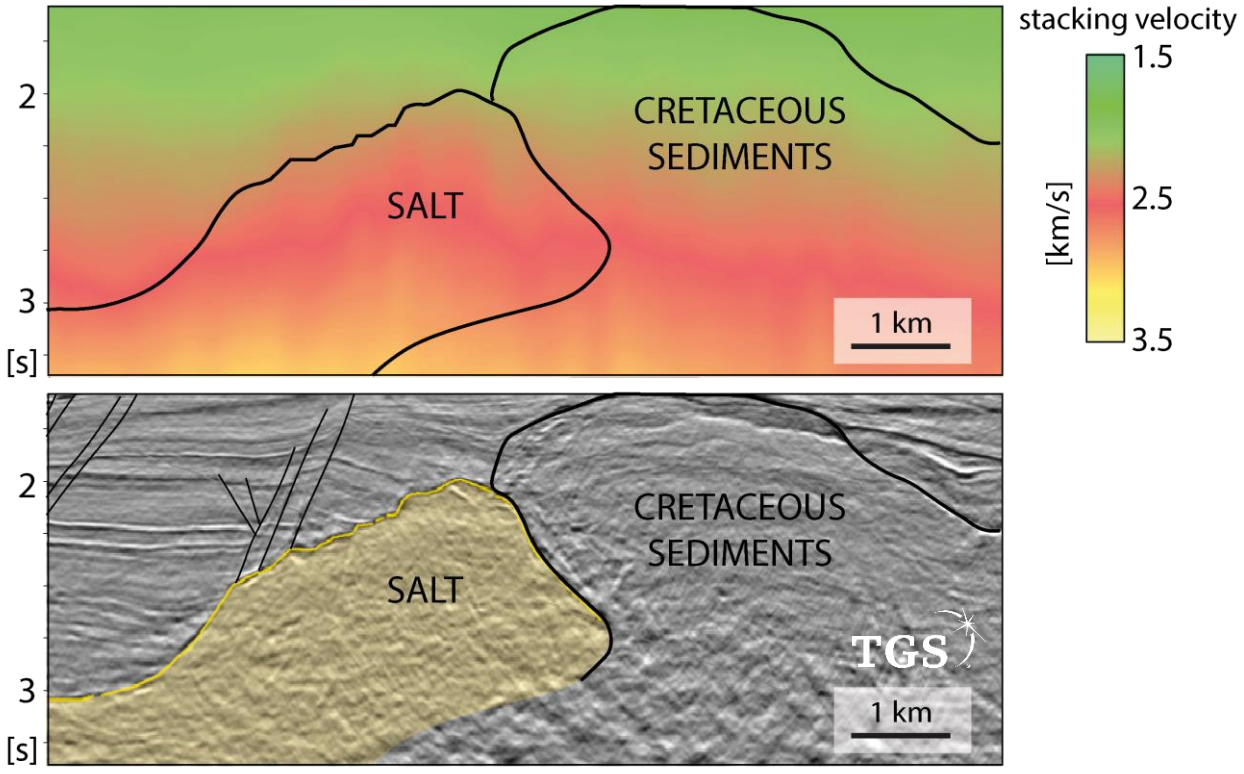

***Figure 4.11**: Comparison between the stacking velocity data (above) and the seismic reflection profile from which the velocity data were obtained (below). The velocity data are locally used to distinguish between bodies with comparable seismic facies, as the transparent Senja Ridge and the salt. VE with a velocity of 2000 m/s: 2X. Seismic data courtesy of TGS.*

❖ **Potential field data**: As seen in chapter II.2 (Introduction on gravity and magnetic potential methods), the use of potential field data is an important constrain when interpreting salt structures, especially when used together and when their regional extension allows to visually distinguish between the regional trends and the local variations. The deep sedimentary basin are generally magnetically quiet zones without strong differences in Bouguer gravity anomalies, and are good to visualize the **negative gravity and magnetic anomalies** related to the salt presence (Olesen *et al.*, 2010).

Particularly interesting for our study was the **Bouguer gravity anomaly**, in particular the 30 km high pass filtered one (Figure 4.9.4) where it is possible to delineate the position of the major structures of the Southwestern Barents Sea, with maximum values corresponding to a basement high (Senja Ridge) and minimum values corresponding to the deeper basins because of the lower density of the sedimentary sequence compared to the basement rocks. Together with this pattern, and characterized by a smaller wavelength of values change, can be identified the presence of local lower values of Bouguer gravity anomalies. These partly correspond in the Sørvestsnaget Basin to the position of three complex structures characterized by transparent seismic facies and partially interpreted in literature as evaporitic bodies. The difficulty in the interpretation is due here to the partial sovrapposition between the Senja Ridge basement high (i.e. positive gravity anomalies) and some sectors of the salt bodies (i.e. negative gravity anomalies), with a resulting lower magnitude of the registered Bouguer anomalies.
Another limit of this method consists in the impossibility to detect thin layers of salt and to distinguish between different shapes and depth combinations, and in the reciprocal cancellation of negative and positive anomalies. Moreover, the resolution is way lower than the one of the seismic reflection data.
Particularly useful is the **integration between Bouguer gravity anomalies and stacking velocity data**. In fact, the geological bodies at the origin of high stacking velocities and transparent facies can be determined through the differences in the Bouguer gravity anomaly: the structures of high velocity and low Bouguer anomaly are interpreted as salt, while the high Bouguer anomaly and high velocity ones are interpreted as crustal structures (e.g. Senja Ridge).

It is from the **integration of the geophysical data** -together with the wells ones- all along the interpretation process that we were able to obtain the results presented in the next subchapters:

- The **seismic stratigraphy (chapter IV.B.1.2)** is mostly the result of the integration between seismic reflection data and wells data. We recognized and interpreted the main horizons and unconformities of the last 66 Ma, a fundamental step not only to have information about the sedimentary setting in the area but also to date faults activity and salt tectonics.
- The **structural analysis (chapter IV.B.1.3)** is the result of the seismic data interpretation of the different families of faults, namely the normal faults of the basin opening, the polygonal faults and the salt related ones, as well as some compressional structures.
- The **salt tectonics and salt related structures (chapter IV.B.1.4)** is the result of the detailed seismic data interpretation of three geological bodies interpreted as allochthonous salt, and the analysis of the geometries of their overburden in terms of thickness, age, depositional geometries and post depositional deformation. In particular, we obtained the following results:

  .Map of the top of the 3 major allochtonous salt bodies with high level of confidence. The top of the allochthonous salt structures was interpreted every 8^{th} inlines and crosslines, and after the Vatmax application the final resolution of the grids is 12.5 m.

  .Map of the base of the allochtonous salt body with medium level of confidence because of the locally very low amplitude of this reflector. The base of the allochthonous salt structures has been interpreted every 32^{th} to 8^{th} inlines and crosslines.

.Isopach map of the **thickness of the allochtonous salt bodies**. The uncertainty about the thickness is direct consequence of the uncertainties about the allochthonous salt base.

An attempt has been done to interpret the autochthonous layer of salt in the 2D and 3D seismic dataset. The interpretation of this horizon has not a good reliability mostly because the horizons constrained by wells and interpreted in the 3D dataset are quite younger, being the older one the base of the Cenozoic; consequently, there is not a strong constrain for what concerns the Permian position in terms of depth (seconds two-ways-time). A possible solution to this problem would be the use of gravimetric data to model the shape of the deep autochthonous salt, adding an important information about the Sørvestsnaget Basin.

IV.B.1.2. Seismic stratigraphy

We interpreted six stratigraphic units in the Southern Sørvestsnaget Basin (Figure 4.9.3), based on the different seismic facies recognized in the data and on the knowledge derived by well data and literature.

Three **allochthonous structures** interpreted in the area (A, B, C in Figure 4.10) present a high amplitude positive anomaly at the top, transparent seismic facies, negative Bouguer gravity anomaly and high velocity of the seismic waves. These characteristics, together with the intrusive nature of these structures and the geological history of the Barents Sea, strongly suggest that these are the mobile evaporitic components (i.e. mostly halite) of the **Gipsdalen Group** deposited in the Barents Sea during **Permo-Carboniferous**, as already proposed by Knutsen and Larsen (1997). Due to the topic of this thesis, we dedicate to the detailed description of these structures the subchapter IV.B.1.4.

The **Paleozoic to Mesozoic sediments** are interpreted as a single seismic unit without established internal divisions, due to the absence of constraints as drillings recovery. The seismic facies visualized in the seismic dataset, most likely dated Cretaceous, presents parallel reflectors in the basin and transparent seismic facies or parallel reflectors on the Senja Ridge (Figure 4.9). Reduced amounts of these sediments are present above some of the allochthonous salt structures. Regional crustal faults dislocate this sequence, and near the salt tectonics structures the horizons are deformed, tilted and upturned.
The horizon marking the passage between the Mesozoic and the Cenozoic in the Carlsen 3D cube is located at a depth between 1.15 s TWT -in correspondence with the Senja Ridge structural high- and maximum values of more than 4.5 s TWT on the eastern and western sides of salt structure A. This horizon locally merges with the top of the salt interpreted in the area, which constitutes local highs in the Base Cenozoic grid. Considering the important amount of sediments related to the Northern Hemisphere Glaciations, we divided the thickness of the Cenozoic sediments in Tertiary and Quaternary.
The **Tertiary sedimentary sequence (Figure 4.12)** is regionally isopach with a thickness of around 1 s TWT, but with a local strong influence of the Senja Ridge and of the salt structures representing local minima (0.1 s TWT), while maximum thickness is associated to the depocenter related to salt structure A (up to almost 3 s TWT). The **Paleocene** seismic unit presents parallel internal reflectors, and locally fan shaped strata and onlapping geometries. This sedimentary sequence is strongly

deformed near and above the salt structures. While the **Lower Eocene** has a seismic facies similar to the Paleocene, with parallel horizons and local growth geometries, the Top Early Eocene surface, mostly erosional in the area, marks a change in the inclination of the horizons.
The **Upper Eocene to Pliocene** is characterized by parallel reflectors and onlapping geometries, and a strong inclination towards W, as well as the presence of polygonal faults result of the fluid expulsion. The polygonal faults, visible in most of the seismic profiles presented in this chapter, are recognizable also in figure 4.10 respectively in the central and western part of the time slices at 2000 and 2500 s TWT. The base of the Pleistocene represents in the region the base of the glacial sedimentary wedge, locally presenting erosional features and marking the beginning of a series of seismic unit marked by medium amplitude high frequency parallel reflectors.
Different subunits have been interpreted in the area, based on the numerous intraglacials surfaces, the wells information and the westward inclination of the horizons, higher on the older deposits and gradually less marked in the most recent ones.

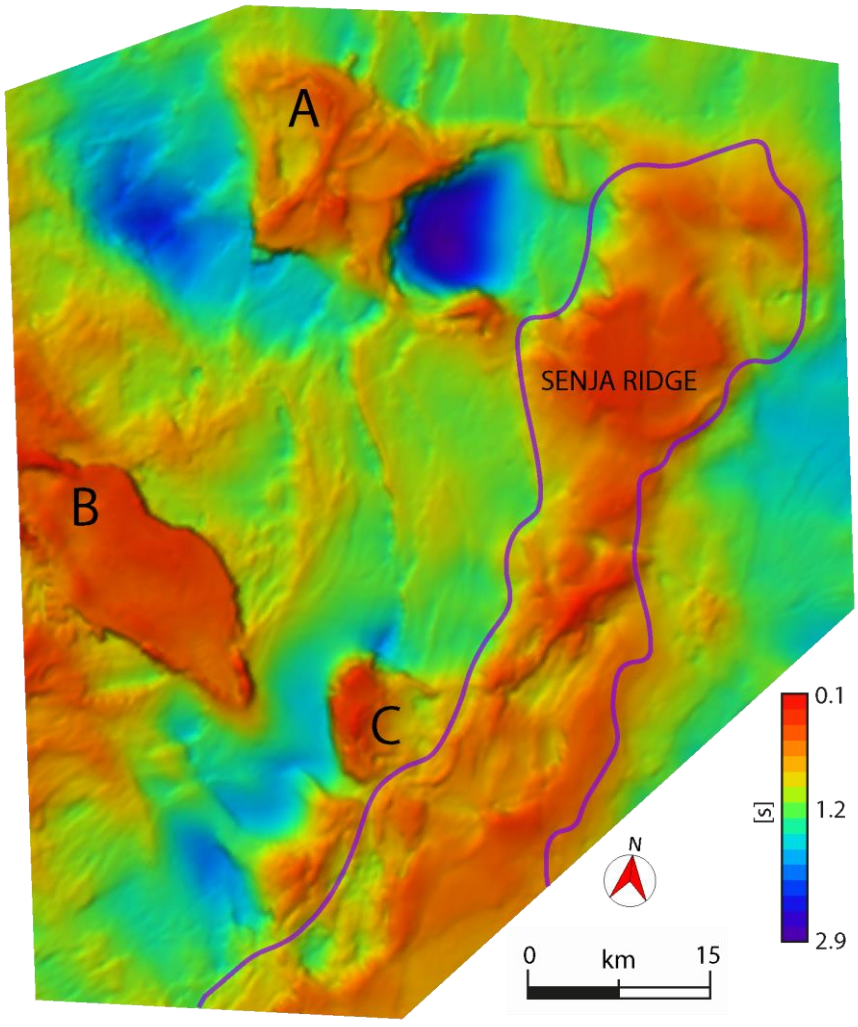

***Figure 4.12**: Thickness map of the Tertiary deposits, i.e. between the beginning of the Cenozoic (66 Ma) and the Upper Regional Unconformity (2.6 Ma). Minimum values correspond to the Senja Ridge (marked in violet) and the salt structures A, B and C, while values of up to 2.9 s TWT characterize the depocenter of salt structure A.*

An intraglacial surface dated 2.1 Ma marks a stronger change in the inclination of the horizons, that become subparallel to the seafloor. The isopach map of the Quaternary deposits shows a thickness range between 0.2 s TWT to 1.9 sTWT, smoothly increasing towards west **(Figure 4.13)**. Despite the time span of the Quaternary sedimentation is less than 1/20 of the Tertiary one, a very important

volume of sediments was deposited, with a sedimentary wedge of up to 2 km thick. Locally, lower values of sediment thickness are registered in correspondence with the salt bodies. On the thickness map of the Quaternary deposits the effect of the crustal faults is not visible anymore, while are visible the glacial erosion marks and the effect of the salt structures presence, which correspond once again to a thinning of the sediments layer. The details of thickness change related to the salt structures will be described in detail in subchapter IV.B.1.4.

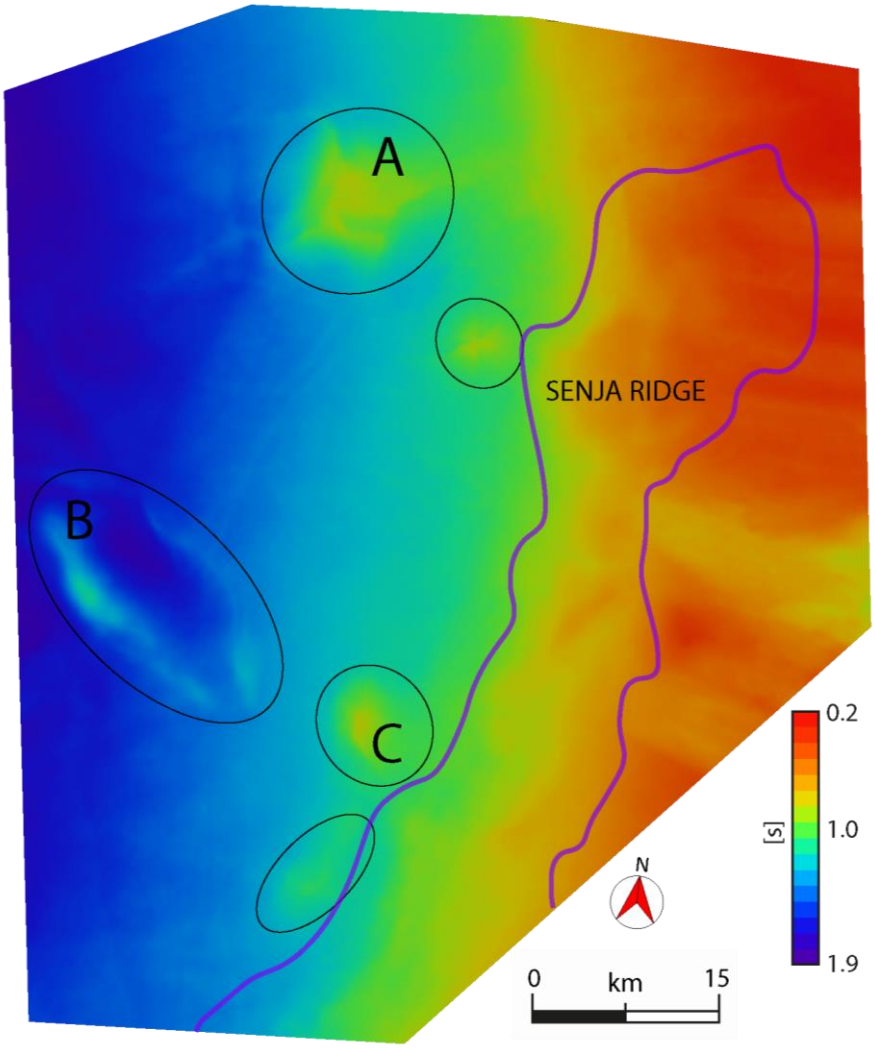

***Figure 4.13**: Thickness map of the Quaternary deposits, i.e. between the Upper Regional Unconformity (2.6 Ma) and the seafloor. The trend of thickening towards west is locally disrupted by the highs due to the salt structures A, B and C.*

IV.B.1.3. Structural analysis

Different families of faults related to crustal and to salt tectonics have been mapped in the 3D seismic dataset, allowing the compilation of a structural map of the area **(Figure 4.14).** The categorization of the faults is based on their mechanisms of formation, and we distinguish between crustal faults, salt related faults, and polygonal faults. In addition to these, some anticlines interpreted in the western area will be briefly discussed.

- The regional normal faults of direction NW to W control the basin architecture and divide the Senja Ridge from the deepest basin (Figures 4.14.1 and 4.14.4). The interpretation of the normal regional faults is mainly the result of the offset analysis of the stratigraphic markers in the seismic profiles (Figures 4.9.1 and 4.9.3) and in the horizons grids (Figure 4.14.4), as well

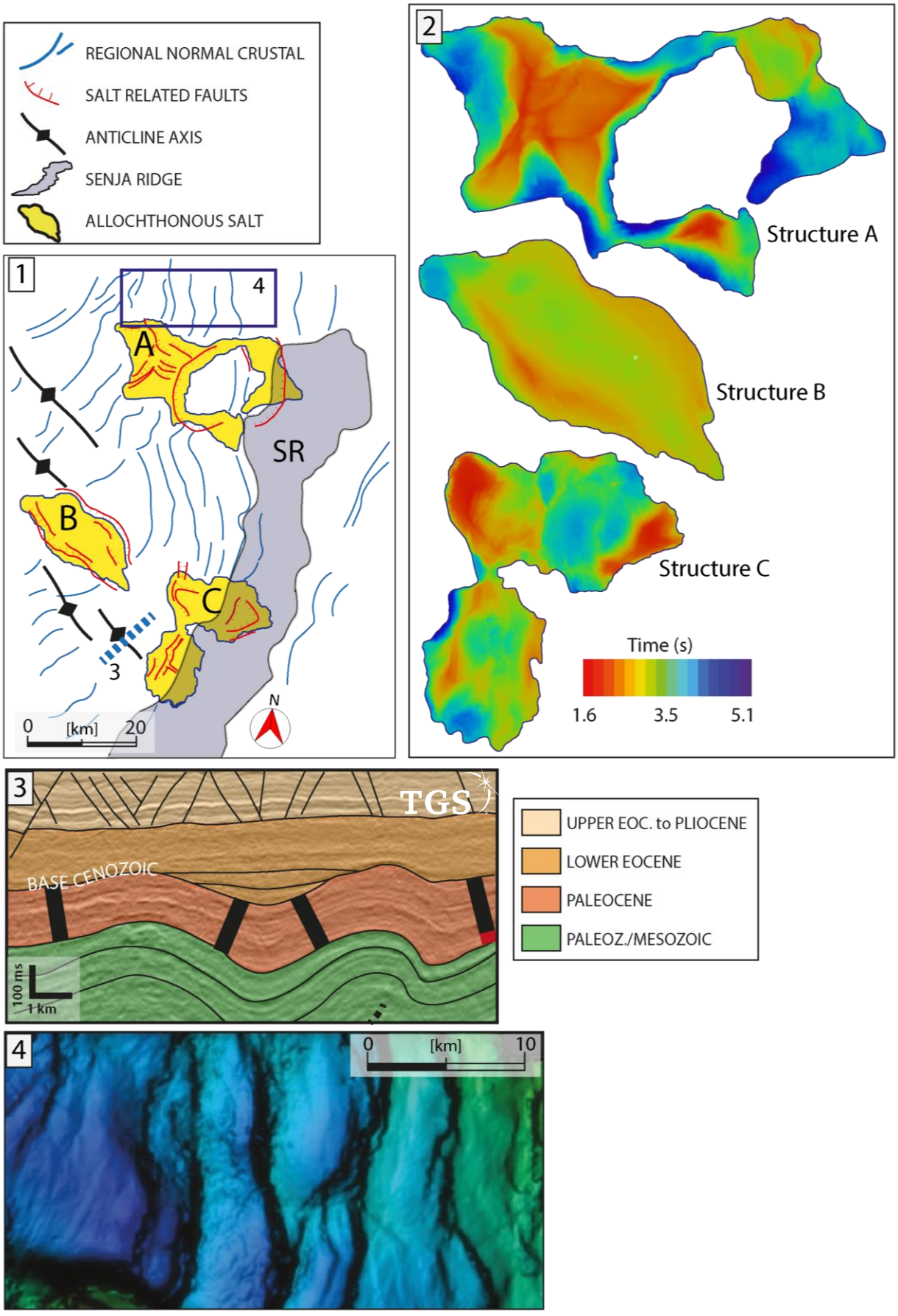

***Figure 4.14**: (caption on next page)*

***Figure 4.14**: Structural setting. **1.** Structural map of the study area from seismic data interpretation, with position of the crustal and salt related faults and the anticlines axes, and the position of the interpreted salt structures A, B and C. The blue rectangle and the dotted blue line show respectively the position of the detail of the Base Cenozoic horizon (.4) and of the seismic profile (.3). **2.** Depth in time of the three salt structures top, between 1.6 and 5.1 s. Structures A, B and C are respectively the northern, western and southern one in the 3D dataset. **3.** Detail of a seismic profile perpendicular to the anticline axis (position in Figure 4.14.1). **4.** Crustal faults expression on the Base Cenozoic horizon (position in Figure 4.14.1). Seismic data courtesy of TGS.*

as the interpretation of the 3D dataset time slices (Figure 4.10). These faults, that present throws of more than 500 ms and a distance between them in the order of a few kilometers, have been previously mapped by Kristensen *et al.* (2018) in the Sørvestsnaget Basin, with partial sovrapposition with our study area. Most of the crustal faults tip out upwards in the Paleocene (Figure 4.9.3), while some reach the mid Eocene horizon above the Senja Ridge, with more limited throws. The deep termination of these faults is not imaged in the seismic data due to the limits of seismic penetration.

- The **faults related to salt tectonics** that are imaged in the seismic data are **multidirectional** and diachronous faults -mostly normal but occasionally reverse- located above or around the allochthonous salt structures (Figures 4.9 and 4.14). These faults are particularly interesting in terms of fluid migrations **(Figure 4.15)** and for the datation of the most recent movements of salt tectonics, evidenced by the Quaternary horizons dislocation **(Figure 4.16)**.

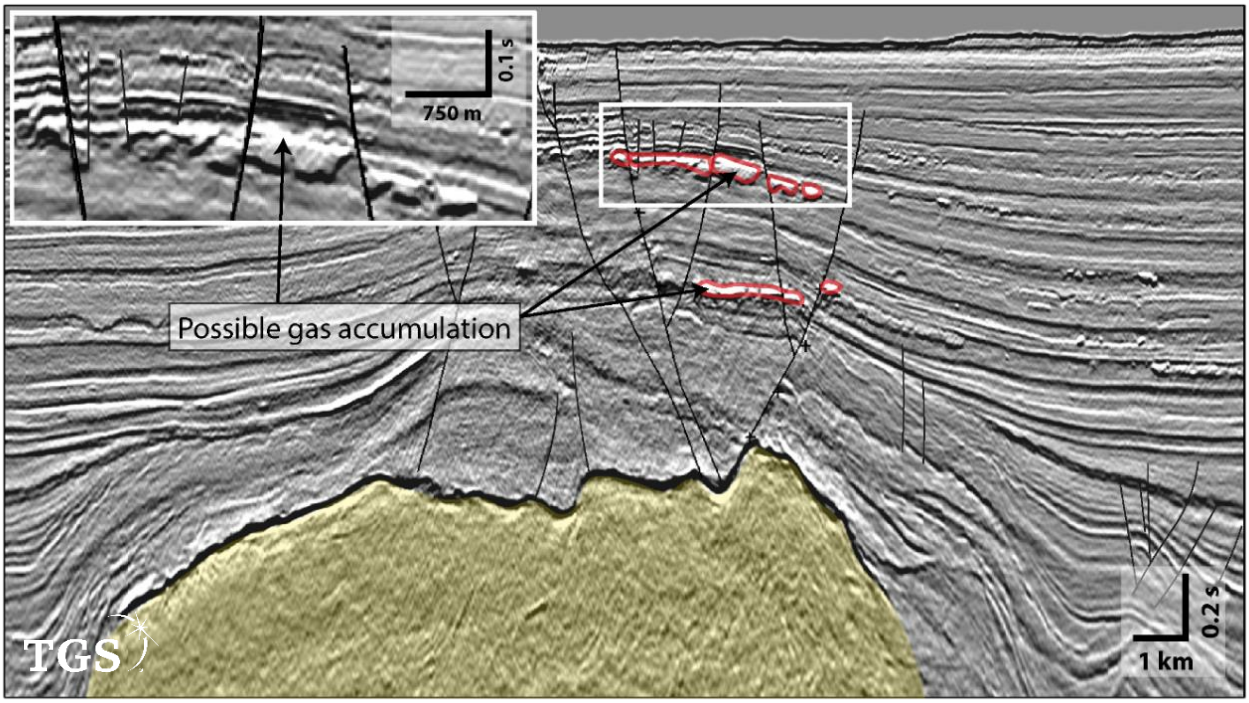

***Figure 4.15**: Detail of the salt related faults above salt structure A (in yellow), with the bright spots identified along the fault highlighted in red. The white rectangle marks the position of the zoom. VE with a seismic velocity of 2000m/s: 5X. Seismic data courtesy of TGS.*

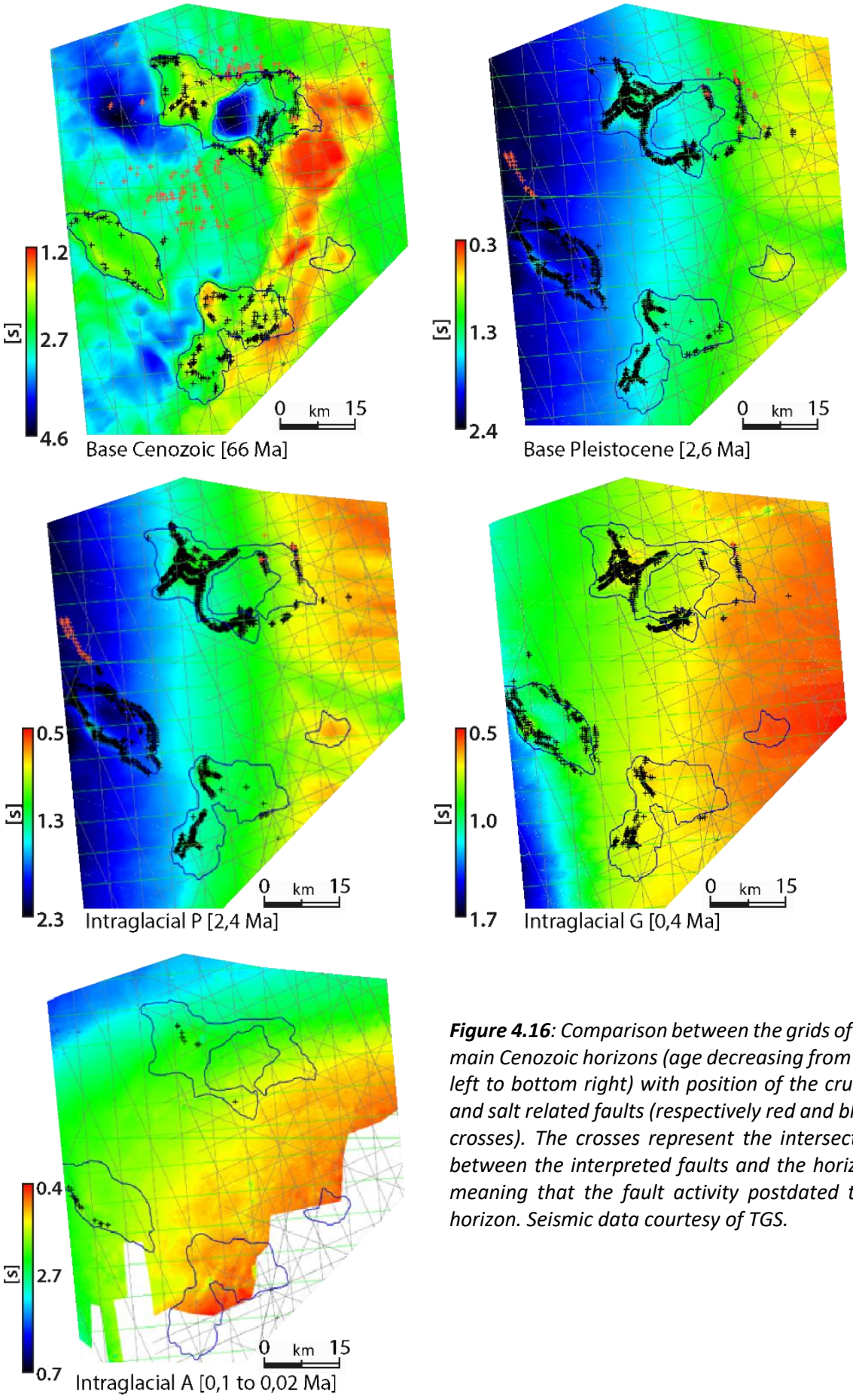

***Figure 4.16**: Comparison between the grids of the main Cenozoic horizons (age decreasing from top left to bottom right) with position of the crustal and salt related faults (respectively red and black crosses). The crosses represent the intersection between the interpreted faults and the horizon, meaning that the fault activity postdated that horizon. Seismic data courtesy of TGS.*

In fact, the salt-related faults are often the most recent sign of deformation –dislocating horizons up to 0.2 Ma and rarely up to present day. Moreover, thanks to their characteristic geometry and to the fact that they are active in the area millions of years more recently than the crustal faults, they constitute an indication for the **detection of limited salt thicknesses**, difficult to observe on the seismic data or on the Bouguer gravity anomaly.

The faults pattern above the salt structures is locally associated to **bright spots**, i.e. areas of high amplitude negative polarity reflections (Figure 4.15). Their position along the salt related faults suggest that they are possible gas accumulation related to the migration of gas along these faults. Salt-related faults, the only actives in recent times, become the preferential path for the rise of gas towards the younger layers.

Given the importance of the salt-related faults, their quantity and variability in terms of geometry and recent activity, we mapped every 8th inlines and crosslines the main –in terms of vertical and lateral extension- salt faults. From the extensive mapping of salt-related faults and the datation of the overburden horizons, we obtained a **regional trend of the salt related faults datation** in our area (Figure 4.16).

As visible from the comparison between the salt faults interpretation and the main Pleistocene horizons, at 2.6 Ma the salt faults activity was widespread, while the percentage of salt related faults reaching a certain horizon gradually decreases towards the younger ones, with drastic reduction between 0.4 Ma and the last glacial maximum, dated 0.1 to 0.02 Ma. The seabed does not present signs of dislocation due to faults activity, and there seems to be no correlation between the position of the pockmarks imaged on the seafloor and the position of the salt related faults.

- Another family of faults interpreted in the 3D dataset is the **polygonal faulting** in the upper Eocene deposits (Figure 4.9). These are multidirectional, closely spaced non-tectonic faults, consequence of fine-grained sediment compaction and fluid expulsion at the end of Eocene (Safronova *et al.*, 2012). These faults, as well as the salt related ones, can have an influence on the fluid flow.

At the western limit of the 3D seismic dataset we interpreted some **anticlines, synclines and fault propagation folds** (Figures 4.14.1 and 4.14.3). The axis of anticlines and synclines has a NW-SE direction, parallel to the western salt structure major axis and sub-orthogonal to regional crustal faults geometry. As visible in the seismic profile perpendicular to the axis of the anticlines (Figure 4.14.3), the Paleocene layers present an almost constant thickness and are strongly deformed, while the strata deposited during Lower Eocene shows onlapping geometries, and parallel and undeformed horizons (i.e. infilling geometries), testifying a compressive episode very limited temporally marking the passage between Paleocene and Eocene. These structures, attributable to compressional tectonics and reasonably not related to salt deformation, were previously partly identified in the area by Kristensen *et al.* (2018), that interpreted them as consequence of transtentional tectonics related to the Senja Fracture Zone.

Some recent faults activity –active up to at least 2.4 Ma - was interpreted at the western limit of the dataset, in close proximity to the western allochthonous salt structure (Figures 4.9.3 and 4.16). Their nature will be object of future studies.

A positive gravity and magnetic anomaly at the south-eastern limit of the Sørvestsnaget Basin, developed in N-S and NNE-SSW direction for a total length of 80 km (Figure 4.9.4), corresponds in

our dataset to the **Senja Ridge**, a high crustal anomaly most likely formed by layered intrusions consequence of crustal extension. The seismic facies varies between transparent and chaotic to deformed parallel stratification with the faults cutting the Mesozoic horizons tipping out upward at the erosional base Cenozoic surface. Some faults activity above the Senja Ridge persisted during Middle Eocene. The different nature of this structure compared to the surrounding Sørvestsnaget sediments is also highlighted by the stacked velocity data (Figure 4.9.2), showing higher values in the Senja Ridge structure. Active during different phases, the Senja Ridge became a positive submarine structure during Early Cenozoic (Ryseth *et al.*, 2003), as testified by the Upper Eocene onlapping on the high (Figure 4.9).

IV.B.1.4. Salt tectonics and salt-related structures

The presence of three massive structures, attributable for seismic characteristics and for Bouguer gravity anomalies to salt bodies, has a huge impact both on the Cenozoic sedimentation and on the fault pattern and consequent fluid migration. We mapped the geomorphology of the allochthonous salt top with a bin size of 12.5 m (Figure 4.14.2), for a total surface of around **750 km²** and a depth range between **1.6 and 5.1 s TWT**. As already mentioned, the autochthonous salt layer is too deep to be imaged, so doubts persist for what concerns the geometry of the connection between the allochthonous and authochthonous salt.

The salt structures described here, although sharing some features, deeply differ one from the other, and will be therefore described –and later discussed- separately. Due to the heterogeneity, structures A and C are further subdivided in several segments.

- ### Structure A

Located between the western side of the Senja Ridge and the deep Sørvestsnaget Basin, the northern structure –from now on **salt structure A**- is constituted by a **main salt body (A1) connected to two minor segments (A2 and A3)**, these ones partly overlapping with the Senja Ridge on the eastern side **(Figure 4.17)**. Segment A2 have been previously interpreted as a separate salt body of limited dimensions (Knutsen and Larsen, 1997), while the connection between the 3 segments is well visible in our 3D dataset. The top of the salt has a total area of **309 km²** and a depth between 1.7 and 3.9 s TWT, i.e. between 1.9 and 4.3 km below sea level using a velocity of 2.2 km/s for the conversion. The top of the salt, as visible in Figure 4.17, shows salt cusps that correspond to the shallowest positions of this horizon, separated by convex areas presenting the higher values of **RMS amplitude** (Figure 4.17.2) potentially attributable to caprock.

The thickness of the allochthonous salt (Figure 4.17.3) is between 0 and 2.7 s TWT, i.e. 0 to 5.4 km calculated, with a certain level of uncertainty due to the very low amplitude of the base salt horizon. The major thickness corresponds to the central part of sector A1, while the salt layer thins towards the edges of the salt structure. Particularly thin is the salt in the southeastern part, in which the interpreted presence of salt in an area of around 40 km² of lateral extension has been suggested by the geometry of the faults (Figure 4.14.1). The isopach map of the salt thickness does not consider the possible presence of a root of the structures, potentially still connecting it to the autochthonous salt. To improve the calculation of this thickness map could be useful to model the gravity anomalies and do a gravity inversion.

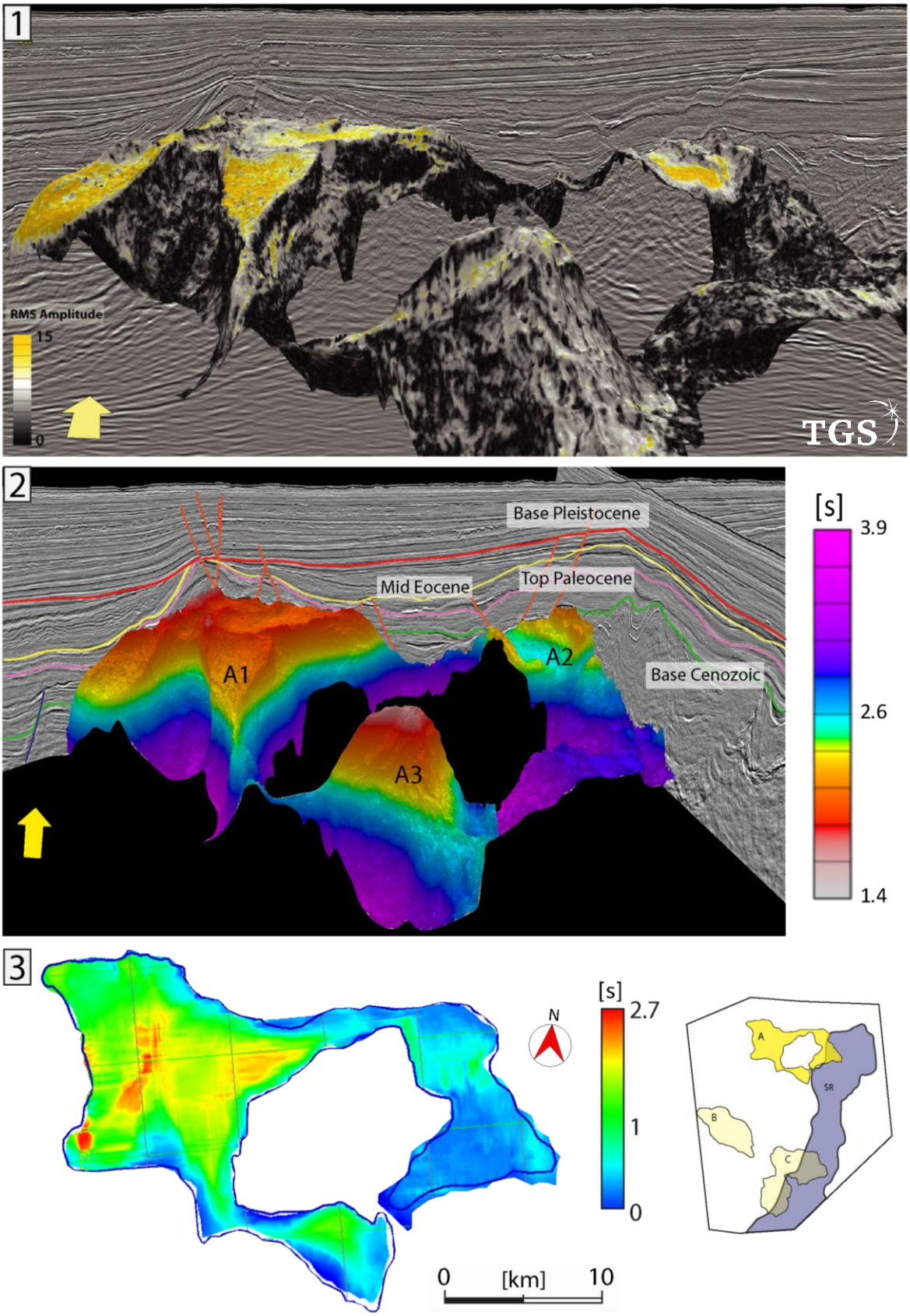

***Figure 4.17**: Salt structure A. **1.**: 3D visualization of the RMS amplitude seismic attribute applied on the Top Salt horizon of salt body A, and seismic profile imaging the area. The yellow arrow shows the north direction. **2.**: 3D visualization of Top Salt horizon of salt body A, and seismic profile imaging the area with interpretation of the main seismic horizons. The allochthonous salt structure has been divided in sectors A1, A2 and A3, due to the differences in the geometry and evolution. **3.**: Thickness of the allochthonous salt structure A, in s TWT. Maximum thickness value is more than 5 km. Seismic data courtesy of TGS.*

To the complexity of the salt structure is also associated an elaborate pattern of **salt related faults** (Figure 4.14.1 and 4.15). The faults of sectors A1 and A2 are mostly faults that extend from the salt cusps, while a fault of tens of km length surrounds the western side of the depocenter dividing the three sectors. In proximity of the Senja Ridge (A2), some faults active up to the Quaternary mark the upslope position of the allochthonous salt. To these salt related faults is associated, as already mentioned, the presence of bright spots (Figure 4.15).

Segment A1 (Figure 4.18) constitutes the **main body** in terms of salt volume, with a calculated thickness of up to 5 km but with a significant degree of uncertainty.

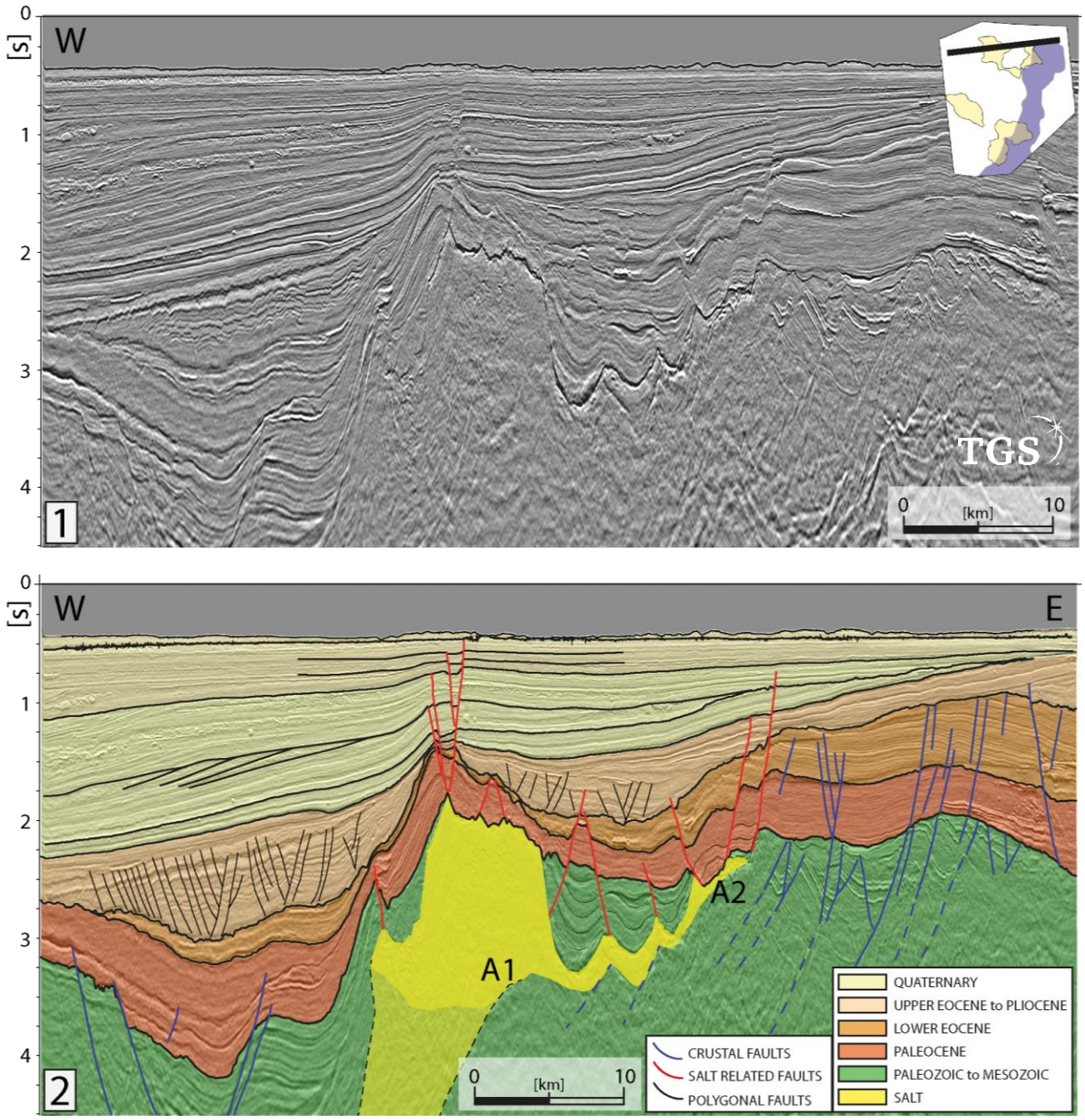

***Figure 4.18**: Seismic reflection profile imaging sector A1, uninterpreted **(1.)** and interpreted **(2.).** Due to the uncertainties on the geometry of the base of the salt, the possible salt shape is marked with dotted lines. VE with a seismic velocity of 2000m/s: 8X. Seismic data courtesy of TGS.*

The **salt cusps** geometries described for the whole salt structure are well visible in this sector, while the infilling geometries between the cusps are partly cancelled by erosion. Except for some localized Mesozoic blocks, the top of the salt is in direct contact with the Paleocene sediments, which are thinner above the salt -but without evidences of growth strata- and present steep internal reflectors testifying the important tilting following the deposition.

Connected to Segments A1 by a salt tongue and located at the western flank of the Senja Ridge, **segment A2 (Figure 4.19)** is a smaller salt body of only **500 meters** estimated salt thickness. Salt horns mark the NE and SW boundaries of the structure, and some indented faults extend from the **salt horns** and terminates in the Quaternary sediments, with a calculated fault offset of more than 300 meters in the Paleocene sequence. For what concerns the Paleocene and Early Eocene units above the salt, the thickness is comparable to the one in the surrounding areas but slightly higher in correspondence with the central part of the salt body, forming an **anticline** dated Lower Eocene.

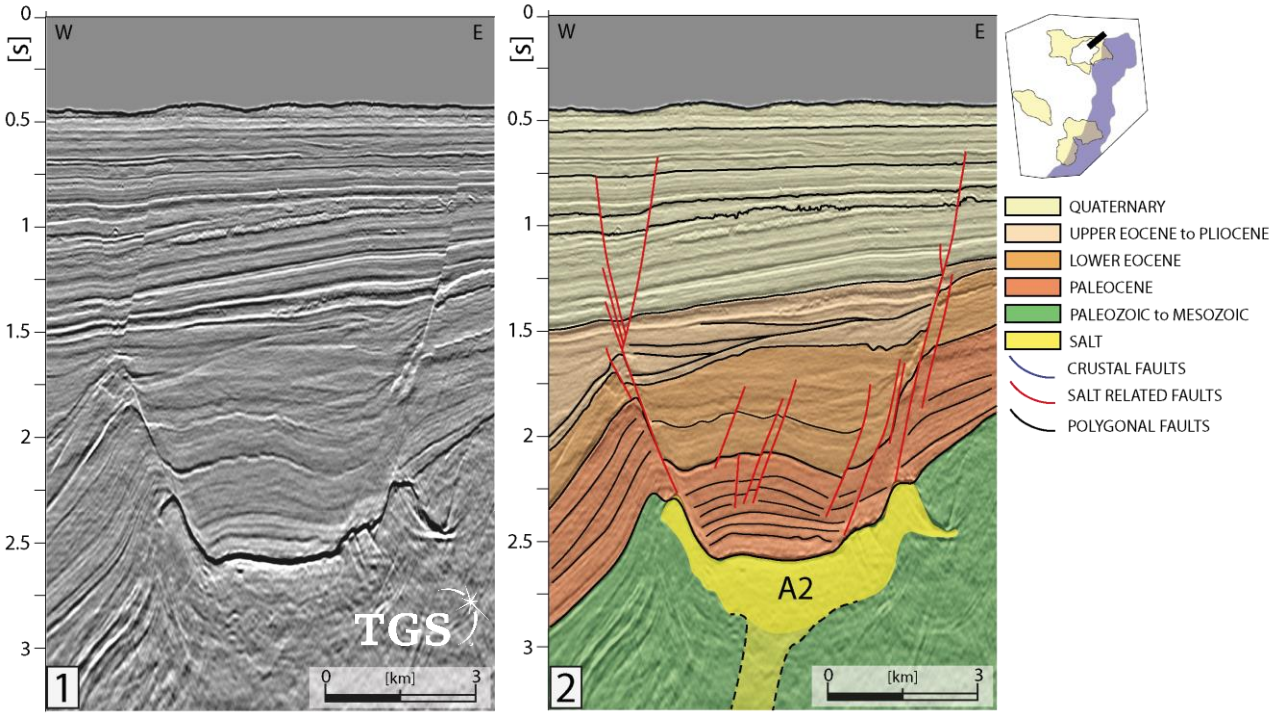

***Figure 4.19**: Detail of the seismic reflection profile imaging sector A2, uninterpreted **(1.)** and interpreted **(2.).** VE with a seismic velocity of 2000m/s: 4.2X. Seismic data courtesy of TGS.*

This geometry indicates a syn-salt tectonic sedimentation, that will be examined in the discussion.

The top of salt structure A reaches the shallowest position in **segment A3 (Figure 4.20)**, with values of 1.4 s TWT below sea level, a thickness around 1.5-2 km and **no sign of diapir fall**. Here the oldest detectable geometries of growth are dated late Cretaceous, with uplifted and tilted horizons and slightly fan shaped geometries (Figure 4.20.1). The Paleocene registers evident fan shaped geometries, with thinner layers towards the salt structure testifying the phase of maximum growth of the structure. The Upper Paleocene to Eocene shows onlapping horizons and limited deformation, and the deformation during Quaternary is limited to the movement along the salt-related faults, active up to few hundreds of thousands years ago. The conformation of the normal faults and of the horizons above segment A3 testify the presence of a crestal graben active up to Eocene.

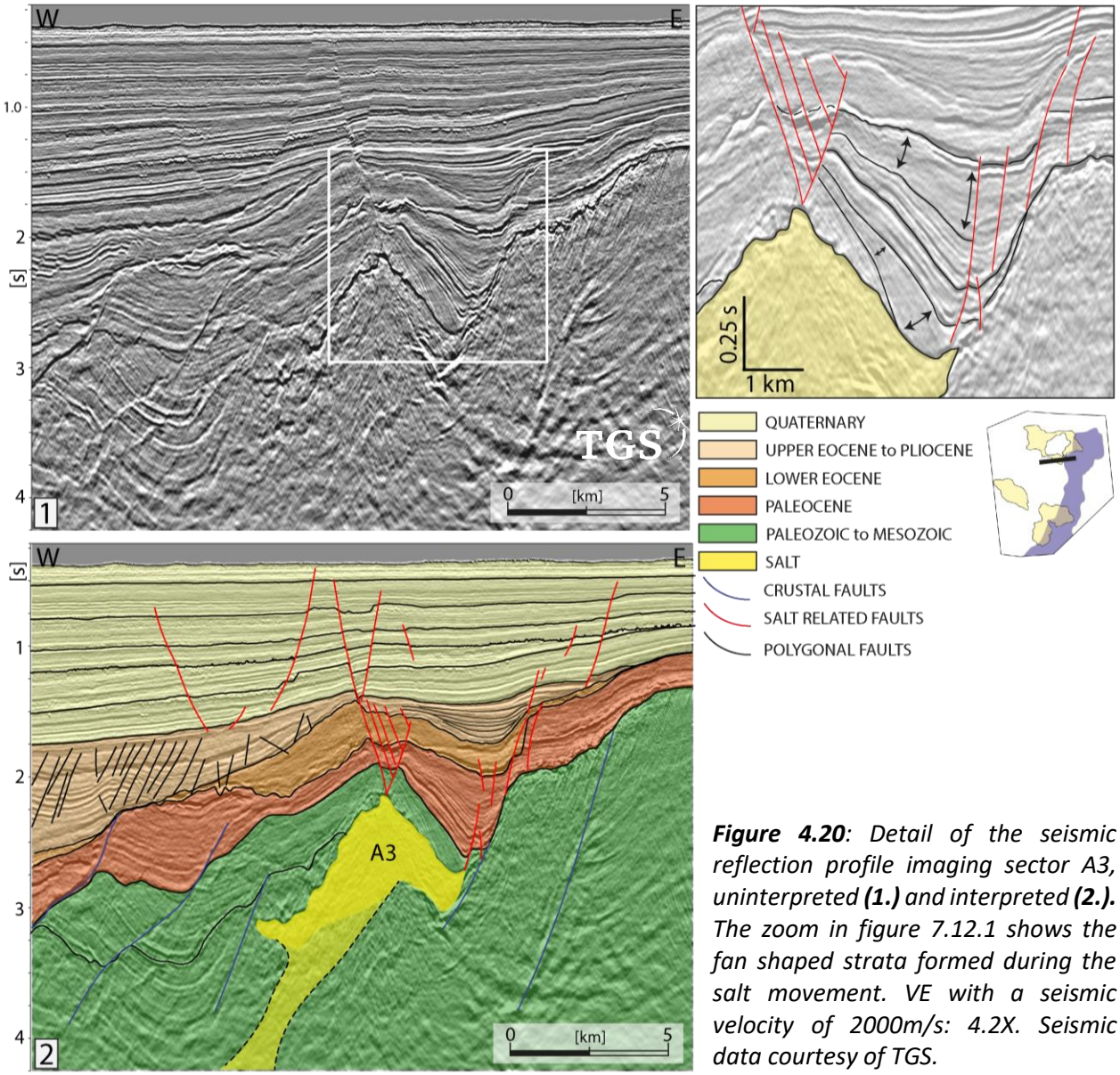

***Figure 4.20**: Detail of the seismic reflection profile imaging sector A3, uninterpreted **(1.)** and interpreted **(2.).** The zoom in figure 7.12.1 shows the fan shaped strata formed during the salt movement. VE with a seismic velocity of 2000m/s: 4.2X. Seismic data courtesy of TGS.*

Enclosed between segments A1, A2 and A3, a **Eocenic-Pliocenic depocenter** is clearly visible both in the seismic data **(Figure 4.21)** and in the time slices at 2000, 2500, 3000 ms (Figure 4.10), as well as in the Tertiary sediments isopach map (Figure 4.12). The Paleocene seismic sequence has constant thickness, and the horizons are deformed in a syncline geometry. The Lower Eocene sequence shows the first marks of a syndepositional movement, with the thickness of the layer thinning mainly towards sector A2 and thickening in the central part of the depocenter. Also the Upper Eocene has a marked thinning and onlap geometries towards sector A2, but with a lighter deformation compared to the previous layer. The situation changes during Pliocene, when the sediments thin and onlap towards sector A1. The end of the activity of this depocenter is dated Upper Eocene to Pliocene.

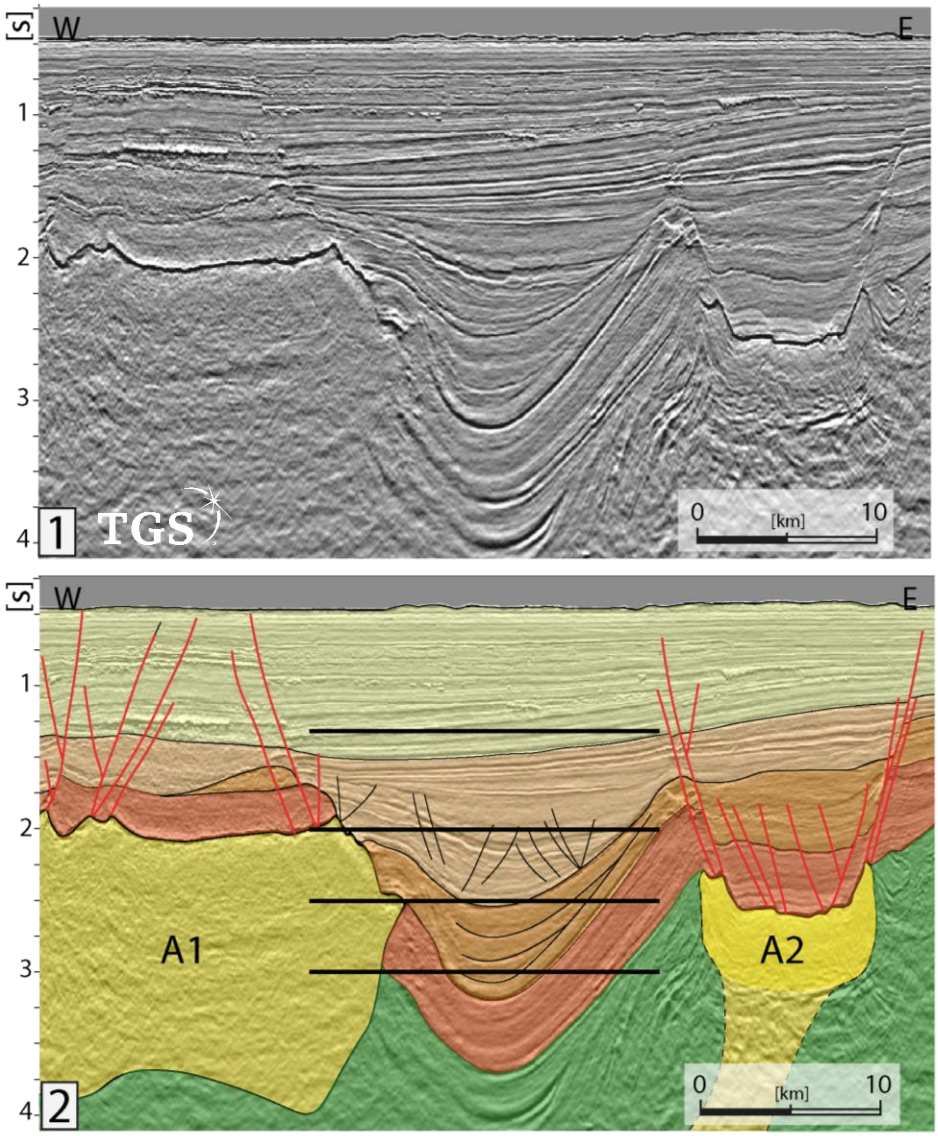

***Figure 4.21**: Detail of the seismic profile imaging the depocenter located between A1 and A2, uninterpreted **(1.)** and interpreted **(2.),** and position of the timeslices of figure 4.10 (black horizontal lines). VE with a seismic velocity of 2000m/s: 8X. Seismic data courtesy of TGS.*

- **Structure B**

Located in proximity of the Senja Fracture Zone and near the compressional structures, **salt structure B (Figure 4.22)** presents a regular elliptical shape in map view, elongated in a NW-SE direction. The top of the salt has a surface of 175 km² and a depth between 1.8 and 3.1 s TWT, shallower in the southwestern part and deeper in the central part (Figure 4.22.2), and a calculated maximum thickness of around 3 km of salt (Figure 4.22.3). This salt structure has a trend of thickening towards the center, rather symmetrical but with a more abrupt thickening towards southwest. The northeastern margin of the structure, slightly deeper than the southwestern one, has **salt cusps** geometries **(Figure 4.23)**, while the convex zone has high **RMS** amplitude values also thanks to the relatively flat top of the salt (Figure 4.22.1). The geometry of the **base of the salt** is partly visible, and results to have a shape rather similar to the top, with a depth in the central part of almost 4 s TWT. Where the salt is thin enough, it is possible to visualize that the allochthonous salt lays on the steps of the rotated faulted blocks.

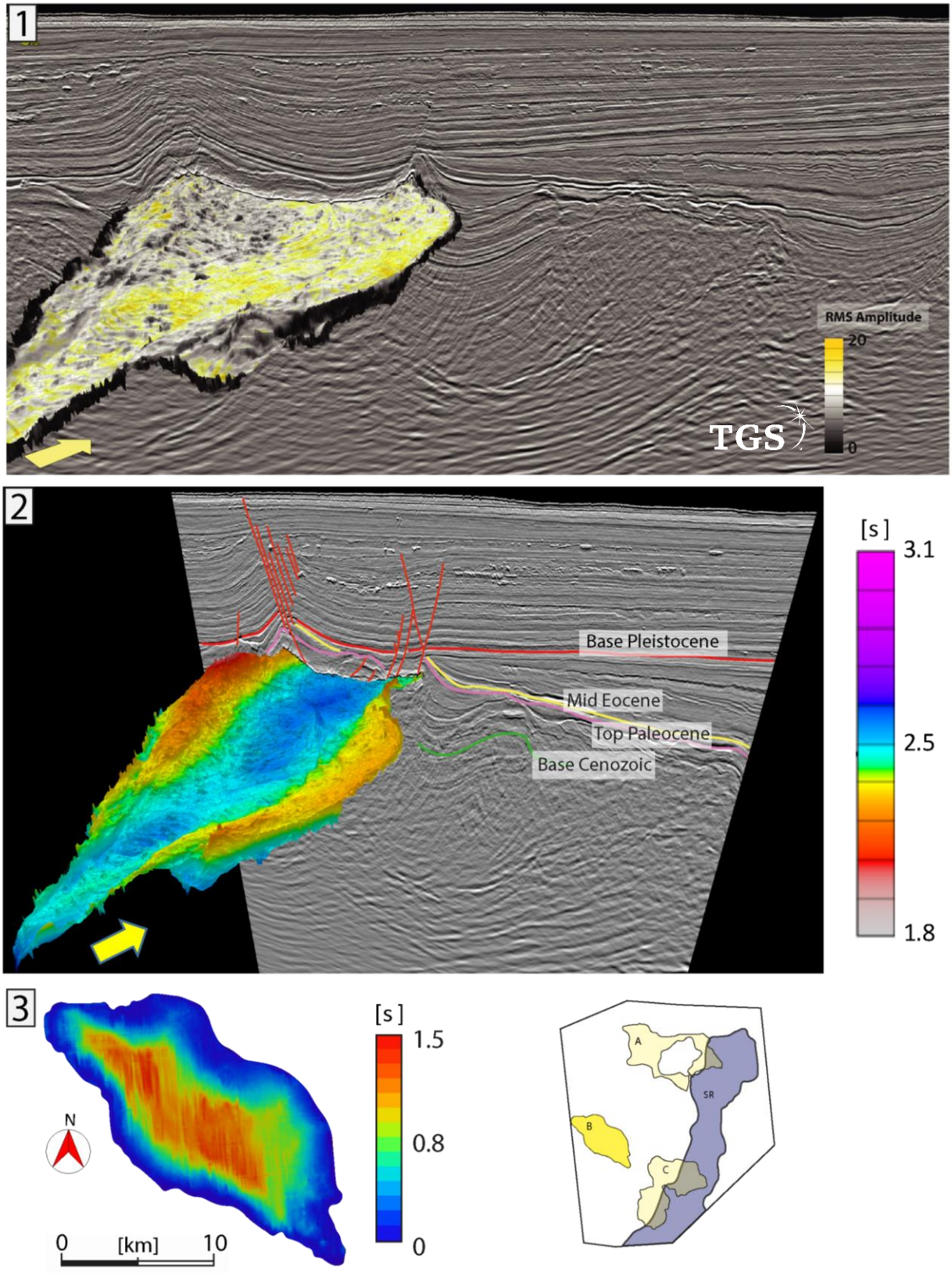

***Figure 4.22**: Salt structure B. **1.** 3D visualization of the RMS amplitude seismic attribute applied on the Top Salt horizon of salt body B, and seismic profile imaging the area. The yellow arrow shows the north direction. **2.** 3D visualization of Top Salt horizon of salt body B, and seismic profile imaging the area with interpretation of the main seismic horizons. **3.** Thickness of the allochthonous salt structure B, in s TWT. Maximum thickness value is around 3 km. Seismic data courtesy of TGS.*

The fault pattern above the salt follows the shape of the salt structure (Figure 4.14), with a graben along the southwestern side and a graben and semi-graben along the northeastern one. Numerous minor faults along a salt related anticline are present on the NW part **(Figure 4.23)**.

As visible in the SW-NE seismic profile (Figure 4.23), the base of the Cenozoic corresponds here with the top of the salt. The thickness of the sedimentary sequence above this allochthonous salt body is significantly thicker compared to structures A and C (Figure 4.13), but the sediments are mostly Paleocene for lack of deposition or successive erosion of Upper Eocene to Pliocene sediments, limiting the possibility to reconstruct the salt movement during Paleogene.

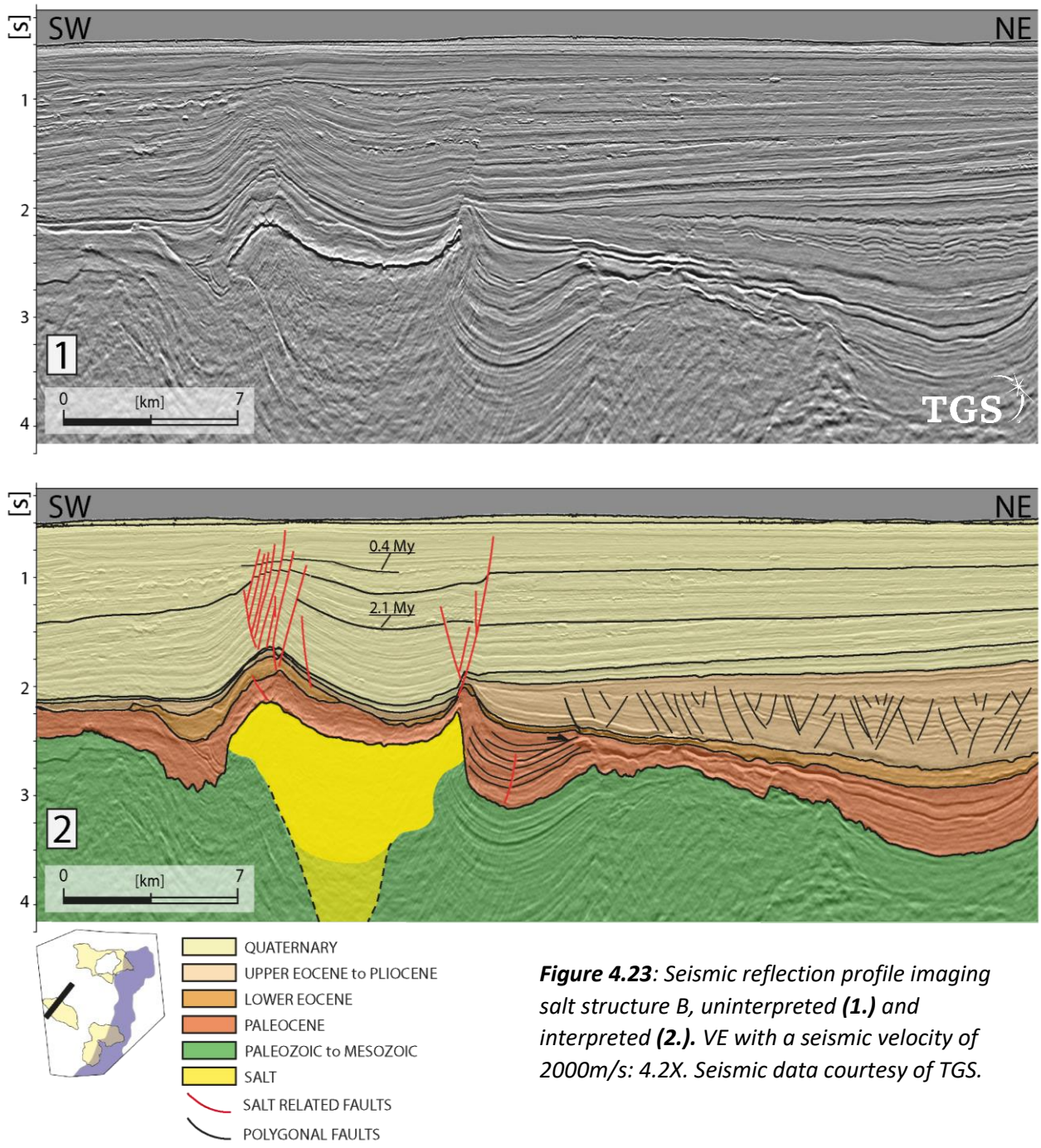

***Figure 4.23**: Seismic reflection profile imaging salt structure B, uninterpreted **(1.)** and interpreted **(2.).** VE with a seismic velocity of 2000m/s: 4.2X. Seismic data courtesy of TGS.*

At the northeastern margin of the salt we interpreted a Cretaceous to Lower Paleocene sequence showing no significant thickness variations but marked anticline geometry, sign of a pre-kinematic deposition followed by deformation, and an Upper Paleocene sequence presenting infilling geometries, suggesting that the formation of the allochthonous salt body predates the end of the Paleocene. For what concerns the Pleistocene sedimentation, constituting most of the salt overburden, we distinguish between sediments older than 0.4 Ma deformed by an anticline at SW, and more recent sediments onlapping on this anticline and presenting minor deformation.

- ## Structure C

The southern salt structure C **(Figure 4.24)** is in proximity and partial sovrapposition with the southern Senja Ridge (Figure 4.14.1). Interpreted in literature as a diapir of 16 km² (Knutsen and Larsen, 1997), it actually has a total surface of **262 km²** and irregular geometries of the base and top, with a depth of the top between **1.3 and 3.9 s TWT**, the deeper values corresponding to the thinner salt. The maximum calculated thickness reaches almost 5 km in the segments C1, C2, and on the western side of C4, while in C3 the salt results particular thin, with local salt welds. Between the three allochthonous salt structures analyzed here, structure C registers the lowest values of RMS amplitude.

In the seismic reflection profile of direction NW-SE **(Figure 4.25)** are visible two areas of major salt thickness (C1 and C2) connected by a thinner salt layer (C3), the latter covered by 1 km of Cretaceous sediments cut by a graben-like fault pattern. These faults are coeval with the crustal faults in the area, but their geometry is influenced by the presence of salt, that leads to shorter wavelength and a multidirectionality of faulting. On the NW side, the Paleocene and Lower Eocene sediments are tilted and uplifted by the growth of segment C1, and the Paleocene layers are thinner above the salt segment. The Lower Eocene presents both onlapping horizons, fan shaped strata and post depositional deformation, as well as partial erosion, while the Upper Eocene strata have onlapping geometries and limited deformation. Minimum deformation is registered after the end of the Eocene.

In the southwestern part of the profile (Figure 4.25), segment C2 crosscuts the Cretaceous sediments but no sign of salt-related deformation is present in the Cenozoic sediments. Due to the absence of clear salt tectonics deformation and fault patterns above C2, there are still some doubts about the nature of this segment, which, however, appears to show a negative gravity anomaly compatible with a salt body. A confirmation would be possible from a detailed Bouguer gravity anomalies survey. Connecting segments C1 and C2, segment C3 is a thinner layer of salt of few hundreds meter thickness with salt anticlines filling the space formed by the normal faults in the Mesozoic layers. This segment is particularly interesting because the geometries of reactive diapirism - that we will discuss in further detail in the discussion chapter- are particularly clear. Sector C4 presents an important salt thickness in the western area, and above it a crestal graben was active at least up to 0.4 Ma (Figures 4.14.1 and 4.16)

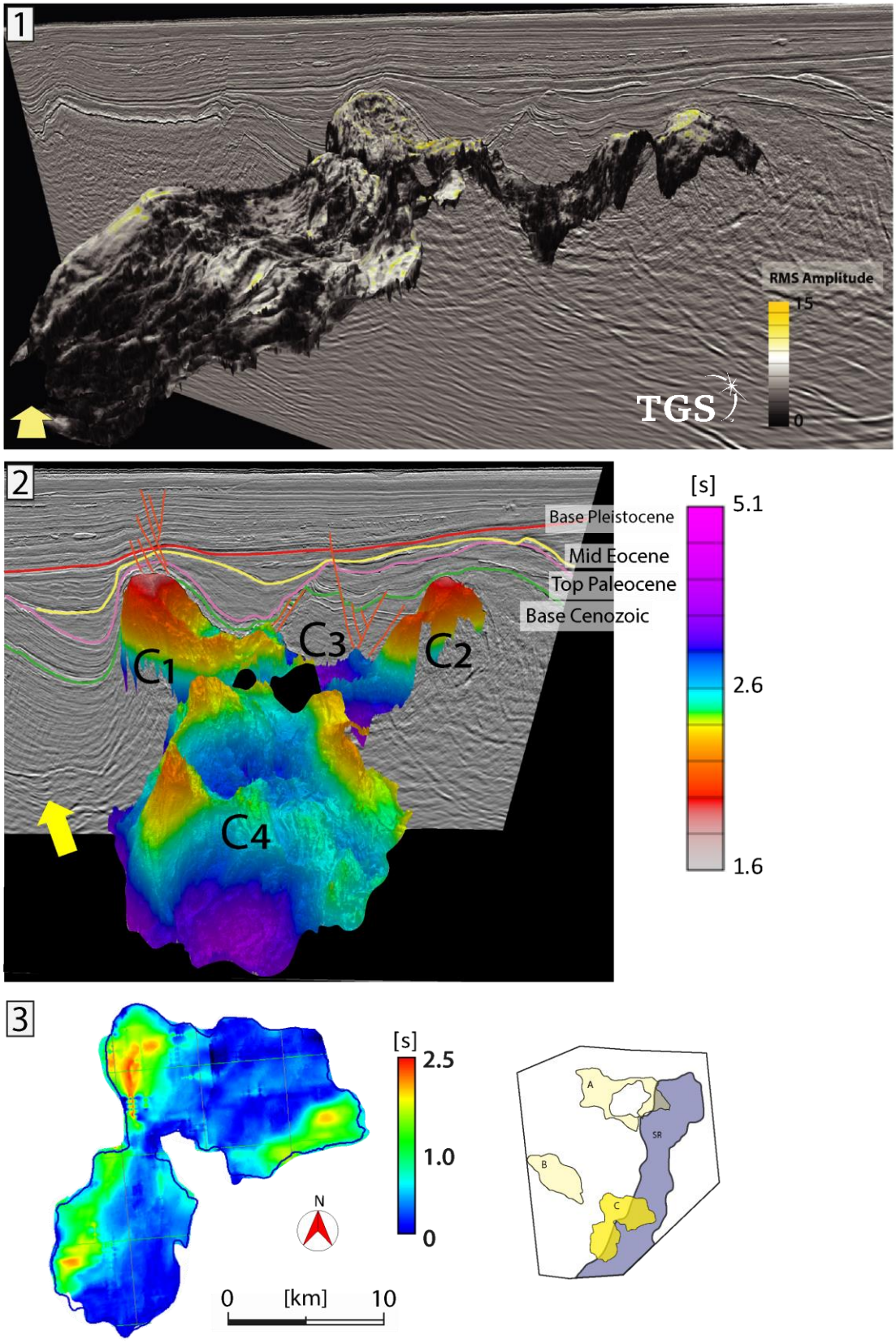

***Figure 4.24**: Salt structure C. **1**. 3D visualization of the RMS amplitude seismic attribute applied on the Top Salt horizon of salt body C, and seismic profile imaging the area. The yellow arrow shows the north direction. **2.** 3D visualization of Top Salt horizon of salt body C, and seismic profile imaging the area with interpretation of the main seismic horizons. The allochthonous salt structure has been divided in sectors C1, C2, C3 and C4. **3.** Thickness of the allochthonous salt structure C, in sTWT. Maximum thickness value is around 5 km. Seismic data courtesy of TGS.*

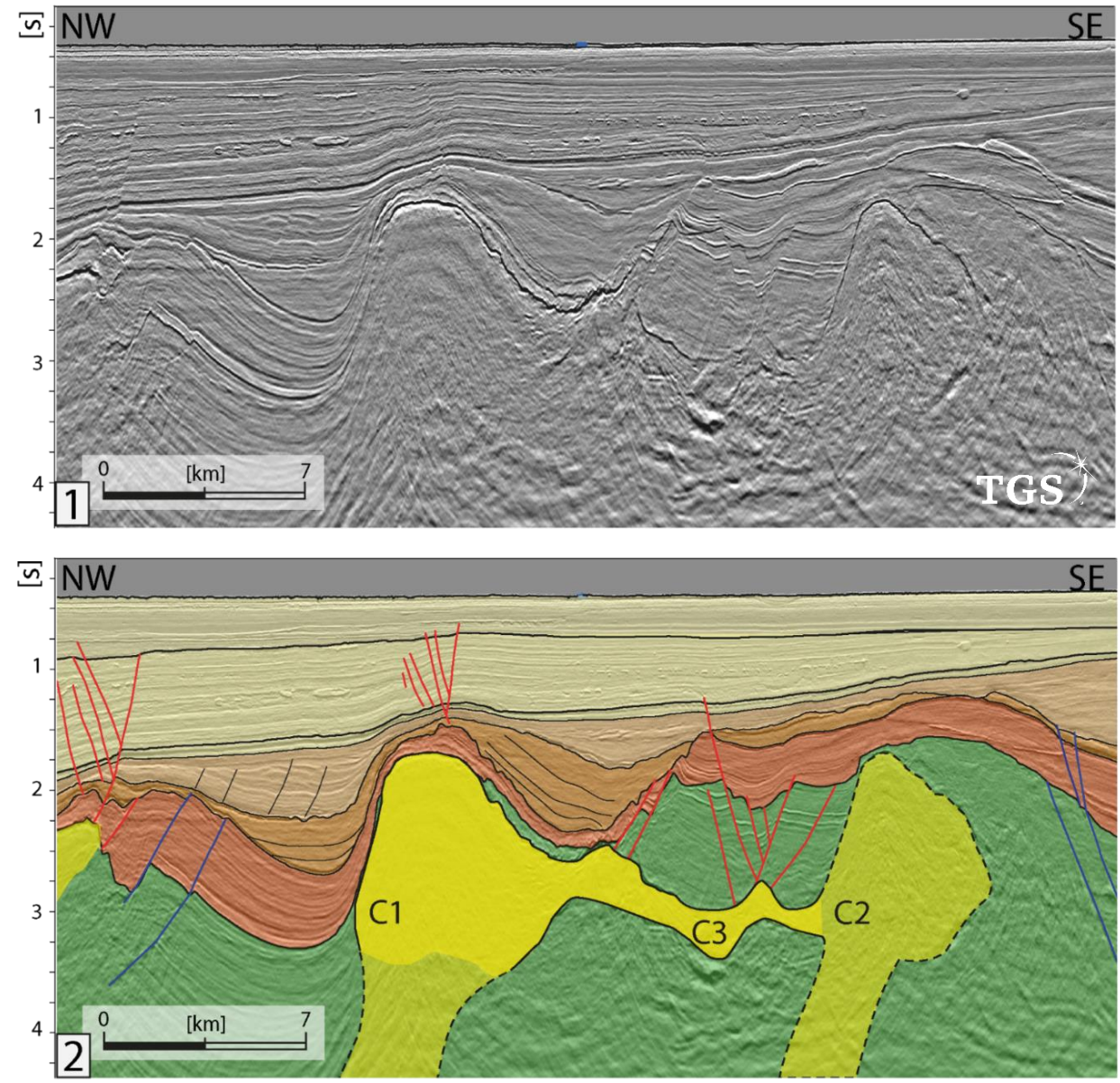

***Figure 4.25**: Seismic reflection profile imaging salt structure C, uninterpreted **(1.)** and interpreted **(2.).** The uncertainties about sector C2 are highlighted by the dotted line. VE with a seismic velocity of 2000m/s: 4.2X. Seismic data courtesy of TGS.*

IV.B.2. Analogue modelling of the Sørvestsnaget Basin salt tectonics

Following the interpretation of the geophysical data, we formulated some hypothesis on the formation of allochthonous salt structures in response to regional extensional tectonics, as well as on their recent development in a post-rift phase.

In particular, given the heterogeneity of the allochthonous salt imaged in the area, we decided to focus on the formation and evolution of the northern salt structure A **(Figure 4.26)** where the elements to consider for the modelization are, starting from the older sedimentary sequence, the followings:

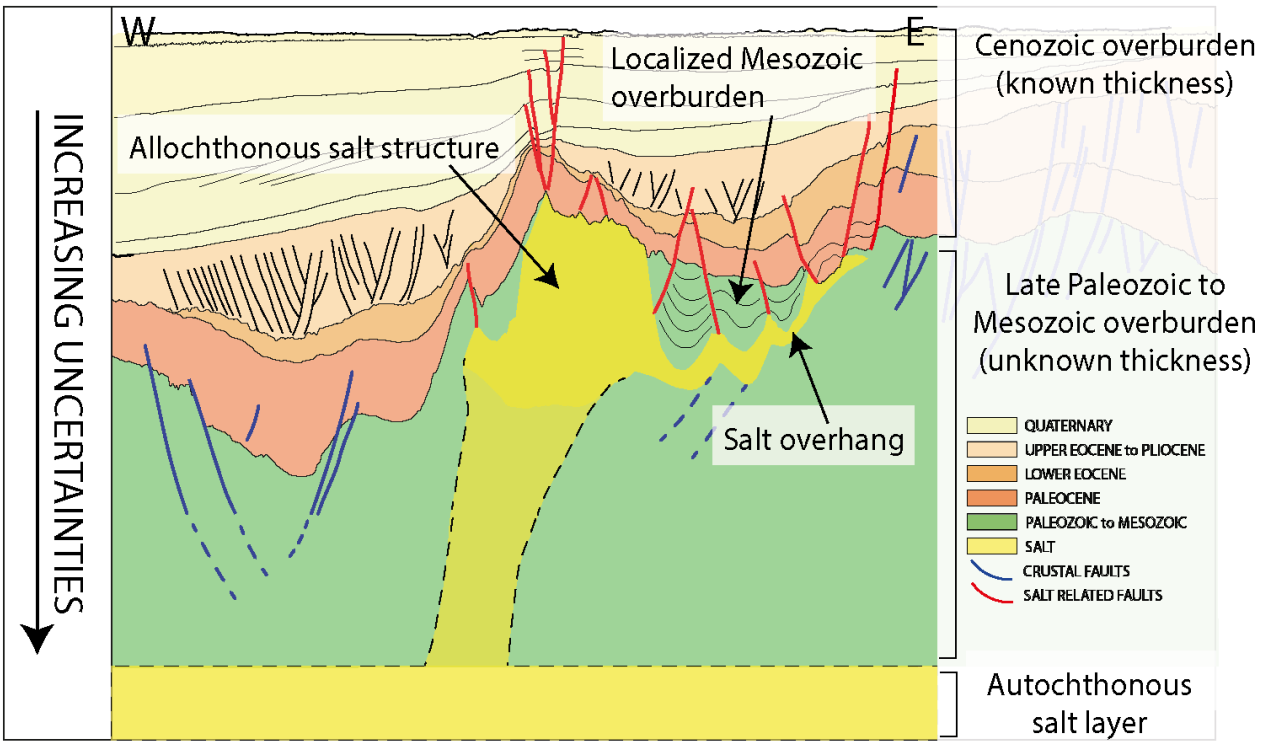

***Figure 4.26**: Schematization of the elements to model based on the seismic interpretation of Figure 4.18: an autochthonous salt layer, a Late Paleozoic to Mesozoic overburden, an allochthonous salt structure with a salt overhang, a localized late Mesozoic overburden and the thick Cenozoic sedimentary sequence. The Late Paleozoic to Mesozoic overburden and the autochthonous salt layer are not to scale due to the lack of seismic imaging at that depth.*

.A layer of **autochthonous salt**, which depth, thickness and distribution are not imaged in the seismic data due to the several km-thick layer of overburden sediments. Due to the uncertainties, we use a isopach silicone layer in the models.

.A **thick Late Paleozoic-Mesozoic overburden** partly imaged in the seismic data, which total thickness is unknown. Crustal faults (blue lines and dotted lines in figure 4.26) cut this sequence.

.An **allochthonous salt** structure, well imaged in the seismic data, composed by a main body and a several km long overhang. Different phases of movement of this structure, both syn- and post- crustal tectonics, have been recognized from the interpretation of seismic reflection data in the area. Recent salt movement postdates the end of the crustal faults

activity, and salt related faults (red ones in the figures) cut the overburden up to horizons as young as 20k years.

.A **localized Late Mesozoic overburden** is present above the salt overhang, and cut by numerous faults.

.A **thick Cenozoic sedimentary sequence** occupy a big portion of the imaged subsoil. More than half of the volume of this sedimentary sequence is composed of Quaternary sediments, due to the high sedimentation rate during the glacial and interglacial events.

Based on these observed elements, we produced some analogue models to reconstruct the long-lived movement of salt in the Southern Sørvestsnaget Basin in reaction to an extensional crustal tectonics and to clarify the mechanisms of recent salt tectonics in the area, i.e. the influence of localized sedimentation and a slope formation on the late (post-crustal tectonics) salt deformation. As well as in the models of the Algerian margin (Chapter III.C.2), the salt layer will be modelled through a layer of silicone, while the brittle behavior of the rocks will be modelled through layers of sand (granulometry 125-315 µm). Different models have been done between end of March and April 2021, with the collaboration of Etienne Van Broeck during his stage of bachelor at the University of Lille.

IV.B.2.1. Experimental protocol

Scaling: We used a 1:10 000 geometrical scaling in our model, so 1 cm of material corresponds to 1 km in the natural example. As already mentioned, there is a strong level of uncertainty about the thickness of autochthonous salt and the Late Paleozoic to Mesozoic overburden. Therefore, the thickness used in the model will be more related to technical aspects than to a scale reproduction of the hypothesized actual dimensions.

Salt thickness scaling: The thickness of the initial layer of silicone we use in the model is based on our considerations about what thickness of silicone -if we consider it as homogeneous in the area- is necessary to have enough material to develop an allochtonous silicone structure, and able to move fast enough to respect our technical constrains. A layer of silicone too thick would result in faster salt tectonics and a difficulty in the slicing of the model.

Overburden thickness scaling: Because of the same problem of data penetration, the **Late Paleozoic to Mesozoic overburden** is not to scale, and its thickness has been decided based on the possibility to properly model an allochthonous salt structure, i.e. what thickness of sand is necessary to have enough pressure above the silicone layer for the development of the silicone structure. Different protocols of deposition in terms of thickness and geometries will be applied in the different models.

For the **Cenozoic overburden**, well visible in the seismic data, the scaling was mostly based on seismic data interpretation. Being the model produced before we had access to the TGS interval velocities data, we used a seismic velocity of 2000 m/s to convert the Cenozoic brittle overburden thickness and 4000 m/s for the salt one. This level of approximation is reasonable in the case of analogue models, where the objective is to recreate a simplified version of the natural example.

In terms of **temporal scale**, the duration of the different phases of the model is mostly dependent by two factors:

- The **silicon mobility**, which in turn depends on other factors such as temperature, sand content in the recycled silicone etc. The time necessary to produce the interpreted structures varies also due to the thickness of the autochthonous salt layer, which is unknown in the area.
- Constrains related to the laboratory accessibility during the night **(human constrains)**: we had to pause the sedimentation during the night due to the impossibility to spend the night in the laboratory, but due to the viscous rheology of the silicone the model did not stop moving.

Experimental box

For this model we built a very simple box, with four fixed walls and no motor to deform the box during the experiment. The base of the box is a metal table on which we positioned two glass panels of 1 meter each in a E-W direction and two wood panels of 50 cm each in a N-S direction. The result is a delimited rectangle of 92 x 50 cm, and the maximum possible height of the model is constrained by the glass panels (20 cm height) **(Figure 4.27)**. After the first model, we realized that the table that served as the base of the box was not sturdy enough and a curvature of the base of the model was produced when the load of silicone and sand became important, consequently a new box model was built to have a more stable base while maintaining the dimensions of the previous one. As marked in figure 4.27, the box is divided in different areas based on the actions that will be carried out during the experimental procedure.

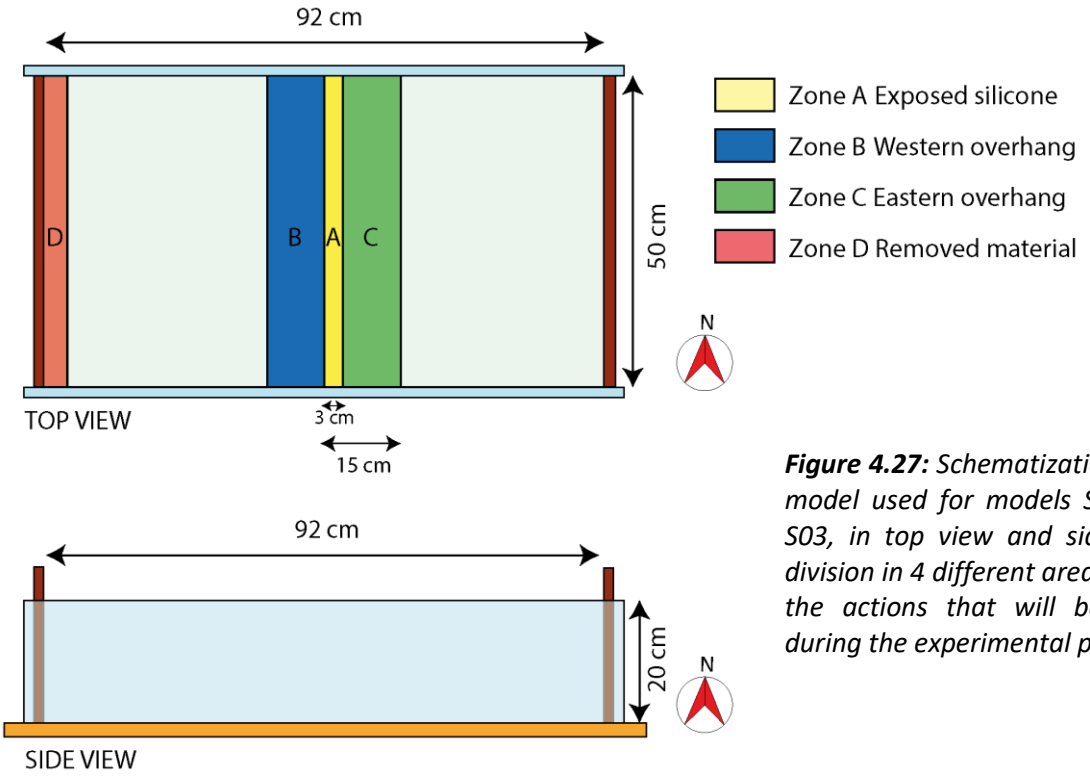

Figure 4.27: *Schematization of the box model used for models S01, S02 and S03, in top view and side view. The division in 4 different areas is based on the actions that will be performed during the experimental procedure.*

Zone A: located in the center of the box model in a N-S direction, this area of 5 x 90 cm marks the position where the thickness of the overburden will be reduced by means of a vacuum to leave space to the main silicone structure to form.

Zones B and C: these represent the surface where the silicone overhangs will develop. The western overhang (Zone B) will be removed manually from the model, while the eastern overhang (Zone C) will be kept in the model to analyze the secondary salt tectonics. Above the overhang of zone C will be added some localized sedimentation.

Zone D: at the western limit of the box model, this part of the model is strongly affected by edge effects, and silicone and sand will be regularly removed during the experiments to create a free edge and leave space to the model to develop.

The experimental protocol for this model can be schematically divided in two main phases. During the first one the allochthonous silicon structure is formed, while during the second one we analyze the post-tectonics evolution of the allochthonous structure:

1. **Modelling of the extensional phase:** We know from literature and from the seismic reflection data that the Sørvestsnaget Basin has undergone long lived extensional crustal tectonics. The most efficient way to model a phase of extensional crustal tectonics -also to have a control on the position in which the modelled salt structure will develop- is through its consequence, i.e. a thinning of the overburden. Therefore, we remove sand from the central part of the box model through a vacuum to model this localized thinning. This way of recreating the extensional tectonics is particularly convenient because it does not need a driving motor. Moreover, it allows to decide the position of the salt structure, that can therefore be located at the center of the box, far from the edge effects and with enough space for the overhangs to develop.
2. **Post tectonics evolution of the allochthonous salt:** As visible in the seismic data, salt tectonics has been active in the area for a long time after the end of crustal tectonics. In particular, the recent salt movement above a salt overhang will be analyzed in terms of possible mechanisms, i.e. gravity gliding or spreading.

We produced three analogue models, differing mostly in terms of overburden thickness and dimensions of the allochthonous salt structures while maintaining the same scaling and experimental box dimensions. The experimental design for every model is summarized in Tables 4.1-3, where all the actions carried out during the experiment (e.g. chronology, layers material and thickness, etc.) are recorded to allow the reproducibility of the model. This is followed by a general comment on the various stages, and a discussion on the models results. The differences between the three models procedures and the results will be briefly described, while the comparison between the result of analogue modelling and seismic data interpretation will be discussed in chapter IV.B.3. (Discussion and intermediate conclusions).

IV.B.2.2 Model S01

- ## Experimental procedure

Being the first one produced about this area, this model has mostly the objective of calibrating the different parameters for the later models, mainly in terms of thickness of the autochthonous silicone layer and thickness of the sand layers **(Table 4.1)**. It will also allow us to evaluate the timing of the formation of the allochthonous silicone structure to calibrate the timing of the models onset.

The silicone layer (layer 1**,** Table 4.1) has to be prepared at least 24 h before the beginning of the model, in order for it to flatten and lose all the possible air bubble trapped in it. When the silicone is ready we add four layers of sand (layers 2 to 5 of table 4.1) representing the pre-salt tectonics sedimentation. The model starts when we aspire the whole thickness of sand above zone A, creating space in the overburden **(Figure 4.28.1)**. Due to the friction angle of the sand (around 30°), an area of 50 cm x 3 cm of silicone is exposed, while the upper section of the graben is around 10 cm large. The sand removal results in differential loading on the silicone layer, that immediately starts to move with visible deformation of the overburden already at T=15'. When the top of the silicone wall reaches the same height as the overburden, we add two layers of sand on the whole model (T=40', layers 6 and 7) representing the syn-salt tectonics sedimentation. The silicone structures continue growing during the deposition of these layers.

Time	Layer	Material/activity	Thickness [cm]	Sand color	Top color	Location
-24h00'	1	Silicone	3	/	/	Whole box
-0h15'	2	Medium sand	0.5	White	Green	Whole box
	3	Medium sand	0.5	Red	Blue	Whole box
	4	Medium sand	0.5	White	Red	Whole box
	5	Medium sand	0.5	Blue	Blue	Whole box
0h00'	/	Material removed	-4	/	/	Zone A
0h40'	6	Medium sand	0.5	White	Black	Whole box
	7	Medium sand	0.5	Lavender	Blue	Whole box
2h00'	8	Medium sand	0-2	Red	Green	Whole box
	/	Slope 3.3° W	/	/	/	/
3h10'	/	Material removed	Up to -8	/	/	Zone D
18h00'	/	Silicone removed	/	/	/	Zone B
	9-10	Medium sand	0.5	White	Red/brown	Zone C
20h35'	/	Material removed	-6.5-8.5	/	/	Zone D
	11	Medium sand	0.2-2	Green	Red	Whole box
25h10'	Final layer	Medium sand	> 2	White	/	Whole box

Table 4.1: *Experimental procedure of model S01.*

After adding another layer of sand of thickness variable between 0 and 2 cm (layer 8, T=2h) the box model is tilted westward of 3.3°. This does not reflect the reconstruction of the evolution of the area based on the seismic data interpretation, so we have to keep this in mind when interpreting the model results. Around one hour after the tilting of the box model, material is removed from zone C, to give space to the system to develop, and faults and grabens forms perpendicularly to the tilting direction (Figure 4.28.2). Between T=3h10' and T=18h no material is added or removed from the box model due to the overnight break. The model continues moving overnight, forming silicone overhangs and normal faults and grabens in the sand layers (Figure 4.28.3). The extension in the overburden results in reactive diapirism also on the eastern side. At T=18h, we remove the overhang in B cutting it without deforming the underlying sand (Figure 4.28.4). To model the sediments present on the eastern overhang we add two thin layers of sand -for a total thickness of 0.5 cm- on zone C (layers 9 and 10). In around 30', the first faults start to form (Figure 4.28.5).

After the formation of the first faults in zone C, we remove sand and silicone from zone D and add on zone C a layer of sand (layer 11, T=20h35') strongly variable in thickness, because the model

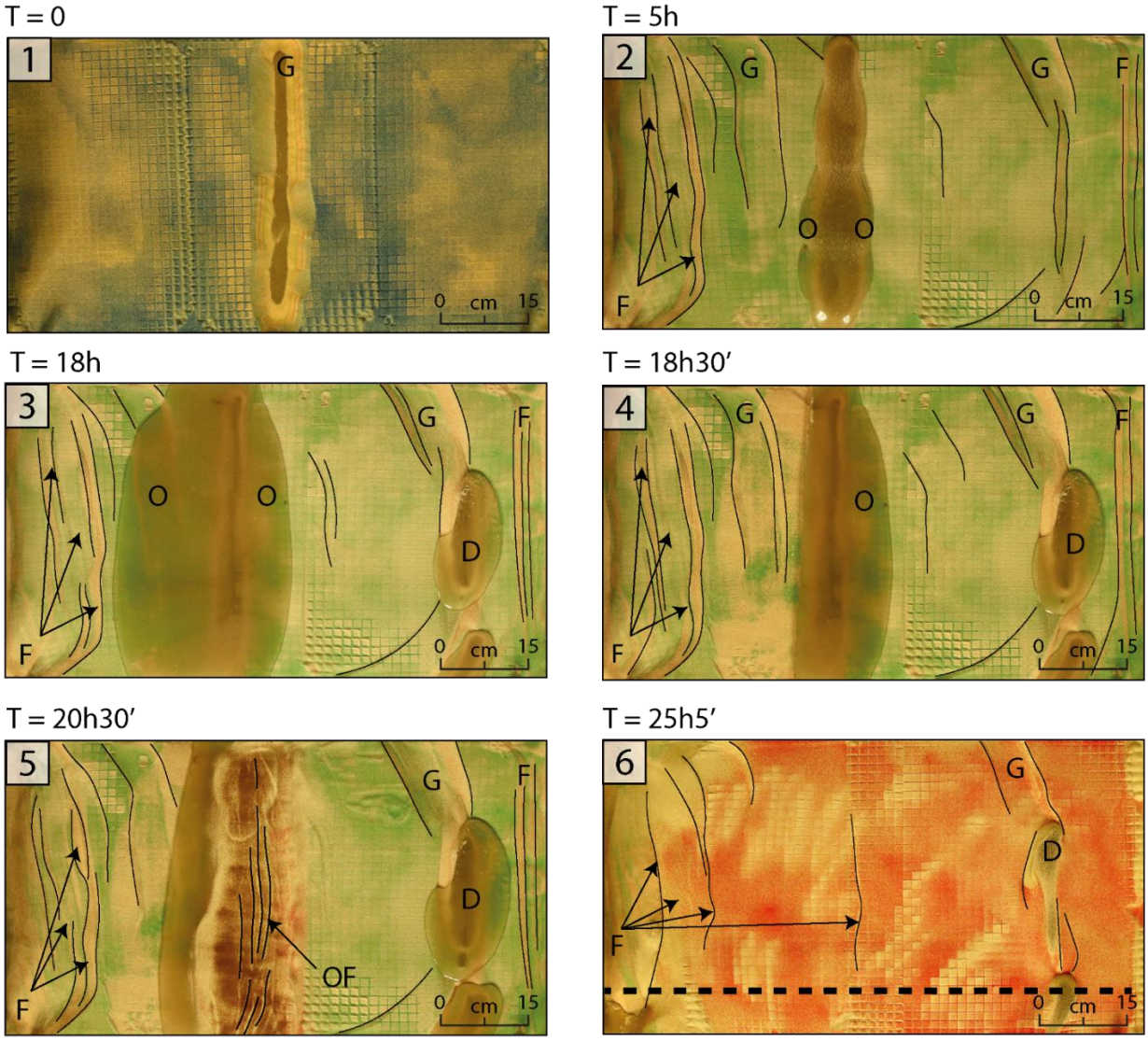

***Figure 4.28**: Model S01, evolution of the Top View between time T=0 and T=25h5'. **1.** T=0, the model presents a graben in zona A. **2.** At T=5h, the silicone grew in an allochthonous structure, that evolves forming overhangs (O). As a result of the tilting of the model (3.3° westward) we have formation of extensional faults (F) and grabens (G). Despite the faults develop in a mainly N-S direction, a curvature is present due to the edge effects. **3.** After the overnight development, extensive overhangs are present, with major dimensions on the western one due to the slope direction. Some silicone 'diapirs' (D) grow up to reaching the surface on the eastern side of the box. **4.** Removal of the western overhang. **5.** After localized sedimentation is added on the eastern overhang, numerous overhang faults (OF) form at few cm distance one from the other. These have a shorter wavelength compared to the faults formed as a consequence of the box model tilting. **6.** Towards the end of the model, we can recognize N-S normal faults on the entire surface of the model. Position of the section S01-03 shown in figure 4.29 is marked with the black dotted line.*

presents -as we can see in figure 4.28.5- both graben geometries and positive salt structures. Normal faults form on the model surface after few minutes.

At time T=25h10', we block the model adding a layer of sand of at least 2 cm. This last, thick layer of sand has the role of blocking the silicone deformation thanks to the important pressure on all the model, and to allow us to wet the sand without ruining the geometries of the sand layers. A wet model is necessary to be able to cut it and visualize the internal structures formed. The water is added in various steps to be sure to wet also the sand below the overburden for capillarity.

After 12 hours, we remove the southern glass panel and slice at irregular intervals in a E-W direction. The position of every slice is based on the structures we found (i.e. more we are interested in a particular structure, smaller will be the distance between the sections), therefore is decided during the operation. We cut 10 sections, at a distance from the southern limit of the box of 1.7, 4.5, 7.2, 9.7, 12.7, 20, 26, 31.2, 37.2 and 43.6 cm.

- ## Results and discussion

As visible in the EW section S01-03 **(Figure 4.29)**, the thickness of the silicone layer is good both for the formation of the salt structures and to have a clean cut of the sections. A slightly thicker layer could increase the velocity of formation of some silicone structures, and will therefore be used in the next model (S02). During this first experiment we observed several phases of salt tectonics:

.Reactive salt tectonics of the main structure between T=0 to T= 40' and **active salt tectonics** of the main structure starting at T=40 and at different steps up to the end of the model. The active salt tectonics geometries are difficult to visualize in the model because the sand has a low friction angle. Despite these difficulties, some typical geometries of active diapirism are visible in figure 4.29 (e.g. upturned horizons of layer 7, anticline geometries of layer 11). Salt tectonics also occurs as a result of the box model tilting and consequent extensional tectonics in the eastern part of the model. This extensional tectonic produces reactive diapirism recognizable by the geometries that we see only when the model is cut (eastern part of figure 4.29). These structures evolve to form allochthonous salt structures with overhangs.

.Secondary salt tectonics above the overhang is present in zone C since T=20h30'. The faults developed above the salt overhang are visible in the top view in figure 4.28.5, and in section S01-03 of Figure 4.29 above the eastern overhang where the tilted blocks are separated by normal faults, and salt rollers form along the faults. Considering that the slope was already present during this phase, we can consider that these faults mostly formed for gravity gliding.

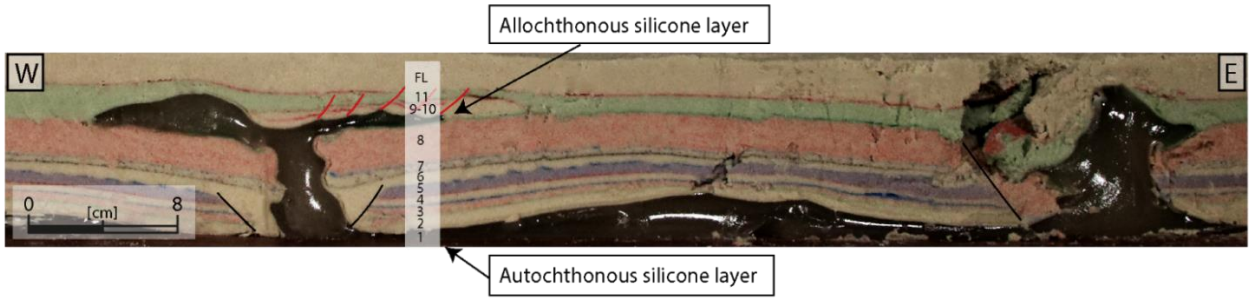

***Figure 4.29**: Section S01-03, at 7.2 cm from the southern limit of the box model. In black are interpreted the normal faults result of the simulated extensional tectonics and in red the normal faults above the overhang, result of the gravity gliding above the salt overhang. The numbers represent the layers deposited on the model (Table 4.1).*

Aspects to be improved in the following models

This first model was used to calibrate the following, so we analyze here some points of this first experience that could be improved in the following models:

- I**n this model we added the slope before the beginning of the overhangs formation,** while in the seismic data results this tilting postdates the overhang formation and the beginning of the Quaternary. This has been done to evaluate the obtained geometries and the eventual

differences with the natural example, and in the next model we will simulate the same timing interpreted in the seismic data.

- The last layer of the model is thinner than in the natural example, because due to the constrain of lab accessibility we had to block the model at T=25h10'. This first experiment allowed us to calibrate the time necessary to add the whole overburden thickness, that will be considered in the next model.

IV.B.2.3. Model S02

• Experimental procedure

Considering that some explanations of the actions carried out have already been provided during the description of model S01, here we will mostly emphasize the differences with model S01.
As discussed at the end of the previous model, we use here a slightly thicker layer of silicone (3.2 cm, Layer 1, **Table 4.2**) to facilitate the silicone structures formation. Based on the fast development of the silicone structure that we observed in model S01, we decide to start model S02 with a thicker pre-kinematic layer, adding to the box model 6 layers of 0.5 cm (Layers 2 to 7), so 1 cm more than in model S01.

Time	Layer	Material/activity	Thickness [cm]	Sand color	Top color	Location
-24h00'	1	Silicone	3.2	/	/	Whole box
-0h45'	2	Medium sand	0.5	White	Green	Whole box
	3	Medium sand	0.5	Orange	Black	Whole box
	4	Medium sand	0.5	White	Blue	Whole box
	5	Medium sand	0.5	Chocolate	Red	Whole box
	6	Medium sand	0.5	White	Brown	Whole box
	7	Medium sand	0.5	Red	Orange	Whole box
0h00'	/	Material removed	-3	/	/	Zone A
7h05'	8	Medium sand	Up to 1	White	Green	Whole box -A
22h00'	/	Silicone removed				Zone B
	9	Medium sand	0.2 to. 1	Blue	Blue	Zone C
25h00'	10	Medium sand	Around 1	Orange	Orange	Whole box
		Material removed	-8.2	/	/	Zone D
		Slope 3.3° W				
27h15'	11	Medium sand	Around 1	White	Blue	Whole box
28h40'	12	Medium sand	Around 0.5	Green	Green	Whole box
29h40'	Final Layer	Medium sand	> 2	White	/	Whole box

***Table 4.2**: Experimental procedure of model S02.*

As in model S01, the pre-kinematic sand layer is removed from zone A through a vacuum **(T=0)** and the silicone starts to deform **(Figure 4.30.1)**. At T=6h30', the overhangs are forming (Figure 4.30.2) but the movement is very slow so we decide to add another layer of sand (Layer 8, T=7h05', Figure 4.30.3) to increment the pressure on the autochthonous silicone layer. This layer of sand is placed everywhere except in zone A, to leave the allochthonous salt structure the space to continue to develop. As in the previous model, there is a long stop in the sedimentation during the night. After the development of the overhangs during the night (Figure 4.30.4), we cut the overhang of zone B and add sediments above the overhang of zone C (Figure 4.30.5), as in model S01. As soon as the first faults form on the western overhang overburden, we add 1 cm of sand on the whole model (T=25h) and we tilt the table 3.3° westward. This time the tilting of the box model postdates the

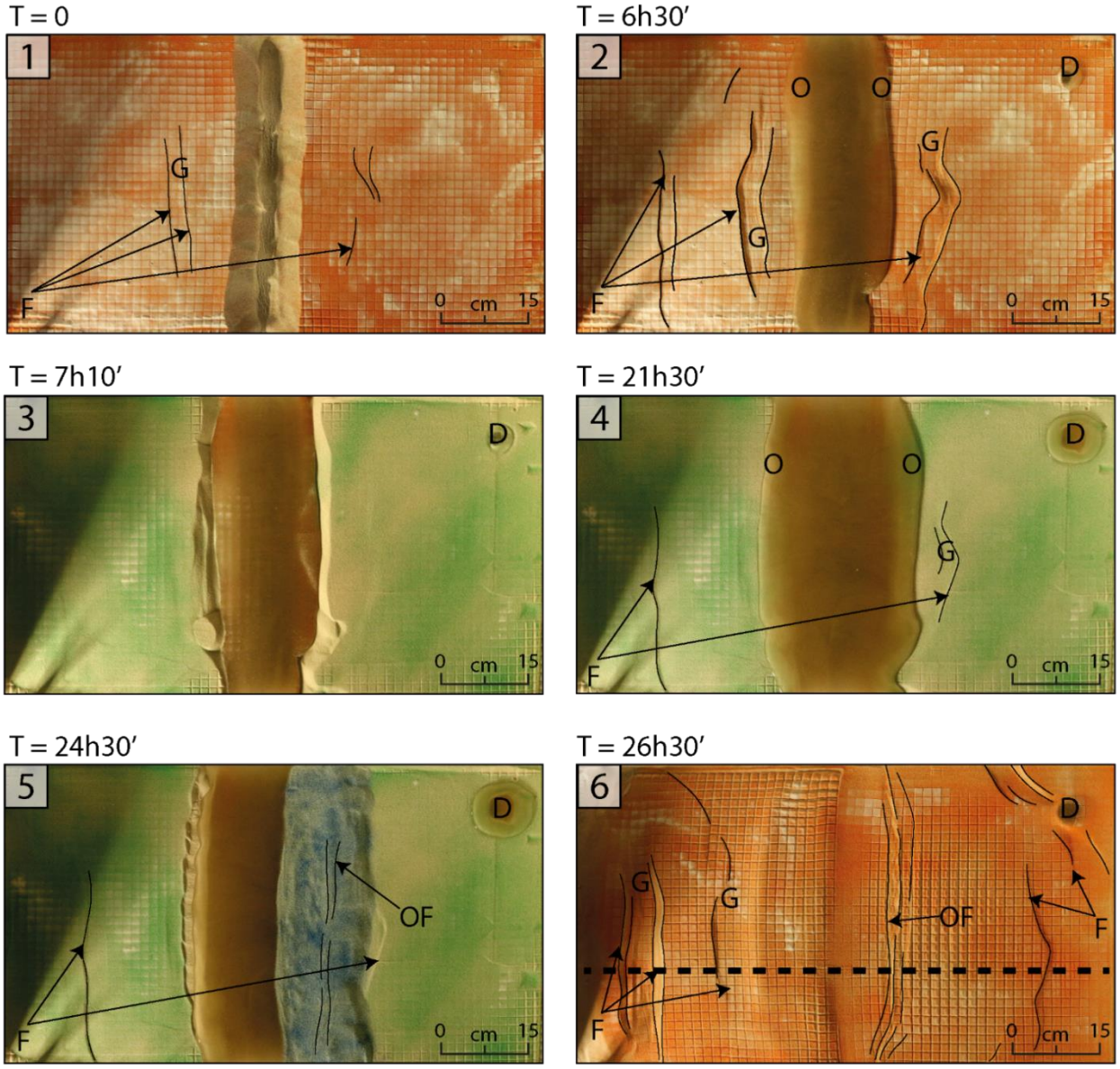

***Figure 4.30**: Model S02, evolution of the Top View between time T=0 and T=26h30'. **1.** T=0, beginning of the model with a graben in zone A. Instantaneously some normal faults (F) and grabens (G) form both at the eastern and western side of the model, parallel to zone A. **2.** At T=6h30', the silicone grew in an allochthonous structure, that evolved forming overhangs (O). Faults and grabens that developed since the very beginning of the experiment go on growing, and more normal faults formed towards west. A diapir (D) forms in the northeastern part of the box. **3.** At T=7h10' another layer of sand is added to the model without covering the silicone structure. **4.** After the overnight development, two overhangs are present on the eastern and western side of the main allochthonous structure (T=21h30'). The extensional structures (normal faults "F" ad grabens "G") are again visible. **5.** After part of the western overhang is manually removed, localized sedimentation is added on the eastern overhang. Short wavelength overhang faults (OF) formed at T=24h30'. **6.** As a result of the tilting of the model (3.3° westward) extensional faults and grabens form on the whole model. Position of the section shown in figure 4.31 is marked with the black dotted line.*

overhang formation and the following sediments deposition, as in the natural example. A thicker overburden of the allochthonous salt structure is added to this model compared to the previous one, with 2.5 cm of sand plus a thick layer of sand to block the model. Water is added during 12 hours. When the model is wet, we remove the southern glass panel and slice at irregular intervals in a E-W direction. We cut 16 sections, at a distance from the southern limit of the box of 2, 4.4, 7.1,

10.2, 12.1, 14.6, 17, 19.3, 23, 26.7, 29, 31.5, 34.2, 37, 41 and 46.1 cm. The northern sections (14 to 16, mainly) are particularly disturbed by the presence of the growing silicone structure, visible on the surface of the model in Figure 4.31.

- ## Results and Discussion

As well as in the previous model, the phase of **reactive diapirism** is perfectly represented here, and the phase of **active diapirism** is more difficult to model but is very clear in the upturned horizons of section S02-07 **(Figure 4.31)** and in the deformation of the last layers of the model. A circular diapir developed towards the east very early during the modelling (Figure 4.30.2); this could be the result to the differential pressure that sometimes can be created during the deposition of the first layers of sand, that take some time to flatten.

Contrary to the previous one, in this model some **normal faults** formed in the overburden very early during the silicone deformation (Figure 4.30.1), symmetrical at the eastern and western side of the model. Considering that they appeared before the tilting of the box model, these faults are consequence of the silicone movement towards the area of lower pressure (zone A). These faults are visible in section S02-07 (Figure 4.31), where we can see the offset of the faults in the sand layers and the reactive silicone structures that form as a consequence. Future studies could focus on the possible influence of the autochthonous salt on the geometry and wavelength of the crustal faults in the Southern Sørvestsnaget Basin, and how this could give some hints on the autochthonous salt distribution in the area.

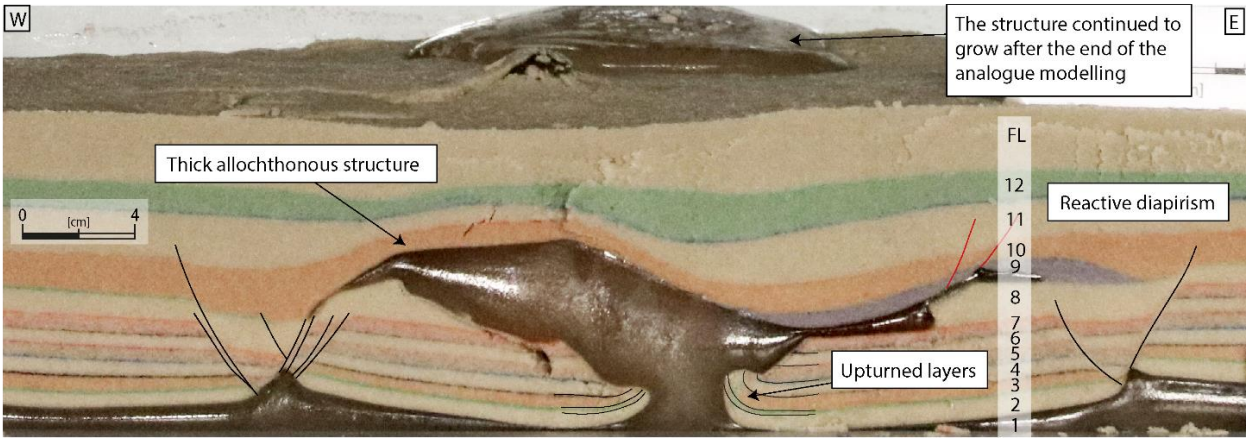

***Figure 4.31**: Section S02-07, at 17 cm from the southern limit of the box model. We can appreciate the extensional faults both above the autochtonous silicone (black lines) and above the overhang (red lines), these last one result of the gravity spreading and later of the gravity gliding above the salt overhang. The numbers represent the layers deposited on the model (Table 4.2).*

The normal **faults localized above the overhang** (Figure 4.30.5) show very clearly the gravity gliding above the eastern overhang. In contrast with the previous model, the localized sedimentation above the overhang (zone C) is added before the tilting of the model, and the formation of the faults we see in 4.30.5 is therefore consequence of pure gravity spreading. In the following phases, after the tilting of the box model, we can assume that the deformation interpreted above the overhang is a hybrid phenomenon of gravity gliding and gravity spreading.

Aspects to be improved in the following models:

- As a consequence of the overdimensioned allochthonous silicone structure formed -partly due to the localized sedimentation of layer 8 (Table 4.2)-, we needed to add a thickness of sediments higher than the scaled value, in order to slow down the rapidly deforming silicone. After the end of the model, a silicone structure continued to grow despite the important amount of sand added on top to stop the model, compromising the model in terms of scaling of the allochthonous overburden thickness but also in terms of timing, because the silicone movement continued after the end of the sand layers' deposition. Moreover, the excessive silicone thickness influenced the quality of the model's slicing, through deformation and fractures in the sand layers.
- The last layers of the model are thicker than in the natural example. This is a consequence of the previous point and the necessity to slow down the structure, so will be solved paying attention to avoid the formation of an excessively thick allochthonous silicone structure.

IV.B.2.4. Model S03

• Experimental procedure

From the analysis of the results of the two previous models -and keeping in mind the few points that could be improved- we produced the third model (S03, **Table 4.3**).

Time	Layer	Material/activity	Thickness [cm]	Sand color	Top color	Location
-24h00'	1	silicone	3	/	/	whole box
-0h20'	2	medium sand	1	blue	black	whole box
	3	medium sand	1	white	orange	whole box
0h00'	/	material removed	-2	/	/	zone A
0h36'	4	medium sand	1	red	green	whole box
2h40'	5	medium sand	1	white	blue	whole box
18h25'	/	silicone removed	/	/	/	zone B
	6	medium sand	0.5	orange	red	zone C
19h55'	7	medium sand	1.2	green	orange	whole box
20h00'	/	material removed	-8.5	/	/	Zone D
	/	Slope 3.3° W	/	/		whole box
20h55'	8	medium sand	1	chocolate	red	whole box
24h45'	/	material removed	-9.5	/	/	Zone D
28h10'	Final layer	medium sand	> 2	white	/	whole box

***Table 4.3**: Experimental procedure of model S03.*

Considering that 3 cm of silicone were sufficient for model S01, we used this thickness for model S03 to avoid the problems of excessive silicone growth we had in model S02. The first sedimentation above the autochthonous silicone layer is reduced to 2 cm (as in S01) and only two layers, in order to shorten the sedimentation phase and possibly avoid the differential pressure related to it. As soon as we remove the sand from zone A (T=0), the silicone starts to move and normal faults form on both sides in a N-S direction **(Figure 4.32.1 and 4.32.2)**.

We add two sand layers of 1 cm each (Layer 4 and 5) on the whole box at T=36' and at T=2h40', to simulate the phases of active diapirism and force the vertical development of the structure. As well

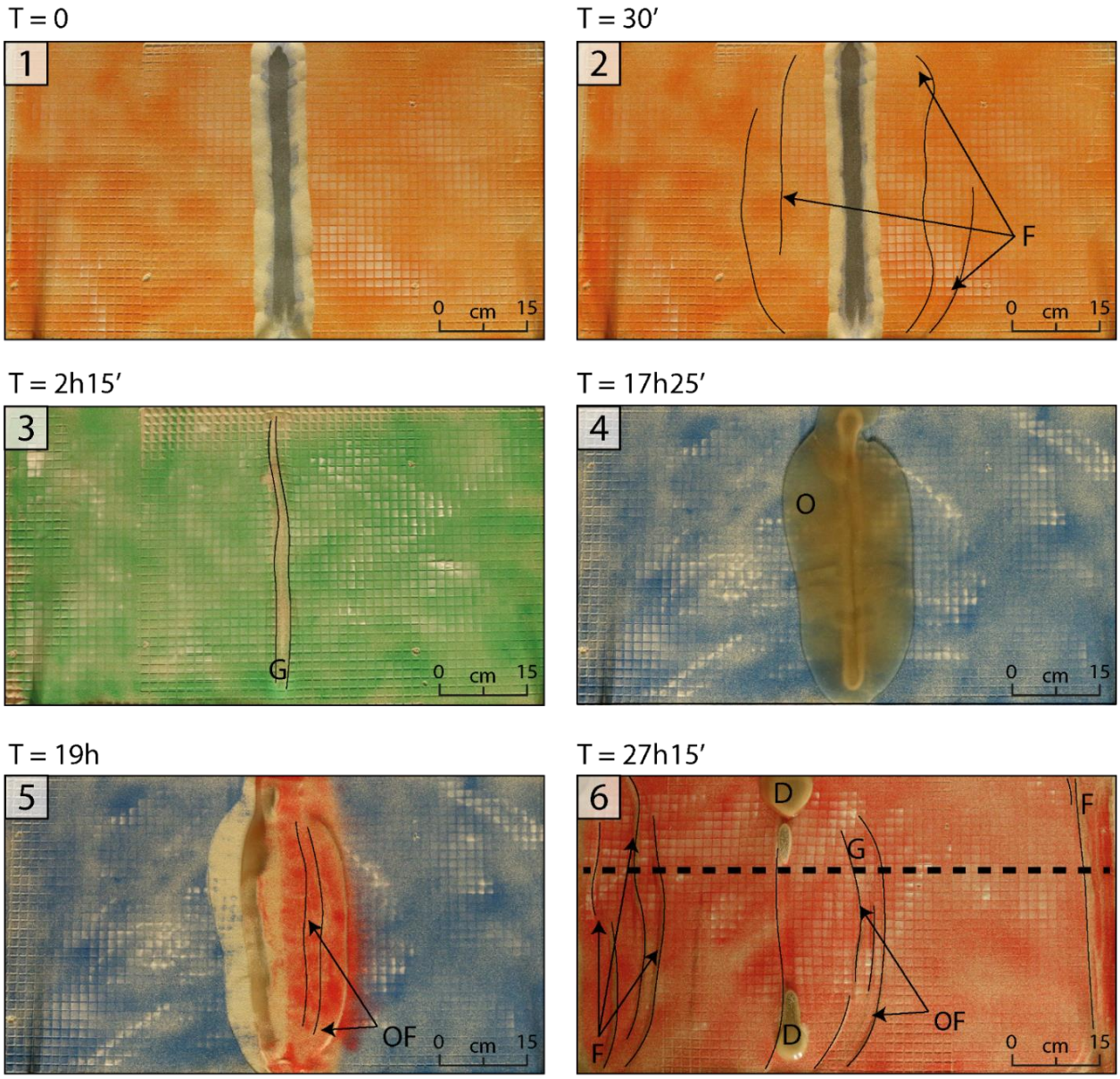

***Figure 4.32**: Model S03, evolution of the Top View between time T=0 and T=27h15'. **1.** T=0, beginning of the model. **2.** Very early during the experiment (T=30') normal faults (F) form both at the eastern and western side of the model, parallel to zone A. **3.** Another layer of sand is added on the whole model, and at T=2h15' the presence of a crestal graben is well visible in zone A. **4**. After the overnight development, the silicone grows in an allochthonous structure, that evolves forming overhangs (O) (T=17h25') on the eastern and western side of the main allochthonous structure. **5.** The western overhang is manually removed, and localized sedimentation is added on the eastern overhang (T=18h25'). Short wavelength overhang faults (OF) form at T=19h. **6.** As a result of the tilting of the model (3.3° westward) extensional faults and grabens form on the whole model, along which some silicone 'diapirs' (D) that reach the model surface in zone A. The normal faults above the buried overhang have a slightly shorter wavelength compared the other ones. Position of the section shown in figure 4.33 is marked with the black dotted line.*

as in the previous models, the overnight break is the phase in which the overhangs develop. At time T=18h25', we remove the western one (zone B) and add localized sedimentation on the eastern one (zone C) (Figures 4.32.4 and 4.32.5). Another layer of 1.2 cm is added at T=19h55', and few minutes later the model is tilted 3.3° westward. After one hour, one more cm of sand is added and the model is blocked at time T=28h10'. In this model the scaling of the Late Mesozoic to Cenozoic overburden was entirely based on the geometrical scaling, i.e. the thickness of the sand layers respected the

scaling of the layers thickness in the natural example: we used an average thickness of 0.5 cm for the Mesozoic overburden of the overhang (0.3 to 0.8 s TWT in the seismic data), 1.2 cm for the Tertiary and Early Quaternary sequence before the tilting of the margin (around 1.2 s TWT above the overhang) and 1 cm for the post tilting layer (around 1 s TWT in the data).

- ## Results and Discussion

Increasing the thickness of the first layers of the overburden and reducing their number worked well to limit differential pressure on the silicone layer and consequent silicone deformation. On the other hand, thicker sand layers reduced the possibility to visualize minor faults and deformations in the model's sections. In order to prevent the formation of an excessively thick allochthonous silicone structure similar to the one of model S02, we avoided the localized sedimentation that caused the problematic silicone shape in the previous model. Here again, we can visualize quite well the reactive and active diapirism geometries. The upturned horizons that we saw in section S02-07 are not well represented here, but active salt tectonics is well testified by the N-S crestal graben (Figure 4.32.3). The faults on the primary overburden that were well visible in top view of model S02 are present also in the first phases of model S03 (4.32.2), and are partly visible in section S03-13 **(Figure 4.33).**

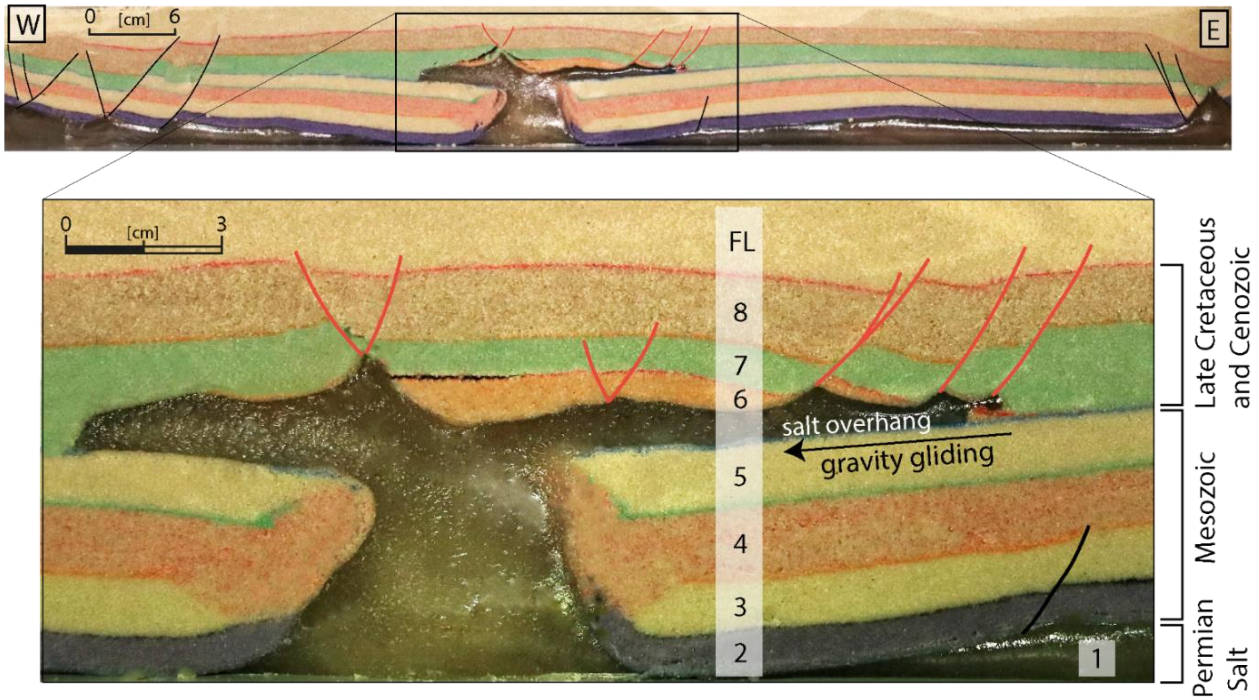

***Figure 4.33**: Section S03-13, at 34.2 cm from the southern limit of the box model. Extensional faults are present above the autochtonous silicone (black line) and above the overhang (red lines), these last one result of the gravity spreading and later of the gravity gliding above the salt overhang. The numbers represent the layers deposited on the model (Table 4.3). The normal faults marked in blue at the eastern and western limit of the model are result of the model tilting (east) and the material removal from zone D (west).*

The limited development of these faults compared to the previous model is probably related to the lower amount of silicone and primary brittle overburden, but both testify the effect of the silicone flow. The salt tectonics related to the overhang presence is particularly well represented in this model, with listric faults and salt rollers, as well as tilted blocks of sand above the overhang (Figure

4.33). In the top view (Figure 4.32.6) we can appreciate the localized normal faults that mark the position of the overhang even after the later sedimentation.

IV.B.2.5. Outcomes of the study

In order to simulate the long lived salt tectonics in the Southern Sørvestsnaget Basin and analyze the different phases of salt movement, we have developed some analogue modelling of silicone and sand. In these models we tested the influence of crustal extension on salt structures initiation, the formation of allochthonous salt structures and salt overhangs, and the effect of the co-presence of an overhang, localized sedimentation and tilting of the area on the post-tectonics deformation of the salt. In our models we recognize two distinct phases of salt tectonics:

- **A phase of reactive and active diapirism** is mainly the consequence of the simulated extensional crustal tectonics through the formation of differential pressure on the silicone layer. During this first phase, the salt grows vertically. In addition to this, we noticed the formation of extensional faults in the sand layers, with a development roughly parallel to the main salt structures. These are most likely the result of the movement of the silicon towards the main silicone structure and the consequent deformation of the silicone overburden.
- In the second phase the diapirism leads to the formation of allochthonous silicone bodies and overhangs, beginning the phase of the **allochthonous salt tectonics**. We actually observed that the geometries of the faults formed above the overhang as a result of gravity gliding and spreading (model S01) or pure spreading (models S02 and S03) are comparable, making impossible a distinction of the two mechanism in the natural example. Even after the sedimentation of various layers of sand, the area above the overhang continues to be a preferential zone of deformation.

The diapir falls that we interpreted in the seismic data cannot be modelled here and probably has an influence on the fact that the salt continues growing in the last phases (e.g. deformation of the model surface even after the last layers deposition). We suggest to repeat the experiment using the same procedure of S03 (Table 4.3) but using a movable wall in order to apply few cm of extension after the deposition of layer 6. The implications of the models result on the understanding of salt tectonics in the Southern Sørvestsnaget Basin will be discussed in the next subchapter (IV.B.3. Discussion and intermediate conclusions).

IV.B.3. Discussion and intermediate conclusions

• Discussion

Despite the only salt imaged in the seismic reflection data is allochthonous and there are no images available about the autochthonous salt, we can assert that the presence of salt in the Sørvestsnaget Basin is reconductable to the Gipsdalen Group deposited during Permo-Carboniferous. The presence of these allochthonous structures does not give complete information about the nature of the **LES (Layered Evaporitic Sequence)** deposited in the Sørvestsnaget Basin, because the imaged evaporite is just the migrated material (halite) while the gypsum, anhydrite and carbonates potentially deposited could not migrate from the autochthonous layer. Based on the detailed seismic interpretation of the current geomorphology of the salt structures, the geometry of the crustal and salt related faults and the critical analysis of the geometries of the salt overburden, together with the know-how in terms of the Southwestern Barents geological history and the results of the analogue models, we propose a reconstruction of the salt movement from the deposition to the actual geometries, in terms of both timing and mechanisms **(Table 4.4)**.

	CRUSTAL TECTONICS	SALT TECTONICS		
		STRUCTURE A	STRUCTURE B	STRUCTURE C
QUATERNARY	Glacio-isostatically controlled crustal movements : tilting of the margin towards west	A1: Gliding above the overhang, general growth A2: Minor movement A3: Minor movement	**Major salt reorganization** inside the allochthonous salt structure towards SW (0.4 Ma)	C1: Active diapirism (limited) C2: No movement C3: No movement
UPPER EOCENE TO PLIOCENE	Phases of formation of the Senja Ridge	A1: Active diapirism A2: Last phase of diapir fall A3: Latest growth during Upper Eocene	The erosion hides the movement	C1: Active diapirism (limited) C2: No movement C3: No movement
LOWER EOCENE	Formation of anticlines at the transition between Paleocene and Lower Eocene (SW area)	A1: Diapir fall. A2: Mock-turtle anticline formation A3: Limited movement	Growth, but the erosion hides the movement	C1: **Active diapirism** C2: No movement C3: Reactive diapirism
PALEOCENE	Extensional tectonics during Early Paleocene	A1: (re)active diapirism A2: Depocenter formation A3: **(re)active diapirism**	Growth of the NE flank	C1: (re)active diapirism? C2: No movement C3: **Reactive diapirism**
CRETACEOUS MESOZOIC	Rifting due to the propagation of the N-Atlantic	Formation of allochthonous salt structures		
		The salt moves for **reactive/active diapirism** as a result of the extensional tectonics		
PERMIAN	Northward drift of the shelf, climate shift and basin drowning	**Evaporites deposition**		

Table 4.4: *Synthesis of the crustal movement and of the evolution of the different salt structures.*

The history of the Sørvestsnaget Basin counts different pulses of crustal and salt tectonics, resulting in hundreds of millions years of deformation that are partly imaged in our data. Due to the impossibility to image the deeper reflectors with seismic reflection data, the reconstruction of the initial phases of salt tectonics is based on the crustal tectonics history of the area (Faleide *et al.*, 2008, Smelror *et al.*, 2009, Gernigon *et al.*, 2014) and on the models of salt deformation in extensional settings (Vendeville and Jackson, 1992a). On the other hand, we have a very high quality image of the top of the allochthonous salt and a great age control on the Cenozoic strata imaged in high-resolution, and we can thus precisely define the salt movement in this Era, with the only limit of the sediment erosion and absence of sedimentation.

The **reconstructed salt tectonics in the Southern Sørvestsnaget Basin** has been divided in different phases, more uncertain for the early evolution and with a higher level of detail for the Cenozoic ones, direct consequence of the higher resolution of the sediments imaging.

Phase 1 - Salt diapirs initiation. Considering that the regional tectonics is composed, as partly visible in our data, by **different phases of extension** between the Triassic and the Eocene, we suggest that salt tectonics began shortly after the salt deposition, during the **extensional tectonics** of the Triassic. The inhomogeneous thinning, result of the extensional tectonics, created grabens and half-grabens, with consequent **differential load** of the brittle overburden on the salt and formation of the first salt structures for **reactive diapirism** below the thinned overburden (Vendeville and Jackson 1992a) (chapter 1.2.2.b). When the overburden becomes thinner than the threshold value, the salt structures can start to grow for **active diapirism** (Vendeville and Jackson, 1992a). If the salt reaches a position at or very near the surface, the growth continues for **passive diapirism**, with the top of the salt maintaining its shallower position while sediments deposit around. Despite we are confident that the salt moved as a consequence of the extensional tectonics, we do not have any constrain in terms of the possible different phases of reactive, active, and passive diapirism, potentially reiterated different times and not necessarily in this order. Most likely, some of the salt structures were aborted during this phase and never reached the depths range imaged in the seismic data.

Phase 2 - Mesozoic formation of allochthonous structures. The allochthonous component of the salt structures started to develop before the end of the Mesozoic, as testified by the presence of Cretaceous sediments above the sheet like salt bodies (Figures 4.18 and 4.25). Generally, the formation of these allochthonous salt bodies is the consequence of a salt growth rate exceeding the sedimentation rate, and can be therefore the result of an acceleration of the salt movement or a slowdown of the sedimentation. This type of growth has in fact been modeled in analogue models through a long phase of absence of sedimentation, which resulted in the formation of silicone overhangs (horizontal developments) (Figure 4.28.3) that then continued their vertical movement as a result of subsequent sedimentation (Figure 4.33 and **4.34.2**).

Phase 3 - Paleocene salt tectonics. From this phase on, the geometries in the overburden that testify the movement of salt are more clearly identifiable in our data, and we can therefore appreciate the strong differences in the evolution of the three salt structures, and even the different or diachronous developments of the various segments of a single allochthonous salt body (Table 4.4). After the formation of the allochthonous salt structures, we recognized another phase of extensional tectonics during Paleocene as testified by the regional crustal faults in the region. Coevally and most likely consequence of it, there is a pulse of salt tectonics. In sector A1 this is testified by thickness differences in the Paleocene layers, but their successive deformation partly hides the depositional geometries.

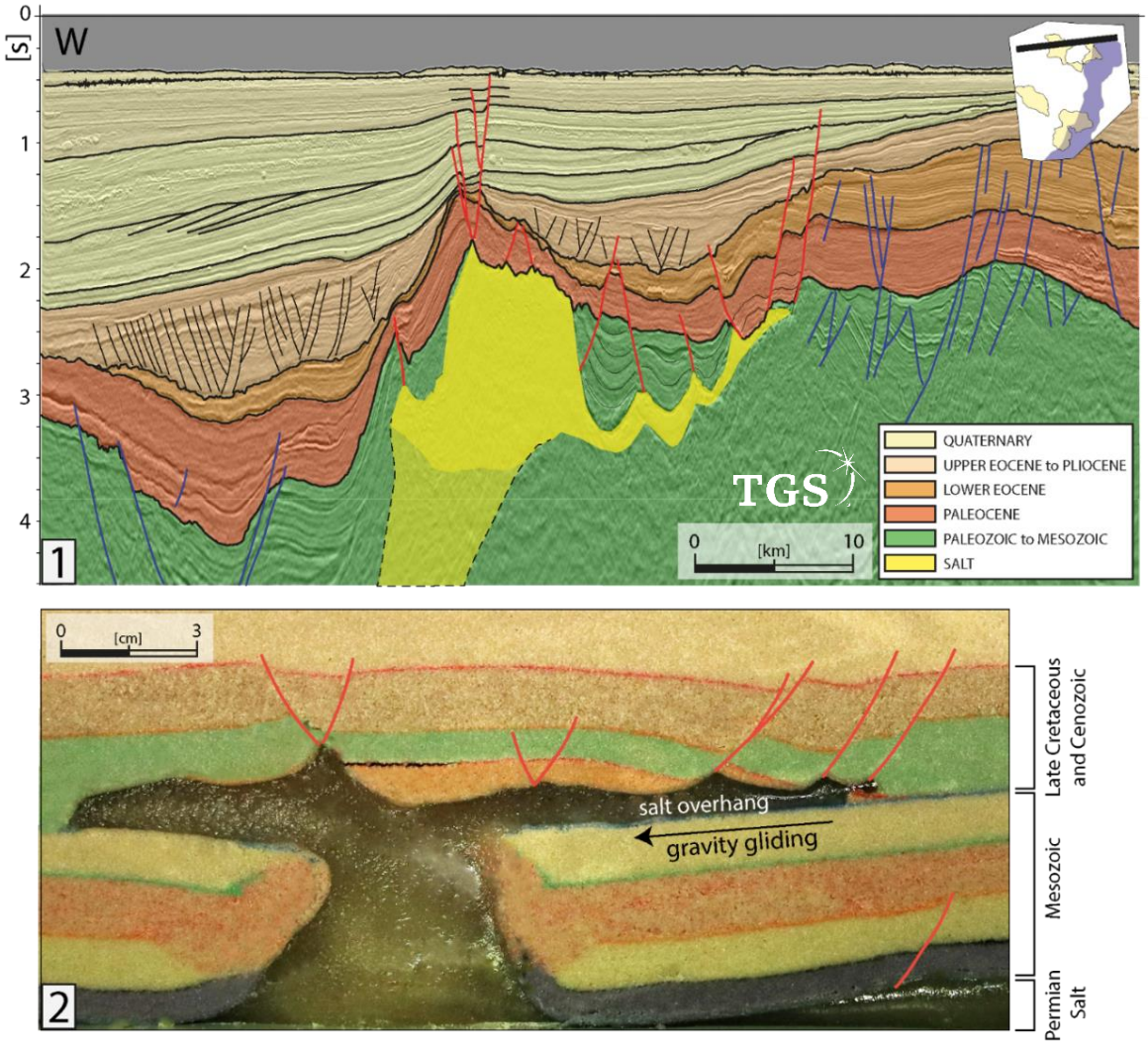

Figure 4.34: *Comparison between the seismic imaging of salt structure A* ***(1.)*** *and analogue modelling S03 simulating the effect of a 3.3° westward tilting on the geometries of salt overhang and overburden* ***(2.).***

The growth phase is particularly well visible in the fan shaped strata of sector A3 (Figure 4.20) that has during Paleocene its maximum growth phase. Due to its simultaneity with the extensional tectonics, we suggest it to be the result of the reactive and active diapirism and consequent influx of salt from the autochthonous layer. Synchronous with this growth is the beginning of the deposition of brittle sediments above **segment A2**, testified by the slightly **thicker Paleocene layer** in the central part of the segment **(Figure 4.35)**.

In sector **C3** it is clearly imaged the effect of the extensional tectonics on the salt layer, with the geometries typical of the reactive diapirism infilling the space in the overburden left by the graben formation **(Figures 4.36.1 and 4.36.3)**. This reactive diapirism aborted in sector C3, where its evolution was impeded by the reduced amount of salt and the important thickness of the Mesozoic overburden. The same reactive diapirism mechanism very likely helped in the growth of segments **C1 and C4**, but the geometry testifying the reactive phase of salt tectonics have been erased by the successive salt tectonics and by sediment erosion. No sign of deformation of **C2** has been detected in the data.

Higher uncertainties surround the growth of the **western structure (B)**, due to the limited thickness of the Paleogene sediments above the allochthonous salt. The uptilted horizons of the

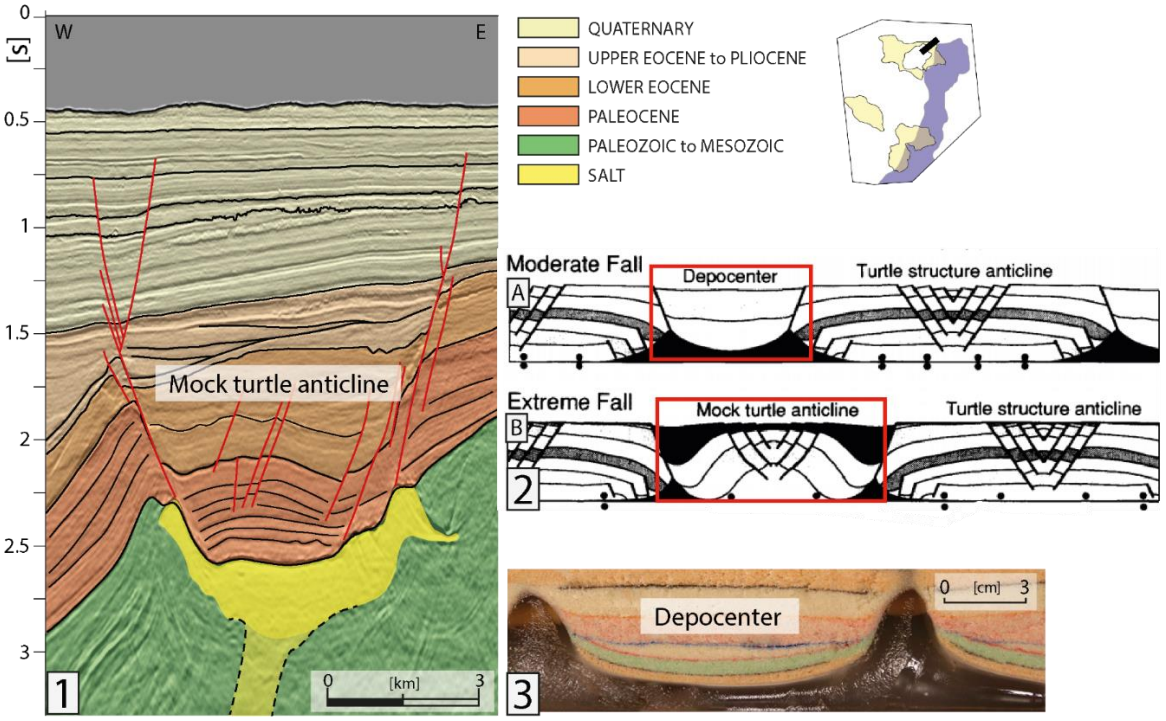

Figure 4.35: *Mechanism of formation of the geometries of sector A2 overburden* ***(1.)****. In the schematization of Vendeville and Jackson (1992)* ***(2.)****, during the diapir fall a depocenter forms above a falling salt structure* ***(3.)****. The latest stage of the evolution of the depocenter is the inversion of the overburden geometries and the formation of the mock-turtle anticline* ***(1. and 2B.)****.* ***3.*** *Analogue modelling of sand and silicone simulating the formation of a brittle depocenters between the growing salt structures.*

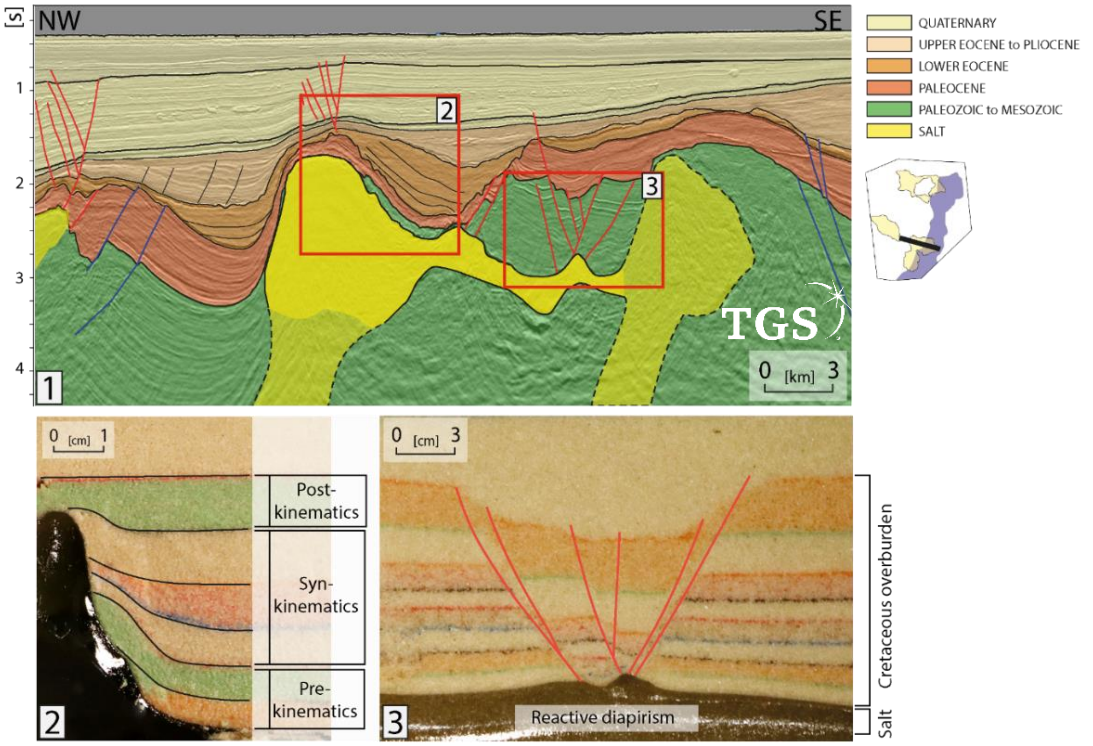

Figure 4.36: *Co-presence of reactive and active diapirism in structure C. The active diapirism in C1* ***(1.)*** *shows a pre-kinematic layer (Cretaceous and Paleocene), a synkinematic layer (Lower Eocene) and a post-kinematic one with later minor deformation, comparable to the ones of analogue model B02 of* ***2.*** *On the other side, in sector C3 the deformation is the result of reactive diapirism, with geometries comparable to the analogue model S02 in* ***3.***

Cretaceous and early Paleogene, and the infilling geometries in the Paleocene sediments at the NE of structure B (Figure 4.23), prove that a phase of growth predates the end of the Paleocene.

Phase 4 - Lower Eocene phase of growth and fall. As known in literature (Vendeville and Jackson, 1992b), the extensional tectonics that favors the growth of salt structures can also lead to diapir fall, as a consequence of a salt supply insufficient to maintain the growth of the salt while the width of the salt structure is increased by the extension. The diapir fall often results in the formation of salt cusps -that can be considered as a 'high water mark' of the shallowest salt position- and areas of subsidence at the top of the salt (Vendeville and Jackson, 1992b), and can therefore be dated through the interpretation of the collapsed blocks of overburden and the collapse-infilling sediments. The salt cusps on the top of salt structure A (Figures 4.17 and 4.18) have been interpreted as the result of a phase of diapir fall (Perez-Garcia *et al.*, 2013), but due to the erosion at the top of the positive salt structure, as well as the lack of clear internal reflection of the Eocene above the salt, it is difficult to date in detail the diapir fall, that we estimate occurred during Lower Eocene thanks to infilling geometries interpreted in this layer (Figure 4.18). The same issue occurs also for the datation of **segment A2**, but here the more limited deformation during Neogene preserved most of the sediments geometries. In fact, after the development of a depocenter during Paleocene, the movement along the faults and the thickness differences testify a phase of diapir fall during Early Eocene to Pliocene (Figure 4.35). The resulting geometries –an inverted sincline with faults cutting the newly formed anticline- are reconductable to the mock-turtle anticline structure (Figure 4.35.2B), defined by Jackson and Vendeville (1992b) as a turtle anticline that developed on the crest of a subsiding diapir. Less information is available for what concerns the Paleogene evolution of the western structure, due to the limited sediment thickness already mentioned.
The Lower Eocene geometries above segment **C1** (Figure 4.36) testify the phase of maximum growth of this structure, with geometries comparable to the ones we see in the analogue model of figure 4.36.2 as a result of active diapir growth. Sectors C2 e C3 have no marks of movement except for minor activity along a salt fault above C3.

Phase 5 - Upper Eocene to Pliocene. In our data the sediments of this phase are mostly characterized by onlap/infilling geometries above and in close proximity to the allochthonous salt structures, and by a deformation that varies between the different sectors. Above sector A1 the sediments of Upper Eocene to Pliocene pinch out and are later slightly deformed, while above A2, A3 and C1 the movement is limited to slight deformation of the onlapping horizons and few faults offsetting the horizons. This suggests that the phase of movement following the deposition of the Upper Eocene to Pliocene is limited to the salt structures with major volume of salt that therefore grows for active diapirism, while for the minor ones the movement is limited. Doubts persist on salt structure B, while C2 and C3 show no movement.

Phase 6 - Quaternary evolution of the salt structures. The salt movement during Quaternary, reconstructed in detail thanks to the thick sequence of glacial sediments, differs between the three salt structures. The Quaternary sediments are locally deformed with anticlines and synclines, and ubiquitous faults with exception for part of the southern salt structure (sector C2 and C3). Glacial events and the thick sedimentary wedge deposited in the Sørvestsnaget Basin led to the **tilting of the margin**, visible in the inclination of the horizons older than 2.1 Ma (Figure 4.36).

In structure A, the most recent signs of activity are in A1, in which the important volume of halite allows the structure to continue the movement despite the fast glacial sedimentation. Activity along the normal faults is present also above A2, with the most recent deformation slightly postdating the tilting of the margin (Figure 4.34.1). Considering the quite limited amount of salt in A2 and in the overhang connecting it to A1, we suggest that secondary salt tectonics above A2 happened here as a consequence of the tilting of the margin, and is mostly the consequence of gravity gliding. However, we must keep in mind that in our models S01 to S03 the same geometries of faults above the overhang were produced both as a result of the box model tilting (S01, Figures 4.28.5 and 4.29) and as a result of a localized sedimentation (S02 and S03, Figures 4.30, 4.32.5-6 and 4.34.2). Therefore, we suggest that a compresence of **gravity gliding and gravity spreading** is plausible during the evolution of the area. Gravity spreading would be predominant in the first phase, when it reactivates the faults already formed for crustal extension in the Early Paleocene. This phase of gravity spreading would be active up to the Upper Eocene, as testified by the faults above the overhang (Figure 4.18 and 4.34), with gravity gliding becoming predominant after the tilting of the margin around 2 Ma, when the base of A2 and of the overhang stops being flat and becomes therefore motor of the salt deformation. This late movement could also be partly responsible for the more recent growth of sector A1, that we mainly attribute to active diapirism but could be boosted by some salt flow from the overhang.

For what concerns structure B, the salt horn on the northeastern side and the salt related anticline on the southwestern one testify a **reorganization of the salt inside the allochthnous salt body**, with a certain amount of salt that moved between the northeastern and the southwestern side and consequently deformed the overburden creating fan shaped strata while the salt moved towards southwest. As visible in **Figure 4.37**, a pre-kinematic layer is deposited above the salt structure up to 2.1 Ma, while a synkinematic sequence is deposited between 2.1 and 0.4 Ma. Minor movements along the salt related faults are present up to 0.1 to 0.02 Ma. For what concerns the mechanisms of this recent deformation, two different hypotheses have been formulated.

1. The **tilting of the margin**: the salt reorganization inside the structure and the consequent anticline formation in the overburden sediments slightly postdates the major tilting of the margin, that could therefore be considered responsible for the movement.
2. **Recent fault activity** near the margin: some recent faults activity, younger than 2.4 Ma, is visible at the western limit of the 3D dataset, parallel to the major axis of the western salt structure (Figure 4.16). Future studies will investigate if these faults could possibly be consequence of a presence of salt not detected in the data, or if on the contrary the recent movement of the salt in this structure could be partly consequence of a recent localized crustal movement.

The southern structure shows a minor phase of active diapirism in C1, and minor activity along the faults in C4.

The fact that on the seabed there is no trace of deformation linked to salt, nor in terms of anticlines and synclines or faults offsets, is not necessarily a sign that the movement of the salt structures is over. In fact, considering the high sedimentary rate and the fact that salt tectonics is not an instantaneous phenomenon, we can consider that salt deformation is still active and that especially

the sectors with the highest amount of salt (A1 and C1) will go on deforming. The future evolution in terms of geometries and timing of movement will depend on the forces at play and future sedimentation and erosion.

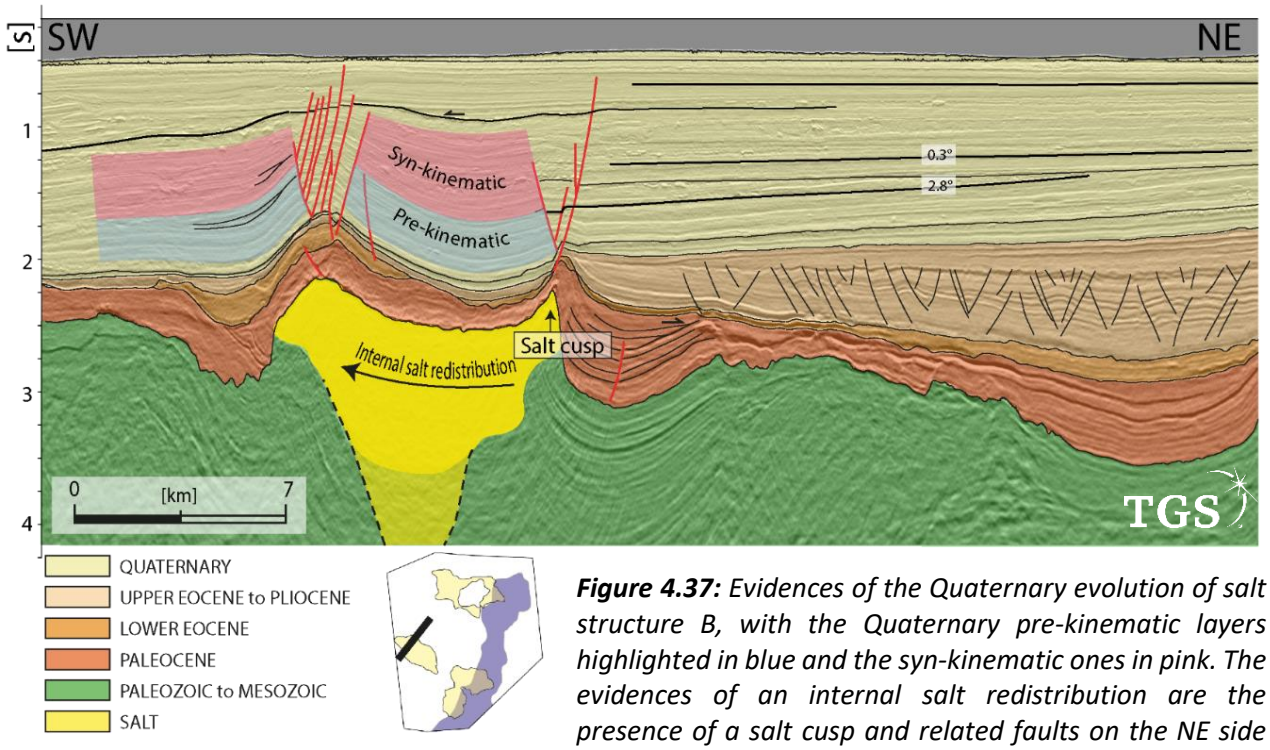

Figure 4.37: *Evidences of the Quaternary evolution of salt structure B, with the Quaternary pre-kinematic layers highlighted in blue and the syn-kinematic ones in pink. The evidences of an internal salt redistribution are the presence of a salt cusp and related faults on the NE side and the anticline of the SW side overburden.*

Influence of the compressional tectonics on the shape of the Western salt structure

The compressional features present at the western limit of the dataset are considered in literature as the result of strain partitioning due to the right-lateral oblique plate motion (Kristensen *et al.*, 2018) and mark the passage between the Paleocene and the Eocene. Considering that the major axis of the western salt structure (B) is parallel to the major axis of development of these anticlines and synclines, we suggest that the compressional stress had an influence on the shape of salt structure B. A possible explanation would be the tendency of the salt to flow into the low pressure cores of the anticlines (Jackson and Hudec, 2017), but the literature on this subject is scarce. This part of the work might benefit from some analogue and numerical modelling studying the different factors acting concurrently at the western boundary of the dataset.

• Intermediate conclusions

The detailed interpretation of the very high quality 3D dataset, together with 2D regional profiles, potential field data and wells constrain led to the mapping in the Southern Sørvestsnaget Basin of the regional crustal faults and compressional structures, together with the interpretation of the main Cenozoic seismic units and of three allochthonous salt structures and salt related faults. In this study we focused in particular on the geometries of these massive salt structures, which were already partially described in literature but never with this resolution; moreover, we show that these salt bodies are much more extended than previously described. The integration of the geological history of the Barents Sea with the interpreted dataset led to the reconstruction of around 300 Ma of salt movement, both in terms of dating and mechanisms. The high complexity of

the salt structures -highlighted by 3D visualization and seismic attributes- is mostly attributable to the intense and multi-phase tectonic movements of this basin. For what concerns the older phases of salt movement, it was not possible to analyze the geometries of growth in the surrounding sediments because of the depth, and the reconstruction is therefore based on the crustal tectonics history of the area and on the models of salt deformation in extensional settings, that suggest reactive and active diapirism as the most efficient mechanisms for the evaporites to vertically migrate for several km. On the other hand, we analyzed in detail the Cenozoic evolution of the allochthonous salt structures, showing that diachronous movements and different mechanisms of salt tectonics coexist in the southern Sørvestsnaget Basin, resulting in the impossibility to generalize the salt movement at a basin scale. This part of the recent evolution has been analyzed with the help of analogue models, that have highlighted how the salt overhang becomes a preferential point of deformation and how gravity spreading and gravity gliding act both at different times of the evolution of the allochthonous structure. Moreover, salt cusps and mock-turtle anticlines interpreted in the seismic dataset testify phases of diapir falls most likely related to crustal extension. The Quaternary evolution of the salt structures is strongly related to the tilting of the margin in response to the glacial sedimentary wedge deposition, and mostly consists in an internal redistribution of salt inside the allochthonous salt bodies, suggesting very limited connections with the autochthonous salt.

Chapter V: GENERAL DISCUSSION AND CONCLUSIONS

In this work we analyzed the timing and mechanisms of salt tectonics in the Western Mediterranean and Southwestern Barents Sea, and discussed in detail the interaction between salt and crustal tectonics in each of the three case studies. Different timing and mechanisms of salt tectonics have been encountered not only in the different study areas, but even in areas just few tens of kilometers distant (as in the case of the Algerian margin), or between separate allochthonous salt structures that due to differences in salt volume, local stress direction or position of the sedimentary wedge present a markedly different development, as in the case of the Sørvestsnaget Basin. The results of the study show therefore the high variability of the salt tectonics deformation as a result of differing geological settings. Both in the Mediterranean and in the Barents Sea the salt presence, distribution and geometry has been used as a proxy to decipher crustal movements, often not well imaged in the seismic profiles due to the screening effect of the halite on the seismic data and hidden by the ductile behaviour of the salt.

In the Western Mediterranean the salt layer deposited during the Messinian Salinity Crisis (5.6 Ma), so salt tectonics is relatively young, the overburden is limited to the Late Messinian and Plio-Quaternary sedimentation and the marks of the first stages of salt deformation are usually imaged. In this study we analyzed two margins of the Western Mediterranean presenting structural similarities (e.g. back-arc context formation).

On the Western Sardinian starved margin the main mechanism of salt tectonics is gravity gliding, resulting from the basinward slope of the base salt, while the Rhone Deep Sea Fan thick sedimentary sequence influences the salt structures geometries towards the center of the Sardo-Provencal Basin. On the Southwestern Sardinian margin salt deformation is very locally influenced by the presence of a crustal strike slip fault recognized in this study as part of the North Balearic Fracture Zone, and reactivated after the end of the Messinian Salinity Crisis.

On the sector of the Algerian margin analyzed in this study, salt tectonics is mostly the result of the reactivation in compression of the margin and the consequent uplift of certain areas, that leads to gravity gliding. Salt tectonics started early in all the area for downbuilding, and led to the formation of polygonal minibasins which evolution was influenced by both the uplift of the plateau offshore Dellys and by the differential sedimentary load due to river inputs. Gravity gliding is also present and highlight the uplift of the Hannibal High.

Very different is the situation in the southern Sørvestsnaget Basin (Southwestern Barents Sea), where the salt deposited during Permo-Carboniferous and the Mesozoic extensional tectonics due to the Atlantic Ocean opening led to reactive and active salt diapirism, with formation of allochthonous salt structures and successive fall of part of them. After the long-lived phase of crustal extension, the Quaternary glacial sedimentary wedge led to glacio-isostatically controlled crustal movements, that locally resulted in an internal redistribution of the salt in the allochthonous salt structures for gravity gliding. Part of the hypothesis on the salt tectonics mechanisms in the Algerian margin and Sørvestsnaget Basin were confirmed through analogue modelling.

It results clear in this study that salt tectonics is an extremely complex phenomenon, that depends on a large number of factors. Some of these factors are well visible in the seismic reflection data, as

the sedimentary load of the deep-sea fans –often visible in the bathymetric data-, the slope of the salt base, the presence of crustal normal faults etc., and can therefore be measured (e.g. degrees of slope) and taken into account when we decipher the mechanisms of salt tectonics and their relative role in the deformation of a certain salt body. On the other hand, some of the factors that influence salt tectonics are not visible in the seismic data. First of all, the initial distribution of salt is unknown. As we saw in the case of the Algerian margin and confirmed by analogue modelling, the ductile nature of the salt in geological times, together with salt dissolution and chemical transformation, leads to a lack of information about the original salt thickness, that becomes therefore another unknown element in our equation. Even the sedimentary load may not be visible in the data due to successive erosion, making it difficult to recognize the gravity spreading phenomena. Obviously what can and cannot be imaged with the seismic reflection data also depends on the data characteristics in terms of resolution and penetration, and for what concerns the 2D data it also depends on the number and direction of the seismic reflection profiles.

- **Differences and similarities between the Mediterranean salt and the Arctic salt**

The complex topic of the interaction between salt and crustal tectonics has been addressed in this thesis analyzing both the Mediterranean and the Arctic salt giants. These two areas are strongly different in terms of geological settings, and also the evaporitic layers that represent their common feature is quite unlike. For what concerns the age, the Arctic salt deposited almost 300 Ma earlier (Upper Carboniferous-Early Permian) than the very recent Messinian salt of the Mediterranean. While this does not strongly influence the characteristics of the halite in terms of density and rheological characteristics, it results in completely different stages of development and maturity of the salt structures.

Moreover, the Barents Sea presents multiple phases of rifting that triggered and controlled the salt movement. Older salt deposition also means, in most cases, thicker brittle overburden. While in the Mediterranean the overburden is up to few kilometers thick, leading to the common imaging of both the top and the base of the salt layer, in the Barents Sea it is highly variable, thicker moving towards the western Barents (i.e. towards the Sørvestsnaget Basin) and reaching several kilometers. The thickness of the sediments above the Arctic salt is an obstacle for the correct imaging of the autochthonous evaporitic layer, that locally cannot be interpreted in the seismic data and has to be modelled through potential field data. Another difference between the two salt bodies concerns the salt distribution. While the salt distribution is quite uniform in the Western Mediterranean -with the exceptions of the Tyrrhenian and Valencia basins-, in the Barents Sea the distribution of the evaporites is strongly controlled by the Carboniferous grabens geometry. The original thickness of the salt in the Barents Sea is very difficult to evaluate due to the complexity of the salt structures and to the thick layer of sediments above the source salt layer.

The parallel study of different areas can be very enriching, because some of the informations that we obtained from the Mediterranean Messinian salt can be applied to the study of the Barents Sea Arctic salt, and vice versa. First of all, in the Mediterranean we have a very good imaging of the salt thanks to the reduced thickness of the overburden. Therefore, in the Mediterranean it is relatively easier to study the relationship between salt and crustal tectonics in different crustal tectonic settings (convergence, divergence, strike-slip). The knowledge acquired in the study of the Mediterranean could be applied in the Barents, where there are higher levels of uncertainties.

Moreover, due to the very good constrain in terms of timing of the Messinian salt giant formation, many studies have been focused on the rates of deposition and the hydrological balance necessary to deposit the amount of salt that has been estimated. Improved knowledge from this point of view, on which part of the SaltGiant project was focused, could lead to a more precise datation of the Barents salt deposition and new hints on the climatic conditions.
Another interesting element in the Western Mediterranean is that the sedimentary sequence above the salt is limited and with important regional differences (sediment starved VS sediment nourished margins), helpful for the study of the relationship between the salt giant and the brittle overburden and the resulting geometries. This knowledge can then be applied to the Barents Sea, where more unknown variables are present in the equation.
On the other hand, the study of the Barents Sea gives us information that we can apply to the study of the Mediterranean salt giant. In particular, in the Barents Sea the salt has been drilled several times, while just a few percent of the MSC sequence has been drilled offshore for scientific purpose, and the industrial boreholes results in cuttings instead of complete cores of the sedimentary sequence. The study of the Barents Sea cores could therefore be helpful for rheological studies on the evaporites.
Moreover, analyze salt tectonics structures at a higher level of maturity allows to make hypothesis about the future evolution of the imaged structures.

- **Future prospects**

This work answered to numerous questions in terms of salt tectonics and interaction between salt and crustal tectonics in different study areas, but at the same time it opened a series of questions that will hopefully be object of future studies and potentially of future data acquisition surveys. In particular, it would be interesting to focus on the following topics:

  - Now that we know the precise localization of the recent reactivation of the North Balearic Fracture Zone, it would be useful to acquire more data along this segment of the strike-slip fault, in order to better constrain the geometry and consequently the origin of the compressional strain imaged, possibly caused by the geometry of the strike slip or by the regional stress. Moreover, it would be interesting to deepen the topic of the Mobile Unit influence on the geometry of the flower structure and vice versa, potentially through analogue modelling.
  - For what concerns the Northern Algerian margin, it would be interesting to analyze in more detail the effect of the sedimentary load offshore Béjaïa, where there are very few data available. A seismic profile imaging the offshore limit of this deep-sea fan could give an image of the role of gravity spreading in the evolution of this sector.
  - The area of the Southern Sørvestsnaget Basin has been analyzed in detail thanks to the 3D dataset, but an interpretation of some 2D seismic reflection profiles could help to zoom out on the salt tectonics mechanisms at a more regional scale. Moreover, modelling the gravity inversion could give information on the deeper structure of the basin and the autochthonous salt distribution, not imaged by seismic reflection data. Future analogue modelling could focus on the diapir fall dynamics.

List of Figures and Tables

Chapter I:

Figure 1.13: *Schematization of different salt welds (primary, secondary, tertiary).*

Figure 1.14*: Minibasin geometries.* ***1.****Analogue modelling of a minibasin (this study), with silicone and sand representing respectively the salt layer and the brittle overburden (scale 1:100'000) and* ***.2*** *Schematization of the formation of a minibasin (Peel, 2014).*

Figure 1.15: *Evolution (from top to bottom) of a turtle structure, with the salt marked in black (Peel, 2014). When the structure forms above a subsiding diapir, it is called mock turtle anticline (Vendeville and Jackson, 1992b).*

Figure 1.16*: Theoretical model of gravity gliding and gravity spreading based on the hydraulic heads.* ***1.*** *Schematization of gravity gliding, where the driving mechanism is the elevation head (z).* ***2.*** *Schematization of gravity spreading, where the driving mechanism is the pressure head ($\rho_0/\rho_s)*h_N$. These mechanisms are independent by the density of the overburden if the density is constant. Both gravity gliding and gravity spreading mechanisms result in the formation of three domains: an upslope extension, a midslope translation, and a downslope contraction* ***(3. and 4.)****. Modified after Hudec and Jackson, 2007; Rowan, 2020; Vendeville, 2005.*

Figure 1.17. *Influence of rate and mode of sedimentation on the resulting geometries of gravity gliding (Vendeville, 1987), in a schematization (above) and in the analogue modelling (below). A: low sedimentation rate, uniform sedimentation. B: high sedimentation rate, uniform sedimentation. C: low sedimentation rate, non-uniform sedimentation. D: high sedimentation rate, non-uniform sedimentation.*

Figure 1.18: *Silicone putty of an analogue modelling, simulating the convergent gravity gliding as a result of a concentric 5° slope (Cobbold and Szatmari, 1991).*

Figure 1.19: *Regional seismic profile from the Gabonese passive margin, with the post-rift salt layer interpreted in magenta and the division in extensional, translational and compressional domains (modified after Tari et al., 2003).*

Figure 1.20: *Analogue modelling of gravity spreading in 3D (Gaullier and Vendeville, 2005).* ***1.*** *The presence of a brittle, semicircular lobe of sediments above a silicone layer lead to the evolution of the system thanks to the plastic behaviour of the silicone and the consequent gravity spreading. As a result of radial gravity spreading, both radial (5) and concentric (6) normal faults form in the brittle overburden, and concentric folds form in front of the lobe. Radial grabens (7) and concentric grabens (8) can be identified.* ***2.*** *The schematization in of the concentric (CF) and radial (RF) faults shows that the two tipologies of faults form due to the increase of both the radius and the perimeter.*

Figure 1.21: *The Gulf of Mexico.* ***1.*** *Detailed bathymetry of the Bureau of Ocean Energy Management with approximate position of Figure 1.21.3 and zoom of the minibasins geometry on the seafloor.* ***2.*** *Schematization of minibasins evolution above a salt nappe (Rowan et al., 1999).* ***3.*** *Cross-section of the northern Gulf of Mexico continental margin (Galloway, 2008).*

Figure 1.22: *Schematization of the evolution of a salt diapir for downbuilding* (Nikolinakou et al., 2017*, modified after Barton, 1933).*

Figure 1.23: 1. *Contractional salt tectonics in the case of thin-skinned deformation and* ***.2*** *in the case of thick-skinned deformation due to basin inversion, after Letouzey et al. (1995).*

Figure 1.24: *SW-NE cross section of the Southwestern Alpine belt, showing La Robine minibasin and the compressed salt walls (Célini et al., 2020).*

Figure 1.25: *Schematization of the phases of reactive, active and passive diapirism during thin-skinned extension (Vendeville and Jackson 1992a). From the calculation of Jackson et al. (1994), the thickness of the roof has to be <20% of the thickness of the nearby sediments flanking the diapir to initiate the salt movement.*

Figure 1.26: *Analogue modelling B03 (this study) with silicone and sand representing respectively the salt layer and the brittle overburden, scale 1:100'000. The dimension of the black arrows is a qualitative*

*representation of the different pressure of the overburden on the silicone layer (black), which result in the initiation of reactive diapirism**.** The white arrows represent the movement of silicone in the model.*

***Figure 1.27:** Analogue modelling S01 (this study) with silicone and sand representing respectively the salt layer and the brittle overburden, scale 1 :100'000. The growth of the salt diapir for active diapirism leads to the formation of faults in the overburden above the diapir (i.e. keystone graben or crestal faults).*

***Figure 1.28:** Analogue modelling B01 (this study) with silicone and sand representing respectively the salt layer and the brittle overburden, scale 1 :100'000. The white layer, crosscut by the silicone, testify the passive growth of the structure (passive diapirism).*

***Figure 1.29:** Schematic rise and fall of diapirs during sedimentation (Vendeville and Jackson, 1992b). **1.** Regional extension during the reactive rise of diapirs. **2.** Passive rise of the salt structur. **3. to 5.** Initiation and progression of the salt structures fall, up to the formation of the mock-turtle anticline (5).*

***Figure 1.30**: The Central North Sea. **1.** Seismic profile of the Dutch Graben, southern North Sea (VSA, 2022, seismic data from Fugro). The salt deposited in a rift basin and the salt structures -salt walls and salt domes- grew for downbuilding during sediment accumulation, and folds and mini-basins formed in response to movement of underlying salt. **2.** Seismic profile of an extensional ramp-flat system later compressed (Stewart, 2007).*

Chapter II:

***Figure 2.1: 1.** Schematized image of the seismic reflection acquisition offshore. **2.** Raypaths examples and resulting oscillographic trace showing the effects of interference and tuning **(.2)**. After Verma (1986) and Ashcroft (2011).*

***Figure 2.2:** Relationship between velocity of the seismic signal (km/s) and density of the geological material (g/cc). Evaporitic materials as salt, dolomites and anhydrites do not follow the main trend, and have high velocity compared to their relatively low density (Ashcroft, 2011).*

***Table 2.1:** Physical properties of main evaporitic minerals (Jones and Davison, 2014)*

***Figure 2.3**: The IFZ (Inner Fresnel zone) here schematized represents the bigger zone of reinforcement (+) of the seismic signal. Zone marked by '-' are the areas of cancellation of the signal (Ashcroft, 2011).*

***Figure 2.4:** Time and frequency domains can be considered complementary, so if one domain is compressed, the other one is extended. The wavelet c) can be considered a standard one, while d) is the ideal spike with white frequency spectrum (from Ashcroft, 2011).*

***Figure 2.5:** Multiples are secondary reflections that can have interbed or intrabed raypath. a) surface multiple b) ghosting c) water reverberation d) peg-leg multiple (from Ashcroft, 2011).*

***Figure 2.6:** Comparison between seismic data pre and post PSTM (Pre-Stack Time Migration). **1.** In the pre-processing the imaging of the salt is challenging. **2.** The migration removed the ringing and improved the imaging of the faults and the base salt, and the continuity of the deeper reflectors (5.5 s TWT).*

***Figure 2.7**: Schematization of the multibeam echosounder acquisition. **1.** The intersection between the transmit and the receive beams represents the area imaged by the instrument (blue rectangle) (Zwolak, 2015). **2.** Both the intensity of the signal, i.e. backscatter imagery (on the left), and the time delay, i.e. the bathymetry (right) are registered (https://www.flotteoceanographique.fr).*

***Figure 2.8:** Relationship between the geoid (blue line), the ellipsoid (black) and the terrain surface (brown line) (Forsberg et al., 2022).*

***Figure 2.9**: Gravity field of a sphere (Dentith and Mudge, 2014). The gravity measured values **(.1)** above the spherical source **(.2)** is the result of the two fields due to the Earth and the sphere, respectively blue and red in the representation **(.3)**.*

Figure 2.10: *Induced magnetic field of a spherical source:* ***1.*** *at the magnetic north pole* ***2.*** *at mid latitude northern hemisphere* ***3.*** *at the magnetic equator and* ***4.*** *at mid latitude southern hemisphere. The TMI is the scalar strength of the field (Dentith and Mudge, 2014).*

Figure 2.11*: Position of the 3 datasets used for this study: the Northern Algerian margin and the Western Sardinian margin in the Western Mediterranean, and the Sørvestsnaget Basin in the Southwestern Barents Sea.*

Table 2.2*: Characteristics of the dataset used on the Western Sardinian margin.*

Figure 2.12: *Position of the datasets used for this study on the Western Sardinian margin: MS (pink lines), CROP (yellow lines) and WS (blue lines). The position of the area is marked in Figure 2.10. NBFZ: North Balearic Fracture Zone. HMA: Hamilcar Magnetic Anomaly. EBE: Emile Baudot Escarpment.*

Figure 2.13*: Position of the datasets used for the study on the Algerian margin: MARADJA I (black lines), MARADJA II (blue lines), SH73 (pink lines) and ALE77 (red lines). The red star shows the location of well 371. The position of the area is marked in Figure 2.11.*

Figure 2.14*: Variations in amplitude as a function of the frequency (amplitude spectra) of the 3 seismic reflection datasets on the Algerian margin.*

Figure 2.15*:* ***1.*** *Location of the study area in the Southwestern Barents Sea with position of the main highs, platforms and basins.* ***2.*** *Detail of the 3D dataset and wells position in the Southern Sørvestsnaget Basin with position of the main structural elements.*

Table 2.4: *Characteristics of the different dataset used for the study of the salt tectonics in the SW Barents Sea. All the data are property of TGS.*

Figure 2.16*: Seismic stratigraphy classifications.* ***1.*** *Schematization of the main seismic units' characteristics* ***2.*** *Schematized geometry of the reflectors terminations.* ***3.*** *Reflector classification based on the continuity, frequency and amplitude of the reflection. After Catuneanu et al., (2011); Mitchum et al., (1977) and Vail et al., (1977).*

Figure 2.17*: Data integration in the Algerian margin.* ***1.*** *Grid of the top salt.* ***2.*** *Bathymetric data.* ***3.*** *Possible correction of the grid. The grid of the salt top strongly depends on the position of the seismic profiles (yellow thin lines), but it can partly be corrected with the bathymetric data if the salt structures deform the seafloor. We can therefore track the 3D geometry of the salt structures in the area (.3). While the illustrated corrections have not been applied to the maps presented here, they have been considered during the analysis of the salt tectonics in the area.*

Figure 2.18*: Flowchart of the seismic data interpretation. For details, see text.*

Figure 2.19*: Volume attribute calculator in HIS Kingdom software.*

Figure 2.20*: Comparison between the different gridding algorithms available in Kingdom Software and applied on the salt top horizon, divided in mathematical modelling algorithms (upper line) and data adaptive algorithms (bottom line). All the calculated grids presented in this work have been constrained by a polygon, delimitating the area in which a seismic facies is present. The segment of seismic reflection profiles shows the cubic spine and gradient projection algorithms results (dark red line), applied on the data (yellow line).*

Figure 2.21*: Original sketch of the first analogue models applied to geology, from Sir James Hall (1815).*

Chapter III:

Figure 3.1: *Bathymetric map of the Mediterranean (from GeoMapApp) with the location of the study areas in relationship with the Messinian salt deposits (MU) and the main structural lineaments (Domzig et al., 2006; Jolivet et al., 2006; Lofi et al., 2011a; Lymer et al., 2018). In red are marked the two study areas in the Western*

Mediterranean: 1 – the Western Sardinian passive margin and 2 – the recently reactivated in compression Northern Algerian margin.

Figure 3.2: *Morpho-bathymetry of the Mediterranean Sea (Brosolo et al., 2012), with the shelf break (blue line) and the limit of the abyssal plain (black line). ABB: Algero-Balearic Basin; AdS: Adriatic Sea; AlB: Alboran Basin; DSF: deep-sea fan; GiS: Gibraltar Strait; Gol: Gulf of Lions; HH: Hannibal High; IoB: Ionian Basin; LPB: Liguro-Provencal Basin; SiS: Sicily Strait; TyB: Tyrrhenian Basin; VaT: Valencia Trough.*

Figure 3.3*: Reconstruction of the Western Mediterranean geological evolution:* ***1.*** *Priabonian* ***2.*** *Early Aquitanian* ***3.*** *Langhian* ***4.*** *Tortonian and* ***5.*** *present day situation with position of the schematized margins architectures of figure 3.4. (Romagny et al., 2020).*

Figure 3.4*: Comparison between the nowadays continental and oceanic crust thickness in different margins:* ***1.*** *The Western Sardinia margin* ***2.*** *The Algerian margin, position in figure 3.3.5. OC: Oceanic Crust; CC: Continental Crust; OCT: Ocean-Continent Transition. Aïdi et al. (2018).*

Figure 3.5*: Location of the transfer zones and nature of the crust in the Mediterranean region (*Jolivet *et al.*, 2021b*). 1: West Anatolia Transfer Zone, 2: Central Aegean Shear Zone, 2b: Kephalonia transfer fault; 3: western limit of the Calabria accretionary wedge, 4: transfer zone along the northern limit of the Southern Tyrrhenian oceanic/exhumed mantle domain, 5: 41st parallel fault, 6: Alps/Apennines transition, 7: Catalan-Baleares Sicily Transfer Zone (CBSTZ), 8: Central transfer zone (Valencia basin), 9: Transition between the Liguro-Provençal and Algerian basins, 10: Betic Cordillera, northern limit of the Alboran Sea, 11: Rif, southern limit of the Alboran Sea, 12: Trimiti transfer zone.*

Figure 3.6*: Map of the Western Mediterranean with the amount of deformation and strain regime (white arrows) of the highlighted active areas, while the grey arrows indicate the direction of the African plate with respect to the Eurasian plate (Nocquet and Calais, 2004). Juxtaposed is the map of the distribution of the earthquake with a magnitude of 5 or more in the Western Mediterranean between 1922 and 2022 (USGS catalogue 2022), which position corresponds to the area of maximum strain.*

Figure 3.7: 1. *Bathymetric and topographic map of the study area, with the pattern of thrusts on the Algerian margin. After Babonneau et al. (2017), Bougrine et al. (2019), Déverchère et al. (2005), Domzig et al. (2006).* ***2.*** *Detail of the Tenes region with the main geological features identified (Domzig et al., 2006).*

Figure 3.8: *NS-SE seismic profile ECORS 1, Gulf of Lions, showing the deepening of the Miocene depositional environment, the Messinian Trilogy and the Plio-Quaternary sedimentary sequence (Leroux et al., 2015).*

Figure 3.9*: Preparation of the Flexotir sphere (photo CNEXO-Laubier), seismic reflection method used to image the subsoil during the 70's.*

Figure 3.10: *The MSC scenario proposed during CIESM (2008), explanations in the text.*

Figure 3.11*: Gypsum crystals from the Sicilian outcrops of the Messinian Salinity Crisis deposits (Gessi di Cattolica).*

Figure 3.12: *Schematic distribution and characteristics of the Messinian deposits in the Western Mediterranean.* ***1.*** *Map of the present-day extent of the oceanic crust and MU deposits, together with the main structural lineaments (after Domzig et al., 2006; Jolivet et al., 2006; Lofi et al., 2011a; Lymer et al., 2018) and position of the DSDP drilling site 134 (leg XIII) (Ryan et al., 1973).* ***2.*** *Details of the drilling site 134 recoveries: nodular gypsum in a matrix of dolomitic marl and silt -similar to the nowadays Sabkhas environment-, spherules of anhydrite in a dolomitic matrix and an interbedding of halite, silt and anhydrite (modified after Ryan et al., 1973).* ***3.*** *Schematization of the MSC surfaces and units in the Western Mediterranean (Lymer et al., 2018 after Lofi et al., 2011a).* ***4.*** *The Messinian Salinity Crisis deposits of the Western Mediterranean as imaged in the seismic reflection profiles.* ***5.*** *Velocities of the seismic waves in the Plio-Quaternary and Messinian sediments from velocity forward modelling (Leprêtre et al., 2013). The velocity of the p-waves in the Messinian sequence has values between 3.9 km/s and 4.2 km/s, higher for the MU and lower for LU and UU.*

Figure 3.13: *The Messinian Erosion Surface (MES), the Top Surface (TS) and the Bottom Surface (BS) in the Western Mediterranean (Cameselle and Urgeles, 2017).*

Figure 3.14: *Seismic reflection profile showing the MU and UU in the western Tyrrhenian basin (Gaullier et al., 2014).*

Figure 3.15: 1. *Bathymetric map of the Sardo-Provencal and Eastern Algero-Balearic basins and position of the multichannel seismic reflection dataset (blue lines). Marked in red is the position of the seismic profiles that follow. NBFZ: North Balearic Fracture Zone. HMA: Hamilcar Magnetic Anomaly. EBE: Emile Baudot Escarpment.* ***2.*** *Seismostratigraphic units interpreted in the dataset, based on the nomenclature of Lofi et al. (2011) and datation of CIESM (2008), modified after Geletti et al. (2014). The absence of drilling of the pre-salt sediments makes it impossible to place temporally these horizons, which could be Messinian (i.e. Lower Unit) or pre-Messinian.*

Figure 3.16: *Detail of seismic profile WS10_13.* ***1.*** *Uninterpreted* ***2.*** *Interpreted.* ***3.*** *Zoom of the pull-up effect on the base salt horizon. VE at the seafloor: 5.8X. The maximum calculated angle of the base salt is 4°.*

Figure 3.17: *Seismic profile WS10-03 on the northeastern Sardinian margin.* ***1.*** *Uninterpreted* ***2.*** *Interpreted. V.E:~ 8X.*

Figure 3.18: 1. *Gradient projection grid of the base of the MU in the whole dataset and* ***2.*** *Detail of the salt base grid (flex gridding algorithm) in the area of higher density of data. Minimum values of 1.9 s TWT depth are registered on the Sardinian slope, while the maximum values of almost 6 s TWT are at the northwestern limit of the dataset.*

Figure 3.19: *Isobaths map of the top of the Mobile Unit in the area. Values range is between 3 and 5.9 s TWT, with increasing values towards the center of the basin and maximum depth values towards north.*

Figure 3.20: *Thickness map of the brittle cover, i.e. the PQ and UU deposits, on the Western Sardinian margin, with contour interval 0.3 s TWT. In red is marked the limit of the Rhone Deep Sea Fan influence, and the red arrows show the direction of the sedimentary influx.*

Figure 3.21: *Line drawing of CROP seismic reflection profile imaging between the Sardinian slope to the center of the basin, and zooms. Modified after Finetti (2005). VE: 6.7 X.*

Figure 3.22: *Seismic profile MS044, southwestern Sardinian margin.* ***1.*** *Uninterpreted* ***2.*** *Interpreted. VE: 4X.*

Figure 3.23: *Seismic profile MS043, southwestern Sardinian margin.* ***1.*** *Uninterpreted* ***2.*** *Interpreted. VE: 4X.*

Figure 3.24: *Seismic profile MS099, southwestern Sardinian margin.* ***1.*** *Uninterpreted* ***2.*** *Interpreted. VE: 4.8X.*

Figure 3.25: 1. *CROP profile line drawing, position in Figure 3.25.2****. 2.*** *Isobath map of the base of the MU.*

Figure 3.26: *Top View of model BO3, modelling the early salt tectonics* ***(1.)*** *and the gravity gliding consequence of the tilting of the box model* ***(2. and 3.)****, and section of the model at the end of the experiment* ***(.4)****. Gaullier et al., in prep.*

Figure 3.27: *Retrodeformation of the crustal structure interpreted in seismic reflection profile MS044.* ***1.*** *The sedimentary sequence of the MSC is deposited.* ***2.*** *The sequence is offset by transtension, leading to the formation of a negative flower structure (http://earthquake.usgs.gov).* ***3.*** *The early Pliocene sedimentary sequence fills the bathymetric low.* ***4.****The sequence is deformed by the transpressional stress* ***5.*** *The deposition of the Pleistocene sequence postdates the crustal activity.*

Figure 3.28: *Bathymetric and topographic map of the Algerian margin, with marked the position of the seismic reflection dataset and the division in western (zone 1: 2°20' to 4°E, 36°40' to 37°20'N), eastern (zone 2: 4 to 6° E, 36° 35' to 37°30' N) and northern (zone 3: 3°40' E to 5°E, 37°25' to 38°20'N) sectors.*

Figure 3.29: *Detail of seismic profile MARADJA 01-97, with the seismostratigraphic units interpreted in the dataset, based on the nomenclature of Lofi et al. (2011) and datation of CIESM (2008). VE: 4X****.***

Figure 3.30: .1: *Isobath map of the base of the Mobile Unit on the Algerian margin, with contour lines every 0.2 s TWT and values between 4.0 and 5.5 s TWT. The geometry of this grid is partly deformed by the presence of pull-ups (see text for details).* ***2.*** *Detail of the base of the Mobile Unit in Zone 1, with contour lines every 0.2 s TWT. The position of the thrusts is from Déverchère et al. (2005) and Domzig et al. (2006), while the dashed red line shows the division between the uplifted plateau, the slope and the deep area.*

Figure 3.31*:* ***1.*** *Isobath map of the top of the Mobile Unit on the Algerian margin, with contour lines every 0.5 and values between 3.6 and 5.4 s TWT. The apparent distribution of the salt structures is strongly dependent from the position of the seismic lines, particularly in areas of well-developed salt tectonics, in which the apparent distribution of the salt structures in the map is limited by the position of the seismic profiles.* ***2.*** *Detail of the base of the MU in Zone 1, with contour lines every 0.4 s TWT and values between 3.7 and 5.4 s TWT. As in Figure 3.30, the dashed red line shows the division between the uplifted plateau, the slope and the deep area.*

Figure 3.32: *Thickness map of Mobile Unit on the Algerian margin, with contour lines every 0.5 s TWT and values between 0 and 1.6 s TWT, corresponding respectively to the structural highs and to the bigger salt diapirs of Zone 1.*

Figure 3.33*: Thickness map of the Upper Unit on the Algerian margin, with contour lines every 0.4 s TWT and values between 0 and 0.7 s TWT, with the lower ones corresponding to the structural highs and to the major salt diapirs.*

Figure 3.34: *Thickness map of the Plio-Quaternary deposits on the Algerian margin with contour lines every 0.5 s TWT. This map presents the higher areal extension, due to the greater ease in interpreting these shallower deposits and to the fact that they are present ubiquitously in all the seismic profiles.*

Figure 3.35: 1. *Thickness map of the brittle cover, i.e. Upper Unit and Plio-Quaternary deposits, on the Algerian margin with contour line every 0.5 s TWT and values between 0 and 2 s TWT. A major depocenter is present around 5°20' E, while minimum values are northward (i.e. Hannibal High).* ***2.*** *Zoom of the brittle cover thickness on area 1, with contour lines every 0.3 s TWT and values between 0 and 1.8. The two depocenters are here related to the sediments of the Algiers Ridge and to the piggy-back basin above the uplifted plateau.*

Figure 3.36*:* ***1.*** *Seismic profile MDJ01-03, parallel to the margin offshore Algiers and Boumerdes, highlighting the presence of an uplifted area and a deeper one, connected by a slope. The black rectangle marks the position of figures 3.36.2, 3.36.3 and 3.36.4. VE: 8.8X.* ***2.*** *Detail of seismic profile MDJ01-03 located on the uplifted plateau. VE: 5.6 X* ***.3:*** *Detail of seismic profile MDJ01-03 located on the slope, at the transition between the uplifted plateau and the slope. The presence of extensional faults in the UU marks the extensional salt tectonics domain. VE: 5.6 X* ***4.*** *Detail of seismic profile MDJ01-03 in the deep basin, imaging the major salt structure of this study area. VE: 5.6 X*.

Figure 3.37*: Seismic profile MDJ01-95, perpendicular to the margin in the area of the uplifted plateau.* ***1.*** *Uninterpreted* ***2.*** *Interpreted. The red arrows represent the supposed position of the thrust that leads to the formation of the anticlines, with major uncertainties concerning the one at km 40, where the visualization of the pre-salt geometries is disturbed by the presence of a salt diapir. VE: 5.6 X.*

Figure 3.38*: Seismic profile MDJ01-96, perpendicular to the margin in the area of the uplifted plateau.* ***1.*** *Uninterpreted* ***2.*** *Interpreted. The profiles perpendicular to the margin show some piggy back geometries (Déverchère et al., 2005a) due to the thrusts rooted below the Messinian sediments, that is also responsible for the southward slope of the base of the salt in this seismic profile. The red arrow represents the supposed position of the thrust that leads to the formation of the anticline. The black dotted line divides the Plio-Quaternary sediments in two subsets: a lower sequence in which are co-present the effects of the salt and crustal tectonics (i.e. anticlines and thickening of the sequence towards south) and an upper one in which the horizons geometries are exclusively the result of the thrust activity. VE: 5.6 X.*

Figure 3.39: 1. *Detail of seismic profile MDJ 01-04, parallel to the margin and imaging the structures related to the minibasins, and* ***2.*** *The multibeam bathymetry data acquired during the MARADJA survey, allowing to interpret in 3D the salt structures which results to be annular salt ridges surrounding polygonal minibasins.*

Onlapping horizons and fan-shaped strata geometries are already present in the sediments that pre-date the end of the MSC. VE: ~6.7X.

***Figure 3.40**: Seismic profile ALE 77-33-1 parallel to the coast line, in zone 2.* **1.** Uninterpreted **2.** Interpreted, *with position of the zoom of figures **.3** ad **.4** (uninterpreted and interpreted) (VE: 4.5 X). VE:~22.5 X The dotted lines represent the acoustic basement.*

***Figure 3.41:** Seismic profile MDJ 02 -70, perpendicular to the coastline in zone 2. **1.** Uninterpreted **2.** Interpreted. V.E.:~ 5X. As visible in the zoom **(.3)**, the UU has different thickness along the seismic profile, and apparent downlap geometries are interpreted in the lower Plio-Quaternary.*

Figure 3.42**: Seismic profile MDJ01-01 (V.E.~ 22 X), imaging the area of the Hannibal High, **1.** Uninterpreted **2.** Interpreted, with marked the position of the zoom of figure **3.

***Figure 3.43:** Isobath map of the base of the Mobile Unit and schematization of the elements of the model representing the uplift of a plateau in an area characterized by the presence of a salt layer. The red arrows represent the slopes direction in the base salt, while the green ones represent the tectonic stress in the area.*

***Figure 3.44:** Schematization of the box model used for models A01 and A02, in top view and side view. The division in different areas is based on the nature of sediments (brittle and ductile) and on the actions that will be performed during the experimental procedure. A change in the size of zone A and of the plate has been made between model A01 and 02, therefore both the values are present in the schematization.*

***Table 3.1:** Experimental procedure of model A01.*
***Figure 3.45**: Model A01, evolution of the top view between time T=4h30' and T=29h40' (end of the model). **1.** T=4h30', the uplifted plateau is well developed and the first faults form above it. **2.** At T=7h, E-W and N-S faults (F) are present on the eastern side of the box model, while NE-SW faults connect the uplifted plateau of the eastern side of the model to the uplifted area on the SW. Folds (FO) are well developed at the limit between areas A and B. **3.** After the overnight development (T=22h25') the silicone reached the surface of the model through the extensional faults. Minibasins geometries (MB) start to be visible on the model surface. **4.** After another layer of sedimentation, the minibasins geometries (MB) are clearer on the uplifted plateau, and the N-S and E-W faults are visible only at the northern and western limits of the plateau. **5.** Towards the end of the model, the minibasins geometries are more and more clear. The position of the section 01-20 and 01-02 is marked with the black dotted line.*

***Figure 3.46**: Section A01-02, cut in a N-S direction and located at 3 cm from the western limit of the box model (position in Figure 3.44). In black are interpreted the reverse faults of the pop-up, result of the compressional stress applied to the model. The silicone layer is thinned above the uplifted plateau, and forms thick structures towards the southern part of the model.*

***Figure 3.47**: **1.** Section A01-20 (E-W direction) located at 31 cm from the northern limit of the box model. In red are interpreted the normal faults above the silicone layer, result of the downslope movement of the silicone due to the plateau uplift. Silicone anticlines formed downslope. **2.** The minibasins interpreted in top view (Figure 3.45) are particularly well visible in the zoom on the slope, where the sediments form turtle-back geometries.*

***Table 3.2:** Experimental procedure of model A02.*

***Figure 3.48**: Model A02, evolution of the Top View between time T=0 and 12h15' (end of the model). **1.** Beginning of the model. **2.** At T=5h35', folds (FO) are well developed at the limit between areas A and B in the eastern part, and towards the center of the model in the western one. A NE-SW fault (F) connects the uplifted plateau of the eastern side of the model to the uplifted area on the SW. **3.** At time T=7h15', sand depocenters of 4-6 cm are added, in order to simulate the irregular sedimentation at the deep sea fans. Minibasins geometries (MB) start to be visible on the model surface. **4.** After another layer of sedimentation, the minibasins geometries (MB) are partly visible on the uplifted plateau. **5.** At time T=12h15', the minibasins geometries are well visible on the slope connecting the uplifted plateau to the deeper western area. N-S and*

E-W faults are partly visible, but their special development is limited by the presence of minibasins. The position of the section 02-02, 02-05 and 02-13 is marked with the black dotted line.

Figure 3.49: *Section A02-02, in a N-S direction and located 5.7 cm from the eastern glass wall. The double slope direction, both southward and northward, leads to gravity gliding in the two directions.*

Figure 3.50: *E-W sections A02-05* ***(1.)*** *and A02-13* ***(2.)****, located respectively at 6.5 and 25.5 cm from the northern limit of the box model. In .1 the salt structures develop without the influence from the compressional stress, while in .2 the plateau uplift affects the silicone layer producing gravity gliding towards west.*

Figure 3.51: *Reconstruction of the evolution of Zone 1 since the MU deposition, and position (in .4) of the following figures. Doubts exist on the geometry of the area during the deposition of the MU* ***(1.)****, but after the MU deposition the area was flat. While the UU was depositing, the first salt structures formed ubiquitously for downbuilding* ***(2.)****, and before the end of the Messinian Salinity Crisis the eastern plateau started to uplift, leading to gravity gliding westward* ***(3.).*** *Despite crustal tectonics is still active in the area, recent salt tectonics characterize only the slope and part of the abyssal plain, where the salt walls are thicker* ***(4.).***

Figure 3.52*: Growth geometries in the UU in seismic profile MDJ01-03* ***(1.)****, parallel to the margin. The beginning of the salt movement predates the end of the MSC, while no activity is present during the late Plio-Quaternary. Similar geometries have been identified in the analogue models* ***(2.)****, where the silicone structures started to form very early during the UU deposition.*

Figure 3.53: *Comparison between the geometries interpreted in the seismic reflection profile parallel to the margin MDJ01-03* ***(1.)*** *and the interpretation of the geometries in analogue model A02* ***(2.)****.*

Figure 3.54: *Seismic profile MDJ01-96. VE: 5.6 X. The brittle overburden is here divided in a pink sequence of crustal and salt tectonics co-presence, an onlapping violet sequence towards the end on the salt related deformation, and a light blue sequence of crustal deformation (piggy-back geometries).*

Figure 3.55: *Comparison between the geometries of the model surface* ***(1.)*** *and the bathymetric data* ***(2.)****.*

Figure 3.56: *Comparison between the base of the Mobile Unit with marked the slope directions (red arrows), the isopach map of the brittle sedimentary cover (the dotted red line shows the limit of the Algiers Ridge) and the minibasins position (oval detail of the bathymetry).*

Figure 3.57: *Reconstruction of the northward gravity gliding and consequent salt structures formation. After the deposition of the lower UU* ***(1.)****, salt starts to glide towards north forming the first salt structures* ***(2. and 3.)****. The northward movement of the salt leads to deflation of the firstly formed structures and formation of new structures downslope* ***(4.),*** *leading to the geometries interpreted in the seismic reflection profile MDJ02-70.*

Figure 3.58: *Flattening of the top of the UU, showing the onlapping geometries and the lateral thickness changes of this unit.*

Figure 3.59: *Reconstruction of the evolution of zone 3 as a consequence of the Hannibal High uplift. After the MU deposition* ***(1.)****, the UU deposited on an already uplifted structure* ***(2.).*** *The uplift of the Hannibal High results in gravity gliding downslope* ***(2. and 3.)****. Despite the crustal activity is still active and deformation is visible on the seafloor, salt tectonics seems to have stopped towards the end of the Quaternary* ***(4.).***

Chapter IV:

Figure 4.1*: Structural map of the Sørvestsnaget Basin, Henriksen et al. (2011).*

Figure 4.2*: Geodynamic evolution of the North Atlantic and Arctic regions (Smelror et al., 2009).*

Figure 4.3*: Schematic (min./max.) model of lateral ice extension in the Barents Sea region during the Late Plio-Pleistocene time period (black stippled lines: maximum; white transparent polygons: minimum. The three different phases contain themselves strong fluctuations in the glacial size. Knies et al. (2009).*

***Figure 4.4**: Main highs and basins of the SW Barents Sea and position of the study area. **1.** The black rectangle marks the position of figure 4.4.2. GH: Gardarbanken High; LH: Loppa High; BB: Bjornaya Basin; HB: Hammerfest Basin; NB: Nordkapp Basin; NH: Norsen High; SD: Svalis Dome; SH: Stappen High; SR: Senja Ridge; VH: Veslemoy High; VVP: Vestbakken Volcanic Province. Compiled after Henriksen et al. (2011). **2.** Position of the TGS 3D dataset and wells in the southern Sørvestsnaget Basin structural map, and position of the seismic profile of Figure 4.6. Compiled after Lasabuda et al. (2018), bathymetry from Emodnet bathymetry.*

***Figure 4.5**: Lithostratigraphic column of the Southwestern Barents Sea, which the main regional tectonic events from the Paleozoic to the present (Omosanya et al., 2017).*

***Figure 4.6**: General section showing the stratigraphy of the Tromso and Sørvestsnaget basins, divided by the Senja Ridge (modified after Lasabuda et al., 2018). Location in Figure 4.4.2.*

***Figure 4.7**: 2D Seismic reflection profile of a Salt Diapir in the northern Tromsø Basin (Rowan and Lindsø, 2017).*

***Figure 4.8**: **1.** Position in map of the previous studies in the area. **2.** First map of the salt structures in the southern Sørvestsnaget Basin by Knutsen and Larsen (1997) and **3.** Mapping of the main horizons above a salt structure in the Southern Sørvestsnaget Basin (Perez-Garcia et al., 2013).*

***Figure 4.9:** Integrated use of the available data. **1.** Seismic reflection profile (position in figure 4.9.4) of the 3D Carlsen dataset. The positive and negative amplitudes reflections are respectively black and white. VE at the seafloor: 7.7 X. **2.** Seismic reflection profile with superimposed the stack velocity values and the relative value of the 30 km high-pass filtered Bouguer gravity anomaly (red line), this last highlighting a difference in density of the subsoil. **3.** Interpreted seismic profile, result of the integration between seismic reflection data and the velocity data derived from it, Bouguer gravity anomaly and wells data. The division in faults families is based on their genesis: crustal faults (blue), salt related faults (red) and polygonal faults (black). **4.** Relative values of Bouguer gravity anomaly, 30 km high-pass filtered. The black line shows the position of the seismic profile in 4.9.1, .2, .3. Seismic data courtesy of TGS.*

***Figure 4.10**: Time slices of the 3D dataset at 1300, 2000, 2500 and 3000 ms TWT. In violet is marked the position of the Senja Ridge and in yellow the position of the interpreted allochthonous salt structures (respectively A, B and C from north to south). Seismic data courtesy of TGS.*

***Figure 4.11**: Comparison between the stacking velocity data (above) and the seismic reflection profile from which the velocity data were obtained (below). The velocity data are locally used to distinguish between bodies with comparable seismic facies, as the transparent Senja Ridge and the salt. VE with a velocity of 2000 m/s: 2X. Seismic data courtesy of TGS.*

***Figure 4.12**: Thickness map of the Tertiary deposits, i.e. between the beginning of the Cenozoic (66 Ma) and the Upper Regional Unconformity (2.6 Ma). Minimum values correspond to the Senja Ridge (marked in violet) and the salt structures A, B and C, while values of up to 2.9 s TWT characterize the depocenter of salt structure A.*

***Figure 4.13**: Thickness map of the Quaternary deposits, i.e. between the Upper Regional Unconformity (2.6 Ma) and the seafloor. The trend of thickening towards west is locally disrupted by the highs due to the salt structures A, B and C.*

***Figure 4.14**: Structural setting. **1.** Structural map of the study area from seismic data interpretation, with position of the crustal and salt related faults and the anticlines axes, and the position of the interpreted salt structures A, B and C. The blue rectangle and the dotted blue line show respectively the position of the detail of the Base Cenozoic horizon (.4) and of the seismic profile (.3). **2.** Depth in time of the three salt structures top, between 1.6 and 5.1 s. Structures A, B and C are respectively the northern, western and southern one in the 3D dataset. **3.** Detail of a seismic profile perpendicular to the anticline axis (position in Figure 4.14.1). **4.** Crustal faults expression on the Base Cenozoic horizon (position in Figure 4.14.1). Seismic data courtesy of TGS.*

***Figure 4.15**: Detail of the salt related faults above salt structure A (in yellow), with the bright spots identified along the fault highlighted in red. The white rectangle marks the position of the zoom. VE with a seismic velocity of 2000m/s: 5X. Seismic data courtesy of TGS.*

***Figure 4.16**: Comparison between the grids of the main Cenozoic horizons (age decreasing from top left to bottom right) with position of the crustal and salt related faults (respectively red and black crosses). The crosses represent the intersection between the interpreted faults and the horizon, meaning that the fault activity postdated that horizon. Seismic data courtesy of TGS.*

***Figure 4.17**: Salt structure A. **1.**: 3D visualization of the RMS amplitude seismic attribute applied on the Top Salt horizon of salt body A, and seismic profile imaging the area. The yellow arrow shows the north direction. **2.**: 3D visualization of Top Salt horizon of salt body A, and seismic profile imaging the area with interpretation of the main seismic horizons. The allochthonous salt structure has been divided in sectors A1, A2 and A3, due to the differences in the geometry and evolution. **3.**: Thickness of the allochthonous salt structure A, in s TWT. Maximum thickness value is more than 5 km. Seismic data courtesy of TGS.*

***Figure 4.18**: Seismic reflection profile imaging sector A1, uninterpreted **(1.)** and interpreted **(2.).** Due to the uncertainties on the geometry of the base of the salt, the possible salt shape is marked with dotted lines. VE with a seismic velocity of 2000m/s: 8X. Seismic data courtesy of TGS.*

***Figure 4.19**: Detail of the seismic reflection profile imaging sector A2, uninterpreted **(1.)** and interpreted **(2.).** VE with a seismic velocity of 2000m/s: 4.2X. Seismic data courtesy of TGS.*

***Figure 4.20**: Detail of the seismic reflection profile imaging sector A3, uninterpreted **(1.)** and interpreted **(2.).** The zoom in figure 7.12.1 shows the fan shaped strata formed during the salt movement. VE with a seismic velocity of 2000m/s: 4.2X. Seismic data courtesy of TGS.*

***Figure 4.21**: Detail of the seismic profile imaging the depocenter located between A1 and A2, uninterpreted **(1.)** and interpreted **(2.),** and position of the timeslices of figure 4.10 (black horizontal lines). VE with a seismic velocity of 2000m/s: 8X. Seismic data courtesy of TGS.*

***Figure 4.22**: Salt structure B. **1.** 3D visualization of the RMS amplitude seismic attribute applied on the Top Salt horizon of salt body B, and seismic profile imaging the area. The yellow arrow shows the north direction. **2.** 3D visualization of Top Salt horizon of salt body B, and seismic profile imaging the area with interpretation of the main seismic horizons. **3.** Thickness of the allochthonous salt structure B, in s TWT. Maximum thickness value is around 3 km. Seismic data courtesy of TGS.*

***Figure 4.23**: Seismic reflection profile imaging salt structure B, uninterpreted **(1.)** and interpreted **(2.).** VE with a seismic velocity of 2000m/s: 4.2X. Seismic data courtesy of TGS.*

***Figure 4.24**: Salt structure C. **1**. 3D visualization of the RMS amplitude seismic attribute applied on the Top Salt horizon of salt body C, and seismic profile imaging the area. The yellow arrow shows the north direction. **2.** 3D visualization of Top Salt horizon of salt body C, and seismic profile imaging the area with interpretation of the main seismic horizons. The allochthonous salt structure has been divided in sectors C1, C2, C3 and C4. **3.** Thickness of the allochthonous salt structure C, in sTWT. Maximum thickness value is around 5 km. Seismic data courtesy of TGS.*

***Figure 4.25**: Seismic reflection profile imaging salt structure C, uninterpreted **(1.)** and interpreted **(2.).** The uncertainties about sector C2 are highlighted by the dotted line. VE with a seismic velocity of 2000m/s: 4.2X. Seismic data courtesy of TGS.*

***Figure 4.26**: Schematization of the elements to model based on the seismic interpretation of Figure 4.18: an autochthonous salt layer, a Late Paleozoic to Mesozoic overburden, an allochthonous salt structure with a salt overhang, a localized late Mesozoic overburden and the thick Cenozoic sedimentary sequence. The Late Paleozoic to Mesozoic overburden and the autochthonous salt layer are not to scale due to the lack of seismic imaging at that depth.*

Figure 4.27: *Schematization of the box model used for models S01, S02 and S03, in top view and side view. The division in 4 different areas is based on the actions that will be performed during the experimental procedure.*

Table 4.1: *Experimental procedure of model S01.*

Figure 4.28*: Model S01, evolution of the Top View between time T=0 and T=25h5'.* ***1.*** *T=0, the model presents a graben in zona A.* ***2.*** *At T=5h, the silicone grew in an allochthonous structure, that evolves forming overhangs (O). As a result of the tilting of the model (3.3° westward) we have formation of extensional faults (F) and grabens (G). Despite the faults develop in a mainly N-S direction, a curvature is present due to the edge effects.* ***3.*** *After the overnight development, extensive overhangs are present, with major dimensions on the western one due to the slope direction. Some silicone 'diapirs' (D) grow up to reaching the surface on the eastern side of the box.* ***4.*** *Removal of the western overhang.* ***5.*** *After localized sedimentation is added on the eastern overhang, numerous overhang faults (OF) form at few cm distance one from the other. These have a shorter wavelength compared to the faults formed as a consequence of the box model tilting.* ***6.*** *Towards the end of the model, we can recognize N-S normal faults on the entire surface of the model. Position of the section S01-03 shown in figure 4.29 is marked with the black dotted line.*

Figure 4.29*: Section S01-03, at 7.2 cm from the southern limit of the box model. In black are interpreted the normal faults result of the simulated extensional tectonics and in red the normal faults above the overhang, result of the gravity gliding above the salt overhang. The numbers represent the layers deposited on the model (Table 4.1).*

Table 4.2*: Experimental procedure of model S02.*

Figure 4.30*: Model S02, evolution of the Top View between time T=0 and T=26h30'.* ***1.*** *T=0, beginning of the model with a graben in zone A. Instantaneously some normal faults (F) and grabens (G) form both at the eastern and western side of the model, parallel to zone A.* ***2.*** *At T=6h30', the silicone grew in an allochthonous structure, that evolved forming overhangs (O). Faults and grabens that developed since the very beginning of the experiment go on growing, and more normal faults formed towards west. A diapir (D) forms in the northeastern part of the box.* ***3.*** *At T=7h10' another layer of sand is added to the model without covering the silicone structure.* ***4.*** *After the overnight development, two overhangs are present on the eastern and western side of the main allochthonous structure (T=21h30'). The extensional structures (normal faults "F" ad grabens "G") are again visible.* ***5.*** *After part of the western overhang is manually removed, localized sedimentation is added on the eastern overhang. Short wavelength overhang faults (OF) formed at T=24h30'.* ***6.*** *As a result of the tilting of the model (3.3° westward) extensional faults and grabens form on the whole model. Position of the section shown in figure 4.31 is marked with the black dotted line.*

Figure 4.31*: Section S02-07, at 17 cm from the southern limit of the box model. We can appreciate the extensional faults both above the autochtonous silicone (black lines) and above the overhang (red lines), these last one result of the gravity spreading and later of the gravity gliding above the salt overhang. The numbers represent the layers deposited on the model (Table 4.2).*

Table 4.3*: Experimental procedure of model S03.*

Figure 4.32*: Model S03, evolution of the Top View between time T=0 and T=27h15'.* ***1.*** *T=0, beginning of the model.* ***2.*** *Very early during the experiment (T=30') normal faults (F) form both at the eastern and western side of the model, parallel to zone A.* ***3.*** *Another layer of sand is added on the whole model, and at T=2h15' the presence of a crestal graben is well visible in zone A.* ***4****. After the overnight development, the silicone grows in an allochthonous structure, that evolves forming overhangs (O) (T=17h25') on the eastern and western side of the main allochthonous structure.* ***5.*** *The western overhang is manually removed, and localized sedimentation is added on the eastern overhang (T=18h25'). Short wavelength overhang faults (OF) form at T=19h.* ***6.*** *As a result of the tilting of the model (3.3° westward) extensional faults and grabens form on the whole model, along which some silicone 'diapirs' (D) that reach the model surface in zone A. The normal faults above the buried overhang have a slightly shorter wavelength compared the other ones. Position of the section shown in figure 4.33 is marked with the black dotted line.*

Table 4.4: *Synthesis of the crustal movement and of the evolution of the different salt structures.*

Figure 4.34: *Comparison between the seismic imaging of salt structure A* ***(1.)*** *and analogue modelling S03 simulating the effect of a 3.3° westward tilting on the geometries of salt overhang and overburden* ***(2.).***

Figure 4.35: *Mechanism of formation of the geometries of sector A2 overburden* ***(1.)****. In the schematization of Vendeville and Jackson (1992)* ***(2.)****, during the diapir fall a depocenter forms above a falling salt structure* ***(3.)****. The latest stage of the evolution of the depocenter is the inversion of the overburden geometries and the formation of the mock-turtle anticline* ***(1. and 2B.)****.* ***3.*** *Analogue modelling of sand and silicone simulating the formation of a brittle depocenters between the growing salt structures.*

Figure 4.36: *Co-presence of reactive and active diapirism in structure C. The active diapirism in C1* ***(1.)*** *shows a pre-kinematic layer (Cretaceous and Paleocene), a synkinematic layer (Lower Eocene) and a post-kinematic one with later minor deformation, comparable to the ones of analogue model B02 of* ***2.*** *On the other side, in sector C3 the deformation is the result of reactive diapirism, with geometries comparable to the analogue model S02 in* ***3.***

Figure 4.37: *Evidences of the Quaternary evolution of salt structure B, with the Quaternary pre-kinematic layers highlighted in blue and the syn-kinematic ones in pink. The evidences of an internal salt redistribution are the presence of a salt cusp and related faults on the NE side and the anticline of the SW side overburden.*

References

Afilhado, A., Moulin, M., Aslanian, D., Schnürle, P., Klingelhoefer, F., Nouzé, H., Rabineau, M., Leroux, E., Beslier, M.-O., 2015. Deep crustal structure across a young passive margin from wide-angle and reflection seismic data (The SARDINIA Experiment) – II. Sardinia's margin. Bull. Société Géologique Fr. 186, 331–351. https://doi.org/10.2113/gssgfbull.186.4-5.331.

Aïdi, C., Beslier, M.-O., Yelles-Chaouche, A.K., Klingelhoefer, F., Bracene, R., Galve, A., Bounif, A., Schenini, L., Hamai, L., Schnurle, P., Djellit, H., Sage, F., Charvis, P., Déverchère, J., 2018. Deep structure of the continental margin and basin off Greater Kabylia, Algeria – New insights from wide-angle seismic data modeling and multichannel seismic interpretation. Tectonophysics 728–729, 1–22. https://doi.org/10.1016/j.tecto.2018.01.007.

Alsop, G.I., Weinberger, R., Levi, T., Marco, S., 2015. Deformation within an exposed salt wall: Recumbent folding and extrusion of evaporites in the Dead Sea Basin. J. Struct. Geol. 70, 95–118. https://doi.org/10.1016/j.jsg.2014.11.006.

Andreetto, F., Aloisi, G., Raad, F., Heida, H., Flecker, R., Agiadi, K., Lofi, J., Blondel, S., Bulian, F., Camerlenghi, A., Caruso, A., Ebner, R., Garcia-Castellanos, D., Gaullier, V., Guibourdenche, L., Gvirtzman, Z., Hoyle, T.M., Meijer, P.T., Moneron, J., Sierro, F.J., Travan, G., Tzevahirtzian, A., Vasiliev, I., Krijgsman, W., 2021. Freshening of the Mediterranean Salt Giant: controversies and certainties around the terminal (Upper Gypsum and Lago-Mare) phases of the Messinian Salinity Crisis. Earth-Sci. Rev. 216, 103577. https://doi.org/10.1016/j.earscirev.2021.103577.

Ashcroft, W., 2011. A Petroleum Geologist's Guide to Seismic Reflection. Wiley & Sons. 176 p.

Auzende, J.-M., Bonnin, J., Olivet, J.-L., Pautot, G., Mauffret, A., 1971. Upper Miocene Salt Layer in the Western Mediterranean Basin. Nat. Phys. Sci. 230, 82–84. https://doi.org/10.1038/physci230082a0.

Auzende, J.M., Olivet, J.L., Bonnin, J., 1972. Une structure compressive au nord de l'Algérie ? Deep Sea Res. Oceanogr. Abstr. 19, 149–155. https://doi.org/10.1016/0011-7471(72)90047-2.

Ayadi, A., Dorbath, C., Ousadou, F., Maouche, S., Chikh, M., Bounif, M.A., Meghraoui, M., 2008. Zemmouri earthquake rupture zone (Mw 6.8, Algeria): Aftershocks sequence relocation and 3D velocity model. J. Geophys. Res. Solid Earth 113. https://doi.org/10.1029/2007JB005257.

Babonneau, N., Cattaneo, A., Ratzov, G., Déverchère, J., Yelles-Chaouche, A., Lateb, T., Bachir, R.S., 2017. Turbidite chronostratigraphy off Algiers, central Algerian margin: A key for reconstructing Holocene paleo-earthquake cycles. Mar. Geol., Subaquatic paleoseismology: records of large Holocene earthquakes in marine and lacustrine sediments 384, 63–80. https://doi.org/10.1016/j.margeo.2016.10.017.

Badley, M.E., Gibson, B., 1987. Practical seismic interpretation. The Journal of the Acoustical Society of America 82, 1100 (1987); https://doi.org/10.1121/1.395350

Barrère, C., Ebbing, J., Gernigon, L., 2009. Offshore prolongation of Caledonian structures and basement characterisation in the western Barents Sea from geophysical modelling. Tectonophysics 470, 71–88. https://doi.org/10.1016/j.tecto.2008.07.012.

Barton, D.C., 1933. Mechanics of Formation of Salt Domes with Special Reference to Gulf Coast Salt Domes of Texas and Louisiana. AAPG Bull. 17, 1025–1083.

Bellucci, M., Aslanian, D., Moulin, M., Rabineau, M., Leroux, E., Pellen, R., Poort, J., Del Ben, A., Gorini, C., Camerlenghi, A., 2021. Salt morphologies and crustal segmentation relationship: New insights from the Western Mediterranean Sea, Earth-Science Reviews, Vol. 222, 103818, ISSN 0012-8252, https://doi.org/10.1016/j.earscirev.2021.103818.

Bellwald, B., Planke, S., Lebedeva-Ivanova, N., Piasecka, E.D., Andreassen, K., 2019. High-resolution landform assemblage along a buried glacio-erosive surface in the SW Barents Sea revealed by P-Cable 3D seismic data. Geomorphology 332, 33–50. https://doi.org/10.1016/j.geomorph.2019.01.019.

Berthelot, A., Solberg, A.H.S., Gelius, L.-J., 2013. Texture attributes for detection of salt. J. Appl. Geophys. 88, 52–69. https://doi.org/10.1016/j.jappgeo.2012.09.006.

Billi, A., Faccenna, C., Bellier, O., Minelli, L., Neri, G., Piromallo, C., Presti, D., Scrocca, D., Serpelloni, E., 2011. Recent tectonic reorganization of the Nubia-Eurasia convergent boundary heading for the closure of the western Mediterranean. Bull. Société Géologique Fr. 182, 279–303. https://doi.org/10.2113/gssgfbull.182.4.279.

Blondel, S., Bellucci, M., Evans, S., Del Ben, A., Camerlenghi, A., 2021. ontractional salt deformation in a recently inverted basin: Miocene to current salt deformation within the central Algerian basin. Basin Res. https://doi.org/10.1111/bre.12673

Boucart, J., 1958. Problèmes de Géologie sous-marine, Masson Editeur. Paris. 127 p.

Bougrine, A., Yelles-Chaouche, A.K., Calais, E., 2019. Active deformation in Algeria from continuous GPS measurements. Geophys. J. Int. 217, 572–588. https://doi.org/10.1093/gji/ggz035.

Brosolo L, Mascle J, Mascle B (2012) Morpho-bathymetry of the Mediterranean Sea; 1:4.000.000 scale. Commission for the geological map of the world.

Brun, J.-P., Fort, X., 2011. Salt tectonics at passive margins: Geology versus models. Mar. Pet. Geol. 28, 1123–1145. https://doi.org/10.1016/j.marpetgeo.2011.03.004.

Brun, J.-P., Mauduit, T.P.-O., 2009. Salt rollers: Structure and kinematics from analogue modelling. Mar. Pet. Geol. 26, 249–258. https://doi.org/10.1016/j.marpetgeo.2008.02.002.

Callot, J.-P., Célini, N., Jourdon, A., Legeay, E., Mouthereau, F., Le Pourhiet, L., and Ringenbach, J.-C.: The role of salt in mountain building, from minibasin formation to orogen dynamic, EGU General Assembly 2022, Vienna, Austria, 23–27 May 2022, EGU22-2767, https://doi.org/10.5194/egusphere-egu22-2767, 2022.

Callot, J.-P., Trocmé, V., Letouzey, J., Albouy, E., Jahani, S., Sherkati, S., 2012. Pre-existing salt structures and the folding of the Zagros Mountains. Geol. Soc. Lond. Spec. Publ. 363, 545–561. https://doi.org/10.1144/SP363.27.

Camerlenghi, A., Del Ben, A., Hübscher, C., Forlin, E., Geletti, R., Brancatelli, G., Micallef, A., Saule, M., Facchin, L., 2020. Seismic markers of the Messinian salinity crisis in the deep Ionian Basin. Basin Res. 32, 716–738. https://doi.org/10.1111/bre.12392.

Cameselle, A.L., Urgeles, R., 2016. Large-scale margin collapse during Messinian early sea-level drawdown: the SW Valencia trough, NW Mediterranean 576–595. https://doi.org/10.1111/bre.12170.

Canva, A., Thinon, I., Peyrefitte, A., Couëffé, R., Maillard, A., Jolivet, L., Martelet, G., Lacquement, F., Guennoc, P., 2020. The Catalan magnetic anomaly: Its significance for the crustal structure of the Gulf of Lion passive margin and relationship to the Catalan transfer zone. Mar. Pet. Geol. 113, 104174. https://doi.org/10.1016/j.marpetgeo.2019.104174.

Capron, A., Déverchère, J., Gaullier, V., Le Roy, S., Mercier de Lépinay, B., Yelles, A.K., 2011. Algerian margin – Regional Setting. in: J. Lofi et al., Eds, Atlas of the Messinian Seismic Markers in the Mediterranean and Black Seas. – Mém. Soc. Géol. Fr., n.s., 179, and World Gological Map Commission, 72 p.

Carminati, E., Doglioni, C., 2005. Mediterranean Tectonics, in: Encyclopedia of Geology. pp. 135–146. https://doi.org/10.1016/B0-12-369396-9/00135-0.

Carminati, E., Doglioni, C., Gelabert, B., Panza, G.F., Raykova, R.B., Roca, E., Sabat, F., Scrocca, D., 2012. Evolution of the Western Mediterranean, in: Regional Geology and Tectonics: Phanerozoic Passive Margins, Cratonic Basins and Global Tectonic Maps. Elsevier, pp. 436–470. https://doi.org/10.1016/B978-0-444-56357-6.00011-1.

Carter, N.L., Hansen, F.D., 1983. Creep of rocksalt. Tectonophysics 92, 275–333. https://doi.org/10.1016/0040-1951(83)90200-7.

Cattaneo, A., Babonneau, N., Dan, G., Déverchère, J., Domzig, A., Gaullier, V., Lepillier, B., de Lépinay, B.M., Nouguès, A., Strzerzynski, P., Sultan, N., Yelles, K., 2010. Submarine Landslides Along the Algerian Margin: A Review of Their Occurrence and Potential Link with Tectonic Structures, in: Mosher, D.C., Shipp, R.C., Moscardelli, L., Chaytor, J.D., Baxter, C.D.P., Lee, H.J., Urgeles, R. (Eds.), Submarine Mass Movements and Their Consequences, Advances in Natural and Technological Hazards Research. Springer Netherlands, Dordrecht, 28, pp. 515–525. https://doi.org/10.1007/978-90-481-3071-9_42.

Catuneanu, O., Galloway, W.E., Kendall, C.G.S.C., Miall, A.D., Posamentier, H.W., Strasser, A., Tucker, M.E., 2011. Sequence stratigraphy: methodology and nomenclature. Newsl. Stratigr. 44, 173–245. https://doi.org/10.1127/0078-0421/2011/0011.

Cedeño, A., Rojo, L.A., Cardozo, N., Centeno, L., Escalona, A., 2019. The Impact of Salt Tectonics on the Thermal Evolution and the Petroleum System of Confined Rift Basins: Insights from Basin Modeling of the Nordkapp Basin, Norwegian Barents Sea. Geosciences 9, 316. https://doi.org/10.3390/geosciences9070316.

Célini, N., Callot, J.-P., Ringenbach, J.-C., Graham, R., 2020. Jurassic Salt Tectonics in the SW Sub-Alpine Fold-and-Thrust Belt. Tectonics 39, e2020TC006107. https://doi.org/10.1029/2020TC006107.

Cherchi, A., Montadert, L., 1982. Oligo-Miocene rift of Sardinia and the early history of the Western Mediterranean Basin. Nature 298, 736–739. https://doi.org/10.1038/298736a0.

CIESM, 2008. The Messinian Salinity Crisis from mega-deposits to microbiology - A consensus report. in: F. Briand, Ed., CIESM Workshop Monographs N° 33, Monaco, 168.

Clark, S.A., Glorstad-Clark, E., Faleide, J.I., Schmid, D., Hartz, E.H., Fjeldskaar, W., 2014. Southwest Barents Sea rift basin evolution: comparing results from backstripping and time-forward modelling. Basin Res. 26, 550–566. https://doi.org/10.1111/bre.12039.

Clauzon, G., Suc, J.-P., Popescu, S.-M., Melinte-Dobrinescu, M.C., Quillévéré, F., Warny, S.A., Fauquette, S., Armijo, R., Meyer, B., Rubino, J.-L., Lericolais, G., Gillet, H., Çağatay, M.N., Ucarkus, G., Escarguel, G., Jouannic, G., Dalesme, F., 2008. Chronology of the Messinian events and paleogeography of the Mediterranean regions s.l., in: F. Briand, Ed., The Messinian Salinity Crisis from Mega-Deposits to Microbiology. in: F. Briand, Ed., CIESM Workshop monographs, 2008. N° 33, Monaco, 31-38.

Cobbold, P., Rossello, E., Vendeville, B., 1989. Some experiments on interacting sedimentation and deformation above salt horizons. Bull. Société Géologique Fr. V, 453–460. https://doi.org/10.2113/gssgfbull.V.3.453.

Cobbold, P.R., Szatmari, P., 1991. Radial gravitational gliding on passive margins. Tectonophysics 188, 249–289. https://doi.org/10.1016/0040-1951(91)90459-6.

Cooke, D., Sena, A., O'Donnell, G., Muryanto, T., Ball, V., 1999. What is the best seismic attribute for quantitative seismic reservoir characterization?, in: SEG Technical Program Expanded Abstracts, 1999. Society of Exploration Geophysicists, pp. 1588–1591. https://doi.org/10.1190/1.1820829.

Cornée, J.-J., Maillard, A., Conesa, G., Garcia, F., Saint Martin, J.-P., Sage, F., Münch, P., 2008. Onshore to offshore reconstruction of the Messinian erosion surface in Western Sardinia, Italy: Implications for the Messinian salinity crisis. Sediment. Geol. 210, 48–60. https://doi.org/10.1016/j.sedgeo.2008.06.005.

Couvering, J.A.V., Castradori, D., Cita, M.B., Hilgen, F.J., Rio, and D., 2000. The base of the Zanclean Stage and of the Pliocene Series. Episodes J. Int. Geosci. 23, 179–187. https://doi.org/10.18814/epiiugs/2000/v23i3/005.

Cunneen, J., Crowe, W., Peters, G., 2015. Using potential field data to map salt distribution in the Western Officer Basin, Western Australia. ASEG Ext. Abstr. 2015, 1–2. https://doi.org/10.1071/ASEG2015ab072.

Cutbill, J.L., Challinor, A., 1965. Revision of the Stratigraphical Scheme for the Carboniferous and Permian Rocks of Spitsbergen and Bjørnøya. Geol. Mag. 102, 418–439. https://doi.org/10.1017/S0016756800053693.

Dal Cin, M., Del Ben, A., Mocnik, A., Accaino, F., Geletti, R., Wardell, N., Zgur, F., Camerlenghi, A., 2016. Seismic imaging of Late Miocene (Messinian) evaporites from Western Mediterranean back-arc basins. Pet. Geosci. 22, 297–308. https://doi.org/10.1144/petgeo2015-096.

Dan, G., Sultan, N., Cattaneo, A., Déverchère, J., Yelles, K., 2010. Mass-transport deposits on the Algerian Margin (Algiers Area): Morphology, Lithology and Sedimentary Processes.Iin: Submarine Mass Movements and Their Consequences, edited by: Mosher, D., Moscardelli, L., Baxter, C. D. P., Urgeles, R., Shipp, R. C., Chaytor, J. D., and Lee, H. J., Adv. Nat. Technol. Haz., Springer 28, 527–539.

Davis, D.M., Engelder, T., 1985. The role of salt in fold-and-thrust belts. Tectonophysics, Collision Tectonics: Deformation of Continental Lithosphere 119, 67–88. https://doi.org/10.1016/0040-1951(85)90033-2.

Del Ben, A., Mocnik, A., Camerlenghi, A., Geletti, R., Zgur, F., 2018. Western Sardinia, in: J. Lofi et al., Eds, Atlas of the Messinian Seismic Markers in the Mediterranean Sea. Volume 2. - Mem. Soc. Géol. Fr. 2018., t. 181, and Commission for the Geological Map of the World, 72 p. pp. 32–34.

Dentith, M.C., Mudge, S., 2014. Geophysics for the Mineral Exploration Geoscientist. Cambridge University Press. HB ISBN: 9780521809511.

Déverchère, J., de Lepinay, B.M., Cattaneo, A., Strzerzynski, P., Calais, E., Domzig, A., Bracene, R., 2010. Comment on Zemmouri earthquake rupture zone (M-w 6.8, Algeria): Aftershocks sequence relocation and 3D velocity model by A. Ayadi et al. J. Geophys. Res.-Solid Earth 115, 1–6. https://doi.org/10.1029/2008JB006190.

Déverchère, J., K, Y., Domzig, A., de Lépinay, B., J.p, B., Gaullier, V., Bracène, R., Calais, E., Bruno, S., Kherroubi, A., Roy, P., H, P., Dan-Unterseh, G., 2005a. Active thrust faulting offshore Boumerdes, Algeria, and its

relations to the 2003 Mw 6.9 earthquake. Geophys. Res. Lett. 32, L04311. doi:10.1029/2004GL021646.

Déverchère, J., Yelles, K., Domzig, A., Lépinay, B.M.D., Cattaneo, A., Gaullier, V., Kherroubi, A., 2005b. Overall tectonic pattern of the Algerian margin: evidences for active folding and thrusting from the 2003 and 2005 MARADJA cruises 1. CIESM Congress 38, p. 82.

Diegel, F.A., Karlo, J.F., Schuster, D.C., Shoup, R.C., Tauvers, and P.R., 1995. Cenozoic Structural Evolution and Tectono-Stratigraphic Framework of the Northern Gulf Coast Continental Margin in: M. P. A. Jackson, D. G. Roberts, and S. Snelson, eds., Salt tectonics: a global perspective: AAPG Memoir 65, 109–151. https://doi.org/10.1306/M65604C6

Domzig, A., Yelles, K., Le Roy, C., Déverchère, J., Bouillin, J.-P., Bracène, R., Mercier de Lépinay, B., Le Roy, P., Calais, E., Kherroubi, A., Gaullier, V., Savoye, B., Pauc, H., 2006. Searching for the Africa–Eurasia Miocene boundary offshore western Algeria (MARADJA'03 cruise). Comptes Rendus Geosci. 338, 80–91. https://doi.org/10.1016/j.crte.2005.11.009.

Driussi, O., Maillard, A., Ochoa, D., Lofi, J., Chanier, F., Gaullier, V., Briais, A., Sage, F., Sierro, F., Garcia, M., 2015. Messinian Salinity Crisis deposits widespread over the Balearic Promontory: Insights from new high-resolution seismic data. Mar. Pet. Geol., The Messinian events and hydrocarbon exploration in the Mediterranean 66, 41–54. https://doi.org/10.1016/j.marpetgeo.2014.09.008.

Duval, B., Cramez, C., Jackson, M.P.A., 1992. Raft tectonics in the Kwanza Basin, Angola. Mar. Pet. Geol. 9, 389–404. https://doi.org/10.1016/0264-8172(92)90050-O.

Faleide, J.I., Gudlaugsson, S.T., Jacquart, G., 1984. Evolution of the western Barents Sea. Mar. Pet. Geol. 1, 123–150. https://doi.org/10.1016/0264-8172(84)90082-5.

Faleide, J.I., Solheim, A., Fiedler, A., Hjelstuen, B.O., Andersen, E.S., Vanneste, K., 1996. Late Cenozoic evolution of the western Barents Sea-Svalbard continental margin. Glob. Planet. Change, Impact of Glaciations on Basin Evolution: Data and Models from the Norwegian Margin and Adjacent Areas 12, 53–74. https://doi.org/10.1016/0921-8181(95)00012-7.

Faleide, J.I., Tsikalas, F., Breivik, A.J., Mjelde, R., Ritzmann, O., Engen, O., Wilson, J., Eldholm, O., 2008. Structure and evolution of the continental margin off Norway and the Barents Sea. Episodes. 2008, 31, 82-91.

Faleide, J.I., Vågnes, E., Gudlaugsson, S.T., 1993. Late Mesozoic-Cenozoic evolution of the south-western Barents Sea in a regional rift-shear tectonic setting. Mar. Pet. Geol. 10, 186–214. https://doi.org/10.1016/0264-8172(93)90104-Z.

Fichler, C., Rueslåtten, H., Gram, C., Ingebrigtsen, A., Olesen, O., 2007. Salt Interpretation with Special Focus on Magnetic Data, Nordkapp Basin, Barents Sea, in: EGM 2007 International Workshop. https://doi.org/10.3997/2214-4609-pdb.166.C_OP_06.

Finetti, I.R., 2005. CROP Project: Deep Seismic Exploration of the Central Mediterranean and Italy. Elsevier. Science - 794 p.

Forsberg, R., Strykowski, G., Tscherning, C.C., 2022. Great Britain's GPS Height Corrector Surface.

Gabrielsen, R.H., 1984. Long-lived fault zones and their influence on the tectonic development of the southwestern Barents Sea J. Geol. Soc. London 141, 651-662.

Gabrielsen, R.H., Faerseth, R.B., Jensen, L.N., 1990. Structural elements of the Norwegian continental shelf. Pt. 1. The Barents Sea region. Norwegian Petroleum Directorate.

Gac, S., Hansford, P.A., Faleide, J.I., 2018. Basin modelling of the SW Barents Sea. Mar. Pet. Geol. 95, 167–187. https://doi.org/10.1016/j.marpetgeo.2018.04.022.

Gaullier, V., 1993. Diapirisme salifère et dynamique sédimentaire dans le basin Liguro-provençal : Données sismique et modèles analogiques. Thèse de Doctorat de l'Université Paris VI, 327 p.

Gaullier, V., Bellaiche, G., 1996. Liguro-Provencal diapirism: the effects of residual topography below the Messinian salt decollement. Insights from analogue modelling. Oceanogr. Lit. Rev. 8, 803.

Gaullier, V., Chanier, F., Lymer, G., Vendeville, B.C., Maillard, A., Thinon, I., Lofi, J., Sage, F., Loncke, L., 2014. Salt tectonics and crustal tectonics along the Eastern Sardinian margin, Western Tyrrhenian: New insights from the "METYSS 1" cruise. Tectonophysics 615–616, 69–84. https://doi.org/10.1016/j.tecto.2013.12.015.

Gaullier V., Loncke L., Vendeville B., Déverchère J., Droz L., Obone Zue Obame E.M., and Mascle J., 2008. Salt tectonics in the deep Mediterranean: indirect clues for understanding the Messinian Salinity Crisis.

In CIESM 2008. The Messinian Salinity Crisis from mega-deposits to microbiology – A consensus report. CIESM Workshop Monographs (F. Briand, Ed.), 33, 168 pages, Monaco, 91-96.

Gaullier, V., Vendeville, B.C., 2005. Salt tectonics driven by sediment progradation: Part II—Radial spreading of sedimentary lobes prograding above salt. AAPG Bull. 89, 1081–1089. https://doi.org/10.1306/03310503064.

Ge, H., Jackson, M.P.A., Vendeville, B.C., 1997. Kinematics and Dynamics of Salt Tectonics Driven by Progradation1. AAPG Bull. 81, 398–423. https://doi.org/10.1306/522B4361-1727-11D7-8645000102C1865D.

Gearing, P., Gearing, J.N., Lytle, T.F., Lytle, J.S., 1976. Hydrocarbons in 60 northeast Gulf of Mexico shelf sediments: a preliminary survey. Geochim. Cosmochim. Acta 40, 1005–1017. https://doi.org/10.1016/0016-7037(76)90043-0.

Geletti, R., Zgur, F., Del Ben, A., Buriola, F., Fais, S., Fedi, M., Forte, E., Mocnik, A., Paoletti, V., Pipan, M., Ramella, R., Romeo, R., Romi, A., 2014. The Messinian Salinity Crisis: New seismic evidence in the West-Sardinian Margin and Eastern Sardo-Provençal basin (West Mediterranean Sea). Mar. Geol. 351, 76–90. https://doi.org/10.1016/j.margeo.2014.03.019.

Gennesseaux, M., Vanney, J.R., 1979. Carte bathymétrique du bassin algéro-provencal. CR Somm Soc Géol Fr. 191–194.

George, M., Olakunle, O.K., Emil, J.S., P., A., 2017. Seismic interpretation and characterization of anhydrite caprocks in the Tromsø Basin, SW Barents Sea. Mar. Geol. 390, 36–50. https://doi.org/10.1016/j.margeo.2017.04.013.

Gernigon, L., Brönner, M., Dumais, M.-A., Gradmann, S., Grønlie, A., Nasuti, A., Roberts, D., 2018. Basement inheritance and salt structures in the SE Barents Sea: Insights from new potential field data. J. Geodyn. 119, 82–106. https://doi.org/10.1016/j.jog.2018.03.008.

Gernigon, L., Brönner, M., Roberts, D., Olesen, O., Nasuti, A., Yamasaki, T., 2014. Crustal and basin evolution of the southwestern Barents Sea: From Caledonian orogeny to continental breakup: Evolution of the Barents Sea. Tectonics 33, 347–373. https://doi.org/10.1002/2013TC003439.

Granado, P., Urgeles, R., Sàbat, F., Albert-Villanueva, E., Roca, E., Muñoz, J.A., Mazzuca, N., Gambini, R., 2016. Geodynamical framework and hydrocarbon plays of a salt giant: the NW Mediterranean Basin. Pet. Geosci. 22, 309–321. https://doi.org/10.1144/petgeo2015-084.

Gussow, W.C., 1968. Salt Diapirism: Importance of Temperature, and Energy Source of Emplacement 153, 16–52.

Haidar, S., Déverchère, J., Graindorge, D., Arab, M., Medaouri M., Klingelhoefer, F., 2022. Back-arc dynamics controlled by slab rollback and tearing: a reappraisal of seafloor spreading and kinematic evolution of the Eastern Algerian basin (western Mediterranean) in Middle-Late Miocene. Tectonics 41, e2021TC006877. 10.1002/essoar.10506942.1

Hall, J., On the vertical position and convolutions of certain strata and their relationship with granite, Transactions of the Royal Society of Edinburgh, 7, 79-108, 1815.

Halpert, A., Clapp, R.G., 2016. Salt body segmentation with dip and frequency attributes, Stanford Exploration Project, vol.136, 2008

Hassaan, M., Faleide, J.I., Gabrielsen, R.H., Tsikalas, F., Grimstad, S., 2021a. Interplay between base-salt relief, progradational sediment loading and salt tectonics in the Nordkapp Basin, Barents Sea – Part II. Basin Res. 33, 3256–3294. https://doi.org/10.1111/bre.12602.

Hassaan, M., Inge Faleide, J., Helge Gabrielsen, R., Tsikalas, F., 2021b. Effects of basement structures and Carboniferous basin configuration on evaporite distribution and the development of salt structures in Nordkapp Basin, Barents Sea—Part I. Basin Res. 33, 2474–2499. https://doi.org/10.1111/bre.12565.

Hegazy, T., AlRegib, G., 2014. Texture attributes for detecting salt bodies in seismic data, in: SEG Technical Program Expanded Abstracts 2014. Society of Exploration Geophysicists, pp. 1455–1459. https://doi.org/10.1190/segam2014-1512.1.

Heida, H., Raad, F., Garcia-Castellanos, D., Jiménez-Munt, I., Maillard, A., Lofi, J., 2021. Flexural-isostatic reconstruction of the Western Mediterranean during the Messinian Salinity Crisis: Implications for water level and basin connectivity. Basin Res. 34. 10.1111/bre.12610. https://doi.org/10.1111/bre.12610.

Henriksen, E., Ryseth, A., Larssen, G.B., Heide, T., Rønning, K., Sollid, K., Stoupakova, A., 2011. Chapter 10 Tectonostratigraphy of the greater Barents Sea: implications for petroleum systems. *Geological Society, London, Memoirs* (2011), 35 (1): 163 https://doi.org/10.1144/M35.10.

Hsü, K.J., Cita, M.B., Ryan, W.B.F., 1973b. The origin of the Mediterranean evaporites. In: Ryan, W.B.F., Hsü, K.J., et al. (Eds.), Initial Reports of the Deep Sea Drilling Project, 13. U. S. Government Printing Office, Washington, pp. 1203–1231. https://doi.org/10.2973/dsdp.proc.42-1.155.1978.

Hubbert, M.K., 1937. Theory of scale models as applied to the study of geologic structures. Geol. Soc. Am. Bull. 1459–1520.

Hübscher, C., Beitz, M., Dümmong, S., Gradmann, S., Meier, K., Netzeband, G.L., 2008. Stratigraphy, fluid dynamics and structural evolution of the Messinian Evaporites in the Levantine Basin, Eastern Mediterranean Sea, in: F. Briand, Ed., The Messinian Salinity Crisis from Mega-Deposits to Microbiology - CIESM Workshop monographs, 33, Monaco.

Hudec, M.R., Jackson, M.P.A., 2007. Terra infirma: Understanding salt tectonics. Earth-Sci. Rev. 82, 1–28. https://doi.org/10.1016/j.earscirev.2007.01.001.

Hughes Clarke, J.E., 2018. Multibeam Echosounders, in: Micallef, A., Krastel, S., Savini, A. (Eds.), Submarine Geomorphology, Springer Geology. Springer International Publishing, Cham, pp. 25–41. https://doi.org/10.1007/978-3-319-57852-1_3.

Jackson, M. P. A., 1995, Retrospective salt tectonics, in: M. P. A. Jackson, D. G. Roberts, and S. Snelson, eds., Salt tectonics: a global perspective: AAPG Memoir 65, p. 1-28.

Jackson, M.P.A., Hudec, M.R., 2017. Salt Tectonics: Principles and Practice. Cambridge University Press, Cambridge. https://doi.org/10.1017/9781139003988.

Jackson, M.P.A., Talbot, C.J., 1986. External shapes, strain rates, and dynamics of salt structures 19.

Jackson, M.P.A., Vendeville, B.C., Schultz-Ela, D.D., 1994. Structural Dynamics of Salt Systems. Annu. Rev. Earth Planet. Sci. 22, 93–117. https://doi.org/10.1146/annurev.ea.22.050194.000521.

Jolivet, L., Augier, R., Robin, C., Suc, J.-P., Rouchy, J.M., 2006. Lithospheric-scale geodynamic context of the Messinian salinity crisis. Sediment. Geol. 188–189, 9–33. https://doi.org/10.1016/j.sedgeo.2006.02.004.

Jolivet, L., Baudin, T., Calassou, S., Chevrot, S., Ford, M., Issautier, B., Lasseur, E., Masini, E., Manatschal, G., Mouthereau, F., Thinon, I., Vidal, O., 2021a. Geodynamic evolution of a wide plate boundary in the Western Mediterranean, near-field versus far-field interactions. BSGF - Earth Sci. Bull. 192, 48. https://doi.org/10.1051/bsgf/2021043.

Jolivet, L., Faccenna, C., 2000. Mediterranean extension and the Africa-Eurasia collision. Tectonics 19, 1095–1106. https://doi.org/10.1029/2000TC900018.

Jolivet, L., Menant, A., Roche, V., Le Pourhiet, L., Maillard, A., Augier, R., Do Couto, D., Gorini, C., Thinon, I., Canva, A., 2021b. Transfer zones in Mediterranean back-arc regions and tear faults. Bull. Société Géologique Fr. 192. https://doi.org/10.1051/bsgf/2021006.

Jones, I.F., Davison, I., 2014. Seismic imaging in and around salt bodies. Interpretation 2, SL1–SL20. https://doi.org/10.1190/INT-2014-0033.1.

Kastens, K.A., Mascle, J., Auroux, C., et al. (Eds.), 1987. Proc. ODP, Init. Repts., 107. College Station, TX (Ocean Drilling Program). https://doi.org/10.2973/odp.proc.ir.107.1987.

Knies, J., Matthiessen, J., Vogt, C., Laberg, J.S., Hjelstuen, B.O., Smelror, M., Larsen, E., Andreassen, K., Eidvin, T., Vorren, T.O., 2009. The Plio-Pleistocene glaciation of the Barents Sea–Svalbard region: a new model based on revised chronostratigraphy. Quat. Sci. Rev. 28, 812–829. https://doi.org/10.1016/j.quascirev.2008.12.002.

Knies, J., Matthiessen, J., Vogt, C., Stein, R., 2002. Evidence of 'Mid-Pliocene (˜3 Ma) global warmth' in the eastern Arctic Ocean and implications for the Svalbard/Barents Sea ice sheet during the late Pliocene and early Pleistocene (˜3 – 1.7 Ma). Boreas 31, 82–93. https://doi.org/10.1111/j.1502-3885.2002.tb01058.x.

Knutsen, S.-M., Larsen, K.I., 1997. The late Mesozoic and Cenozoic evolution of the Sørvestsnaget Basin: A tectonostratigraphic mirror for regional events along the Southwestern Barents Sea margin? Mar. Pet. Geol. 14, 27–54. https://doi.org/10.1016/S0264-8172(96)00039-6.

Knutsen, S.-M., Skjold, L.-J., Skott, P.H., 1992. Palaeocene and Eocene development of the Tromsø Basin sedimentary response to rifting and early sea-floor spreading in the Barents Sea area. Nor. Geol. Tidsskr. 17.

Koefoed, O., 1981. Aspects of Vertical Seismic Resolution. Geophys. Prospect. 29, 21–30. https://doi.org/10.1111/j.1365-2478.1981.tb01008.x

Koson, S., Chenrai, P., Choowong, M., 2014. Seismic Attributes and Their Applications in Seismic Geomorphology. Bulletin of Earth Sciences of Thailand, Vol. 6, 1-19.

Koyi, H., Talbot, C.J., Torudbakken, B.O., 1995a. Analogue models of salt diapirs and seismic interpretation in the Nordkapp Basin, Norway. Pet. Geosci. 1, 185–192. https://doi.org/10.1144/petgeo.1.2.185.

Koyi, H., Talbot, C.J., Tørudbakken, B.O., 1995b. Salt Tectonics in the Northeastern Nordkapp Basin, Southwestern Barents Sea, in: M. P. A. Jackson, D. G. Roberts, and S. Snelson, Eds., Salt Tectonics: A Global Perspective. p. Chapter 21, 437-447.

Krijgsman, W., Blanc-Valleron, M.-M., Flecker, R., Hilgen, F.J., Kouwenhoven, T.J., Merle, D., Orszag-Sperber, F., Rouchy, J.-M., 2002. The onset of the Messinian salinity crisis in the Eastern Mediterranean (Pissouri Basin, Cyprus). Earth Planet. Sci. Lett. 194, 299–310. https://doi.org/10.1016/S0012-821X(01)00574-X.

Krijgsman, W., Hilgen, F.J., Raffi, I., Sierro, F.J., Wilson, D.S., 1999. Chronology, causes and progression of the Messinian salinity crisis. Nature 400, 652–655. https://doi.org/10.1038/23231.

Kristensen, T.B., Rotevatn, A., Marvik, M., Henstra, G.A., Gawthorpe, R.L., Ravnås, R., 2018. Structural evolution of sheared margin basins: the role of strain partitioning. Sørvestsnaget Basin, Norwegian Barents Sea. Basin Res. 30, 279–301. https://doi.org/10.1111/bre.12253.

Larssen, G.B., 2002. Upper Paleozoic lithostratigraphy of the southern Norwegian Barents Sea, Norwegian Petroleum Directorate, 145.

Lasabuda, A., Laberg, J.S., Knutsen, S.-M., Høgseth, G., 2018. Early to middle Cenozoic paleoenvironment and erosion estimates of the southwestern Barents Sea: Insights from a regional mass-balance approach. Mar. Pet. Geol. 96, 501–521. https://doi.org/10.1016/j.marpetgeo.2018.05.039.

LeCompte, P., 1965. Creep in rock salt. J. Geol. 469–484.

Leprêtre, A., Klingelhoefer, F., Graindorge, D., Schnurle, P., Beslier, M.O., Yelles, K., Déverchère, J., Bracene, R., 2013. Multiphased tectonic evolution of the Central Algerian margin from combined wideangle and reflection seismic data off Tipaza, Algeria. J. Geophys. Res. Solid Earth 118, 3899–3916. https://doi.org/doi:10.1002/jgrb.50318, 2013.

Leprêtre, R., Lamotte, D.F. de, Combier, V., Gimeno-Vives, O., Mohn, G., Eschard, R., 2018. The Tell-Rif orogenic system (Morocco, Algeria, Tunisia) and the structural heritage of the southern Tethys margin. BSGF - Earth Sci. Bull. 189, 10. https://doi.org/10.1051/bsgf/2018009.

Leroux, E., Aslanian, D., Rabineau, M., Moulin, M., Granjeon, D., Gorini, C., Droz, L., 2015. Sedimentary markers in the Provençal Basin (western Mediterranean): a window into deep geodynamic processes. Terra Nova, 27(2), 122–129. doi: 10.1111/ter.12139

Letouzey, J., Colletta, B., Vially, R., Chermette, J.C., 1995. Evolution of Salt-Related Structures in Compressional Settings, in: Jackson, M.P.A., Roberts, D.G., Snelson, S. (Eds.), Salt Tectonics: A Global Perspective. American Association of Petroleum Geologists, p. 0. https://doi.org/10.1306/M65604C3.

Letouzey, J., Sherkati, S., 2004. Salt Movement, Tectonic Events, and Structural Style in the Central Zagros Fold and Thrust Belt (Iran), in: Post, P.J., Olson, D.L., Lyons, K.T., Palmes, S.L., Harrison, P.F., Rosen, N.C. (Eds.), Salt Sediment Interactions and Hydrocarbon Prospectivity Concepts, Applications and Case Studies for the 21st Century. SEPM Society for Sedimentary Geology, p. 0. https://doi.org/10.5724/gcs.04.24.0753.

Lines, L.R., Newrick, R.T., 2004. Fundamentals of Geophysical Interpretation. Society of Exploration Geophysicists. https://doi.org/10.1190/1.9781560801726.

Lofi, J., Déverchère, J., Gaullier, V., Herve, G., Gorini, C., Guennoc, P., Loncke, L., Maillard, A., Sage, F., Thinon, I., 2011a. Seismic Atlas of the Messinian Salinity Crisis markers in the Mediterranean and Black Seas, Mém. Soc. Géol. Fr., n.s., 179, and World Geological Map Commission, 72 p.

Lofi, J., Gorini, C., Berné, S., Clauzon, G., Tadeu Dos Reis, A., Ryan, W.B.F., Steckler, M.S., 2005. Erosional processes and paleo-environmental changes in the Western Gulf of Lions (SW France) during the Messinian Salinity Crisis. Mar. Geol. 217, 1–30. https://doi.org/10.1016/j.margeo.2005.02.014.

Lofi, J., Sage, F., Déverchère, J., Loncke, L., Maillard, A., Gaullier, V., Thinon, I., Gillet, H., Guennoc, P., Gorini, C., 2011b. Refining our knowledge of the Messinian salinity crisis records in the offshore domain

through multi-site seismic analysis. Bull. Société Géologique Fr. 182, 163–180. https://doi.org/10.2113/gssgfbull.182.2.163.

Loncke, L., Vendeville, B.C., Gaullier, V., Mascle, J., 2010. Respective contributions of tectonic and gravity-driven processes on the structural pattern in the Eastern Nile deep-sea fan: insights from physical experiments. Basin Res. 22, 765–782. https://doi.org/10.1111/j.1365-2117.2009.00436.x

Lymer, G., Lofi, J., Gaullier, V., Maillard, A., Thinon, I., Sage, F., Chanier, F., Vendeville, B.C., 2018. The Western Tyrrhenian Sea revisited: New evidence for a rifted basin during the Messinian Salinity Crisis. Mar. Geol. 398, 1–21. https://doi.org/10.1016/j.margeo.2017.12.009.

Maillard, A., Gaullier, V., Vendeville, B.C., Odonne, F., 2003. Influence of differential compaction above basement steps on salt tectonics in the Ligurian-Provençal Basin, northwest Mediterranean. Mar. Pet. Geol. 20, 13–27. https://doi.org/10.1016/S0264-8172(03)00022-9.

Maillard A., Gaullier V., Lézin C., Chanier F., Odonne F., Lofi J., 2020a. New onshore/offshore evidence of the Messinian Erosion Surface from key areas: The Ibiza-Balearic Promontary and the Orosei-Eastern Tyrrhenian margin. BSGF – Earth Sciences Bulletin*,* 191 : 9, https://doi.org/10.1051/bsgf/2020007.

Maillard, A., Gorini, C., Mauffret, A., Sage, F., Lofi, J., Gaullier, V., 2006. Offshore evidence of polyphase erosion in the Valencia Basin (Northwestern Mediterranean): Scenario for the Messinian Salinity Crisis. Sediment. Geol., The Messinian Salinity Crisis Revisited 188–189, 69–91. https://doi.org/10.1016/j.sedgeo.2006.02.006.

Maillard, A., Jolivet, L., Lofi, J., Thinon, I., Couëffé, R., Canva, A., Dofal, A., 2020b. Transfer zones and associated volcanic province in the eastern Valencia Basin: Evidence for a hot rifted margin? Mar. Pet. Geol. 119, 104419. https://doi.org/10.1016/j.marpetgeo.2020.104419.

Maillard, Mauffret, 1999. Crustal structure and riftogenesis of the Valencia Trough (north-western Mediterranean Sea). Basin Res. 11, 357–379. https://doi.org/10.1046/j.1365-2117.1999.00105.x.

Mangerud, J., Jansen, E., Landvik, J.Y., 1996. Late Cenozoic history of the Scandinavian and Barents Sea ice sheets. Glob. Planet. Change 12, 11–26. https://doi.org/10.1016/0921-8181(95)00009-7.

Manzi, V., Lugli, S., Lucchi, F.R., Roveri, M., 2005. Deep-water clastic evaporites deposition in the Messinian Adriatic foredeep (northern Apennines, Italy): did the Mediterranean ever dry out? Sedimentology 52, 875–902. https://doi.org/10.1111/j.1365-3091.2005.00722.x.

Mauffret, A., Durand de Grossouvre, B., Tadeu Dos Reis, A., Gorini, C., Nercessian, A., 2001. Structural geometry in the eastern Pyrenees and western Gulf of Lion (Western Mediterranean). J. Struct. Geol. 23, 1701–1726. https://doi.org/10.1016/S0191-8141(01)00025-6.

Mauffret, A., Frizon de Lamotte, D., Lallemant, S., Gorini, C., Maillard, A., 2004. E-W opening of the Algerian Basin (Western Mediterranean). Terra Nova 16, 257–264. https://doi.org/10.1111/j.1365-3121.2004.00559.x.

Mauffret, A., Maldonado, A., Campillo, A.C., 1992. Tectonic framework of the eastern Alboran and western Algerian Basins, western Mediterranean. Geo-Mar. Lett. 12, 104–110. https://doi.org/10.1007/BF02084919.

Mauffret, A., Pascal, G., Maillard, A., Gorini, C., 1995. Tectonics and deep structure of the north-western Mediterranean Basin. Mar. Pet. Geol. 12, 645–666. https://doi.org/10.1016/0264-8172(95)98090-R.

Medaouri, M., Déverchère, J., Graindorge, D., Bracene, R., Badji, R., Ouabadi, A., Yelles-Chaouche, K., Bendiab, F., 2014. The transition from Alboran to Algerian basins (Western Mediterranean Sea): Chronostratigraphy, deep crustal structure and tectonic evolution at the rear of a narrow slab rollback system. J. Geodyn., SI: Geodynamic evolution of the Alboran domain 77, 186–205. https://doi.org/10.1016/j.jog.2014.01.003.

Meinhold, R. 1956. Bemerkungen zur Frage des Salzaufstieges. Freib Forsch C 22 156–165.

Micallef, A., Camerlenghi, A., Garcia-Castellanos, D., Cunarro Otero, D., Gutscher, M.-A., Barreca, G., Spatola, D., Facchin, L., Geletti, R., Krastel, S., Gross, F., Urlaub, M., 2018. Evidence of the Zanclean megaflood in the eastern Mediterranean Basin. Sci. Rep. 8, 1078. https://doi.org/10.1038/s41598-018-19446-3.

Mitchum, R.M., Vail, P.R., Thompson, S., 1977. Seismic Stratigraphy and Global Changes of Sea Level: Part 2. The Depositional Sequence as a Basic Unit for Stratigraphic Analysis., in: Payton, C. E. (Ed.), Seismic Stratigraphy – Applications to Hydrocarbon Exploration. American Association of Petroleum Geologists Memoir, pp. 53–62.

Mjelde, R., Breivik, A.J., Elstad, H., Ryseth, A.E., Reidar, J., Opsal, J.G., Shimamura, H., Murai, Y., Nishimura, Y., 2002. Geological development of the Sørvestsnaget Basin, SW Barents Sea, from ocean bottom seismic, surface seismic and potential field data. Nor. J. Geol. 20.

Mjelde, R., Breivik, A.J., Raum, T., Mittelstaedt, E., Ito, G., Faleide, J.I., 2008. Magmatic and tectonic evolution of the North Atlantic. J. Geol. Soc. 165, 31–42. https://doi.org/10.1144/0016-76492007-018.

Montadert, L., Letouzey, J., Mauffret, A., 1978. Messinian event: seismic evidence., in: Hsü, K.J., Montadert, L., et al. (Eds.), Leg 42. Initial Reports of the Deep Sea Drilling Project, Vol. 42, Part I., U.S. Govt. Printing Office, Washington, D.C., p. 1037–1050.

Montadert, L., Sancho, J., Fail, J.P., Debyser, J., Winnock, E., 1970. De l'âge tertiaire de la série salifère responsable des structures diapiriques en Méditerranée Occidentale (Nord-Est des Baléares). C. R. Acad. Sci., 217, 812–815.

Moulin M., Klingelhoefer F., Afilhado A., Aslanian D., Schnurle P., Nouzé H., Rabineau M., Beslier M.-O. and Feld A., 2015. Deep crustal structure across a young passive margin from wide-angle and reflection seismic data (The SARDINIA Experiment) – I. Gulf of Lion's margin. Bulletin de la Société géologique de France, 186 (4-5), 309-330.

Mukherjee, S., Misra, A., 2017. Atlas of Structural Geological Interpretation from Seismic Images.

Nagihara, S., Sclater, J.G., Beckley, L.M., Behrens, E.W., Lawver, L.A., 1992. High heat flow anomalies over salt structures on the Texas Continental Slope, Gulf of Mexico. Geophys. Res. Lett. 19, 1687–1690. https://doi.org/10.1029/92GL00976.

Nalpas, T., Le Douaran, S., Brun, J.-P., Unternehr, P., Richert, J.-P., 1995. Inversion of the Broad Fourteens Basin (offshore Netherlands), a small-scale model investigation. Sediment. Geol. 95, 237–250. https://doi.org/10.1016/0037-0738(94)00113-9.

Nesteroff, W.D., 1973. Un modèle pour les evaporites messiniennes en méditerranée, des bassins peu profonds avec des dé pots d'évaporites lagunaires, in: Messinian Events, Drooger, C. W., et al., Eds.,. pp. 68–81.

Nettleton, L.L., 1971. Elementary gravity and magnetics for geologists and seismologists. Geophys. Monogr. Ser. 1.

Nettleton, L.L., 1934. Fluid Mechanics of Salt Domes1. AAPG Bull. 18, 1175–1204. https://doi.org/10.1306/3D932C74-16B1-11D7-8645000102C1865D.

Nikolinakou, M.A., Heidari, M., Hudec, M.R., Flemings, P.B., 2017. Initiation and growth of salt diapirs in tectonically stable settings: Upbuilding and megaflaps. AAPG Bull. 101, 887–905. https://doi.org/10.1306/09021615245

Nilsen, K.T., Vendeville, B.C., Johansen, J.-T., 1995. Influence of Regional Tectonics on Halokinesis in the Nordkapp Basin, Barents Sea. Salt Tecton. Glob. Perspect. Ed. MPA Jackson DG Roberts Snelson 413–436.

Nocquet, J.-M., Calais, E., 2004. Geodetic Measurements of Crustal Deformation in the Western Mediterranean and Europe. Pure Appl. Geophys. 161, 661–681. https://doi.org/10.1007/s00024-003-2468-z.

Obone-Zue-Obame, E.M., Gaullier, V., Sage, F., Maillard, A., Lofi, J., Vendeville, B., Thinon, I., Rehault, J.-P., 2011. The sedimentary markers of the Messinian salinity crisis and their relation with salt tectonics on the Provençal margin (western Mediterranean): results from the "MAURESC" cruise. Bull. Société Géologique Fr. 182, 181–196. https://doi.org/10.2113/gssgfbull.182.2.181.

Olesen, O., Brönner, M., Ebbing, J., Gellein, J., Gernigon, L., Koziel, J., Lauritsen, T., Myklebust, R., Pascal, C., Sand, M., Solheim, D., Usov, S., 2010. New aeromagnetic and gravity compilations from Norway and adjacent areas: methods and applications. Geol. Soc. Lond. Pet. Geol. Conf. Ser. 7, 559–586. https://doi.org/10.1144/0070559.

Omosanya, K.O., Zervas, I., Mattos, N.H., Alves, T.M., Johansen, S.E., Marfo, G., 2017. Strike-Slip Tectonics in the SW Barents Sea During North Atlantic Rifting (Swaen Graben, Northern Norway): Strike-slip faults in extensional domain. Tectonics 36, 2422–2446. https://doi.org/10.1002/2017TC004635.

Orszag-Sperber, F., 2006. Changing perspectives in the concept of "Lago-Mare" in Mediterranean Late Miocene evolution. Sediment. Geol., The Messinian Salinity Crisis Revisited 188–189, 259–277. https://doi.org/10.1016/j.sedgeo.2006.03.008.

Ottes, W., Lambregts, P., Barkooky, A.E., 2008. The Messinian Salinity Crisis in the Nile Delta: chasing shallow marine reservoirs in a deep-water basin, in: F. Briand, Ed., The Messinian Salinity Crisis from Mega-Deposits to Microbiology - CIESM Workshop monographs, 33, Monaco, 107-110.

Peel, F., 2014. How do salt withdrawal minibasins form? Insights from forward modelling, and implications for hydrocarbon migration. Tectonophysics 630. https://doi.org/10.1016/j.tecto.2014.05.027.

Peel, F., Hossack, C.J.T., J.R., 1995. Genetic Structural Provinces and Salt Tectonics of the Cenozoic Offshore U.S. Gulf of Mexico: A Preliminary Analysis 153–175. AAPG Memoir 65.

Perez-Garcia, C., Safronova, P.A., Mienert, J., Berndt, C., Andreassen, K., 2013. Extensional rise and fall of a salt diapir in the Sørvestsnaget Basin, SW Barents Sea. Mar. Pet. Geol. 46, 129–143. https://doi.org/10.1016/j.marpetgeo.2013.05.010.

Planke, S., Trulsvik, M., Myklebust, R., Kjølhamar, B., 2012. Geophysical Atlas of The Barents Sea.

Poort, J., Lucazeau, F., Le Gal, V., Dal Cin, M., Leroux, E., Bouzid, A., Rabineau, M., Palomino, D., Battani, A., Akhmanov, G.G., Ferrante, G.M., Gafurova, D.R., Si Bachir, R., Koptev, A., Tremblin, M., Bellucci, M., Pellen, R., Camerlenghi, A., Migeon, S., Alonso, B., Ercilla, G., Yelles-Chaouche, A.K., Khlystov, O.M., 2020. Heat flow in the Western Mediterranean: Thermal anomalies on the margins, the seafloor and the transfer zones. Mar. Geol. 419, 106064. https://doi.org/10.1016/j.margeo.2019.106064.

Rabineau, M., Leroux, E., Aslanian, D., Bache, F., Gorini, C., Moulin, M., Molliex, S., Droz, L., dos Reis, A.T., Rubino, J.L., Guillocheau, F., Olivet, J.L., 2014. Quantifying subsidence and isostatic readjustment using sedimentary paleomarkers, example from the Gulf of Lion. Earth Planet. Sci. Lett. 388, 353–366. https://doi.org/10.1016/j.epsl.2013.11.059.

Ramberg, H., 1981. The role of gravity in orogenic belts. Geol. Soc. Lond. Spec. Publ. 9, 125–140. https://doi.org/10.1144/GSL.SP.1981.009.01.11.

Ravelo, A.C., Andreasen, D.H., Lyle, M., Olivarez Lyle, A., Wara, M.W., 2004. Regional climate shifts caused by gradual global cooling in the Pliocene epoch. Nature 429, 263–267. https://doi.org/10.1038/nature02567.

Rehault, Boillot, Mauffret, A., 1984. The Western Mediterranean Basin Geological Evolution. Mar. Geol. 447–477.

Robertson, E.C., Robie, R.A., Books, K.G., 1958. Physical properties of salt, anhydrite and gypsum: preliminary report, Trace Elements Memorandum. 1048. https://doi.org/10.3133/tem1048

Romagny, A., Jolivet, L., Menant, A., Bessiere, E., Maillard, A., Canva, A., Gorini, C., Augier, R., 2020. Detailed tectonic reconstructions of the Western Mediterranean region for the last 35 Ma, insights on driving mechanisms. BSGF - Earth Sci. Bull. 191. https://doi.org/10.1051/bsgf/2020040

Ronnevik, H., Beskow, B., Jacobsen, H.P., 1982. Structural and Stratigraphic Evolution of the Barents Sea, Can. Soc. Pet. Geol., Mem. 431–440.

Roveri, M., Bassetti, M.A., Ricci Lucchi, F., 2001. The Mediterranean Messinian salinity crisis: an Apennine foredeep perspective. Sediment. Geol. 140, 201–214. https://doi.org/10.1016/S0037-0738(00)00183-4.

Roveri, M., Manzi, V., Bergamasco, A., Falcieri, F.M., Gennari, R., Lugli, S., Schreiber, B.C., 2014. Dense shelf water cascading and Messinian Canyons: A new scenario for the Mediterranean salinity crisis. Am. J. Sci. 314, 751–784. https://doi.org/10.2475/05.2014.03.

Rowan, M., 2020. Salt- and shale-detached gravity-driven failure of continental margins. Regional Geology and Tectonics (Second Edition), pp. 205–234. https://doi.org/10.1016/B978-0-444-64134-2.00010-9.

Rowan, M.G., 2017. An Overview of Allochthonous Salt Tectonics, in: Permo-Triassic Salt Provinces of Europe, North Africa and the Atlantic Margins. Elsevier, pp. 97–114. https://doi.org/10.1016/B978-0-12-809417-4.00005-7.

Rowan, M.G., Giles, K.A., 2021. Passive versus active salt diapirism. AAPG Bull. 105, 53–63. https://doi.org/10.1306/05212020001.

Rowan, M.G., Jackson, M.P.A., Trudgill, B.D., 1999. Salt-Related Fault Families and Fault Welds in the Northern Gulf of Mexico1. AAPG Bull. 83, 1454–1484. https://doi.org/10.1306/E4FD41E3-1732-11D7-8645000102C1865D.

Rowan, M.G., Lindsø, S., 2017. Salt Tectonics of the Norwegian Barents Sea and Northeast Greenland Shelf, in: Permo-Triassic Salt Provinces of Europe, North Africa and the Atlantic Margins. Elsevier, pp. 265–286. https://doi.org/10.1016/B978-0-12-809417-4.00013-6.

Rowan, M.G., Peel, F.J., Vendeville, B.C., Gaullier, V., 2012. Salt tectonics at passive margins: Geology versus models – Discussion. Mar. Pet. Geol. 37, 184–194. https://doi.org/10.1016/j.marpetgeo.2012.04.007.

Ryan, W.B. f., 1976. Quantitative evaluation of the depth of the western Mediterranean before, during and after the Late Miocene salinity crisis. Sedimentology 23, 791–813. https://doi.org/10.1111/j.1365-3091.1976.tb00109.x.

Ryan, W.B.F., Cita, M.B., 1978. The nature and distribution of Messinian erosional surfaces — Indicators of a several-kilometer-deep Mediterranean in the Miocene. Mar. Geol., Messinian erosional surfaces in the Mediterranean 27, 193–230. https://doi.org/10.1016/0025-3227(78)90032-4.

Ryan, W.B.F., Hsü, K.J., Cita, M.B., Dumitrica, P., Lort, J.M., Mayne, W., Nesteroff, W.D., Pautot, G., Stradner, H., Wezel, F.C., 1973. Initial reports of the deep sea drilling project. US Gov. Print. Off. Wash. 13, 32.

Ryseth, A., Augustson, J.H., Charnock, M., Haugerud, O., Midbøe, P.S., Opsal, J.G., Sundsbø, G., 2003. Cenozoic stratigraphy and evolution of the Sørvestsnaget Basin, southwestern Barents Sea. Nor. J. Geol. 24.

Sættem, J., Poole, D.A.R., Ellingsen, L., Sejrup, H.P., 1992. Glacial geology of outer Bjørnøyrenna, southwestern Barents Sea. Mar. Geol. 103, 15–51. https://doi.org/10.1016/0025-3227(92)90007-5.

Safronova, P., Andreassen, K., Laberg, J., Vorren, T., 2012. Development and post-depositional deformation of a Middle Eocene deep-water sandy depositional system in the Sørvestsnaget Basin, SW Barents Sea. Mar. Pet. Geol. 36, 83–99. https://doi.org/10.1016/j.marpetgeo.2012.06.007.

Sage, F., Déverchére, J., Von Gronefeld, G., Gaullier, V., Gorini, C., Maillard, A., Cornée, J.-J., 2011. Western Sardinia, in: J. Lofi et al., Eds, Atlas of the Messinian Seismic Markers in the Mediterranean and Black Seas _ Mem. Soc. Géol. Fr. 2011, 179, and World Geological Map Commission, 72 p.

Sage, F., Gronefeld, G.V., Déverchère, J., Gaullier, V., Maillard, A., Gorini, C., 2005. Seismic evidence for Messinian detrital deposits at the western Sardinia margin, northwestern Mediterranean. Mar. Pet. Geol. 22, 757–773. https://doi.org/10.1016/j.marpetgeo.2005.03.007.

Savoye, B., Piper, D.J.W., 1991. The Messinian event on the margin of the Mediterranean Sea in the Nice area, southern France. Mar. Geol. 97, 279–304. https://doi.org/10.1016/0025-3227(91)90121-J.

Schellart, W.P., Strak, V., 2016. A review of analogue modelling of geodynamic processes: Approaches, scaling, materials and quantification, with an application to subduction experiments. J. Geodyn., 100, 7–32. https://doi.org/10.1016/j.jog.2016.03.009

Schettino, A., Turco, E., 2006. Plate kinematics of the Western Mediterranean region during the Oligocene and Early Miocene 26. Geophys. J. Int. 166 (3), 1398–1423. doi:10.1111/j.1365- 246X.2006.02997.x.

Selli, R., 1973. An outline of the Italian Messinian., in: Drogger, C.W., Broekman, J.A., Hageman, J., Hantelman, J.J., Marks, P., Meulenkamp, J.E., Schmidt, R.R. (Eds.), Messinian Events in the Mediterranean. Koninklijke Nederlandse Akademie Van Wetenschappen, North-Holland Publishing Company, Amsterdam, London. pp. 150–171.

Simm, R., Bacon, M., 2014. Seismic Amplitude. an Interpreters Handbook, Cambridge University Press. ed., 280 p.

Sirota, I., Enzel, Y., Lensky, N.G., 2018. Halite focusing and amplification of salt layer thickness: From the Dead Sea to deep hypersaline basins. Geology 46, 851–854. https://doi.org/10.1130/G45339.1.

Sirota, I., Ouillon, R., Mor, Z., Meiburg, E., Enzel, Y., Arnon, A., Lensky, N.G., 2020. Hydroclimatic Controls on Salt Fluxes and Halite Deposition in the Dead Sea and the Shaping of “Salt Giants.” Geophys. Res. Lett. 47, e2020GL090836. https://doi.org/10.1029/2020GL090836.

Smelror, M., Petrov, O.V., Birger Larssen, G., 2009. Atlas - Geological history of the Barents Sea. NGU.

Soto, J.I., Déverchère, J., Hudec, M.R., Medaouri, M., Badji, R., Gaullier, V., Leffondré, P., 2022. Crustal structures and salt tectonics on the margins of the western Algerian Basin (Mediterranean Region). Mar. Pet. Geol. 144, 105820. https://doi.org/10.1016/j.marpetgeo.2022.105820.

Spathopoulos, F., 1996. An insight on salt tectonics in the Angola Basin, South Atlantic. Geol. Soc. Lond. Spec. Publ. 100, 153–174. https://doi.org/10.1144/GSL.SP.1996.100.01.11.

Stewart, S.A., 2007. Salt tectonics in the North Sea Basin: a structural style template for seismic interpreters. Geol. Soc. Lond. Spec. Publ. 272, 361–396. https://doi.org/10.1144/GSL.SP.2007.272.01.19.

Sulli, A., 2000. Structural framework and crustal characteristics of the Sardinia Channel Alpine transect in the central Mediterranean. Tectonophysics 324, 321–336. https://doi.org/10.1016/S0040-1951(00)00050-0.

Tari, G., Molnar, J., Ashton, P., 2003. Examples of salt tectonics from West Africa: A comparative approach. Geol. Soc. Lond. Spec. Publ. 207, 85–104. https://doi.org/10.1144/GSL.SP.2003.207.5.

Vågnes, E., Gabrielsen, R.H., Haremo, P., 1998. Late Cretaceous–Cenozoic intraplate contractional deformation at the Norwegian continental shelf: timing, magnitude and regional implications. Tectonophysics 300, 29–46. https://doi.org/10.1016/S0040-1951(98)00232-7.

Vail, P.R., Mitchum, R.M., Thompson, S., 1977. Seismic Stratigraphy and Global Changes of Sea Level: Part 4. Global Cycles of Relative Changes of Sea Level. pp. 83–98.

Vendeville, B. C., 1987. Champs de failles et tectonique en extension : Modélisation expérimentale (PhD thesis). Université Rennes 1.

Vendeville, B.C., 2005. Salt tectonics driven by sediment progradation: Part I—Mechanics and kinematics. AAPG Bull. 89, 1071–1079. https://doi.org/10.1306/03310503063.

Vendeville, B., Cobbold, P., 1987. Glissements gravitaires synsédimentaires et failles normales listriques: Modèles expérimentaux. Comptes Rendus Académie Sci. Paris 305, 1313–1319.

Vendeville, B.C., 1998. Remobilization of Salt Structures by Sediment Progradation: Experimental Models and Potential Applications to the Gulf of Mexico and Other Continental Margins. AAPG Discovery Series 1(1998).

Vendeville, B.C., 2000. Remobilization of Salt Structures by Sediment Progradation: Experimental Models and Potential Applications to the Gulf of Mexico and Other Continental Margins. AAPG Special Volumes.

Vendeville, B.C., Jackson, M.P.A., 1992a. The rise of diapirs during thin-skinned extension. Mar. Pet. Geol. 9, 331–354. https://doi.org/10.1016/0264-8172(92)90047-I.

Vendeville, B.C., Jackson, M.P.A., 1992b. The fall of diapirs during thin-skinned extension. Mar. Pet. Geol. 9, 354–371. https://doi.org/10.1016/0264-8172(92)90048-J.

Verma, R.K., 1986. Offshore seismic exploration. Data acquisition, processing, and interpretation. Gulf Publishing Co.,Houston, TX.

Warren, J.K., 2006. Evaporites: Sediments, Resources and Hydrocarbons. Springer, Berlin, 1036 p. http://dx.doi.org/10.1007/3-540-32344-9.

Warren, J.K., 2010. Evaporites through time: Tectonic, climatic and eustatic controls in marine and nonmarine deposits. Earth-Sci. Rev. 98, 217–268. https://doi.org/10.1016/j.earscirev.2009.11.004.

Weinberger, R., Begin, Z.B., Waldmann, N., Gardosh, M., Baer, G., Frumkin, A., Wdowinski, S., 2006. Quaternary rise of the Sedom diapir, Dead Sea basin. in: Special Paper 401: New Frontiers in Dead Sea Paleoenvironmental Research. https://doi.org/10.1130/2006.2401(03).

White, R.E., Simm, R., 2003. Tutorial: good practice in well ties. First Break 21. 75-83. https://doi.org/10.3997/1365-2397.21.10.25640

Widess, M.B., 1973. How thin is a thin bed? Geophysics 38 (6) 1176–1180. doi:10.1190/1.1440403.

Wu, S., Bally, A.W., Cramez, C., 1990. Allochthonous salt, structure and stratigraphy of the north-eastern Gulf of Mexico. Part II: Structure. Mar. Pet. Geol. 7, 334–370. https://doi.org/10.1016/0264-8172(90)90014-8.

Yelles, K., Lammali, K., Mahsas, A., Calais, E., Briole, P., 2004. Coseismic deformation of the May 21st, 2003, Mw = 6.8 Boumerdes earthquake, Algeria, from GPS measurements. Geophys. Res. Lett. 31. https://doi.org/10.1029/2004GL019884.

Yilmaz, Ö., 2001. Seismic Data Analysis, Investigations in Geophysics. Society of Exploration Geophysicists. https://doi.org/10.1190/1.9781560801580.

Ziegler, A.M., Scotese, C.R., Barrett, S.F., 1982. Mesozoic and Cenozoic Paleogeographic Maps, in: Brosche, P., Sündermann, J. (Eds.), Tidal Friction and the Earth's Rotation II. Springer, Berlin, Heidelberg, pp. 240–252. https://doi.org/10.1007/978-3-642-68836-2_17.

Zwolak, K., 2015. Underwater objects' detection system choice for harbor surveillance purposes. Zesz. Nauk. Akad. Mar. Wojennej 200, 1–1. https://doi.org/10.5604/0860889X.1161261.

Annex A: Other activities

The results of this thesis have been presented to many international conferences, in person or online after the beginning of the Covid-19 pandemic. Moreover, I have been convener of the salt tectonics sessions at EGU in 2020, 2021 and 2022, taking care of part of the abstract review and session coordination.

- ## Poster presentations

Travan, G., Gaullier, V., and Vendeville, B.C., 2019. Highlights on the interactions between salt tectonics and crustal tectonics in the Mediterranean. EGU General Assembly 2019, Vienna, Austria, 7-12 April, Geophysical Research Abstracts, Vol. 21, EGU2019-13613.

Travan, G., Gaullier, V., and Vendeville, B.C., 2019. Highlights on the interactions between salt tectonics and crustal tectonics in the Mediterranean. Journée des Doctorants IRePSE- Sciences de la Matière, du Rayonnement e de l'Environnement, Lille, France, 3 October.

Travan, G., Bellwald, B., Planke, S., Gaullier, V., Maharjan, D., Vendeville, B.C., 2020. Relationship between salt and crustal tectonics in the Sørvestsnaget Basin, SW Barents Sea. MEDSALT Final Symposium, Piran, Slovenia, 25-27 February.

- ## Oral presentations

Travan, G., Gaullier, V., Vendeville, B.C., 2018. Analogue modelling of combined crustal and Messinian salt deformation in Mediterranean. SaltGiant Workshop, Palermo, Italy, 26-29 November.

Gaullier, V., Chanier, F., Schmitt, F. G., Lymer, G., Watremez, L., Maillard, A. L., Thinon, I., Sage, F., **Travan, G.**, Graveleau, F., Caroir, F., 2019. The Eastern Sardinian Margin: From Rifting to Hyper-extension and Post-rift reactivation in a Backarc Setting. American Geophysical Union, Fall Meeting 2019, San Francisco, 9-13 December, 2019AGUFM.T33F0425G.

Bellwald, B., **Travan, G.**, Planke, S., Maharjan, D., Faleide, J.I., Gaullier, V., and Myklebust, R., 2020. Permo-Carboniferous Salt Messing Up the Cenozoic Stratigraphy of the Sørvestnaget Basin, SW Barents Sea. 34th Nordic Geological Winter Meeting 2020 (NGWM20), Geological Society of Norway, University of Oslo, Norway, 8-10 January.

Travan, G., Bellwald, B., Planke, S., Gaullier, V., Maharjan, D., Vendeville, B.C., 2020. Relationship between salt and crustal tectonics in the Sørvestsnaget Basin, SW Barents Sea. EGU General Assembly 2020, online, 4-8 May. EGU2020-17586, https://doi.org/10.5194/egusphere-egu2020-17586.

Travan, G., Gaullier, V., Vendeville, B.C., 2020. Relationships between salt tectonics and crustal tectonics in the Sørvestsnaget Basin (SW Barents Sea) and in the Algerian Margin (Western Mediterranean). 3rd SaltGiant Workshop, online, 2-3 June.

Travan, G., Gaullier, V., Vendeville, B.C., 2021. Interactions between salt and crustal tectonics: Examples of the Western Mediterranean and SW Barents Sea. 4th SaltGiant Workshop, online, 2-4 March.

Travan, G., Gaullier, V., Vendeville, B.C., Déverchère, J., Raad, F., Lofi, J., 2021. Gravity gliding and spreading in a compressional setting: the example of the Algerian margin. EGU General Assembly 2021, online, 19–30 April, EGU21-11948, https://doi.org/10.5194/egusphere-egu21-11948

Travan, G., Gaullier, V., Bellwald, B., Maharjan, D., Planke, S., 2021. Long-lived salt tectonics in the SW Barents Sea: The giants of the Sørvestsnaget Basin. SaltGiant Short Course, Banja Luka, Bosnia and Herzegovina, 4-6 October.

Travan, G., Bellwald, B., Planke, S., Gaullier, V., Maharjan, D., Vendeville, B.C., Myklebust, R., 2021. Salt tectonics processes in the Sørvestsnaget Basin, SW Barents Sea. AAPG Evaporite Processes and Systems: Integrating perspectives, online, 18-20 October.

Gaullier, V., **Travan, G.,** Vendeville, B.C., Déverchère, J., Raad, F., Lofi, J., 2021. Interactions between crustal contraction and gravity-driven salt tectonics offshore Algeria: Insights from seismic data and new analogue modelling. AGU Fall meeting 2021. New Orleans, 13-17 December.

Travan, G., Gaullier, V., Vendeville B.C. and Déverchère J., 2022. Messinian salt deformation offshore Algeria: the role of crustal tectonics and sedimentary load on the observed geometries. EGU General Assembly 2022, Vienna, Austria, 3-8 April, EGU22-12073, https://doi.org/10.5194/egusphere-egu22-12073.

Travan, G., Gaullier, V. and Déverchère, J., 2022. Multidirectional salt gravity gliding and minibasins formation: the case study of the reactivated Algerian margin. SaltGiant Final Event, Paris, France, 17-19 May.

- ## Session convener

EGU 2020, May 2020, online. Co-convener of session TS13 - Salt basins: from deposition to deformation

EGU 2021, May 2021, online. Co-convener of session TS11.1 Salt and shale tectonics

EGU 2022, May 2022, Vienna (Austria). Co-convener of session TS11.1 Salt and shale tectonics

- **Saltgiant activities**

A plan of formation (both specific, interdisciplinary and soft-skills related) is included in the SaltGiant project. One of the main objectives of the SaltGiant ETN is to train the PhD candidates to a multidisciplinary approach, both creating networks and collaborations between Universities, Research Institutes and industry, both broadening the personal knowledge of the single students with field courses, short courses and transferable skills trainings. The pandemic that stopped the international travels during different Covid-19 waves did not stop the events, that were partly held online and partly delayed to moments of open borders. The attended Saltgiant and Medsalt events are the following:

. SaltGiant workshop and first Transferrable skills workshop, November 2018, Palermo (Italy).

. MedSalt training school “The Messinian Salinity Crisis from a fieldwork perspective”, April 2019, Sorbas (Spain).

. SaltGiant field trip “Introduction to MSG geology”, May 2019, Sicily (Italy).

. SaltGiant workshop and second Transferrable skills workshop, June 2019, Trieste (Italy).

. SaltGiant Short Course «Numerical Modelling in the Earth Sciences: Philosophy, methods and applications of numerical and analogue modelling in the Earth Sciences », October 2019, Utrecht University (Netherlands).

. Medsalt final symposium, February 2020, Piran (Slovenia).

. SaltGiant Mid-term meeting, May 2020, online.

. SaltGiant Transferable skills 3 « Managing research », April and May 2021, online.

. SaltGiant Social Sciences Short Course, June 2021, Paris (France).

. SaltGiant Short Course and workshop, October 2021, Banja Luka ad Tuzla (Bosnia and Herzegovina)

. Dead Sea field course, November 2021, Dead Sea.

. SaltGiant final event, May 2022, Paris (France).

- **Oceanographic cruises**

  - Participation to the 5 days “GEOBAS” Survey (Party Chief: Gaullier, October 2018) in the English Channel, aimed at teaching to the GEOBAS master’s students the principles of seismic reflection data acquisition and the practical work of Sparker profiles acquisition (procedure, safety issues, possible problems during the acquisition and how to solve them).

  - Participation to ten days of the « METYSS 4 » Survey (Party Chief: Gaullier, June 2019) in the Western Tyrrhenian, during which we acquired sparker profiles on the Eastern Sardinian margin.

- **Dissemination**

  - Participation to the SaltGiant blog (https://thesaltgiantfellowship.wordpress.com/)
    - *"About Dr. Ilaria Capua, the loss of scientific credibility and the amplifying effect of the press"*
    - *"History of salt tectonics studies"*
  - Participation to the SaltGiant newsletters (https://www.saltgiant-etn.com/dissemination/)
  - Participation to « Fêtes de la Mer », July 2019, Boulogne-sur-Mer (France): practical demonstrations of analogue modelling for the public.

- **Other activities**

  - Member of the « Commission Mixte » of the « Département des Sciences de la Terre – Laboratoires de Recherche (LOG, EEP, LGCGE) ».

  - Participation to the CNFH (Commission Nationale Flotte Hauturière) MEDSALT oceanographic cruise proposal, aimed at sampling the massive salt deposits that formed in the Mediterranean during the Messinian Salinity Crisis in order to study their dynamics and their associated microbial communities (Aloisi G., Lofi J., Rabaute A., Camerlenghi A.).

Annex B: The Lago Mare controversy

One of the topics still much debated regarding the Messinian Salinity Crisis is how and when the salinity crisis ended. The spirit of interdisciplinarity and international collaboration represented by the project SaltGiant led to the publication of the paper "**Freshening of the Mediterranean Salt Giant: controversies and certainties around the terminal (Upper Gypsum and *Lago*-Mare) phases of the Messinian Salinity Crisis"** (Andreetto et al., 2021, https://doi.org/10.1016/j.earscirev.2021.103577), published on the Earth-Science Reviews scientific journal (impact factor: 12.413 in 2021). More than 20 co-authors of different nationalities, institutes and disciplines collaborated on the writing of a manuscript of 47 pages which takes into consideration the literature and the data, from the geochemical to the geophysical ones, of the onshore and offshore Mediterranean. Our contribution focuses in particular on the presence and detectability of the Lago Mare sequence offshore, namely in the seismic reflection profiles and in the core recoveries, with a focus on the Tyrrhenian and Alboran basins.

How to cite: Andreetto, F., Aloisi, G., Raad, F., Heida, H., Flecker, R., Agiadi, K., Lofi, J., Blondel, S., Bulian, F., Camerlenghi, A., Caruso, A., Ebner, R., Garcia-Castellanos, D., Gaullier, V., Guibourdenche, L., Gvirtzman, Z., Hoyle, T.M., Meijer, P.T., Moneron, J., Sierro, F.J., Travan, G., Tzevahirtzian, A., Vasiliev, I., Krijgsman, W., 2021. Freshening of the Mediterranean Salt Giant: controversies and certainties around the terminal (Upper Gypsum and Lago-Mare) phases of the Messinian salinity crisis. Earth-Sci. Rev., 216, 103577, pp. 1-47, 10.1016/j.earscirev.2021.103577

Earth-Science Reviews 216 (2021) 103577

Contents lists available at ScienceDirect

Earth-Science Reviews

journal homepage: www.elsevier.com/locate/earscirev

Freshening of the Mediterranean Salt Giant: controversies and certainties around the terminal (Upper Gypsum and Lago-Mare) phases of the Messinian Salinity Crisis

F. Andreetto [a,*], G. Aloisi [b], F. Raad [c], H. Heida [d], R. Flecker [e], K. Agiadi [f], J. Lofi [c], S. Blondel [g], F. Bulian [h], A. Camerlenghi [g], A. Caruso [i], R. Ebner [j], D. Garcia-Castellanos [d], V. Gaullier [k], L. Guibourdenche [b], Z. Gvirtzman [l,m], T.M. Hoyle [a,n], P.T. Meijer [j], J. Moneron [l,m], F.J. Sierro [h], G. Travan [k], A. Tzevahirtzian [i], I. Vasiliev [o], W. Krijgsman [a]

[a] Paleomagnetic Laboratory "Fort Hoofddijk", Dept. of Earth Sciences, Utrecht University, Budapestlaan 17, 3584 CD Utrecht, The Netherlands
[b] Université de Paris, Institut de physique du globe de Paris, CNRS, F-75005 Paris, France
[c] Géosciences Montpellier, CNRS, Université de Montpellier, Montpellier, France
[d] Geosciences Barcelona, GEO3BCN, CSIC, Solé i Sabarís s/n, Barcelona, Spain
[e] BRIDGE, School of Geographical Sciences and Cabot Institute, University of Bristol, University Road, Bristol BS8 1SS, United Kingdom
[f] Department of Palaeontology, University of Vienna, Althanstraße 14 (UZA II), 1090 Vienna, Austria
[g] Istituto Nazionale di Oceanografia e di Geofisica Sperimentale (OGS), Trieste, Italy
[h] Department of Geology, University of Salamanca, Salamanca, Spain
[i] Dipartimento di Scienze della Terra e del Mare, Università degli studi di Palermo, via Archirafi 20-22, 90123 Palermo, Italy
[j] Department of Earth Sciences, Utrecht University, Utrecht, The Netherlands
[k] Univ. Lille, CNRS, Univ. Littoral Côte d'Opale, UMR 8187, LOG, Laboratoire d'Océanologie et de Géosciences, F 59000, Lille, France
[l] Geological Survey of Israel, Jerusalem 95501, Israel
[m] Institute of Earth Sciences, The Hebrew University of Jerusalem, Israel
[n] CASP, West Building, Madingley Rise, Madingley Road, Cambridge CB3 0UD, United Kingdom
[o] Senckenberg Research Biodiversity and Climate Research Centre, Senckenberganlage 25, 60325 Frankfurt am Main, Germany

ARTICLE INFO

Keywords:
Messinian Salinity Crisis
Mediterranean stratigraphy
Connectivity proxies
Paleogeography
Paratethys
Lago-Mare

ABSTRACT

The late Miocene evolution of the Mediterranean Basin is characterized by major changes in connectivity, climate and tectonic activity resulting in unprecedented environmental and ecological disruptions. During the Messinian Salinity Crisis (MSC, 5.97-5.33 Ma) this culminated in most scenarios first in the precipitation of gypsum around the Mediterranean margins (Stage 1, 5.97-5.60 Ma) and subsequently > 2 km of halite on the basin floor, which formed the so-called Mediterranean Salt Giant (Stage 2, 5.60-5.55 Ma). The final MSC Stage 3, however, was characterized by a "low-salinity crisis", when a second calcium-sulfate unit (Upper Gypsum; substage 3.1, 5.55-5.42 Ma) showing (bio)geochemical evidence of substantial brine dilution and brackish biota-bearing terrigenous sediments (substage 3.2 or Lago-Mare phase, 5.42-5.33 Ma) deposited in a Mediterranean that received relatively large amounts of riverine and Paratethys-derived low-salinity waters. The transition from hypersaline evaporitic (halite) to brackish facies implies a major change in the Mediterranean's hydrological regime. However, even after nearly 50 years of research, causes and modalities are poorly understood and the original scientific debate between a largely isolated and (partly) desiccated Mediterranean or a fully connected and filled basin is still vibrant. Here we present a comprehensive overview that brings together (chrono)stratigraphic, sedimentological, paleontological, geochemical and seismic data from all over the Mediterranean. We summarize the paleo-environmental, paleohydrological and paleoconnectivity scenarios that arose from this cross-disciplinary dataset and we discuss arguments in favour of and against each scenario.

* Corresponding author.
E-mail address: f.andreetto@uu.nl (F. Andreetto).

https://doi.org/10.1016/j.earscirev.2021.103577
Received 1 November 2020; Received in revised form 4 February 2021; Accepted 25 February 2021
Available online 3 March 2021

1. Introduction

At the end of the Miocene, orbital and tectonic drivers combined to alter the amount of water delivered to the Mediterranean Basin by the Atlantic Ocean from the west, the brackish Eastern Paratethys (i.e. Euxinic-Caspian Basin system) from the east and the major peri-Mediterranean freshwater drainage systems (e.g. African rivers and Rhône; Griffin, 2002; Gladstone et al., 2007; Van der Laan et al., 2006; Hilgen et al., 2007; Ryan, 2009; Flecker et al., 2015; Marzocchi et al., 2015, 2016, 2019; Simon et al., 2017; Krijgsman et al., 2018; Capella et al., 2020). The changes in extra and intrabasinal connectivity resulted in unprecedented paleoceanographic and paleohydrological budget changes that led to a relatively short-lived environmental and ecological crisis (approx. 660 kyr; 5.97-5.33 Ma), for which the term Messinian Salinity Crisis (MSC) was coined (Selli, 1954, 1960). Most conspicuous was the rapid accumulation of several kilometers of halite (i.e. ~1 million km^3) on the Mediterranean abyssal plains (e.g. Hsü, 1972; Ryan, 1973; Montadert et al., 1978; Haq et al., 2020). This happened within 50 kyr, from 5.60-5.55 Ma, according to Roveri et al. (2014a) and Manzi et al. (2018), or in >300 kyr, when starting at 5.97 Ma, as put forward by Meilijson et al. (2018, 2019).

During the ~200 kyr lapse (i.e. MSC Stage 3 following Roveri et al., 2014a; Fig. 1a) between the end of salt precipitation (5.55 Ma) and the restoration of the still enduring marine conditions (5.33 Ma), the Mediterranean underwent a sequence of paleohydrological and base-level changes that are the topic of intense and long-standing debates. The initial and still widely endorsed hypothesis was that the Mediterranean Sea, following the major drawdown event that led to halite deposition (i.e. Stage 2), maintained the isolated, deeply-desiccated geography containing a series of hypersaline (substage 3.1; 5.55-5.42 Ma) and hyposaline (substage 3.2; 5.42-5.33 Ma) ponds which only received water from local streams and were colonized by Black Sea organisms carried by aquatic migratory birds (Fig. 1b; e.g. Ruggieri, 1967; Decima and Sprovieri, 1973; Decima and Wezel, 1971, 1973; Cita et al., 1978; Müller et al., 1990; Benson and Rakic-El Bied, 1991; Benson et al., 1991; Müller and Mueller, 1991; Butler et al., 1995; Orszag-Sperber et al., 2000; Rouchy et al., 2001; Kartveit et al., 2019; Madof et al., 2019; Camerlenghi et al., 2019; Caruso et al., 2020; Raad et al., 2021). As morphological and seismic reflection studies at the Strait of Gibraltar documented a ~400 km long erosional trough connecting the Gulf of Cadiz (Atlantic Ocean) to the Mediterranean Sea, this scenario of a lowered Mediterranean Sea was promptly linked to the termination of the MSC (McKenzie, 1999; Blanc, 2002; Garcia-Castellanos et al., 2009, 2020). This conclusion has recently been reinforced by the discovery of vast chaotic deposits sitting at the claimed Miocene/Pliocene transition in the area of the Malta Escarpment-Ionian Abyssal Plain (Micallef et al., 2018, 2019; Spatola et al., 2020).

In more recent years, the desiccated basin model was challenged by the observation of deposits that are uniform in terms of sedimentology and stratigraphic architecture (Roveri et al., 2008a), ostracod content (Gliozzi et al., 2007; Stoica et al., 2016) and geochemistry (McCulloch and De Deckker, 1989; García-Veigas et al., 2018; Andreetto et al., 2021) throughout the Mediterranean marginal belt and of $\delta D_{n\text{-alkanes}}$ and $\delta D_{alkenones}$ sharing similarities with the coeval Atlantic Ocean and Black Sea, respectively (Vasiliev et al., 2017). A model of a (relatively) full Mediterranean Sea developed (Fig. 1c), where the debate mainly concerns the provenance of the hydrological fluxes and the resultant hydrochemical composition of the water mass. In this scenario, the Mediterranean was first, during substage 3.1, transformed into a new gypsum-precipitating basin filled with marine and continent-derived

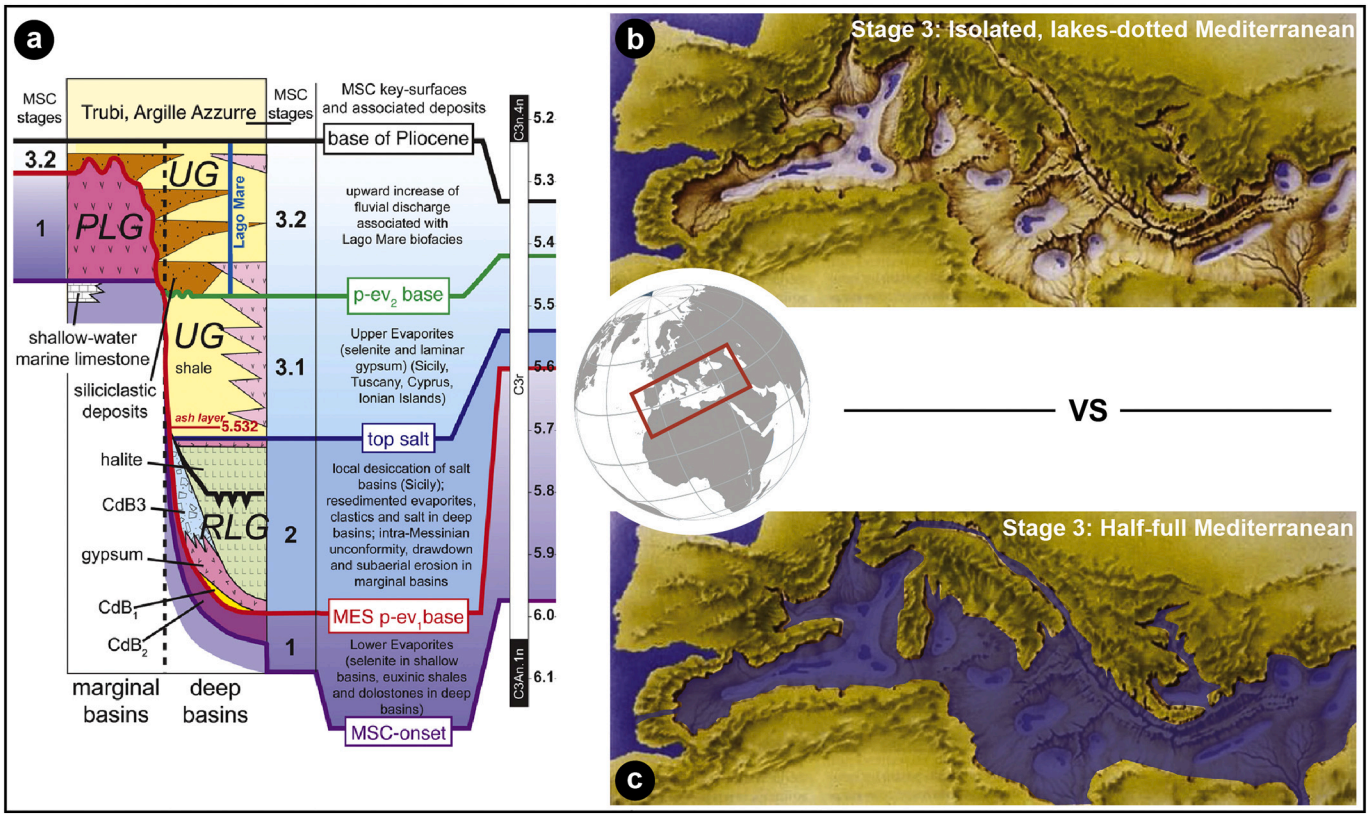

Fig. 1. (a) Consensus chronostratigraphic model for the MSC events (Roveri et al., 2014a). Stage 3, here of interest, spans between 5.55 Ma and 5.332 Ma, the astronomical ages of the base of the Upper Gypsum Unit (following Manzi et al., 2009) and Trubi Formation (Van Couvering et al., 2000) in the Sicilian Eraclea Minoa section, respectively. CdB: Calcare di Base; PLG: Primary Lower Gypsum; RLG: Resedimented Lower Gypsum; UG: Upper Gypsum. (b), (c) Map of the Mediterranean region showing the two extreme and mutually exclusive paleoenvironmental scenarios proposed to have featured the Mediterranean during Stage 3 (see discussion in Chapter 7; modified after Krijgsman et al., 2018).

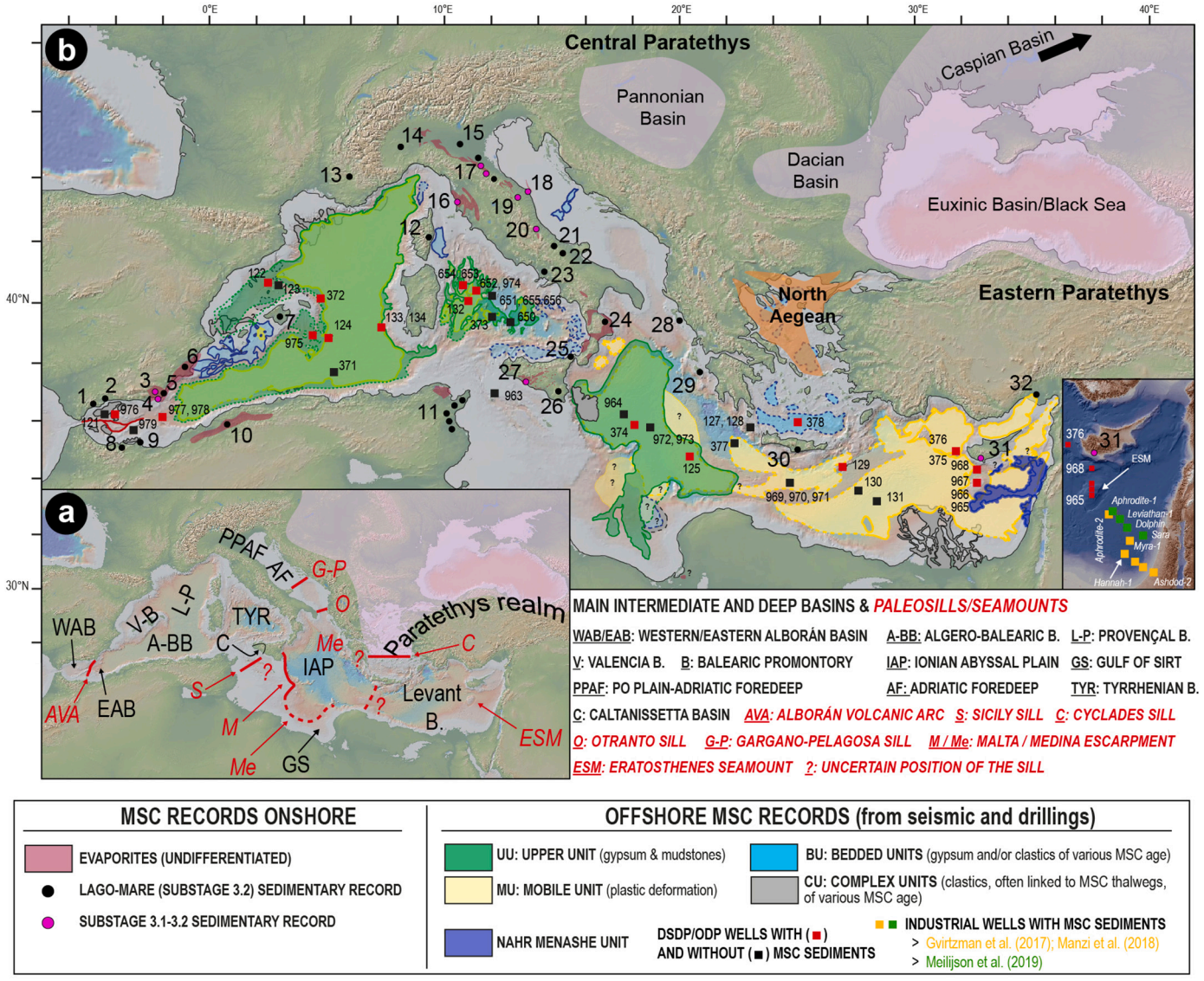

Fig. 2. Map of the Mediterranean Basin (modified from Lofi, 2018) showing: a) the location of the key intermediate and deep basins as well as physical thresholds that influenced the connectivity history of the Mediterranean; b) the onshore (i.e. basins and/or sections) and offshore (DSDP/ODP/Industrial drill sites) localities where deposits attributed to MSC Stage 3 have been studied. Mixed assemblages of Paratethyan-like ostracods and foraminifera are known from all mentioned onshore localities and some offshore locations (see text). The present-day spatial extent of the MSC seismic units, except for the Lower Unit, is also shown. The paleogeography of the (Eastern and Central) Paratethys and of the North Aegean domain is contoured after Van Baak et al. (2017) and Krijgsman et al. (2020a), respectively. W-E onshore localities: 1-6 Betic Cordillera (SE Spain): 1-Marbella and 2-Malaga basins (Guerra-Merchán et al., 2010); 3-Sorbas Basin (Roveri et al., 2009, 2019a); 4-Nijar Basin (Fortuin and Krijgsman, 2003); 5-Vera Basin (Fortuin et al., 1995); 6-Bajo Segura Basin (Soria et al., 2005, 2008a, 2008b); 7-Mallorca (Mas and Fornós, 2020); 8-Melilla Basin (Rouchy et al., 2003); 9-Boudinar Basin (Merzeraud et al., 2019); 10-Chelif Basin (Rouchy et al., 2007); 11-Sahel area (Frigui et al., 2016); 12-Aléria Basin and 13-Rhône Valley (Carbonnel, 1978); 14-Piedmont Basin (Dela Pierre et al., 2011, 2016); 15-Po Plain (Ghielmi et al., 2010, 2013; Amadori et al., 2018); 16-Fine Basin (Cava Serredi section; Carnevale et al., 2006a, 2008). 17-21 Apennine system: Romagna sections (17, Roveri et al., 1998), Trave section (18, Iaccarino et al., 2008), Maccarone section (19, Bertini, 2006, Grossi et al., 2008; Sampalmieri et al., 2010; Pellen et al., 2017), Colle di Votta (20)-Fonte dei Pulcini (21)-Stingeti (22) sections (Cosentino et al., 2005, 2012, 2013, 2018), Mondragone 1 well (23, Cosentino et al., 2006), Crotone Basin (24, Roveri et al., 2008a); 25-27 Sicily: Villafranca Tirrena (25) and Licodia Eubea (26) sections (Sciuto et al., 2018), Caltanissetta Basin (27, Manzi et al., 2009); 28-Corfu (Pierre et al., 2006); 29-Zakinthos (Karakitsios et al., 2017b); 30-Crete (Cosentino et al., 2007); 31-Cyprus (Rouchy et al., 2001; Manzi et al., 2016a); 32-Adana Basin (Radeff et al., 2016).

waters (e.g. Manzi et al., 2009; Roveri et al., 2014c; Flecker et al., 2015; Vasiliev et al., 2017; García-Veigas et al., 2018; Grothe et al., 2020). Then, during substage 3.2, it became a brackish lake-sea comparable to the present-day Black Sea or Caspian Sea (Roveri et al., 2008a; Stoica et al., 2016; Andreetto et al., 2021), depending on whether a marine connection with the Atlantic was active (Manzi et al., 2009; Roveri et al., 2014b, 2014c; Flecker et al., 2015; Marzocchi et al., 2016; Vasiliev et al., 2017; García-Veigas et al., 2018) or not (e.g. McCulloch and De Deckker, 1989; Roveri et al., 2008a), and with a base-level fluctuating by hundreds of meters with precessional periodicity (Fortuin and Krijgsman, 2003; Ben Moshe et al., 2020; Andreetto et al., 2021). In the relatively full scenario, the revival of marine conditions is ascribed to either connectivity changes (Marzocchi et al., 2016) or to a moderate sea-level rise (Andreetto et al., 2021). In contrast, Carnevale et al. (2006a, 2006b, 2008, 2018) and Grunert et al. (2016), based on the recovery of fish remains ascribed to marine species, proposed that fully marine conditions were in force in the Mediterranean already at the end of substage 3.1.

After nearly 50 years of research on both onshore and offshore localities (Fig. 2), the observations backing up the competing desiccated and full-basin Mediterranean models remain extremely difficult to reconcile. Uncertainties regarding the chronostratigraphic framework of Stage 3 deposits, the origin and migration of its characteristic biota, the meaning of the data derived from the applied geochemical techniques and the relationship between the Mediterranean and its surrounding water bodies (i.e. Atlantic Ocean, Indian Ocean and Paratethys) all inhibit a clear understanding of the Mediterranean base-level and its hydrochemical structure.

In this paper we attempt to summarize all the existing, but heavily scattered, data resulting from ~50 years of cross-disciplinary studies with the aim of providing a comprehensive overview of the stratigraphic arrangement of Stage 3 onshore and offshore deposits, as well as of their sedimentological, paleontological, geochemical and seismic properties. Subsequently, we assemble the observations favoring both end-member scenarios of a relatively desiccated and relatively full Mediterranean. Finally, we focus on novel future analytical techniques and approaches that have the potential to constrain Mediterranean base-level during MSC Stage 3 as well as the changing hydrological fluxes and connectivity phases between the intra-Mediterranean basins and the neighboring Atlantic Ocean and Paratethyan domains as a mean of reconstructing the state of the art of the complex history of this enigmatic period of the Mediterranean history once and for all.

2. The terminal Stage 3 of the MSC

2.1. Historic overview of nomenclature and concepts

The final phase of the MSC (i.e. substage 3.2), also known as “Lago-Mare”, finds its sedimentary expression in cyclically-arranged terrigenous and evaporitic sediments hosting unique faunal assemblages of ostracods, mollusks and dinoflagellate cysts (dinocysts). They are related, at species level, to those inhabiting, during the Miocene, the brackish basins of the Paratethys realm (e.g. Gliozzi et al., 2007; Stoica et al., 2016). But what exactly is the “Lago-Mare”? This widely employed expression in the MSC literature encompasses a variety of meanings that make its application doubtful and misleading. The root of the wording “Lago-Mare” is to be found in the Russian scientific literature of the late 1800s. Nikolai Andrusov (1890) used the corresponding Russian term with a geographical and chronological connotation in reference to the series of central-eastern European basins that during the Miocene turned from marine settings to desalinized semi-isolated lakes with an endemic fresh-brackish water biota association (e.g. Popov et al., 2006 and references therein). The original monograph of Andrusov (1890) was not widely available outside Russia, but his attendance of international conferences allowed his research to spread outside the Russian borders. From the publications of the French geologists Suzette Gillet (Gillet, 1932, 1933) and Maurice Gignoux (Gignoux, 1936a) we can state with relative certainty that the original meaning of the word “Lago-Mare” (here reported with the French counterpart “Lac-Mer”) had its provenance in the Russian literature:

> *“[…] An isolation of the basin, that became a brackish, isolated basin. Then, a uniform fauna populated this immense lac-mer which was divided […] into Pannonian basin, […] Dacique Basin, and Euxin and Caspian basin […]”* (Gillet, 1932).
>
> *“[…] During the Volhynien (Sarmatique inferior) there was a lac-mer of uniform fauna that extended through all the eastern Europe. […] and the fauna of the eastern regions of that huge lac-mer was completely differenciated* [sic] *from the one in the western regions. […]”* (Gillet, 1933).
>
> *“[…] The Pontien fauna is not anymore a fauna characteristic of an internal saline sea, as in the Sarmantien, but is a fauna of a “desalinated lagoon”, a lac-mer, as the Russian geologists named it. […]”* (Gignoux, 1936b).

In the late 19th (Capellini, 1880) and 20th century (Ogniben, 1955; Ruggieri, 1962, 1967; Decima, 1964), late Messinian ostracod- and mollusk-bearing deposits in the Mediterranean were described at several Italian localities. Initially, the expressions “*Congeria* beds” (Capellini, 1880) and "*Melanopsis* beds" (Ruggieri, 1962) were used. Later on, Ruggieri (1967) pointed out the affinity of these faunal elements with those of the Pontian of the Paratethys. Consequently, he speculated on a feasible Paratethys-like paleoenvironmental configuration for the Mediterranean in the latest Messinian and he coined the Italian translation (i.e. "Lago-Mare") from the French “Lac-Mer” in reference to the shallow-water lakes claimed to be widely distributed across the Mediterranean. Progress in the 1970s in onshore and offshore exploration highlighted the temporally well-constrained distribution of the Paratethyan organisms in the Mediterranean (Carbonnel, 1978). On this premise, Hsü et al. (1978a) proposed to use "Lago-Mare" to "*designate the latest Messinian oligohaline environment, postdating evaporite deposition and predating Pliocene marine sedimentation […] in order to distinguish it from "lac mer" which, strictly speaking, was a Paratethyan environment*". Notwithstanding the new definition, in various parts of the text they used "Lago-Mare" to refer to the Paratethyan lakes (pp. 1071-1072: "*[…] The upper Messinian Mediterranean was floored by a series of desert basins, some with salt lakes, prior to inundation by the Lago-Mare.*"), thus giving rise to the confusion on how to use the term properly.

In the most recent stratigraphic overview of the MSC (Fig. 1a; Roveri et al., 2014a), the terminal MSC stage is called Stage 3, which is in turn subdivided into substages 3.1 and 3.2 (also termed Lago-Mare). Beside such a chronostratigraphic definition, the term “Lago-Mare” has also been used for a typical biofacies of the late Messinian Mediterranean (e.g. Fortuin et al., 1995; Gliozzi, 1999; Gliozzi and Grossi, 2008; Sciuto et al., 2018), for the pelitic beds encasing the Paratethyan-related fauna (i.e. a lithofacies; e.g. Fortuin and Krijgsman, 2003; Sciuto et al., 2018), as the name of an informal lithostratigraphic unit (usually distinguished by its fossil content) sandwiched between the Sicilian Upper Gypsum and the Arenazzolo Fm. (Fig. 4b; Clauzon et al., 2005; Londeix et al., 2007; Popescu et al., 2009; Bache et al., 2012) and to denote multiple (3 to 4) spilling events of the Paratethys into the Mediterranean (Clauzon et al., 2005, 2015; Popescu et al., 2007, 2009, 2015; Suc et al., 2011; Bache et al., 2012; Do Couto et al., 2014; Frigui et al., 2016; Mas and Fornós, 2020).

This being a review, we use the widely employed definition of the model of Roveri et al., 2014a) (Fig. 1a) and regard the Lago-Mare as a “phase of massive biota migration from the Paratethys realm, cyclostratigraphically constrained between 5.42 Ma and 5.332 Ma (Roveri et al., 2008a; Grossi et al., 2011), during which the Mediterranean sedimentary environments underwent an impressive freshening”. Nevertheless, we call for caution in the use of this definition of “Lago-Mare” in future studies, since 5.42 Ma as the (astronomical) age of the first entrance of Paratethyan organisms into the Mediterranean is likely

to be incorrect (see subsection 5.1) and evidence of 'impressive freshening' are already present much earlier (e.g. at Eraclea Minoa; Vasiliev et al., 2017; García-Veigas et al., 2018).

2.2. Development of a chronostratigraphic framework

Issues of the timing and duration of the MSC only began to be tackled in the 1990s, in parallel with discussion concerning the nature of its extreme paleoenvironments (Schmalz, 1969; Hsü et al., 1973a, 1973b, 1973c, Hsü et al., 1978a, 1978b; Nesteroff, 1973; De Benedetti, 1982). While published models (Butler et al., 1995; Clauzon et al., 1996; Krijgsman et al., 1999a; Rouchy and Caruso, 2006) mostly converged on the (astronomical) age of the marine replenishment at the beginning of the Pliocene (5.332 Ma; Van Couvering et al., 2000), there were disagreements about the age of the onset of the MSC (synchronous vs diachronous) and of specific events within it (see discussion in Roveri et al., 2014a). Among these, the work of Krijgsman et al. (1999a) has obtained wide consensus. Their cyclostratigraphic tuning and correlation of continuous and bio-magnetostratigraphically constrained pre-evaporitic sections in Spain (Sorbas), Sicily (Gibliscemi/Falconara) and Greece (Metochia) resulted in a synchronous age of 5.96±0.02 Ma for the MSC onset (later refined to 5.97 Ma by Manzi et al., 2013). The astronomical ages for the onset (Krijgsman et al., 1999a) and termination (Van Couvering et al., 2000) of the MSC are not contentious since the characteristic sedimentary cyclicity and sediments' properties (e.g. color of the lithologies and biota content) of the pre- and post-MSC successions fit robustly with the insolation curve (see also Van der Laan et al., 2006 and Topper and Meijer, 2015).

The cyclic arrangement of the MSC sediments (Fig. 3a) led scientists to interpret that the same cyclostratigraphic approach could be used to gain precise dates for events within the MSC (e.g. Hilgen et al., 1995; Vai, 1997; Krijgsman et al., 1999b, 2001), bypassing the challenge posed by the unsuitability of the classic biomagnetostratigraphic tools for the MSC successions. Characteristic interference patterns of eccentricity and precession have been tentatively recognized in the Sicilian Eraclea Minoa section (see subsection 3.8; Van der Laan et al., 2006). However, clear orbital signals are typically poorly expressed in MSC records and, when they are present, like in Sicily, they are not (vertically) repeated with sufficient frequency to establish clear phase relations with the astronomical cyclicity. For this reason, the simple counting of cycles with no analysis of cyclostratigraphic pattern in proxy records has mostly been employed as a correlation method (Roveri et al., 2008a; Manzi et al., 2009; Manzi et al., 2016a; Cosentino et al., 2013).

The age of the base of Stage 3 is largely determined by correlating the sedimentary cycles of the Upper Gypsum unit (UG) at Eraclea Minoa (Sicily) with the astronomical curve La2004 (Laskar et al., 2004). The UG sedimentary cyclicity consists of alternating gypsum and mudstone beds of variable thickness (Figs. 5g-i; see subsection 3.8). Precessional variation of the Mediterranean freshwater budget tied tightly to the African monsoon and Atlantic storms are the drivers interpreted to lie behind the gypsum-mudstone cycles (e.g. Marzocchi et al., 2015, 2019; Simon et al., 2017). Variations of the freshwater discharge cause the pycnocline to shift vertically, resulting in brine concentration and gypsum precipitation during to the arid/dry phases of the precession cycles (precession maxima-insolation minima) and brine dilution and mudstone deposition during the humid/wet phases (precession minima-insolation maxima) (Van der Laan et al., 2006; Manzi et al., 2009). Two different tuning options exist in literature (Van der Laan et al., 2006 versus Manzi et al., 2009; Fig. 3a):

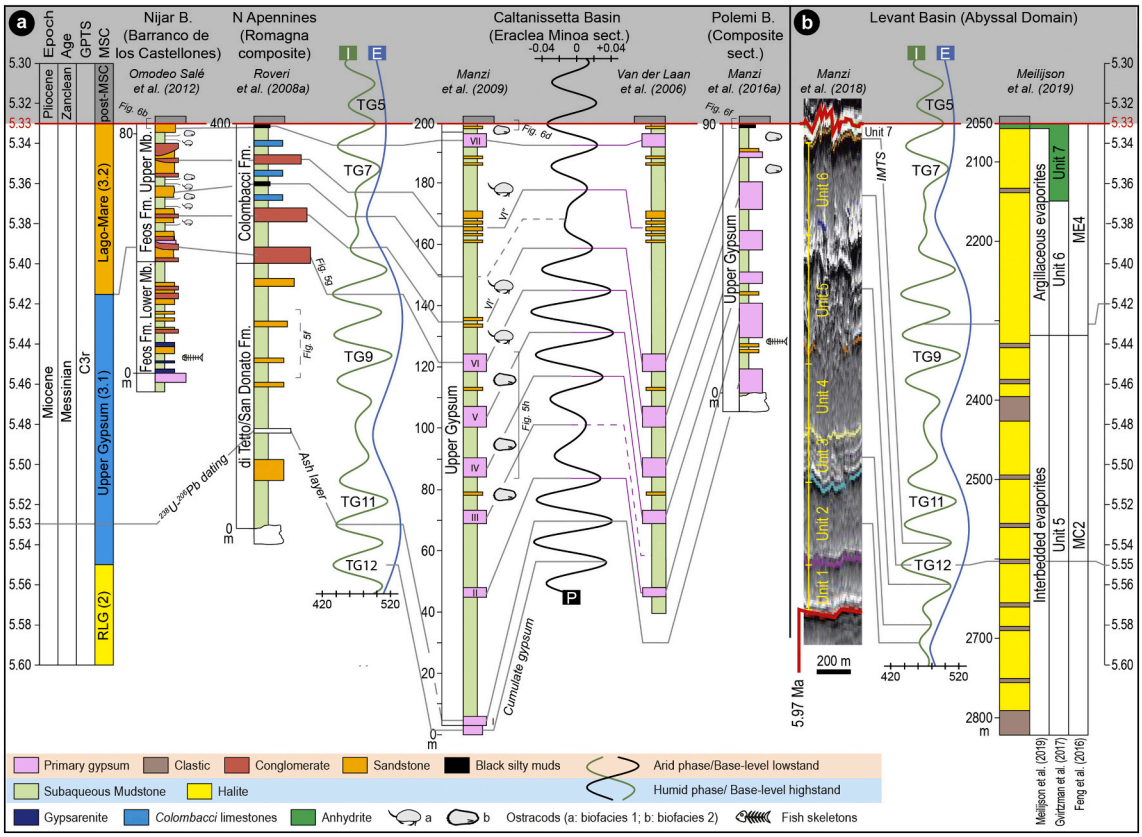

Fig. 3. (a), (b) Available astronomical tunings to astronomic curves of climatic precession (P), 100 kyr eccentricity (E) and 65°N insolation curve (I) of Laskar et al. (2004) of the lithological cyclicity of onshore Stage 3sections (a) and of the seismic cycles and/or well logs (gamma ray and resistivity) of the MU in the Levant Basin (b). Tunings of onshore sections in (a) are carried out downward from the M/P boundary (conformable in all sections). Astronomically-tuned glacial (even numbers) and interglacial (odd numbers) stages (i.e. TG) as defined by Hodell et al. (1994) are also indicated.

1. Van der Laan et al. (2006) tentatively recognized sedimentary patterns that they correlated with the astronomical curves by using the same phase relationships between the sedimentary cycles and the astronomical cycles as are seen in Plio-Pleistocene sapropel-bearing marine successions of the Mediterranean (Hilgen, 1991). The four closely spaced gypsum beds III to VI were regarded as a cluster, i.e. the sedimentary expression of a 100 kyr eccentricity maximum (Hilgen, 1991; Strasser et al., 2006), whereas the preceding and following evaporite-free marly interval were attributed to a phase of low-amplitude precession oscillations caused by a 100 kyr eccentricity minimum (Fig. 3a). Tuning downward from the conformable Miocene/Pliocene boundary (Fig. 6d) and arguing that the precession peak at ~5.38 Ma, which has an extremely low amplitude, is not expressed in the sedimentary record, Van der Laan et al. (2006) correlated gypsums III to VI with the four successive precession/insolation peaks of the 100 kyr eccentricity maximum dated around 5.44 Ma and the overlying and underlying gypsum-free marly interval fell within 100 kyr eccentricity minimum cycles (Fig. 3a, right log). This tuning resulted in an astronomical age of ~5.51 Ma for the first gypsum bed in their log (i.e. gypsum II in the log of Manzi et al., 2009), and an approximate duration of 175 kyr for Stage 3 as whole.
2. An alternative tuning by Manzi et al., 2009; Fig. 3a, left log) argued that every precessional/insolation peak must have an expression in the rock record. Manzi et al. (2009) agreed with the solution of Van der Laan et al. (2006) on the sedimentary inexpressiveness of the (barely visible) insolation minima peak at ~5.38 Ma. However, these authors considered the insolation minima peaks immediately above and below of too low amplitude to promote the conditions required for gypsum precipitation, but also too high not to have some sedimentary expression. They therefore identified sandstone horizons VI' and VI" as the sedimentary response to these weak insolation/precession signals. The addition of two precessional cycles (i.e. a total of 9) resulted in an astronomical solution that was adjusted one precessional cycle lower than that of Van der Laan et al. (2006), translating into an age of 5.53 Ma for the base of the UG and a total duration of ~200 kyr for Stage 3. But the more conspicuous difference between the two astronomical solutions discussed lies in the timing at which gypsum precipitation occurred, restricted to the 100 kyr eccentricity maxima according to Van der Laan et al. (2006), extended to the 100 kyr eccentricity minima by Manzi et al. (2009).

An age of 5.53 Ma for the first gypsum bed was also obtained by the astronomical tuning of the Upper Gypsum in Cyprus (Manzi et al., 2016a), but there the tuning is performed just by following the recognition, from the base up, of 6 gypsum beds just like in Sicily and therefore arguing for a bed-to-bed correlation with the Sicilian gypsums I-VI. In the consensus model of Roveri et al. (2014a) the base of Stage 3 coincides with the base of the Sicilian UG, placed by Manzi et al. (2009) at 5.55 Ma (Fig. 1A). However, in the model of Manzi et al. (2009) this age is attributed to a cumulate gypsum horizon interpreted as laterally equivalent of the Halite (i.e. Stage 2), and therefore implying the kickoff of Stage 3 at 5.53 Ma (Fig. 3a).

The post-evaporitic successions of the Romagna (Cusercoli and Sapigno sections; Roveri et al., 1998) and Marche (e.g. Trave and Maccarone sections; Iaccarino et al., 2008; Cosentino et al., 2013) areas provided evidence that led to the splitting of Stage 3 into substage 3.1 and 3.2. In the resulting composite section (Roveri et al., 2008a), a shift in the sedimentary facies and stacking pattern is observed (see description in subsection 3.7). Correlation of the sedimentary cyclicity in Romagna was from the (conformable) base of the Pliocene downwards (or from an U-Pb-dated ash layer upward; Cosentino et al., 2013) and linked three fluvial conglomerates and two black mudstone layers of unknown sedimentological significance to the arid phases of the precession cycles (Fig. 3a; Roveri et al., 2008a). The greater thickness of the oldest conglomerate was possibly assumed to be evocative of an oscillation of the amplitude of the corresponding precession minima peak rather than the amplitude of the peaks responsible for the formation of the other facies. This approach resulted in an age of 5.42 Ma for the first conglomerate (i.e. the substage 3.1/3.2 transition; Fig. 5g) and an approximate duration of 90 kyr for substage 3.2 (the Lago-Mare phase). The same astronomical age is obtained by tuning the Upper Member of the Feos Formation in the Nijar Basin (Omodeo-Salé et al., 2012), where four pelite-conglomerate cycles plus one sandstone capped by the Miocene/Pliocene boundary mark the interval attributed to Stage 3.2 (Fortuin and Krijgsman, 2003).

Although the substage 3.1/3.2 transition is linked to a major Mediterranean-scale hydrological re-organization possibly coinciding with the migration of the Paratethyan biota (Roveri et al., 2008a; Grossi et al., 2011), the facies change used for its definition is hardly recognizable elsewhere (see Chapter 3). As such, other tools have been used to equip fragmentary and/or lithological cyclicity-lacking sections with an age model: the (highly controversial) ostracod biozonation (see subsection 5.1; e.g. Stoica et al., 2016; Karakitsios et al., 2017a; Cosentino et al., 2018; Caruso et al., 2020) and the astronomical tuning of magnetic susceptibility records (e.g. Fonte dei Pulcini section, Central Apennines; Cosentino et al., 2012).

Comparison of Atlantic oxygen isotope records (Van der Laan et al., 2005, 2006) and the chronostratigraphy of Roveri et al. (2014a) revealed that Stage 3 sedimentation started during a prominent global eustatic lowstand associated with oxygen isotope (glacial) stage TG12, followed by a latest Messinian deglacial interval which comprised multiple obliquity- and possibly precession-forced global eustatic phases. As documented by Hodell et al. (2001) (later revised by Drury et al., 2018), Van der Laan et al. (2006) and Roveri et al. (2014a), the marine replenishment of the Mediterranean did not coincide with any major deglaciation, so non-eustatic causes of the Zanclean megaflood hypothesis are required.

3. Onshore domain: key sections, sedimentary expression and faunal content

3.1. The Alborán region

The westernmost outcrops of Stage 3 deposits in the Mediterranean are located in the Alborán region, close to the present-day Strait of Gibraltar (Fig. 2b). MSC deposits on the margins of this region are poorly developed, possibly because of a late Tortonian uplift that raised the margins above the Mediterranean water level (López-Garrido and Sanz de Galdeano, 1999). Near Malaga, however, two facies associations consisting of m-thick conglomerate-sandstone beds alternating with laminated pelites are documented in the Rio Mendelín section (informally referred to as "LM unit"; Guerra-Merchán et al., 2010) and attributed to (part of) the Lago-Mare phase (Fig. 4a) based on their paleontological content. These sediments are squeezed between the Paleozoic basement units, with an erosive contact and associated angular unconformity, and the Pliocene, from which they are separated by another erosional surface draped by conglomeratic accumulations (Fig. 6a). A well-preserved and diverse *in situ* Paratethyan-type ostracod and molluskan fauna (i.e. *Lymnocardiinae* and *Dreissenidae*) typical of shallow waterbodies (up to 100 m deep; Grossi et al., 2008; Gliozzi and Grossi, 2008) with low salinities (5-18‰) is reported from the pelitic units (Guerra-Merchán et al., 2010). The overlying Pliocene in the deeper depocenters starts with 30 m-thick littoral conglomerates with marine mollusks passing progressively upwards into deeper water facies, while fan deltas developed at the basin margins (López-Garrido and Sanz de Galdeano, 1999; Guerra-Merchán et al., 2010, 2014). Notably, the overall thickness of the Pliocene deposits reaches 600 m. The detailed regional studies by López-Garrido and Sanz de Galdeano (1999) and Guerra-Merchán et al. (2014) concluded that accommodation space was created during (Zanclean) sedimentation by local fault-driven subsidence, and that movement on these faults only reversed at the end of the Zanclean causing uplift.

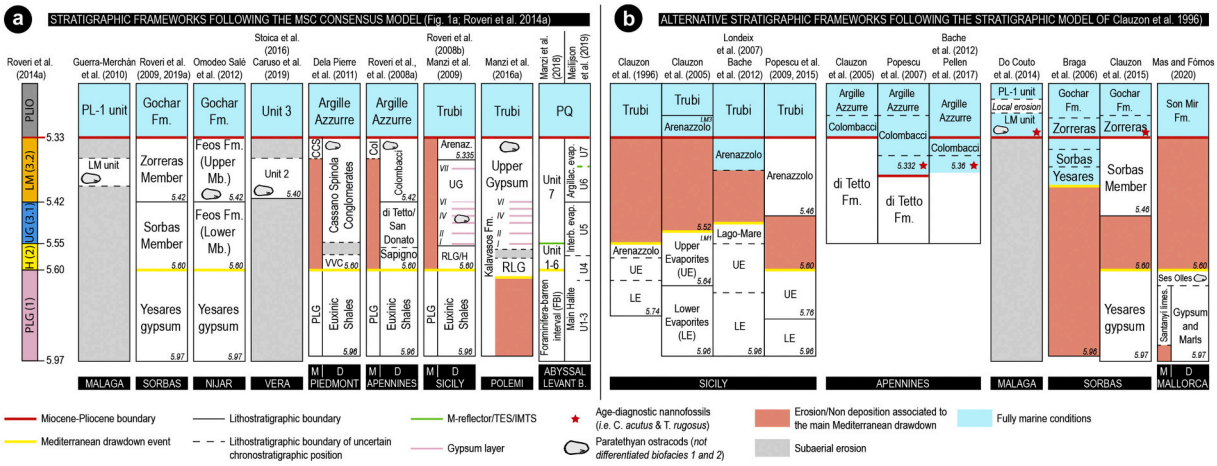

Fig. 4. Schematic overview of different chronostratigraphic models for some of the Messinian successions presented in Chapter 3. Note the large controversies in timing, duration and chronostratigraphic position of the main erosion phase between models in (a) and (b). Models in (a) follow the recently established MSC chronostratigraphic model of Roveri et al. (2014a), according to which the Mediterranean base-level dropped and halite deposited on sea floor during Stage 2 and the Upper Gypsum/Upper Evaporites-Lago-Mare sequence followed. Models in (b) were proposed following the alternative scenario of Clauzon et al. (1996, 2005), which envisaged two Lago-Mare episodes (LM1 and LM3) that occurred before and after the main Mediterranean drawdown event, during which LM2 was deposited in the deep desiccated basins (Do Couto et al., 2014; Popescu et al., 2015; see Roveri et al., 2008c and Grothe et al., 2018 for further explanations). Note, in (b), the shifting of the position of the main erosional phase in Sicily through time as well as the time of the marine replenishment in the Apennines.

An alternative scenario, based on the finding of (a few) specimens of the nannofossil *Ceratolithus acutus*, ascribed the LM unit of Guerra-Merchán et al. (2010) to the earliest Zanclean (Fig. 4b; Do Couto et al., 2014).

On the southern Alborán margin in Morocco, latest Messinian deposits are reported from the Boudinar and Melilla basins (Fig. 2b). Up to 100 m-thick chaotic deposits containing selenite gypsum fragments, azoic conglomerates, sandstones yielding planktic foraminifera and nannofossils and lacustrine limestones are capped by early Pliocene marine marls (Rouchy et al., 2003; Azdimousa et al., 2006; Cornée et al., 2016; Merzeraud et al., 2019). Due to their stratigraphic position, these continental to lacustrine deposits are interpreted as the local expression of the Lago-Mare phase (Cornée et al., 2016) or alternatively as Zanclean successions (Azdimousa et al., 2006).

3.2. Algeria

The Chelif Basin in Algeria (Fig. 2b) displays the typical marginal Messinian succession comprising Tortonian to lower Messinian blue marls, diatomite-bearing sediments (Tripoli unit), cyclically-arranged primary evaporites (13 couplets), ostracod-rich post-evaporitic deposits and Zanclean foraminiferal marls (Rouchy et al., 2007). The post-evaporitic sediments show a great lateral variability in both thickness (from few meters up to 125 m) and facies. They are mainly dominated by terrigenous clastic lithologies, associated in the marginal areas with sandy carbonates and stromatolitic limestones. A mixed faunal assemblage of non-marine (Paratethyan-like ostracods) and marine (benthic and planktic foraminifera) organisms is present, showing an increase in ostracod species diversity from the bottom to the top (Rouchy et al., 2007).

3.3. Neogene basins of the Eastern Betics (Spain)

The external Neogene basins (Sorbas, Nijar, Vera and Bajo Segura) of the eastern Betic Cordillera (SE Spain; Fig. 2b) represent an important laboratory for understanding Messinian events. In particular, the Sorbas and Nijar basins preserve two allegedly continuous successions spanning the entire MSC (e.g. Roveri et al., 2009; Omodeo-Salé et al., 2012). The two basins are similar in many respects. Their stratigraphic organization, for example, suggests they were connected for much of the late Miocene up until MSC Stage 1 (Fortuin and Krijgsman, 2003), which is represented by the gypsiferous Yesares Member (e.g. Lu, 2006). However, facies differences are prominent in the Stage 3 formations according to the chronostratigraphic frameworks of Roveri et al. (2009) for the Sorbas Basin and Omodeo-Salé et al. (2012) for the Nijar Basin (Fig. 4a). Lithostratigraphically, two members are discerned between the Yesares Member and the basal Zanclean: the Sorbas and Zorreras members in the Sorbas Basin (Figs. 4a, 5a) and the lower and upper members of the Feos Fm. in Nijar (Figs. 3a, 4a; Roep et al., 1998; Krijgsman et al., 2001; Fortuin and Krijgsman, 2003; Braga et al., 2006; Roveri et al., 2009, 2019a; Omodeo-Salé et al., 2012).

The Sorbas Member (see Roep et al., 1998 and Aufgebauer and McCann, 2010 for a more detailed sedimentological description) consists of three overlapping coarsening-upward depositional sequences made of offshore clays and marls passing upward into shelf muds and coastal sandstone bodies. Still unclear is the chemistry of the subaqueous environment during the formation of the Sorbas Member and the provenance of the water fluxes. These shallow-water deposits are conformably replaced upward by the Zorreras Member that comprises alternations of reddish siltstones and sandstones (Fig. 5a) organized in five (or eight) lithological cycles expressing continental environments (Martín-Suárez et al., 2000; Aufgebauer and McCann, 2010). Up to four lenticular white limestone beds bearing brackish Paratethyan-like ostracods (*Cyprideis, Loxocorniculina djafarovi* and freshwater species of the family Limnocytheridae), bivalves and *Chara* oogonia (Roep and Harten, 1979; Aufgebauer and McCann, 2010) are found interrupting the fluviatile sequence (Fig. 5a) and are linked to either episodic flooding by local rivers (Braga et al., 2006; Aufgebauer and McCann, 2010) or episodic Mediterranean ingressions (Fortuin and Krijgsman, 2003; Andreetto et al., 2021). A correct interpretation of the paleodepositional environment of these limestone beds is crucial for the discussion concerning the Mediterranean base-level position during the Lago-Mare phase. In fact, if the Sorbas Basin was relatively shallow during Zorreras deposition (50-100 m; Roveri et al., 2019a, 2020), repeated and sudden Mediterranean incursions would indicate that the Mediterranean Basin was relatively full and that its base level was oscillating, possibly with precessional periodicity (Andreetto et al., 2021). The contact between the Zorreras Mb. and the overlying nearshore Pliocene (<50 m depositional paleodepth; Roveri et al., 2019a) in the Sorbas Basin is conformable and expressed differently around the

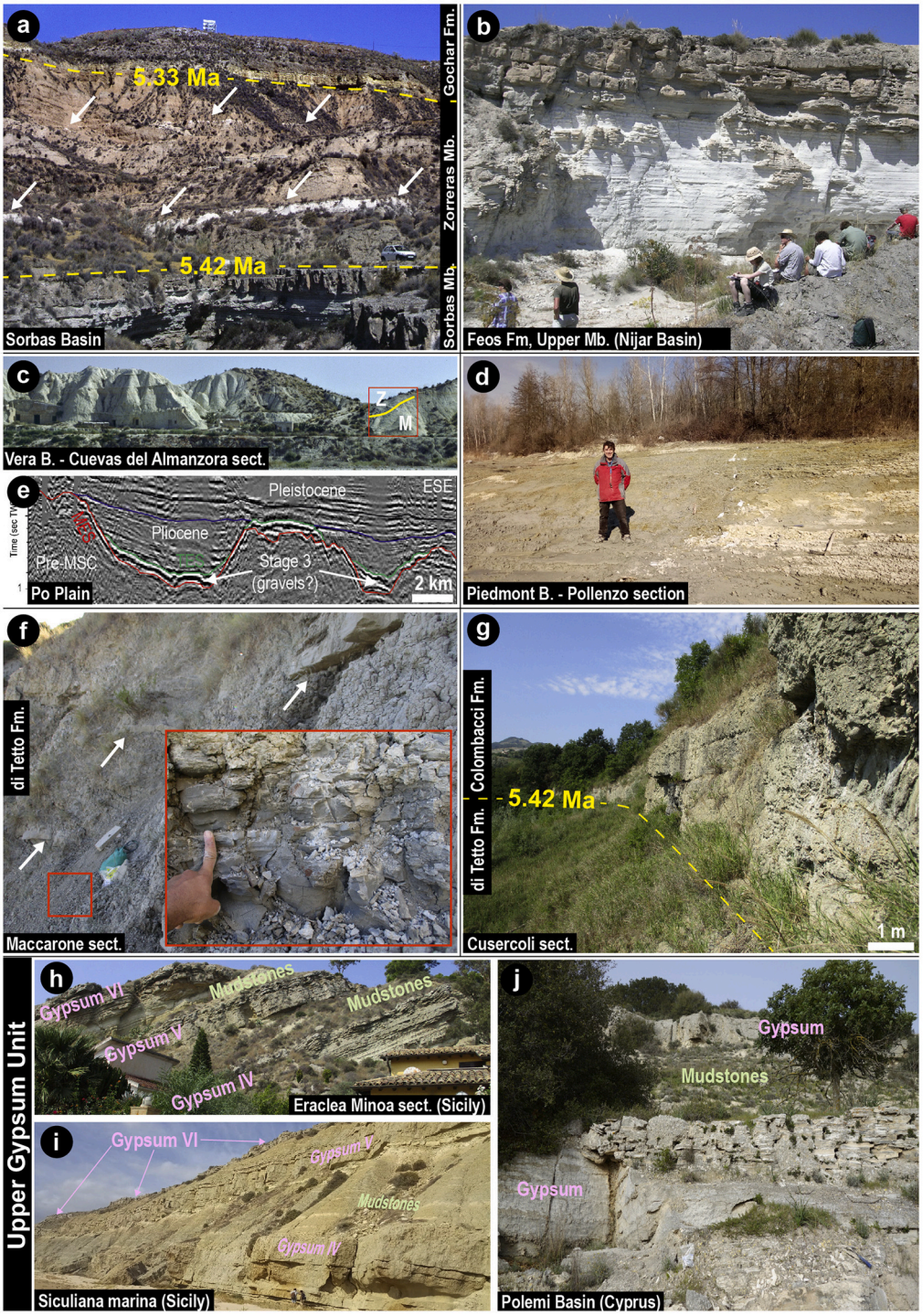

Fig. 5. Sedimentary expression of Stage 3 from selected onshore Mediterranean localities. (a) Photograph from the Sorbas Basin showing the red continental sediments of the Zorreras member with intercalated white limestones (white arrows; from Andreetto et al., 2021). The conformable resting of the Zorreras Mb. above the Sorbas Mb. and underneath the Gochar Fm. of Pliocene age is also appreciable. Car for scale. (b) One typical lithological (and precessional) cycle of the Upper Mb. of the Feos Fm. in the Nijar Basin, here constituted by an ostracod-bearing, white and laminated mudstone bed overlain by an azoic fluvial sandstone (courtesy of Anne Fortuin). (c) Panoramic view of the Cuevas del Almanzora section (from Andreetto et al., 2021). Red rectangle indicates the position of the section straddling the Messinian (M)/Zanclean (Z) transition and studied by Fortuin et al. (1995), Stoica et al. (2016), Caruso et al. (2020) and Andreetto et al. (2021). Buildings for scale. (d) The sub-unit a of the Piedmont Basin composed of azoic grey mudstones grading into yellowish, mammal-rich overbank deposits. (e) WNW-ESE seismic profile in the Po Plain showing incised valleys filled during Stage 3 by suggested clastic deposits and sealed by deep-water turbidites in the Zanclean (modified from Amadori et al., 2018). (f) Typical aspect of the di Tetto/San Donato Formation in the Northern Apennines composed by grey mudstones (detail in the inset) with interbedded sandstone bodies (white arrows). The picture is taken from the Maccarone section. (g) The di Tetto Fm.-Colombacci Fm. transition in the Cusercoli area (Eastern Romagna, Fig. 2b), defined by the facies change underlined by the appearance of a fluvial conglomerate. This lithostratigraphic boundary also corresponds to substage 3.1/3.2 boundary of Roveri et al. (2014a). (h), (i), (l) Lithological cycles of the Upper Gypsum Unit in Eraclea Minoa (h), Siculiana Marina (i) and Polemi (l) sections. Cycles are several m-thick and primarily composed by beds of primary gypsum alternating with mudstones bearing Paratethyan ostracods (at least in Eraclea Minoa).

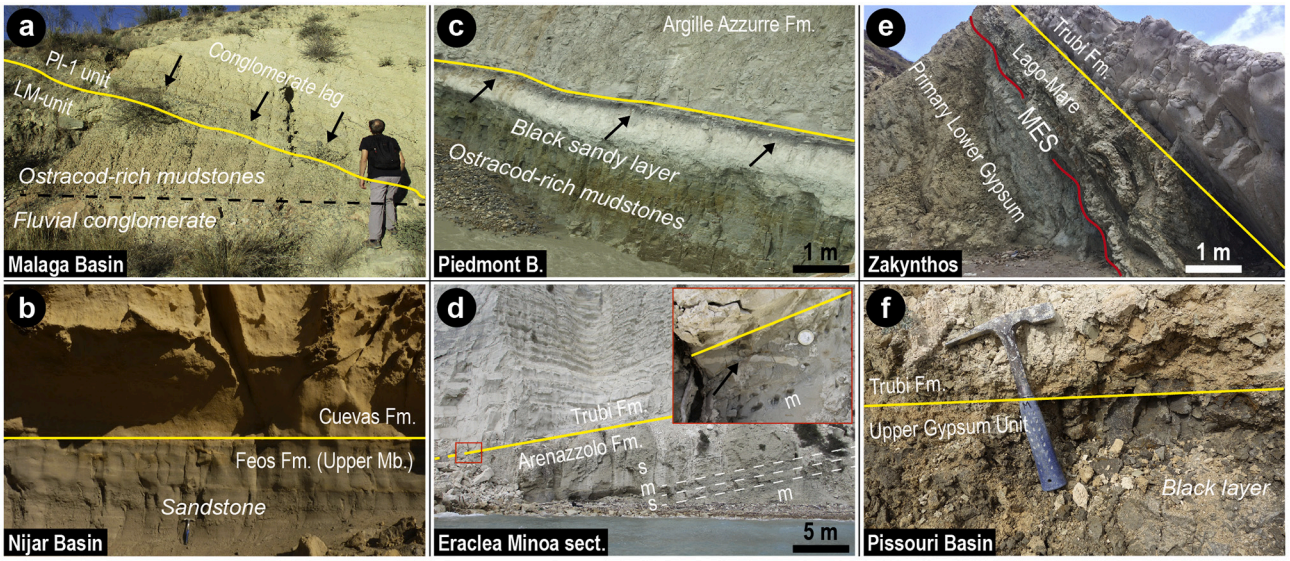

Fig. 6. Photographs of the Miocene/Pliocene boundary (yellow lines) from selected onshore Mediterranean localities. (a) Erosive M/P transition in the Mendelín section (Malaga Basin). Note the conglomeratic lag draping the erosional surface and sharply overlain by foraminifera-rich marls. (b) Conformable stratigraphic contact between the uppermost Messinian sandstone of the Feos Fm. and the Zanclean biocalcarenites of the Cuevas Fm. in the Barranco de los Castellones section, Nijar Basin (hammer for scale; modified from Andreetto et al., 2021). (c) The Messinian/Zanclean boundary in the Pollenzo section (Piedmont Basin) marked by a characteristic black layer interbedded between Paratethyan ostracods-rich mudstones and marine foraminifera-rich marls (modified from Dela Pierre et al., 2016). (d) Uppermost segment of the Eraclea Minoa section (Caltanissetta Basin, Sicily) displaying the (non erosive) contact between the Pliocene Trubi Formation above and the sandy Arenazzolo Formation below. The inset is a close view of the transition, which occurs above a ~50 cm-thick burrowed mudstone horizon rich in Paratethyan ostracods and marine foraminifera. (e) Lago-Mare sediments in the Kalamaki section (Zakynthos) unconformable, through an erosional surface (i.e. the Messinian Erosional Surface, MES), over the PLG unit and also unconformable beneath the Trubi Fm. (modified from Karakitsios et al., 2017b). (f) Close view of the M/P boundary in the Pissouri Basin, where the foraminifera-rich Trubi marls lie above a black layer (paleosol according to Rouchy et al., 2001).

basin, ranging from a bivalves-rich bed overlain by a yellow, fossiliferous calcarenite floored by a gravelly lag deposit (Mather et al., 2001) to a grey marl horizon with marine foraminifera assemblages followed by a second shell-rich bed (Roveri et al., 2019a). Similar to the situation in Malaga, the rare identification of *Ceratolithus acutus* in sediments of the continental Zorreras Mb. led Clauzon et al. (2015) to put forward an alternative chronostratigraphic and paleoenvironmental interpretation for the Sorbas MSC succession, shifting the Zorreras Mb. into the Pliocene (Fig. 4b) and thus associating the presence of brackish Paratethyan-like ostracods with exchanges between the Mediterranean and Paratethys following the Mediterranean re-filling, at high sea level.

In the Nijar Basin (Fig. 2b), the latest Messinian Feos Formation is bracketed at the base and top by an erosional surface along the basin margins and its correlative conformity in the deeper parts (Fig. 3a; Fortuin and Krijgsman, 2003; Aguirre and Sánchez-Almazo, 2004; Omodeo-Salé et al., 2012). The Lower Feos Member consists of azoic, graded and locally slumped siliciclastic-carbonate beds alternating with gypsarenites and gypsiltites and including a laterally continuous Mn-rich bed (Fortuin and Krijgsman, 2003; Omodeo-Salé et al., 2012). In the basin center (e.g. Barranco de los Castellones section; Fig. 3a) the Upper Feos member comprises four complete lithological cycles of m-thick conglomerate to sandstone beds alternating with laminated pelites (Fig. 5b), and one incomplete cycle, which only consists of a sandstone horizon conformably capped by the Pliocene Cuevas Fm. (Fig. 6b; Fortuin and Krijgsman, 2003). A rich fauna of mixed brackish ostracods and marine foraminifera is found in all four pelitic beds (Bassetti et al., 2006). Its origin is questionable. These ostracods were regarded as endemic to the Mediterranean and inhabiting endorheic lakes by Bassetti et al. (2006). However, later they were shown to have been misidentified and were instead considered Paratethys-derived by Stoica et al. (2016; see subsection 5.1). Planktonic and deep-water benthic foraminifera are widely considered reworked by Fortuin and Krijgsman (2003), Bassetti et al. (2006) and Omodeo-Salé et al. (2012), in place by Aguirre and Sánchez-Almazo (2004).

In the Vera Basin (Fig. 2b), in situ gypsum deposits are missing because of widespread erosion or non-deposition and MSC deposits are only represented by ~12 m of laminated varicolored marly clays (Unit 2 Fig. 4a), which are best exposed in the Cuevas del Almanzora section (Fortuin et al., 1995; Fig. 5c). These clays contain a well-preserved and diversified *in situ* fauna of Paratethyan-like ostracod and shallow-water, benthic foraminifera mixed with physically reworked (mostly from the lower Messinian Abad marls) planktic and deep-water benthic foraminifera (Fortuin et al., 1995; Stoica et al., 2016; Caruso et al., 2020). The marly clays are assigned by Stoica et al. (2016) and Caruso et al. (2020) to (roughly) the whole late Messinian Lago-Mare phase (Fig. 4a) based on the ostracod biozonation of Grossi et al. (2011) and are considered to represent either sedimentation in an isolated lake subject to base-level and salinity fluctuations (Caruso et al., 2020) or deposition in a coastal lagoon that was connected to the water mass filling the open Mediterranean (Stoica et al., 2016; Andreetto et al., 2021). Similar to Malaga, these sediments are topped by an erosive surface draped by a conglomeratic accumulation which is overlain by the open marine fauna-rich sediments of the basal Zanclean (Fortuin et al., 1995; Caruso et al., 2020). This erosion feature likely indicates that the Miocene/Pliocene transition followed a base-level lowstand in the Vera Basin.

Stage 3 deposits (Garrucha Fm.) in the easternmost basin of the Betic Cordillera, the Bajo Segura Basin (Fig. 2b), are bounded below and above by two erosional surfaces related to lowered Mediterranean base-levels and discontinuously present due to the widespread fluvial erosion that occurred at the Miocene/Pliocene boundary (Soria et al., 2005, 2008a, 2008b). The Garrucha Fm. shows a maximum thickness of 100 m in its type section (Soria et al., 2007, 2008b). It consists of 20-50 cm thick sandstone bodies interrupting a dominantly marly succession deposited in a subaqueous environment inhabited by *Cyprideis* sp. and

euryhaline, shallow-water benthic foraminifera (*Ammonia beccarii*, *Elphidium granosum*, *Elphidium macellum*, *Haynesina germanica* and *Quinqueloculina laevigata*). Planktic foraminifera are also observed and for a long time were considered to be physically reworked (Soria et al., 2005, 2008b). However, some stratigraphic levels contain dwarf tests of long-ranging taxa such as *Globoturborotalita decoraperta*, *Globigerina bulloides*, and *Neogloboquadrina spp*. which recently have been interpreted as being *in-situ* mostly due to the absence of notable signs of reworking (Corbí and Soria, 2016). Among these dwarf taxa is *Neogloboquadrina acostaensis* (dextral; Corbí and Soria, 2016). Since this group is mainly dextral in the latest Messinian Atlantic successions (e.g. Sierro et al., 1993; Bassetti et al., 2006), this may indicate that Atlantic inflow to the Mediterranean occurred during the late Messinian and the base level of the Mediterranean was high enough to reach the marginal Bajo Segura Basin. The Miocene/Pliocene boundary is, once again, marked by an erosional surface which outlines up to 200 m deep paleovalleys engraved down into the pre-MSC sediments and filled with conglomerates and sandstones of claimed coastal and shallow marine environments (Soria et al., 2005, 2008b; García-García et al., 2011; Corbí et al., 2016).

3.4. Mallorca

Mallorca, which constitutes an emerged segment of the Balearic Promontory (Fig. 2), does not expose the classical MSC evaporite sequence. Instead, two main MSC-related units are found above late Tortonian-Messinian reefal carbonates (Reef Complex Unit) and beneath the Pliocene: the Santanyí limestones and the Ses Olles Formation (Mas and Fornós, 2020 and references therein). The Santanyí limestones are microbialites and oolite-dominated sediments in which a baleen whale neurocranium has been found (Mas et al., 2018a). This unit was interpreted either as a Terminal Carbonate Complex (TCC) laterally equivalent to the Primary Lower Gypsum (PLG) which has been drilled in the deeper parts of the bay of Palma (Mas and Fornós, 2020) or as time-equivalent to the Reef Complex Unit (e.g. Arenas and Pomar, 2010; Suárez-González et al., 2019). The Ses Olles Formation consists of marls, sandy-marls and marly-calcareous lacustrine deposits rich in in-situ freshwater *Chara* spp., brackish water Paratethyan-like mollusks and ostracods and littoral benthic foraminifera (*Elphidium* sp., *Ammonia* sp.).

The upper contact of the Ses Olles Formation with the Pliocene corresponds to an erosional ravinement surface draped by a transgressive lag of coastal deposits usually containing coquinas and/or conglomerates (Mas, 2013, 2015; Mas and Fornós, 2020). The lower contact of the Ses Olles Formation with the Santanyí limestones is sporadically marked by a well-developed reddish paleosol (Mas, 2013, 2015; Mas and Fornós, 2020), which indicates that a (unquantified) period of subaerial exposure occurred before the emplacement of the Ses Olles Fm. However, in their more recent study, Mas and Fornós (2020) surprisingly conclude that the Ses Olles Formation has a conformable contact with the Santanyí limestones, ascribed to part of Stage 1. This led Mas and Fornós (2020) to conclude that the emplacement of the Ses Olles Fm. pre-dated the MSC peak and that the erosional surface marking the Miocene/Pliocene boundary is associated with a 270 kyr hiatus linked to the main MSC base-level drawdown (Fig. 4b). This conclusion is, however, in disagreement with the unconformity at the base of the Ses Olles Fm., which instead points to the deposition of the Ses Olles Fm. (and therefore to the arrival of the Paratethyan fauna in Mallorca) at some point during Stage 3 of Roveri et al. (2014a).

3.5. Piedmont Basin

The Piedmont Basin (NW Italy) contains the northernmost record of the MSC (Fig. 2b). The terminal MSC sediments (i.e. the Cassano Spinola Conglomerates Fm.) overlay pre-MSC units, the PLG deposits (Gessoso Solfifera Fm.) or reworked evaporites (Valle Versa chaotic complex, VVC) and underly the Zanclean marls of the Argille Azzurre Fm. (Dela Pierre et al., 2011).

The Cassano Spinola Conglomerates is splitted in two sub-units by Dela Pierre et al. (2016). Sub-unit *a* consists of azoic grey mudstones turning to yellowish silty mudstones (Fig. 5d) typified by in situ root traces, paleosols and mud cracks and including three/four intercalated lens-shaped, cross-bedded conglomeratic layers (Ghibaudo et al., 1985; Dela Pierre et al., 2011, 2016). Abundant land plant leaves and a diverse terrestrial vertebrate fauna are found in the yellowish siltstones, which have been interpreted as overbank deposits (Harzhauser et al., 2015; Colombero et al., 2017 and references therein). In this continental interval, a low-diversity fish fauna consisting of otoliths of marine and Paratethyan species is found (Grunert et al., 2016; Carnevale et al., 2018; Schwarzhans et al., 2020). These otoliths were Sr-dated to the early-middle Miocene (Grunert et al., 2016). Nevertheless, they were concluded not to be physically reworked, but rather to have been transported by large marine predators, therefore implying a Piedmont Basin-(marine) Mediterranean connection was in force (Grunert et al., 2016; see subsection 5.6). Sub-unit *b* (i.e. Strati a Congeria *sensu*Sturani, 1973) is made of grey mudstones bearing a mixture of in-situ brackish water mollusks (Sturani, 1973; Esu, 2007) and ostracods (Trenkwalder et al., 2008) of Paratethyan affinity along with physically reworked foraminifera and calcareous nannofossils (Trenkwalder et al., 2008; Violanti et al., 2009). The transition to the Pliocene Argille Azzurre Fm. is sharp above a characteristic black and azoic sandy layer (Fig. 6c) rich in terrigenous and intrabasinal (i.e., glaucony and phosphates) grains and disarticulated valves of both brackish-water and continental bivalves, but barren of in-situ fossils (Trenkwalder et al., 2008). The occurrence, at its top and directly below the Argille Azzurre Fm., of abundant *Thalassinoides* trace fossils filled with Pliocene sediments led Trenkwalder et al. (2008) and Dela Pierre et al. (2016) to interpret the top surface of this layer as an omission surface. This surface indicates a period of basin starvation (and therefore a hiatus) due to a sudden increase in water-depth, ascribed by Trenkwalder et al. (2008) to the Zanclean reflooding. This hiatus may have lasted for only part of the late Messinian (Violanti et al., 2009; Dela Pierre et al., 2016) or may have endured into the Pliocene (Trenkwalder et al., 2008).

3.6. Po Plain

To the east, the Messinian sediments in the Piedmont Basin disappear beneath the km-thick Plio-Quaternary succession of the Po Plain-Adriatic Foredeep (PPAF; Fig. 2a). By definition of Ghielmi et al. (2010) and Amadori et al. (2018), the PPAF includes two main elongated depocenters enclosed within the northern Apennines to the South and the Southern Alps to the North: the easternmost portion of the Po Plain and the whole present-day northern Adriatic Sea. Here, for simplicity, we include in the definition of PPAF also its westernmost depocenters of the Western Po Plain Foredeep.

The Messinian-Pleistocene sedimentary sequence, studied through the integration of seismic and borehole observations, is mostly represented by thick sequences of turbidite deposits in the foreland depocenter passing, towards the margins, to fluvial and deltaic systems related to the proximity of the marginal thrust-fold-belts (Cipollari et al., 1999; Ghielmi et al., 2010, 2013; Rossi et al., 2015a; Rossi, 2017). During MSC Stage 1, primary evaporites and dolomicrites were deposited in some shallow-water settings, while evaporitic deposition was inhibited in the deep-water settings, where it was replaced by deposition of anoxic mudstones (Ghielmi et al., 2010). Instead, the post-evaporitic deposits consist of large thicknesses (up to 1 km) and volumes of coarse-grained clastics (LM1 and LM2 of Rossi and Rogledi, 1988; ME3 or Fusignano Fm. of Ghielmi et al., 2010; ME4 of Ghielmi et al., 2013; ME3b and possibly ME3a of Rossi et al., 2015a). Several authors (Ghielmi et al., 2010, 2013; Rossi et al., 2015a; Amadori et al., 2018; Cazzini et al., 2020) showed that these post-evaporitic sediments are the infilling of ca. N-S and NW-SE trending, V-shaped valleys (Fig. 5e). These valleys were carved at least as far as 50 km into the Alps, to a

depth up to 1 km into the pre- and syn-evaporitic Messinian deposits and nicely shape the present-day river network of the southern Alps (Amadori et al., 2018).

Different mechanisms for the incision have been proposed, with major implications for the desiccated vs full Mediterranean controversy (Figs. 1b-c). Ghielmi et al. (2010, 2013), Rossi et al. (2015a), Amadori et al. (2018) and Cazzini et al. (2020) ascribed the valley incision along the PPAF northern margin to fluvial erosion, whose basinward shifting was triggered by the Stage 2 Mediterranean drawdown, estimated to have been around 800-900 m (Ghielmi et al., 2013; Amadori et al., 2018). In this case, Stage 3 deposition in the PPAF occurred in endorheic lakes fed by the Alpine rivers and kept isolated until the Zanclean, when the sudden sea-level rise following the Zanclean reflooding was enough to bypass morphological highs (e.g. Gargano-Pelagosa and/or Otranto paleosills) located in the southern Adriatic foredeep (Fig. 2a; see Pellen et al., 2017; Amadori et al., 2018; Manzi et al., 2020). Conversely, Winterberg et al. (2020) suggested that the over-deepened valleys on the southern slope of the Alps are related to Pleistocene glacial erosion. Although Winterberg et al. (2020) do not address the paleoenvironment during the Messinian, this interpretation does not rule out the possibility that (at least part of) Stage 3 sedimentation occurred in a PPAF connected to the Mediterranean water mass and that no catastrophic reflooding occurred at the Miocene/Pliocene boundary. The conclusion of a non-catastrophic refilling was also drawn by Pellen et al. (2017) on the basis of the onshore Adriatic record (see subsection 3.7).

3.7. Apennine system

The Messinian deposits resurface to the south of the PPAF sector and extensive sections are found in several basins on both the foreland domain (Adriatic side of the partially uplifted Apennine chain), subjected to compressional tectonics during the late Messinian, and the back-arc domain (Tyrrhenian side), contemporaneously affected by extension (Fig. 2b; Cipollari et al., 1999; Schildgen et al., 2014; Cosentino et al., 2018). Overall, the MSC record of the Apennines is subdivided into an evaporitic and post-evaporitic interval squeezed in between two marine units (Messinian Euxinic Shales Fm. at the base and Zanclean Argille Azzurre Fm. atop; Fig. 4a). Different vertical motions related to ongoing Apenninic tectonics resulted in the deposition of Stage 3 sediments with highly variable sedimentary expression and stratigraphic resolution from basin to basin. The post-evaporitic deposits are alternatively found resting unconformably, with an erosional contact associated to an angular unconformity, above the alternations of the Gessoso Solfifera Fm./PLG, or conformably above evaporitic-free cycles lateral equivalent of the marginal PLG (Fig. 4a; e.g. Roveri et al., 1998, 2008a). This led to the conclusion that both shallow and deep-water successions are present in the Apennine foredeep system (Roveri et al., 2001).

The physical-stratigraphic model developed for the post-evaporitic interval in the Romagna area (i.e. Northern Apennines) and applied to the whole Apennine domain was subdivided into two allounits (named p-ev$_1$ and p-ev$_2$) based on a basin-wide shift in facies, overall stacking patterns and depositional trends (i.e. progradational and retrogradational, respectively; Roveri et al., 1998, 2001, 2005, 2008a; Manzi et al., 2005, 2007, 2020). Allounit p-ev$_1$ only accumulated in deep-water settings (e.g. Cusercoli, Sapigno, Maccarone and Trave sections; Roveri et al., 1998; Iaccarino et al., 2008; Cosentino et al., 2013) during the subaerial exposure of the basin margins (e.g. Vena del Gesso Basin, Monticino quarry, Pellen et al., 2017). It starts with resedimented clastic evaporites (i.e. Sapigno Fm.) followed by a coarsening- and shallowing-upward succession (i.e. di Tetto or San Donato Fm.) of mudstones with intercalated turbiditic sandstones (Fig. 5f) and a volcaniclastic marker bed dated initially by ^{40}Ar-^{39}Ar at ~5.5 Ma (Odin et al., 1997) and later by ^{238}U-^{206}Pb at 5.5320±0.0046/0.0074 Ma (Cosentino et al., 2013; Fig. 3a). Allounit p-ev$_2$ (i.e. Colombacci Fm.) occurs in the deeper depocenters in 4/5 sedimentary cycles consisting of three > 5 m-thick coarse-grained bodies (conglomerates and sandstones) and two black-colored mudstone beds alternating with fine-grained mudstones/clays with intercalated three micritic limestones (known in literature as *Colombacci* limestones; Figs. 3a, 5g; Bassetti et al., 2004). By contrast, an incomplete Colombacci Fm. deposited in the shallower thrust-top basins (e.g. Vena del Gesso Basin and Molise sections; Pellen et al., 2017; Cosentino et al., 2018). The p-ev$_2$ cycles have been interpreted as reflecting the alternation of wet (mudstones and Colombacci limestones in Eastern Romagna) and dry (coarse-grained facies and Colombacci limestones in the Maccarone section) phases controlled by Milankovitch-driven climatic factors (Fig. 3a; Roveri et al., 2008a; Cosentino et al., 2013) and, as such, they have been used for the astronomical tuning of the Colombacci Fm. to the Lago-Mare phase (Figs. 3a, 4a; see subsection 2.2). By contrast, Clauzon et al. (2005) and Popescu et al. (2007) moved the Colombacci Fm. into the Pliocene (Fig. 4b). However, this conclusion has been proven to rely on wrong stratigraphic and paleontological arguments (see Roveri et al., 2008c, Grothe et al., 2018 and subsection 5.5). Substage 3.2 records in the Apennines do not always contain the three prominent conglomeratic facies as in Romagna, but only laminated to massive clays with sandy intercalations equivalent to the ones typifying substage 3.1 records (e.g. Maccarone section; Sampalmieri et al., 2010; Cosentino et al., 2013; Fig. 5f). The absence of a lithological cyclicity that clearly mimics an orbital signal largely hampered the astronomical tuning of these clay-dominated sections, although an attempt has been made with the Maccarone section (Cosentino et al., 2013). The only exception is represented by the Fonte dei Pulcini section, which has been equipped with an age framework by astronomical tuning of the magnetic susceptibility record (Cosentino et al., 2012). Despite the lack of outstanding lithological changes these sections are often provided with a lithostratigraphic subdivision using the same nomenclature as in the Romagna area. When applied, the di Tetto Fm.-Colombacci Fm. boundary is placed high in the sections, i.e. few tens of meters underneath the Miocene/Pliocene boundary, resulting in a much different thickness of the formations compared to the Romagna area.

Stage 3 sediments are poorly exposed on the Tyrrhenian Sea onshore side of Italy (Fig. 2b). The best known succession crops out in the Cava Serredi quarry in the Fine Basin (Tuscany; Bossio et al., 1978, 1993; Carnevale et al., 2006b, 2008). Here the MSC has a thickness of ~150 m, of which only the uppermost ~100 m are attributed, without clear arguments, to Stage 3 by Carnevale et al. (2006b). The lowermost ~40 m of the Stage 3 unit consists of mudstone with alternating sandstone bodies which have been attributed to Roveri et al. (1998)'s p-ev$_1$ allounit, while the uppermost ~60 m form the p-ev$_2$ allounit and include two prominent conglomerate bodies alternating with mudstones interbedded with sandstone horizons and black, organic-rich layers (Carnevale et al., 2006b). A few and more fragmented sections are also described on the Tyrrhenian Sea side of Italy by Cipollari et al. (1999).

The Miocene/Pliocene boundary is variably expressed through the Apennine system: unconformable above the ostracod-bearing clays and highlighted by erosional surfaces draped by conglomeratic accumulations (e.g. Stingeti section in Molise; Cosentino et al., 2018), conformable above 0.5-1 m-thick black mudstones similar to how it is observed in Piedmont and of equally unknown paleoenvironmental significance (e.g. Romagna area and Maccarone section; Roveri et al., 1998; Gennari et al., 2008) or conformable above the ostracod-rich mudstones (e.g. Maccarone and Fonte dei Pulcini sections; Cosentino et al., 2005, 2012, 2013; Sampalmieri et al., 2010).

All p-ev$_1$ deposits studied are almost devoid of in-situ biota, except for fish otoliths and three fish skeletons found in the upper substage 3.1 part of Cava Serredi (Carnevale et al., 2006b). The p-ev$_2$/Colombacci deposits, instead, host typical Paratethyan assemblages of brackish-water mollusks, ostracods, dinocysts and fish (Bassetti et al., 2003; Bertini, 2006; Popescu et al., 2007; Grossi et al., 2008; Iaccarino et al., 2008; Cosentino et al., 2012, 2018; Schwarzhans et al., 2020). A diverse array of marine fossils (benthic and planktic foraminifera, calcareous nannofossils, dinocysts and fish otoliths and skeletons) has also been

reported from the horizons containing these Paratethyan taxa (Bertini, 2006; Carnevale et al., 2006a; Popescu et al., 2007; Pellen et al., 2017). While the autochthony of ostracods, when considered, is unquestioned, the allochthonous vs autochthonous character of the other mentioned fossils is disputed and still unclear (see Chapter 5).

3.8. Sicily

The MSC record is widely exposed on Sicily, mainly in the Caltanissetta Basin and in scattered locations on the Hyblean Plateau (i.e. Ragusa-Siracusa area) and the Messina area (Fig. 2b; Butler et al., 1995; Manzi et al., 2009; Sciuto et al., 2018). Like the Northern Apennines, it shows a complex distribution and variable stratigraphy that mirrors the structuring of Sicily into basins with different characters, geometries and depocenters which subsided at different times and rates (Butler et al., 1995; Catalano et al., 2013). This structural setting permitted the simultaneous deposition of shallow and intermediate-water sediments (Roveri et al., 2008b). Mostly found in the Caltanissetta Basin, these intermediate-water successions have for decades been considered the onshore counterpart of the offshore evaporitic trilogy seen in seismic data from the Western Mediterranean Basin (Decima and Wezel, 1973). More recently, Raad et al. (2021) attempted a similar onshore-offshore correlation but with the intermediate Central Mallorca Depression. The currently endorsed stratigraphic model (Fig. 4a), refined over the years by Decima and Wezel (1971, 1973), Decima et al. (1988), Butler et al. (1995), García-Veigas et al. (1995), Rouchy and Caruso (2006), Roveri et al. (2008b) and Manzi et al. (2009), envisages two 'evaporitic cycles'. The 'First cycle', overlying both alluvial and deep-water sediments (Tripoli Fm., Licata Fm. and Terravecchia Fm.; see Maniscalco et al., 2019 and references therein), comprises the disputed Calcare di Base (Manzi et al., 2011, 2016b vs Caruso et al., 2015), PLG or Gessi di Cattolica Fm. (Decima and Wezel, 1973; Lugli et al., 2010) and the Halite Unit (Lugli et al., 1999). The 'Second cycle' comprises the Upper Gypsum (UG) or Gessi di Pasquasia Fm., which is only present in depocenters of the Caltanissetta Basin (see Manzi et al., 2009 for a detailed overview), sporadically overlain by the siliciclastic Arenazzolo Fm. (Decima and Wezel, 1973; Cita and Colombo, 1979). The whole succession is sealed by the Pliocene marine Trubi Fm. (Fig. 4a). The two evaporite cycles are separated by an erosional surface (MES) associated with an angular discordance broadly linked to the main Mediterranean drawdown event (e.g. Butler et al., 1995; Roveri et al., 2008b). Clauzon et al. (1996), however, placed the MES at the Arenazzolo Fm.-Trubi Fm. transition, implying that the entire evaporitic deposition in the Caltanissetta Basin pre-dated the offshore one, but they do not provide evidence of erosion at that level. In more recent publications from the same research group, the MES is shifted towards the base of the Arenazzolo Fm. (e.g. Bache et al., 2012), again without evidence of major erosion, and different ages are assigned (see Fig. 4b and Grothe et al., 2018 for details).

The Upper Gypsum successions are commonly incomplete in many of the Caltanissetta Basin sections (Pasquasia-Capodarso, Casteltermini, Alimena, Nicosia, Siculiana-Marina; Decima and Sprovieri, 1973; Rouchy and Caruso, 2006; Manzi et al., 2009; Fig. 5i). In the most complete section, Eraclea Minoa (Fig. 3a), the Upper Gypsum Unit consists of 6 (Van der Laan et al., 2006) to 7 (Manzi et al., 2009) primary gypsum beds with a repetitive internal organization of facies (see Schreiber, 1997 and Manzi et al., 2009 for facies description) interbedded with marls and lenticular terrigenous sandstone bodies, gypsarenites and gypsrudites (Fig. 5h). Two of the terrigenous sandstone bodies are highlighted by Manzi et al. (2009) in the thick (~60 m), *Cyprideis agrigentina*-rich (Grossi et al., 2015), marly interval dividing gypsum VI and VII for its alleged astronomical significance (Fig. 3a; see subsection 2.2). A mixed (physically reworked) marine (foraminifera and dinocysts) and (*in-situ*) brackish biota (ostracods and dinocysts) of Paratethyan origin characterizes the marly interbeds from at least gypsum III upwards (following the investigations carried on the Eraclea Minoa section; Bonaduce and Sgarrella, 1999; Rouchy and Caruso, 2006; Londeix et al., 2007; Grossi et al., 2015; Fig. 3a). Calcareous nannofossils have been found along with the above organisms in a more northerly location by Maniscalco et al. (2019) and considered reworked. Above the last gypsum, the ~6-7 m-thick Arenazzolo Fm. is found, represented by reddish arkosic cross-laminated and poorly consolidated sand (Bonaduce and Sgarrella, 1999; Roveri et al., 2008b) and interpreted as the expression of a shallow-water delta, albeit without a sedimentological investigation (e.g. Decima and Wezel, 1973; Cita and Colombo, 1979). The whole Stage 3 sequence is conformably overlain by the Zanclean marine Trubi Fm. in the basin center (e.g. at Eraclea Minoa and Capo Rossello; Fig. 6d; Brolsma, 1975; Cita and Colombo, 1979; Van Couvering et al., 2000; Rouchy and Caruso, 2006; Manzi et al., 2009; Fig. 6d) and unconformably in the shallower, marginal areas (Manzi et al., 2009; Roveri et al., 2019b). Only Decima and Wezel (1973) and Raad et al. (2021) report the Miocene/Pliocene transition in the key, intermediate water-representative section of Eraclea Minoa as erosive. However, they do not provide evidence (e.g. photographic documentation) for the presence of an erosional unconformity and, moreover, Raad et al. (2021) erroneously refer to Cita and Colombo (1979), where no erosion is mentioned at the M/P boundary in Eraclea Minoa.

The bathymetric jump between the <100 m of water depth during the late Messinian and the >200 m at the base of the Trubi Fm. is often regarded as a key onshore evidence of the sudden and catastrophic Mediterranean-Atlantic re-connection at the Miocene/Pliocene boundary (e.g. Caruso et al., 2020). However, the real depth of the base of the Trubi is all but obvious. In fact, variable estimates have been proposed based on the observed benthic foraminifera and/or psychrospheric ostracods at Capo Rossello and Eraclea Minoa: 200-500 m (Decima and Wezel, 1973), 600-800 m (Sgarrella et al., 1997, 1999; Barra et al., 1998), 1400-2400 m (Cita and Colombo, 1979).

3.9. Greece

Several MSC localities are reported from the Greek Ionian Islands (Corfu, Cephalonia and Zakynthos) and from Crete (Fig. 2b).

On the NW coast of Corfu (Aghios Stefanos section), the PLG unit is missing and only a 32 m-thick cyclically-arranged terrigenous succession is present comprising three m-thick conglomerate beds alternating with fine-grained deposits rich in unspecified species of brackish water ostracods (Pierre et al., 2006).

In the southern part of Zakynthos, an evaporitic succession composed of eight gypsum cycles (Kalamaki section) occurs above marine marly deposits (Karakitsios et al., 2017b). These gypsum beds were initially ascribed to the UG unit (Pierre et al., 2006) and later to the PLG (Karakitsios et al., 2017b). The gypsum unit is overlain by approximately ~13 m of siltstones and marls with scattered, cm-thick beds of sandstones, conglomerates and carbonates with nodular texture (Pierre et al., 2006; Karakitsios et al., 2017b). Although no ostracods are reported from this interval, due to its stratigraphic position the post-evaporitic unit is correlated to the Lago-Mare phase (Karakitsios et al., 2017b). Except for the rare presence of marine nannofossils (*Ceratolithus acutus* together with *Reticulofenestra zancleana)* just below the Miocene/Pliocene boundary, only reworked marine fauna has been reported from the post-evaporitic package (Karakitsios et al., 2017b). This dominantly terrigenous succession is unconformably overlain by the Zanclean Trubi Formation (Fig. 6e; Karakitsios et al., 2017b).

MSC deposits on Crete (e.g. Meulenkamp et al., 1979; Delrieu et al., 1993; Cosentino et al., 2007; Roveri et al., 2008a; Zachariasse et al., 2008, 2011) were deposited in Miocene extensional, fault-bound basins driven by tectonic subsidence that ceased in the late Pliocene and Pleistocene (Van Hinsbergen and Meulenkamp, 2006). Because of the strong tectonic and eustatic sea-level-related fragmentation of the stratigraphic record, reconstructing the late Miocene stratigraphy of Crete has not been straightforward (Zachariasse et al., 2008, 2011). Several primary and clastic gypsum facies are recognized, but their

correlation with the MSC stratigraphy is disputed (see Cosentino et al., 2007; Roveri et al., 2008a, 2014a; Zachariasse et al., 2008). Coarse-grained, mammal-bearing terrigenous facies irregularly alternating with marls are in places found unconformably overlying the gypsum and separated from the Pliocene facies by an erosion surface (see Meulenkamp et al., 1979; Delrieu et al., 1993; Cosentino et al., 2007). In two localities on the Messarà Plain, Cosentino et al. (2007) described a highly diversified ostracod fauna with Paratethyan affinity in some marly intervals.

Messinian evaporites and/or Lago-Mare deposits are also reported from the North Aegean region onshore in the Strymon Basin (Snel et al., 2006; Suc et al., 2015; Karakitsios et al., 2017a) and Dardanelles region (Melinte-Dobrinescu et al., 2009) and offshore (Prinos-Nestos Basin; Karakitsios et al., 2017a), but recent integrated studies suggested that the sections studied by the above listed authors are older than the MSC (see Krijgsman et al., 2020a, 2020b). In particular, Krijgsman et al. (2020a) proposed that for most, if not all, of the MSC the North Aegean was a brackish water, mostly Paratethyan-fed basin restricted by the Cyclades sill to the south (Fig. 2a) and forming a passageway for Paratethyan overspill waters towards the Mediterranean.

3.10. Cyprus

MSC deposits on Cyprus outcrop in the Pissouri, Psematismenos, Mesaoria and Polemi basins on the southerly fringe of the Troodos massif (Fig. 2b; Rouchy et al., 2001; Manzi et al., 2016a). According to Rouchy et al. (2001) and Orszag-Sperber et al. (2009), sediments belonging to all MSC stages of Roveri et al. (2014a) are preserved in the Cypriot basins. By contrast, Robertson et al. (1995) and Manzi et al. (2016a) considered that PLG evaporites on Cyprus are only present as fragments reworked within a chaotic unit (the Lower Gypsum and Intermediate breccia units of Orszag-Sperber et al., 2009) and that the only *in situ* evaporites belong to the overlying Upper Gypsum Unit, which encompasses the whole of Stage 3 (Figs. 3a, 4a). A continuous, Eraclea Minoa-like section is not known in Cyprus (Manzi et al., 2016a). The best exposure of the lower 60 m of this unit is found in the Polemi Basin (Manzi et al., 2016a). It comprises up to six gypsum beds (the lower three of which are mainly selenitic, while the upper three are predominantly laminated; Fig. 3a). Gypsum beds range in thickness from 1 to 6 m and are separated by laminated marls (Fig. 5j) occasionally interbedded with conglomerates and sandstones (e.g. between the 5th and 6th gypsum layers; Rouchy, 1982; Rouchy et al., 2001; Manzi et al., 2016a). The sixth gypsum bed is reported by Rouchy et al. (2001) to be hollowed in the upper part with the cavities filled with overlying sediments. The similarity of the cyclicity and facies association of this Cyprus succession with the substage 3.1 interval of the Sicilian UG led Manzi et al. (2016a) to propose a bed-to-bed correlation and to recognize the substage 3.1/3.2 boundary at the top of the last gypsum bed (Fig. 3a). According to Orszag-Sperber et al. (2000) and Rouchy et al. (2001), this chronostratigraphic boundary coincides with a Mediterranean-scale sea-level drop, a conclusion that arises from the interpretation of the cavities in the uppermost gypsum as the product of karstic dissolution following a prolonged period of subaerial exposure.

The sedimentary sequence overlying the last gypsum bed and assigned by Manzi et al. (2016a) to the Lago-Mare phase lacks a clear and rhythmic sedimentary cyclicity. In the Pissouri Basin this interval (up to 25-30 m-thick) mostly consists of conglomerates, sandstones, limestones, paleosols (which appear as dm to m-thick dark marly horizons, in one case with pulmonated gastropods) and subordinated clay-marly horizons (Rouchy et al., 2001). By contrast, in the Polemi sections the clay-marly facies dominates this interval (Rouchy et al., 2001). *In situ* fresh-brackish water species of articulated mollusks (*Limnocardiidae*, *Melanopsis*), Paratethyan (*Loxocorniculina djafarovi*, *Euxynocythere praebaquana*) and Mediterranean (*Cyprideis agrigentina*) ostracods and foraminifera (*Ammonia beccarii*), *Characeae*, abundant fragments of the marine euryhaline fish *Clupeidae* and a fish skeleton of the euryhaline *Aphanius crassicaudus* are described from some of the substage 3.1 and 3.2 fine-grained facies and within the terrigenous laminae of some *balatino* gypsum (Orszag-Sperber et al., 2000; Rouchy et al., 2001; Orszag-Sperber, 2006; Manzi et al., 2016a). The upward change in diversity of the ostracod fauna seen elsewhere (e.g. Malaga, Nijar, Vera, Apennines and Eraclea Minoa) is not reported in Cyprus but this may be because no detailed study of ostracod assemblages in Stage 3 sediments has been published. The Miocene/Pliocene boundary, near Polemi village is described by Manzi et al. (2016a) as a sharp contact above a dark, organic-rich layer (Fig. 6f). It appears to be similar to the boundary reported from Piedmont (Fig. 6c; Trenkwalder et al., 2008; Dela Pierre et al., 2016) and Northern Apennines (Gennari et al., 2008; Grossi et al., 2008), if not for the presence, in Cyprus, of (possibly) in-situ *Cyprideis agrigentina* (Manzi et al., 2016a). A layer with the same field appearance, thickness (~ 1 m) and stratigraphic position is reported in Pissouri by Rouchy et al. (2001), which they interpreted as a paleosol based on mottling, oxidized roots, carbonate concretions and plant fragments.

3.11. Southern Turkey

The tectonically active, during the Miocene, thrust-top basin of Adana in southern Turkey (Radeff et al., 2017) retains the most complete and better exposed easternmost successions of the MSC (Fig. 2b), whose deposits were attributed to the Handere Fm. (Cosentino et al., 2010; Radeff et al., 2016).

MSC Stage 3 finds expression in a >1 km thick continental unit unconformable, through an erosional surface, above the pre-evaporitic, Stage 1 anhydrite-shale alternations (Radeff et al., 2016) and resedimented gypsum-bearing Stage 2 deposits (Cosentino et al., 2010; Cipollari et al., 2013). This unit mainly consists of fluvial coarse- and fine-grained deposits representing channel fill and overbank deposits. Sporadically, some fine-grained intercalations are found containing a mixed brackish (ostracod) and marine (foraminifera and calcareous nannofossils) fauna. The ostracod fauna has affinity with the Paratethyan fauna but, unlike to many other Mediterranean onshore localities, is poorly diversified, with monospecific assemblages of *Cyprideis agrigentina* (Avadan section and T-191 borehole; Cipollari et al., 2013) or with *Cyprideis agrigentina* accompanied by rare to abundant specimens of *Loxoconcha muelleri*, *Euxinocyhere* (*Maeotocythere*) *praebaquana*, and *Loxoconcha* sp. (Adana section; Faranda et al., 2013). Ostracods are often associated with *Ammonia beccarii* and rare *Elphidium* and *Cribroelphidium*, which are the only foraminifera considered as autochthonous. Conversely, the entire nannoflora is interpreted as physically reworked (Cipollari et al., 2013; Faranda et al., 2013).

The Handere Fm. is followed by early Zanclean marine sediments (Avadan Fm.) deposited, according to the paleoecology of the benthic foraminifera species recognized, at bathymetries ranging from 200 to 500 m (Cipollari et al., 2013). The lithological nature of the Miocene/Pliocene boundary in the Adana Basin is not clear, but it occurs either above the continental or subaqueous, ostracod-bearing facies.

A similar stratigraphic sequence is present in the subsurface. Here, however, chaotic gypsum-bearing deposits are not found and two halite bodies ~20 and ~170 m-thick are present, separated and followed by fluvial gravels, sands and silts (Cipollari et al., 2013).

3.12. Summary of the onshore Stage 3 record

Most of the onshore Stage 3 records formed in shallow marginal Mediterranean basins, which underwent substantial uplift from the Messinian till nowadays and are assumed to have had their depocenter at ~200 to 50 m below the Atlantic level during the late Messinian (Roveri et al., 2014a, 2019a; Radeff et al., 2016, 2017). The Caltanissetta Basin (Sicily), some basins along the Apennines and (possibly) Cyprus represent, instead, possible onshore representative of intermediate basins. The nature and duration of these records is quite variable,

and there are only six sections that may record an entire Stage 3 sequence (i.e. Sorbas, Nijar, Northern Apennines, Eraclea Minoa and Cyprus; Fig. 3a). Reasons for the fragmentary nature of the Stage 3 sedimentary record include different durations of subaerial exposure following the Stage 2 drawdown, local tectonics and associated syn-depositional erosion and deposition. One of the consequences of this is that any sedimentary cyclicity that resulted from orbital fluctuations is typically either less well developed or poorly preserved, making the chronology of Stage 3 rather uncertain or controversial in places.

Despite this variability, several fairly consistent characteristics are widely expressed. These are:

1) Stage 3 sedimentation follows a period of intensive tectonic and/or eustatic-driven erosion of the margins, as demonstrated by the frequent presence of erosional unconformities and/or chaotic Stage 2 deposits (RLG unit);
2) Stage 3 lithologies are mostly terrigenous (conglomerates, sandstones and mudstones) and deposited in a variety of continental (fan delta, fluvial channels and alluvial plains) and shallow water environments (endorheic lakes or water bodies connected with the Mediterranean water mass is the riddle). Carbonate intercalations are sometimes present (e.g. Sorbas Basin and *Colombacci* limestones in the Apennines). Stage 3 gypsum is only found in deeper-water intermediate basins of Caltanissetta in Sicily and Cyprus.
3) A diversified fossil assemblage with Paratethyan affiliation (ostracods, dinocysts, mollusks) is commonly found in the shallow-water sediments of Lago-Mare successions. Only in the intermediate Caltanissetta Basin (Sicily) do these diversified Paratethyan forms (only ostracods) occur earlier, in the sediments from substage 3.1. Where these have been studied in detail, these assemblages typically show an increase in diversity with time (possibly every wet phase of the precession cycles). Some of these sediments also contain marine fossils and there is controversy over whether these are *in situ* and contemporaneous or reworked.
4) In outcrop, the Miocene/Pliocene boundary has four main sedimentary expressions: erosive and followed by a conglomeratic lag (e.g. Malaga, Vera, Mallorca; Fig. 6a); conformable above continental facies (e.g. Nijar Basin; Fig. 6b); conformable above ostracod-rich mudstones (e.g. Eraclea Minoa; Fig. 6d); sharp contact above a black layer of still largely unknown paleoenvironmental significance (Piedmont, Apennines and Cyprus; Fig. 6c, f).

For a better understanding of how Stage 3 developed across the Mediterranean these marginal records now need to be considered alongside the evidence from intermediate to deep offshore settings.

We note that alternative chronostratigraphic frameworks have been proposed for several onshore (Malaga, Sorbas, Mallorca, Apennines, Sicily) and offshore (Sites 134B, 976B, 978A) locations (see Fig. 4b for references), but we have omitted them as they are shown to rely on incorrect (bio)stratigraphic arguments (see Roveri et al., 2008c, Grothe et al., 2018 and subsection 5.5).

4. Offshore domain

The offshore Mediterranean is a complex array of variable-depth and morphologically complex subbasins framed by morphological highs or sills. Traditionally it is divided into two main domains (Fig. 2a), the Western and Eastern Mediterranean, with the intervening divide (or Sicily sill) situated in the Sicily channel at present with a maximum depth of 316 m. The Alborán Basin, the depressions on the Balearic Promontory, the Corsica, Valencia, Algero-Balearic, Liguro (or Sardo)-Provençal and Tyrrhenian basins belong to the "Western Mediterranean" (Fig. 2a). The Adriatic foredeep, the Ionian, Sirte, Aegean and Levant basins belong in the "Eastern Mediterranean" (Fig. 2a). Smaller-sized depressions, again surrounded by sills of variable depth, are identified and labelled within each of these subbasins.

Although the exact topography and hypsometry of the Messinian Mediterranean is difficult to reconstruct, this present-day geography is generally assumed to have been in place, with five main differences: (1) the Alborán Basin was split into a Western (WAB) and Eastern Alborán (EAB) by a volcanic arc (Booth-Rea et al., 2018); (2) the Tyrrhenian Basin was only partly opened (Lymer et al., 2018); (3) the precise depth and width of the ancient Sicily Sill are difficult to estimate, but may have been much deeper than today (~300 m; Meijer and Krijgsman, 2005Jolivet et al., 2006). Paleodepth estimations for the Messinian configuration range from 380 m (Just et al., 2011) to 430 m (Garcia-Castellanos et al., 2009); (4) one or two sills were present at the southern termination of the Adriatic foredeep (Pellen et al., 2017; Amadori et al., 2018; Manzi et al., 2020); (5) the North Aegean was partially isolated from the Mediterranean by the Cyclades Sill and with high Paratethys affinity (Krijgsman et al., 2020a). Following the schematic classification of the Messinian sub-basins by Roveri et al. (2014a), all these subbasins are regarded as either intermediate (i.e. relatively deep-water, 200–1000 m) or deep (water depth > 1000 m).

Compared with the onshore domain, the offshore basins hold a far greater percentage of the total volume of MSC sediments (Ryan, 1973; Haq et al., 2020). The architecture, geometry and main lithologies of the MSC and younger deposits are well known thanks to the high density of seismic data and the fact that evaporites (halite particularly) are easily identified on seismic profiles due to their unusual seismic properties, especially compared to those of terrigenous and carbonate sediments (see Lofi et al., 2011a, 2011b; Lofi, 2018; Haq et al., 2020). However, the detailed lithological, sedimentological, paleontological and geochemical nature and their chronostratigraphy are still poorly constrained offshore because these cannot be univocally defined on the basis of seismic data alone (Roveri et al., 2019b) and direct information about these deep MSC successions is limited to a small number of cores (16) drilled during the DSDP (Ryan et al., 1973; Hsü et al., 1978b) and ODP (Kastens et al., 1987; Comas et al., 1996; Emeis et al., 1996) drilling campaigns that penetrated exclusively the uppermost tens of meters of the deep MSC suite in very scattered localities (Fig. 2b). Only recently, access to industrial boreholes crossing the base of the halite in the deep Levant Basin has been granted, providing a rare glimpse of the deep MSC deposits in the easternmost part of the Mediterranean (Gvirtzman et al., 2017; Manzi et al., 2018; Meilijson et al., 2018, 2019).

The MSC is commonly described as tripartite ('Messinian trilogy' after Montadert et al., 1978) in the Western Mediterranean (Lower-Mobile-Upper units: LU-MU-UU, respectively). However, in the Ionian Basin is described as bipartite (MU-UU) by Camerlenghi et al. (2019) while according to Lofi et al. (2011a), Gvirtzman et al. (2013, 2017), Lofi (2018) and Camerlenghi et al. (2019), the Levant Basin consists of the MU and the UU is only present locally and possibly represented by evaporite-free terrigenous accumulations (Kartveit et al., 2019; Madof et al., 2019). The lack of many age constraints within the offshore MSC successions hampers unambiguous correlation with onshore sequences (Fig. 1a; Roveri et al., 2014a). Nevertheless, different authors have proposed onshore-offshore correlation of specific events (e.g. onset, Ochoa et al., 2015; and termination of the MSC, Biscaye et al., 1972, Iaccarino et al., 1999) and stratigraphic schemes (Decima and Wezel, 1971; Raad et al., 2021) based on and biostratigraphic evidence (Cosentino et al., 2006), $^{87}Sr/^{86}Sr$ isotope ratios (Roveri et al., 2014b; Gvirtzman et al., 2017; Manzi et al., 2018) and astronomical tuning of the deep seismic record (Ochoa et al., 2015, 2018; Manzi et al., 2018; Meilijson et al., 2018, 2019). Here we focus on the seismic and

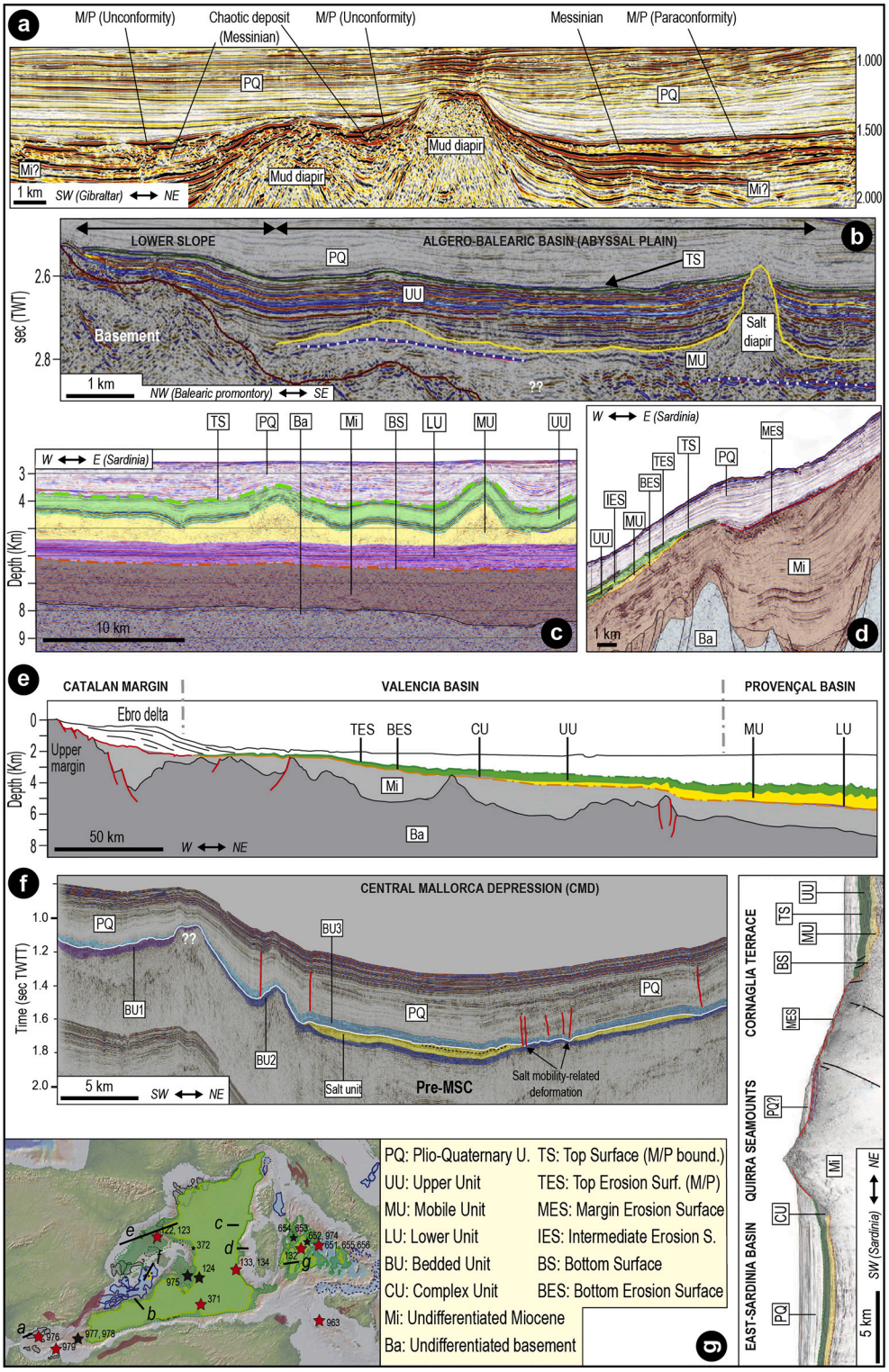

Fig. 7. Seismic profiles from intermediate-deep Western Mediterranean basins containing MSC markers/units. (a) Seismic reflection line CAB01-104 from the WAB (modified from Booth-Rea et al., 2018). The line shows the variable geometry of the inferred M/P boundary, erosive in proximity of mud diapirs, (para)conformable in tectonically undisturbed sectors. Chaotic reflectors are occasionally imaged below the inferred M/P boundary. (b) Seismic profile SF12-09 imaging the lower slope of the south Algero-Balearic margin and part of the Algero-Balearic abyssal plain (modified from Mocnik et al., 2014). Here a high reflecting and horizontally stratified UU covers a thin layer of MU evidenced by salt diapirism. Note the concordant deformation of the UU and MU. (c) Line MS-39 from the abyssal plain of the Liguro-Provençal Basin showing the Messinian trilogy and non-erosive bottom and top surfaces (BS and TS; Dal Cin et al., 2016). Halokinesis of MU gives rise to domes that deform the UU and PQ units. (d) Interpreted seismic profile from the lower-middle slope of the west Sardinian margin (modified from Dal Cin et al., 2016). Thin MU and UU are present on the lower slope, while on the middle slope (and upper slope here not shown) they converge in the margin erosion surface MES. (e) Line drawing of seismic line imaging from the Catalan margin (or Ebro Basin) to the abyss of the Liguro-Provençal basin (modified from Maillard et al., 2011b). Note the pinch out of the MU in the Valencia Basin and of the UU in the Ebro Basin, which is MSC free. (f) Interpreted seismic profile Simbad 15 crossing the depocenter of the CMD showing all the MSC units and erosional surfaces (modified from Raad et al., 2021). (g) Interpreted seismic profile MYS40 illustrating the MU-UU-PQ units in the East-Sardinia Basin and Cornaglia Terrace, separated by the MSC deposits-free Quirra Seamounts (modified from Lymer et al., 2018).

geological (core-derived)[1] properties of the Upper Unit (and laterally grading/interfingering sediments when present), stratigraphically below the Plio-Quaternary deposits (PQ) suggesting that it belongs to (at least part of) Stage 3.

4.1. Western Alborán Basin and westernmost East Alborán Basin

The Alborán Basin has received particular attention because of its proximity to the Gibraltar Corridor (Estrada et al., 2011; Popescu et al., 2015 and references therein). Evaporites only occur on the eastern side of the EAB (which is treated in subsection 4.2; Fig. 2a). To the west of the volcanic archipelago (Booth-Rea et al., 2018, i.e. the WAB) and immediately to the east on the western side of the EAB only terrigenous sediments occur in the MSC interval (Booth-Rea et al., 2018; de la Peña et al., 2020). Sediments at the Miocene/Pliocene boundary appear in the seismic reflection data as parallel reflectors with increasing reflectivity (Comas et al., 1996, 1999; Booth-Rea et al., 2018). Locally, just below the M discontinuity, some of the reflectors suggest a chaotic seismic facies (Fig. 7a; Booth-Rea et al., 2018; Bulian et al., 2021). Miocene sediments with a maximum thickness of 100 m have been recovered from two out of nine holes drilled in the region (ODP 976B, 978A; Comas et al., 1996, 1999). These sediments mostly consist of claystones, siltstones and sandstones with *Chondrites* and *Zoophycos* ichnofacies at site 976B and include a conglomerate close to the Miocene/Pliocene boundary at Site 978A. The lack of age-diagnostic fossils hampers their correlation with the Geologic Time Scale (GTS). However, the presence, high in the Miocene section, of an oligotypic association of ostracods (*Candona* sp., *Loxoconcha muelleri*, and *Cyprideis* sp.) with different stages of growth (Site 978A; Iaccarino and Bossio, 1999) and Paratethyan dinocysts (including *Galeacysta etrusca*; see subsection 5.2; Popescu et al., 2015) indicates a latest Messinian (substage 3.2) age and brackish paleodepositional conditions. Foraminifera and nannofossils are also present, but all species recognized are of no help in narrowing down the paleoenvironmental interpretation because they are considered either definitely or likely to be reworked (Iaccarino and Bossio, 1999). By contrast, Popescu et al. (2015) interpreted some species of calcareous nannofossils (*Reticulofenestra pseudoumbilicus*, *Discoaster quinqueramus*, *Ceratolithus acutus*, *Triquetrorhabdulus rugosus*, *Amaurolithus primus*) and marine dinocysts as autochthonous.

The nature of the Miocene/Pliocene boundary is also uncertain. According to some authors, the "M" discontinuity is a high-amplitude reflector with evidence of erosion attributed to subaerial processes (Estrada et al., 2011; Urgeles et al., 2011) and locally (e.g. close to Site 121; Ryan et al., 1973) associated with an angular unconformity that abruptly truncates the upper Miocene deposits and morphological highs (Comas et al., 1999; Estrada et al., 2011; Garcia-Castellanos et al., 2020). Although the M-reflector was drilled at Sites 976B, 977A and 978A, a lithological contact was only recovered at Site 976B coinciding with a major erosional surface between the early Messinian and the base of the Pliocene (Bulian et al., 2021). Only at Site 978A (and possibly 977A) was a few meters of what may be the contact interval recovered (Comas et al., 1996). This comprises a 25 m-thick cemented succession containing pebbles of volcanic and sedimentary rocks likely to derive from the Alborán substrate (46R, 620.9-630.67 mbsf, between the Pliocene-bearing core 45R and the Messinian-bearing core 47R; Comas et al., 1996). In contrast, Booth-Rea et al. (2018) concluded that the M-reflector is an unconformity only close to the mud diapirs and owes its erosive shape and angular discordance to the activity of these structures (Fig. 7a). In more undisturbed sectors these authors argue that the boundary is a paraconformity with no evidence of erosion (Fig. 7a). The lack of Messinian erosion in the shallow regions of the WAB margins has prompted the hypothesis that this area did not desiccate during the MSC (Booth-Rea et al., 2018; de la Peña et al., 2020). This contradicts much of the interpretation made of the DSDP and ODP cores of this interval in the Alborán Sea. The succession recovered by drilling from beneath the Pliocene comprises gravels that contain a mixed Miocene fauna. These sediments and their faunal content are thought to have been reworked from older sediments exposed as Alborán substrate with no evidence of an extensive wet Lago Mare interval immediately before the Zanclean (Comas et al., 1996).

Two W-E-aligned erosional channels straddling the Strait of Gibraltar and stretching for 390 km from the easternmost Gulf of Cádiz (Atlantic Ocean) into the Alborán Basin are clearly observed in seismic profiles (Garcia-Castellanos et al., 2009; Estrada et al., 2011). There is disagreement, however, concerning the timing and nature of their formation. These incisions are classically considered to occur at the very top of the MSC suite (when present) and to be the consequence of the Zanclean megaflood (Garcia-Castellanos et al., 2009, 2020; Estrada et al., 2011 among others). More recently, Krijgsman et al. (2018) highlighted that an accurate age determination for these channel incisions is lacking and that they might have been formed earlier during the MSC as a result of the Mediterranean-Atlantic gateway currents. Interpretation of E-W seismic profiles across the Alborán Basin combined with mammal records in Africa and Iberia led Booth-Rea et al. (2018) to suggest the existence of an emergent volcanic archipelago that temporarily connected southeastern Iberia with northern Africa, separating an open marine, Atlantic-influenced West Alborán Basin realm from a restricted, hydrologically complex Mediterranean realm to the east.

4.2. Eastern Alborán, Algero-Balearic and Liguro-Provençal basins

From the eastern margin of the EAB as far east as the Tyrrhenian coast of Italy, the Messinian (evaporites-bearing) trilogy LU-MU-UU is found and sealed by the PQ. The MU and UU are interpreted to fill the deepest depocenters (Algero-Balearic, Valencia and Liguro-Provençal basins; with minor interruptions due to seamounts) and the lower slope domain, where they comprise ~500 to ~800 m of UU and ~1000 m of MU/halite (Figs. 7b-d; Camerlenghi et al., 2009; Lofi et al., 2011a, 2011b; Geletti et al., 2014; Mocnik et al., 2014; Dal Cin et al., 2016; Lofi, 2018). Upslope, a thinner, possibly incomplete UU is locally described on the middle-upper continental slopes of Western Corsica (Guennoc et al., 2011) and Sardinia (Mocnik et al., 2014; Dal Cin et al., 2016) and the northern (Maillard et al., 2006) and southern (Maillard and Maufret, 2013; Mocnik et al., 2014; Dal Cin et al., 2016) flanks of the Balearic Promontory, even though the structural settings of these locations are mostly dominated by erosion (Fig. 7d). MSC evaporites are absent on the continental shelves bordering the deep Algero-Balearic and Liguro-Provençal basins, where the PQ directly overlies the MES which, in turn, cuts through the middle Miocene deposits (Gorini et al., 2005; Lofi et al., 2005). The only late Messinian sediments are present as Complex Units (Gulf of Lion, Bessis, 1986; Gorini et al., 2005; Lofi et al., 2005; Algerian Basin, Medaouri et al., 2014; Arab et al., 2016; Fig. 7e). CUs can have various origin (Lofi et al., 2011a, 2011b), but when identified at the outlet of drainage systems, they are commonly interpreted as Messinian clastics supplied by rivers (Lofi et al., 2005). In the Gulf of Lion, the MES is a high angle unconformity with substantial erosion along highly rugged relief thought to have been generated by fluvial incision (Lofi et al., 2005). In contrast, Roveri et al. (2014c) suggested that the drainage networks visible on the seismic could be of subaqueous origin.

When not involved in MU-related deformation processes, the UU appears as a highly reflective series of flat reflectors alternating with less reflective, but concordant, reflectors (Figs. 7b-c; Lofi et al., 2011a, 2011b) aggrading in the basin center and onlapping the margins

[1] Lithostratigraphic and biostratigraphic information from DSDP and ODP cores are primarily extracted from the Scientific Shipboard Party documents, accessible from https://www.marum.de/en/Research/Cores-at-BCR.html. These documents are referenced in the text as follows: Ryan et al. (1973): DSDP 120-134; Hsü et al. (1978b): DSDP 371-378; Kastens et al. (1987): ODP 650-656; Comas et al. (1996): ODP 974-979; Emeis et al. (1996): ODP 963-973.

(Fig. 7b; Camerlenghi et al., 2009; Lofi et al., 2011a, 2011b; Geletti et al., 2014; Mocnik et al., 2014; Dal Cin et al., 2016). The aggrading nature, shelf-ward thinning and the onlap terminations of the UU are interpreted as evidence of sedimentation in a lake with fluctuating base level (e.g. Lofi et al., 2005; Lofi et al., 2011a). In the abyssal plains (Figs. 2a, 7c), nine to ten cycles have been interpreted on high resolution seismic profiles as corresponding to gypsum-marl alternations (Geletti et al., 2014; Mocnik et al., 2014). At Sites 124 and 372, ~40-50 m of the UU have been drilled at the feet of the east Menorca continental rise and the northern Menorca slope, where 3-4 gypsum-marl cycles are recognized (Fig. 2b; Ryan et al., 1973; Hsü et al., 1978a). Primary gypsum facies are widely overprinted by post-depositional diagenetic processes, but the still recognizable laminated and clastic primary textures indicate precipitation at the water-air interface and emplacement by gravity flows, respectively (Lugli et al., 2015). The marl interbeds are made from stiff to firm dolomitic mud containing substantial quantities of detrital material intercalated with current-bedded sandstones and, at Site 124, with diatomites (Ryan et al., 1973). *Cyprideis* sp. specimens are reported from some mudstone interbeds at Site 372, while dwarf planktonic foraminifera are present just below the Miocene/Pliocene boundary at Site 124 (Ryan et al., 1973).

The Miocene/Pliocene boundary coincides with the top of the UU where present (labelled TES when erosional and TS when conformable; Lofi et al., 2011a, 2011b). In the abyssal plain-lower slope domain it appears to be undulating, although this geometry is related to the deformation of the underlying salt (Figs. 7b-c), and it actually corresponds to a sharp surface lacking signs of erosion (Lofi et al., 2011a, 2011b; Geletti et al., 2014; Mocnik et al., 2014). By contrast, the UU-PQ boundary commonly appears strongly erosional in the middle-upper slope and shelf domain, where it coincides with the MES (Fig. 7d; Lofi et al., 2005; Maillard et al., 2006; Geletti et al., 2014; Mocnik et al., 2014). Among the six DSDP-ODP Sites drilled in this region (Fig. 2b), only Hole 975B recovered the Miocene/Pliocene boundary (Iaccarino and Bossio, 1999; Marsaglia and Tribble, 1999). Here the Messinian is a few centimeters thick and consists of banded micritic silty clays with minor calcareous siltstones to sandstones typified by a diverse faunal assemblage consisting of dwarf planktonic foraminifera, *Ammonia tepida* tests and brackish Paratethyan ostracods (*Loxocorniculina djafarovi*, *Euxinocythere praebaquana*, *Amnicythere idonea*, *Leptocythere limbate*, *Candona* sp., and *Cyprideis* sp.; Iaccarino and Bossio, 1999).

Halite is present at the bottom of Hole 134 drilled within the UU (Ryan et al., 1973; Sage et al., 2005; Lugli et al., 2015). High-resolution seismic profiles from both the Algero-Balearic and Ligurian-Provençal basins confirm the presence of a halite layer high in the UU sequence (Geletti et al., 2014; Mocnik et al., 2014). This layer is up to 50 m thick (Dal Cin et al., 2016) and is correlated with an erosional surface (called IES: Intermediate Erosional Surface by Lofi et al., 2011a, 2011b) associated with an angular unconformity which is better developed on the lower slope (Fig. 7d). Geletti et al. (2014) and Mocnik et al. (2014) interpreted this layer as autochtonous and indicative of at least one important sea level drop during UU deposition. However, this intra UU halite layer is always described from areas strongly affected by salt diapirism (just like in the Ionian Abyssal Plain; see subsection 4.6.1) and is never found in adjacent, undisturbed areas (see Camerlenghi et al., 2009; Geletti et al., 2014; Mocnik et al., 2014; Dal Cin et al., 2016), two features that may suggest it has an allochthonous origin.

Site 134 shows evidence of a “desiccation crack" cutting through a sandy silt layer interbedded with unaffected laminated halite (Hsü et al., 1973c). Unfortunately, the core photograph of this crack has been published in two different orientations (Hsü et al., 1973a, 1973b), leading both Hardie and Lowenstein (2004) and Lugli et al. (2015) to question the evidence for subaerial desiccation. Because of these ambiguities, we suggest to dismiss this example from the book of evidence.

4.3. Valencia Basin

The Valencia Basin (VB; Fig. 2a) is an aborted rift formed during the late Oligocene-early Miocene opening of the back-arc Liguro-Provençal Basin (e.g. Jolivet et al., 2006). It is located between the Spanish Ebro Margin to the west and the Balearic Promontory to the east, while it grades into the Liguro-Provençal Basin to the E/NE (Fig. 7e; Maillard and Mauffret, 2006; Maillard et al., 2006).

Numerous exploratory boreholes exist on the western Ebro margin. These boreholes, tied to seismic data, confirm that MSC-related sediments on the northwestern shelf are missing (Fig. 7e; Urgeles et al., 2011; Pellen et al., 2019). The only MSC feature present is a prominent erosional surface (the MES) incising Serravallian-early Messinian sediments (Urgeles et al., 2011). By contrast, on the southwestern and southern part of the margin, well data show the presence of evaporitic sediments (e.g. Delta L and Golfo de Valencia D1 boreholes; Del Olmo, 2011; Del Olmo and Martín, 2016; Lozano, 2016). Del Olmo and Martín (2016) described these evaporites as primary selenites and ascribed them to MSC Stage 1 (their unit M7). Lozano (2016) described the same evaporitic deposits in the same boreholes as ‘white anhydrites’, leaving open the question as to whether the anhydrite is primary (sabhka’s) or secondary at the expense of a primary gypsum facies. On the eastern margin of the VB boreholes and seismic studies suggest there are no MSC units with only a prominent MES cutting pre-MSC sediments (Driussi et al., 2015; Raad et al., 2021). All authors conclude that the shelves of VB were exposed to subaerial erosion during and following the main drawdown.

MSC deposits are also absent along the slopes and, where present, consist of coarse- and fine-grained terrigenous facies filling valleys largely related to fluvial incision (Fig. 7e; Stampfli and Höcker, 1989).

A different situation features in the depocenter. Despite its present-day depth of > 2000 m, no MU is observed in the depocenter, as the salt pinches-out at the edge of the deeper Provençal Basin (Fig. 7e). Only the seismic properties of UU suggest that it is roughly continuous from the Provençal Basin into the VB (Fig. 7e; see subsection 4.2), although it thins from ~1000 m to < 500 m. The UU is characterized by aggrading and onlapping geometries towards the slopes, where it also thins out until it disappears along the middle-upper slope (Fig. 7e; Maillard et al., 2006; Cameselle and Urgeles, 2017). Maillard et al. (2006), Urgeles et al. (2011), Cameselle et al. (2014) and Cameselle and Urgeles (2017) all stated that the UU formed during an important Mediterranean-level lowstand (~1000 m). Several Complex Units (CU), with different origin, have been observed and described as belonging to the MSC (Cameselle and Urgeles, 2017).

DSDP Site 122, drilled at the mouth of a valley incision, recovered a few meters of sand-gravels made of well-rounded basalt, marine limestones, nodules of crystalline gypsum and mollusk fragments in a clay-silty matrix rich in deep-water benthonic foraminifera and early Pliocene nannofossils, all interpreted as erosional products of the VB seabed (Ryan et al., 1973). The uppermost Messinian in two industrial wells (Ibiza Marino and Cabriel boreholes; see Lozano, 2016) is represented by intercalations of clastic gypsum/anhydrite and marls (unit M8-P1 of Del Olmo and Martín, 2016). These are interpreted as turbidites sourced from the shelf and/or slope during a lowstand phase of the Mediterranean base level (Del Olmo, 2011; Del Olmo and Martín, 2016; Cameselle and Urgeles, 2017).

In seismic profiles, the UU/PQ transition (M-reflector or TES) is locally both sharp and smooth (in more distal settings) and erosional (in more proximal settings; Fig. 7e). Maillard and Mauffret (2006) indicate that the smooth parts have been caused by increasing fresh water influx during the Lago-Mare phase, leading to dissolution of the evaporites, and the rough erosional segments are of subaerial origin. For Cameselle and Urgeles (2017), the top of the UU is a smooth and conformable downlap surface, representing the rapid inundation of the basin with only local minor erosional features.

4.4. Balearic Promontory

Sticking out from the surrounding deep-water locations, the Balearic Promontory (BP; Fig. 2a) is a continental high that has undergone tectonic extension since the late Serravallian (Roca and Guimera, 1992; Sabat et al., 2011). During the Messinian, it comprised in topographic lows/subbasins at different water depths and separated by structural highs/sills (Maillard et al., 2014; Driussi et al., 2015; Roveri et al., 2019b; Raad et al., 2021). The area has been the subject of multiple studies (Maillard et al., 2014; Driussi et al., 2015; Ochoa et al., 2015; Roveri et al., 2019b; Raad et al., 2021) and several controversies arose after the publication of Roveri et al. (2019b).

The first controversy concerns the Messinian paleodepth of the BP's subbasins. According to Roveri et al. (2019b) the subbasins were shallow during the Messinian and acquired today's paleodepths following a strong post-MSC subsidence; Maillard and Mauffret (2011), Maillard et al. (2014) and Raad et al. (2021), instead, consider the tectonic movements in the BP to have been minor since the late Miocene (Messinian) and the region to have been already structured as it is today during the MSC. Well-to-seismic ties in the shallower basins closer to the Spanish coast (i.e. Bajo Segura, San Pedro and Elche basins) comprise up to 14 Stage 1 primary gypsum-marl cycles similar to the onshore PLG unit (Lugli et al., 2010) truncated at the top by the MES (Soria et al., 2008a, 2008b; Ochoa et al., 2015). At first, Ochoa et al. (2015) concluded that all sediments overlying the MES are Pliocene in age. A later re-appraisal of the same downhole logging data and cuttings led Ochoa et al. (2018) to attribute the first ~13 m-thick micritic and evaporite-free sediments to the late Messinian (stage 2 or 3 of the MSC according to the authors). The MSC stratigraphy of the shallowest offshore basins of the BP closely resembles that described from cores and outcrops onshore Mallorca (see subsection 3.4; Roveri et al., 2019b).

High resolution seismic reflection data in the Central Mallorca Depression (CMD) highlighted up to 500 m of MSC deposits made of a Bedded Unit (BU) and a thin salt layer (Maillard et al., 2014; Driussi et al., 2015). This BU has never been drilled and, therefore, lacks lithological and chronostratigraphic constraints. Two contrasting chronostratigraphic and lithological interpretations are proposed: Roveri et al. (2019b) ascribed these sediments to Stage 2 and 3 and suggested that only reworked evaporites and halite are present. By contrast, following the seismostratigraphic description of Maillard et al. (2014), Ochoa et al. (2015) and Raad et al. (2021) inferred the presence of Stage 1 gypsum also in the CMD.

Raad et al. (2021) made a step forward by disclosing a possible tripartition of the BU unit (Fig. 7f). In their seismostratigraphic framework, Raad et al. (2021) noticed that the uppermost evaporite-bearing unit (called BU3), ~120 m-thick in the CMD, has geometric, stratigraphic and facies analogies with the astronomically-tuned UG unit of the Caltanissetta Basin (Fig. 3a) that endorse its attribution to Stage 3. Similar to the UU in the deepest basins (see subsection 4.2), BU3 consists of up to 9 low- and medium-amplitude reflectors that are interpreted as alternating terrigenous and gypsum beds (Maillard et al., 2014; Raad et al., 2021). Reflectors are parallel and continuous in the more distal areas, while they appear more chaotic in the more proximal sectors (Raad et al., 2021). The base of BU3 coincides with the erosional top of the salt, interpreted as created by salt exposure, dissolution and locally salt gliding towards the depocenter (Fig. 7f; Raad et al., 2021). By contrast, the top of BU3, which corresponds to the Miocene/Pliocene boundary, is largely flat without signs of erosion (Fig. 7f; Maillard et al., 2014; Raad et al., 2021). An irregular geometry is sometimes visible, but is likely to be related to deformation of the underlying salt (Fig. 7f; Raad et al., 2021).

4.5. Tyrrhenian Basin

The Tyrrhenian Basin to the east of Sardinia is a back-arc basin that opened by continental rifting and oceanic spreading related to the eastward migration of the Apennine subduction system from middle Miocene to Pliocene times (Gaullier et al., 2014; Lymer et al., 2018; Loreto et al., 2020 and references therein). Three main domains are traditionally identified (Lymer et al., 2018 and references therein): 1) the East Sardinia Basin, with present-day water depths between 200-2000 m consisting of a system of seamounts and depressions that do not contain MSC sediments (Lymer et al., 2018); 2) the Cornaglia Terrace (2000-3000 m deep), a wide, flat area with dispersed structural highs; 3) the Tyrrhenian Basin *s.s.*, with water depths varying from 3000-3600 m. Whether the Tyrrhenian Basin acquired the present-day topography and hypsometry before the MSC (Lymer et al., 2018) or at least part of it (e.g. Eastern Sardinia margin, where Site 654 is located, and Northern Tyrrhenian) was much shallower (possibly comparable to the Caltanissetta Basin; Roveri et al., 2014b) and underwent extension and subsidence during the Messinian-Pliocene (e.g. Kastens and Mascle, 1990; Loreto et al., 2020) is still unresolved.

The MSC units in seismic profiles from the Tyrrhenian Basin (Fig. 7g) are very similar to the ones described in the Algero-Balearic and Liguro-Provençal basins (Fig. 7b-c; Gaullier et al., 2014; Lymer et al., 2018). ODP Sites 652, 653 and 654 confirmed the seismic-inferred lithological nature of UU as consisting, of gypsum-mudstone alternations (8 are counted at Site 654; Kastens et al., 1987; Borsetti et al., 1990; Roveri et al., 2014b). Intercalations of ripple–cross-laminated, fine-grained, azoic sandstones occur within the mudstone intervals in places (Cita et al., 1990; Iaccarino and Bossio, 1999). In some mudstone samples, the ostracod *Cyprideis* sp. (Site 654) and *Candona* sp. (DSDP Hole 974B) and the foraminifera *Ammonia beccarii* and *Ammonia tepida* have been found, indicating a shallow-water (< 50 m) brackish environment (see subsections 5.1 and 5.4; Cita et al., 1990; Iaccarino and Bossio, 1999). $^{87}Sr/^{86}Sr$ isotope ratios of UU gypsum and planktic foraminifera of the overlying Pliocene (Unit 1 at Site 654) show values much lower (from 0.708627 to 0.708745) and roughly equivalent (from 0.708935 to 0.709112) to coeval ocean water (~0.709020-30; McArthur et al., 2012), respectively (Müller et al., 1990; Müller and Mueller, 1991). Similar $^{87}Sr/^{86}Sr$ values were obtained from the gypsum cored at Site 652 (0.708626-0.708773; Müller and Mueller, 1991).

The Miocene/Pliocene boundary at DSDP Site 132 is placed above a cross-bedded sand rich in quartz, mica, pyrite, rounded fragments of gypsum and specimens of *Ammonia beccarii* and *Elphidium macellus* (Ryan et al., 1973). In the adjacent ODP Site 653 a similar sandstone is found slightly below the biostratigraphically-defined Messinian/Pliocene boundary and ~70 cm of grey mudstones with foraminifera and nannofossils of undisclosed provenance are squeezed in between (Cita et al., 1990). These mudstones also contain rare dwarf planktic foraminifera (*Globorotalia acostaensis*, *Orbulina universa*, and *Globigerina bulbosa*; Cita et al., 1990).

Overall, the uppermost Messinian sediments of the Tyrrhenian Basin are interpreted as having been deposited in lakes with periodic episodes of increased salinity and dilution under the strong influence of high energy rivers and, perhaps ocassionally, of the Atlantic (Cita et al., 1990; Müller et al., 1990; Müller and Mueller, 1991).

4.6. Ionian Basin

The deepest basin in the Mediterranean today is the Ionian Basin, with its lowest point at 5,267 meters. The so-called Ionian Abyssal Plain (IAP) is bounded on all sides by pre-MSC structural highs (Fig. 2a; Camerlenghi et al., 2019): the Malta Escarpment to the west; the Medina Escarpment to the south separating it from the Gulf of Sirt (Fig. 8a); the Gargano-Pelagosa and/or Otranto sill to the north dividing it from the Adriatic Foreland and, finally, an unnamed sill to the east, separating the IAP from the Levant Basin. Evidence from recent high-resolution seismic studies across the region have been used to support Stage 3 desiccation models (e.g. Hsü et al., 1978a, 1978b; Bowman, 2012; Micallef et al., 2018, 2019; Camerlenghi et al., 2019; Spatola et al., 2020).

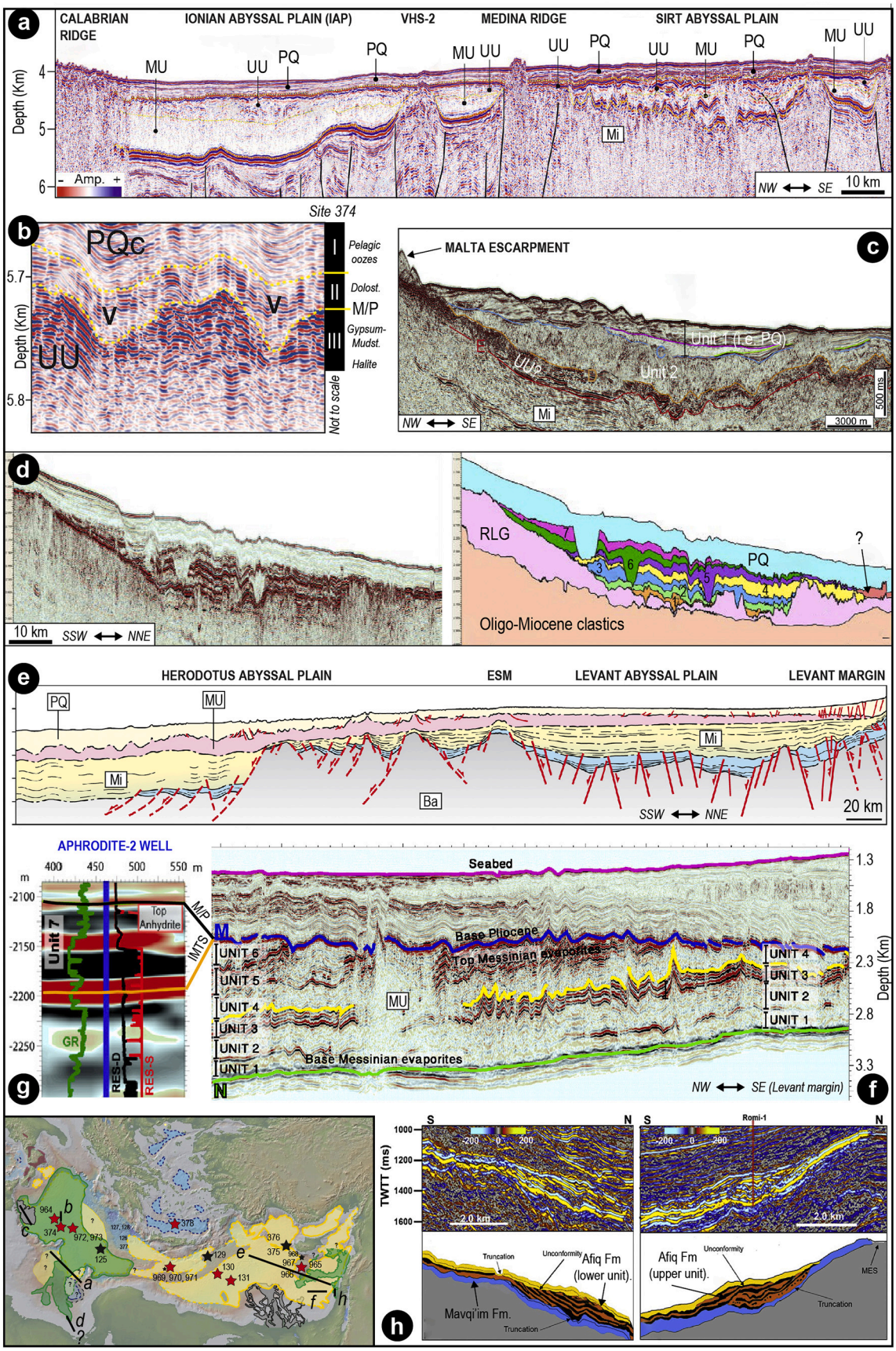

(caption on next page)

Fig. 8. Seismic profiles from intermediate-deep Eastern Mediterranean basins containing MSC markers/units (see Fig. 7 for abbreviations). (a) High-resolution seismic line MS27 imaging the PQ and the uppermost MSC's UU and MU in the Ionian Abyssal Plain and Gulf of Sirt (modified from Camerlenghi et al., 2019). Note how the MSC units are thinner, more difficult to distinguish and more deformed in the Sirt Abyssal Plain than in the IAP. PQ, UU and MU all onlap the structural highs of the Medina Ridge and VHS-2 sill. (b) High-resolution imaging of the lower part of the Plio-Quaternary (PQc unit) and upper part of the Messinian (UU) in the IAP (Camerlenghi et al., 2019). The MSC-PQ boundary is a highly irregular surface, describing apparent V-shaped incisions (symbol V) of controversial origin (see subsection 4.6.1 for insights). Note the coherent deformation of PQc with the underlying MSC sequence and the absence of fluvial facies within the incisions (Unit II is made of lower Pliocene dolomitic marls recovered in Site 374 drilled nearby the seismic line; see text). (c) Multichannel seismic reflection profile MEM-07-203 running approximately parallel to the Malta Escarpment and showing the relationship between Unit 2 of Micallef et al. (2018) with the overlying and underlying Zanclean and Messinian sediments, respectively (modified from Spatola et al., 2020). (d) Uninterpreted (left) and interpreted (right) seismic profiles showing the cyclic and channelized nature of the uppermost Messinian observed in the offshore Sirt Basin (modified from Bowman, 2012). (e) Interpreted 2D regional WNW–ESE seismic profile crossing the continental shelf and offshore Levant Basin and the Herodotus Abyssal Plain (Jagger et al., 2020). Note the lateral continuity of the Messinian MU. (f) Seismic profile from the Levant Basin showing the 6 sub-units distinguished inside the MU as well as its lower (N-reflector) and upper (M-reflector) boundaries (modified from Gvirtzman et al., 2013). (g) High-resolution seismic reflection image with wireline logs from Aphrodite-2 well illustrating that M-reflector previously considered as top evaporitic sequence and M/P boundary here consists of a ~100-m-thick unit (i.e. Unit 7 of Gvirtzman et al., 2017) in which different layers are distinguished (modified from Gvirtzman et al., 2017). (h) Interpreted and uninterpreted seismic profiles imaging the Mavqi'im and Afiq formations described in the canyons on the Levant continental margin (modified from Ben Moshe et al., 2020).

4.6.1. Ionian Abyssal Plain

The typical "trilogy" of seismic units representing the MSC deposition in the Western Mediterranean is recognized also in the IAP by Gallais et al. (2018) and Mocnik et al. (2018). However, Camerlenghi et al. (2019) states the MSC sequence in the IAP is ~1,300 m-thick and composed of only two units (Fig. 8a). The lowermost 150-700 m-thick Mobile Unit (MU) is seismically transparent without discernible bedding and with diapiric structures, all features diagnostic of halite. By contrast, the 350-1,000 m-thick Upper Unit (UU) alternates highly reflective with acoustically transparent reflectors (Figs. 8a-b), similar to those described of the UU sequences of the Western Mediterranean (Figs. 7b-c). These are therefore assumed to represent gypsum-mudstone cycles (Camerlenghi et al., 2019). The uppermost 80 m of UU has been recovered from DSDP Site 374 (Hsü et al., 1978b), confirming the presence of gypsum (both primary cumulate and clastic; Lugli et al., 2015) alternating with mudstones (Unit III; Hsü et al., 1978b). These mudstones are largely barren of *in situ* fossils. However, the presence of some foraminifera and siliceous microfossils led Cita et al. (1978) and Hsü et al. (1978a) to suggest that sporadic marine incursions, possibly from the Indian Ocean, took place during Stage 3. Similar to Site 372, the basal part of Hole 374 intercepted one thin (~3.5 m) halite layer within the UU (Hsü et al., 1978b).

The UU and the overlying Zanclean (subunit PQc of Camerlenghi et al., 2019) reflectors are conformably folded throughout most of the abyssal plain, locally showing chaotic internal structure, irregular folding mimicking V-shaped incisions and truncations (Fig. 8b; Camerlenghi et al., 2019). These features are interpreted by Camerlenghi et al. (2019) as fluvial valleys carved in subaerially exposed evaporites by the Eso-Sahabi fluvial system, the closest fluvial drainage network to the area (see Micallef et al., 2018) that drained Libya in the late Miocene (Griffin, 2002) and has been traced across the Gulf of Sirt offshore (Sabato Ceraldi et al., 2010; Bowman, 2012). Several arguments counteract this interpretation: 1) the coherent, deformation, mostly of post-Messinian age, of both the UU and the lower Zanclean; 2) the absence of fluvial facies above the bottom of the "valleys", which instead correspond to a mudstone interval that underwent post-depositional dolomitization (Unit II; see below; Fig. 8b); 3) the unlikelihood that the Eso-Sahabi fluvial system managed to bypass the Medina Ridge divide (Fig. 8a). Alternatively, the apparent incisions at the M/P boundary in the IAP may represent post-sedimentary folds resulting from post-Messinian tectonic and/or salt movements-driven deformation (e.g. Mocnik et al., 2018). At Site 374 the Miocene/Pliocene boundary has been recovered (Unit II), but its primary nature (likely a mudstone) is obscured by diagenesis (cementation by dolomite; Hsü et al., 1978b). A lithified dolostone at the (seismic) predicted depth of the M-Horizon is a characteristic of several sites. Sometimes this interval has been recovered (e.g. Sites 125 and 374; Ryan et al., 1973; Hsü et al., 1978b; Comas et al., 1996); at others the hard lithology is inferred by the torqueing of the drill string (resistance to turning) accompanied by bouncing of the drill bit at the (e.g. Sites 122, 124, 125, 132, 133 and 134; Ryan et al., 1973). Dolomitization was (Hsü et al., 1973a, 1973b; Ryan et al., 1973) and still is (e.g. Ryan, 2009) largely considered a "*diagnostic feature of tidal (sabkha) sediments*" (Friedman, 1973, *pp.* 705). Its occurrence at locations with present-day water depth exceeding 2000 m was therefore considered strong evidence that the Mediterranean floor was subaerially exposed prior to the Zanclean marine replenishment (e.g. Ryan et al., 1973). It is, however, now widely accepted that dolomite precipitation is not exclusive of sabkha environments, but rather is a common process also in bottom sediments under a relatively deep water column (see Dela Pierre et al., 2012, 2014 and references therein). In the specific case of the offshore Mediterranean's M/P boundary on the Ionian Abyssal Plain, already in the '70s dolomitization was thought to have occurred after burial (Hsü et al., 1978b), a conclusion recently reinforced by McKenzie et al. (2017).

4.6.2. Malta Escarpment

At the foot of the Malta Escarpment, Micallef et al. (2018, 2019) and Spatola et al. (2020) amalgamated the MU and UU into one seismic unit, Unit 3, which is separated from the Plio-Quaternary marine sediments (Unit 1) by Unit 2, a chaotic transparent seismic package (Fig. 8c). Unit 2 has a maximum thickness of 760-860 m, a volume of 1430–1620 km^3 and a wedge-shaped geometry that thins eastwards, disappearing before reaching the IAP (Micallef et al., 2018). Micallef et al. (2018) and Spatola et al. (2020) proposed a lithological/sedimentological interpretation of this chaotic body, suggesting it is composed of well-sorted sediments of the Pelagian Platform to the west of the Malta Escarpment, with coarser material at the mouth grading into more distal finer sediments. This chaotic body has recently been attributed to the Zanclean megaflood during its passage from the western to the eastern Mediterranean via a gateway located in south-eastern Sicily (Micallef et al., 2018, 2019; Spatola et al., 2020). Given the rapidity of the reflooding ($\leq$ 2 years, Garcia-Castellanos et al., 2009, 2020), this interpretation implies rapid mass deposition. Other interpretations of this Unit 2 include being the result of extensive marine mass movement (Polonia et al., 2011), being folded UU (Butler et al., 2015) or being a complex unit built during lower sea level phases (Lofi et al., 2011a, 2011b).

4.6.3. Gulf of Sirt

The Gulf of Sirt (or Sirt embayment; Figs. 2a, 8a), the offshore extension of the Sirt Basin onshore Libya (Griffin, 2002 and references therein), is cross-cut by high-density seismic and well datasets as a result of oil potential of the region (Fiduk, 2009). However, only few studies have tackled the MSC (e.g. Hallett, 2002; Fiduk, 2009; Bowman, 2012).

In the Sirt embayment the MSC unit(s) is unevenly distributed in sub-basins controlled by a pre-existing topography, there is little distinction between the MU and UU, the overall thickness of the MSC unit(s) is lower and the degree of deformation is higher than in the adjacent IAP (Fig. 8a; Camerlenghi et al., 2019). The presence of halite in the Sirt

embayment is debated, but most authors think it is absent (see Fiduk, 2009; Sabato Ceraldi et al., 2010; Lofi, 2018; Jagger et al., 2020; Fig. 2b). Bowman (2012) distinguishes seven seismic units within the MSC-related sequence (Fig. 8d). On the basis of high-resolution 3D and 2D data, each seismic unit has been interpreted consisting of clastics filling erosional channels cutting up to 100 m deep and wide (Fig. 8d) and evaporites (gypsum and anhydrite) alternating with precessional cyclicity (Bowman, 2012). The presence of anhydrite in the topmost part of the sequence is confirmed by the B1 NC 35A well (Hallett, 2002). Sabato Ceraldi et al. (2010) and Bowman (2012) envisaged a three-step evolution of each unit: 1) evaporitic deposition during precession maxima in a dried out Sirt embayment; 2) erosion of the valleys during the arid-wet transition fed by the Eso-Sahabi paleofluvial system; 3) filling of the valleys with the fluvial sediments during the wet phase. Based on this chronostratigraphic interpretation, the evaporite cycles should be time equivalent to most of Stage 3, with the upper four seismic units reflecting the Lago-Mare phase (Fig. 1a).

4.7. Levant Basin

4.7.1. Abyssal plain

Old seismic data in the Levant Basin show an up to 2 km-thick, high velocity, acoustically transparent sequence bounded by the N-reflector at the base and the M-reflector at the top (Figs. 8e-f; Ryan, 1978; Netzeband et al., 2006). This sequence thickens and extends for tens of kilometers towards WNW and thins eastward along the continental margin (Fig. 8e), where the N and M-reflectors converge forming the condensed MSC section of the Mavqiim and Afiq formations (described in subsection 4.7.2; Gvirtzman et al., 2017; Manzi et al., 2018). High resolution 2D and 3D industrial seismic and well data from the southern Levant Basin revealed that this transparent sequence is largely made of pure halite with internal stratification picked out by diatomite, clay- and clastic-rich layers that allowed the division of the sequence into six subunits, basinward-tilted and truncated at the top by the flat TES (Fig. 8f; Gvirtzman et al., 2013, 2015, 2017; Feng et al., 2016, 2017; Manzi et al., 2018; Meilijson et al., 2018, 2019). Clastic beds ~3 to 20 m-thick are abundant in the highly reflective and chaotic Unit 5 (i.e. Interbedded evaporites of Meilijson et al., 2019; MC2 unit of Feng et al., 2016; Figs. 3b, 4a), where they are interbedded with evaporites (probably halite with minor occurrences of anhydrite) varying in thickness from ~6 to 30 m (Manzi et al., 2018; Meilijson et al., 2019). Paleontological analyses of cuttings probably belonging to one of the clastic beds revealed the presence of a few mollusk fragments, ostracods, echinoid spines and a relatively rich assemblage of benthic and planktic foraminifera which Meilijson et al. (2019) concluded to be reworked. Based on seismic and well-log data, clastic intercalations (probably of clays, silts and sands) within a halite-dominated sequence are thought to persist in the overlying Unit 6, although they diminish in thickness and frequency (Gvirtzman et al., 2013; Feng et al., 2016; Meilijson et al., 2019). The expression of the end of the MSC is highly controversial. Until recently, the M-reflector of Ryan (1978) (later renamed as the Top Erosion Surface, TES; Lofi et al., 2011a, 2011b) bounding Unit 6 at the top was considered to be the Miocene/Pliocene boundary (Fig. 8f; Ryan, 1978; Gvirtzman et al., 2013; Feng et al., 2016). Instead, Gvirtzman et al. (2017) showed that in higher resolution seismic data the M-reflector/TES is a bundle of reflectors forming a distinct layer (Unit 7) overlying a truncation surface (i.e. Unit 6/7 boundary) that they re-labelled intra-Messinian truncation surface (IMTS; Fig. 8g) and ascribed to subaqueous dissolution rather than subaerial incision (e.g. Bertoni and Cartwright, 2007; Lofi et al., 2011a, 2011b; Kartveit et al., 2019; Madof et al., 2019). This conclusion was recently corroborated by the independent study of Kirkham et al. (2020). Analysis of gamma-ray and resistivity logs in three deep basin wells (Aphrodite-2, Myra-1, Sara-1; Fig. 2b) and correlation with the Or-South-1 well (located between the deep basin and the shelf) showed that Unit 7 maintains a constant thickness of ~100 m-thick and consists of clastic-rich anhydrite of undisclosed provenance. Meilijson et al. (2019)'s lithological interpretation of industrial boreholes slightly farther to the NE (Fig. 2b) give Unit 7 a significantly smaller thickness (5 m; Fig. 3b). Independent studies offshore Lebanon and Syria (Kartveit et al., 2019; Madof et al., 2019) describe a unit (Nahr Menashe complex) interpreted as a thicker (up to 300 m; Madof et al., 2019), but lateral equivalent of Gvirtzman et al. (2017)'s Unit 7. Based on its channelized morphology identified upslope near the Lebanese coast, Kartveit et al. (2019) and Madof et al. (2019) interpreted the Nahr Menashe Unit and the IMTS underneath as fluvial in origin, deposited/formed on a subaerially exposed floor of the Levant Basin. Six (Madof et al., 2019) to eight (Madof and Connell, 2018) lobes were identified and are proposed to have stacked with precessional frequency. The Nahr Menashe sequence has been correlated by the same authors with the Abu Madi Fm. located within the Messinian canyons offshore Egypt (Abdel Aal et al., 2000; Loncke et al., 2006; Abdel-Fattah, 2014), the Handere Formation offshore Turkey (Radeff et al., 2017) and with the Eosahabi deposits offshore Libya (Bowman, 2012). This interpretation implies a low base-level during the final stage of the MSC.

Manzi et al. (2018) and Meilijson et al. (2018, 2019) attempted astronomical dating of the abyssal MSC succession of the Levant Basin by integrating biostratigraphy on the pre-MU succession, reflector counting within the MU (only Meilijson et al., 2019) and well-log data (Fig. 3b). They achieved two contrasting results that gave rise to an outstanding controversy (Figs. 3b, 4a). Manzi et al. (2018) proposed that Stage 1 in the deep Levant is represented by a foraminifera-barren, evaporite-free shales interval labelled FBI (foraminifer barren interval) observed in the deep Aprodite-2 well and in the more proximal Myra-1 well. In this interpretation Unit 7 comprises the whole of Stage 3 (with the IMTS corresponding to the Stage 2/3 transition) and all halite deposition took place in ~50 kyr estimated during Stage 2 of the MSC (Fig. 1a; Roveri et al., 2014a). By contrast, the FBI is not present in the Dolphin well targeted by Meilijson et al. (2019), which is located in an intermediate position between the Aprodite-2 and Myra-1 wells studied by Manzi et al., 2018; Fig. 2b). Instead, in the Dolphin well a relatively open-marine, foraminifera-rich sequence extends below the (conformable) base of the MU, placed in correspondence to a ~2 to 5.5 m-thick anhydrite/shale (Unit 0; Manzi et al., 2018 and Meilijson et al., 2018, respectively). Astronomical tuning of the ~33 cycles counted in the MU in the Dolphin well, which are assumed to be precessional, results in the Main Halite body (i.e. Unit 0-4 of Gvirtzman et al., 2013 and Manzi et al., 2018) spanning MSC Stage 1 and 2, the Interbedded Evaporites/Unit 5 covering substage 3.1 and the Argillaceous Evaporites/Unit 6-7 to encompass the Lago-Mare phase (Figs. 3b, 4a). In this interpretation from Meilijson et al. (2019), halite deposition in the Levant Basin started in Stage 1 and persisted throughout the entire MSC, including Stage 3, during which more allochthonous material was delivered to the basin (Fig. 3b). Madof and Connell (2018) and Madof et al. (2019) also attempted an astronomical tuning of the Nahr Menashe Unit, concluding that it spans throughout substage 3.2 and part of substage 3.1. Feng et al. (2016) claim, however, that the impressive thickness of clastics found in the Levantine MU is more indicative of distinct short-term events (shorter than the precession cycle) associated with transport of extraordinary power and magnitude.

Late Messinian sediments have also been recovered at several DSDP (129, 375, 376; Ryan et al., 1973; Hsü et al., 1978b) and ODP Sites (965, 967, 968; Emeis et al., 1996), but the assignment of the retrieved sediments to seismostratigraphic units is problematic. Nevertheless, they provide several key nuggets of precious information about the Stage 3 paleoenvironment:

- Sites 965 and 966, located roughly on the crest of the Eratosthenes Seamount, just south of Cyprus (Fig. 2b), recovered soil structures above the evaporites indicating exposure above sea level (Robertson, 1998a, 1998b; Maillard et al., 2011a; Reiche et al., 2016).
- ODP Sites 967 and 968, located at the base of the northern and southern slope of Eratosthenes Seamount (Fig. 2b), respectively,

revealed the presence, within the MSC interval, of calcareous turbidites with Cyprus-derived clasts and clays containing *Ammonia tepida*, *Cyprideis pannonica* and *pulmonate gastropods* (Blanc-Valleron et al., 1998; Robertson, 1998a,b; Reiche et al., 2016).
- Abundant *Cyprideis pannonica* specimens were also recovered from DSDP Sites 375 and 376 drilled on the crest of the Florence Rise, west of Cyprus (Fig. 2b; Hsü et al., 1978b).
- Abundant, well-preserved *Ammonia* tests and *Cyprideis* specimens are also known from Site 129A (Fig. 2b), occurring with dwarf planktonic foraminifera (Ryan et al., 1973).

All the evidence listed above suggest that a base-level fall leading to subaerial exposure occurred at some point(s) during Stage 3 in the Eastern Mediterranean (Ryan, 2009). However, it must be kept in mind that both the Florence Rise and Eratosthenes Seamount are likely to have been much more elevated during the Messinian than they are today because of Pliocene-Quaternary subsidence related to the Cyprus subduction zone (Robertson, 1998a, 1998b; Maillard et al., 2011a; Reiche et al., 2016).

Sites 375 and 376 display several discrete layers of primary and clastic gypsum interbedded in the *Cyprideis*-rich mudstones (McCulloch and De Deckker, 1989; Lugli et al., 2015). This succession shares several similarities with sites drilled in the Western Mediterranean (e.g. ODP 654A) and Ionian Basin (DSDP 374), where they have been correlated with the seismic Upper Unit (see subsections 4.5 and 4.6). This may suggest that a Western Mediterranean-like gypsum-bearing UU was also locally deposited in the easternmost abyss of the Mediterranean (see Güneş et al., 2018).

4.7.2. Levant continental margin

Evaporitic and non-evaporitic deposits are buried beneath PQ deposits (Yafo Formation) along the Levant continental margin, where they are mostly preserved within canyons carved underwater in pre-Messinian time (Druckman et al., 1995; Lugli et al., 2013). Within the Afiq canyon, Druckman et al. (1995) distinguished three formations in the Messinian sequence: the evaporitic Mavqi'im Formation, 115 m-thick and mostly composed of anhydrite in places interbedded with micritic limestones; the Be'eri Formation, cmprising gypsum; the Afiq Formation, varying in thickness from 30 to 90 m and consisting of conglomerates, sandstones and marls interpreted as representing fluvial and lacustrine-marsh environments (Druckman et al., 1995). The Afiq Fm. is only present in the deepest portions of the canyon where it overlies the Mavqi'im Fm. By contrast, the Be'eri gypsum is only found along the canyon shoulders covered by the Pliocene, at elevations $>$ 600 m with respect to the Mavqi'im Fm. Based on Sr values, Druckman et al. (1995) attributed the Mavqi'im Fm. to MSC Stage 1, the Be'eri Fm. to substage 3.1 and the Afiq Fm. to the Lago-Mare phase. These authors also suggested that gypsum precipitation occurred under subaqueous conditions, with the water level ~600 m (i.e. the difference in altitude between the Mavqi'im and Be'eri fms.) higher during the deposition of the Be'eri Fm. Two base-level falls of approximately the same magnitude are thought to have occurred between the evaporitic phases and after Mavqi'im deposition. A lowstand phase was therefore in force during Afiq deposition (Druckman et al., 1995).

However, combining stratigraphic, sedimentological and geochemical (Sr isotopes) considerations, Lugli et al. (2013) revealed the clastic nature of both the Mavqi'im and Be'eri evaporites and suggested the persistent drowning of the canyon(s), filled with turbidites (Lugli et al., 2013). Due to the presence of clastic evaporites, Gvirtzman et al. (2017) suggested that the Mavqiim Formation is a condensed section encompassing MSC Stage 2 and early Stage 3, while the evaporite-free Afiq Formation represents the Lago-Mare phase.

Ben Moshe et al. (2020) ascribed (at least part of) the Afiq Fm. to the whole of Stage 3 as a wedge-shape clastic complex lying on top of the Mavqi'im Fm. and with the basal surface corresponding to the correlative conformity of the MES developed landward, at the expense of the Mavqi'im Fm (Fig. 8h). Ben Moshe et al. (2020) distinguished a lower sub-unit composed of clastic gypsum and with fore-stepping and down-stepping internal geometry typical of progradational wedges, and an upper sub-unit containing anhydrite fragments and marls with Lago-Mare fauna (e.g. *Cyprideis torosa*; Rosenfeld, 1977) and with seismic characteristics typical of a transgressive systems tract. Incisions are reported throughout the Afiq Fm. at different depths, while erosional surfaces bound both sub-units (Ben Moshe et al., 2020). In particular, the surface capping the upper subunit and correlated to the M horizon or TES basinward (see subsection 4.7.1) shows dendritic drainage patterns of gullies and channels (Ben Moshe et al., 2020).

Ben Moshe et al. (2020) identify the variation of base level specifically during Stage 3 by analyzing the morphology of truncation surfaces bounding the Afiq Formation on the continental margin of the Levant Basin. This suggests high amplitude fluctuations of base-level in the order of one hundred meters, with development of subaerial erosion surfaces and the deposition of clastics and incision by fluvial drainage systems that occurred during the lowstand phases, while aggradational units (of unknown lithological nature) accumulated during the high-stand phases. According to their analysis, base level dropped down to a maximum 535 m during Afiq deposition (i.e. below the maximum 430 m estimated paleodepth of the Sicily Sill; Garcia-Castellanos et al., 2009), implying hydrological disconnection between the Eastern and Western basins at various times during Stage 3. A regression to 615-885 m is proposed to have occurred at the top of the Afiq Fm., pre-dating the abrupt refilling at the base of the Zanclean (e.g. Micallef et al., 2018, 2019; Garcia-Castellanos et al., 2020; Spatola et al., 2020).

4.8. Summary of the offshore Stage 3 record

Knowledge of the Stage 3 sequence offshore is mainly based on the integration of seismic interpretations and analysis of material recovered from fragmentary and unevenly distributed DSDP/ODP/industrial cores.

- MSC sediments are absent on the eroded continental shelves bordering the deep basins, except in the Messinian thalwegs and at their mouth. Here the PQ lies directly above the MES which, in turn, cuts through the pre-MSC deposits (Fig. 7e). A similar stratigraphic arrangement is found along the middle-upper slopes (Fig. 7d), although the presence of a thin, possibly incomplete UU in morphological depressions is sometimes postulated. Seamounts also lack MSC Stage 3 sediments and are strongly incised by the MES (Fig. 7g).
- The thick UU is widespread and roughly present everywhere in the abyssal plains from west of the Alborán volcanic arc to the eastern edge of the Ionian Basin (Fig. 2b). In the abyssal plains its seismic facies appears homogeneous, comprising parallel and relatively continuous high amplitude reflections (Figs. 7b-c). The UU pinches out towards the foot of continental slopes and seamounts (Figs. 7b, d-g), where it can be irregularly bedded or relatively well bedded (Lofi et al., 2011a, 2011b). The uppermost part of the Bedded Units (defined in depressions physically disconnected from the abyssal plains and, therefore, from the UU; e.g. CMD and Corsica Basin; Maillard et al., 2014; Thinon et al., 2016; Raad et al., 2021) shows seismic features comparable to those of the UU.
- Drill Sites revealed that the reflections of relatively high amplitude in seismic profiles correspond to gypsum and mudstone alternations with sporadic intercalations of massive to cross-bedded sandstones. Some mudstone interbeds contain low-diversity assemblages of benthic organisms (ostracods, foraminifera and diatoms) indicative of shallow to neritic environments. Except for dwarfed forms of planktonic foraminifera and the monospecific nannofossil assemblages described

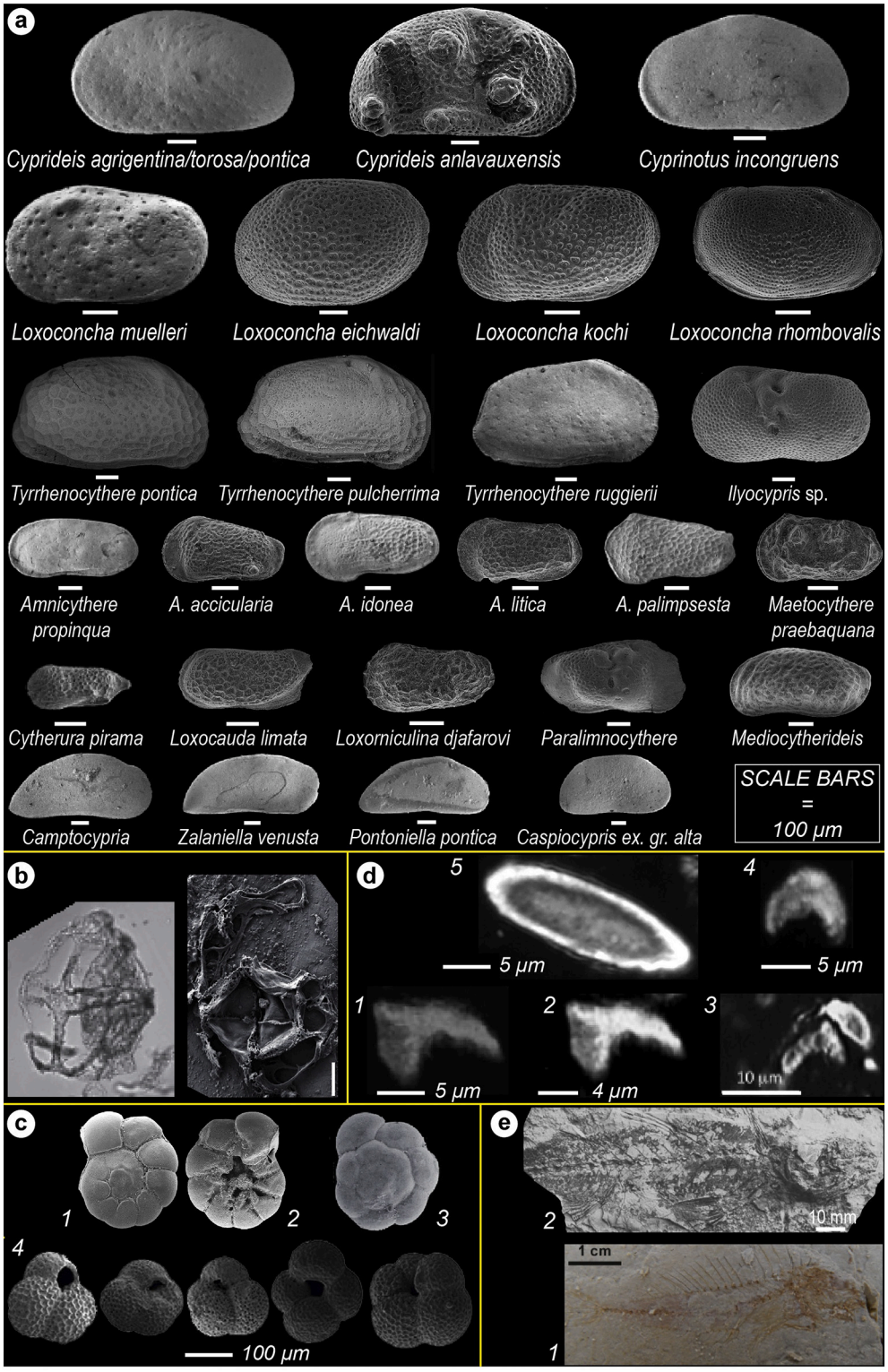

Fig. 9. Photomicrographs of the key micro- and macrofossils featuring Stage 3 sediments. (a) Scanning electron microscope (SEM) photographs of the more common Paratethyan ostracod species in substage 3.1 and 3.2 sediments (compiled from Stoica et al., 2016, Cosentino et al., 2018 and Sciuto et al., 2018). (b) Photomicrographs of the Paratethyan dinoflagellate cyst *Galeacysta etrusca* under the optical microscope (left) and SEM (right) (modified from Do Couto et al., 2014 and Grothe et al., 2018). Scale=20 µm. (c) SEM microphotographs of the euryhaline, shallow-water benthic foraminifera *Ammonia beccarii* (1-spiral side, 2-umbilical side) and *Ammonia tepida* (3-spiral side; Carnevale et al., 2019) and of the dwarf fauna of planktonic foraminifera from the Bajo Segura Basin (4; Corbí and Soria, 2016). (d) Photographs in polarized light (crossed nicols) of some specimens of *Ceratolithus acutus* (1-3) described in the Lago-Mare unit of Malaga (1-Do Couto et al., 2014), the Zorreras Mb. of Sorbas (2-Clauzon et al., 2015) and the Colombacci Fm. of the Northern Apennines (3-Popescu et al., 2017) and of destroyed (4) and intact (5) ascidian spicules of *Micrascidiscus* sp. (Golovina et al., 2019). Note that *C. acutus* specimens closely resemble ascidian spicules of *Micrascidiscus* sp., which may lead to misinterpretation of the C. acutus (see Golovina et al., 2019), and that pictures 1 and 2 are identical, despite they are attributed to samples taken from two different localities. (e) Articulated skeletons of marine fish from substage 3.1 mudstone horizons in Cyprus (1-*Aphanius crassicaudus*; Manzi et al., 2016a) and substage 3.2 deposits in Cava Serredi (2-*Mugil cf. cephalus*; Carnevale et al., 2018).

by Castradori (1998), the rest of planktonic foraminifera and nannofossils are largely regarded as reworked.

- The deep Levant Basin contains a ~1.8-2.0 km-thick MU (Figs. 8e-f), consisting of 6 to 7 seismic units depending on the resolution of the seismic employed. In high resolution seismic data, the lateral equivalent of part of the UU is identified as a ~100-m-thick, clastic-rich, anhydrite layer (Unit 7 of Gvirtzman 1207) offshore Israel, thickening to 300 m offshore Lebanon (Nahr Menashe complex, Madof et al., 2019). The Levant Basin still has major controversies concerning the timing of halite deposition (~50 kyr vs ~550 kyr; Manzi et al., 2018 vs Meilijson et al., 2019), the origin of the clastic accumulations overlying the halite (fluvial vs subaqueous) and the presence or absence of gypsum-mudstone cycles.
- Apart from the halite flow-related deformation, the Miocene/Pliocene boundary (i.e. UU/PQ transition) is conformable in intermediate (e.g. Balearic Promontory) and deep (WAB, EAB, Algero-Balearic, Liguro-Provençal, Tyrrhenian, Ionian and Levant) depocenters, while it shows signs of erosion on the shelf domain and along the upper-middle continental slopes and seamounts. Clear arguments of floor exposure at the M/P boundary are absent in all drill sites but 978A.

5. The paleontological perspective

Paleontological data have been used to define and identify Stage 3 sediments, but have also been a source of profound contention over the interpretation of its paleoenvironmental and paleohydrological nature. Biotic groups impacted by the evolution of the gateways linking the Mediterranean with the Atlantic, Indian Ocean and Paratethys include marine species (e.g. foraminifera, calcareous nannofossils, fish) and brackish water-species (ostracods, fish, mollusks and dinocysts endemic or with affinity to species of the Paratethys region) that were unable to migrate when these corridors were closed, and terrestrial species (e.g. mammals) that, conversely, got across the gateway during periods of exposure (see Colombero et al., 2017; Booth-Rea et al., 2018; Mas et al., 2018b). Analysis of these faunal datasets provides key insights into likely gateway dimensions and the timing of their opening, restriction and closure (e.g. Palcu et al., 2017). Furthermore, they are a key constraint on the water sources likely to have been affecting the Mediterranean during MSC Stage 3.

5.1. Ostracods

Ostracods are by far the most prolific faunal group during Stage 3. Brackish species are known from both land sections and deep-sea cores across the whole Mediterranean (see Fig. 2b for sites and references; Fig. 9a). Two characteristic biofacies are commonly distinguished: Biofacies 1 (Bonaduce and Sgarrella, 1999) or *Cyprideis* assemblage (Iaccarino and Bossio, 1999) consists of an monospecific population of *Cyprideis* species or of an oligotypic population dominated by *Cyprideis* species alongside rare specimens of *Tyrrhenocythere ruggierii*, *Loxoconcha kochi*, *Loxoconcha muelleri* and *Caspiocypris alta*); Biofacies 2 (Bonaduce and Sgarrella, 1999) or *Loxocorniculina djafarovi* assemblage (Iaccarino and Bossio, 1999) has a higher species diversity characterized by the abundant occurrence of truly Paratethyan species belonging to the genera *Amnicythere*, *Loxoconcha*, *Loxocauda*, *Cytheromorpha*, *Cyprinotus* and *Tyrrenhocythere* (see species names in Fig. 9a). The number of species reported in the onshore sections is variable, ranging from a dozen (e.g. Caruso et al., 2020) to more than sixty (e.g. Gliozzi et al., 2007; Grossi et al., 2008). This variability is not explained, but it may result from the application of different taxonomic concepts that resulted in the recognition of more or fewer species (Stoica et al., 2016) or from local environmental conditions that differed from basin to basin and resulted in different patterns of colonization.

Compared to the onshore domain, the ostracod fauna offshore is impoverished. Monospecific assemblages of *Cyprideis* sp. (Sites 372, 129A, 376, 654A, 967, 968; Ryan et al., 1973; Cita et al., 1990) or oligospecific assemblages dominated by *Cyprideis* and rare specimens of *Candona* sp. (Hole 974B, Iaccarino and Bossio, 1999) and L. *muelleri* (Hole 978, Iaccarino and Bossio, 1999) are the more widely reported. Interestingly, these assemblages are always associated with *Ammonia* sp. tests and, in some cases, with other species of shallow-water, euryhaline benthic foraminifera (see subsection 5.4). Only in Hole 975, close to the M/P boundary is a more heterotypic ostracod assemblage found (*Euxinocythere praebaquana*, *Amnicythere idonea*, *Leptocythere limbate, Loxocorniculina djafarovi, Candona sp.,* and *Cyprideis* sp.; Iaccarino and Bossio, 1999) and lacking of euryhaline benthic foraminifera. The likely cause of the widespread barrenness of ostracods in most of the offshore samples is perhaps because environmental conditions in the deep basins (depth and/or salinity) where not suitable to permit population by this benthic fauna (see below for the ecological requirements; e.g. Hsü et al., 1978b in reference to Site 374). Finally, one must bear in mind that studying these organisms require much more material (some hundreds of grams) than the quantity of core sediments usually processed (i.e. ~10 cm^3; Iaccarino and Bossio, 1999).

The paleoecology (salinity and depth ranges) of Stage 3 ostracods has been based on both observations of few species that still live in the Caspian and Black seas today and have affinities with the Stage 3 species and on the interpretation of sedimentological, geochemical and mineralogical data of the surrounding sediments (see Gliozzi and Grossi, 2008 and Grossi et al., 2008 for insights). Biofacies 1 is thought to represent very shallow water environments (i.e. <15 m) with salinity fluctuating between mesohaline and hypersaline when the euryhaline *Cyprideis* is dominant. Instead, more stable oligo-mesohaline water is inferred when the other species are more abundant in Biofacies 1. The variegated Biofacies 2, on the other hand, is thought to represent somewhat deeper environments (up to 100 m) and less salty conditions (oligo-low mesohaline; Gliozzi and Grossi, 2008; Grossi et al., 2008; Caruso et al., 2020).

Some authors consider the time when the Paratethyan ostracods arrived in the Mediterranean to be well constrained (e.g. Roveri et al., 2008a; Grossi et al., 2011; Cosentino et al., 2018) by the scarce occurrence of the first Paratethyan immigrant *Loxoconcha muelleri* 20 cm below the ash layer in the Colla di Votta section, which has a ^{238}U-^{206}Pb age of 5.5320±0.0074 Ma (Cosentino et al., 2013), and in the chaotic deposits of the Adana Basin, ascribed to Stage 2 (Faranda et al., 2013). Instead, the first appearance of *Loxocorniculina djafarovi* has been considered to coincide with the biofacies 1-2 shift and to have occurred Mediterranean-wide synchronously at 5.40 Ma (Roveri et al., 2008a; Grossi et al., 2011; Cosentino et al., 2013). Roveri et al. (2008a) also showed Biofacies 2 diversity as increasing linearly through the Lago-Mare phase, reaching its maximum diversity just beneath the Miocene/Pliocene boundary and before disappearing in the Pliocene. Following the claimed synchronicity of the FO of both *Loxoconcha muelleri* and *Loxocorniculina djafarovi*, Roveri et al. (2008a) and Grossi et al. (2011) recognized one biozone in each biofacies: the *Loxoconcha muelleri* Biozone, spanning from 5.59 to 5.40 Ma, and the *Loxocorniculina djafarovi* Biozone, whose boundaries correspond respectively to the first (5.40 Ma) and last occurrence (5.33 Ma) of *L. djafarovi* in the Mediterranean. This biozonation, erected by Grossi et al. (2011), is often used for dating incomplete successions (e.g. Vera Basin; Stoica et al., 2016; Caruso et al., 2020). However, the first appearance of a diversified ostracod assemblage (including *Loxocorniculina djafarovi*) occurred in already cycle 3 of the Sicilian Upper Gypsum at Eraclea Minoa (Fig. 3a; Grossi et al., 2015), which has an astronomical age of 5.45 Ma (Van der Laan et al., 2006) or 5.47 Ma (Manzi et al., 2009). Furthermore, the sudden appearance of Biofacies 2 and its linear, upward increase in diversity have not been recognized in localities like Nijar and Malaga, where biofacies 1 and 2 are found stacked in more than one lithological (possibly precession-controlled) cycle in the Lago-Mare succession (Bassetti et al., 2006; Guerra-Merchán et al., 2010). These findings argue that the appearance of Paratethyan ostracods in the Mediterranean may

not have been synchronous, therefore casting serious doubts upon the biostratigraphic relevance of the Mediterranean ostracods.

Except for *Cyprideis* specimens, where species attribution is debated (see discussion in Stoica et al., 2016), the affinity of all other ostracod species observed in Mediterranean Stage 3 sediments (Fig. 9a) with those of the Eastern Paratethys basins (i.e. Dacian, Euxinic and Caspian) has been demonstrated in several publications (e.g. Ruggieri, 1967; Gliozzi et al., 2007; Stoica et al., 2016; Sciuto et al., 2018). Only Bassetti et al. (2003, 2006) have questioned the Paratethyan affinity by suggesting that species from the Northern Apennines and Nijar Basin have ambiguous affinities with Paratethyan fauna as described in the mainly Russian literature from the '60-'70s. However, these differences between the late Messinian Mediterranean and Paratethyan ostracods resulted from misidentifications and/or a different use of species nomenclature (Stoica et al., 2016). Recently acquired knowledge of the Pontian assemblages of the Dacian, Euxinic and Caspian basins now permit to trace the provenance of Mediterranean Stage 3 ostracod species from the entire Black Sea region (Stoica et al., 2016) and, for a few species, from the Dacian (Stoica et al., 2013; Lazarev et al., 2020), Caspian (Van Baak et al., 2016) and North Aegean (see references in Krijgsman et al., 2020a) basins.

The means by which the ostracods travelled from the Paratethys to and across the Mediterranean during Stage 3 is as crucial for reconstructing the Stage 3 paleoenvironment as it is poorly addressed in onshore studies or overlooked in seismic and computational studies. Two migratory mechanisms have been suggested:

1) the aerial dispersion of ostracods through the migration of aquatic birds (Benson, 1978; Caruso et al., 2020); this hypothesis was proposed because, in a Mediterranean concluded to have been desiccated, it was the only possible migration mechanism.

2) direct aqueous migration by the ostracods themselves (which are planktonic in the larval stage) through the establishment of similar paleoenvironmental conditions; by this mechanism, the dispersion of Paratethyan ostracod fauna from right across the Mediterranean requires E-W intraconnection and a Mediterranean water-level high enough to reach the marginal basins (Gliozzi et al., 2007; Stoica et al., 2016; Sciuto et al., 2018; Sciuto and Baldanza, 2020).

Finally, Carnevale et al. (2006a, 2006b, 2008, 2018) recognized the Paratethyan affinity of the Mediterranean Stage 3 species but, in view of their occurrence with *in-situ* species of marine fish, they suggested that Stage 3 ostracods descended from a Paratethyan stock that migrated into the Mediterranean well before the MSC and survived the extreme salinity conditions of Stage 1 and 2 in marginal, fresher water refugia. In this scenario the brackish water ostracod assemblages found in Stage 3 have no paleoecological significance for Stage 3 paleoenvironment (Carnevale et al., 2006a, 2006b, 2008, 2018). However, there are two, unflagged problems with this hypothesis: 1) the Mediterranean-Central Paratethys connection through the Trans-Tethyan gateway in Slovenia already closed in the early Tortonian (Kováč et al., 2007; Sant et al., 2017; Palcu et al., 2017); 2) No Paratethyan ostracod species have been found in the Mediterranean before the MSC (see Gliozzi et al., 2007).

5.2. Dinoflagellate cysts

Dinoflagellate cysts (dinocysts) are the fossil remains of unicellular protists that live in the upper water column of many water bodies (e.g. Zonneveld et al., 2013; Mudie et al., 2017). They can be used as paleoenvironmental indicators and for biostratigraphy, providing the ages of speciation and extinction events, as well as supplying evidence of age diagnostic dispersals of characteristic taxa/assemblages. Influxes of these microorganisms into a basin may occur as the result of interconnection with another basin and dinocysts can therefore be useful indicators of the open gateways between adjacent basins and the resultant changes in conditions (e.g. Grothe et al., 2018). In the case of the MSC, presence of *in situ* marine and/or Paratethys dinocyst assemblages in a marginal basin are likely to indicate the presence of Atlantic and/or Eastern Paratethys water (respectively) in the Mediterranean and (relatively) high water level conditions (e.g. Pellen et al., 2017).

Palynological studies on the late Messinian Mediterranean dinocysts record are rather scarce, confined to a limited number of outcrops (Malaga Basin, Do Couto et al., 2014; Northern Apennines, Bertini, 2006; Popescu et al., 2007; Iaccarino et al., 2008; Cosentino et al., 2012; Pellen et al., 2017; Caltanissetta Basin, Londeix et al., 2007) and deep wells (976B, 977A, 978A and 134B, Popescu et al., 2015). These studies describe substage 3.1 as being barren of dinocysts. By contrast, substage 3.2 dinocyst assemblages are diverse particularly a few meters/tens of meters below the Miocene/Pliocene boundary and show recurrent vertical variation in abundance between brackish, Paratethyan-type taxa and marine stenohaline and euryhaline species. Taxa with Paratethyan affinities are largely considered to be autochthonous by all aforementioned authors. The extent to which reworking may have affected the marine assemblages is more controversial and debated between none (in Malaga and in the Apennines; Popescu et al., 2007; Do Couto et al., 2014; Pellen et al., 2017), partial (in the uppermost part of the Sicilian Upper Gypsum; Londeix et al., 2007) and total (in the Apennines; e.g. Bertini, 2006; Iaccarino et al., 2008; Cosentino et al., 2012). Given the extent of the implications (i.e. re-establishment of a Mediterranean-Atlantic flow or connection earlier than the Zanclean; e.g. Pellen et al., 2017), this is an issue that will require further clarification.

A key dinocyst influencing our understanding of the late Miocene Lago-Mare phase is *Galeacysta etrusca* (Fig. 9b; see Bertini and Corradini, 1998; Popescu et al., 2009 and Grothe et al., 2018 for more insights). This species was originally described from sediments in the Mediterranean (Corradini and Biffi, 1988), but has since been discovered in much older deposits in Paratethys (Magyar et al., 1999a, 1999b). The earliest recorded occurrence of *Galeacysta etrusca* is in sediments from the Pannonian Basin dated at ~8 Ma (Magyar et al., 1999a, 1999b). It subsequently dispersed throughout Paratethys at ~6 Ma and was present in the Black Sea throughout the MSC interval (Grothe et al., 2014, 2018). Despite a Mediterranean-Eastern Paratethys connection that is thought to have been established at ~6.1 Ma (Krijgsman et al., 2010; Van Baak et al., 2016; Grothe et al., 2020), *G. etrusca* is not found in the Mediterranean during MSC Stages 1, 2 and 3.1 (5.97-5.42 Ma; Bertini, 2006, Londeix et al., 2007, Manzi et al., 2007, Iaccarino et al., 2008, Gennari et al., 2013) and is only reported in the uppermost part of the Lago-Mare phase, very close to the transition to the Pliocene (e.g. Bertini, 2006; Londeix et al., 2007; Popescu et al., 2007; Iaccarino et al., 2008; Cosentino et al., 2012; Pellen et al., 2017). This implies that *Galeacysta etrusca* may have migrated from Paratethys into the Mediterranean after 5.42 Ma or that environmental conditions in the Mediterranean and in its marginal basins were only suitable for this species (and more generally the whole dinocysts Paratethyan contingent) to proliferate in the uppermost Messinian. Several authors report multiple occurrences of *Galeacysta etrusca* within the Zanclean (e.g. Clauzon et al., 2005; Londeix et al., 2007; Popescu et al., 2007, 2015; Do Couto et al., 2014; Clauzon et al., 2015), but these interpretations are based on the use of an alternative stratigraphic model for the MSC sections (Fig. 4b; see Grothe et al., 2018 for details).

5.3. Diatoms

Among the fresh-brackish organisms found in Stage 3 sediments are also species of diatoms. To date (and to our knowledge), there are no onshore studies that have ever looked for these organisms. By contrast, two samples from DSDP Site 124 in the Algero-Balearic Basin (Fig. 2b) revealed the presence of littoral planktonic forms accompanied by brackish water, and even freshwater, euryhaline, benthonic, and epiphytic species in considerable numbers (Hajós, 1973). Diatoms of undisclosed paleoecological significance are also reported from the ~60 cm-thick mudstone bed between an anhydrite and halite bed found in the last core of Site 134 (Ryan et al., 1973). According to Hajós (1973) and Ryan (2009), the diatoms found in these drill cores attest to an

extremely low salinity and a base level in the Balearic and Valencia basins below wave action. Further study of these indicative species and a wider distribution is required to apply this interpretation more generally.

5.4. Foraminifera

A reasonably diverse benthic and planktic foraminiferal assemblage containing no age-diagnostic taxa have been found co-occurring with the brackish Paratethyan fauna in both the onshore and offshore record throughout the Mediterranean (Fig. 2b for localities and references).

The benthic foraminifera assemblage is dominated by euryhaline representatives of the genus *Ammonia*, which today dwell in marginal marine (lagoons, estuaries, fjords and deltas) and lacustrine environments at depths < 50 m and tolerate salinities of up to 50‰ (Milker and Schmiedl, 2012; Consorti et al., 2020). *Ammonia tepida* and *Ammonia beccari* (Fig. 9c) are by far the most abundant species in both onshore (see Fig. 2b for localities and references) and offshore (e.g. Site 968A, Blanc-Valleron et al., 1998; Sites 375, 376, 965-968, Orszag-Sperber, 2006) localities, where they co-occur with ostracods belonging to Biofacies 1. Other commonly occurring benthic euryhaline taxa are *Elphidium* sp., *Cribroelphidium excavatum*, *Haynesina* sp., *Nonion* sp., *Quinqueloculina* sp., *Discorbis* sp. and T*richohyalus* sp., *Brizalina dentellata*, *Bulimina echinate* and *Bolivina* spp. (Ryan et al., 1973; Hsü et al., 1978a, 1978b; Rouchy et al., 2001, 2003, 2007; Iaccarino et al., 2008; Caruso et al., 2020). These species are frequently mixed with poorly preserved and older in age bathyal species (e.g. Caruso et al., 2020).

Planktic foraminifera are represented both by species whose last occurrence pre-dates the MSC (e.g. *Praeorbulina* spp., *Paragloborotalia partimlabiata*, P. *siakensis*, *Neogloquadrina atlantica praeatlantica*, *Globigerinoides subquadratus*, *Globorotalia saheliana, Globorotalia conomiozea, Acarinina sp., Hedbergella sp.*) and by taxa with extended biostratigraphic ranges (e.g. *Sphaeroidinellopsis seminulina, Turborotalita quinqueloba*, *Globorotalia miotumida, Globoturborotalita decoraperta*, *Neogloboquadrina acostaensis*, *Neogloboquadrina* spp., *Orbulina universa*, *Globigerinoides trilobus, Globigerinoides obliquus, Globorotalia scitula, Globigerina bulloides*, *G. Mediterranea* and *G. humerosa*; see Fig. 2b for references).

The mixing of foraminifera species with different ecological and salinity requirements and the widespread agreement that the brackish Paratethyan fauna are autochthonous (see subsection 5.1) has always complicated the interpretation of the origin of the foraminiferal assemblages. Among the benthic species, *Ammonia* taxa and the other benthic euryhaline taxa are generally considered autochthonous because they are typically well-preserved and their ecological and salinity requirements could be compatible with those of the Paratethyan ostracods.

The habitat of these benthic foraminifera today in environments both influenced by and disconnected from the open ocean indicates that the Stage 3 sediments in which they occur were deposited in a shallow-water environment subject to salinity fluctuations (Caruso et al., 2020 and references therein), but they do not provide insights into the water provenance. By contrast, the poor preservation, older age and low diversity of the bathyal taxa strongly suggest that these species are reworked (Bassetti et al., 2006; Iaccarino et al., 2008; Caruso et al., 2020). Their mode of life is also incompatible with the shallower water elements of the faunal assemblage. The planktic species which went extinct before the MSC are also undoubtedly reworked (Iaccarino et al., 2008; Caruso et al., 2020). It is more challenging to discriminate between i*n situ* and reworked specimens of the long range Neogene taxa. Most of them are considered to be reworked because of their scarcity, their occurrence with *in-situ* brackish organisms and their poor preservation (e.g. Iaccarino et al., 2008; Caruso et al., 2020). A more complex controversy surrounds the long-range dwarf specimens (Fig. 9c) occurring in onshore substage 3.1 (di Tetto Fm. in the Trave section; Iaccarino et al., 2008) and Lago-Mare sediments (Upper Mb. of the Nijar Feos Fm., Fortuin and Krijgsman, 2003; Aguirre and Sánchez-Almazo, 2004; Bassetti et al., 2006; Sorbas Basin, Roveri et al., 2019a; Bajo Segura Basin, Corbí and Soria, 2016; Colombacci Fm. in Northern Apennines localities, Casati et al., 1976; Colalongo et al., 1976; Rio and Negri, 1988; Popescu et al., 2007; Cyprus, Rouchy et al., 2001) and in some offshore localities (e.g. Sites 124, 125, 129A, 132, 134, 372, 376, 653, 974B, 975, 978; Cita, 1973; Cita et al., 1978; Kastens et al., 1987; Cita et al., 1990; Iaccarino and Bossio, 1999). This fauna is variably interpreted as:

1) reworked and size-sorted during transport, therefore lacking any paleoenvironmental significance (e.g. Kastens et al., 1987; Iaccarino and Bossio, 1999; Fortuin and Krijgsman, 2003; Bassetti et al., 2006);

2) *in situ* and indicating normal marine conditions (Aguirre and Sánchez-Almazo, 2004; Braga et al., 2006) or temporary Atlantic incursions (Rouchy et al., 2001);

3) *in situ* and indicative of high-stress environments (Keller and Abramovich, 2009), such as restricted and/or diluted marine environments (Corbí and Soria, 2016; Corbí et al., 2016, 2020). However, the paleoecological significance of dwarfism in foraminifer tests is not well understood and, given its potential implications for the Lago-Mare environment, it needs to be explored in greater detail.

5.5. Calcareous nannofossils and the C. acutus conundrum

Calcareous nannofossils are the fossil remains of coccolithophores, single-celled marine algae which dwell in the eutrophic and photic zone of the ocean (e.g. Ziveri et al., 2004). The potential recognition of marine calcareous nannofossils in marginal Stage 3 deposits would therefore have implications for the Mediterranean base-level and the hydrological riddle of MSC Stage 3. However, like foraminifera and dinocysts, the *in situ* versus reworking issue also impacts the nannoflora.

MSC Stage 3 is crossed by three important nannofossil bio-events astronomically calibrated in the ocean record: the top of *Discoaster quinqueramus* at 5.537 Ma, the base of *Ceratolithus acutus* at 5.36 Ma and the top of *Triquetrorhabdulus rugosus* at 5.231 Ma (Backman et al., 2012; Agnini et al., 2017). Most of the (few) studies that addressed the nannoflora component of Stage 3 deposits did not report taxa belonging to the biozones defined by these bio-events, but only taxa of Cenozoic and Cretaceous age, clearly physically reworked (e.g. Sites 132, 134, 653, 654A, 967A, 969B, Ryan et al., 1973; Hsü et al., 1978b; Müller et al., 1990; Castradori, 1998; Piedmont Basin, Trenkwalder et al., 2008; Violanti et al., 2009; Trave, Fonte dei Pulcini and Stingeti sections and Mondragone well in the Apennines, Cosentino et al., 2006, 2012, 2018; Iaccarino et al., 2008). An exception is the nannoflora observed in the uppermost Messinian sediments at Sites 978A, 975B and 967A (Levant Basin; Fig. 2b). Here, among the plethora of reworked and long-ranging Neogene taxa, Castradori (1998) reported the anomalous abundance of *Sphenolithus* spp (mostly *Sphenolithus gr abies/moriformis*). Although the assemblage points to the absence of a primary marine signature, the unlikely possibility that reworking and/or sorting lies behind the observed peak of *Sphenolithus* spp. led Castradori (1998) to conclude that at least one incursion of marine water occurred during the (uppermost) Lago-Mare.

By contrast, some authors (i.e. Popescu et al., 2007, 2015; Do Couto et al., 2014; Clauzon et al., 2015; Pellen et al., 2017) described the nannofossil assemblage the Lago-Mare LM Unit in Malaga, the Zorreras Member in Sorbas, the uppermost di Tetto/Colombacci Fm. in some Apenninic localities and offshore in the Alborán Basin as having good preservation and showing no erratic fluctuations, all characteristics that led to their interpretation as autochthonous and to the conclusion that these sediments were deposited in a Mediterranean already replenished of Atlantic water (Fig. 4b). In addition, these authors reported the low abundance, but continuous presence of the biostratigraphic markers for the Zanclean *Triquetrorhabdulus rugosus* and *Ceratolithus acutus* (Fig. 9d) below the formally defined Miocene/Pliocene boundary (Van Couvering et al., 2000) in several onshore and offshore Mediterranean (as wells as Paratethyan) localities (see Popescu et al., 2017 for details and a

complete list of finding locations).

Such findings (especially that of *C. acutus*) are in sharp disagreement with most of the existing literature and have resulted in an important debate amongst the MSC community (e.g. Popescu et al., 2007, 2008 vs Roveri et al., 2008c and Stoica et al., 2016 vs Popescu et al., 2017), not only for their paleoenvironmental implications (i.e. presence of Atlantic water in the Mediterranean), but also for the chronostratigraphic repercussions (Fig. 4b). The chronostratigraphic value of *C. acutus* lies in its short temporal distribution straddling the M/P boundary (astrochronologically calibrated at 5.332 Ma; Van Couvering et al., 2000; Lourens et al., 2004). However, the corresponding biozone is established in oceanic areas (Zone CNPL1: 5.36-5.05 Ma; Backman et al., 2012; Agnini et al., 2017) and is considered not applicable to the Mediterranean region during the MSC due to the harsh physicochemical conditions that are unsuitable for marine biota (Di Stefano and Sturiale, 2010). The interpretation of these nannofossil assemblages in the westernmost areas of the Mediterranean has been countered with several observations: (1) the observation of these age-diagnostic taxa is often not replicated by other studies (e.g. Roveri et al., 2008a; Van Baak et al., 2015; Krijgsman et al., 2020b); (2) *Ceratolithus acutus* is very rare also in fully marine open-ocean sediments (e.g. Di Stefano and Sturiale, 2010); (3) despite being rare in the late Messinian Mediterranean, this species has never been documented together with other long-range taxa, generally predominant in the assemblage, in Stage 3 deposits (see discussion in Krijgsman et al., 2020b). Recently, Golovina et al. (2019) showed that the morphology and size of *C. acutus* overlaps with the shape and dimensions of destroyed ascidian spicules (i.e. calcareous elements produced by benthic tunicates; Fig. 9d), providing an explanation for erroneous identification of *C. acutus* in the Black Sea Basin (Golovina et al., 2019) and perhaps in the western Mediterranean Lago-Mare sediments as well.

5.6. Fish

Fossil fish remains provide information about salinity and depth and have been used to contradict the brackish nature of the Lago-Mare deposits by Carnevale et al. (2006a, 2006b, 2008, 2018) and Grunert et al. (2016). Euryhaline fish species inhabit marine to brackish environments and dominate settings with strong salinity variations while stenohaline fish have specific salinity requirements (marine, brackish, or freshwater) and cannot survive under different conditions. Demersal fish (i.e. those living in or immediately above the sea floor) have specific depth requirements, whereas pelagic fish occupy the water column within a wide range of depth variable from species to species. Fossil fish remains are found either as articulated or disarticulated skeletal parts, including teeth and otoliths, which are identified to the species level. Articulated fish skeletons typically indicate autochthonous deposition because of the difficulty in reworking and transporting intact skeletons. Otoliths and fish teeth are much more likely to be transported.

Otoliths and rare articulated skeletons (Fig. 9e) of marine and Paratethyan species have been reported from Stage 3 deposits, but commonly huge volumes of sediment are required to find even quite small numbers of these fossils (e.g. 20 tons from Moncucco, 6 tons from Cava Serredi, 700 kg from Capanne di Bronzo; Schwarzhans et al., 2020), much more than what is expected for normal marine deposits (i.e. $<$ 30 kg; Agiadi et al., 2017; Karakitsios et al., 2017b).

Substage 3.1 sediments contain articulated skeletons (Fig. 9e) of the marine fish species *Lampanyctus licatae* and *Maurolicus muelleri*, and the shallow water, euryhaline species *Aphanius crassicaudus* in the Lower Feos Member in the Nijar Basin (de la Chapelle and Gaudant, 1987) and the marls of the first UG cycle in the Polemi Basin (Manzi et al., 2016a; Fig. 3a). Cava Serredi (Tuscany), Verduno and Moncucco (Piedmont) are the only other localities in which fish remains (only otoliths) in (claimed) substage 3.1 sediments are known (Carnevale et al., 2006a, 2008, 2018; Grunert et al., 2016).

The more diverse and abundant ichtyofaunal record occurs in substage 3.2 in a few marginal sections on the Italian peninsula (Ciabot Cagna in the Piedmont Basin; Cava Serredi and Podere Torricella in Tuscany; Capanne di Bronzo, La Vicenne and Ca' Ciuccio in thrust-top basins of the Northern and Central Apennines). The Lago-Mare fish remains mainly comprise otoliths of both euryhaline and stenohaline taxa indicative of marine, brackish, and freshwater habitats (Carnevale et al., 2018). Three articulated skeletons of the euryhaline marine taxa *Mugil* cf. *cephalus* (Fig. 9e), the marine Indo-Pacific species *Spratelloides gracilis* and of *Gobius* sp. have been identified at Cava Serredi in a horizon $<$ 1 m below the Miocene/Pliocene boundary (Carnevale et al., 2006b). The dominant stenohaline families in these assemblages are Gobiidae, a family of demersal fish occupying shallow-water marine, brackish and freshwater environments, and Myctophidae, which are marine mesopelagic fish that live below 200 m depth during the day, but feed at night in surface waters. A recent review of the Tortonian-Zanclean Gobiidae of the Mediterranean (Schwarzhans et al., 2020) showed that the otoliths of this family, described by Carnevale et al. (2006a, 2008, 2018) and Grunert et al. (2016) as belonging to marine Atlantic species, instead belong to brackish and freshwater species of Paratethyan affinity inhabiting sheltered prodelta environments. In fact, no normal marine demersal taxa were recognized in these assemblages by Schwarzhans et al. (2020). As for the Myctophidae, the vast majority of the taxa belonging to this family were recovered in Moncucco and Verduno from alluvial plain silty mudstones along with terrestrial mammals (Dela Pierre et al., 2011; Colombero et al., 2017 and references therein), pointing to a physically reworked origin. When $^{87}Sr/^{86}Sr$ isotope ratios are measured (Carnevale et al., 2008; Grunert et al., 2016), the resulting Sr-based age of the otoliths is $>$ 7 Ma, therefore further arguing against their in-situ origin. Since the good preservation of the otoliths suggests they did not suffer physical reworking (Carnevale et al., 2006a, 2006b, 2008, 2018; Grunert et al., 2016), predators foraging in open marine settings and migrating to marginal environments are proposed as a way out of the enigma (Carnevale et al., 2008, 2018; Grunert et al., 2016; Colombero et al., 2017). However, Carnevale et al. (2006a) also rule out that so well preserved otoliths may have suffered post-mortem transport and action of the digestive acids in the stomach of predators. Rare findings of Myctophidae from Ciabot Cagna (3 species), Cava Serredi (1 species), Capanne di Bronzo (1 species) and Podere Torricella (6 species) (Carnevale et al., 2018) are all from sections where the host sediments have not been studied in sufficient detail to be clear about the *in situ* or reworked nature of the fossil assemblage. This lack of sedimentological uncertainty also extends to the stratigraphic position of many samples, because a stratigraphic log is provided for only a few sections (i.e. Ca' Ciuccio, Cava Serredi and Moncucco; Carnevale et al., 2006a, 2006b). What this stratigraphic information suggests is that euryhaline fish taxa are widespread throughout substage 3.2, whereas strictly Myctophidae, which are an oceanic, marine stenohaline species, only occur very close to the base of the Pliocene, plausibly corresponding to the uppermost lithological cycle in substage 3.2 (~5.35-5.33 Ma; Carnevale et al., 2018).

5.7. Summary of the Stage 3 paleontological record

The aquatic fossil record of MSC Stage 3 indicates that substage 3.1 in onshore sections is mostly barren, while diverse assemblages characterize substage 3.2 deposits. By contrast, the deep record as a whole contains relatively few, low diversity assemblages. This might be as a consequence either of the limited sample locations recovered from the offshore areas (see Fig. 2b) or because the environmental conditions in the intermediate-deep basins were less favorable for sustaining the life forms typical of the onshore domain. Nevertheless, the assemblages that are found in both marginal and deep locations comprise mixed brackish and marine species.

Brackish species are mostly represented by ostracods and dinocysts (and mollusks here not addressed because poorly studied; see Esu, 2007 and Guerra-Merchán et al., 2010). Prominent is the affinity of these late

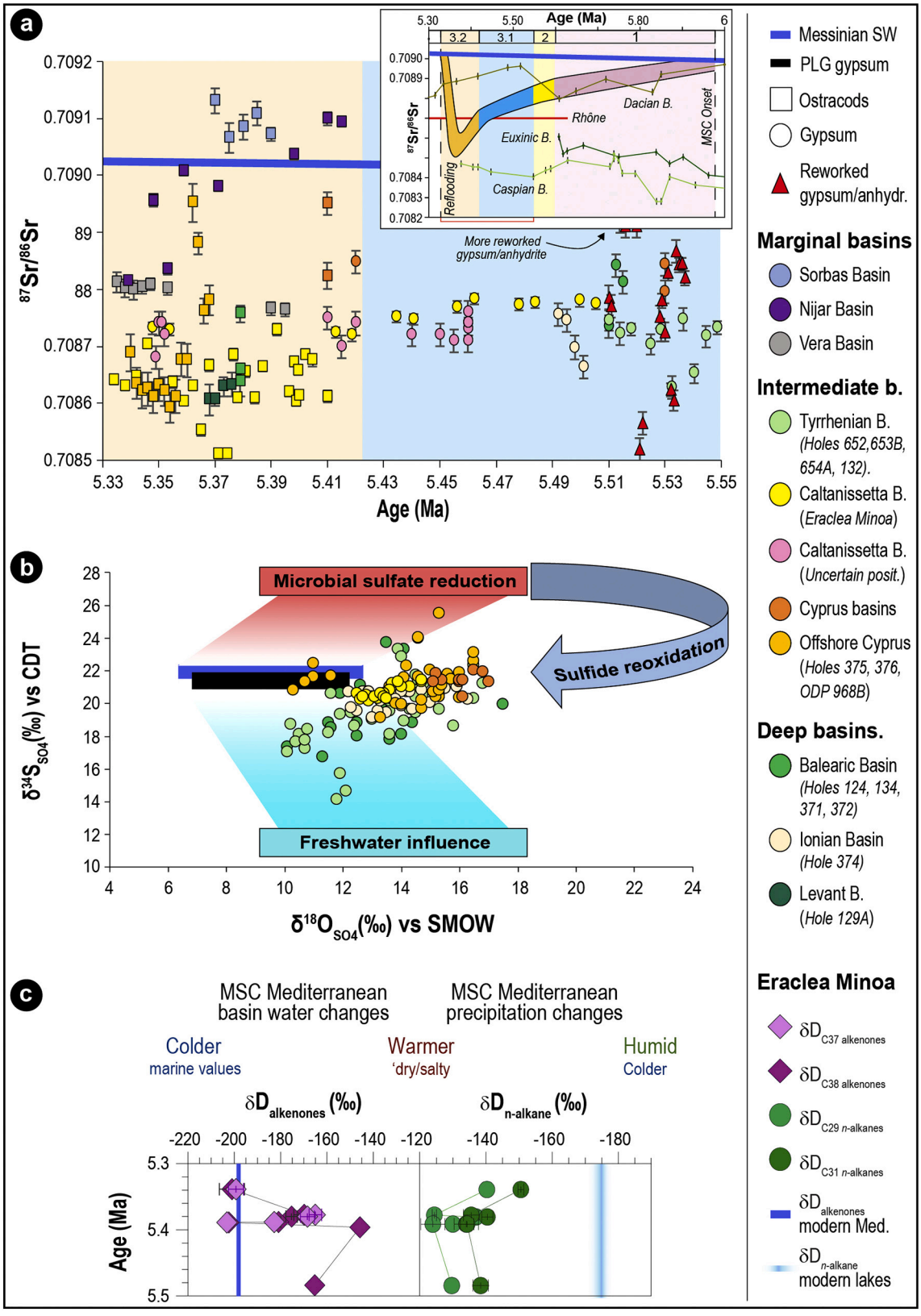

(caption on next page)

Fig. 10. Isotopic record of MSC Stage 3 for the Mediterranean Basin. (a) Compilation of MSC Stage 3 $^{87}Sr/^{86}Sr$ isotope data sourced from ostracod valves and gypsum crystals (see Supplementary material 1 and subsection 6.1 for references). Data are plotted with the global $^{87}Sr/^{86}Sr$ seawater curve (McArthur et al., 2012). Error bars indicate analytical error, which is so small in some cases that no error bars are visible at this scale. To not complicate the figure, horizontal error bars have not been added for the sections/cores unprovided of a chronostratigraphic framework and for which age uncertainties are present (i.e. all but Nijar and Vera basins, Eraclea Minoa and onshore Cyprus; see Fig. 3). Note that none of the $^{87}Sr/^{86}Sr$ isotope ratios but one from Nijar plot on the ocean curve. In the inset is shown the Mediterranean Sr record for the entire MSC as well as the time-equivalent Eastern Paratethys record (modified after Andreetto et al., 2021). (b) Plot of $\delta^{34}S_{SO4}$ and $\delta^{18}O_{SO4}$ in Stage 3 gypsum and anhydrite beds from onshore and offshore localities (see Supplementary material 1 and subsection 6.2 for references). No measures are available from the marginal basins, where gypsum did not deposit during Stage 3. The dark blue and black rectangles represent the sulfate isotopic composition of the Global Messinian ocean and Stage 1 (PLG) evaporites, respectively. The light blue area represents the sulfate isotopic composition of mixtures of Messinian marine waters with non-marine sources. The red area represents the isotopic composition of the residual sulfate ion in a basin where marine Messinian sulfate is consumed by microbial sulfate reduction to produce H_2S. The arrow represents the isotope trajectory of dissolved sulfate resulting from the mixing of residual ^{34}S-enriched sulfate produced by MSR and ^{34}S-depleted sulfate produced by H_2S oxidation. All the published $\delta^{34}S_{SO4}$ and $\delta^{18}O_{SO4}$ values are provided corrected with the fractionation factors $\delta^{34}S$=+1.65‰ and $\delta^{18}O$=+3.5‰ to smooth the isotopic fractionation effects experienced by dissolved sulfate and to reason on values reproducing the isotopic composition at the time of gypsum precipitation. (c) δD isotopes of C_{29} and C_{31}*n*-alkanes and C_{37} and C_{38} long chain alkenones recorded in the Stage 3 gypsums and marls of the Eraclea Minoa section (modified from Vasiliev et al., 2017). Blue lines indicate the values recorded in the present day lacustrine settings for the *n*-alkanes (Sachse et al., 2006) and in the alkenones from the Mediterranean in the recent times (Van der Meer et al., 2007). Error bars indicate standard errors of the mean.

Messinian Mediterranean brackish species with the same species that were simultaneously dwelling in the Eastern Paratethyan basins (Dacian, Euxinic and Caspian) and in the North Aegean. Since these organisms were not present in the Mediterranean at any time before the MSC, they are considered, with a broad consensus, as *in situ*. This conclusion is further corroborated by the mixing of adult and juvenile forms in the ostracod assemblages and by the good preservation of the specimens, which do not show typical evidence of physical reworking like abrasion, dissolution, or fragmentation. Still problematic is the time of their arrival in the Mediterranean and their likelihood as biostratigraphic tool. From our review it seems more likely that truly Paratethyan species of ostracods entered the Mediterranean already during substage 3.1, when they colonized intermediate-deep settings, while they entered the marginal basins at different times during substage 3.2. As for dinocysts, characteristic is their occurrence only in the uppermost Messinian. However, it must be noted that samples from the substage 3.1 interval are rarely processed for dinocysts, especially in age model-equipped sections (Fig. 3a). The route followed by the Paratethyan immigrants is equally contested and important for paleoenvironmental and paleohydrological interpretations. In view of a desiccated Mediterranean, their migration can only have taken place passively by means of aquatic migratory birds. Conversely, the homogeneity of the ostracod assemblages throughout the Mediterranean marginal basins is more indicative of the presence of a water body fed by Eastern Paratethys and connecting all Mediterranean subbasins, therefore implying relatively high water-level conditions (at least at times when ostracod-bearing sediments deposited; see Andreetto et al., 2021).

Marine assemblages are composed by foraminifera, nannofossils, dinocysts and calcareous nannofossils. Their reworked or *in situ* nature is in many cases contested but critical for paleoenvironmental interpretation. The picture that emerges from our review is that an open marine signature is questionable in the foraminifera, nannofossils, dinocyst and fish records, as well as in other biotic groups (e.g. corals, echinoids and mammals) here not tackled (and for which we refer the reader to Dominici et al., 2018 and Carnevale et al., 2019). All marine representatives of the above mentioned categories were reintroduced into the Mediterranean only at the beginning of the Pliocene and at the expense of the Paratethys species that, instead, disappeared. Collectively, these observations lead us to conclude that the marine model as conceived by Carnevale et al. (2006a, 2006b, 2008, 2018) and Grunert et al. (2016) has no foundation and therefore will not be further discussed.

6. The geochemical perspective

Variations in the water sources draining into the Mediterranean are expected to be reflected also in (geo)chemical properties of the paleodepositional environments. Important information about the nature of the connectivity framework of the Mediterranean can be gained by interpreting geochemical signals that respond to the presence or absence of an exchange with a chemically-unique water body. Four main geochemical proxies have been applied so far to MSC Stage 3 sedimentary and paleontological records. These includes both radiogenic (Sr isotope ratios) and stable isotopes (sulfate and oxygen) measured on fossils and minerals and hydrogen isotopes on molecular biomarkers. This section summarizes the dataset available for geochemical proxies (Fig. 10; Supplementary material 1) and its interpretation(s) for MSC Stage 3.

6.1. Strontium isotope ratios ($^{87}Sr/^{86}Sr$)

The available strontium isotope data for Stage 3 (Fig. 10a; Supplementary material 1) derive from measurements on both Ca-bearing fossils (ostracod valves, mollusk shells, fish otoliths; Fig. 9a) and minerals (calcite and gypsum), where Sr^{2+} dissolved in an aqueous solution substitutes Ca atoms due to their similar ionic radius (e.g. Hajj et al., 2017). Here we screen the available dataset and discuss only results that (1) reflect the original primary isotopic signal, i.e. the isotopic signal of the fluid at time of shell calcification or mineral precipitation, and (2) for which timing of mineral precipitation can be constrained. This screening excludes bulk carbonate samples (e.g. *Colombacci* limestones; Bassetti et al., 2004), which contain carbonate compounds of various and/or unknown provenance, measurements from mollusk shells and otoliths (e.g. Carnevale et al., 2008; Grunert et al., 2016; Roveri et al., 2019a), because they are made of mineral phases easily altered during diagenesis (e.g. aragonite; Marcano et al., 2015), and data coming from reworked material (e.g. all reworked gypsum or transported foraminifera). $^{87}Sr/^{86}Sr$ isotope ratios have also been measured by Müller and Mueller (1991) and Roveri et al. (2014b) on the halite beds recovered at Sites 134, 374 and 376 (Ryan et al., 1973; Hsü et al., 1978b). Although they provide interesting interpretative aspects, we do not consider these Sr measurements because the position of Sr in the crystal lattice of halite is unknown and the removal of all contaminants, that is not a straightforward procedure (see Meilijson et al., 2019), is not clear it was achieved by Müller and Mueller (1991) and Roveri et al. (2014b). As a matter of fact, there is no consistency between data generated from roughly the same interval in Core 134 by Müller and Mueller (1991) (0.708968) and Roveri et al. (2014b) (0.708800-0.708896). Added to this is the uncertainty over the provenance of halite in Sites 134 and 374 (see subsections 4.2 and 4.6.1), which violates both criteria mentioned above.

The general trend of the Mediterranean $^{87}Sr/^{86}Sr$ isotope ratio during the MSC deviates from the ocean curve towards the less radiogenic values of the major peri-Mediterranean rivers and Paratethys and returns abruptly to oceanic values at the Miocene/Pliocene boundary (Fig. 10a inset). This trend is regarded to reflect the progressive restriction of Mediterranean-Atlantic exchange and the relative increase in

the proportion of non-marine source waters (Topper et al., 2011; Roveri et al., 2014a). At first glance it seems that each MSC Stage was characterized by a well-defined range of Sr ratios (Fig. 10a inset), an observation that led Roveri et al. (2014b) to attribute a chronostratigraphic value to MSC $^{87}Sr/^{86}Sr$ ratios. A closer look, however, shows that MSC substages are anything but homogeneous with respect to $^{87}Sr/^{86}Sr$ ratios. At least in the marginal basins, local lithological differences in the catchments (each lithology carries a unique $^{87}Sr/^{86}Sr$ fingerprint; see subsection 8.1.1) explain the different Sr isotopic compositions from basin to basin (see Schildgen et al., 2014; Modestou et al., 2017; Andreetto et al., 2021), therefore arguing against the use of $^{87}Sr/^{86}Sr$ ratios for chronostratigraphic purposes in the MSC record.

Most of the data characterizing substage 3.1 (Fig. 10a) are from the Eraclea Minoa gypsum (Fig. 5h). These data define a narrow range of Sr isotope ratios between 0.708747 and 0.708793 (García-Veigas et al., 2018). Similar values were reported from both Eraclea Minoa and the nearby Siculiana Marina section (0.708710-0.708760; Keogh and Butler, 1999; Fig. 5i). The dominance of Sicily samples gives the appearance of a consistent Sr isotope signal for gypsum beds. However, data points from elsewhere (Cyprus, Manzi et al., 2016a; DSDPs 122, 371 and 372 in the Algero-Balearic Basin, ODPs 652, 653 and 654 in the Tyrrhenian Basin, DSDP 374 in the Ionian Basin; Müller et al., 1990; Müller and Mueller, 1991; Roveri et al., 2014b) display a wider range (from ~0.7087 to 0.708847; Fig. 10a) that may indicate a different hydrological regime for each basin (e.g. Müller et al., 1990; Müller and Mueller, 1991; Ryan, 2009). The one published Sr isotope value for ostracods found within one of the marl interbeds at Eraclea Minoa also has a lower value outside the typical Sicily gypsum range (Grossi et al., 2015). This suggests that a different hydrological regime may also have characterised precession minima stages of the precessional cycle.

The Sr isotope dataset for the Lago-Mare phase includes the lowest values measured on MSC sediments (~0.7085 from between gypsum VI and VII at Eraclea Minoa; Fig. 3a; Grossi et al., 2015) and the widest range of ratios spanning from 0.7085 to 0.7091, which is above coeval oceanic values (Fig. 10a). Again, the conspicuously high Sr isotope values in substage 3.2 come from two areas, the marginal basins of southern Spain (Andreetto et al., 2021 and references therein; Figs. 5a-c) and the intermediate Polemi Basin on Cyprus (McCulloch and De Deckker, 1989). The lower values are drawn from right across the intermediate-deep Mediterranean (Algero-Balearic, Sicily, Levant; Fig. 2a) and are therefore more likely to represent a Mediterranean-wide Sr isotope signal.

New Sr isotope data from Eastern Paratethys (i.e. Dacian and Caspian basins; Fig. 2b) are now available for the interval corresponding to MSC Stage 3 (inset Fig. 10a). The $^{87}Sr/^{86}Sr$ ratios of the Dacian Basin (0.708865-0.708982; Vasiliev et al., 2010; Grothe, 2016) are slightly lower than coeval ocean water (0.709020), but much higher than coeval Mediterranean values. However, the Dacian Basin is regarded as highly restricted from the Mediterranean throughout the MSC (Vasiliev et al., 2010). By contrast, the Caspian has very low values (0.708402 to 0.708473, Grothe et al., 2020) which are thought to reflect both the very low Sr isotope ratio of the Volga river (0.708020; Vasiliev et al., 2010 and references therein) and some input from the Mediterranean (Grothe et al., 2020).

6.2. Sulfate isotopes

Sulfur isotopic investigations have been carried out only on sulfate minerals (gypsum and more rarely anhydrite) of the MSC Stage 3 deposits with samples drawn from both onshore intermediate sequences (Caltanissetta Basin and Cypriot basins) and deep basinal records (Sites 122, 124, 125A, 132, 134, 372, 374, 375, 376, 652, 653, 654, 968, 969, 970; Fig. 10b; Fontes et al., 1973; Pierre, 1974, 1982; Pierre and Fontes, 1978; Ricchiuto and McKenzie, 1978; Pierre and Rouchy, 1990; Blanc-Valleron et al., 1998). Because the incorporation of dissolved sulfate into gypsum produces a nearly constant fractionation of $\delta^{18}O$ (+3.5‰) and $\delta^{34}S$ (+1.65‰) at earth surface temperatures (Thode and Monster, 1965; Lloyd, 1968; Warren, 2016), $\delta^{18}O$ and $\delta^{34}S$ isotopic values measured in gypsum should be corrected with the above mentioned fractionation factors in order to reconstruct the sulfate isotopic composition of the basin waters at the time of gypsum formation.

The deep Mediterranean samples exhibit a wide range of $\delta^{34}S_{SO4,}$ but the majority of samples display $\delta^{34}S_{SO4}$ values between 18 and 22‰, strongly indicative of a marine origin of the sulfate forming the gypsum (Fig. 10b; Fontes et al., 1973; Pierre, 1974, 1982; Pierre and Fontes, 1978; Pierre and Rouchy, 1990; Blanc-Valleron et al., 1998). The $\delta^{34}S_{SO4}$ values lower than marine sulfate in the dataset are generally considered to represent a greater influence of continental sulfate input to the basin (Fig. 10b; Pierre, 1974; Pierre and Fontes, 1978; Pierre and Rouchy, 1990). By contrast, the data display $\delta^{18}O_{SO4}$ isotopic values that deviate substantially from marine $\delta^{18}O_{SO4}$ values towards higher values (Fig. 10). This is consistent with the influence of sulfate produced by reoxidation of reduced sulfur compounds generated by microbial sulfate reduction (MSR; Kaplan and Rittenberg, 1964; Brunner and Bernasconi, 2005; Sim et al., 2011; Leavitt et al., 2013). The microbial use of SO_4^{2-} leads to an equilibration of $\delta^{18}O_{SO4}$ with ambient water oxygen, whereas the $\delta^{34}S_{SO4}$ returns towards its initial value as a higher fraction of sulfide produced by MSR is re-oxidated. This mechanism has been suggested for Sites in the Algero-Balearic, Tyrrhenian and Ionian basins and offshore Cyprus (Pierre, 1974; Pierre and Fontes, 1978; Pierre and Rouchy, 1990). Although some authors have suggested that partial equilibration of sulfate oxygen toward $\delta^{18}O_{H2O}$ values of the basin enriched in heavy oxygen isotopes by evaporation have led to an increase in $\delta^{18}O_{SO4}$ values without significant changes in $\delta^{34}S_{SO4}$ (Fontes et al., 1973; Pierre, 1974; Ricchiuto and McKenzie, 1978), this hypothesis seems highly unlikely as the abiotic equilibration between sulfate and water oxygen take about 20 Myr at normal marine pH (Lloyd, 1968; Longinelli and Craig, 1967; Turchyn et al., 2006). Moreover, the microbial sulfate reduction process is supported by the presence of pyrite at Sites 132, 654A and 968 (Pierre, 1982; Pierre and Rouchy, 1990; Blanc-Valleron et al., 1998) and the existence of filaments of possible microbial origin at Site 654A (Pierre and Rouchy, 1990).

The sulfate isotopic values reported by Longinelli (1979) and Pierre (1982) from the Upper Gypsum of Eraclea Minoa (Caltanissetta Basin, Sicily) are considerably more scattered than those from a recent study by García-Veigas et al., 2018; Fig. 10b). Such discrepancies are probably a consequence of different sample selection: García-Veigas et al. (2018) analyzed only pristine whitish selenite and balatino samples, while Longinelli (1979) and Pierre (1982) analyzed all types of gypsum-bearing samples such as "gypsiferous marl" and gypsum laminae intercalated in carbonate or diatomaceous intervals. These less pristine samples probably contain high quantities of ^{34}S-depleted solid sulfides or diagenetic gypsum formed by oxidation of sulfides (see Liu et al., 2017 for more details on this process) and are therefore unlikely to be representative of the primary gypsum facies. Once these data are excluded, the Eraclea Minoa sulfate values ($\delta^{18}O_{SO4}$ from 12.4 to 14.6‰ and $\delta^{34}S_{SO4}$ from 21.0 to 22.3‰) suggest a marine origin of the sulfate and stable redox conditions during gypsum deposition (Fig 9.b; García-Veigas et al., 2018). Interestingly, the Eraclea Minoa sulfate values are in compliance with the isotopic values ($\delta^{18}O_{SO4}$=15.2 to 16.8‰; $\delta^{34}S_{SO4}$= 20.4 to 21.9‰) measured by Pierre (1982) in the Polemi Basin (Cyprus).

6.3. Hydrogen isotopes on molecular biomarkers

From the point of view of the application of organic geochemistry proxies, the Miocene Mediterranean Basin received little attention so far, with biomarker-based proxies that have been mostly applied to (a limited number of) pre-MSC sequences (Tzanova et al., 2015; Herbert et al., 2016; Mayser et al., 2017; Natalicchio et al., 2017, 2019; Vasiliev et al., 2019) and pre-Stage 3 sedimentary records (Lower Evaporites on Sicily, Andersen et al., 2001; Vena del Gesso Basin, Sinninghe Damsté

et al., 1995 and Vasiliev et al., 2017; Levant Basin, Meilijson et al., 2019). To date, only one study analyzed Stage 3 samples (Vasiliev et al., 2017). This study used compound specific hydrogen isotope (δD) analyses, measured on both terrestrial (long chain C_{29} and C_{31}*n*-alkanes; Sachse et al., 2006) and aquatic (alkenones; Englebrecht and Sachs, 2005) biomarkers from the gypsum beds of the Upper Gypsum at Eraclea Minoa to reconstruct the hydrological cycle during gypsum precipitation.

Both $\delta D_{C29n\text{-alkane}}$ and $\delta D_{alkenones}$ results (Fig. 10c) suggested that conditions in Sicily were significantly dryer than today, with highly enriched values of $\delta D_{C29n\text{-alkanes}}$ (up to −125‰). The $\delta D_{alkenones}$ varied between values suggesting evaporative conditions (−125‰) and values typical for present-day $\delta D_{alkenones}$ in the Mediterranean (−203‰) (Vasiliev et al., 2017).

No time-equivalent biomarker data from the open ocean settings are currently available. Instead, Vasiliev et al. (2017) compared their Mediterranean data with data from the Black Sea (DSDP 42B Hole 380 and Taman peninsula; Vasiliev et al., 2013, 2015). The Upper Gypsum $\delta D_{n\text{-alkanes}}$ were more enriched when compared to their time equivalent deposits of the DSDP 42B 380 borehole of the Black Sea (−180‰). This probably reflects the more intracontinental position of the Black Sea which commonly translates into more depleted values for $\delta D_{precipitation}$ used by the vegetation, resulting in more depleted $\delta D_{C29n\text{ -alkanes}}$. However, there is a 30 to 40‰ enrichment relative to present in the $\delta D_{n\text{-alkanes}}$ (i.e. $\delta D_{precipitation}$) in both Mediterranean and Paratethys domains, indicating concurrent changes in both areas during the latest phase of the MSC.

Both the Mediterranean and Paratethyan samples contain $\delta D_{alkenones}$ with low values (~-200‰) (Fig. 10c) leading Vasiliev et al. (2017) to suggest that either the surface water from the Upper Gypsum was derived from the Black Sea, or that the Mediterranean and Paratethys were exchanging surface water during gypsum precipitation. Similarity between the relative contribution of the C_{37}, C_{38} and C_{39} alkenones at Eraclea Minoa and one of the Black Sea samples may suggest common alkenone producers for the two areas, again supporting the idea of a Mediterranean-Paratethys connection during Stage 3 (Vasiliev et al., 2017).

A final speculative insight from this biomarker dataset is that the relative contribution of alkenones found in the Upper Gypsum of Eraclea Minoa is strikingly similar to present-day open marine samples, even though *Emiliania huxleyi*, the principal ocean alkenone producer today, did not exist in the late Miocene. Vasiliev et al. (2017) suggested that this could imply the existence of a connection to the open ocean during Upper Gypsum deposition in Sicily (i.e. throughout Stage 3; Fig. 3a).

6.4. Oxygen isotopes

Oxygen stable isotope data ($\delta^{18}O$) are available from bulk samples (Rouchy et al., 2001, 2003, 2007; Pierre et al., 2006; Cosentino et al., 2012), gypsum (Pierre and Fontes, 1978; Ricchiuto and McKenzie, 1978; Lugli et al., 2007), mollusk shells (Carnevale et al., 2008; Grunert et al., 2016) and ostracod valves (Cosentino et al., 2012; Grossi et al., 2015).

For all the sub-basins for which there is latest Messinian data (e.g. Sites 974 and 975; Eraclea Minoa section, Sicily; Aghios Stefanos section, Corfu; Kalamaki section, Zakynthos; Pissouri Basin, Cyprus; Rouchy et al., 2001, Pierre et al., 2006), each has its own range of oxygen isotopic compositions and its own degree of variability. Values from above the Miocene/Pliocene boundary regain seawater values of 0.3 to 1 ‰ (e.g. Pierre et al., 2006).

In marginal marine settings and lakes, the controls over $\delta^{18}O$ are poorly constrained as oxygen does not respond simply to the freshwater flux, but to a combination of variables such as temperature, rainfall and evaporation (e.g. Placzek et al., 2011). Freshwater input may contribute to the signal, resulting in $\delta^{18}O$ more negative than seawater (0.3‰ to 0.8‰ SMOW; Dettman et al., 2004), but under prevailing evaporating conditions it is likely that the $\delta^{18}O$ will be primarily influenced by evaporation, leading to $\delta^{18}O$ more positive than seawater (e.g. Dettman et al., 2004), making any data very difficult to interpret. Furthermore, the lack of a unique $\delta^{18}O$ signature for each water source makes oxygen isotopes a difficult tracer proxy to use.

6.5. Summary of the Stage 3 geochemical dataset

The variety of paleoenvironmental and connectivity proxies applied to MSC Stage 3 record provide valuable insights into the hydrological conditions during Stage 3. The more outstanding results from all discussed proxies are that:

1) Paleodepositional subaqueous environments where gypsum was precipitating and ostracods and biomarker-producers were thriving were strongly dominated by non-oceanic inputs;
2) an indisputable marine signal is absent and only regained above the M/P boundary.

Sulfate and oxygen isotopes are currently difficult to use for water provenance reconstruction because the non-marine sources (local and major rivers and Eastern Paratethys) that are likely to be of influence lack distinctive isotopic signatures and, especially for oxygen, respond to a combination of controls (e.g. temperature, rainfall, evaporation) with local variability. $\delta^{34}S_{SO4}$ are claimed by several authors to be an evidence of the presence of an Atlantic inflow ($\delta^{34}S_{SO4}$=22‰; Turchyn and Schrag, 2004) in a Mediterranean strongly affected by non-marine waters (Manzi et al., 2009, 2016a; García-Veigas et al., 2018 among others). However, the same values can be obtained by means of the recycling of PLG deposits (~23‰; Lu et al., 2001; Lugli et al., 2010; García-Veigas et al., 2018).

Similarities between the $\delta D_{alkenones}$ of the Upper Gypsum at Eraclea Minoa and coeval Black Sea sediments and $\delta D_{n\text{-alkanes}}$ similar to present-day marine settings, suggest that Eastern Paratethys and the Atlantic were simultaneously contributing to the Mediterranean hydrological budget. $^{87}Sr/^{86}Sr$ isotope ratios are a useful water-mass tracer because each water body carries a unique Sr isotope fingerprint (see subsection 8.1.1). Our plotting of Stage 3 $^{87}Sr/^{86}Sr$ isotope values (Fig. 10a) highlights the large geographical variability of the values and the sharp division between Sr isotope ratios measured in marginal basins versus those in intermediate-deep water locations. This is only noticeable in substage 3.2, since no (or not enough) material suitable for Sr analysis is present in substage 3.1 deposits from the marginal basins. Some authors see this variability as an indication of isolated subbasins with unique hydrological conditions driven by their catchment rivers (e.g. Müller et al., 1990; Müller and Mueller, 1991; Ryan, 2009). If some degree of connection was present, it involved only neighbouring basins (e.g. Tyrrhenian subbasins; Müller et al., 1990; Müller and Mueller, 1991). A recent comparison of the Sr isotope record of the Spanish marginal basins of Sorbas, Nijar and Vera with the Sr isotope ratios likely to have typified the local riverine sources demonstrated that a local sources-mixed signal expected from an endorheic lake in that location is absent. In this instance mixing of intrabasinal water sources with a non-marine Mediterranean water mass is used to explain the measured values (Andreetto et al., 2021). If this explanation is more widely applicable, then it may result in a re-interpretation of the spread of Sr isotope data from the latest Messinian interval.

To conclude, geochemical proxies have great potential to test the different scenarios, but data are currently too numerically and geographically limited to be robust.

7. Paleoenvironmental scenarios for freshening the salt giant: desiccated versus full Mediterranean

The riddle of the Mediterranean environmental and hydrological conditions during Stage 3 is a highly debated topic and it is key to understanding the means by which open marine conditions were restored

at the base of the Zanclean and on the potential impact that the Atlantic-Mediterranean re-connection had on the Atlantic and global climate (Flecker et al., 2015; Capella et al., 2019). In this chapter, the paleoenvironmental scenarios, in terms of base-level position (desiccated or full Mediterranean) and hydrological configuration (connections to the Atlantic and/or Paratethys), proposed for the Mediterranean during Stage 3 are described, as well as the different timings of the reflooding (instantaneous, gradual, step-like increments). The low-salinity Stage 3 followed the hypersaline Stage 2 and the transition between the two likely influences the plausibility of the various paleoenvironmental scenarios proposed for the terminal stage. We therefore first summarize the current understanding of the configuration of the Mediterranean during Stage 2 and the enduring controversies (see Roveri et al., 2014a for a more extensive review).

7.1. Stage 2 (5.59-5.55 Ma): formation of the Mediterranean salt giant

Numerical modelling based on hydrological budget calculations shows that in order to reach salinity levels compatible with halite saturation and to accumulate the substantial thicknesses of halite observed in the seismic profiles (Ryan, 1973; Haq et al., 2020), the Atlantic-Mediterranean gateway needs to have permitted inflow from the Atlantic, but may have completely blocked outflow (Blanc, 2002; Krijgsman and Meijer, 2008). Numerical models also showed that without Atlantic inflow into the Mediterranean Sea its base level is forced to drop on time scales in the order of a few thousand years by virtue of the basin's negative hydrological budget, where more water is lost to the atmosphere by evaporation than is received from rainfall and river runoff (e.g. Meijer and Krijgsman, 2005; Krijgsman and Meijer, 2008; Simon et al., 2017). The idea of a drawdown is supported by several arguments: (1) the widespread presence, from the margins to the slopes, of the Messinian Erosional Surface cutting through Stage 1 and pre-MSC deposits and canyon incisions following today's drainage networks (e.g. Chumakov, 1973; Clauzon, 1982; Lofi et al., 2005, 2011a, 2011b; Loget et al., 2006; Maillard et al., 2006, 2020; Estrada et al., 2011; Just et al., 2011; Urgeles et al., 2011; Amadori et al., 2018; Lymer et al., 2018; Cazzini et al., 2020; Figs. 5e, 7e); (2) their morphology interpreted as subaerial in origin; (3) the clastic fans at the outlet of the valleys onlapped by Stage 3 deposits and interpreted as fluvial accumulations (e.g. Lofi et al., 2005; Maillard et al., 2006; Pellen et al., 2019). A number of studies have tried to quantify the magnitude of the sea-level fall by compensating for the isostatic vertical motion since the Messinian to obtain the original depth of the erosional features and Messinian deposits. However, this depends on the assumptions about when the drawdown occurred relative to the halite precipitation: before (e.g. Cartwright and Jackson, 2008; Bache et al., 2009, 2012), during (e.g. Ryan, 2008, 2009) or after (e.g. Ryan, 1978; Bertoni and Cartwright, 2007; Lofi et al., 2011a, 2011b). How shallow the Mediterranean became during Stage 2 is also a matter of disagreement. Estimates in the Western Mediterranean vary from a maximum drawdown of 2500 m (Ryan, 1976) to 1000-1500 m (Bache et al., 2012) in the Gulf of Lion, 800-1200 m in the Balearic promontory (Mas et al., 2018b) and 400 m in the Ebro delta region (Frey-Martinez et al., 2004). A later backstripping analysis of this delta yielded a drawdown of ~1300 m (Urgeles et al., 2011). East of the Sicily sill, backstripping studies estimated base-level drops of 1800-2000 m in the Ionian basin (Micallef et al., 2018, 2019; Camerlenghi et al., 2019; Spatola et al., 2020), 800-900 m in the Adriatic foredeep and Po plain (Ghielmi et al., 2013; Amadori et al., 2018), 800-1300 m (Ben-Gal et al., 2005), 600 (Druckman et al., 1995) and 800 m (Cartwright and Jackson, 2008) in the Levant Basin.

None of these quantifications could unequivocally constrain the timing of the drawdown within the MSC sequence, but numerical modeling studies show that, if the blocking of the outflow was controlled by a tectonic uplift counteracted by inflow erosion across the Strait of Gibraltar, then the expected drawdown of the Mediterranean Sea should be moderate (< 400 m; and possibly harmonic) due to an equilibrium between incision and uplift before the complete blocking of inflow and larger (up to complete desiccation) only after tectonic uplift overcame incision rates (Garcia-Castellanos and Villaseñor, 2011). The same model suggests that the initiation of halite precipitation might overlap in time with the late primary gypsum deposition, right before the full disconnection from the Atlantic Ocean.

The interpretation of the deep evaporites and their associated seismic markers (erosional surfaces and deep engravings along the shelf-slope

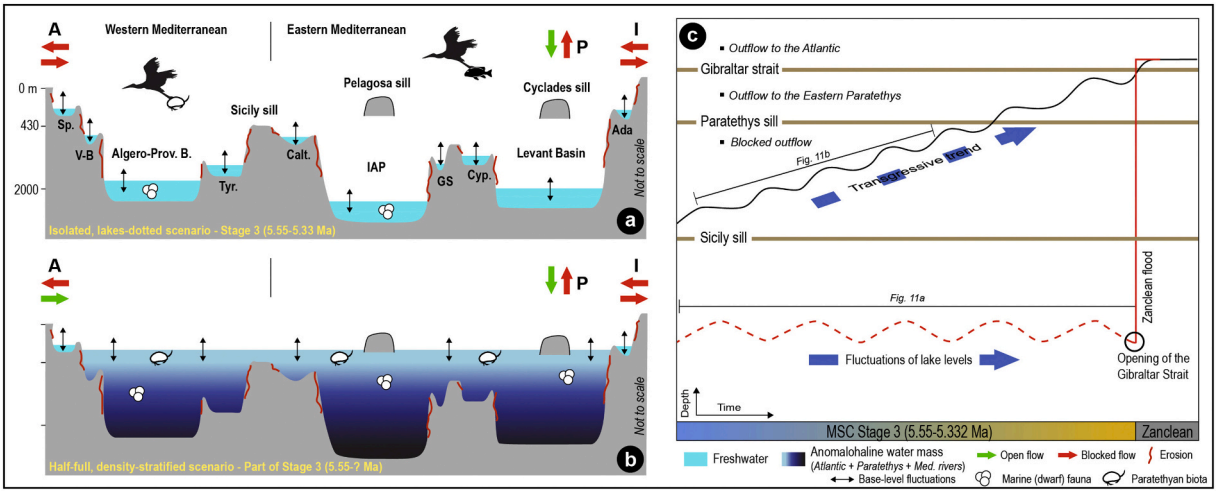

Fig. 11. (a), (b) Schematic W-E profiles across the Mediterranean Basin showing the contrasting paleoenvironmental, paleohydrological and paleoconnectivity interpretations proposed for Stage 3. When a water flow is present (green arrow) from and/or to an extra-Mediterranean water mass (i.e., A: Atlantic Ocean; I: Indian Ocean; P: Eastern Paratethys), the direction of the arrow gives the direction of flow. For simplicity, water added by the major and local rivers is not shown, but it adds to the hydrological budget at any time in each scenario. Note the main difference between the isolated (a) and density-stratified (b) scenario lies in the connectivity framework (Atlantic connection closed and negligible influence from the Paratethys in the isolated scenario; influence from both Atlantic and Paratethys in the density-stratified scenario), which affects the position of the base level of the Mediterranean water mass and its hydrochemistry (see extensive discussion in subsection 7.2). Abbreviations: Sp.: SE Spain; V-B: Valencia Basin; Tyr: Tyrrhenian Basin; Calt: Caltanissetta Basin; IAP: Ionian Abyssal Plain; GS: Gulf of Sirt; Cyp: Cyprus; Ada: Adana Basin. See Fig. 2 for the geographic position of each basin. (c) Schematic plot showing the evolution of the Mediterranean base-level during Stage 3 according to both the isolated (red line) and half-full (black line) scenarios. The critical sills for controlling intra- and extra-Mediterranean connectivity are also shown.

systems) is not straightforward. Recently, it was suggested that the deep evaporitic facies and the seismic morphological features could have been produced without a significant drop of the Mediterranean base-level, therefore promoting the persistence of a relatively deep-water Mediterranean basin even during halite deposition (Lugli et al., 2013, 2015; Roveri et al., 2014b). For example, Roveri et al. (2014c) proposed that downslope flows of dense, hypersaline waters sourced from evaporation in shallower water areas could have generated both the observed shelf-slope erosion and have created a deep brine, supersaturated in the ions necessary for precipitating halite. These subaqueous hyperpycnal flows are consistent with the observed clastic evaporites that filled the Levant margin canyons (Lugli et al., 2013) and, more generally, with the widespread presence of Complex Units at the outlet of the MES drainage systems (see Lofi et al., 2005, 2011a, 2011b; Lofi, 2018). These sediments are dominated by reworked PLG that would have been exposed by a sea-level fall as little as 200 m (Lugli et al., 2010). However, the hypersaline environment that is presumed to be established by these hyperpycnal flows during the deposition of the RLG is in contrast with the occurrence of the Paratethyan ostracod *L. muelleri* within the clastic evaporites (RLG) in several marginal sections (e.g. Adana Basin, Faranda et al., 2013; Radeff et al., 2016, 2017).

Whatever the state of Mediterranean base-level during Stage 2, the more commonly used chronostratigraphic model for the MSC (Fig. 1a; Roveri et al., 2014a) states that massive halite precipitation ceased at 5.55 Ma and was superseded by an environment that, with precession periodicity (Fig. 3a), cycled between gypsum precipitation and conditions that saw fresh-brackish organisms thriving. The question is whether these conditions cycled homogeneously in several isolated lakes or in basins largely connected to the same Atlantic and Eastern Paratethys-influenced water mass (Fig. 11).

7.2. Stage 3 (5.55-5.33 Ma): resumption of (upper) gypsum precipitation and Paratethys fauna invasion

7.2.1. An isolated Mediterranean dotted by sabkhas and lakes

The first and long-lasting paleoenvironmental interpretation of the evaporite-bearing UG/UU units and (possibly) time-equivalent evaporite-free units (e.g. LM Unit in Malaga, Sorbas and Zorreras Mb. in Sorbas, Feos Fm. in Nijar, Cassano Spinola Conglomerates in Piedmont, San Donato/Colombacci fms. in the Apennines, Handere Fm. in Turkey) envisaged their sedimentation in a Mediterranean mostly isolated from the Paratethys (which may have added water only to some basins in the Eastern Mediterranean) and totally isolated from the Atlantic where, in each subbasin, continental settings (e.g. alluvial plains, river channels, alluvial fans, playa lakes, sabkhas) alternated/interfingered with shallow, endorheic lakes (Figs. 11a, c; e.g. Ruggieri, 1962, 1967; Decima and Sprovieri, 1973; Decima and Wezel, 1973; Friedman, 1973; Hsü et al., 1973a, 1973b, 1973c, Hsü et al., 1978a, 1978b; Ryan et al., 1973; Selli, 1973; Sturani, 1973; Sissingh, 1976; Benson, 1978; Bossio et al., 1978; Cita et al., 1978, 1990; Ricchiuto and McKenzie, 1978; Ryan, 1978, 2008, 2009; Cita and Colombo, 1979; Orszag-Sperber and Rouchy, 1979; Ghibaudo et al., 1985; Müller et al., 1990; Benson and Rakic-El Bied, 1991; Benson et al., 1991; Müller and Mueller, 1991; Orszag-Sperber et al., 2000; Rouchy et al., 2001, 2003, 2007; Blanc, 2002; Lofi et al., 2005, Lofi et al., 2011b; Bassetti et al., 2006; Rouchy and Caruso, 2006; Bertoni and Cartwright, 2007; Cameselle and Urgeles, 2017; Amadori et al., 2018; Camerlenghi et al., 2019; Kartveit et al., 2019; Madof et al., 2019; Ben Moshe et al., 2020; Caruso et al., 2020; Cazzini et al., 2020; Raad et al., 2021). The full disconnection is also supported by observations that support an abrupt Zanclean reflooding (e.g. Blanc, 2002; Micallef et al., 2018, 2019; Garcia-Castellanos et al., 2020; Spatola et al., 2020), since a rapid outburst flood requires a large sea level difference prior to the flood that can only be developed in a scenario of a full Mediterranean-Atlantic disconnection (Garcia-Castellanos et al., 2009; Garcia-Castellanos and Villaseñor, 2011). Although rarely explicitly stated, all these studies must assume that:

1) all Paratethyan biota (and possibly other organisms of undisclosed provenance like diatoms) migrated passively via aquatic migratory birds across the entire Mediterranean (Fig. 11a; Benson, 1978; Benson and Rakic-El Bied, 1991; Caruso et al., 2020);
2) chemical and physical conditions (brackish water and water depth not exceeding 100 m; e.g. Hajós, 1973; Gliozzi and Grossi, 2008) that allowed alternated conditions suitable for gypsum to precipitate and Paratethyan biota and euryhaline benthic foraminifera to thrive were related to changes in the local freshwater budget;
3) The marine isotopic signals in UU/UG gypsum (Fig. 10) are entirely the reflection of the lithologies that are leached by continental waters in surficial and/or underground drainage areas (e.g. Ryan, 2009; Raad et al., 2021);
4) Stage 3 gypsum precipitated in extremely shallow-water (playa lakes) to completely dried environments (sabkhas) and the excessive sulfate necessary is completely derived from "clastic reworking, dissolution, re-precipitation and diagenesis of materials belonging to the PLG and halite of the previous MSC Stage 2" (Ryan, 2009).

Observations supporting a Mediterranean isolated throughout Stage 3 and only at the mercy of local freshwater inputs (Fig. 11a) are: (1) the lack of evidence for in situ marine fauna and flora in UU (e.g. Ryan et al., 1973; Hsü et al., 1978a; Cita et al., 1990; Ryan, 2009; Lofi et al., 2011a); (2) the shallow-water mode of life and highly likely in-situ nature of ostracods and euryhaline, shallow-water benthic foraminifera observed in DSDP/ODP wells from intermediate and deep basins (e.g. Cita et al., 1978; Iaccarino and Bossio, 1999; Figs. 9a-c); (3) the bathymetric contrast (up to several hundred meters) between the late Messinian paleoenvironments and the marine Zanclean on top (e.g. Cita and Colombo, 1979; Bonaduce and Sgarrella, 1999; Caruso et al., 2020); (4) the presence of paleosols in Cyprus (Orszag-Sperber et al., 2000; Rouchy et al., 2001) and on the crest of the Eratosthenes seamount (Robertson, 1998a, 1998b); (5) the erosional features preserved both offshore on the continental shelves and lower-middle slope domain and interpreted in most seismic stratigraphic studies as the result of subaerial exposure (e.g. Lofi et al., 2005; Lofi et al., 2011b; Lymer et al., 2018; Ben Moshe et al., 2020); (6) the pinching out of the UU/BU units towards evaporite-free pre-Messinian structural highs (Figs. 7b-g; Figs. 8a, e; Ryan, 2009; Lymer et al., 2018; Camerlenghi et al., 2019; Raad et al., 2021); (7) the more abundant terrigenous clasts and reworked calcareous fossils in Stage 3 samples compared to the overlying, deep-water Pliocene (Ryan et al., 1973; Hsü et al., 1978b; Ryan, 2009); (8) the erosional nature of the M-reflector/TES/IMTS in the Levant Basin (Figs. 8e-g), by some linked to subaerial exposure of the Levant seafloor (e.g. Bertoni and Cartwright, 2007; Lofi et al., 2011a, 2011b; Maillard et al., 2011a) before the emplacement of deposits interpreted as fluvial from seismic observations (Bowman, 2012; Radeff et al., 2017; Leila et al., 2018; Kartveit et al., 2019; Madof et al., 2019). Furthermore, (9) isolated hydrological circuits with unique chemical composition are regarded by Camerlenghi et al. (2019) as the most plausible explanation for the W-E change in the MSC sedimentary expression in the deep basins, represented by the trilogy LU-MU-UU in the Algero-Balearic and Liguro-Provençal basins, missing the LU in the Tyrrhenian and (possibly) Ionian basins, by terrigenous deposits with hiatuses in the WAB and Adriatic foredeep and by halite, anhydrite and clastics in the Levant Basin (Interbedded and Argillaceous evaporites of Meilijson et al., 2019; Fig. 3b).

The main problems with the isolated scenario lasting throughout Stage 3 are: (1) it does not provide an explanation neither for the homogeneity of Paratethyan ostracod assemblages in the marginal basins (e.g. Gliozzi et al., 2007; Stoica et al., 2016), an aspect difficult to explain when fauna migration takes place passively via either birds or wind, nor for the biomarkers (Vasiliev et al., 2017), which cannot be transported effectively by aquatic birds; (2) it does not explain the mismatch between $^{87}Sr/^{86}Sr$ isotope ratios measured on marginal ostracods and Sr values expected from endorheic lakes fed with local

freshwaters (e.g. Andreetto et al., 2021); 3) it misses to substantiate, with geochemical arguments, the precipitation of gypsum in lakes, a process that is everything but straightforward (see Warren, 2016 for insights); 4) except for the salt-bearing basins, the source(s) of solutes which makes freshwater-fed endorheic lakes brackish and causes similar physico-chemical conditions to exist in each lake is also difficult to explain in the context of a Mediterranean only at the mercy of local rivers.

7.2.2. *The half-full, density-stratified Mediterranean scenarios*

An alternative concept to the isolated scenario envisages the Mediterranean connected with the Atlantic and/or the Eastern Paratethys and relatively full of water connecting the different subbasins (Fig. 11b). To our knowledge, this scenario was first developed by McCulloch and De Deckker (1989) on the basis of the similar $^{87}Sr/^{86}Sr$ ratios from marginal (Spain and Cyprus) and deep (Levantine and Algero-Balearic) basins. This intuition was a significant departure from the far more in vogue desiccated scenario (see conclusion of Hsü et al., 1973b), and for this was long overlooked. Sr isotope ratios lower than contemporary ocean water led McCulloch and De Deckker (1989) to conclude that a brackish water mass created by the mixing of water from the peri-Mediterranean rivers (e.g. Nile, Rhône and African rivers that no longer flow today, etc.; see Griffin, 2002 and Gladstone et al., 2007) with water of the Eastern Paratethys filled the Mediterranean, resembling the Caspian Sea today. This conclusion is consistent with the impoverished (or absent) marine fauna and flora of Stage 3 sediments and the enhanced assemblage of fresh-brackish water biota (see subsection 5.7; Figs. 9a-c), but is problematic as a viable origin for Stage 3 gypsum to precipitate at depth. Furthermore, climate models for the late Miocene fail to fill the Mediterranean Basin with fluvial and Paratethys waters alone (Gladstone et al., 2007; Marzocchi et al., 2016, 2019; Simon et al., 2017). A marine contribution is therefore required to fill the Mediterranean (Marzocchi et al., 2016). In the event, the contribution is most likely to have derived from the Atlantic via the Gibraltar Corridor (Flecker et al., 2015; Booth-Rea et al., 2018; Krijgsman et al., 2018) either through a karst system (Krijgsman et al., 2018) or an emerged volcanic archipelago in the Alborán Basin (Booth-Rea et al., 2018). In fact, although an Indian Ocean contribution was proposed (Cita et al., 1978; Hsü et al., 1978a) and the possibility discussed (Ryan, 2009; Vai, 2016), palinspastic reconstructions concluded that the Neo-Tethys Mediterranean-Indian Ocean connection via southern Turkey and Iran already closed before the Tortonian (Rögl, 1998; Popov et al., 2004; Gargani et al., 2008; Bialik et al., 2019; Gülyüz et al., 2020), while a seaway via the Red Sea and Gulf of Aden, although not completely ruled out (e.g. Schütz, 1994; Bosworth et al., 2005; Gargani et al., 2008; Ryan, 2009), is highly contested (e.g. Meulenkamp and Sissingh, 2003; Segev et al., 2017).

In light of this, Roveri et al. (2014c), Gvirtzman et al. (2017), Vasiliev et al. (2017), García-Veigas et al. (2018) and Grothe et al. (2020) suggested that the Mediterranean was likely density-stratified during this interval as a result of the simultaneous influx of isotopically-different marine and non-marine (major Mediterranean rivers and Eastern Paratethys) water sources (Fig. 11b). This connectivity framework resulted in a brackish layer carrying low-salinity (mostly Paratethyan) biota (Gliozzi et al., 2007; Stoica et al., 2016; Grothe et al., 2018, 2020; Figs. 9a-b) to lay on top of a more saline layer formed by Atlantic-derived seawater from which UU/UG gypsum (Figs. 5h-j, 7b-g, 8a-d), that facies analyses demonstrated to result from subaqueous deposition (Hardie and Lowenstein, 2004; Lugli et al., 2015), precipitated at intermediate and greater depths (e.g. García-Veigas et al., 2018). A dense, anoxic deep-water mass, possibly inherited from Stage 2, is envisaged at the bottom of the Mediterranean by Marzocchi et al. (2016) and García-Veigas et al. (2018), albeit without conclusive arguments, and by Gvirtzman et al. (2017) following the observation that the tilted halite body of the Levant Basin was simultaneously eroded landward and preserved basinward (Fig. 8f).

This scenario accounts for the erosive/non-depositional features (Figs. 5e, 6a, e) and continental/lacustrine facies (Figs. 5a-b, d-g) widespread around the margins and shelves and suggestive of a Mediterranean base-level somewhat lower than the Atlantic level suggesting a one-way inflow from both the Atlantic and the Eastern Paratethys after Stage 2 (e.g. Marzocchi et al., 2016; Figs. 11b, c), a connectivity configuration that effectively translates in a half-full Mediterranean (e.g. Krijgsman and Meijer, 2008). Refilling as a result of persistent Atlantic inflow, in part perhaps because of the latest Messinian deglaciation (see subsection 2.2; Van der Laan et al., 2006; Hilgen et al., 2007), would have resulted in the establishment of two-way exchange first with the Paratethys at some point during the Lago-Mare phase and later, i.e. slightly before or at the Messinian/Zanclean boundary, with the Atlantic Ocean (Fig. 11c; Marzocchi et al., 2016). The moment the Mediterranean base-level reached the sill with the adjacent water body (Paratethys and Atlantic) and a two-way exchange was initiated, the density contrast will have prompted an enhanced inflow into the Mediterranean (Marzocchi et al., 2016). The overall transgressive trend leading to the Zanclean marine replenishment was accompanied by base-level fluctuations in the order of 400±100 m every precessional cycle (Fig. 11c; Fortuin and Krijgsman, 2003; Ben Moshe et al., 2020; Andreetto et al., 2021). These fluctuations are ascribed to switch in the Mediterranean freshwater budget driven by the African summer monsoon and Atlantic winter storms (e.g. Marzocchi et al., 2015, 2019; Simon et al., 2017). Since higher freshwater discharge rates occur at precession minima times and their Stage 3 sedimentary expression is considered to be the mudstone intervals (Fig. 3a; Manzi et al., 2009), mudstone interbeds (both onshore and offshore; e.g. Figs. 5h-j) represent the highstand episodes (e.g. Manzi et al., 2009; Roveri et al., 2008a; Omodeo-Salé et al., 2012; Fig. 3), while continental facies onshore (e.g. conglomerates in the Apennines; Fig. 5g) and offshore (clastic beds in the Levant Basin) and gypsum beds (Algero-Balearic, Liguro-Provencal, CMD, Tyrrhenian, Caltanissetta, Ionian, Sirte and Polemi-Pissouri basins; Figs. 5h-j) represent the lowstand (e.g. Roveri et al., 2008a; Manzi et al., 2009; Meilijson et al., 2019; Fig. 3). If Atlantic was the major source of sulfate for Stage 3 gypsum (e.g. García-Veigas et al., 2018) and an intervening, relatively shallow (Sicily) sill was establishing Western and Eastern Mediterranean division during the MSC (e.g. Garcia-Castellanos et al., 2009, 2020; Micallef et al., 2018), the presence of Stage 3 gypsum to the east of the Sicily sill (Fig. 2b) implies that the Mediterranean base level never dropped below the (maximum estimated) paleodepth of the sill (i.e. ~430 m; Garcia-Castellanos et al., 2009) during Stage 3 and Western and Eastern Mediterranean remained connected also during the arid (lowstand) phases of the precession cycles.

A Mediterranean step-wise refilled and at times filled with water up to the marginal belt agrees with: (1) Paratethyan biota being present only in intermediate-deeper settings during substage 3.1, but more widespread including marginal settings during substage 3.2; (2) the W-E homogeneity of Paratethyan ostracod assemblages around the Mediterranean marginal belt (Gliozzi et al., 2007; Stoica et al., 2016; Sciuto et al., 2018; Sciuto and Baldanza, 2020; Fig. 9a); (3) the presence, in marginal basins, of Paratethyan fish (Bannikov et al., 2018; Schwarzhans et al., 2020), dinocysts (e.g. Pellen et al., 2017; Fig. 9b) and biomarkers (Vasiliev et al., 2017; Fig. 10c); (4) the occurrence of a monospecific assemblage of abundant *Sphenolithus* spp. just below the M/P boundary at ODP Sites 978, 975 and 967 (Castradori, 1998); (5) the requirement of water from the Mediterranean to explain the Sr isotope ratios of ostracods that inhabited marginal subaqueous environments (Andreetto et al., 2021); (6) the Atlantic-like sulfate values (although variably diluted and affected by microbial processes; Fig. 10b) of the UU/UG gypsum beds (García-Veigas et al., 2018); (7) the presence of long chain alkenones in the Sicilian UG beds similar to those observed in present-day marine settings (Fig. 10c; Vasiliev et al., 2017).

Major problems also exist with the half-full stratified scenario: (1) it does not provide a proper mechanism for gypsum precipitation at several hundreds, or thousands, meters water depth; (2) it fails to explain how unquestionable shallow-water (< 50 m) benthic organisms

such as *Ammonia tepida* and *Cyprideis* sp. could survive at hundreds of meters of depth and beyond; (3) it does not provide an explanation for the high abundance of coarse-grained detritus at intermediate and deep-water locations, especially when compared to deep-water Pliocene samples, as well as for the broad absence of MSC deposits in the shelf domain; (4) a persistent Atlantic inflow without outflow seems to be a configuration that cannot be maintained stable for ~200 kyr. Indeed, models coupling the inflow of marine waters with the erosion of the gateway channel concluded that, if the Mediterranean level was lowered by at least several hundred meters below present sea level, any small overtopping of water from the Atlantic would inevitably trigger a fast refill of the basin that, if responsible for the erosion trough the Alborán Basin, should have involved an unprecedented water discharge and be completed within a few years or less (Garcia-Castellanos et al., 2020 and references therein). The scenario arising from Meilijson et al., 2019, Figs. 3b, 4a) is also problematic for a high base-level Mediterranean. In order to simultaneously reach precipitation of gypsum and halite in different basins sharing the same water, the water has to be of high salinity and stratified. Simon and Meijer (2017) demonstrated that this can be achieved with slow overturning circulation, but it is currently unclear how realistic this process is.

7.3. Demise of the MSC (5.33 Ma): the Zanclean marine replenishment

The conspicuous and abrupt transition to normal marine sediments in the Mediterranean is globally and historically important because it is the origin of the stratigraphic position of the Miocene/Pliocene boundary (Van Couvering et al., 2000). From an ocean perspective, it is not an ideal stratigraphic location being difficult to locate from biozone data even in the adjacent Atlantic (Hodell et al., 2001; Krijgsman et al., 2004; Van den Berg et al., 2015). However, from a Mediterranean perspective it provides a clear and unambiguous end to the MSC and the restoration of normal marine conditions. All evidence show that the onset of the Zanclean marine replenishment followed a period of relative lowstand that exposed all the Mediterranean margins (see subsection 3.12; Figs. 6a-b, f) and kept intermediate and deep basins underwater (see subsection 4.8). Yet again, the key dispute concerns the exact depth of the Mediterranean base level preceding the Miocene/Pliocene transition.

Building on the isolated Mediterranean scenario, base level immediately before the early Zanclean was more than thousand kilometers below eustatic sea level (Fig. 10e; e.g. Hsü et al., 1973a; Blanc, 2002; Loget et al., 2006; Garcia-Castellanos et al., 2009; Pérez-Asensio et al., 2012; García-Alix et al., 2016; Amadori et al., 2018; Micallef et al., 2018, 2019; Camerlenghi et al., 2019; Kartveit et al., 2019; Madof et al., 2019; Ben Moshe et al., 2020; Caruso et al., 2020; Cazzini et al., 2020; Mas and Fornós, 2020; Spatola et al., 2020). Hydrodynamic erosional models allowed a reinterpretation of the erosional features across the strait of Gibraltar (Campillo et al., 1992; Blanc, 2002) suggesting that a sudden breach of the Mediterranean-Atlantic divide at Gibraltar resulted in a vast cascade of Atlantic water that refilled the entire Mediterranean in less than 2 years (i.e. rates of ten meters per day) spilling first into the Western Mediterranean (see the extensive review in Garcia-Castellanos et al., 2020) and then, after reaching the level of the Sicily sill, pouring into the Eastern Mediterranean (Micallef et al., 2018, 2019; Ben Moshe et al., 2020; Spatola et al., 2020). This concept of catastrophic refilling has led to terms such as “Zanclean flood” or “deluge”. Evidence supporting the catastrophic flood mechanism mostly comes from the seismic reflection dataset and includes: 1) the presence of >250 m deep and 390-km-long incisions on both sides of the Gibraltar Strait (Garcia-Castellanos et al., 2020); 2) the detection of (allegedly) Pliocene-aged chaotic sedimentary bodies stretching for kilometers in the Alborán Basin (Garcia-Castellanos et al., 2020 and references therein) and Ionian Basin at the foot of the Malta Escarpment (Micallef et al., 2018, 2019; Spatola et al., 2020; Fig. 8c). A further argument is the bathymetric jump of several hundred meters between the late Messinian and the early Pliocene sediments (e.g. Caruso et al., 2020; Fig. 6d).

Instantaneous sea level rise is not the only possible refilling model. Bache et al. (2012) suggested the reflooding occurred in two steps at ~5.60 Ma, accompanied by a moderate (≤ 500 m) rise, followed by a rapid rise of 600-900 m at around 5.46 Ma tracking the deposition of the deep basin evaporites and resulting from the collapse of the Gibraltar divide. There is also the reconnection model that follows from a Stage 3 Mediterranean that is already relatively full and with the base level possibly oscillating of 400 ± 100 m with precessional frequency (Fig. 10h; Fortuin and Krijgsman, 2003; Ben Moshe et al., 2020; Andreetto et al., 2021). In this case, only a sea level rise of a few hundred meters is required to restore the Mediterranean to the Atlantic level (Fig. 10h), which was hypothesized to have occurred in the last precessional cycle of the Messinian (Marzocchi et al., 2016; Fig. 3a).

In detail, the re-establishment of a fully marine faunal diversity and oceanic geochemistry (e.g. $^{87}Sr/^{86}Sr$ ratios and $\delta^{18}O$) occurred more gradually over one or more precessional cycles in the earliest Zanclean (e.g. Iaccarino et al., 1999; Pierre et al., 1998, 2006; Cipollari et al., 2013; Roveri et al., 2019a; Bulian et al., 2021). This suggests that stressed ecological conditions at first only suitable for opportunistic organisms to survive (e.g. Bulian et al., 2021) developed (or persisted) in the Mediterranean as marine replenishment occurred (e.g. Rouchy et al., 2003). One possible mechanism for achieving this may be the physico-chemical turnover in the water column triggered by the re-established two-way exchange with the Atlantic which, for reasons that are largely unknown, took time (at least oneprecession cycle; Pierre et al., 2006) to displace surficial Paratethyan water and restore normal marine conditions (Marzocchi et al., 2016).

8. Methods and proxies to better reconstruct base level and connectivity changes

Chronological uncertainty and spatial variability limit the use of both sedimentological and paleontological information to achieve a comprehensive and coherent basin-wide interpretation of the conditions and drivers of Stage 3 environments and water levels. Alternative methods are therefore required to clarify connectivity relationships and constrain base-level conditions. This section explores the principles and potential of geochemical, backstripping and numerical modelling techniques that could be used to further test existing hypotheses and enhance understanding of the complex environmental conditions experienced by the Mediterranean during the latest Messinian.

8.1. Geochemical proxies

Radiogenic strontium isotopes. Radiogenic strontium isotope ratio ($^{87}Sr/^{86}Sr$) is a widely applied geochemical tool in provenance studies, including the reconstruction of the hydrological circuit and connectivity of basins with little or null oceanic entries. Its potential to detect the provenance of the hydrological fluxes derives from the unique $^{87}Sr/^{86}Sr$ ratio that typifies each water source and from the negligible effects of isotopic fractionation during the liquid-solid transition (see Hajj et al., 2017).

Mineral phases precipitating in endorheic lakes uptake Sr with $^{87}Sr/^{86}Sr$ ratio that reflects the mixing of all feeding surficial and underground streams and whose $^{87}Sr/^{86}Sr$ fingerprint hinges on the composition and age of watershed bedrock (see Peucker-Ehrenbrink and Fiske, 2019; Andreetto et al., 2021 and references therein). When river water mixes with seawater such as in the oceans, semi-enclosed basins or estuaries, mineral phases uptake Sr with oceanic $^{87}Sr/^{86}Sr$ ratios because the high oceanic Sr concentration (~7.8 mg/l today; Veizer, 1989) masks the impact of the ~100 times lower concentrated continental Sr-sources (~0.0780 mg/l; Palmer and Edmond, 1992). This is valid as long as a certain ratio of continental-marine water mixing is fulfilled, beyond which $^{87}Sr/^{86}Sr$ ratios deviate towards the $^{87}Sr/^{86}Sr$ ratios of the non-marine source(s) (Ingram and Sloan, 1992). For the

Mediterranean to attain non-marine $^{87}Sr/^{86}Sr$ ratios (like during the MSC), Topper et al. (2014) calculated a mixing of at least 1:4 (Atlantic: freshwater) to be required.

If Mediterranean subbasins hosted endorheic lakes (Figs. 10c, e), the $^{87}Sr/^{86}Sr$ isotope ratios measured on ostracod valves or gypsum crystals of each lake are expected to generate a scattered distribution by virtue of the different geology in the hinterland of each basin. By contrast, some degree of connection between different basins and the Mediterranean water mass (Figs. 10d, f) is expected to result in more homogeneous $^{87}Sr/^{86}Sr$ ratios because, although isotopically-different, local rivers mix with a water mass that has the same $^{87}Sr/^{86}Sr$ value and (much higher) Sr concentration for each basin (Andreetto et al., 2021). In this scenario, differences in the $^{87}Sr/^{86}Sr$ ratios between basins are likely the reflection of the different $^{87}Sr/^{86}Sr$ ratio of the local input in each basin (Andreetto et al., 2021). The application of numerical models assists to identify and quantify the different water sources feeding the basin(s) in question and (e.g. Placzek et al., 2011; Topper et al., 2011, 2014; Doebbert et al., 2014; Rossi et al., 2015b; Modestou et al., 2017; Grothe et al., 2020; Andreetto et al., 2021).

Sulfate isotopes. When sulfate-bearing minerals precipitate in a basin they uptake dissolved S and O with $\delta^{34}S_{SO4}$ and $\delta^{18}O_{SO4}$ isotopic composition that, once corrected for the fractionation effects during liquid-solid transition (see subsection 6.2), can be assimilated to that of the mother brine. The higher concentrated source of sulfate is seawater (with present-day $\delta^{34}S_{SO4}$=21.15±0.15‰ and $\delta^{18}O_{SO4}$=8.67±0.21‰, Johnston et al., 2014; with Messinian values of ~22±0.2‰ for the $\delta^{34}S_{SO4}$ and ~9±2‰ for the $\delta^{18}O_{SO4}$; Turchyn and Schrag, 2004; Markovic et al., 2016; Masterson et al., 2016). Significantly higher inputs from the ~1000 times less concentrated riverine freshwater (both surficial and underground) with respect to the ocean water (more than 1:5 according to Lu et al., 2001) can modify the marine $\delta^{34}S_{SO4}$ and $\delta^{18}O_{SO4}$ isotopic composition of the mother brine (Utrilla et al., 1992; Lu et al., 2001) and have it deviated from that of the ocean (Lu et al., 2001). This deviation is normally towards lower values, because river-derived dissolved sulfate is generally depleted in heavy isotopes ^{34}S and ^{18}O compared to oceanic sulfate because these isotopes mainly come from the oxidation of ^{34}S-depleted pyrite (FeS_2) on the continents and to a lesser extent from the dissolution of older sulfate-bearing minerals (Claypool et al., 1980; Turchyn and Schrag, 2004; Burke et al., 2018). However, when marine sulfate is preferentially leached in the catchment, ^{34}S of the freshwater-dissolved sulfate and [SO_4^{2-}] likely increase, therefore reducing the continental-marine mixing ratio necessary to deviate the resulting sulfate isotopic signature away from marine values. Unfortunately, the sulfate isotopic composition is not provided for a number of major Mediterranean rivers (Burke et al., 2018) nor for the Eastern Paratethys and it is hardly assessed with the catchment-forming lithologies (Liu et al., 2017; Burke et al., 2018), making sulfate isotopes still an unsuitable tracer of non-marine water provenance in Mediterranean subbasins.

Deviation of $\delta^{34}S_{SO4}$ and $\delta^{18}O_{SO4}$ from the marine average can also be the result of isotopic fractionation during microbial sulfate reduction (MSR; Fritz et al., 1989; Berner, 1999). MSR produces ^{34}S-depleted hydrogen sulfide (~0 to 70‰ lighter than initial sulfate; Brunner and Bernasconi, 2005; Sim et al., 2011; Leavitt et al., 2013) and induces the enrichment in ^{34}S and ^{18}O of the residual sulfate pool (Kaplan and Rittenberg, 1964; Thode and Monster, 1965; Turchyn et al., 2006; Wortmann et al., 2007). Therefore, if isotopically light H_2S produced by MSR leaves the system as a sulfide mineral (most likely pyrite), the resulting dissolved sulfate would have $\delta^{34}S_{SO4}$ and $\delta^{18}O_{SO4}$ isotopic signatures higher than the oceanic one (Brunner et al., 2005). However, if the MSR-produced H_2S is re-oxidized back to sulfate through abiotic or microbial sulfide oxidation, isotopically light sulfate will be brought back to the ^{34}S-enriched sulfate pool, producing little or no enrichment in ^{34}S observed in the resulting sulfate (Gomes and Johnston, 2017 and references therein; Pellerin et al., 2019). Slight deviations from marine $\delta^{18}O_{SO4}$ and $\delta^{34}S_{SO4}$ values of sulfate reflect both biological sulfur cycling and/or freshwater riverine inputs (e.g. Utrilla et al., 1992; Lu et al., 2001; Turchyn et al., 2009) (Fig. 10b). Untangling the relative importance of these processes is key to understanding the Mediterranean sulfur isotope record and gleaning paleoenvironmental insights into Stage 3.

Hydrogen isotopes. Organic geochemistry biomarker-based tools can be used as independent proxies for reconstructing sea surface temperatures, relative changes in the basin hydrology and, indirectly, salinity. Basin water properties are reflected in a variety of life forms. Different types of organisms produce specific organic compounds that serve as molecular biomarkers. These large biomolecules record the changes in the hydrogen isotopic composition of the water used by different groups of biomarker producers (i.e. different organisms). The principle behind the method is to measure δD on biomarkers produced in Mediterranean Sea waters (e.g. alkenones, produced by a few species of haptophyte coccolithophores algae) during the MSC and compare the results with the δD signals retrieved from biomarkers produced in the open ocean ideally at the same time intervals. The influence of precipitation on the changes in hydrological budget can be monitored by measuring the δD of long chain *n*-alkanes (Sachse et al., 2006), biomarkers predominantly produced by higher terrestrial plants that rely on precipitation for plant growth, therefore reflecting the changes in the δD of the precipitation. The extreme base level drop(s) suggested for the Mediterranean during the MSC would, in principle, indicate a negative precipitation (P) + runoff (R) – evaporation (E) ratio. Such a negative water budget (E>P+R) results in waters increasingly enriched in δD whereas, a positive water balance (E<P+R) results instead in a negative shift of δD values. The analysis of compound specific δD of alkenones, long and short chain *n*-alkanes can be used to constrain E/(P+E) relationships.

8.2. Backstripping analyses

Backstripping uses paleobathymetry, sea level and sediment thickness to quantify the tectonic and isostatic components of subsidence. If tectonic subsidence or uplift history are known relative to the current position and depth of paleoshoreline markers, an inverse approach allows base level to be estimated. A number of approaches have been applied to the MSC, using erosional surfaces (e.g. Amadori et al., 2018), terraces (Micallef et al., 2018) or fluvial network characteristics (Urgeles et al., 2011) as paleoshoreline indicators. The relief on erosional features has also been used to estimate minimum base-level variation (Frey-Martinez et al., 2004).

Apart from the quantitative constraints on base level that backstripping provides, consideration of the regional implications of isostatic subsidence and the gravitational impact of redistributing water masses (such as in the cascading model of Roveri et al., 2014c; Fig. 10b) and evaporite precipitation is important in gateway regions like Gibraltar, which due to their shallow and restricted nature are exceptionally sensitive to vertical motions. Here, both flexural effects and gravitational effects on local sea level on the Atlantic side of the strait has the potential to influence Mediterranean-Atlantic connectivity driving paleoenvironmental changes in the basin itself (Coulson et al., 2019).

8.3. Modelling

Numerical models can be used complementary to lab- and field-based studies, or to find answers to open questions by testing the physical plausibility of hypotheses and their compatibility with the available sedimentological/stratigraphic/paleontological/geochemical data, which have to constrain model results and not adjust to it. For example, whether gypsum beds in marginal/intermediate basins can precipitate at the same time as the halite in deep basins is an intriguing question that circulates in the MSC literature (e.g. Van Couvering et al., 1976), but whether this is physically and geochemically possible is yet to be answered. In a first model analysis, Simon and Meijer (2017) found that the required stratification can indeed be achieved for specific

conditions including a slow overturning circulation. A different approach is needed to determine whether such slow circulation is to be expected or if other scenarios should be considered. A thermo-haline stratification that enables coeval precipitation of two evaporites for a considerable time span might also influence the degree of heterogeneity of other parameters, such as strontium concentration. Previous models showed the influence of the Atlantic Ocean and major rivers (Topper et al., 2014) and of evaporation (Flecker et al., 2002) on the Sr value of a basin with restricted oceanic inflow and assuming a homogeneous distribution of strontium throughout the water column (Flecker et al., 2002; Topper et al., 2011, 2014; Modestou et al., 2017), but it is uncertain if this holds true in conditions of water stratification. New insights into this behavior would have consequences for the way the strontium dataset (Fig. 10a) must be interpreted. Another loose end where the model approach can provide insight relates to the question whether a high water level could have been reached without an inflow from the Atlantic. Climate simulations conducted by Gladstone et al. (2007), Simon et al. (2017) and Marzocchi et al. (2019) indicate that this is not possible with today's bathymetry. A quantitative analysis exploring the Mediterranean water level reached in different situations (i.e. with or without an Atlantic or Paratethys in and outflow) and with information on the Mediterranean hypsometry that may be provided by isostatic restoration of the seafloor topography (flexural backstripping) could help understanding how the Messinian Salinity Crisis ended.

9. Certainties, open problems and future directions

Our understanding of the nature of MSC Stage 3 has evolved considerably over the last fifty years. However, there are still such disparate models for the paleoenvironmental conditions and basin connectivity that led to Stage 3 deposition and that express the challenges that the study of this interval presents: it is a relatively short interval and its sedimentary expression varies spatially. It is no surprise that the main point of contention lies in reconciling the observations from seismic profiles and well data, which are largely interpreted as favoring the desiccated scenario, with the sedimentological, paleontological and geochemical data from the marginal basins record, largely discontinuous and unaddressed from seismic-based and computational-based studies and mainly supporting the full-Mediterranean hypothesis.

To a large extent this mismatch is the result of the lack of intersection of the two datasets. Some Stage 3 onshore localities are meticulously studied from the stratigraphic, sedimentological, paleontological and geochemical point of view, showing remarkably consistent and homogenous trends and patterns (as previously highlighted by Roveri et al., 2008a). However, changes at precessional and subprecessional scale are difficult to trace from one exposure to another and are well below the level of seismic resolution, making onshore-offshore correlation at this scale impossible. Even correlation between onshore sections is problematic since most of the stratigraphic sections are incomplete, with erosion surfaces at the bottom and/or top (i.e. the Miocene/Pliocene boundary), and this lack of stratigraphic continuity frustrates attempts to constrain ages by cyclostratigraphy. A future focus on strengthening the available chronostratigraphic framework (Fig. 3) and making it inclusive of the fragmented outcrops is required to better understand the paleoenvironmental and paleohydrological changes suffered by the Mediterranean marginal belt through time. The successful drilling of the three IODP proposals currently in the scheduling pool (see Camerlenghi and Aloisi, 2020), all of which propose to recover Stage 3 sediments, will also provide transformative information enabling far better offshore-onshore correlation and interpretation of currently enigmatic seismic data. In the meantime, re-evaluation of existing DSDP and ODP material, particularly through the application of more novel geochemical techniques and, where possible, access to material collected during industrial drilling would be helpful for understanding the deep Mediterranean Basin during this interval.

Extensive paleontological studies have established that Stage 3 contains *in situ* biota assemblages of Paratethyan provenance implying brackish water conditions. More problematic is the differentiation of in situ and reworked marine microfauna and flora and the paleoecological significance of dwarfism in marine calcareous microfossils/algae. These have important repercussions for the Mediterranean connectivity and base-level reconstruction.

The geochemical dataset for Stage 3, particularly strontium isotopes and hydrogen isotopes on biomarkers, is both demonstrably valuable in providing key constraints on connectivity and environmental conditions, and frustratingly inadequate in terms of data distribution. It has great potential as a constraint on quantitative sensitivity analysis of the different hydrochemistry scenarios that follow from the endmember Stage 3 hypotheses, but substantially more data is required.

An approach which combines geological, geochemical, geophysical and paleontological data with numerical modelling (e.g. climate simulations, backstripping analyses and paleoceanographic models) will provide a more accurate reconstruction of Mediterranean paleogeography and the processes that occurred during the final phase of the Messinian Salinity Crisis.

Data availability

The compilation of strontium, sulfate and hydrogen isotope data plotted in figure 9, as well as some of the available, and here not (graphically) shown, oxygen isotope values is accessible in separate excel spreadsheets (Supplementary material 1).

Declaration of Competing Interest

The authors whose names are listed immediately below certify that they have NO affiliations with or involvement in any organization or entity with any financial interest (such as honoraria; educational grants; participation in speakers' bureaus; membership, employment, consultancies, stock ownership, or other equity interest; and expert testimony or patent-licensing arrangements), or non-financial interest (such as personal or professional relationships, affiliations, knowledge or beliefs) in the subject matter or materials discussed in this manuscript.

Acknowledgments

We thank the entire SALTGIANT community for many profitable workshops that inspired the development of this manuscript. This research was supported by the project SALTGIANT-Understanding the Mediterranean Salt Giant, a European project which has received funding from the European Union's Horizon 2020 research and innovation program, under the Marie Sklodowska-Curie [grant agreement No 765256]. We greatly thank the two reviewers Domenico Cosentino and William Ryan and the editor Alessandra Negri for the fruitful comments provided that led to a substantial improvement of the manuscript.

Appendix A. Supplementary data

Supplementary data to this article can be found online at https://doi.org/10.1016/j.earscirev.2021.103577.

References

Abdel Aal, A., El Barkooky, A., Gerrits, M., Meyer, H., Schwander, M., Zaki, H., 2000. Tectonic evolution of the eastern Mediterranean Basin and its significance for hydrocarbon prospectivity in the ultradeepwater of the Nile Delta. Lead. Edge 19, 1086–1102. https://doi.org/10.1190/1.1438485.

Abdel-Fattah, M.I., 2014. Petrophysical characteristics of the messinian abu madi formation in the baltim east and north fields, offshore Nile delta, Egypt. J. Pet. Geol. 37 (2), 183–195.

Agiadi, K., Antonarakou, A., Kontakiotis, G., Kafousia, N., Moissette, P., Cornée, J.-J., Manoutsoglou, E., Karakitsios, V., 2017. Connectivity controls on the late Miocene

eastern Mediterranean fish fauna. Int. J. Earth Sci. 106, 1147–1159. https://doi.org/10.1007/s00531-016-1355-7.
Agnini, C., Monechi, S., Raffi, I., 2017. Calcareous nannofβossil biostratigraphy: historical background and alication in Cenozoic chronostratigraphy. Lethaia 50 (3), 447–463.
Aguirre, J., Sánchez-Almazo, I.M., 2004. The Messinian post-evaporitic deposits of the Gafares area (Almeria-Nijar basin, SE Spain). A new view of the "Lago-Mare" facies. Sediment. Geol. 168, 71–95.
Amadori, C., Garcia-Castellanos, D., Toscani, G., Sternai, P., Fantoni, R., Ghielmi, M., Di Giulio, A., 2018. Restored topography of the Po Plain-Northern Adriatic region during the Messinian base level drop-Implications for the physiography and compartmentalization of the paleo-Mediterranean basin. Basin Res. 30 (6), 1247–1263. https://doi.org/10.1111/bre.12302.
Andersen, N., Paul, H.A., Bernasconi, S.M., McKenzie, J.A., Behrens, A., Schaeffer, P., Albrecht, P., 2001. Large and rapid climate variability during the Messinian salinity crisis: evidence from deuterium concentrations of individual biomarkers. Geology 29, 799–802.
Andreetto, F., Matsubara, K., Beets, C.J., Fortuin, A.R., Flecker, R., Krijgsman, W., 2021. High Mediterranean water-level during the Lago-Mare phase of the Messinian Salinity Crisis: insights from the Sr isotope records of Spanish marginal basins (SE Spain). Paleogeogr. Paleoclimatol. Paleoecol. 562.
Andrusov, D., 1890. Les Dreissenidae fossiles et actuelles d'Eurasie. Geol. Min. 25, 1–683 (in Russian).
Arab, M., Rabineau, M., Déverchère, J., Bracene, R., Belhai, D., Roure, F., Marok, A., Bouyahiaoui, B., Granjeon, D., Andriessen, P., Sage, F., 2016. Tectonostratigraphic evolution of the eastern Algerian margin and basin from seismic data and onshore-offshore correlation. Mar. Pet. Geol. 77, 1355–1375. https://doi.org/10.1016/j.marpetgeo.2016.08.021.
Arenas, C., Pomar, L., 2010. Microbial deposits in upper Miocene carbonates, Mallorca, Spain. Paleogeogr. Paleoclimatol. Paleoecol. 297 (2), 465–485.
Aufgebauer, A., McCann, T., 2010. Messinian to Pliocene transition in the deep part of the Sorbas Basin, SE Spain-a new description of the depositional environment during the Messinian Salinity Crisis. Neues Jahrbuch für Geologie und Paläontologie-Abhandlungen 259 (2), 177–195.
Azdimousa, A., Poupeau, G., Rezqi, H., Asebriy, L., Bourgois, J., Ait Brahim, L., 2006. Geodynamique des bordures meridionales de la mer d'Alboran; alication de la stratigraphie sequentielle dans le bassin neogene de Boudinar Rif oriental. Maroc. Bull. Inst. Sci. Rabat 28, 9–18.
Bache, F., Olivet, J.-L., Gorini, C., Rabineau, M., Baztan, J., Aslanian, D., Suc, J.-P., 2009. Messinian erosional and salinity crisis: view from the Provence basin (Gulf of Lions, western Mediterranean). Earth Planet. Sci. Lett. 286, 139–157.
Bache, F., Popescu, S.-M., Rabineau, M., Gorini, C., Suc, J.-P., Clauzon, G., Olivet, J.-L., Rubino, J.-L., Melinte-Dobrinescu, M.C., Estrada, F., Londeix, L., Armijo, R., Meyer, B., Jolivet, L., Jouannic, G., Leroux, E., Aslanian, D., Reis, A.T.D., Mocochain, L., Dumurdžanov, N., Zagorchev, I., Lesić, V., Tomić, D., Namık Çağatay, M., Brun, J.-P., Sokoutis, D., Csato, I.T., Ucarkus, G., Çakır, Z., 2012. A two-step process for the reflooding of the Mediterranean after the Messinian Salinity Crisis. Basin Res. 24, 125–153. https://doi.org/10.1111/j.1365-2117.2011.00521.x.
Backman, J., Raffi, I., Rio, D., Fornaciari, E., Pälike, H., 2012. Biozonation and biochronology of Miocene through Pleistocene calcareous nannofossils from low and middle latitudes. Newsl. Stratigr. 45, 221–244.
Bannikov, A.F., Schwarzhans, W., Carnevale, G., 2018. Neogene Paratethyan croakers (Teleostei, Sciaenidae). Riv. Ital. Paleontol. Stratigr. 124, 535–571.
Barra, D., Bonaduce, G., Sgarrella, E., 1998. Paleoenvironmental bottom water conditions in the early Zanclean of the Capo Rossello area (Agrigento, Sicily). Boll. Soc. Paleontol. Ital. 37, 61–88.
Bassetti, M.A., Miculan, P., Lucchi, F.R., 2003. Ostracod faunas and brackish-water environments of the late Messinian Sapigno section (northern Apennines, Italy). Paleogeogr. Paleoclimatol. Paleoecol. 198 (3-4), 335–352.
Bassetti, M.A., Manzi, V., Lugli, S., Roveri, M., Longinelli, A., Lucchi, F.R., Barbieri, M., 2004. Paleoenvironmental significance of Messinian post-evaporitic lacustrine carbonates in the northern Apennines, Italy. Sediment. Geol. 172 (1–2), 1–18.
Bassetti, M.A., Miculan, P., Sierro, F.J., 2006. Evolution of depositional environments after the end of Messinian Salinity Crisis in Nijar basin (SE Betic Cordillera). Sediment. Geol. 188-189, 279–295.
Ben Moshe, L., Ben-Avraham, Z., Enzel, Y., Schattner, U., 2020. Estimating drawdown magnitudes of the Mediterranean Sea in the Levant basin during the Lago Mare stage of the Messinian Salinity Crisis. Mar. Geol. 106215 https://doi.org/10.1016/j.margeo.2020.106215.
Ben-Gal, Y., Ben-Avraham, Z., Buchbinder, B., Kendall, C.G.S.C., 2005. Post-Messinian evolution of the Southeastern Levant Basin based on two-dimensional stratigraphic simulation. Mar. Geol. 221 (1-4), 359–379.
Benson, R.H., 1978. The paleoecology of the ostracods of DSDP Leg 42A. In: Hsü, K., Montadert, L. (Eds.), Initial Reports of the Deep-Sea Drilling Project, 42. U.S. Government Printing Office, Washington, pp. 777–787.
Benson, R.H., Rakic-El Bied, K., 1991. The Messinian parastratotype at Cuevas de Almanzora, Vera Basin, SE Spain; refutation of the deep-basin, shallow-water hypothesis? Micropaleontology 37 (3), 289–302.
Benson, R.H., Rakic-El Bied, K., Bonaduce, G., 1991. An important current reversal (influx) in the Rifian Corridor (Morocco) at the Tortonian-Messinian boundary: the end of Tethys Ocean. Paleoceanography 6 (1), 165–192.
Berner, R.A., 1999. Atmospheric oxygen over Phanerozoic time. Proc. Natl. Acad. Sci. 96, 10955.
Bertini, A., 2006. The Northern Apennines palynological record as a contribute for the reconstruction of the Messinian paleoenvironments. Sediment. Geol. 188, 235–258.
Bertini, A., Corradini, D., 1998. Biostratigraphic and paleoecological significance of Galeacysta etrusca in the "Lago-Mare" facies from the Mediterranean area (Neogene). Dino NTNU Vitensk. Mus. Rapp. Bot. ser. 6, 15–16. Abstract.
Bertoni, C., Cartwright, J., 2007. Major erosion at the end of the Messinian Salinity Crisis: evidence from the Levant Basin, Eastern Mediterranean. Basin Res. 19, 1–18.
Bessis, F., 1986. Some remarks on the study of subsidence of sedimentary basins. Application to the Gulf of Lions margin (Western Mediterranean). Mar. Pet. Geol. 3, 37–63.
Bialik, O.M., Frank, M., Betzler, C., Zammit, R., Waldmann, N.D., 2019. Two-step closure of the Miocene Indian Ocean Gateway to the Mediterranean. Sci. Rep. 9 (1), 1–10. https://doi.org/10.1038/s41598-019-45308-7.
Biscaye, P.E., Ryan, W.B.F., Wezel, F.C., 1972. Age and nature of the Pan-Mediterranean subbottom reflector M. The Mediterranean Sea 83–90.
Blanc, P.L., 2002. The opening of the Plio-Quaternary Gibraltar Strait: assessing the size of a cataclysm. Geodin. Acta 15, 303–317.
Blanc-Valleron, M.-M., Rouchy, J.-M., Pierre, C., Badaut-Trauth, D., Schuler, M., 1998. Evidence of Messinian nonmarine deposition at site 968 (Cyprus lower slope). In: Proceedings of the Ocean Drilling Program, Scientific Results. ODP Sci. Results 160, Texas, USA, pp. 43–445.
Bonaduce, G., Sgarrella, F., 1999. Paleoecological interpretation of the latest Messinian sediments from southern Sicily (Italy). Soc. Geol. Ital. Mem. 54, 83–91.
Booth-Rea, G., Ranero, R., Grevemeyer, I.C., 2018. The Alboran volcanic-arc modulated the Messinian faunal exchange and salinity crisis. Sci. Rep. 8 https://doi.org/10.1038/s41598-018-31307-7.
Borsetti, A.M., Curzi, P.V., Landuzzi, V., Mutti, M., Ricci Lucchi, F., Sartori, R., Tomadin, L., Zuffa, G.G., 1990. Messinian and pre-Messinian sediments from ODP Leg 107 Sites 652 and 654 in the Tyrrhenian Sea: sedimentologic and petrographic study and possible comparisons with Italian sequences. In: Kastens, K.A., Mascle, J., et al. (Eds.), Proceedings of the Ocean Drilling Program, Scientific Results, 107, pp. 169–186.
Bossio, A., Esteban, M., Giannelli, L., Longinelli, A., Mazzanti, R., Mazzei, R., Ricci Lucchi, F., Salvatorini, G., 1978. Some aspects of the upper Miocene in Tuscany. In: Messinian Seminar, vol. 4. Pacini, Pisa, 88 pp.
Bossio, A., Costantini, A., Lazzarotto, A., Liotta, D., Mazzanti, R., 1993. Rassegna delle conoscenze sulla stratigrafia del Neoautoctono toscano. Mem. Soc. Geol. Ital. 49, 17–98.
Bosworth, W., Huchon, P., Mc Clay, K., 2005. The Red Sea and Gulf of Aden Basins. J. Afr. Earth Sci. 43, 334–378.
Bowman, S.A., 2012. A comprehensive review of the MSC facies and their origins in the offshore Sirt Basin, Libya. Pet. Geosci. 18, 457–469. https://doi.org/10.1144/petgeo2011-070.
Braga, J.C., Martín, J.M., Riding, R., Aguirre, J., Sanchez-Almazo, I.M., Dinares-Turell, J., 2006. Testing models for the Messinian salinity crisis: the Messinian record in Almería, SE Spain. Sediment. Geol. 188-189, 131–154. https://doi.org/10.1016/j.sedgeo.2006.03.002.
Brolsma, M.J., 1975. Lithostratigraphy and Foraminiferal assemblages of the Miocene/Pliocene transitional strata at Capo Rossello and Eraclea Minoa (Sicily, Italy): Kon. Ned. Akad. Wetensch. Amsterdam Proc 78, 1–40.
Brunner, B., Bernasconi, S.M., 2005. A revised isotope fractionation model for dissimilatory sulfate reduction in sulfate reducing bacteria. Geochim. Cosmochim. Acta 69, 4759–4771.
Brunner, B., Bernasconi, S.M., Kleikemper, J., Schroth, M.H., 2005. A model for oxygen and sulfur isotope fractionation in sulfate during bacterial sulfate reduction processes. Geochim. Cosmochim. Acta 69, 4773–4785.
Bulian, F., Sierro, F.J., Santiago, L., Jiménez-Espejo, F.J., Bassetti, M.A., 2021. Messinian West Alboran Sea record in the proximity 1 of Gibraltar: early signs of Atlantic-Mediterranean gateway restriction. Mar. Geol. 434.
Burke, A., Present, T.M., Paris, G., Rae, E.C.M., Sandilands, B.H., Gaillardet, J., Peucker-Ehrenbrink, B., Fischer, W.W., McClelland, J.W., Spencer, R.G.M., Voss, B.M., Adkins, J.F., 2018. Sulfur isotopes in rivers: Insights into global weathering budgets, pyrite oxidation, and the modern sulfur cycle. Earth Planet. Sci. Lett. 496, 168–177.
Butler, R.W.H., Likhorish, W.H., Grasso, M., Pedley, H.M., Ramberti, L., 1995. Tectonics and sequence stratigraphy in Messinian Basins, Sicily: constraints on the initiation and termination of the Mediterranean salinity crisis. Geol. Soc. Am. Bull. 107, 425–439.
Butler, R.W.H., Maniscalco, R., Sturiale, G., Grasso, M., 2015. Stratigraphic variations control deformation patterns in evaporite basins: Messinian examples, onshore and offshore Sicily (Italy). J. Geol. Soc. 172, 113–124.
Camerlenghi, A., Aloisi, V., 2020. Uncovering the Mediterranean Salt Giant (MEDSALT)-Scientific Networking as Incubator of Cross-disciplinary Research in Earth Sciences. Eur. Rev. 28 (1), 40–61. https://doi.org/10.1017/S1062798719000255.
Camerlenghi, A., Accettella, D., Costa, S., Lastras, G., Acosta, J., Canals, M., Wardell, N., 2009. Morphogenesis of the SW Balearic continental slope and adjacent abyssal plain, Western Mediterranean Sea. Int. J. Earth Sci. 98, 735–750.
Camerlenghi, A., Del Ben, A., Hübscher, C., Forlin, E., Geletti, R., Brancatelli, G., Micallef, A., Saule, M., Facchin, L., 2019. Seismic markers of the Messinian salinity crisis in the deep Ionian Basin. Basin Res bre.12392. https://doi.org/10.1111/bre.12392.
Cameselle, A.L., Urgeles, R., 2017. Large-scale margin collapse during Messinian early sea-level drawdown: the SW Valencia trough, NW Mediterranean. Basin Res. 29, 576–595. https://doi.org/10.1111/bre.12170.
Cameselle, A.L., Urgeles, R., De Mol, B., Camerlenghi, A., Canning, J.C., 2014. Late Miocene sedimentary architecture of the Ebro Continental Margin (Western Mediterranean): implications to the Messinian Salinity Crisis. Int. J. Earth Sci. 103 (2), 423–440.

Campillo, A.C., Maldonado, A., Mauffret, A., 1992. Stratigraphic and Tectonic evolution of the Western Alboran Sea late Miocene to recent. Geo-Mar. Lett. 12, 165–172.
Capella, W., Flecker, R., Hernández-Molina, F.J., Simon, D., Meijer, P.T., Rogerson, M., Sierro, F.J., Krijgsman, W., 2019. Mediterranean isolation preconditioning the Earth System for late Miocene climate cooling. Sci. Rep. 9 (1), 1–8. https://doi.org/10.1038/s41598-019-40208-2.
Capella, W., Spakman, W., van Hinsbergen, D.J., Chertova, M.V., Krijgsman, W., 2020. Mantle resistance against Gibraltar slab dragging as a key cause of the Messinian Salinity Crisis. Terra Nova 32 (2), 141–150. https://doi.org/10.1111/ter.12442.
Capellini, G., 1880. Gli strati a Congerie o la formazione gessoso solfifera nella provincia di Pisa e nei dintorni di Livorno. Mem. R. Accad. Lincei., Cl. Sci. Fis. Mat. Nat. 5, 1–64.
Carbonnel, G., 1978. La zone à Loxoconcha djaffarovi Schneider (ostracodes, Miocène supérieur) ou le Messinien de la vallée du Rhône. Rev. Micropaleontol. 21 (3), 106–118.
Carnevale, G., Landini, W., Sarti, G., 2006a. Mare versus Lago-mare: marine fishes and the Mediterranean environment at the end of the Messinian Salinity Crisis. J. Geol. Soc. 163 (1), 75–80. https://doi.org/10.1144/0016-764904-158.
Carnevale, G., Caputo, D., Landini, W., 2006b. Late Miocene fish otoliths from the Colombacci Formation (Northern Apennines, Italy): implications for the Messinian 'Lago-mare'event. Geol. J. 41 (5), 537–555. https://doi.org/10.1002/gj.1055.
Carnevale, G., Longinelli, A., Caputo, D., Barbieri, M., Landini, W., 2008. Did the Mediterranean marine reflooding precede the Miocene/Pliocene boundary? Paleontological and geochemical evidence from upper Messinian sequences of Tuscany, Italy. Paleogeogr. Paleoclimatol. Paleoecol. 257, 81–105. https://doi.org/10.1016/j.paleo.2007.09.005.
Carnevale, G., Dela Pierre, F., Natalicchio, M., Landini, W., 2018. Fossil marine fishes and the "Lago Mare" event: Has the Mediterranean ever transformed into a brackish lake? Newsl. Stratigr. 51, 57–72. https://doi.org/10.1127/nos/2016/0343.
Carnevale, G., Gennari, R., Lozar, F., Natalicchio, M., Pellegrino, L., Dela Pierre, F., 2019. Living in a deep desiccated Mediterranean Sea: An overview of the Italian fossil record of the Messinian salinity crisis. Boll. Soc. Paleontol. Ital. 58, 109–140. https://doi.org/10.4435/BSPI.2019.04.
Cartwright, J.A., Jackson, M.P.A., 2008. Initiation of gravitational collapse of an evaporitic basin margin: the Messinian saline giant, Levant Basin, eastern Mediterranean. Geol. Soc. Am. Bull. 120, 399–413.
Caruso, A., Pierre, C., Blanc-Valleron, M.M., Rouchy, J.M., 2015. Carbonate deposition and diagenesis in evaporitic environments: the evaporative and sulphur-bearing limestones during the settlement of the Messinian Salinity Crisis in Sicily and Calabria. Palaeogeogr. Palaeoclimatol. Palaeoecol. 429, 136–162. https://doi.org/10.1016/j.palaeo.2015.03.035.
Caruso, A., Blanc-Valleron, M.M., Da Prato, S., Pierre, C., Rouchy, J.M., 2020. The late Messinian "Lago-Mare" event and the Zanclean Reflooding in the Mediterranean Sea: new insights from the Cuevas del Almanzora section (Vera Basin, South-Eastern Spain). Earth Sci. Rev. 200, 102993 https://doi.org/10.1016/j.earscirev.2019.102993.
Casati, P., Bertozzi, P., Cita, M.B., Longinelli, A., Damiani, V., 1976. Stratigraphy and paleoenvironment of the Messinian "Colombacci" Formation in the periadriatic trough. A pilot study. Memorie della Società Geologica Italiana 16, 173–195.
Castradori, D., 1998. Calcareous nannofossils in the basal Zanclean of the Eastern Mediterranean Sea: remarks on paleoceanography and sapropel formation. In: Robertson, A.H.F., Emeis, K.C., Richter, C., Camerlenghi, A. (Eds.), Proceedings of the Ocean Drilling Program. US Government Printing Office, Washington, pp. 113–123. Scientific Results 160.
Catalano, R., Valenti, V., Albanese, C., Accaino, F., Sulli, A., Tinivella, U., Morticelli, M. G., Zanolla, C., Giustiniani, M., 2013. Sicily's fold–thrust belt and slab roll-back: the SI. RI. PRO. seismic crustal transect. J. Geol. Soc. 170 (3), 451–464.
Cazzini, F.F., Amadori, C., Bosino, A., Fantoni, R., 2020. New seismic evidence of the Messinian paleomorphology beneath Lake Maggiore area (Italy). Ital. J. Geosci. 139 (2), 195–211. https://doi.org/10.3301/IJG.2019.26.
Chumakov, I.S., 1973. Pliocene and Pleistocene deposits of the Nile valley in Nubia and upper Egypt. In: Ryan, W.B.F., Hsu, K.J., et al. (Eds.), Initial Reports of the Deep Sea Drilling Project, 13. US Govern. Print. Office, Washington, DC, pp. 1242–1243.
Cipollari, P., Cosentino, D., Gliozzi, E., 1999. Extension-and compression-related basins in central Italy during the Messinian Lago-Mare event. Tectonophysics 315 (1-4), 163–185.
Cipollari, P., Cosentino, D., Radeff, G., Schildgen, T.F., Faranda, C., Grossi, F., Gliozzi, E., Smedile, A., Gennari, R., Darbas, G., Dudas, F.Ö., Gürbüz, K., Nazik, A., Echtler, H., 2013. Easternmost Mediterranean evidence of the Zanclean flooding event and subsequent surface uplift: Adana Basin, southern Turkey. Geol. Soc. Lond., Spec. Publ. 372 (1), 473–494. https://doi.org/10.1144/SP372.5.
Cita, M.B., 1973. Inventory of biostratigraphical findings and problems. Init. Rep. Deep-Sea Drill. Proj. 13 (2), 1045–1065.
Cita, M.B., Colombo, L., 1979. Sedimentation in the latest Messinian at Capo Rossello (Sicily). Sedimentology 26, 497–522.
Cita, M.B., Wright, R.C., Ryan, W.B.F., Longinelli, A., 1978. Messinian paleoenvironments. In: Hsü, K.J., Montadert, L., et al. (Eds.), Initial Reports of the Deep Sea Drilling Project, 42. U.S. Government Printing Office, Washington D.C, pp. 1003–1035.
Cita, M.B., Santambrogio, S., Melillo, B., Rogate, F., 1990. Messinian Paleoenvironments: New Evidence from the Tyrrhenian Sea (ODP LEG 107). In: Proceedings of the Ocean Drilling Program, Scientific Results, 107, pp. 211–227.
Clauzon, G., 1982. Le canyon messinien du Rhône: Une preuve decisive du "dessicated deep basin model" (Hsu , Cita et Ryan, 1973). Bull. Soc. Geol. Fr. 24, 231–246.
Clauzon, G., Suc, J.-P., Gautier, F., Berger, A., Loutre, M.F., 1996. Alternate interpretation of the Messinian salinity crisis, controversy resolved? Geology 24, 363–366.
Clauzon, G., Suc, J.P., Popescu, S.M., Marunteanu, M., Rubino, J.L., Marinescu, F., Melinte, M.C., 2005. Influence of Mediterranean sea-level changes on the Dacic Basin (Eastern Paratethys) during the late Neogene: the Mediterranean Lago Mare facies deciphered. Basin Res. 17 (3), 437–462. https://doi.org/10.1111/j.1365-2117.2005.00269.x.
Clauzon, G., Suc, J.-P., Do Couto, D., Jouannic, G., Melinte-Dobrinescu, M.C., Jolivet, L., Quillévéré, F., Lebret, N., Mocochain, L., Popescu, S.-M., Martinell, J., Doménech, R., Rubino, J.-L., Gumiaux, C., Warny, S., Bellas, S.M., Gorini, C., Bache, F., Rabineau, M., Estrada, F., 2015. New insights on the Sorbas Basin (SE Spain): the onshore reference of the Messinian salinity crisis. Mar. Pet. Geol. 66, 71–100. https://doi.org/10.1016/j.marpetgeo.2015.02.016.
Claypool, G.E., Holser, W.T., Kaplan, I.R., Sakai, H., Zak, I., 1980. The age curves of sulfur and oxygen isotopes in marine sulfate and their mutual interpretation. Chem. Geol. 28, 199–260.
Colalongo, M.L., Cremonini, G., Farabegoli, E., Sartori, R., Tampieri, R., Tomadin, L., 1976. Paleoenvironmental study of the "Colombacci" Formation in Romagna (Italy): the cella section. Mem. Soc. Geol. Ital. 16, 197–216.
Colombero, S., Alba, D.M., D'Amico, C., Delfino, M., Esu, D., Giuntelli, P., Harzhauser, M., Mazza, P.P.A., Mosca, M., Neubauer, T.A., Pavia, G., Pavia, M., Villa, A., Carnevale, G., 2017. Late Messinian mollusks and vertebrates from Moncucco Torinese, north-western Italy. Paleoecological and paleoclimatological implications. Palaeontol. Electron. 1–66, 20.1.10A.
Comas, M.C., Zahn, R., Klaus, A., et al., 1996. Proceedings of the Ocean Drilling Program, Initial Reports, v. 161: College Station, Texas, Ocean Drilling Program.
Comas, M.C., Platt, J.P., Soto, J.I., Watts, A.B., 1999. 44. The origin and tectonic history of the Alboran Basin: Insights from leg 161 results: Proceedings of the Ocean Drilling Program. Sci. Res. 161, 555–580.
Consorti, L., Sabbatino, M., Parente, M., 2020. Insights on the paleoecology of Ammonia (Foraminifera, Rotalioidea) from Miocene carbonates of central and southern Apennines (Italy). Palaeogeogr. Palaeoclimatol. Palaeoecol. 110105 https://doi.org/10.1016/j.palaeo.2020.110105.
Corbí, H., Soria, J.M., 2016. Late Miocene-early Pliocene planktonic foraminifer event-stratigraphy of the Bajo Segura basin: a complete record of the western Mediterranean. Mar. Pet. Geol. 77, 1010–1027. https://doi.org/10.1016/j.marpetgeo.2016.08.004.
Corbí, H., Soria, J.M., Lancis, C., Giannetti, A., Tent-Manclús, J.E., Dinarès-Turell, J., 2016. Sedimentological and paleoenvironmental scenario before, during, and after the Messinian Salinity Crisis: The San Miguel de Salinas composite section (western Mediterranean). Mar. Geol. 379, 246–266. https://doi.org/10.1016/j.margeo.2016.05.017.
Corbí, H., Soria, J.M., Giannetti, A., Yébenes, A., 2020. The step-by-step restriction of the Mediterranean (start, amplification, and consolidation phases) preceding the Messinian Salinity Crisis (climax phase) in the Bajo Segura basin. Geo-Mar. Lett. 1–21. https://doi.org/10.1007/s00367-020-00647-7.
Cornée, J.J., Munch, P., Achalhi, M., Merzeraud, G., Azdimousa, A., Quillevere, F., Melinte-Dobrinescu, M., Chaix, C., Ben Moussa, A., Lofi, J., Seranne, A., Moissette, P., 2016. The Messinian erosional surface and early Pliocene reflooding in the Alboran Sea: new insights from the Boudinar basin. Morocco. Sediment. Geol. 333, 115–129. https://doi.org/10.1016/j.sedgeo.2015.12.014.
Corradini, D., Biffi, U., 1988. Etude des dinokystes a la limite Messinien-Pliocene dans la coupe Cava Serredi, Tos cane, Italie. Bulletin des Centres de Recherche Exploration-Production Elf-Aquitaine 12 (1), 221–236.
Cosentino, D., Cipollari, P., Mastro, S.L., Giampaolo, C., 2005. High-frequency cyclicity in the latest Messinian Adriatic foreland basin: insight into paleoclimate and paleoenvironments of the Mediterranean Lago-Mare episode. Sediment. Geol. 178 (1–2), 31–53. https://doi.org/10.1016/j.sedgeo.2005.03.010.
Cosentino, D., Federici, I., Cipollari, P., Gliozzi, E., 2006. Environments and tectonic instability in central Italy (Garigliano Basin) during the late Messinian Lago-Mare episode: new data from the onshore Mondragone 1 well. Sediment. Geol. 188, 297–317. https://doi.org/10.1016/j.sedgeo.2006.03.010.
Cosentino, D., Gliozzi, E., Pionzi, G., 2007. The late Messinian Lago-Mare episode in the Mediterranean Basin: preliminary report on the occurrence of Paratethyan ostracod fauna from central Crete (Greece). Geobios 40 (3), 339–349. https://doi.org/10.1016/j.geobios.2007.01.001.
Cosentino, D., Darbaş, G., Gürbüz, K., 2010. The Messinian salinity crisis in the marginal basins of the peri-Mediterranean orogenic systems: examples from the central Apennines (Italy) and the Adana Basin (Turkey). EGUGA 2462.
Cosentino, D., Bertini, A., Cipollari, P., Florindo, F., Gliozzi, E., Grossi, F., Lo Mastro, S., Sprovieri, M., 2012. Orbitally forced paleoenvironmental and paleoclimate changes in the late postevaporitic Messinian of the central Mediterranean Basin. GSA Bull. 124 (3-4), 499–516. https://doi.org/10.1130/B30462.1.
Cosentino, D., Buchwaldt, R., Sampalmieri, G., Iadanza, A., Cipollari, P., Schildgen, T.F., Hinnov, L.A., Ramezani, J., Bowring, S.A., 2013. Refining the Mediterranean "Messinian gap" with high-precision U-Pb zircon geochronology, central and northern Italy. Geology 41, 323–326. https://doi.org/10.1130/G33820.1.
Cosentino, D., Bracone, V., D'Amico, C., Cipollari, P., Esu, D., Faranda, C., Frezza, V., Gliozzi, E., Grossi, F., Gupperrieri, P., Iadanza, A., Kotsakis, D., Soulié-Märsche, I., 2018. The record of the Messinian salinity crisis in mobile belts: insights from the Molise allochthonous units (southern Apennines, Italy). Paleogeogr. Paleoclimatol. Paleoecol. 503, 112–130. https://doi.org/10.1016/j.paleo.2018.04.028.
Coulson, S., Pico, T., Austermann, J., Powell, E., Moucha, R., Mitrovica, J.X., 2019. The role of isostatic adjustment and gravitational effects on the dynamics of the Messinian salinity crisis. Earth Planet. Sci. Lett. 525, 115760.

Dal Cin, M., Del Ben, A., Mocnik, A., Accaino, F., Geletti, R., Wardell, N., Zgur, F., Camerlenghi, A., 2016. Seismic imaging of late Miocene (Messinian) evaporites from western Mediterranean back-arc basins. Pet. Geosci. 22, 297–308. https://doi.org/10.1144/petgeo2015-096.

De Benedetti, A., 1982. The problem of the origin of the salt deposits in the Mediterranean and of their relations to other salt occurrences in the Neogene formations of the contiguous regions. Mar. Geol. 49, 91–114.

de la Chapelle, G., Gaudant, J., 1987. Decouverte de deux nouveaux gisements de poissons fossiles messiniens dans le bassin de Nijar-Carboneras (Andalousie Orientale): Signification paleoecologique et implications paleogeographiques.

de la Peña, L.G., Ranero, C.R., Gràcia, E., Booth-Rea, G., 2020. The evolution of the westernmost Mediterranean basins. Earth Sci. Rev. 103445.

Decima, A., 1964. Ostracodi del Gen. Cyprideis JONES del Neogene e del Quaternario italiani. Paleont. Italica, 57, p. 81.

Decima, A., Sprovieri, R., 1973. Comments on late Messinian microfaunas in several sections from Sicily. In: Drooger, C.W. (Ed.), Messinian Events in the Mediterranean. North-Holland Pub. Co, Amsterdam, pp. 229–234.

Decima, A., Wezel, F.C., 1971. Osservazioni sulle evaporiti Messiniane della Sicilia centro-meridionale. Rivista Mineraria Siciliana 130-134, 172–187.

Decima, A., Wezel, F.C., 1973. Late Miocene evaporites of the Central Sicilian Basin. In: Ryan, W.B.F., Hsu, K.J. (Eds.), Initial Reports of the Deep Sea Drilling Project, vol. 13. U.S. Gov. Print. Off, Washington, DC, pp. 1234–1240.

Decima, A., Schreiber, B.C., McKenzie, J.A., 1988. The origin of "evaporative" limestones: an example from the Messinian of Sicily (Italy). J. Sediment. Petrol. 58-2, 256–272.

Del Olmo, W.M., 2011. The Messinian in the Gulf of Valencia and Alboran Sea (Spain): paleogeography and paleoceanography implications. Rev. Soc. Geol. Esp. 24, 1–22.

Del Olmo, W.M., Martín, D., 2016. The Messinian record of Spanish onshore and offshore data (Atlantic Ocean and Western Mediterranean Sea). Pet. Geosci. 22 (4), 291–296.

Dela Pierre, F., Bernardi, E., Cavagna, S., Clari, P., Gennari, R., Irace, A., Lozar, F., Lugli, S., Manzi, V., Natalicchio, M., Roveri, M., Violanti, D., 2011. The record of the Messinian salinity crisis in the Tertiary Piedmont Basin (NW Italy): The Alba section revisited. Paleogeogr. Paleoclimatol. Paleoecol. 310, 238–255. https://doi.org/10.1016/j.paleo.2011.07.017.

Dela Pierre, F., Clari, P., Bernardi, E., Natalicchio, M., Costa, M., Cavagna, S., Lozar, F., Lugli, S., Manzi, V., Roveri, M., Violanti, D., 2012. Messinian carbonate-rich beds of the Tertiary Piedmont Basin (NW Italy): microbially-mediated products straddling the onset of the salinity crisis. Palaeogeogr. Palaeoclimatol. Palaeoecol. 34, 78–93. https://doi.org/10.1016/j.palaeo.2012.05.022.

Dela Pierre, F., Clari, P., Natalicchio, M., Ferrando, S., Giustetto, R., Lozar, F., Lugli, S., Manzi, V., Roveri, M., Violanti, D., 2014. Flocculent layers and bacterial mats in the mudstone interbeds of the Primary Lower Gypsum unit (Tertiary Piedmont Basin, NW Italy): archives of paleoenvironmental changes during the Messinian salinity crisis. Mar. Geol. 335, 71–87. https://doi.org/10.1016/j.margeo.2014.05.010.

Dela Pierre, F., Natalicchio, M., Lozar, F., Bonetto, S., Carnevale, G., Cavagna, S., Clari, P., Colombero, S., Violanti, D., 2016. The northermost record of the Messinian salinity crisis (Piedmont Basin, NW Italy). Geol. F. Trips 8, 1–58. https://doi.org/10.3301/GFT.2016.03.

Delrieu, B., Rouchy, J.M., Foucault, A., 1993. La surface d'erosion finimessinienne en Crète centrale (Grèce) et sur le pourtour méditerranéen: Rapports avec la crise de salinité méditerranéenne. Comptes rendus de l'Académie des sciences. Série 2, Mécanique, Physique, Chimie, Sciences de l'univers, Sciences de la Terre 316, no. 4, pp. 527–533.

Dettman, D.L., Flessa, K.W., Roopnarine, P.D., Schöne, B.R., Goodwin, D.H., 2004. The use of oxygen isotope variation in shells of estuarine mollusks as a quantitative record of seasonal and annual Colorado River discharge. Geochim. Cosmochim. Acta 68 (6), 1253–1263.

Di Stefano, A., Sturiale, G., 2010. Refinements of calcareous nannofossil biostratigraphy at the Miocene/Pliocene Boundary in the Mediterranean region. Geobios 43 (1), 5–20.

Do Couto, D., Popescu, S.-M., Suc, J.-P., Melinte-Dobrinescu, M.C., Barhoun, N., Gorini, C., Jolivet, L., Poort, J., Jouannic, G., Auxietre, J.-L., 2014. Lago Mare and the Messinian salinity crisis: evidences from the Alboran Sea (S. Spain). Mar. Pet. Geol. 52, 57–76. https://doi.org/10.1016/j.marpetgeo.2014.01.018.

Doebbert, A.C., Johnson, C.M., Carroll, A.R., Beard, B.L., Pietras, J.T., Carson, M.R., Norsted, B., Throckmorton, L.A., 2014. Controls on Sr isotopic evolution in lacustrine systems: Eocene green river formation, Wyoming. Chem. Geol. 380, 172–189. https://doi.org/10.1016/j.chemgeo.2014.04.008.

Dominici, S., Danise, S., Benvenuti, M., 2018. Pliocene stratigraphic paleobiology in Tuscany and the fossil record of marine megafauna. Earth Sci. Rev. 176, 277–310.

Driussi, O., Maillard, A., Ochoa, D., Lofi, J., Chanier, F., Gaullier, V., Briais, A., Sage, F., Sierro, F., Garcia, M., 2015. Messinian Salinity Crisis deposits widespread over the Balearic Promontory: insights from new high-resolution seismic data. Mar. Pet. Geol. 66, 41–54. https://doi.org/10.1016/j.marpetgeo.2014.09.008.

Druckman, Y., Buchbinder, B., Martinotti, G.M., Tov, R.S., Aharon, P., 1995. The buried Afiq Canyon (eastern Mediterranean, Israel): a case study of a Tertiary submarine canyon exposed in Late Messinian times. Mar. Geol. 123 (3–4), 167–185.

Drury, A.J., Westerhold, T., Hodell, D., Röhl, U., 2018. Reinforcing the North Atlantic backbone: revision and extension of the composite splice at ODP Site 982. Clim. Past 14 (3), 321–338.

Emeis, K.-C., Robertson, A.H.F., Richter, C., et al., 1996. Proc. ODP, Initial Reports, 160: College Station, TX (Ocean Drilling Program).

Englebrecht, A.C., Sachs, J.P., 2005. Determination of sediment provenance at drift sites using hydrogen isotopes and unsaturation ratios in alkenones. Geochim. Cosmochim. Acta 69, 4253–4265.

Estrada, F., Ercilla, G., Gorini, C., Alonso, B., Vazquez, J.T., García-Castellanos, D., Juan, C., Maldonado, A., Ammar, A., Elabbassi, M., 2011. Impact of pulsed Atlantic water inflow into the Alboran Basin at the time of the Zanclean flooding. GeoMar. Lett. 31, 361–376.

Esu, D., 2007. Latest Messinian "Lago-Mare" Lymnocardiinae from Italy: close relations with the Pontian fauna from the Dacic Basin. Geobios 40 (3), 291–302. https://doi.org/10.1016/j.geobios.2006.10.003.

Faranda, C., Gliozzi, E., Cipollari, P., Grossi, F., Darbaş, G., Gürbüz, K., Cosentino, D., 2013. Messinian paleoenvironmental changes in the easternmost Mediterranean Basin: Adana Basin, southern Turkey. Turk. J. Earth Sci. 22 (5), 839–863. https://doi.org/10.3906/yer-1205-11.

Feng, Y.E., Yankelzon, A., Steinberg, J., Reshef, M., 2016. Lithology and characteristics of the Messinian evaporite sequence of the deep Levant Basin, Eastern Mediterranean. Mar. Geol. 376, 118–131. https://doi.org/10.1016/j.margeo.2016.04.004.

Feng, Y.E., Steinberg, J., Reshef, M., 2017. Intra-salt deformation: implications for the evolution of the Messinian evaporites in the levant basin, eastern Mediterranean. Mar. Pet. Geol. 88, 251–267.

Fiduk, J.C., 2009. Evaporites, petroleum exploration, and the Cenozoic evolution of the Libyan shelf margin, central North Africa. Mar. Pet. Geol. 26 (8), 1513–1527.

Flecker, R., de Villiers, S., Ellam, R.M., 2002. Modelling the effect of evaporation on the salinity-$^{87}Sr/^{86}Sr$ relationship in modern and ancient marginal-marine systems: the Mediterranean Messinian Salinity Crisis. Earth Planet. Sci. Lett. 203, 221–233.

Flecker, R., Krijgsman, W., Capella, W., de Castro Martíns, C., Dmitrieva, E., Mayser, J.P., Marzocchi, A., Modestu, S., Ochoa, D., Simon, D., Tulbure, M., van den Berg, B., van der Schee, M., de Lange, G., Ellam, R., Govers, R., Gutjahr, M., Hilgen, F., Kouwenhoven, T., Lofi, J., Meijer, P., Sierro, F.J., Bachiri, N., Barhoun, N., Alami, A. C., Chacon, B., Flores, J.A., Gregory, J., Howard, J., Lunt, D., Ochoa, M., Pancost, R., Vincent, S., Yousfi, M.Z., 2015. Evolution of the late Miocene Mediterranean-Atlantic gateways and their impact on regional and global environmental change. Earth Sci. Rev. 150, 365–392. https://doi.org/10.1016/j.earscirev.2015.08.007.

Fontes, J.-C., Letolle, R., Nesteroff, D., Ryan, W.B.F., 1973. Oxygen, Carbon, Sulfur and Hydrogen stable isotopes in carbonate and sulfate mineral phases of Neogene evaporites, sediments and in interstitial waters. Texas A.M University, O.D.P.C.S., TX, United States (Ed.). In: Initial Reports of the Deep Sea Drilling Project, Covering Leg 13 of the Cruises of the Drilling Vessel Glomar Challenger Lisbon, Portugal to Lisbon, Portugal, August-October 1970., United States, pp. 788–796.

Fortuin, A.R., Krijgsman, W., 2003. The Messinian of the Nijar basin (SE Spain): sedimentation, depositional environments and paleogeographic evolution. Sediment. Geol. 160, 213–242.

Fortuin, A.R., Kelling, J.M.D., Roep, T.B., 1995. The enigmatic Messinian -Pliocene section of Cuevas del Almanzora (Vera Basin, SE Spain) revisited-erosional features and strontium isotope ages. Sediment. Geol. 97, 177–201.

Frey-Martinez, J.F., Cartwright, J.A., Burgess, P.M., Bravo, J.V., 2004. 3D seismic interpretation of the Messinian Unconformity in the Valencia Basin, Spain. Geol. Soc. Lond. Mem. 29 (1), 91–100.

Friedman, G.M., 1973. Petrographic data and comments on the depositional environment of the Miocene sulfates and dolomites at Sites 124, 132, and 134, western Mediterranean Sea. In: Ryan, W.B.F., Hsü, K.J., et al. (Eds.), Initial Reports of the Deep Sea Drilling Project 13. U. S. Government Printing Office, Washington, pp. 695–708.

Frigui, M., Youssef, M.B., Ouaja, M., 2016. Evidences of "Lago-Mare" episode around the Messinian-Pliocene boundary in eastern Tunisia (central Mediterranean). J. Afr. Earth Sci. 123, 57–74. https://doi.org/10.1016/j.jafrearsci.2016.07.007.

Fritz, P., Basharmal, G.M., Drimmie, R.J., Ibsen, J., Qureshi, R.M., 1989. Oxygen isotope exchange between sulphate and water during bacterial reduction of sulphate. Chem. Geol. 79, 99–105.

Gallais, F., Gutscher, M.A., Graindorge, D., Klaeschen, D., 2018. 12.B&E- Ionian Basin. In J. Lofi (Ed.), Seismic Atlas of the Messinian salinity crisis markers in the Mediterranean sea. Volume 2. - Mémoires de la Société géologique de France, n.s., 2018, t. 181, and Commission for the Geological Map of the World, pp. 41–44.

García-Alix, A., Minwer-Barakat, R., Martín Suárez, E., Freudenthal, M., Aguirre, J., Kaya, F., 2016. Updating the Europe-Africa small mammal exchange during the late Messinian. J. Biogeogr. 43 (7), 1336–1348.

Garcia-Castellanos, D., Villaseñor, A., 2011. Messinian salinity crisis regulated by competing tectonics and erosion at the Gibraltar arc. Nature 480, 359–363. https://doi.org/10.1038/nature10651.

Garcia-Castellanos, D., Estrada, F., Jiménez-Munt, I., Gorini, C., Fernàndez, M., Vergés, J., De Vicente, R., 2009. Catastrophic flood of the Mediterranean after the Messinian salinity crisis. Nature 462, 10. https://doi.org/10.1038/nature08555.

Garcia-Castellanos, D., Micallef, A., Estrada, F., Camerlenghi, A., Ercilla, G., Periáñez, R., Abril, J.M., 2020. The Zanclean megaflood of the Mediterranean-Searching for independent evidence. Earth Sci. Rev. 201, 103061. https://doi.org/10.1016/j.earscirev.2019.103061.

García-García, F., Corbí, H., Soria, J.M., Viseras, C., 2011. Architecture analysis of a river flood-dominated delta during an overall sea-level rise (Early Pliocene, SE Spain). Sediment. Geol. 237, 102–113.

García-Veigas, J., Orti, F., Rosell, L., Ayora, C., Rouchy, J.M., Lugli, S., 1995. The Messinian salt of the Mediterranean: geochemical study of the salt from the Central Sicily Basin and comparison with the Lorca Basin (Spain). Bull. Soc. Géol. Fr 166, 699–710.

García-Veigas, J., Cendón, D.I., Gibert, L., Lowenstein, T.K., Artiaga, D., 2018. Geochemical indicators in Western Mediterranean Messinian evaporites: Implications for the salinity crisis. Mar. Geol. 403, 197–214. https://doi.org/10.1016/j.margeo.2018.06.005.

Gargani, J., Moretti, I., Letouzey, J., 2008. Evaporite accumulation during the Messinian Salinity Crisis: the Suez rift case. Geophys. Res. Lett. 35 (2) https://doi.org/10.1029/2007GL032494.
Gaullier, V., Chanier, F., Lymer, G., Vendeville, B., Maillard, A., Thinon, I., Lofi, J., Sage, F., Loncke, L., 2014. Salt tectonics and crustal tectonics along the Eastern Sardinian margin, Western Tyrrhenian: new insights from the «METYSS 1» cruise. Tectonophysics. https://doi.org/10.1016/j.tecto.2013.12.015.
Geletti, R., Zgur, F., Del Ben, A., Buriola, F., Fais, S., Fedi, M., Forte, E., Mocknik, A., Paoletti, V., Pipan, M., Ramella, R., Romeo, R., Romi, A., 2014. The Messinian Salinity Crisis: new seismic evidence in the West-Sardinian Margin and Eastern Sardo-Provençal basin (West Mediterranean Sea). Mar. Geol. 351, 76–90. https://doi.org/10.1016/j.margeo.2014.03.019.
Gennari, R., Iaccarino, S.M., Di Stefano, A., Sturiale, G., Cipollari, P., Manzi, V., Roveri, M., Cosentino, D., 2008. The Messinian–Zanclean boundary in the Northern Apennine. Stratigraphy 5, 307–322.
Gennari, R., Manzi, V., Angeletti, L., Bertini, A., Biffi, U., Ceregato, A., Rosso, A., 2013. A shallow water record of the onset of the Messinian salinity crisis in the Adriatic foredeep (Legnagnone section, Northern Apennines). Paleogeogr. Paleoclimatol. Paleoecol. 386, 145–164.
Ghibaudo, G., Clari, P., Perello, M., 1985. Litostratigrafia, sedimentologia ed evoluzione tettonico-sedimentaria dei depositi miocenici del margine sud-orientale del bacino terziario ligure-piemontese (Valli Borbera, Scrivia e Lemme). In memoria di Carlo Sturani. Boll. Soc. Geol. Ital. 104 (3), 349–397.
Ghielmi, M., Minervini, M., Nini, C., Rogledi, S., Rossi, M., Vignolo, A., 2010. Sedimentary and tectonic evolution in the eastern Po-Plain and northern Adriatic Sea area from Messinian to Middle Pleistocene (Italy). Rendiconti Lincei 21 (1), 131–166. https://doi.org/10.1007/s12210-010-0101-5.
Ghielmi, M., Minervini, M., Nini, C., Rogledi, S., Rossi, M., 2013. Late Miocene-Middle Pleistocene sequences in the Po Plain-Northern Adriatic Sea (Italy): the stratigraphic record of modification phases affecting a complex foreland basin. Marine and Petroleum Geology, Special Issue: The Geology of the Periadriatic Basin and of the Adriatic Sea 42, 50–81. https://doi.org/10.1016/j.marpetgeo.2012.11.007.
Gignoux, M., 1936a. Géologie stratigraphique, 2°édition. Masson, Paris.
Gignoux, M., 1936b. Géologie stratigraphique, 2°édition. Masson, Paris.
Gillet, S., 1932. Essai de classification du Miocène superieur et du Pliocene inferieur de Roumanie. La Transylvanie et le Banat. Comptes Rendus Hebdomadaires des séances de l'Académie des sciences. Séance 27 Decembre, 1932. Académie des Sciences, Paris.
Gillet, S., 1933. Essai de classification du Miòcene supérieur et du Pliocène inférieur de Roumanie. Le bassin dacique. Comptes Rendus Hebdomadaires des séances de l'Académie des sciences. 01/1933. Académie des Sciences, Paris.
Gladstone, R., Flecker, R., Valdes, P., Lunt, D., Markwick, P., 2007. The Mediterranean hydrologic budget from a Late Miocene global climate simulation. Paleogeogr. Paleoclimatol. Paleoecol. 251 (2), 254–267. https://doi.org/10.1016/j.paleo.2007.03.050.
Gliozzi, E., 1999. A late Messinian brackish water ostracod fauna of Paratethyan aspect from Le Vicenne Basin (Abruzzi, central Apennines, Italy). Paleogeogr. Paleoclimatol. Paleoecol. 151 (1-3), 191–208.
Gliozzi, E., Grossi, F., 2008. Late Messinian lago-mare ostracod paleoecology: a correspondence analysis aroach. Paleogeogr. Paleoclimatol. Paleoecol. 264 (3-4), 288–295. https://doi.org/10.1016/j.paleo.2007.03.055.
Gliozzi, E., Ceci, M.E., Grossi, F., Ligios, S., 2007. Paratethyan ostracod immigrants in Italy during the Late Miocene. Geobios 40 (3), 325–337. https://doi.org/10.1016/j.geobios.2006.10.004.
Golovina, L.A., Radionova, E.P., van Baak, C.G., Krijgsman, W., Palcu, D.V., 2019. A Late Maeotian age (6.7-6.3 Ma) for the enigmatic "Pebbly Breccia" unit in DSDP Hole 380A of the Black Sea. Paleogeogr. Paleoclimatol. Paleoecol. 533, 109269. https://doi.org/10.1016/j.paleo.2019.109269.
Gomes, M.L., Johnston, D.T., 2017. Oxygen and sulfur isotopes in sulfate in modern euxinic systems with implications for evaluating the extent of euxinia in ancient oceans. Geochim. Cosmochim. Acta 205, 331–359.
Gorini, C., Lofi, J., Duvail, C., Dos Reis, A.T., Guennoc, P., Lestrat, P., Mauffret, A., 2005. The Late Messinian salinity crisis and Late Miocene Tectonism: interaction and consequence on the physiography and post-rift evolution of the gulf of Lions margin. Mar. Pet. Geol. 22, 695–712.
Griffin, D.L., 2002. Aridity and humidity: two aspects of the late Miocene climate of North Africa and the Mediterranean. Paleogeogr. Paleoclimatol. Paleoecol. 182 (1-2), 65–91.
Grossi, F., Cosentino, D., Gliozzi, E., 2008. Late Messinian Lago-Mare ostracods and paleoenvironments of the central and eastern Mediterranean Basin. Boll. Soc. Paleontol. Ital. 47 (2), 131–146.
Grossi, F., Gliozzi, E., Cosentino, D., 2011. Paratethyan ostracod immigrants mark the biostratigraphy of the Messinian Salinity Crisis. Joannea Geologie und Paleontologie 11, 66–68.
Grossi, F., Gliozzi, E., Anadón, P., Castorina, F., Voltaggio, M., 2015. Is Cyprideis agrigentina Decima a good paleosalinometer for the Messinian Salinity Crisis? Morphometrical and geochemical analyses from the Eraclea Minoa section (Sicily). Paleogeogr. Paleoclimatol. Paleoecol. 419, 75–89. https://doi.org/10.1016/j.paleo.2014.09.024.
Grothe, A., 2016. The Messinian Salinity Crisis: a Paratethyan perspective (Doctoral dissertation, University Utrecht).
Grothe, A., Sangiorgi, F., Mulders, Y.R., Vasiliev, I., Reichart, G.-J., Brinkhuis, H., Stoica, M., Krijgsman, W., 2014. Black Sea desiccation during the Messinian Salinity Crisis: fact or fiction? Geology 42 (7), 563–566. https://doi.org/10.1130/G35503.1.
Grothe, A., Sangiorgi, F., Brinkhuis, H., Stoica, M., Krijgsman, W., 2018. Migration of the dinoflagellate Galeacysta etrusca and its implications for the Messinian Salinity Crisis. Newsl. Stratigr. 51 (1), 73–91. https://doi.org/10.1127/nos/2016/0340.
Grothe, A., Andreetto, F., Reichart, G.J., Wolthers, M., Van Baak, C.G., Vasiliev, I., Stoica, M., Sangiorgi, F., Middelburg, J.J., Davies, G.R., Krijgsman, W., 2020. Paratethys pacing of the Messinian Salinity Crisis: low salinity waters contributing to gypsum precipitation? Earth Planet. Sci. Lett. 532, 116029 https://doi.org/10.1016/j.epsl.2019.116029.
Grunert, P., Harzhauser, M., Rosenthal, Y., Carnevale, G., 2016. Estuarine Lago Mare fauna from the Tertiary Piedmont Basin indicates episodic Atlantic/Mediterranean exchange during the final stage of the Mediterranean Salinity Crisis. Paleogeogr. Paleoclimatol. Paleoecol. 457, 70–79. https://doi.org/10.1016/j.paleo.2016.06.005.
Guennoc, P., Réhault, J.P., Thinon, I., 2011. West-Corsica Margin: MSC basinal units. In: Lofi, J., et al. (Eds.), Mémoires de la Société géologique de France and World Geological Map Commission ed, pp. 1–72.
Guerra-Merchán, A., Serrano, F., Garcés, M., Gofas, S., Esu, D., Gliozzi, E., Grossi, F., 2010. Messinian Lago-Mare deposits near the strait of Gibraltar (Malaga basin, S Spain). Paleogeogr. Paleoclimatol. Paleoecol. 285 (3-4), 264–276. https://doi.org/10.1016/j.paleo.2009.11.019.
Guerra-Merchán, A., Serrano, F., Hlila, R., El Kadiri, K., de Galdeano, C.S., Garcés, M., 2014. Tectono-sedimentary evolution of the peripheral basins of the Alboran Sea in the arc of Gibraltar during the latest Messinian-Pliocene. J. Geodyn. 77, 158–170. https://doi.org/10.1016/j.jog.2013.12.003.
Gülyüz, E., Durak, H., Özkaptan, M., Krijgsman, W., 2020. Paleomagnetic constraints on the early Miocene closure of the southern Neo-Tethys (Van region; East Anatolia): Inferences for the timing of Eurasia-Arabia collision. Glob. Planet. Chang. 185, 103089. https://doi.org/10.1016/j.gloplacha.2019.103089.
Güneş, P., Aksu, A.E., Hall, J., 2018. Internal seismic stratigraphy of the Messinian evaporites across the northern sector of the eastern Mediterranean Sea. Mar. Pet. Geol. 91, 297–320. https://doi.org/10.1016/j.marpetgeo.2018.01.016.
Gvirtzman, Z., Reshef, M., Buch-Leviatan, O., Ben-Avraham, Z., 2013. Intense salt deformation in the Levant Basin in the middle of the Messinian salinity crisis. Earth Planet. Sci. Lett. 379, 108–119.
Gvirtzman, Z., Reshef, M., Buch-Leviatan, O., Groves-Gidney, G., Karcz, Z., Makovsky, Y., Ben-Avraham, Z., 2015. Bathymetry of the Levant basin: interaction of salt-tectonics and surficial mass movements. Mar. Geol. 360, 25–39. https://doi.org/10.1016/j.margeo.2014.12.001.
Gvirtzman, Z., Manzi, V., Calvo, R., Gavrieli, I., Gennari, R., Lugli, S., Reghizzi, M., Roveri, M., 2017. Intra-Messinian truncation surface in the Levant Basin explained by subaqueous dissolution. Geology 45 (10), 915–918. https://doi.org/10.1130/G39113.1.
Hajj, F., Poszwa, A., Bouchez, J., Guérold, F., 2017. Radiogenic and "stable" strontium isotopes in provenance studies: a review and first results on archaeological wood from shipwrecks. J. Archaeol. Sci. 86, 24–49. https://doi.org/10.1016/j.jas.2017.09.005.
Hajós, M., 1973. 34.5. The Mediterranean diatoms. In: Proceedings of the Ocean Drilling Program: Initial report. Part A, 944.
Hallett, D., 2002. Petroleum Geology of Libya. Elsevier Inc., New York, 503 pp.
Haq, B., Gorini, C., Baur, J., Moneron, J., Rubino, J.L., 2020. Deep Mediterranean's Messinian evaporite giant: how much salt? Glob. Planet. Chang. 184, 103052 https://doi.org/10.1016/j.gloplacha.2019.103052.
Hardie, L.A., Lowenstein, T.K., 2004. Did the Mediterranean Sea dry out during the Miocene? A reassessment of the evaporite evidence from DSDP Legs 13 and 42A cores. J. Sediment. Res. 74, 453–461.
Harzhauser, M., Neubaupper, T.A., Georgopoulou, E., Esu, D., D'Amico, C., Pavia, G., Giuntelli, P., Carnevale, G., 2015. Late Messinian continental and Lago-Mare gastropods from the Tertiary Piedmont Basin. NW Italy. Boll. Soc. Paleontol. Ital. 54, 1–53. https://doi.org/10.4435/BSPI.2015.1.
Herbert, T.D., Lawrence, K.T., Tzanova, A., Peterson, L.C., Caballero-Gill, R., Kelly, C.S., 2016. Late Miocene global cooling and the rise of modern ecosystems. Nat. Geosci. 9, 843–847. https://doi.org/10.1038/ngeo2813.
Hilgen, F.J., 1991. Astronomical calibration of Gauss to Matuyama sapropels in the Mediterranean and implication for the geomagnetic polarity time scale. Earth Planet. Sci. Lett. 104 (2-4), 226–244.
Hilgen, F.J., Krijgsman, W., Langereis, C.G., Lourens, L.J., Santarelli, A., Zachariasse, W. J., 1995. Extending the astronomical (polarity) time scale into the Miocene. Earth Planet. Sci. Lett. 136, 495–510.
Hilgen, F., Kuiper, K., Krijgsman, W., Snel, E., van der Laan, E., 2007. Astronomical tuning as the basis for high resolution chronostratigraphy: the intricate history of the Messinian Salinity Crisis. Stratigraphy 4 (2-3), 231–238.
Hodell, D.A., Benson, R.H., Kent, D.V., Boersma, A., Rakic-el Bied, K., 1994. Magnetostratigraphic, biostratigraphic, and stable isotope stratigraphy of an Upper Miocene drill core from the Salé Briqueterie (northwest Morocco): a high-resolution chronology for the Messinian stage. Paleoceanography 9, 835–855.
Hodell, D.A., Curtis, J.H., Sierro, F.J., Raymo, M.E., 2001. Correlation of late Miocene to early Pliocene sequences between the Mediterranean and North Atlantic. Paleoceanography 16, 164–178.
Hsü, K.J., 1972. Origin of Saline Giants: a critical review after the discovery of the Mediterranean evaporite. Earth-Sci. Rev. 8, 371–396.
Hsü, K.J., Ryan, W.B.F., Cita, M., 1973a. Late Miocene desiccation of the Mediterranean. Nature 242, 240.
Hsü, K.J., Cita, M.B., Ryan, W.B.F., 1973b. The origin of the Mediterranean evaporites. In: Ryan, W.B.F., Hsü, K.J., et al. (Eds.), Initial Reports of the Deep Sea Drilling Project, 13. U. S. Government Printing Office, Washington, pp. 1203–1231.
Hsü, K.J., Montadert, L., Bernouilli, D., Cita, M.B., Erikson, A., Garrison, R.G., Kidd, R.B., Mélières, F., Müller, C., Wright, R., 1978a. History of the Mediterranean salinity

crisis. In: Hsü, K.J., Montadert, L., et al. (Eds.), Initial Reports of the Deep Sea Drilling Project. U.S. Government Printing Office, Washington, DC.
Hsü, K.J., Montadert, L., Bernoulli, D., Bizon, G., Cita, M., Erickson, A., Fabricius, F., Garrison, R.E., Kidd, R.B., Mélières, F., Müller, C., Wright, R.C., 1978b. Initial reports of the deep sea drilling project: DSDP volume XLII Part 1.
Iaccarino, S., Bossio, A., 1999. Paleoenvironment of uppermost Messinian sequences in the western Mediterranean (Sites 974, 975, and 978). In: Proceedings of the Ocean Drilling Program, Scientific Results (Vol. 161, 529-541). College Station, TX: Ocean Drilling Program.
Iaccarino, S.M., Cita, M.B., Gaboardi, S., Gruppini, G.M., 1999. 15. High-Resolution Biostratigraphy at the Miocene/Pliocene boundary in Holes 974b and 975b, Western Mediterranean. In: Proceedings of the Ocean Drilling Program: Scientific Results, Vol. 161, p. 197.
Hsü, K.J., Ryan,, W.B.F., Schreiber, B.C., 1973c. Petrography of a halite sample from Hole 134-Balearic Abyssal Plain. In: Ryan, W.B.F., Hsü, K.J., et al. (Eds.), Initial Reports of the Deep Sea Drilling Project, 13. U. S. Government Printing Office, Washington, pp. 708–711.
Iaccarino, S.M., Bertini, A., Di Stefano, A., Ferraro, L., Gennari, R., Grossi, F., Lirer, F., Manzi, V., Menichetti, E., Ricci Lucchi, M., Taviani, M., Sturiale, G., Angeletti, L., 2008. The Trave section (Monte dei Corvi, Ancona, central Italy): an integrated paleontological study of the Messinian deposits. Stratigraphy 5 (3–4), 281–306.
Ingram, B.L., Sloan, D., 1992. Strontium isotopic composition of estuarine sediments as paleosalinity-paleoclimate indicator. Science 255, 68–72.
Jagger, L.J., Bevan, T.G., McClay, K.R., 2020. Tectono-stratigraphic evolution of the SE Mediterranean passive margin, offshore Egypt and Libya. Geol. Soc. Lond., Spec. Publ. 476 (1), 365–401.
Johnston, D.T., Gill, B.C., Masterson, A., Beirne, E., Casciotti, K.L., Kna, A.N., Berelson, W., 2014. Placing an upper limit on cryptic marine sulphur cycling. Nature 513, 530–533.
Jolivet, L., Augier, R., Robin, C., Suc, J.-P., Rouchy, J.-M., 2006. Lithospheric-scale geodynamic context of the Messinian Salinity Crisis. Sediment. Geol. 188–189, 9–33. https://doi.org/10.1016/j.sedgeo.2006.02.004.
Just, J., Hübscher, C., Betzler, C., Lüdmann, T., Reicherter, K., 2011. Erosion of continental margins in the Western Mediterranean due to sea-level stagnancy during the Messinian Salinity Crisis. Geo-Mar. Lett. 31 (1), 51–64.
Kaplan, I.R., Rittenberg, S.C., 1964. Microbiological fractionation of sulphur isotopes. Microbiology 34, 195–212.
Karakitsios, V., Cornée, J., Tsourou, T., Moissette, P., Kontakiotis, G., Agiadi, K., Manoutsoglou, E., Triantaphyllou, M., Koskeridou, E., 2017a. Messinian salinity crisis record under strong freshwater input in marginal, intermediate, and deep environments: the case of the North Aegean. Paleogr. Paleoclimatol. Paleoecol. 485, 316–335. https://doi.org/10.1016/j.palaeo.2017.06.023.
Karakitsios, V., Roveri, M., Lugli, S., Manzi, V., Gennari, R., Antonarakou, A., Triantaphyllou, M., Agiadi, K., Kontakiotis, G., Kafousia, N., de Rafelis, M., 2017b. A record of the Messinian salinity crisis in the eastern Ionian tectonically active domain (Greece, eastern Mediterranean). Basin Res. 29, 203–233. https://doi.org/10.1111/bre.12173.
Kartveit, K.H., Ulsund, H.B., Johansen, S.E., 2019. Evidence of sea level drawdown at the end of the Messinian salinity crisis and seismic investigation of the Nahr Menashe unit in the northern Levant Basin, offshore Lebanon. Basin Res. 31 (5), 827–840. https://doi.org/10.1111/bre.12347.
Kastens, K.A., Mascle, J., 1990. The geological evolution of the Tyrrhenian Sea: An introduction to the scientific results of ODP Leg 107. In: Proceedings of the Ocean Drilling Program, Scientific Results (Vol. 107, No. 3), p. 26. College Station, TX (Ocean Drilling Program).
Kastens, K.A., Mascle, J., Auroux, C., et al., 1987. Proc. ODP, Init. Repts., 107. College Station, TX (Ocean Drilling Program). https://doi.org/10.2973/odp.proc.ir.107.1987.
Keller, G., Abramovich, S., 2009. Lilliput effect in late Maastrichtian planktic foraminifera: response to environmental stress: Paleogeography. Paleoclimatol. Paleoecol. 284, 47–62.
Keogh, S.M., Butler, R.W.H., 1999. The Mediterranean water body in the late Messinian: interpreting the record from marginal basins on Sicily. J. Geol. Soc. 156 (4), 837–846.
Kirkham, C., Bertoni, C., Cartwright, J., Lensky, N.G., Sirota, I., Rodriguez, K., Hodgson, N., 2020. The demise of a 'salt giant' driven by uplift and thermal dissolution. Earth Planet. Sci. Lett. 531, 115933 https://doi.org/10.1016/j.epsl.2019.115933.
Kováč, M., Andreyeva-grigorovich, A., Bajraktarević, Z., Brzobohatý, R., Filipescu, S., Fodor, L., Harzhauser, M., Nagymarosy, A., Oszczypko, N., Pavelić, D., Rögl, F., Saftić, B., Sliva, U., Studencka, B., 2007. Badenian evolution of the Central Paratethys Sea: paleogeography, climate and eustatic sea-level changes. Geol. Carpathica 58, 579–606.
Krijgsman, W., Meijer, P.T., 2008. Depositional environments of the Mediterranean "Lower Evaporites" of the Messinian salinity crisis: constraints from quantitative analyses. Mar. Geol. 253 (3–4), 73–81. https://doi.org/10.1016/j.margeo.2008.04.010.
Krijgsman, W., Hilgen, F.J., Raffi, I., Sierro, F.J., Wilson, D.S., 1999a. Chronology, causes, and progression of the Messinian salinity crisis. Nature 400, 652–655.
Krijgsman, W., Hilgen, F.J., Marabini, S., Vai, G.B., 1999b. New paleomagnetic and cyclostratigraphic age constraints on the Messinian of the Northern Apennines (Vena del Gesso Basin, Italy). Mem. Soc. Geol. Ital. 54, 25–33.
Krijgsman, W., Fortuin, A.R., Hilgen, F.J., Sierro, F.J., 2001. Astrochronology for the Messinian Sorbas basin (SE Spain) and orbital (precessional) forcing for evaporite cyclicity. Sediment. Geol. 140, 43–60.
Krijgsman, W., Gaboardi, S., Hilgen, F.J., Iaccarino, S., Kaenel, E.D., Laan, E.V.D., 2004. Revised astrochronology for the Ain el Beida section (Atlantic Morocco): no glacio-eustatic control for the onset of the Messinian Salinity Crisis. Stratigraphy 1, 87–101.
Krijgsman, W., Stoica, M., Vasiliev, I., Popov, V.V., 2010. Rise and fall of the Paratethys Sea during the Messinian Salinity Crisis. Earth Planet. Sci. Lett. 290 (1-2), 183–191. https://doi.org/10.1016/j.epsl.2009.12.020.
Krijgsman, W., Capella, W., Simon, D., Hilgen, F.J., Kouwenhoven, T.J., Meijer, P.Th., Sierro, F.J., Tulbure, M.A., van den Berg, B.C.J., van der Schee, M., Flecker, R., 2018. The Gibraltar Corridor: watergate of the Messinian Salinity Crisis. Mar. Geol. 403, 238–246. https://doi.org/10.1016/j.margeo.2018.06.008.
Krijgsman, W., Palcu, D., Andreetto, F., Stoica, M., Mandic, O., 2020a. Changing seas in the late Miocene Northern Aegean: a Paratethyan aroach to Mediterranean basin evolution. Earth Sci. Rev. 103386 https://doi.org/10.1016/j.earscirev.2020.103386.
Krijgsman, W., Stoica, M., Hoyle, T.M., Jorissen, E.L., Lazarev, S., Rausch, L., Bista, D., Alçiçek, M.C., Ilgar, A., van den Hoek Ostende, L.W., Mayda, S., Raffi, I., Flecker, R., Mandic, O., Neubauer, T.A., Wesselingh, F.P., 2020b. The myth of the Messinian Dardanelles: Late Miocene stratigraphy and paleogeography of the ancient Aegean-Black Sea gateway. Paleogeogr. Paleoclimatol. Paleoecol. 110033 https://doi.org/10.1016/j.paleo.2020.110033.
Van der Laan, E., Gaboardi, S., Hilgen, F.J., Lourens, L.J., 2005. Regional climate and glacial control on high-resolution oxygen isotope records from Ain El Beida (latest Miocene, NW Morocco): a cyclostratigraphic analysis in the depth and time domain. Paleoceanography 20. https://doi.org/10.1029/2003PA000995. PA1001.
Van der Laan, E., Snel, E., de Kaenel, E., Hilgen, F.J., Krijgsman, W., 2006. No major deglaciation across the Miocene-Pliocene boundary: integrated stratigraphy and astronomical tuning of the Loulja sections (Bou Regreg area, NW Morocco). Paleoceanography 21. https://doi.org/10.1029/2005PA001193. PA3011.
Laskar, L.J., Robutel, P., Joutel, F., Gastineau, M., Correia, A.C.M., Levrard, B., 2004. A long term numerical solution for the insolation quantities of the Earth. Astron. Astrophys. 428, 261–285.
Lazarev, S., de Leeuw, A., Stoica, M., Mandic, O., van Baak, C.G.C., Vasiliev, I., Krijgsman, W., 2020. From Khersonian drying to Pontian "flooding": Late Miocene stratigraphy and paleoenvironmental evolution of the Dacian Basin (Eastern Paratethys). Glob. Planet. Chang. 103224 https://doi.org/10.1016/j.gloplacha.2020.103224.
Leavitt, W.D., Halevy, I., Bradley, A.S., Johnston, D.T., 2013. Influence of sulfate reduction rates on the Phanerozoic sulfur isotope record. Proc. Natl. Acad. Sci. 110, 11244.
Leila, M., Moscariello, A., Šegvić, B., 2018. Depositional facies controls on the diagenesis and reservoir quality of the Messinian Qawasim and Abu Madi formations, onshore Nile Delta, Egypt. Geol. J. 54 (3), 1797–1813.
Liu, J., Li, S., Zhong, J., Zhu, X., Guo, Q., Lang, Y., Han, X., 2017. Sulfate sources constrained by sulfur and oxygen isotopic compositions in the upper reaches of the Xijiang River, China. Acta Geochimica 36, 611–618.
Lloyd, R.M., 1968. Oxygen isotope behavior in the Sulfate-Water System. J. Geophys. Res. 1896-1977 (73), 6099–6110.
Lofi, J., 2018. Seismic Atlas of the Messinian salinity crisis markers in the Mediterranean sea. Volume 2 - Mémoires de la Société géologique de France, n.s., 2018, t. 181, and Commission for the Geological Map of the World, 72 p. + DVD. https://doi.org/10.10682/2018M ESSINV2.
Lofi, J., Gorini, C., Berne, S., Clauzon, G., Dos Reis, A.T., Ryan, W.B.F., Steckler, M.S., 2005. Erosional processes and paleo-environmental changes in the Western Gulf of Lions (SW France) during the Messinian Salinity Crisis. Mar. Geol. 217, 1–30. https://doi.org/10.1016/j.margeo.2005.02.014.
Lofi, J., Sage, F., Déverchère, J., Loncke, L., Maillard, A., Gaullier, V., Thinon, I., Gillet, H., Guennoc, P., Gorini, C., 2011a. Refining our knowledge of the Messinian salinity crisis records in the offshore domain through multi-site seismic analysis. Bulletin de la Société géologique de France 182 (2), 163–180.
Lofi, J., Déverchère, J., Gaullier, V., Gillet, H., Gorini, C., Guennoc, P., Loncke, L., Maillard, A., Sage, F., Thinon, I., 2011b. Seismic atlas of the "Messinian Salinity Crisis" markers in the Mediterranean and Black seas. Commission for the Geological Map of the World and Memoires de la Société Géologique de France. Nouv. Ser. 72.
Loget, N., Davy, P., Van Den Driessche, J., 2006. Mesoscale fluvial erosion parameters deduced from modelling the Mediterranean sea-level drop during the Messinian (late Miocene). J. Geophys. Res. 111. F03005.
Loncke, L., Gaullier, V., Mascle, J., Vendeville, B., Camera, L., 2006. The Nile deep-sea fan: An example of interacting sedimentation, salt tectonics, and inherited subsalt paleotopographic features. Mar. Pet. Geol. 23, 297–315. https://doi.org/10.1016/j.marpetgeo.2006.01.001.
Londeix, L., Benzakour, M., Suc, J.P., Turon, J.L., 2007. Messinian paleoenvironments and hydrology in Sicily (Italy): the dinoflagellate cyst record. Geobios 40 (3), 233–250. https://doi.org/10.1016/j.geobios.2006.12.001.
Longinelli, A., 1979. Isotope geochemistry of some Messinian evaporates: paleoenvironmental implications. Paleogeogr. Paleoclimatol. Paleoecol. 29, 95–123.
Longinelli, A., Craig, H., 1967. Oxygen-18 variations in sulfate ions in sea water and saline lakes. Science 156 (3771), 56–59.
López-Garrido, A.C., Sanz de Galdeano, C., 1999. Neogene sedimentation and tectonic-eustatic control of the Malaga basin, South Spain. J. Pet. Geol. 22 (1), 81–96.
Loreto, M.F., Zitellini, N., Ranero, C.R., Palmiotto, C., Prada, M., 2020. Extensional tectonics during the Tyrrhenian back-arc basin formation and a new morpho-tectonic map. Basin Res. 33 (1), 138–158.
Lourens, L., Hilgen, F., Shackleton, N.J., Laskar, J., Wilson, D., 2004. The Neogene period. In: Gradstein, F.M., Ogg, J.G., Smith, A.G. (Eds.), A Geologic Time Scale 2004. Cambridge Univ. Press, Cambridge, pp. 409–440.

Lozano, D.O., 2016. Astrobiochronological Constraints on Margin to deep basin correlations across the Balearic Promontory and the Valencia basin (Doctoral dissertation, Universidad de Salamanca).
Lu, F.H., 2006. Lithofacies and water-body record of Messinian evaporites in Nijar Basin, SE Spain. Sediment. Geol. 188, 115–130.
Lu, F.H., Meyers, W.J., Schoonen, M.A., 2001. S and O (SO4) isotopes, simultaneous modeling, and environmental significance of the Nijar Messinian gypsum, Spain. Geochim. Cosmochim. Acta 65, 3081–3092.
Lugli, S., Schreiber, B.C., Triberti, B., 1999. Giant polygons in the Realmonte mine (Agrigento, Sicily): evidence for the desiccation of a Messinian halite basin. J. Sediment. Res. 69, 764–771.
Lugli, S., Bassetti, M.A., Manzi, V., Barbieri, M., Longinelli, A., Roveri, M., 2007. The Messinian "Vena del Gesso" evaporites revisited: characterization of isotopic composition and organic matter. In: Schreiber, B.C., Lugli, S., Bąbel, M. (Eds.), Evaporites through Space and Time. Special Publications, 285. Geological Society, London, pp. 143–154.
Lugli, S., Manzi, V., Roveri, M., Schreiber, B.C., 2010. The Primary Lower Gypsum in the Mediterranean: a newfacies interpretation for the first stage of the Messinian salinity crisis. Paleogeogr. Paleoclimatol. Paleoecol. 297, 83–99. https://doi.org/10.1016/j.paleo.2010.07.017.
Lugli, S., Gennari, R., Gvirtzman, Z., Manzi, V., Roveri, M., Schreiber, B.C., 2013. Evidence of clastic evaporites in the canyons of the Levant Basin (Israel): implications for the Messinian Salinity Crisis. J. Sediment. Res. 83, 942–954. https://doi.org/10.2110/jsr.2013.72.
Lugli, S., Manzi, V., Roveri, M., Schreiber, B.C., 2015. The deep record of the Messinian salinity crisis: evidence of a non-desiccated Mediterranean Sea. Paleogeogr. Paleoclimatol. Paleoecol. 433, 201–218. https://doi.org/10.1016/j.paleo.2015.05.017.
Lymer, G., Lofi, J., Gaullier, V., Maillard, A., Thinon, I., Sage, F., Chanier, F., Vendeville, B.C., 2018. The Western Tyrrhenian Sea revisited: New evidence for a rifted basin during the Messinian Salinity Crisis. Mar. Geol. 398, 1–21. https://doi.org/10.1016/j.margeo.2017.12.009.
Madof, A.S., Connell, S.D., 2018. Northern Levant Basin. In: Lofi, et al. (Eds.), Atlas of the Messinian Salinity Crisis markers in the Mediterranean and Black SeasMémoires de la Société géologique de France 179. World Geological Map Commission, pp. 60–62.
Madof, A.S., Bertoni, C., Lofi, J., 2019. Discovery of vast fluvial deposits provides evidence for drawdown during the late Miocene Messinian salinity crisis. Geology 47 (2), 171–174. https://doi.org/10.1130/G45873.1.
Magyar, I., Geary, D.H., Lantos, M., Müller, P., Süto-Szentai, M., 1999a. Integrated biostratigraphic, magnetostratigraphic and chronostratigraphic correlations of the Late Miocene Lake Pannon deposits. Acta Geol. Hung. 42 (1), 5–31.
Magyar, I., Geary, D.H., Müller, P., 1999b. Paleogeographic evolution of the late miocene Lake Pannon in Central Europe. Paleogeogr. Paleoclimatol. Paleoecol. 147 (3–4), 151–167.
Maillard, A., Mauffret, A., 2006. Relationship between erosion surfaces and Late Miocene Salinity Crisis deposits in the Valencia Basin (northwestern Mediterranean): evidence for an early sea-level fall. Terra Nova 18 (5), 321–329. https://doi.org/10.1111/j.1365-3121.2006.00696.x.
Maillard, A., Mauffret, A., 2011. Valencia through. In: Lofi, et al. (Eds.), Atlas of the Messinian Salinity Crisis markers in the Mediterranean and Black SeasMémoires de la Société géologique de France 179. World Geological Map Commission (72 pp.).
Maillard, A., Mauffret, A., 2013. Structure and present-day compression in the offshore area between Alicante and Ibiza Island (Eastern Iberian Margin). Tectonophysics 591, 116–130.
Maillard, A., Gorini, C., Mauffret, A., Sage, F., Lofi, J., Gaullier, V., 2006. Offshore evidence of polyphase erosion in the Valencia Basin (Northwestern Mediterranean): scenario for the Messinian Salinity Crisis. Sediment. Geol. 188–189, 69–91.
Maillard, A., Hübscher, C., Benkhelil, J., Tahchi, E., 2011a. Deformed Messinian markers in the Cyprus Arc: tectonic and/or Messinian Salinity Crisis indicators? Basin Res. 23, 146–170.
Maillard, A., Lofi, J., Déverchère, J., Gaullier, V., Loncke, L., Sage, F., Thinon, I., Guennoc, P., Gillet, H., Gorini, C., 2011b. Synthesis. In: Lofi, J., Déverchère, J., et al. (Eds.), Seismic Atlas of the Messinian Salinity Crisis Markers in the Offshore Mediterranean Domain. – CCGM & Mém. Soc. géol. Fr., n.s., 179, 72 p.
Maillard, A., Driussi, O., Lofi, J., Briais, A., Chanier, F., Hübscher, C., Gaullier, V., 2014. Record of the Messinian Salinity Crisis in the SW Mallorca area (Balearic Promontory, Spain). Mar. Geol. 357, 304–320. https://doi.org/10.1016/j.margeo.2014.10.001.
Maillard, A., Gaullier, V., Lézin, C., Chanier, F., Odonne, F., Lofi, J., 2020. New onshore/offshore evidence of the Messinian Erosion Surface from key areas: The Ibiza-Balearic Promontory and the Orosei-Eastern Sardinian margin. Découverte de la surface d'érosion messinienne onshore/offshore dans deux lieux clés: le Promontoire Baléares (Ibiza) et la marge est-sarde (Orosei). Bulletin de la Société Géologique de France 191 (1). https://doi.org/10.1051/bsgf/2020007.
Maniscalco, R., Casciano, C.I., Distefano, S., Grossi, F., Di Stefano, A., 2019. Facies analysis in the Second Cycle Messinian evaporites predating the early Pliocene reflooding: the Balza Soletta section (Corvillo Basin, central Sicily). Ital. J. Geosci. 138 (3), 301–316. https://doi.org/10.3301/IJG.2019.06.
Manzi, V., Lugli, S., Ricci Lucchi, F., Roveri, M., 2005. Deep-water clastic evaporites deposition in the Messinian Adriatic foredeep (northern Apennines, Italy): did the Mediterranean ever dry out? Sedimentology 52, 875–902.
Manzi, V., Roveri, M., Gennari, R., Bertini, A., Biffi, U., Giunta, S., Iaccarino, S.M., Lanci, L., Lugli, S., Negri, A., Riva, A., Rossi, M.E., Taviani, M., 2007. The deep-water counterpart of the messinian lower evaporites in the apennine foredeep: the fanantello section (northern Apennines, Italy). Paleogeogr. Paleoclimatol. Paleoecol. 251, 470–499.
Manzi, V., Lugli, S., Roveri, M., Schreiber, B.C., 2009. A new facies model for the Upper Gypsum of Sicily (Italy): chronological and paleoenvironmental constraits for the Messinian salinity crisis in the Mediterranean. Sedimentology 56. https://doi.org/10.1111/j.1365-3091.2009.01063.x, 1937-1960.
Manzi, V., Lugli, S., Roveri, M., Schreiber, B.C., Gennari, R., 2011. The Messinian CdB (Sicily, Italy) revisited. Geol. Soc. Am. Bull. 123, 347–370. https://doi.org/10.1130/B30262.1.
Manzi, V., Gennari, R., Hilgen, F., Krijgsman, W., Lugli, S., Roveri, M., Sierro, F.J., 2013. Age refinement of the Messinian salinity crisis onset in the Mediterranean. Terra Nova 25 (4), 315–322.
Manzi, V., Lugli, S., Roveri, M., Dela, Pierre F., Gennari, R., Lozar, F., Natalicchio, M., Schreiber, B.C., Taviani, M., Turco, E., 2016a. The Messinian salinity crisis in Cyprus: A further step towards a new stratigraphic framework for Eastern Mediterranean. Basin Res. 28, 207–236. https://doi.org/10.1111/bre.12107.
Manzi, V., Gennari, R., Lugli, S., Minelli, N., Reghizzi, M., Roveri, M., Schreiber, B.C., 2016b. Comment on "Carbonate deposition and diagenesis in evaporitic environments: the evaporative and sulphur-bearing limestones during the settlement of the Messinian Salinity Crisis in Sicily and Calabria" by Caruso et al., 2015. Palaeo3, 429, 136e162. Palaeogeogr. Palaeoclimatol. Palaeoecol. 459, 585–596.
Manzi, V., Gennari, R., Lugli, S., Persico, D., Reghizzi, M., Roveri, M., Schreiber, B.C., Calvo, R., Gavrieli, I., Gvirtzman, Z., 2018. The onset of the Messinian salinity crisis in the deep Eastern Mediterranean basin. Terra Nova 30 (3), 189–198. https://doi.org/10.1111/ter.12325.
Manzi, V., Argnani, A., Corcagnani, A., Lugli, S., Roveri, M., 2020. The Messinian salinity crisis in the Adriatic foredeep: evolution of the largest evaporitic marginal basin in the Mediterranean. Mar. Pet. Geol. 115, 104288 https://doi.org/10.1016/j.marpetgeo.2020.104288.
Marcano, M.C., Frank, T.D., Mukasa, S.B., Lohmann, K.C., Taviani, M., 2015. Diagenetic incorporation of Sr into aragonitic bivalve shells: Implications for chronostratigraphic and paleoenvironmental interpretations. Depositional Record 1 (1), 38–52. https://doi.org/10.1016/j.marpetgeo.2020.104288.
Markovic, S., Paytan, A., Li, H., Wortmann, U.G., 2016. A revised seawater sulfate oxygen isotope record for the last 4Myr. Geochim. Cosmochim. Acta 175, 239–251.
Marsaglia, K.M., Tribble, J.S., 1999. Petrography and mineralogy of the uppermost Messinian section and the Pliocene/Miocene boundary at Site 975, Western Mediterranean Sea. In: Proc. ODP, Sci. Results, Vol. 161, pp. 3–20. Ocean Drilling Program College Station, TX.
Martín-Suárez, E., Freudenthal, M., Krijgsman, W., Fortuin, R., 2000. On the age of the continental deposits of the Zorreras Member (Sorbas Basin, SE Spain). Géobios 33, 505–512.
Marzocchi, A., Lunt, D.J., Flecker, R., Bradshaw, C.D., Farnsworth, A., Hilgen, F.J., 2015. Orbital control on late Miocene climate and the North African monsoon: insight from an ensemble of sub-precessional simulations. Clim. Past 11 (10), 1271–1295. https://doi.org/10.5194/cpd-11-2181-2015.
Marzocchi, A., Flecker, R., Van Baak, C.G.C., Lunt, D.J., Krijgsman, W., 2016. Mediterranean outflow pump: an alternative mechanism for the Lago-mare and the end of the Messinian Salinity Crisis. Geology 44, 523–526. https://doi.org/10.1130/G37646.1.
Marzocchi, A., Flecker, R., Lunt, D.J., Krijgsman, W., Hilgen, F.J., 2019. Precessional drivers of late Miocene Mediterranean sedimentary sequences: African summer monsoon and Atlantic winter storm tracks. Paleoceanogr. Paleoclimatol. 34 (12), 1980–1994. https://doi.org/10.1029/2019PA003721.
Mas, G., 2013. Definició i caracterització de la Formació ses Olles (Lago mare, messinià terminal) a l'Illa de Mallorca (illes balears, mediterrània Occidental). Bolletí de la Societat d'Història Natural de Balears 56, 209–231.
Mas, G., 2015. El registre estratigr`afic del Messini`a terminal i del Pliocè a l'illa de Mallorca. Relacions amb la crisi de salinitat de la Mediterrània. PhD Tesis. Universitat de les Iles Balears. http://www.tdx.cat/handle/10803/375904.
Mas, G., Fornós, J.J., 2020. The messinian salinity crisis in Mallorca: New insights for a western mediterranean stratigraphic scenario. Mar. Pet. Geol. 104656 https://doi.org/10.1016/j.marpetgeo.2020.104656.
Mas, G., Bisconti, M., Torres-Roig, E., Juárez, J., Sacarès, J., 2018a. The last whale of the Messinian. First record of a mysticete cetacean from the Mediterranean Messinian Salinity Crisis. In: 1st Paleontological Virtual Congress. Book of Abstracts—Paleontology in the Virtual Era, Vol. 97.
Mas, G., Maillard, A., Alcover, J.A., Fornós, J.J., Bover, P., Torres-Roig, E., 2018b. Terrestrial colonization of the Balearic Islands: New evidence for the Mediterranean sea-level drawdown during the Messinian Salinity Crisis. Geology 46 (6), 527–530. https://doi.org/10.1130/G40260.1.
Masterson, A.L., Wing, B.A., Paytan, A., Farquhar, J., Johnston, D.T., 2016. The minor sulfur isotope composition of Cretaceous and Cenozoic seawater sulfate. Paleoceanography 31, 779–788.
Mather, A., Martín, J.M., Harvey, A.M., Braga, J.C., 2001. A Field Guide to the Neogene Sedimentary Basins of the Almería Province, South-East Spain., 186-189. Blackwell Science, Oxford.
Mayser, J.P., Flecker, R., Marzocchi, A., Kouwenhoven, T.J., Lunt, D.J., Pancost, R.D., 2017. Precession driven changes in terrestrial organic matter input to the Eastern Mediterranean leading up to the Messinian Salinity Crisis. Earth Planet. Sci. Lett. 462, 199–211. https://doi.org/10.1016/j.epsl.2017.01.029.
McArthur, J.M., Howarth, R.J., Shields, G.A., 2012. Strontium isotope stratigraphy. In: Gradstein, F.M., Ogg, J.G., Schmitz, M.D., Ogg, G.M. (Eds.), The Geological Time Scale 2012. Elsevier B.V, Oxford, pp. 127–144.
McCulloch, M.T., De Deckker, P., 1989. Sr isotope constraints on the Mediterranean environment at the end of the Messinian salinity crisis. Nature 342, 62–65.
McKenzie, J.A., 1999. From desert to deluge in the Mediterranean. Nature 400, 613–614.

McKenzie, J.A., Evans, N., Hodell, D., Aloisi, G., Vasconcelos, C., 2017. Subsurface dolomite formation during post-depositional flow of sulphate-bearing fluids from underlying salt giants: Early Pliocene example at DSDP Leg 42A, Site 374, Ionian Abyssal Plain. EGUGA 10166.

Medaouri, M., Déverchère, J., Graindorge, D., Bracene, R., Badji, R., Ouabadi, A., Yelles, K., Bendib, F., 2014. The transition from Alboran to Algerian basins (Western Mediterranean Sea): chronostratigraphy, deep crustal structure and tectonic evolution at the rear of a narrow slab rollback system. J. Geodyn. 77, 186–205. https://doi.org/10.1016/j.jog.2014.01.003.

Meijer, P.T., Krijgsman, W., 2005. A quantitative analysis of the desiccation and re-filling of the Mediterranean during the Messinian Salinity Crisis. Earth Planet. Sci. Lett. 240 (2), 510–520.

Meilijson, A., Steinberg, J., Hilgen, F., Bialik, O.M., Waldmann, N.D., Makovsky, Y., 2018. Deep-basin evidence resolves a 50-year-old debate and demonstrates synchronous onset of Messinian evaporite deposition in a non-desiccated Mediterranean. Geology 46 (3), 243–246. https://doi.org/10.1130/G39868.1.

Meilijson, A., Hilgen, F., Sepúlveda, J., Steinberg, J., Fairbank, V., Flecker, R., Waldmann, N.D., Spaulding, S.A., Bialik, O.M., Boudinot, F.G., Illner, P., Makovsky, Y., 2019. Chronology with a pinch of salt: integrated stratigraphy of Messinian evaporites in the deep Eastern Mediterranean reveals long-lasting halite deposition during Atlantic connectivity. Earth-Sci. Rev. 194, 374–398. https://doi.org/10.1016/j.earscirev.2019.05.011.

Melinte-Dobrinescu, M.C., Suc, J.-P., Clauzon, G., Popescu, S.-M., Armijo, R., Meyer, B., Biltekin, D., Çağatay, M.N., Ucarkus, G., Jouannic, G., Fauquette, S., Çakir, Z., 2009. The Messinian salinity crisis in the Dardanelles region: Chronostratigraphic constraints. Paleogeogr. Paleoclimatol. Paleoecol. 278, 24–39. https://doi.org/10.1016/j.paleo.2009.04.009.

Merzeraud, G., Achalhi, M., Cornee, J.J., Münch, P., Azdimousa, A., Moussa, A.B., 2019. Sedimentology and sequence stratigraphy of the late-Messinian-Early pliocene continental to marine deposits of the Boudinar basin (North Morocco). J. Afr. Earth Sci. 150, 205–223. https://doi.org/10.1016/j.jafrearsci.2018.11.002.

Meulenkamp, J.E., Sissingh, W., 2003. Tertiary paleogeography and tectonostratigraphic evolution of the Northern and Southern Peri-Tethys platforms and the intermediate domains of the African-Eurasian convergent plate boundary zone. Paleogeogr. Paleoclimatol. Paleoecol. 196 (1-2), 209–228.

Meulenkamp, J.E., Dermitzakis, M., Georgiades-Dikeoulia, E., Jonkers, H.A., Boger, A., 1979. Field Guide to the Neogene of Crete. Publication of the Department of Geology and Paleontology, University of Athens, A, 32, pp. 1–32.

Micallef, A., Camerlenghi, A., Garcia-Castellanos, D., Cunarro Otero, D., Gutscher, M.-A. M.A., Barreca, G., Spatola, D., Facchin, L., Geletti, R., Krastel, S., Gross, F., Urlaub, M., Sulli, A., Basilone, L., Basilone, G., 2018. Evidence of the Zanclean megaflood in the eastern Mediterranean Basin. Sci. Rep. 8, 1–8. https://doi.org/10.1038/s41598-018-19446-3.

Micallef, A., Camerlenghi, A., Georgiopoulou, A., Garcia-Castellanos, D., Gutscher, M.-A., Lo Iacono, C., Huvenne, V.A.I., Mountjoy, J.J., Paull, C.K., Le Bas, T., Spatola, D., Facchin, L., Accettella, D., 2019. Geomorphic evolution of the Malta Escarpment and implications for the Messinian evaporative drawdown in the eastern Mediterranean Sea. Geomorphology 327, 264–283. https://doi.org/10.1016/j.geomorph.2018.11.012.

Milker, Y., Schmiedl, G., 2012. A taxonomic guide to modern benthic shelf foraminifera of the western Mediterranean Sea. Palaeontol. Electron. 15 (2), 1–134. https://doi.org/10.26879/271.

Mocnik, A., Camerlenghi, A., Del Ben, A., Geletti, R., Wardell, N., Zgur, F., 2014. The Messinian Salinity Crisis in the West-Mediterranean Basins: comparison between two rifted margins. In: Proceedings of the 33rd GNGTS Conference, Bologna, Vol. 1, pp. 156–163.

Mocnik, A., Del Ben, A., Camerlenghi, A., Geletti, R., Saule, M., 2018. 12. Ionian Basin. In J. Lofi (Ed.), Seismic Atlas of the Messinian salinity crisis markers in the Mediterranean sea. Volume 2. - Mémoires de la Société géologique de France, n.s., 2018, t. 181, and Commission for the Geological Map of the World, pp. 41–44.

Modestou, S., Simon, D., Gutjahr, M., Marzocchi, A., Kouwenhoven, T.J., Ellam, R.M., Flecker, R., 2017. Precessional variability of $^{87}Sr/^{86}Sr$ in the late miocene sorbas basin: An interdisciplinary study of drivers of interbasin exchange. Paleoceanography 32 (6), 531–552.

Montadert, L., Letouzey, J., Mauffret, A., 1978. Messinian event: seismic evidence. In: Hsü, K.J., Montadert, L., et al. (Eds.), Initial Reports of the Deep Sea Drilling Project, 1. US Government Printing Office, Washington, DC, pp. 1037–1050.

Mudie, P.J., Marret, F., Mertens, K.N., Shumilovskikh, L., Leroy, S.A., 2017. Atlas of modern dinoflagellate cyst distributions in the Black Sea Corridor: from Aegean to Aral Seas, including Marmara, Black, Azov and Caspian Seas. Mar. Micropaleontol. 134, 1–152.

Müller, D.W., Mueller, P.A., 1991. Origin and age of the Mediterranean Messinian evaporites: implications from Sr isotopes. Earth Planet. Sci. Lett. 107 (1), 1–12.

Müller, D.W., Mueller, P.A., McKenzie, J.A., 1990. Strontium isotopic ratios as fluid tracers in Messinian evaporites of the Tyrrhenian Sea (western Mediterranean Sea). In: Proceedings of the Ocean Drilling Program, Scientific Results (Vol. 107, 603-614). College Station, Tex.: Ocean Drill. Program.

Natalicchio, M., Birgel, D., Peckmann, J., Lozar, F., Carnevale, G., Liu, X., Hinrichs, K.-U., Dela Pierre, F., 2017. An archaeal biomarker record of paleoenvironmental change across the onset of the Messinian salinity crisis in the absence of evaporites (Piedmont Basin, Italy). Org. Geochem. 113, 242–253.

Natalicchio, M., Dela Pierre, F., Birgel, D., Brumsack, H., Carnevale, G., Gennari, R., Gier, S., Lozar, F., Pellegrino, L., Sabino, M., Schnetger, B., Peckmann, J., 2019. Paleoenvironmental change in a precession-paced succession across the onset of the Messinian salinity crisis: insight from element geochemistry and molecular fossils. Paleogeogr. Paleoclimatol. Paleoecol. 518, 45–61. https://doi.org/10.1016/j.paleo.2019.01.009.

Nesteroff, W.D., 1973. Un modéle pour les évaporites messinienne en Méditerranée, bassins peu profonds avec dépot d'évaporites lagunaires. In: Drooger, C.W. (Ed.), Messinian Events in the Mediterranean. North-Holland Publ. Co., Amsterdam, pp. 68–81.

Netzeband, G., Hübscher, C., Gajewski, G., 2006. The structural evolution of the Messinian evaporites in the Levantine Basin. Mar. Geol. 230, 249–273.

Ochoa, D., Sierro, F.J., Lofi, J., Maillard, A., Flores, J.A., Suárez, M., 2015. Synchronous onset of the Messinian evaporite precipitation: First Mediterranean offshore evidence. Earth Planet. Sci. Lett. 427, 112–124. https://doi.org/10.1016/j.epsl.2015.06.059.

Ochoa, D., Sierro, F.J., Hilgen, F.J., Cortina, A., Lofi, J., Kouwenhoven, T., Flores, J.A., 2018. Origin and implications of orbital-induced sedimentary cyclicity in Pliocene well-logs of the Western Mediterranean. Mar. Geol. 403, 150–164. https://doi.org/10.1016/j.margeo.2018.05.009.

Odin, G.S., Vai, G.B., Cosca, M., Tateo, F., Hunziker, J.C., 1997. Integrated stratigraphy of the Maccarone section. In: Montanari, A., Odin, G.S., Coccioni, R. (Eds.), Miocene Stratigraphy: An Integrated Aroach: Developments in Paleontology and Stratigraphy, 15. Elsevier Science B.V, Amsterdam, Netherlands, pp. 531–545.

Ogniben, L., 1955. Le argille scagliose del Crotonese. Memorie e Note dell'Istituto di Geologia Alicata di Napoli 6, 1–72.

Omodeo-Salé, S., Gennari, R., Lugli, S., Manzi, V., Roveri, M., 2012. Tectonic and climatic control on the Late Messinian sedimentary evolution of the Nijar Basin (Betic Cordillera, Southern Spain). Basin Res. 24, 314–337. https://doi.org/10.1111/j.1365-2117.2011.00527.x.

Orszag-Sperber, F., 2006. Changing perspectives in the concept of "Lago-Mare" in Mediterranean Late Miocene evolution. Sediment. Geol. 188, 259–277. https://doi.org/10.1016/j.sedgeo.2006.03.008.

Orszag-Sperber, F., Rouchy, J.M., 1979. Le Miocène terminal et le Pliocène inférieur au sud de Chypre, livret-guide, 5e séminaire sur le Messinien. Chypre, 60 p.

Orszag-Sperber, F., Rouchy, J.M., Blanc-Valleron, M.M., 2000. La transition Messinien-Pliocène en Méditerranée orientale (Chypre): la période du Lago-Mare et sa signification. Comptes Rendus de l'Académie des Sciences-Series IIA-Earth and. Planet. Sci. 331 (7), 483–490.

Orszag-Sperber, F., Caruso, A., Blanc-Valleron, M.M., Merle, D., Rouchy, J.M., 2009. The onset of the Messinian salinity crisis: insights from Cyprus sections. Sediment. Geol. 217 (1-4), 52–64. https://doi.org/10.1016/j.sedgeo.2009.03.006.

Palcu, D.V., Golovina, L.A., Vernyhorova, Y.V., Popov, S.V., Krijgsman, W., 2017. Middle Miocene paleoenvironmental crises in Central Eurasia caused by changes in marine gateway configuration. Glob. Planet. Chang. 158, 57–71. https://doi.org/10.1016/j.gloplacha.2017.09.013.

Palmer, M.R., Edmond, J.M., 1992. Controls over the strontium isotope composition of river water. Geochim. Cosmochim. Acta 56 (5), 2099–2111.

Pellen, R., Popescu, S.-M., Suc, J.-P., Melinte-Dobrinescu, M.C., Rubino, J.-L., Rabineau, M., Marabini, S., Loget, N., Casero, P., Cavazza, W., Head, M.J., Aslanian, D., 2017. The Apennine foredeep (Italy) during the latest Messinian: Lago Mare reflects competing brackish and marine conditions based on calcareous nannofossils and dinoflagellate cysts. Geobios 50, 237–257. https://doi.org/10.1016/j.geobios.2017.04.004.

Pellen, R., Aslanian, D., Rabineau, M., Suc, J.P., Gorini, C., Leroux, E., Blanpied, C., Silenziario, C., Popescu, S.M., Rubino, J.L., 2019. The Messinian Ebro River incision. Glob. Planet. Chang. 181, 102988 https://doi.org/10.1016/j.gloplacha.2019.102988.

Pellerin, A., Antler, G., Holm, S.A., Findlay, A.J., Crockford, P.W., Turchyn, A.V., Jørgensen, B.B., Finster, K., 2019. Large sulfur isotope fractionation by bacterial sulfide oxidation. Sci. Adv. 5 eaaw1480-eaaw1480.

Pérez-Asensio, J.N., Aguirre, J., Schmiedl, G., Civis, J., 2012. Impact of restriction of the Atlantic-Mediterranean gateway on the Mediterranean Outflow Water and eastern Atlantic circulation during the Messinian. Paleoceanography 27 (3). https://doi.org/10.1029/2012PA002309.

Peucker-Ehrenbrink, B., Fiske, G.J., 2019. A continental perspective of the seawater 87Sr/86Sr record: A review. Chem. Geol. 510, 140–165. https://doi.org/10.1016/j.chemgeo.2019.01.017.

Pierre, C., 1974. Contribution ~ l'Jtude sgdimentologique et isotopique des evaporites messiniennes de la Mediterrane; implications geodynamiques. Thesis, University of Paris.

Pierre, C., 1982. Teneurs en isotopes stables (18O,2H,13C,34S) et conditions de génèse des évaporites marines : Alication à quelques milieux actuels et au Messinien de la Mediterrannée, Ecole Normale Supérieure. Université Paris Sud Orsay, p. 262.

Pierre, C., Fontes, J.-C., 1978. Isotope Composition of Messinian sediments from the Mediterranean Sea as indicators of paleoenvironments and diagenesis, in: Texas A M University, O.D.P.C.S., TX, United States (Ed.), Initial reports of the Deep Sea Drilling, covering Leg 42 of the cruises of the drilling Vessel Glomar Challenger Malaga Spain to Itanbul Turkey. April-May 1975. University of California. Scris Institution of Oceanography. National Science Foundation. National Ocean Sediment Coring Program, pp. 635–650.

Pierre, C., Rouchy, J.M., 1990. Stable isotope composition of carbonates in the Tyrrhenian Sea, Sulement to: Pierre, C; Rouchy, JM (1990): Sedimentary and diagenetic evolution of Messinian evaporites in the Tyrrhenian Sea (ODP Leg 107, Sites 652, 653, and 654): petrographic, mineralogical, and stable isotope records. In: Kastens, K.A., Mascle, J., et al. (Eds.), Proceedings of the Ocean Drilling Program, Scientific Results, College Station, TX (Ocean Drilling Program), 107, pp. 187–210. https://doi.org/10.2973/odp.proc.sr.107.131.1990. PANGAEA.

Pierre, C., Rouchy, J.M., Blanc-Valleron, M.-M., 1998. Sedimentological and stable isotope changes at the Messinian-Pliocene boundary in the eastern Mediterranean.

In: Robertson, A.H.F., Emeis, K.-C., Richter, C., Camerlenghi, A. (Eds.), Proc. O.D.P., Sci. Res, vol. 160. Ocean Drilling Program, College Station, TX, pp. 3–8.
Pierre, C., Caruso, A., Blanc-Valleron, M.M., Rouchy, J.M., Orzsag-Sperber, F., 2006. Reconstruction of the paleoenvironmental changes around the Miocene-Pliocene boundary along a West-East transect across the Mediterranean. Sediment. Geol. 188, 319–340. https://doi.org/10.1016/j.sedgeo.2006.03.011.
Placzek, C.J., Quade, J., Patchett, P.J., 2011. Isotopic tracers of paleohydrologic change in large lakes of the Bolivian Altiplano. Quat. Res. 75 (1), 231–244. https://doi.org/10.1016/j.yqres.2010.08.004.
Polonia, A., Torelli, L., Mussoni, P., Gasperini, L., Artoni, A., Klaeschen, D., 2011. The Calabrian Arc subduction complex in the Ionian Sea: Regional architecture, active deformation, and seismic hazard. Tectonics 30 (5).
Popescu, S.M., Melinte, M.C., Suc, J.P., Clauzon, G., Quillévéré, F., Süto-Szentai, M., 2007. Earliest Zanclean age for the Colombacci and uppermost Di Tetto formations of the "latest Messinian" northern Apennines: New paleoenvironmental data from the Maccarone section (Marche Province, Italy). Geobios 40 (3), 359–373. https://doi.org/10.1016/j.geobios.2006.11.005.
Popescu, S.-M., Melinte, M.-C., Suc, J.-P., Clauzon, G., Quillévéré, F., Süto-Szentai, M., 2008. Marine reflooding of the Mediterranean after the Messinian Salinity Crisis predates the Zanclean GSSP. Reply to the "Comment on 'Earliest Zanclean age for the Colombacci and uppermost Di Tetto formations of the "latest Messinian" northern Apennines: new paleoenvironmental data from the Maccarone section (Marche Province, Italy)'" by Popescu et al. (2007). Geobios 40 (359-373) authored by Roveri et al. Geobios 41, 657-660.
Popescu, S.M., Dalesme, F., Jouannic, G., Escarguel, G., Head, M.J., Melinte-Dobrinescu, M.C., Sütö-Szentai, M., Bakrac, K., Clauzon, G., Suc, J.P., 2009. Galeacysta etrusca complex: dinoflagellate cyst marker of Paratethyan influxes to the Mediterranean Sea before and after the peak of the Messinian Salinity Crisis. Palynology 33 (2), 105–134.
Popescu, S.-M., Dalibard, M., Suc, J.-P., Barhoun, N., Melinte-Dobrinescu, M.C., Bassetti, M.A., Deaconu, F., Head, M.J., Gorini, C., Do Couto, D., Rubino, J.-L., Auxietre, J.-L., Floodpage, J., 2015. Lago Mare episodes around the Messinian-Zanclean boundary in the deep southwestern Mediterranean. Mar. Pet. Geol. 66, 55–70. https://doi.org/10.1016/j.marpetgeo.2015.04.002.
Popescu, S.M., Melinte-Dobrinescu, M.C., Suc, J.P., Do Couto, D., 2017. Ceratolithus acutus (= C. armatus), calcareous nannofossil marker of the marine reflooding that terminated the Messinian salinity crisis: Comment on "Paratethyan ostracods in the Spanish Lago-Mare: More evidence for interbasinal exchange at high Mediterranean sea level" by. Paleogeogr., Paleoclimatol., Paleoecol. 441, 854-870. Paleogeogr. Paleoclimatol. Paleoecol. 485, 986–989. https://doi.org/10.1016/j.paleo.2016.07.011.
Popov, S.V., Rögl, F., Rozanov, A.Y., Steininger, F.F., Shcherba, I.G., Kovac, M., 2004. Lithological-paleogeographic maps of Paratethys-10 maps late Eocene to pliocene.
Popov, S.V., Shcherba, I.G., Ilyina, L.B., Nevesskaya, L.A., Paramonova, N.P., Khondkarian, S.O., Magyar, I., 2006. Late Miocene to Pliocene paleogeography of the Paratethys and its relation to the Mediterranean. Paleogeogr. Paleoclimatol. Paleoecol. 238 (1-4), 91–106.
Raad, F., Lofi, J., Maillard, A., Tzevahirtzian, A., Caruso, A., 2021. The Messinian Salinity Crisis deposits in the Balearic Promontory: an undeformed analog of the MSC Sicilian basins?? Mar. Pet. Geol. 104777 https://doi.org/10.1016/j.marpetgeo.2020.104777.
Radeff, G., Cosentino, D., Cipollari, P., Schildgen, T.F., Iadanza, A., Strecker, M.R., Darbas, G., Gurbuz, K., 2016. Stratigraphic architecture of the upper Messinian deposits of the Adana Basin (southern Turkey): implications for the Messinian salinity crisis and the Taurus petroleum system. Ital. J. Geosci. 135, 408–424.
Radeff, G., Schildgen, T.F., Cosentino, D., Strecker, M.R., Cipollari, P., Darbaş, G., Gürbüz, K., 2017. Sedimentary evidence for late Messinian uplift of the SE margin of the Central Anatolian Plateau: Adana Basin, southern Turkey. Basin Res. 29, 488–514. https://doi.org/10.1111/bre.12159.
Reiche, S., Hübscher, C., Ehrhardt, A., 2016. The impact of salt on the late Messinian to recent tectonostratigraphic evolution of the Cyprus subduction zone. Basin Res. 28 (5), 569–597. https://doi.org/10.1111/bre.12122.
Ricchiuto, T.E., McKenzie, J.A., 1978. Stable Isotopic investigation of Messinian sulfate samples from DSDP. LEG 42. Eastern Mediterranean Sea. In: Texas A M University, O.D.P.C.S., TX, United States (Ed.), Initial reports of the Deep Sea Drilling covering Leg 42 of the cruises of the drilling vessel Glomar Challenger. Malaga, Spain to Istanbul, Turkey. April-May 1975. University of California. Scris Institution of Oceanography, National Science Foundation. National Ocen Sediment Coring Program, pp. 657–660.
Rio, D., Negri, A., 1988. Calcareous nannofossils (Monticino Quarry, Faenza). In: De Giuli, C., Vai, G.B. (Eds.), Fossil Vertebrates in the Lamone Valley, Romagna Apennines. Field Trip Guidebook of the International Workshop "Continental faunas at the Miocene/Pliocene boundary", Faenza, pp. 55–57.
Robertson, A.H.F., 1998a. Late Miocene paleoenvironments and tectonic settings of the southern margin of Cyprus and the Eratosthenes Seamount. In: Robertson, A.H.F., Emeis, K.C., Richter, C., Camerlenghi, A. (Eds.), Proc. ODP, Sci. Res., vol. 160 Ocean Drilling Program, College Station, TX, pp. 453–463.
Robertson, A.H., 1998b. Tectonic significance of the Eratosthenes Seamount: a continental fragment in the process of collision with a subduction zone in the eastern Mediterranean (Ocean Drilling Program Leg 160). Tectonophysics 298 (1-3), 63–82.
Robertson, A.H.F., Eaton, S., Follows, E.J., Payne, A.S., 1995. Depositional processes and basin analysis of Messinian evaporites in Cyprus. Terra Nova 7, 233–253.
Roca, E., Guimera, J., 1992. The Neogene structure of the eastern iberian margin: structural constraints on the crustal evolution of the Valencia trough (western mediterranean). Tectonophysics 203, 203–218.
Roep, Th.B., Van Harten, D., 1979. Sedimentological and ostracodological observations on Messinian post-evaporite deposits in some southeastern Spanish basins. Annales Géologiques des Pays Helleniques 3, 1037–1044.
Roep, T.B., Dabrio, C.J., Fortuin, A.R., Polo, M.D., 1998. Late highstand patterns of shifting and steing coastal barriers and washover-fans (Late Messinian, Sorbas Basina, SE Spain). Sediment. Geol. 116, 27–56.
Rögl, F., 1998. Paleogeographic considerations for Mediterranean and Paratethys seaways (Oligocène to Miocene). Ann. Naturhist. Mus. Wien 9 9 A, 279310.
Rosenfeld, A., 1977. The sieve pores of Cyprideis torosa (Jones, 1850) from the Messinian Mavqi'im Formation in the coastal plain and continental shelf of Israel as an indicator of paleoenvironment. Isr. J. Earth Sci. 26, 89993.
Rossi, M., 2017. Outcrop and seismic expression of stratigraphic patterns driven by accommodation and sediment suly turnarounds: Implications on the meaning and variability of unconformities in syn-orogenic basins. Mar. Pet. Geol. 87, 112–127. https://doi.org/10.1016/j.marpetgeo.2017.03.032.
Rossi, M., Rogledi, S., 1988. Relative sea-level changes, local tectonic setting and basin margin sedimentation in the interference zone between two orogenic belts: seismic stratigraphic examples from Padan foreland basin, northern Italy. In: Fan Deltas: Sedimentology and Tectonic Settings, pp. 368–384.
Rossi, M., Minervini, M., Ghielmi, M., Rogledi, S., 2015a. Messinian and Pliocene erosional surfaces in the Po Plain-Adriatic Basin: Insights from allostratigraphy and sequence stratigraphy in assessing play concepts related to accommodation and gateway turnarounds in tectonically active margins. Marine Petroleum Geol. The Messinian events and hydrocarbon exploration in the Mediterranean 66, 192–216. https://doi.org/10.1016/j.marpetgeo.2014.12.012.
Rossi, C., Vilas, L., Arias, C., 2015b. The Messinian marine to nonmarine gypsums of Jumilla (Northern Betic Cordillera, SE Spain): Isotopic and Sr concentration constraints on the origin of parent brines. Sediment. Geol. 328, 96–114. https://doi.org/10.1016/j.sedgeo.2015.08.007.
Rouchy, J.M., 1982. La crise evaporitique messinienne de Mediterranee: nouvelles propositions pour une interpretation genetique. Thesis, Mem, p. 280. Mus. Natn. Hist. Nat, Paris.
Rouchy, J.M., Caruso, A., 2006. The Messinian salinity crisis in the Mediterranean basin: a reassessment of the data and an integrated scenario. Sediment. Geol. 188, 35–67. https://doi.org/10.1016/j.sedgeo.2006.02.005.
Rouchy, J.M., Orzsag-Sperber, F., Blanc-Valleron, M.M., Pierre, C., Rivière, M., Combourieu-Nebout, N., Panayides, I., 2001. Paleoenvironmental changes at the Messinian-Pliocene boundary in the eastern Mediterranean (southern Cyprus basins): significance of the Messinian Lago-Mare. Sediment. Geol. 145 (1-2), 93–117.
Rouchy, J.M., Pierre, C., Et-Touhami, M., Kerzazi, K., Caruso, A., Blanc-Valleron, M.M., 2003. Late Messinian to Early Pliocene paleoenvironmental changes in the Melilla Basin (NE Morocco) and their relation to Mediterranean evolution. Sediment. Geol. 163 (1-2), 1–27.
Rouchy, J.M., Caruso, A., Pierre, C., Blanc-Valleron, M.M., Bassetti, M.A., 2007. The end of the Messinian salinity crisis: evidences from the Chelif Basin (Algeria). Paleogeogr. Paleoclimatol. Paleoecol. 254 (3–4), 386–417. https://doi.org/10.1016/j.paleo.2007.06.015.
Roveri, M., Manzi, V., Bassetti, M.A., Merini, M., Ricci Lucchi, F., 1998. Stratigraphy of the Messinian post-evaporitic stage in eastern-Romagna (northern Apennines, Italy). G. Geol. 60, 119–142.
Roveri, M., Bassetti, M.A., Ricci Lucchi, F., 2001. The Mediterranean Messinian salinity crisis: an Apennines foredeep perspective. Sediment. Geol. 140, 201–214.
Roveri, M., Boscolo Gallo, A., Rossi, M., Gennari, R., Iaccarino, S.M., Lugli, S., Manzi, V., Negri, A., Rizzini, F., Taviani, M., 2005. The Adriatic foreland record of Messinian events (central Adriatic sea, Italy). GeoActa 4 (139), 158.
Roveri, M., Bertini, A., Cosentino, D., Di Stefano, A., Gennari, R., Gliozzi, E., Grossi, F., Iaccarino, S.M., Lugli, S., Manzi, V., Taviani, M., 2008a. A high-resolution stratigraphic framework for the latest Messinian events in the Mediterranean area. Stratigraphy 5 (3-4), 323–342.
Roveri, M., Lugli, S., Manzi, V., Schreiber, B.C., 2008b. The Messinian Sicilian stratigraphy revisited: new insights for the Messinian salinity crisis. Terra Nova 20 (6), 483–488. https://doi.org/10.1111/j.1365-3121.2008.00842.x.
Roveri, M., Bertini, A., Cipollari, P., Cosentino, D., Di Stefano, A., Florindo, F., Gennari, R., Gliozzi, E., Grossi, F., Iaccarino, S., Lugli, S., Manzi, V., 2008c. Comment on "Earliest Zanclean age for the Colombacci and uppermost Di Tetto formations of the "latest Messinian" northern Apennines: new palaeoenvironmental data from the Maccarone section (Marche Province, Italy)" by Popescu et al. (2007) Geobios 40 (359–373). Geobios 41, 669-675.
Roveri, M., Gennari, R., Lugli, S., Manzi, V., 2009. The Terminal Carbonate Complex: the record of sea-level changes during the Messinian salinity crisis. GeoActa 8 (63), 63–77.
Roveri, M., Flecker, R., Krijgsman, W., Lofi, J., Lugli, S., Manzi, V., Sierro, F.J., Bertini, A., Camerlenghi, A., De Lange, G., Govers, R., Hilgen, F.J., Hübscher, C., Meijer, P.Th., Stoica, M., 2014a. The Messinian salinity crisis: past and future of a great challenge for marine sciences. Mar. Geol. 349, 113–125. https://doi.org/10.1016/j.margeo.2014.02.002.
Roveri, M., Lugli, S., Manzi, V., Gennari, R., Schreiber, B.C., 2014b. High resolution strontium isotope stratigraphy of the Messinian deep Mediterranean basins: implications for marginal to central basins correlation. Mar. Geol. 349, 113–125. https://doi.org/10.1016/j.margeo.2014.01.002.
Roveri, M., Manzi, V., Bergamasco, A., Falcieri, F., Gennari, R., Lugli, S., 2014c. Dense shelf water cascading and Messinian canyons: a new scenario for the Mediterranean salinity crisis. Am. J. Sci. 314, 751–784. https://doi.org/10.2475/05.2014.03].
Roveri, M., Gennari, R., Persico, D., Rossi, F.P., Lugli, S., Manzi, V., Reghizzi, M., Taviani, M., 2019a. A new chronostratigraphic and paleoenvironmental framework

for the end of the Messinian salinity crisis in the Sorbas Basin (Betic Cordillera, southern Spain). Geol. J. 54 (3), 1617–1637. https://doi.org/10.1002/gj.3256.
Roveri, M., Gennari, R., Ligi, M., Lugli, S., Manzi, V., Reghizzi, M., 2019b. The synthetic seismic expression of the Messinian salinity crisis from onshore records: implications for shallow-to deep-water correlations. Basin Res. 31 (6), 1121–1152. https://doi.org/10.1111/bre.12361.
Roveri, M., Lugli, S., Manzi, V., Reghizzi, M., Rossi, F.P., 2020. Stratigraphic relationships between shallow-water carbonates and primary gypsum: insights from the Messinian succession of the Sorbas Basin (Betic Cordillera, Southern Spain). Sediment. Geol. 105678 https://doi.org/10.1016/j.sedgeo.2020.105678.
Ruggieri, G., 1962. La serie marine pliocenica e quaternaria della Val Marecchia: Atti Accad. Sci. Lett. Arti Palermo 19, 1–169.
Ruggieri, G., 1967. The Miocene and later evolution of the Mediterranean sea. Adams and Ager (Eds.). In: Aspects of Tethyan Biogeography: Syst. Ass. Publ. 7, p. 238.
Ryan, W.B.F., 1973. Geodynamic implications of the Messinian crisis of salinity. In: Drooger, C.W. (Ed.), Messinian Events in the Mediterranean. North-Holland Publ. Co., Amsterdam, Netherlands, pp. 26–38.
Ryan, W.B.F., 1976. Quantitative evaluation of the depth of the western Mediterranean before, during and after the late Miocene salinity crisis. Sedimentology 23, 791–813.
Ryan, W.B.F., 1978. Messinian badlands on the southeastern margin of the Mediterranean Sea. Mar. Geol. 27, 349–363.
Ryan, W.B.F., 2008. Modeling the magnitude and timing of evaporative drawdown during the Messinian salinity crisis. Stratigraphy 5, 227–243.
Ryan, W.B.F., 2009. Decoding the Mediterranean salinity crisis. Sedimentology 56 (1), 95–136.
Ryan, W.B.F., Hsü, K.J., Cita, M.B., Dumitrica, P., Lort, P., Maync, W., Nesteroff, W.D., Pautot, P., Stradner, H., Wezel, F.C., 1973. In: Ryan, W.B.F., Hsü, K.J. (Eds.), Initial Reports of the Deep Sea Drilling Project, Vol. 13. U.S. Government Printing Office, Washington, DC, p. 1447.
Sabat, F., Gelabert, B., Rodriguez-Perea, A., Giménez, J., 2011. Geological structure and evolution of Majorca: implications for the origin of the Western Mediterranean. Tectonophysics 510, 217–238.
Sabato Ceraldi, T., Kamel, M., Mason, T., Poole, A., Hossack, J., Slack, J., Fraser, A., 2010. Messinian seismic facies in offshore Sirt Basin Libya and implications for sub-Messinian seismic imaging. In: Paper presented at TOG 2008-Technology of Oil and Gas, Forum and Exhibition, 21-23 October, Tripoli.
Sachse, D., Radke, J., Gleixner, G., 2006. δD values of individual n-alkanes from terrestrial plants along a climatic gradient - implications for the sedimentary biomarker record. Org. Geochem. 37, 469–483.
Sage, F., Von Gronefeld, G., Déverchère, J., Gaullier, V., Maillard, A., Gorini, C., 2005. A record of the Messinian salinity crisis on the western Sardinia margin, northwestern Mediterranean. Mar. Pet. Geol. 22, 757–773.
Sampalmieri, G., Iadanza, A., Cipollari, P., Cosentino, D., Lo Mastro, S., 2010. Paleoenvironments of the Mediterranean Basin at the Messinian hypersaline/hyposaline transition: evidence from natural radioactivity and microfacies of post-evaporitic successions of the Adriatic sub-basin. Terra Nova 22 (4), 239–250. https://doi.org/10.1111/j.1365-3121.2010.00939.x.
Sant, K., Palcu, V., Mandic, D., Krijgsman, O., 2017. Changing seas in the Early-Middle Miocene of Central Europe: a Mediterranean approach to Paratethyan stratigraphy. Terra Nova 29 (5), 273–281.
Schildgen, T.F., Cosentino, D., Frijia, G., Castorina, F., Dudas, F.Ö., Iadanza, A., Sampalmieri, G., Cipollari, P., Caruso, A., Bowring, S.A., Strecker, M.R., 2014. Sea level and climate forcing of the Sr isotope composition of Late Miocene Mediterranean marine basins. Geochem. Geophys. Geosyst. 15, 2964–2983. https://doi.org/10.1002/2014GC005332.
Schmalz, R.F., 1969. Deep-water evaporite deposition, a genetic model. Am. Assoc. Pet. Geol. Bull. 53, 798–823.
Schreiber, B.C., 1997. Field trip to Eraclea Minoa: Upper Messinian. "Neogene Mediterranean Paleoceanography", Excursion Guide Book Palermo-Caltanissetta-Agrigento-Erice (Sicily), 24-27 September 1997, pp. 72–80.
Schütz, K.I., 1994. Structure and stratigraphy of the Gulf of Suez, Egypt, in Interior Rift Basins, edited by S. M. Landon. AAPG Mem. 59, 57–96.
Schwarzhans, W., Agiadi, K., Carnevale, G., 2020. Late Miocene-Early Pliocene evolution of Mediterranean gobies and their environmental and biogeographic significance. Riv. Ital. Paleontol. Stratigr. 126 (3).
Sciuto, F., Baldanza, A., 2020. Full restoration of marine conditions after the late Messinian Mediterranean Lago-Mare phase in Licodia Eubea and Villafranca Tirrena areas (east Sicily). Carnets de géologie.
Sciuto, F., Baldanza, A., Temani, R., Privitera, G., 2018. New reports of Paratethyan ostracods affinity from the Mediterranean Basin (Sicily, Italy). Paleontologia Electronica 21 (1), 1. https://doi.org/10.26879/800.
Segev, A., Avni, Y., Shahar, J., Wald, R., 2017. Late Oligocene and Miocene different seaways to the Red Sea-Gulf of Suez rift and the Gulf of Aqaba-Dead Sea basins. Earth Sci. Rev. 171, 196–219. https://doi.org/10.1016/j.earscirev.2017.05.004.
Selli, R., 1954. Il Bacino del Metauro. Giorn. Geol. 24, 1–294.
Selli, R., 1960. Il Messiniano Mayer-Eymar 1867. Proposta di un neostratotipo. Giornale di Geologia 28, 1–33.
Selli, R., 1973. An outline of the Italian Messinian. In: Drooger, C.W. (Ed.), Messinian Events in the Mediterranean, pp. 150–171. Amsterdam (Kon. Nedl. Akad. Wetensch.).
Sgarrella, F., Sprovieri, R., Di Stefano, E., Caruso, A., 1997. Paleoceanographic conditions at the base of the Pliocene in the Southern Mediterranean Basin. Riv. Ital. Paleontol. Stratigr. 103, 207–220.
Sgarrella, F., Sprovieri, R., Di Stefano, E., Caruso, A., Sprovieri, M., Bonaduce, G., 1999. The Capo Rossello Bore-Hole (Agrigento, Sicily): cyclostratigraphic and paleoceanographic reconstructions from quantitative analyses of the Zanclean foraminiferal assemblages. Riv. Ital. Paleontol. Stratigr. 105, 303–322.
Sierro, F.J., Flores, J.A., Civis, J., Gonza, J.A., France, G., 1993. Late Miocene globorotaliid event-stratigraphy and biogeography in the NE-Atlantic and Mediterranean. Mar. Micropaleontol. 21 (1-3), 143–167.
Sim, M.S., Bosak, T., Ono, S., 2011. Large sulfur isotope fractionation does not require disproportionation. Science 333, 74–77.
Simon, D., Meijer, P.T., 2017. Salinity stratification of the Mediterranean Sea during the Messinian crisis: A first model analysis. Earth Planet. Sci. Lett. 479, 366–376.
Simon, D., Marzocchi, A., Flecker, R., Lunt, D.J., Hilgen, F.J., Meijer, P.T., 2017. Quantifying the Mediterranean freshwater budget throughout the late Miocene: New implications for sapropel formation and the Messinian Salinity Crisis. Earth Planet. Sci. Lett. 472, 25–37.
Sinninghe Damsté, J.S., Frewin, N.L., Kenig, F., De Leeuw, J.W., 1995. Molecular indicators for palaeoenvironmental changes in a Messinian evaporitic sequence (Vena del Gesso, Italy). I: Variations in extractable organic matter of ten cyclically deposited marl beds. Org. Geochem. 23, 471–483.
Sissingh, W., 1976. Aspects of late Cenozoic evolution of the South Aegean ostracode fauna. Paleogeogr., Paleoclimatol., Paleoecol 20, 131–146.
Snel, E., Mărunțeanu, M., Meulenkamp, J.E., 2006. Calcareous nannofossil biostratigraphy and magnetostratigraphy of the upper Miocene and lower Pliocene of the Northern Aegean (Orphanic Gulf-Strimon Basin areas), Greece. Paleogeogr. Paleoclimatol. Paleoecol. 238 (1-4), 125–150. https://doi.org/10.1016/j.paleo.2006.03.022.
Soria, J.M., Caracuel, J.E., Yébenes, A., Fernández, J., Viseras, C., 2005. The stratigraphic record of the Messinian salinity crisis in the northern margin of the Bajo Segura basin (SE Spain). Sediment. Geol. 179 (3), 225–247. https://doi.org/10.1016/j.sedgeo.2005.05.011.
Soria, J.M., Caracuel, J.E., Corbí, H., Dinarès-Turell, J., Lancis, C., Tent-Manclús, J.E., Yébenes, A., 2007. Estratigrafía y biomagnetoestratigrafía del Messiniense en la sección del Garruchal (Cuenca del Bajo Segura). Implicaciones para la Crisis de Salinidad del Mediterráneo. Geogaceta 41, 215–218.
Soria, J.M., Caracuel, J.E., Corbí, H., Dinarès-Turell, J., Lancis, C., Tent-Manclús, J.E., Yébenes, A., 2008a. The Bajo Segura basin (SE Spain): implications for the Messinian Salinity Crisis in the Mediterranean margins. Stratigraphy 5, 259–265.
Soria, J.M., Caracuel, J.E., Corbí, H., Dinarès-Turell, J., Lancis, C., Tent-Manclús, J.E., Viseras, C., Yébenes, A., 2008b. The Messinian-Early Pliocene stratigraphic record in the southern Bajo Segura basin (Betic Cordillera, Spain). Implications for the Mediterranean salinity crisis. Sediment. Geol. 203, 267–288.
Spatola, D., del Moral-Erencia, J.D., Micallef, A., Camerlenghi, A., Garcia-Castellanos, D., Gupta, S., Bohorquez, P., Gutscher, M.A., Bertoni, C., 2020. A single-stage megaflood at the termination of the Messinian salinity crisis: geophysical and modelling evidence from the eastern Mediterranean Basin. Mar. Geol. 106337 https://doi.org/10.1016/j.margeo.2020.106337.
Stampfli, J., Höcker, C.F.W., 1989. Messinian paleorelief from a 3D seismic survey in the Tarrasco concession area (Spanish Mediterranean Sea). Geologie in Minjbouw 68, 201–210.
Stoica, M., Lazăr, I., Krijgsman, W., Vasiliev, I., Jipa, D., Floroiu, A., 2013. Paleoenvironmental evolution of the East Carpathian foredeep during the late Miocene-early Pliocene (Dacian Basin; Romania). Glob. Planet. Chang. 103, 135–148. https://doi.org/10.1016/j.gloplacha.2012.04.004.
Stoica, M., Krijgsman, W., Fortuin, A., Gliozzi, E., 2016. Paratethyan ostracods in the Spanish Lago-Mare: More evidence for intra-basinal exchange at high Mediterranean sea level. Paleogeogr. Paleoclimatol. Paleoecol. 441, 854–870. https://doi.org/10.1016/j.paleo.2015.10.034.
Strasser, A., Hilgen, F.J., Heckel, P.H., 2006. Cyclostratigraphy-concepts, definitions, and alications. Newsl. Stratigr. 42 (2), 75–114.
Sturani, C., 1973. A fossil eel (Anguilla sp.) from the Messinian of Alba (Tertiary Piedmont Basin). Paleoenvironmental and paleogeographic implications. In: Messinian Events in the Mediterranean. K. Nederl. Akad. Wetensch, Amsterdam, pp. 243–255.
Suárez-González, P., Arenas, C., Benito, M.I., Pomar, L., 2019. Interplay between biotic and environmental conditions in presalt Messinian microbialites of the western Mediterranean (Upper Miocene, Mallorca, Spain). Palaeogeogr. Palaeoclimatol. Palaeoecol. 533, 109–242.
Suc, J.-P., Do Couto, D., Melinte-Dobrinescu, M.C., Macaleț, R., Quillévéré, F., Clauzon, G., Csato, I., Rubino, J.-L., Popescu, S.-M., 2011. The Messinian salinity crisis in the Dacic Basin (SW Romania) and early Zanclean Mediterranean-Paratethys high sea-level connection. Paleoecol. 310, 256–272. https://doi.org/10.1016/j.paleo.2011.07.018.
Suc, J.-P., Popescu, S.-M., Do Couto, D., Clauzon, G., Rubino, J.-L., Melinte-Dobrinescu, M.C., Quillévéré, F., Brun, J.-P., Dumurdžanov, N., Zagorchev, I., Lesić, V., Tomić, D., Sokoutis, D., Meyer, B., Macalet, R., Rifelj, H., 2015. Marine gateway vs. fluvial stream within the Balkans from 6 to 5 Ma. Mar. Pet. Geol. 66 (1), 231–245. https://doi.org/10.1016/j.marpetgeo.2015.01.013.
Thinon, I., Guennoc, P., Serrano, O., Maillard, A., Lasseur, E., Réhault, J.P., 2016. Seismic markers of the Messinian Salinity Crisis in an intermediate-depth basin: data for understanding the Neogene evolution of the Corsica Basin (Northern Tyrrhenian Sea). Mar. Pet. Geol. 77, 1274–1296. November 2016. https://doi.org/10.1016/j.marpetgeo.2016.02.017.
Thode, H.G., Monster, J., 1965. Sulfur-Isotope Geochemistry of Petroleum, Evaporites, and Ancient Seas1. In: Young, A., Galley, J.E. (Eds.), Fluids in Subsurface Environments. American Association of Petroleum Geologists, p. 0.
Topper, R.P.M., Meijer, P.T., 2015. The precessional phase lag of Messinian gypsum deposition in Mediterranean marginal basins. Palaeogeogr. Palaeoclimatol. Palaeoecol. 417, 6–16.

Topper, R.P.M., Flecker, R., Meijer, P.T., Wortel, M.J.R., 2011. A box model of the Late Miocene Mediterranean Sea: implications from combined 87Sr/86Sr and salinity data. Paleoceanography 26. https://doi.org/10.1029/2010PA002063. PA3223.

Topper, R.P.M., Lugli, S., Manzi, V., Roveri, M., Meijer, P.T., 2014. Precessional control of Sr ratios in marginal basins during the Messinian salinity crisis? Geochem. Geophys. Geosyst. 15-5, 1926–1944. https://doi.org/10.1002/2013GC005192.

Trenkwalder, S., Violanti, D., D'Atri, A., Lozar, F., Dela Pierre, F., Irace, A., 2008. The Miocene/Pliocene boundary in the Early Pliocene micropaleontological record: new data from the Tertiary Piedmont Basin (Moncucco quarry, Torino Hill, northwestern Italy). Boll. Soc. Paleontol. Ital. 47, 87–103.

Turchyn, A.V., Schrag, D.P., 2004. Oxygen Isotope Constraints on the Sulfur Cycle over the Past 10 Million Years. Science 303, 2004.

Turchyn, A.V., Sivan, O., Schrag, D.P., 2006. Oxygen isotopic composition of sulfate in deep sea pore fluid: evidence for rapid sulfur cycling. Geobiology 4, 191–201.

Turchyn, A.V., Schrag, D.P., Coccioni, R., Montanari, A., 2009. Stable isotope analysis of the Cretaceous sulfur cycle. Earth Planet. Sci. Lett. 285, 115–123.

Tzanova, A., Herbert, T.D., Peterson, L., 2015. Cooling Mediterranean Sea surface temperatures during the Late Miocene provide a climate context for evolutionary transitions in Africa and Eurasia. Earth Planet. Sci. Lett. 419, 71–80. https://doi.org/10.1016/j.epsl.2015.03.016.

Urgeles, R., Camerlenghi, A., Garcia-Castellanos, D., De Mol, B., Garces, M., Verges, J., Haslam, I., Hardman, M., 2011. New constraints on the Messinian sealevel drawdown from 3D seismic data of the Ebro margin, western Mediterranean. Basin Res. 23, 123–145. https://doi.org/10.1111/j.1365-2117.2010.00477.x.

Utrilla, R., Pierre, C., Orti, F., Pueyo, J.J., 1992. Oxygen and sulphur isotope compositions as indicators of the origin of Mesozoic and Cenozoic evaporites from Spain. Chem. Geol. 102, 229–244.

Vai, G.B., 1997. Chapter E3 Cyclostratigraphic estimate of the messinian stage duration. In: Montanari, A., Odin, G.S., Coccioni, R. (Eds.), Miocene Stratigraphy: An Integrated Approach. Dev. Paleontol. Stratigr. 15, 463–476.

Vai, G.B., 2016. Over half a century of Messinian salinity crisis. Bol. Geol. Min. 127 (2), 625–641.

Van Baak, C.G.C., Radionova, E.P., Golovina, L.A., Raffi, I., Kuiper, K.F., Vasiliev, I., Krijgsman, W., 2015. Messinian events in the Black Sea. Terra Nova 27, 433–441. https://doi.org/10.1111/ter.12177.

Van Baak, C.G., Stoica, M., Grothe, A., Aliyeva, E., Krijgsman, W., 2016. Mediterranean-Paratethys connectivity during the Messinian salinity crisis: The Pontian of Azerbaijan. Glob. Planet. Chang. 141, 63–81. https://doi.org/10.1016/j.gloplacha.2016.04.005.

Van Baak, C.G., Krijgsman, W., Magyar, I., Sztanó, O., Golovina, L.A., Grothe, A., Hoyle, T.M., Mandic, O., Patina, I.S., Popov, S.V., Radionova, E.P., Stoica, M., Vasiliev, I., 2017. Paratethys response to the Messinian salinity crisis. Earth Sci. Rev. 172, 193–223. https://doi.org/10.1016/j.earscirev.2017.07.015.

Van Couvering, J.A., Berggren, W.A., Drake, R.E., Aguirre, E., Curtis, G.H., 1976. The terminal Miocene event. Mar. Micropaleontol. 1, 263–286.

Van Couvering, J.A., Castradori, D., Cita, M.B., Hilgen, F.J., Rio, D., 2000. The base of the Zanclean Stage and of the Pliocene Series. Episodes 23, 179–187.

Van den Berg, B.C.J., Sierro, F.J., Hilgen, F.J., Flecker, R., Larrasoaña, J.C., Krijgsman, W., Flores, J.A., Mata, M.P., Martín, E.B., Civis, J., González-Delgado, J. A., 2015. Astronomical tuning for the upper Messinian Spanish Atlantic margin: disentangling basin evolution, climate cyclicity and MOW. Glob. Planet. Chang. 135, 89–103.

Van der Meer, M.T.J., Baas, M., Rijpstra, I.C., Marino, G., Rohling, E.J., Sinninghe Damsté, J.S., Schouten, S., 2007. Hydrogen isotopic compositions of long-chain alkenones record freshwater flooding of the Eastern Mediterranean at the onset of sapropel deposition. Earth Planet. Sci. Lett. 262, 594–600.

Van Hinsbergen, D.J., Meulenkamp, J.E., 2006. Neogene supradetachment basin development on Crete (Greece) during exhumation of the South Aegean core complex. Basin Res. 18 (1), 103–124.

Vasiliev, I., Reichart, G.-J., Davies, G.R., Krijgsman, W., Stoica, M., 2010. Strontium isotope ratios of the Eastern Paratethys during the Miocene/Pliocene transition; Implications for interbasinal connectivity. Earth Planet. Sci. Lett. 292, 123–131. https://doi.org/10.1016/j.epsl.2010.01.027.

Vasiliev, I., Reichart, G.J., Krijgsman, W., 2013. Impact of the Messinian Salinity Crisis on Black Sea hydrology - insights from hydrogen isotopes on molecular biomarkers. Earth Planet. Sci. Lett. 362, 272–282. https://doi.org/10.1016/j.epsl.2012.11.038.

Vasiliev, I., Reichart, G.-J., Grothe, A., Sinninghe Damsté, J.S., Krijgsman, W., Sangiorgi, F., Weijers, J.W.H., van Roij, L., 2015. Recurrent phases of drought in the upper Miocene of the Black Sea region. Paleogeogr. Paleoclimatol. Paleoecol. 423, 18–31.

Vasiliev, I., Mezger, E.M., Lugli, S., Reichart, G.J., Manzi, V., Roveri, M., 2017. How dry was the Mediterranean during the Messinian salinity crisis? Paleogeogr. Paleoclimatol. Paleoecol. 471, 120–133. https://doi.org/10.1016/j.paleo.2017.01.032.

Vasiliev, I., Karakitsios, V., Bouloubassi, I., Agiadi, K., Kontakiotis, G., Antonarakou, A., Triantaphyllou, M., Gogou, A., Kafousia, N., de Rafélis, M., Zarkogiannis, S., Kaczmar, F., Parinos, C., Pasadakis, N., 2019. Large sea surface temperature, salinity, and productivity preservation changes preceding the onset of the Messinian Salinity Crisis in the eastern Mediterranean Sea. Paleoceanogr. Paleoclimatol. 34, 182–202. https://doi.org/10.1029/2018PA003438.

Veizer, J., 1989. Strontium isotopes in seawater through time. Annu. Rev. Earth Planet. Sci. 17 (1), 141–167.

Violanti, D., Trenkwalder, S., Lozar, F., Gallo, L.M., 2009. Micropaleontological analyses of the Narzole core: biostratigraphy and paleoenvironment of the late Messinian and early Zanclean of Piedmont (Northwestern Italy). Boll. Soc. Paleontol. Ital. 48, 167–181.

Warren, J.K., 2016. Evaporites: A geological compendium. Springer.

Winterberg, S., Picotti, V., Willett, S.D., 2020. Messinian or Pleistocene valley incision within the Southern Alps. Swiss J. Geosci. 113 (1), 1–14. https://doi.org/10.1186/s00015-020-00361-7.

Wortmann, U.G., Chernyavsky, B., Bernasconi, S.M., Brunner, B., Böttcher, M.E., Swart, P.K., 2007. Oxygen isotope biogeochemistry of pore water sulfate in the deep biosphere: Dominance of isotope exchange reactions with ambient water during microbial sulfate reduction (ODP Site 1130). Geochim. Cosmochim. Acta 71, 4221–4232.

Zachariasse, W.J., van Hinsbergen, D.J.J., Fortuin, A.R., 2008. Mass wasting and uplift on Crete and Karpathos (Greece) during the Early Pliocene related to beginning of South Aegean left-lateral, strike slip tectonics. Geol. Soc. Am.Bull. 120, 976–993.

Zachariasse, W.J., van Hinsbergen, D.J., Fortuin, A.R., 2011. Formation and fragmentation of a late Miocene supradetachment basin in central Crete: implications for exhumation mechanisms of high-pressure rocks in the Aegean forearc. Basin Res. 23 (6), 678–701. https://doi.org/10.1111/j.1365-2117.2011.00507.x.

Ziveri, P., Baumann, K.H., Bockel, B., Bollmann, J., Young, J., 2004. Present day coccolithophore-biogeography in the Atlantic Ocean. In: Coccolithophores: From Molecular Processes to Global Impact. Springer Verlag, pp. 403–428.

Zonneveld, K.A., Marret, F., Versteegh, G.J., Bogus, K., Bonnet, S., Bouimetarhan, I., Crouch, I.E., Esper, O., 2013. Atlas of modern dinoflagellate cyst distribution based on 2405 data points. Rev. Paleobot. Palynol. 191, 1–197.